

University of Strathclyde

Department of Naval Architecture, Ocean and Marine Engineering

**A NOVEL METHODOLOGY FOR ROBUST, HOLISTIC,
SIMULATION-BASED SHIP DESIGN OPTIMIZATION**

By

Lampros Nikolopoulos

A thesis presented in fulfilment of the requirements for the degree of Doctor of
Philosophy

December 2022

Contents

List of Figures	5
List of Tables	12
Abstract.....	15
Acknowledgements	16
Chapter 1: Introduction.....	17
1.1. Contemporary Challenges for Commercial Shipping	17
1.2. Traditional Approaches in the Ship Design Process.....	21
1.3. Research Aim.....	21
1.4. Objectives	22
1.5. Thesis Structure.....	22
1.6. Summary	23
Chapter 2 - Literature Survey.....	24
2.1. Ship Design Methodologies Overview	24
2.2. Multi-Objective Ship Design Optimization.....	25
2.3. Set-Based Ship Design and Application of Networks Engineering.....	26
2.4. Ship Design Optimization Under Uncertainty	28
2.5. Holistic Ship Design and Optimization.....	33
2.6. Application of Simulation Methods in Ship Design	37
2.7. Application of Surrogate Models in Ship Design.....	40
2.8. Application of Big Data in Ship Design.....	43
2.9. Research Gaps.....	46
2.10. Contribution to the Area of Research.....	47
Chapter 3 : A Robust Holistic Optimization Ship Design Approach (RHODA)	49
Chapter 4: Existing Methods Utilized in RHODA	53
4.1. Geometrical Core and Variation	53
4.2. Cargo Hold Arrangement Modelling.....	58
4.3. Added Resistance in Seaways	59
4.4. Propulsion	89
4.5. Electrical Load Analysis and Diesel Generators Sizing.....	94
4.6. Steam Balance and Composite Boiler Load.....	95

4.7.	Lightship Weight Estimation.....	97
4.8.	Hydrostatics, Trim, Stability and Loadline	102
Chapter 5: Original Research and Developed Methodologies deployed in RHODA.....		104
5.1.	Calm Water Resistance Estimation.....	104
5.2.	Main Engine Dimensioning.....	141
5.3.	Lifecycle Voyages Simulation Environment	146
5.3.1.	Voyage Definition	146
5.3.2.	Use of Big Data for Voyage Simulation	146
5.3.3.	Input Data	149
5.3.4.	Environmental Parameters Modelling.....	150
5.3.5.	Simulation of the Vessel’s Operation	177
5.3.6.	Lifecycle Economic and Environmental Assessment.....	190
5.3.7.	Simulation Code Validation	207
Chapter 6: Bulk Carrier Optimization Case Studies		227
6.1.	Parent Vessel.....	228
6.2.	Trade Routes Definition and Voyage Planning for Simulation.....	231
6.2.1.	Brazil to China Roundtrip.....	231
6.2.2.	Australia to China Roundtrip.....	235
6.3.	Optimization Problem Definition	238
6.3.1.	Definition of the Optimization Problem and Workflow.	238
6.3.2.	Optimization Design Variables	240
6.3.3.	Optimization Design Constraints	242
6.3.4.	Optimization Targets (Design Merits)	244
6.3.5.	Optimization Studies Strategy	246
6.3.6.	Pareto Designs Ranking and Selection.....	249
6.4.	Stage 1: Multi-Objective Optimization (Deterministic)	251
6.4.1.	Optimization Problem Setup.....	251
6.4.2.	Sensitivity Analysis.....	252
6.4.3.	Optimization Results	297
6.4.4.	Design Selection, Ranking and Discussion.....	324
6.4.5.	Discussion Of Results	345

6.5.	Stage 2: Multi-Objective Optimization under Simulation.....	350
6.5.1.	Optimization Problem Setup.....	351
6.5.2.	Sensitivity Analysis.....	352
6.5.3.	Optimization Results.....	381
6.5.4.	Design Selection, Ranking and Discussion.....	391
6.5.5.	Discussion Of Results.....	410
6.6.	Stage 3: Multi-Objective Optimization of Zero Emission Vessel (ZEV) under Simulation and Uncertainty.....	416
6.6.1.	Optimization Problem Setup.....	416
6.6.2.	Sensitivity Analysis.....	426
6.6.3.	Optimization Results.....	437
6.6.4.	Design Selection, Ranking and Discussion.....	442
6.6.5.	Discussion of Results.....	450
Chapter 7: Discussion, Results and Conclusion		458
7.1.	General Remarks.....	458
7.2.	Ship Design Optimization Conclusions and Thesis Contribution.....	462
7.2.1.	What is the effect of Simulation-Based RHODA on the Optimization Process and Targets? 462	
7.2.2.	What is the macroscopic effect of the optimization result?.....	462
7.2.3.	What is the most effective use of IMO Efficiency Indices (EEDI, EEOI etc) in the optimization process?.....	462
7.2.4.	How robust are the Designs generated from the optimization process?.....	463
7.2.5.	Benefits from the use of actual operating data in the optimization process.....	463
7.2.6.	Use in the Design Optimization of Zero Emission Vessels.....	463
7.3.	Future Work and Reception by Industry Stakeholders.....	464
Appendix I – List of Publications.....		465
References		466

List of Figures

Figure 1: GHG Reduction requirements by IMO MEPC72 (DNVGL, 2019).....	18
Figure 2: Capesize Bulk Carrier Freight Rates (1990-2015) (Alizadeh, et al., 2016).....	19
Figure 3: VLCC Freight Rates (2019-2020) (Sand, 2019)	20
Figure 4: Workflow and structure of proposed methodology in the design environment.....	51
Figure 5: Aft Body Meta-Surface modelling in CAESES	56
Figure 6:Midship Parallel Body Meta-Surface modelling in CAESES.....	56
Figure 7:Forebody Meta-Surface modelling in CAESES	57
Figure 8: Hull and SAC after Lackenby Transformation	57
Figure 9: Hull and SAC after Lackenby Transformation	58
Figure 10: Non-Dimensional Added Resistance Comparison Liu vs. Panel Code Results // Laden Condition at 8 Knots Advance Speed	69
Figure 11: Non-Dimensional Added Resistance Comparison Liu vs. Panel Code Results // Laden Condition at 12 Knots Advance Speed	72
Figure 12: Non-Dimensional Added Resistance Comparison Liu vs. Panel Code Results // Laden Condition at 16 Knots Advance Speed	75
Figure 13: Non-Dimensional Added Resistance Comparison Liu vs. Panel Code Results // Ballast Condition at 8 Knots Advance Speed	78
Figure 14: Non-Dimensional Added Resistance Comparison Liu vs. Panel Code Results // Ballast Condition at 12 Knots Advance Speed	81
Figure 15: Non-Dimensional Added Resistance Comparison Liu vs. Panel Code Results // Ballast Condition at 16 Knots Advance Speed	84
Figure 16: Coordinate system and input used in Fujiwara empirical formula for the estimation of added resistance due to wind (Fujiwara, et al., 2005).....	87
Figure 17: Assumed Roughness Increase as a function of Dry-Docking and Special Survey Cycles	88
Figure 18: Flowchart of propeller calculation and propeller design selection.....	93
Figure 19: Distribution of the EHP difference (%) over different speeds – LADEN Condition	110
Figure 20: Distribution of the EHP difference (%) over different speeds – BALLAST Condition	112
Figure 21: Shaft Power prediction error (%) distribution over different speeds – LADEN Condition ...	113
Figure 22: Shaft Power prediction error (%) distribution over different speeds – BALLAST Condition	115
Figure 23: Generalized optimization problem workflow.....	115
Figure 24: Specific Optimization Problem and Design Engine Setup	125
Figure 25: Stages and tools employed for each one	125
Figure 26: Distribution of EHP difference over speeds – LADEN Condition.....	128
Figure 27: Distribution of EHP difference over different speeds – BALLAST Condition	130
Figure 28: Deviation of SHP over different speeds – LADEN Condition	134
Figure 29: Deviation of SHP over different speeds – BALLAST Condition	136
Figure 30: Engine Layout Envelope (MAN, 2020).....	142
Figure 31: Flowchart of Engine Selection Procedure.....	144
Figure 32: Process flow of the data acquisition system.....	147

Figure 33: Filtering process for creating data pool 148

Figure 34: Correlation between Anemometer Readings and Matched Weather Data – BALLAST 151

Figure 35: Correlation between Anemometer Readings and Matched Weather Data – LADEN 151

Figure 36: Histogram of the populated values for Wind Velocity – onboard data 153

Figure 37: Histogram of Gamma PDF simulated data for Wind Velocity -onboard data 153

Figure 38: Histogram of the populated values for Wind Direction – onboard data 154

Figure 39: Histogram of Normal PDF simulated data for Wind Direction – onboard data 154

Figure 40: Histogram of the populated values for Wind Velocity LADEN – matched satellite data 156

Figure 41: Histogram of Normal PDF simulated data for Wind Velocity LADEN – matched satellite data 156

Figure 42: Histogram of the populated values for Wind Direction LADEN– matched satellite data 157

Figure 43: Histogram of Exponential PDF simulated data for Wind Direction LADEN – matched satellite data 157

Figure 44: Histogram of the populated values for Wind Velocity BALLAST – matched satellite data ... 158

Figure 45: Histogram of Lognormal PDF simulated data for Wind Velocity BALLAST – matched satellite data 158

Figure 46: Histogram of the populated values for Wind Direction BALLAST – matched satellite data . 159

Figure 47: Histogram of Exponential PDF simulated data for Wind Direction BALLAST – matched satellite data 159

Figure 48: Histogram of the populated values for Current Velocity LADEN – Brazil Onboard data 161

Figure 49: Histogram of Exponential PDF simulated data for Current Velocity LADEN -Brazil onboard data 161

Figure 50: Histogram of the populated values for Current Velocity LADEN – Australia Onboard data 162

Figure 51: Histogram of Normal PDF simulated data for Current Velocity LADEN -Australia onboard data 162

Figure 52: Histogram of the populated values for Current Velocity BALLAST – Brazil Onboard data . 163

Figure 53: Histogram of Exponential PDF simulated data for Current Velocity BALLAST -Brazil onboard data 163

Figure 54: Histogram of the populated values for Current Velocity BALLAST – Australia Onboard data 164

Figure 55: Histogram of Exponential PDF simulated data for Current Velocity BALLAST -Australia onboard data 164

Figure 56: Histogram of the populated values for Current Direction – onboard data 165

Figure 57: Histogram of Uniform PDF simulated data for Current Direction – onboard data 165

Figure 58: Histogram of the populated values for Current Velocity LADEN – matched satellite data ... 167

Figure 59: Histogram of Exponential PDF simulated data for Current Velocity LADEN – matched satellite data 167

Figure 60: Histogram of populated values for Current Direction LADEN – matched satellite data 168

Figure 61: Histogram of Normal PDF simulated data for Current Direction LADEN – matched satellite data 168

Figure 62: Histogram of the populated values for Current Velocity BALLAST – matched satellite data 169

Figure 63: Histogram of Lognormal PDF simulated data for Current Velocity BALLAST – matched satellite data 169

Figure 64: Histogram of the populated values for Current Direction BALLAST – matched satellite data 170

Figure 65: Histogram of Normal PDF simulated data for Current Direction BALLAST – matched satellite data 170

Figure 66: Correlation of Anemometer Wind Velocity vs. Crew Observed Wave Height 171

Figure 67: Scatter Diagram of Worldwide Sea Regions (DNV, October 2010)..... 173

Figure 68: Process flow of integrated code for simulating vessel’s responses and operation profile 177

Figure 69: Histogram of the populated values for Operating Speed LADEN - Australia 179

Figure 70: Histogram of Normal PDF simulated data for Operating Speed LADEN - Australia 180

Figure 71: Histogram of the populated values for Operating Speed BALLAST - Australia..... 181

Figure 72: Histogram of Normal PDF simulated data for Operating Speed BALLAST - Australia..... 181

Figure 73: Histogram of the populated values for Operating Speed LADEN – Brazil 182

Figure 74: Histogram of Normal PDF simulated data for Operating Speed LADEN - Brazil 182

Figure 75: Histogram of the populated values for Operating Speed BALLAST – Brazil..... 183

Figure 76: Histogram of Normal PDF simulated data for Operating Speed BALLAST - Brazil 183

Figure 77: Wind Velocities and Directions used as input in Simulation Module 185

Figure 78: Engine Envelope of the 6G70ME-C engine (MAN, 2020). 188

Figure 79: Histogram of the populated values for Capesize Earnings from 1990 to 2015. 192

Figure 80: Histogram of lognormal PDF simulated data for TCE Earnings 193

Figure 81: Histogram of the populated values for IFO180 prices from 1990 to 2015..... 197

Figure 82: Histogram of the populated values for IFO380 prices from 1990 to 2015..... 197

Figure 83: Histogram of the populated values for MGO prices from 1990 to 2015..... 198

Figure 84: Histogram of lognormal PDF simulated data for IFO180..... 200

Figure 85: Histogram of lognormal PDF simulated data for IFO380..... 201

Figure 86: Histogram of lognormal PDF simulated data for MGO..... 201

Figure 87: Market scenarios simulated for the vessel’s lifecycle..... 202

Figure 88: Monetary Flows over time modelled for RFR calculation..... 203

Figure 89: EEDI Phased Reduction (International Maritime Organization (IMO), 2016) 204

Figure 90: Timeline of Predicted vs. Actual Delivered Power (P_b in kW) – LADEN / VOYAGE 1 210

Figure 91: Timeline of Deviation of Estimated Shaft Power (%) – LADEN / VOYAGE 1..... 211

Figure 92: Timeline of Predicted vs. Actual Speed Over Ground (SOD in knots) – LADEN / VOYAGE 1 211

Figure 93: Timeline of SOG Estimation Deviation (%) – LADEN / VOYAGE 1 212

Figure 94: Timeline of Estimated vs. Actual Speed Through Water (STW in knots) – LADEN / VOYAGE 1..... 212

Figure 95: Timeline of STW Deviation (%) – LADEN / VOYAGE 1..... 213

Figure 96: Timeline of Predicted vs. Actual Delivered Power (P_b in kW) – LADEN / VOYAGE 2 214

Figure 97: Timeline of Delivered Power Deviation (%) – LADEN / VOYAGE 2.....	215
Figure 98: Frequency Distribution (Histogram) of Shaft Power Deviation – LADEN / VOYAGE 2	215
Figure 99: Timeline of Estimated vs. Actual Speed Over Ground (SOG in knots) – LADEN / VOYAGE 2	215
Figure 100: Timeline of Speed Over ground (SoG) Deviation (%) – LADEN / VOYAGE 2.....	216
Figure 101: Timeline of Estimated vs. Actual Speed Through Water (STW in knots) – LADEN / VOYAGE 2	216
Figure 102: Timeline of Predicted vs. Actual Delivered Power (Pb in kW) – BALLAST / VOYAGE 1.	217
Figure 103: Timeline of Delivered Power Deviation (%) – BALLAST/ VOYAGE 1	218
Figure 104: Timeline of Estimated vs. Actual Speed Over Ground (SoG in knots) – BALLAT / VOYAGE 1	218
Figure 105: Timeline of Speed Over ground (SoG) Deviation (%) – BALLAST / VOYAGE 1	218
Figure 106: Timeline of Predicted vs. Actual Delivered Power (Pb in kW) – BALLAST / VOYAGE 2.	220
Figure 107: Timeline of Delivered Power Deviation (%) – BALLAST/ VOYAGE 2	220
Figure 108: Timeline of Estimated vs. Actual Speed Over Ground (SoG in knots) – BALLAT / VOYAGE 2	221
Figure 109: Timeline of Speed Over ground (SoG) Deviation (%) – BALLAST / VOYAGE 2	221
Figure 110: Timeline of Predicted vs. Actual Delivered Power (Pb in kW) – BALLAST / VOYAGE 3.	222
Figure 111: Timeline of Delivered Power Deviation (%) – BALLAST/ VOYAGE 3	223
Figure 112: Timeline of Estimated vs. Actual Speed Over Ground (SoG in knots) – BALLAT / VOYAGE 3	223
Figure 113: Timeline of Speed Over ground (SoG) Deviation (%) – BALLAST / VOYAGE 2	224
Figure 114: Parametric Cargo Hold Surfaces in CAESES®.....	229
Figure 115: Parametric Cargo Hold Surfaces in CAESES®.....	230
Figure 116: Parametric Cargo Hold Surfaces in CAESES®.....	230
Figure 117: Tubarao to Qingdao Sea Passage (11,358 nautical miles)	231
Figure 118: Ponta De Madeira to Qingdao Sea Passage (12,261 nautical miles).....	231
Figure 119: Leg A – South Atlantic Passage route	232
Figure 120: Leg B – Indian Ocean Passage	233
Figure 121: Leg C – Passage through Malacca and Singapore Straights.....	233
Figure 122: Leg D – Passage from Singapore Straights Eastern Exit to Qingdao.....	234
Figure 123: Newcastle (AU) to Qingdao Sea Passage (4,797 nm).....	235
Figure 124: Port Hedland, Port Walcott to Qingdao Sea Passage (3,696 nm)	235
Figure 125: Leg A - Port Headland to Philippines Sea Passage	236
Figure 126: Leg B - Philippines to Qingdao Sea Passage	236
Figure 127: Leg C - Qingdao to Singapore for bunkering (BALLAST LEG ONLY)	237
Figure 128: Leg A - Singapore IPL to Port Hedland (BALLAST LEG ONLY)	237
Figure 129: The optimization Loop applied.	239
Figure 130: Optimization Pathways examined.	246
Figure 131: Assumed Logarithmic distribution for Utility Functions.....	251

Figure 132: <i>Det_NMAX_01 / EEDI vs. RFR Design Scatter Diagram with Baseline Vessel and Dominant Variants superimposed.</i>	297
Figure 133: <i>Det_NMAX_01 / Required Ballast Water vs. RFR Design Scatter Diagram with Baseline Vessel and Dominant Variants superimposed.</i>	298
Figure 134: <i>Det_NMAX_01 / Required Ballast Water vs. EEDI Design Scatter Diagram with Baseline Vessel and Dominant Variants superimposed.</i>	299
Figure 135: <i>Det_NMAX_01 / RFR Australian Trade vs. RFR Brazilian Trade Design Scatter Diagram</i>	300
Figure 136: <i>Det_NMAX_02 / EEDI vs. RFR Design Scatter Diagram with Baseline Vessel and Dominant Variants superimposed.</i>	301
Figure 137: <i>Det_NMAX_02 / Required Ballast Water vs. RFR Design Scatter Diagram with Baseline Vessel and Dominant Variants superimposed.</i>	302
Figure 138: <i>Det_NMAX_02 / Required Ballast Water vs. EEDI Design Scatter Diagram with Baseline Vessel and Dominant Variants superimposed.</i>	303
Figure 139: <i>Det_NMAX_03 / EEDI vs. RFR Design Scatter Diagram with Baseline Vessel and Dominant Variants superimposed.</i>	304
Figure 140: <i>Det_NMAX_03 / Required Ballast Water vs. RFR Design Scatter Diagram with Baseline Vessel and Dominant Variants superimposed.</i>	305
Figure 141: <i>Det_NMAX_03 / Required Ballast Water vs. EEDI Design Scatter Diagram with Baseline Vessel and Dominant Variants superimposed.</i>	306
Figure 142: <i>Det_WOZMAX_01 / EEDI vs. RFR Design Scatter Diagram with Baseline Vessel and Dominant Variants superimposed.</i>	308
Figure 143: <i>Det_WOZMAX_01 / Required Ballast Water vs. RFR Design Scatter Diagram with Baseline Vessel and Dominant Variants superimposed.</i>	309
Figure 144: <i>Det_WOZMAX_01 / Required Ballast Water vs. EEDI Design Scatter Diagram with Baseline Vessel and Dominant Variants superimposed.</i>	310
Figure 145: <i>Det_WOZMAX_02 / EEDI vs. RFR Design Scatter Diagram with Baseline Vessel and Dominant Variants superimposed.</i>	312
Figure 146: <i>Det_WOZMAX_02 / Required Ballast Water vs. RFR Design Scatter Diagram with Baseline Vessel and Dominant Variants superimposed.</i>	313
Figure 147: <i>Det_WOZMAX_02 / Required Ballast Water vs. EEDI Design Scatter Diagram with Baseline Vessel and Dominant Variants superimposed.</i>	314
Figure 148: <i>Det_WOZMAX_03 / EEDI vs. RFR Design Scatter Diagram with Baseline Vessel and Dominant Variants superimposed.</i>	316
Figure 149: <i>Det_WOZMAX_03 / Required Ballast Water vs. RFR Design Scatter Diagram with Baseline Vessel and Dominant Variants superimposed.</i>	317
Figure 150: <i>Det_WOZMAX_03 / Required Ballast Water vs. EEDI Design Scatter Diagram with Baseline Vessel and Dominant Variants superimposed.</i>	318
Figure 151: <i>Det_WOZMAX_04 / EEDI vs. RFR Design Scatter Diagram with Baseline Vessel and Dominant Variants superimposed.</i>	320

Figure 152: <i>Det_WOZMAX_04*/ Required Ballast Water vs. RFR Design Scatter Diagram with Baseline Vessel and Dominant Variants superimposed.</i>	321
Figure 153: <i>Det_WOZMAX_04* / Required Ballast Water vs. EEDI Design Scatter Diagram with Baseline Vessel and Dominant Variants superimposed.</i>	322
Figure 154: <i>Sensitivity Analysis and Scatter between Nominal and Simulated Required Freight Rate – NMAX Case Study.</i>	376
Figure 155: <i>Sensitivity Analysis and Scatter between Nominal and Simulated Required Freight Rate – WOZMAX Case Study</i>	377
Figure 156: <i>Sensitivity Analysis and Scatter between EEDI and Simulated EEOI – NMAX Case Studies</i>	379
Figure 157: <i>Sensitivity Analysis and Scatter between EEDI and Simulated EEOI – WOZMAX Case Studies</i>	380
Figure 158: <i>Sim_NMAX_01 / EEOI vs. RFR Design Scatter Diagram with Baseline Vessel and Dominant Variants superimposed.</i>	381
Figure 159: <i>Sim_NMAX_01/ Required Ballast Water vs. Simulated RFR Design Scatter Diagram with Baseline Vessel and Dominant Variants superimposed.</i>	382
Figure 160: <i>Sim_NMAX_01 / Required Ballast Water vs. Simulated EEOI Design Scatter Diagram with Baseline Vessel and Dominant Variants superimposed.</i>	384
Figure 161: <i>Sim_WOZMAX_01 / EEOI vs. RFR Design Scatter Diagram with Baseline Vessel and Dominant Variants superimposed.</i>	385
Figure 162: <i>Sim_WOZMAX_01/ Required Ballast Water vs. Simulated RFR Design Scatter Diagram with Baseline Vessel and Dominant Variants superimposed.</i>	386
Figure 163: <i>Sim_WOZMAX_01 / Required Ballast Water vs. Simulated EEOI Design Scatter Diagram with Baseline Vessel and Dominant Variants superimposed.</i>	387
Figure 164: <i>Sim_WOZMAX_02/Simulated EEOI vs. Simulated RFR Design Scatter Diagram with Baseline Vessel and Dominant Variants superimposed.</i>	388
Figure 165: <i>Sim_WOZMAX_02 / Required Ballast Water vs. Simulated RFR Design Scatter Diagram with Baseline Vessel and Dominant Variants and Sim_WOZMAX_01 design scatter superimposed ...</i>	389
Figure 166: <i>Sim_WOZMAX_02 / Required Ballast Water vs. Simulated EEOI Design Scatter Diagram with Baseline Vessel and Dominant Variants and Sim_WOZMAX_01 design scatter superimposed ...</i>	390
Figure 167: <i>Scatter Diagram of Simulation-Based RFR vs Nominal RFR for Sim_WOZMAX_02 Run (2000 designs).</i>	412
Figure 168: <i>Indicative P&ID of the NH3 containment, processing and consumption system</i>	417
Figure 169: <i>Modelling of Load Dependent Ammonia Specific Consumption Scaling Function</i>	420
Figure 170: <i>Modelling of Load Dependent Ammonia Specific Pilot Oil Consumption as a percentage of NH3-SFOC.</i>	420
Figure 171: <i>Membrane Tank Volumetric Cost Ratio (linear modelling).</i>	423
Figure 172: <i>Pricing of ammonia in various regions from 2010 to 2019.</i>	424
Figure 173: <i>Sim_WOZMAX_03 / Simulated RFR of NH3 powered Vessel vs. Simulated RFR of VLSFO powered Vessel with Baseline Vessel superimposed.</i>	435

Figure 174: *Sim_WOZMAX_03 / Simulated RFR of NH3 powered vessel vs Simulated RFR with Laden Consumption covered by Charterers.....* 436

Figure 175: *Sim_WOZMAX_03 / EEDI vs Simulated RFR of NH3 powered Vessel with Baseline Vessel and dominant variants superimposed.....* 437

Figure 176: *Sim_WOZMAX_03 / Required Ballast Water Amount vs Simulated RFR of NH3 powered Vessel with Baseline Vessel and dominant variants superimposed.* 438

Figure 177: *Sim_WOZMAX_03 / Maximum Ammonia Pricing (MAP) vs Simulated RFR of NH3 powered Vessel with Baseline Vessel and dominant variants superimposed.....* 439

Figure 178: *Sim_WOZMAX_03 / Required Time Charter Equivalent Daily Rate (TCE) vs Maximum Ammonia Pricing (MAP).....* 440

Figure 179: *Sim_WOZMAX_03 / Required Time Charter Equivalent Daily Rate (TCE) vs Simulated RFR of NH3 powered Vessel with Baseline Vessel and dominant variants superimposed.* 441

List of Tables

<i>Table 1: Ship Design Optimization Methods taxonomy</i>	24
<i>Table 2: Helicopter Overview of Methods used for RHODA processes</i>	52
<i>Table 3: Taxonomy and Overview of Different Added Resistance Estimation Approaches</i>	60
<i>Table 4: Environmental Conditions Setup for Parent vessel added resistance calculations</i>	65
<i>Table 5: Conditions examined in Liu Methodology Comparison to Panel Code Results</i>	66
<i>Table 6: Non-dimensionalised (with M/E SMCR) electrical load analysis from the parent vessel</i>	95
<i>Table 7: Non-dimensionalised steam balance of parent vessel used here. All original steam consumptions were in kg/h</i>	96
<i>Table 8: Database used for lightship weight estimation calibration</i>	100
<i>Table 9: Loading Conditions examined in Stability Module</i>	102
<i>Table 10: Taxonomy of methods for estimating Calm Water resistance</i>	105
<i>Table 11: Particulars of vessels examined</i>	107
<i>Table 12: Holtrop Constants used as variables in optimization problem and their respective value range – LADEN CONDITION</i>	120
<i>Table 13: Holtrop Constants used as variables in optimization problem and their respective value range – BALLAST CONDITION</i>	124
<i>Table 14: EHP Deviation from Model Tests Prior and After Stage 1 Calibration – LADEN CONDITIONS</i>	131
<i>Table 15: EHP Deviation from Model Tests Prior and After Stage 1 Calibration – BALLAST CONDITION</i>	132
<i>Table 16: Average Deviation of the Delivered Horse Power (%) per vessel – LADEN Condition</i>	137
<i>Table 17: Average Deviation of the Delivered Horse Power (%) per vessel – BALLAST Condition</i>	137
<i>Table 18: Values of Holtrop coefficients after calibration for bare hull resistance</i>	139
<i>Table 19: Engine Models Database</i>	143
<i>Table 20: Inputs of Main Engine Selection Module</i>	144
<i>Table 21: Summary of collected signals used for database generation</i>	147
<i>Table 22: Input Parameters of Seaways Simulation Module</i>	150
<i>Table 23: Fitted Probability Distribution Functions for onboard data - Wind</i>	152
<i>Table 24: Fitted Probability Distribution Functions for matched satellite weather data</i>	155
<i>Table 25: Fitted Probability Distribution Functions for crew observations - Currents</i>	160
<i>Table 26: Fitted Probability Distribution Functions for matched satellite data- Currents</i>	166
<i>Table 27: Global Environmental Model developed and considered</i>	176
<i>Table 28: Fitted Probability Distribution Functions for Operating Speeds in Simulation Model</i>	179
<i>Table 29: Sea States considered for added resistance estimation in seaways</i>	186
<i>Table 30: Simulation Code Output Variables summary</i>	189
<i>Table 31: Fitted Probability Distribution Function for TCE Earnings</i>	193
<i>Table 32: Dry Docking Costs Model developed</i>	195
<i>Table 33: Fuel Cost Probability Functions developed and used</i>	200
<i>Table 34: List of Filters applied for processing Populated Data</i>	208

Table 35: Baseline Vessel Principal Particulars.....	228
Table 36: List and range of design variables of the optimization problem for Newcastlemax Studies.	240
Table 37: List and range of design variables of the optimization problem for WOZMAX Studies.....	241
Table 38: Inequality Constraints used in Optimization Runs	242
Table 39: Overview of Optimization Targets throughout Optimization Studies	244
Table 40: Taxonomy of optimization runs explored.	247
Table 41: Weights used for the utility functions.....	250
Table 42: RFR Sensitivity on Design Variables – Deterministic NEWCASTLEMAX Case Studies	260
Table 43: EEDI Sensitivity on Design Variables – Deterministic NEWCASTLEMAX Case Studies ...	268
Table 44: BW Amount Sensitivity on Design Variables – Deterministic Newcastlemax Case Studies ..	274
Table 45: RFR Sensitivity on Design Variables – Deterministic WOZMAX Case Studies.....	282
Table 46: EEDI Sensitivity on Design Variables – Deterministic WOZMAX Case Studies.....	290
Table 47: BW Amount Sensitivity on Design Variables – Deterministic WOZMAX Case Studies	296
Table 48: Ranking of Optimization Dominant Variants with Utility Functions Scenarios – RUN ID Det_NMAX_01.....	325
Table 49: Ranking of Optimization Dominant Variants with Utility Functions Scenarios – RUN ID Det_NMAX_02.....	326
Table 50: Ranking of Optimization Dominant Variants with Utility Functions Scenarios – RUN ID Det_NMAX_03.....	327
Table 51: Ranking of Optimization Dominant Variants with Utility Functions Scenarios – RUN ID Det_WOZMAX_01	328
Table 52: Ranking of Optimization Dominant Variants with Utility Functions Scenarios – RUN ID Det_WOZMAX_02	329
Table 53: Ranking of Optimization Dominant Variants with Utility Functions Scenarios – RUN ID Det_WOZMAX_03	330
Table 54: Ranking of Optimization Dominant Variants with Utility Functions Scenarios – RUN ID Det_WOZMAX_04	332
Table 55: Principal Particulars of Newcastlemax Dominant Variants (I)	336
Table 56: Principal Particulars of Newcastlemax Dominant Variants (II).....	338
Table 57: Principal Particulars of WOZMAX Dominant Variants (I)	340
Table 58: Principal Particulars of WOZMAX Dominant Variants (II)	342
Table 59: Principal Particulars of WOZMAX Dominant Variants (III).....	344
Table 60: Summary of Optimization Results on Optimization Targets for Dominant Variants // Deterministic Pathway	346
Table 61: RFR Sensitivity on Design Variables – Simulation Driven WOZMAX Case Studies	360
Table 62: EEOI Sensitivity on Design Variables – Simulation Driven WOZMAX Case Studies.....	368
Table 63 : BW Amount Sensitivity of Design Variables– Simulation Driven WOZMAX Case Studies.....	375
Table 64: Ranking of Optimization Dominant Variants with Utility Functions Scenarios – RUN ID Sim_NMAX_01	393

<i>Table 65: Ranking of Optimization Dominant Variants with Utility Functions Scenarios – RUN ID Sim_WOZMAX_01</i>	395
<i>Table 66: Ranking of Optimization Dominant Variants with Utility Functions Scenarios – RUN ID Sim_WOZMAX_02</i>	397
<i>Table 67: Principal Particulars of Sim_NMAX_01 Dominant Variants (I)</i>	399
<i>Table 68: Principal Particulars of Sim_WOZMAX_01 Dominant Variants (II)</i>	401
<i>Table 69: Principal Particulars of Sim_WOZMAX_02 Dominant Variants (III)</i>	403
<i>Table 70: Comparison of Principal Particulars of Dominant Variants of Deterministic vs. Simulation-Based Runs / Newcastlemax Case Study</i>	407
<i>Table 71: Comparison of Principal Particulars of Dominant Variants of Deterministic vs. Simulation-Based Runs / WOZMAX Case Study</i>	409
<i>Table 72: Summary of Optimization Results on Optimization Targets for Dominant Variants // Simulation Driven Pathway</i>	410
<i>Table 73: Performance and Consumption Engine of MAN 7G80-ME-C10.5 LGIA Engine (NH3 powered)</i>	419
<i>Table 74: Performance and Consumption of Conventional “Base” 7G80-ME-C10.5 Engine</i>	419
<i>Table 66: Cost Basis and Non-dimensional costs of cryogenic Membrane Tanks</i>	422
<i>Table 76: Additional CAPEX Decomposition</i>	424
<i>Table 77: Ammonia Pricing Scenarios introduced in RHODA</i>	425
<i>Table 78: MAP Sensitivity on Design Variables – Simulation Driven Zero Emission Vessel Case Studies</i>	434
<i>Table 79: Ranking of Optimization Dominant Variants with Utility Functions Scenarios – RUN ID Sim_WOZMAX_03 (ZEV)</i>	443
<i>Table 80: Principal Particulars of Sim_WOZMAX_02 Dominant Variants (ZEVs)</i>	446
<i>Table 81: Comparison of Deterministic vs. Simulation-Driven and vs. Simulation Driven (NH3 powered) optimization run results</i>	449
<i>Table 82: Summary of Optimization Results on Optimization Targets for Dominant Variants // NH3 Powered Variants</i>	450
<i>Table 83: Comparison of discounted Total Cost of Ownership between Baseline and ID1750</i>	452
<i>Table 84: RFR Sensitivity and Translation to Total Cost of Ownership</i>	453
<i>Table 85: Effect of NH3 pricing on key economic metrics of Sim_WOZMAX_03_ID1750</i>	454
<i>Table 86: Effect of Vessel’s Lifetime on Required Freight – Sim_WOZMAX_03_ID1750</i>	456
<i>Table 87: Effect of Containment System Capacity of RFR of Sim_WOZMAX_03_ID1750</i>	457

Abstract

The herein presented Thesis presents the Author's research work on the field of Ship Design that fulfils the requirements of the Doctor of Philosophy degree. The original scientific research is focused on the field of Ship Design optimization with the novelty of lifecycle simulation from the early ship design stage (basic/preliminary ship design) as well as the use of digital twin models generated based on big data acquired from a fleet of actual vessels. Three different of layers for uncertainty have been added (market uncertainty, environmental and vessel operation uncertainty, method and model error modelling), tightly coupled with a comprehensive voyage simulation framework for the vessel's entire lifecycle (25 years). This Robust Holistic Design Approach (RHODA) has been deployed for formal and Global Ship Design optimization studies and compared against deterministic runs showing a great potential for more effective Design space exploration resulting into more robust dominant variants over different environments and market conditions. To showcase the applicability and potential of the herein proposed RHODA method and Research work, the methodology has been also adapted to be applicable for Zero Emission Vessels (NH₃ powered bulk carriers) and a Global Ship design Optimization case study has been performed for such vessels yielding many interesting design points for the future.

Acknowledgements

The Author would like to acknowledge and thank the people who made it possible and supported him in completing this work, while actively pursuing a career in Commercial Shipping.

My beloved parents, George and Penelope, provided the foundations and context and placed the quest of knowledge, perseverance, curiosity, and integrity at the core of the personal and scientific values of both me and my sister, who also conducts her own Research in the field of analytical Chemistry. My maternal uncle, George Economopoulos, has always been a constant inspiration for his passion, sense of duty and determination on excelling in Cardiovascular Surgery, prompting each member of our family to reach our potential.

My Professor in NTUA, Prof. Dr. Ing. Habil Apostolos Papanikolaou has been the compass of my scientific development. The idea of Holistic Ship Theory, the father of which is our revered professor, is the one I have humbly chosen to further explore and develop with my own research contribution, while using the knowledge, ethos, and scientific principles of his unsurpassed lectures in the Ship Design Laboratory.

The pillar for materializing this contribution has been my supervisor, Professor Evangelos Boulougouris. I will always be grateful for his continuous support, flood of ideas, meticulous review of my work and patience in having a Post Graduate Researcher who is also working full time.

My introduction to the Shipping Industry was initiated thanks to my mentor and guide Mr. Dimitrios Heliotis of Target Marine, who always remains a valued source of counselling. At my first steps in Shipping at Starbulk S.A, I was lucky enough to meet and work with Dr. Petros Kousiounelos, who taught along with myself a great number of young graduates and engineers how to retrieve and assess onboard data and transform them into valuable analysis tools. The data he generously provided formed the core of the mathematical models for this Research work. Later, as a member of the Euronav Ship Management (Hellas) Ltd. team, I had the privilege of working with Mr. Stamatis Bourboulis whose ideas, management skills, way of thinking and exchange of views on Decarbonization Pathways gave me a significant boost for completing this work.

Finally, I will always be grateful to my friends Mr. Kimon Zografakis, Mr. Andreas Kerasiotis, Dr. Eleftherios Dedes, Mr. Michael Pytharoulis, Mr. Alexandros Heliotis, Mr. Pavlos Kanelis and to my beloved wife Marilyn the support of which accompanied me throughout this quest.

Lampros Nikolopoulos

Athens, December 2022

Chapter 1: Introduction

1.1. Contemporary Challenges for Commercial Shipping

While the 19th century has been the age of steam, and the 20th century the age of globalization, the 21st century appears to be the century of digitalization, big data and decarbonization. On July 20th 1969 the team of Astronauts of Apollo 11 that successfully landed on the moon had at their fingertips 32,768 bits of RAM memory for navigating the 953,054-mile round voyage. The average RAM memory of a smartphone at the time of writing is 34,359,738,368 bits. Similarly, ships have evolved in scale and propulsion plants throughout the 20th century, while during the first two decades of the 21st century the emergence of telemetry, data acquisition systems and digitalized applications is prominent.

In parallel, the awareness regarding the phenomenon of Climate Change due to the generation of anthropogenic Green House Gases (GHGs) with effects on global temperature, climate and the balance of the ecosystem has been raised from the late 1970s to date. In 1997 the Kyoto protocol (United Nations, 1997) and in 2015 the Paris Agreement for Climate (United Nations, 2015) solidified the pledge of modern societies and nations towards the deceleration of the carbon footprint. The globalization and emergence of international stock markets in the meantime created a harsh and volatile economic environment that can be easily offset from balance.

The effect of the above operating environment creates two main challenges for modern shipping.

1. First Challenge: Compliance with the societal pledge for decarbonization.

The International Maritime Organization (IMO), being the primary international and inter-governmental regulatory for maritime matters has developed several regulations in the past two decades focusing on Marine Safety (through its Marine Safety Committee – MSC) as well as protection of the Marine Environment (through its Marine Environmental Protection Committee – MEPC).

In April 2018 and during the session of MEPC72 (followed by the session of MEPC73), the International Maritime Organization pledged to reduce by the Year 2050 the GHGs generated by shipping by 50% when compared to the emission levels of 2008, with the intention to reduce more than 70% by the end of the century (International Maritime Organization, 2018). These targets are visualized in (DNVGL, 2019) as per Figure 1.

IMO strategy for major reductions in GHG emissions from shipping

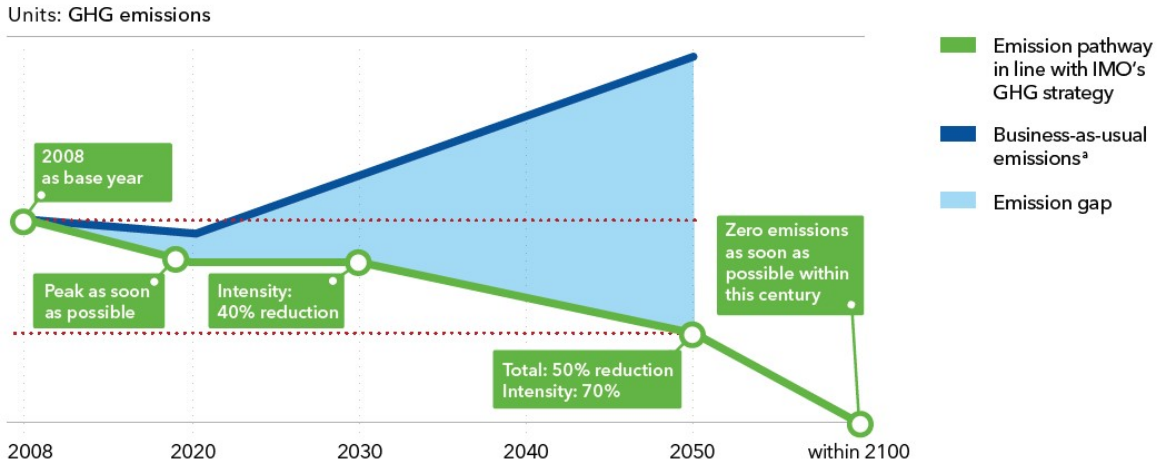


Figure 1: GHG Reduction requirements by IMO MEPC72 (DNVGL, 2019)

In order to tackle that ambitious target, a multi-disciplinary, technological approach in three paths is required:

a. Path 1: Reduction of Energy Demand per ton*mile of cargo.

This path follows the rationale of the minimization of the onboard energy demand to trigger the necessary reduction of the consumed energy in terms of Mega Joules for each unit of transport work (ton-miles). Following this scope of view, technical measures including Design Optimization, hydrodynamic improvement devices, low friction coatings, advanced machinery plants with waste heat recovery as well as operational measures including speed optimization, virtual arrival and voyage planning are included. There are several barriers however to the extent of this reduction, ranging from physical barriers (related to the involved physical phenomena and processes), safety barriers (navigation, structural integrity, manoeuvrability, fire protection), human factor barriers as well as Financial (acquisition and operating costs).

b. Path 2: Introduction of zero-carbon or net-zero carbon fuels.

Another approach would be the generation of energy through the use of zero-carbon fuels that don't emit Greenhouse Gases during the energy release process. An accurate definition and categorization of the term Zero Carbon Energy Sources can be found in Smith (Smith, 2019) below:

“Zero Carbon Energy Sources is intended to be inclusive of fuels derived from zero-carbon electricity, biomass and the use of Carbon Capturing and Storage, but not of Carbon Capture and Use derived energy sources based on the combustion of fossil fuels”

c. Path 3: Introduction of Carbon Taxation and Carbon Capturing technologies.

Carbon taxation used as a means of financing for global decarbonization projects (e.g. reforestation, investment in renewable energy etc.) is the third alternative that can be followed

towards the goal of shipping decarbonization. The potential framework for the implementation of carbon taxation can be found in (Parry, et al., 2018).

2. Second Challenge: Resilience against Volatile Economic Conditions and Freight Markets

The second challenge international shipping transport is facing currently is the exposure to a globalized economy with a multitude of layers of sophisticated and unbalanced relationships that can easily change and spark dramatic effects on the supply and demand tonnage. Historically, shipping has always been volatile as can be seen from the historical freight rates for Capesize bulk carriers depicted in the below Figure 2 (Alizadeh, et al., 2016).

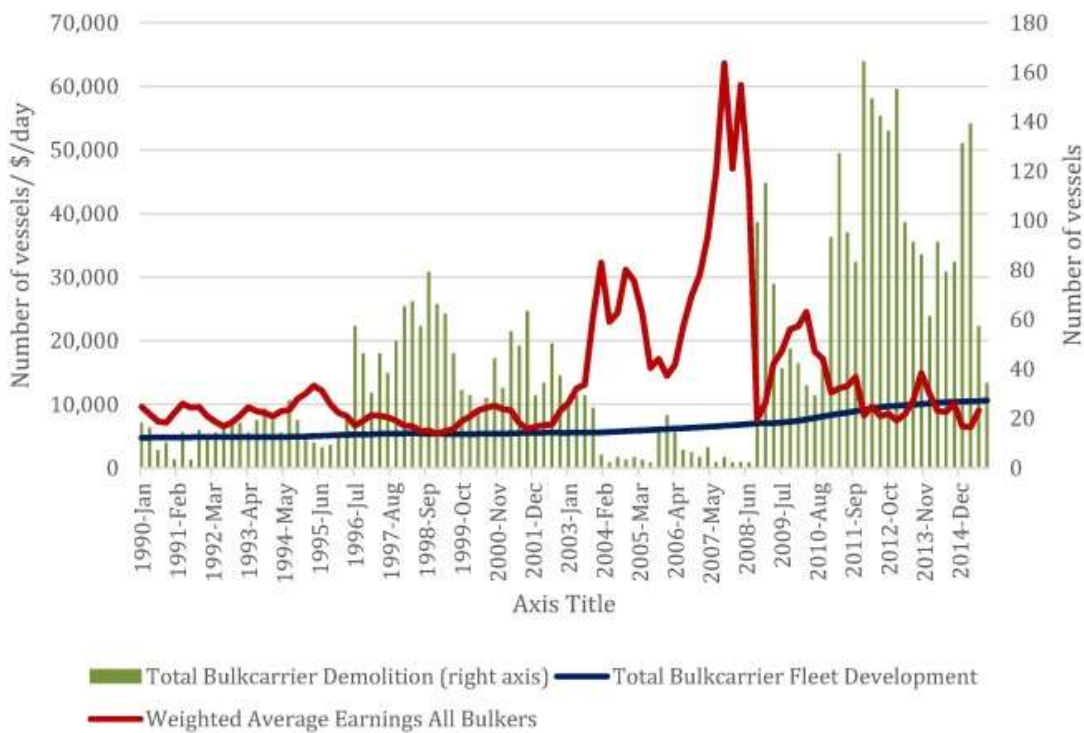
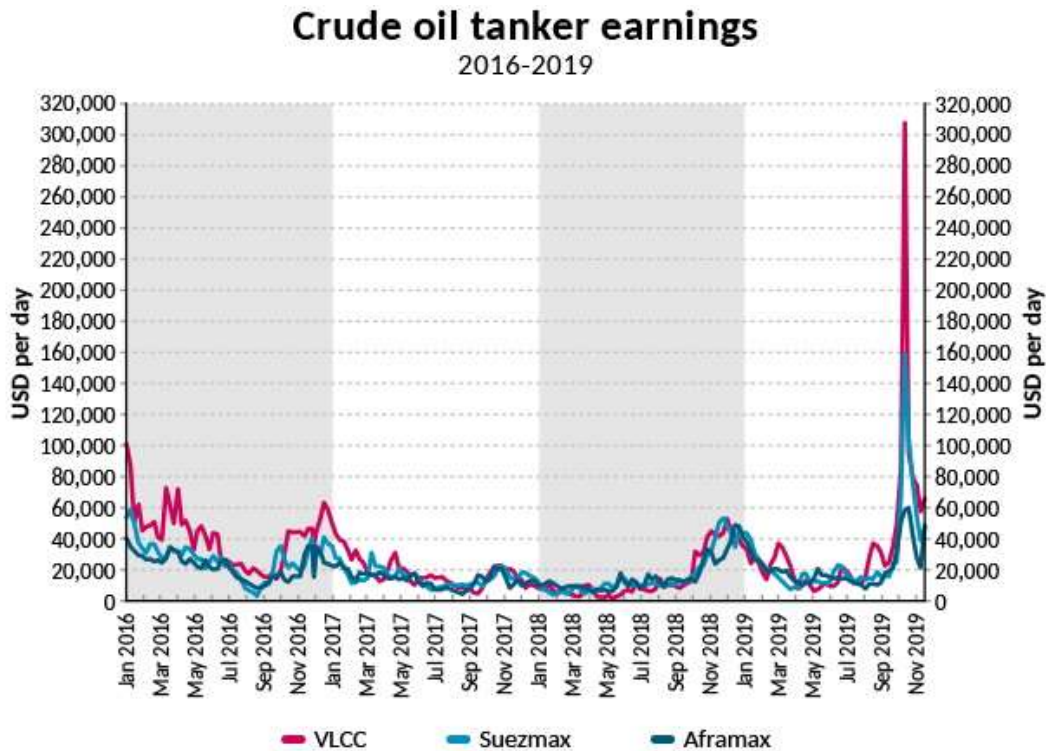


Figure 2: Capesize Bulk Carrier Freight Rates (1990-2015) (Alizadeh, et al., 2016)

The outbreak of trade wars at the time of the writing, further magnifies this volatility, as seen from the earnings in the spot market of VLCC tankers' evolution over the last decade (Sand, 2019).



Source: BIMCO, Clarksons

Figure 3: VLCC Freight Rates (2019-2020) (Sand, 2019)

This uncertainty, apart from the direct negative impact on the cashflows of shipping companies, when combined with their exposure to large capital markets through stock exchange listings can trigger further capital loss and devaluation of the company in very short periods of time. The 2008 global economic crisis and banking crisis that followed, further restricted the lending for investments in shipping, while the newly formed “Poseidon Principles” (Parker, et al., 2019), can provide funding only for environmentally sustainable vessel acquisitions. At the same time, the Operating Expenditure (OPEX) is kept at a constant level, which is on average 6500 USD/day for a Capesize bulker and 9500 USD/day for a VLCC tanker. It is thus evident that in periods of low freight rates, the profitability, monetary flows, and financial sustainability of shipping companies can be at risk.

It is evident from this introduction, that the major two challenges that shipping faces today have both an antagonistic and interdependent nature. On one hand, they have an antagonistic relationship, as compliance with decarbonization requires significant capital investment while it has considerably higher fuel and thus operating costs, making the profitability and economic sustainability of the owning company more difficult. On the other, they are interdependent as decarbonization can be attained only through significant investment.

In such a complex and uncertain environment, the ship designs of the future need to be resilient and robust enough to maintain optimal performance under their actual operating and market conditions. To achieve this, new approaches in the Ship Design and Ship Design Optimization processes that encompass the simulation of the vessel’s actual responses in real seaways and trade

routes as well as accurately depict the design uncertainty and its effect on the candidate vessel performance.

1.2. Traditional Approaches in the Ship Design Process.

In the book *Ship Design and Construction* (Lamb, 2003), Design can be defined as “*the activity involved in producing the drawings (or 3D models), specifications and other data needed to construct an object, in this case a ship*”. The primary objective of the design effort, besides creating the information needed to build the ship, is to satisfy the ship owner’s requirements at a minimum cost. Traditionally, ship design is an iterative process, especially in the early stages. The ultimate result is postulated and then analysed and modified. The modified result is re-analysed and so on until all requirements are satisfied. The reason for the iteration is that ship design up until recently was proven to be too complex to be described by a set of equations that can be solved directly. Instead, educated guesses are made as to hull size, displacement etc. to get the process started and then the initial guesses are modified, as better information becomes available. A typical example of this procedure is the well-known design spiral as defined by (Evans, 1959).

Historically, the first studies in ship design optimization started to appear by the middle of the 1960s with the advances in computer hardware and software technology allowing the integration of computers in several processes of Ship Design, especially those entailing heavy computation and drafting elements. The first computer-aided design software appeared shortly afterwards enabling mathematical parametric exploration of the design space based on simplified formulas for specific economic criteria using gradient-based techniques with notable examples that of Murphy et al. (Murphy, et al., 1965) as well as Nowacki et.al. (Nowacki, et al., 1970).

1.3. Research Aim

The primary objective of the present thesis is to provide a robust and comprehensive methodology and framework for tackling the problem of Ship Design Optimization, which will simulate the vessel’s entire lifecycle from the early design stages based on actually retrieved data from the vessel’s operation. The lifecycle approach proposed herein also includes considerations of the Newbuilding stage (building and acquisition cost modelling under uncertainty) as well as the end of the vessel’s life (scrapping and disposal cost and value). The vessel’s ageing both in terms of residual hull roughness as well as machinery ageing are also considered. Furthermore, the method will be easily adaptable to existing, available design environments commonly used in commercial shipbuilding and shipping. The method will be in such a holistic framework that future research can expand the latter, on one hand for assessing through simulation the application of new fuels, technologies, propulsion plants in existing vessels and on the other, in a more simplified format, used for the economic, lifecycle assessment of future shipping investments.

1.4. Objectives

Following the exploration and definition of the current “state-of-the-art” in ship design, optimization and simulation methods and approaches, the herein presented research work and Thesis objectives are summarized below:

- Introduce a Robust Holistic Optimization Design Approach (RHODA) that uses the simulation of the operation of the vessel's actual voyages throughout its lifecycle and model most of the ship's primary systems and integrates them into a holistic, fully parametric ship design model.
- Calibrate existing empirical methods using actual operating and shipbuilding data for fast, yet accurate estimations for specific calculations where computational methods are intensive and expensive.
- Comprehensively capture multi-layer uncertainty, model and introduce it in the RHODA process and highlight the effect of the latter in the optimization process and results, with the assistance of big volumes of actual operating data (Big Data) and the use of high-end statistical analysis for modelling environmental and economic uncertainty in the simulation environment.
- The exploration of innovative design concepts with the target of optimizing the economic performance while minimizing the lifecycle emissions and economic footprint of the vessel.
- The development of a RHODA-based simulation platform and decision-making mentality for evaluating options and pathways towards decarbonization in the future and well-informed Zero Emission Ship Design decisions in this direction.

1.5. Thesis Structure

In Chapter 2 of the present Thesis, the current “state-of-the-art” in Ship Design and Ship Design Optimization is presented and gaps are identified. Following the identification of gaps, at the end of the chapter, the contribution to the area of research is elaborated. In Chapter 3, an overview of the proposed methodology is presented with Chapter 4 describing existing methods utilized in RHODA while Chapter 5 presents the original research and developed methodologies that have been integrated in the RHODA. In Chapter 6, the main case studies of optimization for large Bulk Carriers (VLOCs) are documented, starting from a deterministic approach, followed by the introduction of simulation in the optimization and then simulation coupled with market uncertainty for a Zero Emission Vessel variant powered with Ammonia (NH₃). In Chapter 7, the optimization results are discussed and analysed. Furthermore, suggestions on the expansion of the herein research works are made and planned. Appendix I contains the list of original research contributions of the Author.

1.6. Summary

In the present Chapter, the driving motive that prompted the rationale of the present research work has been clarified, objectives for the Thesis have been set and the structure of the Thesis has been explained.

Chapter 2 - Literature Survey

2.1. Ship Design Methodologies Overview

The current state-of-the-art in ship design methodology is examined on a 3-year basis upon the closing of each International Marine Design Conference (IMDC) by the IMDC committee. In the 2018 conference, the committee presented its state-of-the-art report as can be found in the literature (Andrews, et al., 2018), reviewing, on a philosophical basis, books and papers on generic design theory and how this can be applied in ship applications. Similar reports with a focus on the “DESIGN FOR X” the notion of designing for a particular merit/operational aspect of the vessel can be found in (Andrews, et al., 2012) and (Papanikolaou, et al., 2009).

An attempt for setting up a taxonomy of the different approaches in Ship Design and Optimization is depicted in the below-developed Table 1 after a critical review of the literature.

Single Objective Ship Design Optimization	Multi-Objective Ship Design Optimization with Computational Methods		Ship Design Optimization with Simulation	Ship Design Optimization Surrogate Models	Set-Based Ship Design	
	Holistic Ship Design Methods	Ship Design Optimization under Uncertainty			Set-Based Design	Networks Engineering
(Murphy, et al., 1965)	(Papanikolaou, 2010)	(Noor, 2005),	(Tillig, et al., n.d.)	(Yan & Huang, n.d.).	(Hannapel, 2012)	(Yuan & Singer, 2018)
(Nowacki, et al., 1970)	(Zaraphonitis, et al., 2012)	(Fusi, et al., 2019)	(Tillig & Ringsberg, 2018)	(Guerrero, et al., n.d.).	(Goodrum, et al., 2018)	(Shields, et al., 2015)
(MacCallum & Duffy, 1989)	(Zaraphonitis, et al., 2013)	(Clarich & Russo, 2019)	(Ferrante, et al., n.d.)	(Guerrero, et al., n.d.)	(Shields, et al., n.d.)	(Killaars, et al., 2015)
(Meyer, 2002)	(Papanikolaou, et al., 2010)	(Hannapel, 2012)	(Sandvik, et al., 2018).	(Couser, et al., n.d.)		(Smith, et al., 2018)
(Mandel & Leopold, 1966)	(Papanikolaou, et al., 2007)	(Hannapel & Vlahopoulos, 2010)	(Alwan, n.d.)			
(Söding & Poulsen, 1974)	(Sames, et al., 2011)	(Plessas & Papanikolaou, 2015)	(Hassani, et al., 2016)			
	(Papanikolaou, et al., 2011)	Plessas, et al., 2018)	(Lu, et al., 2015)			
	(Nikolopoulos, 2012)	(Hiekata, et al., 2015)				
	(Priftis, et al., 2018)	(Diez, et al., 2010)				
	(Koutroukis, et al., 2013)	(Diez & Peri, 2010)				
	(Marzi, 2019)	(Campana, et al., 2015)				
	(Zaraphonitis, et al., 2019).					
	(Maggioncalda, et al., 2019)					

Table 1: Ship Design Optimization Methods taxonomy

A similar taxonomy has been also attempted by (Papanikolaou, et al., 2020) .

For the purpose of the current thesis, a critical review of the current literature State-of-the-Art has been conducted for the below disciplines:

1. Multi-Objective Ship Design Optimization
2. Set-Based Ship Design and the Use of Networks Engineering
3. Holistic Ship Design Optimization
4. Robust Holistic Optimisation Design Approach

Furthermore, the subject critical review has been extended to the below attempts for new approaches in Ship Design that are currently relatively niche and are addressed by and covered by the present Thesis:

1. Application of Surrogate Models in Ship Design.
2. Application of Big Data in Ship Design
3. Application of Simulation in Ship Design

Consequently, the research gap is identified targets are set to fulfil the aim of the Thesis as described in Chapter 1.

2.2. Multi-Objective Ship Design Optimization

An early and established application of Multi-Criteria optimization in Ship Design can be found under the Risk-Based Design Optimization and studies, where the focus lies on the minimization of accidental risk and hazardous occurrences through the minimization (primarily) of consequences of each hazardous occurrence after optimization of the design and arrangements of a vessel. The most comprehensive reference is that of (Papanikolaou, 2009).

The development of a multi-objective deterministic partition-based algorithm by coupling a multi-objective direct type algorithm with an efficient derivative-free algorithm is presented by (Campana, et al., n.d.), with their focus being the improvement of robustness by using derivative-free methods given the risk of algorithm trap in local Pareto solutions inherent in many deterministic methods. The reason for this is that the DIRECT algorithm operates by building finer and finer partitions of the original solution (design) domain. However, when it comes to the actual application of the identification procedure prior to partition the selection of potential Pareto-optimal hyperintervals is a very computationally expensive procedure. To solve that they replaced the identification procedure of DIRECT with a newly proposed multi-objective identification procedure. The new algorithm, when compared to the NSGAII equivalent demonstrates a very good performance with a much better efficiency in terms of purity versus time but with smaller robustness. This algorithm is also applied to the hull form optimization of a 100m high-speed catamaran, aiming at the reduction of the main total resistance in irregular head waves at variable speed and the increase of ship operability by decreasing ship motions. A radial basis function has been used for the interpolation of high-fidelity URANS simulations, with four design variables controlling the global shape modifications of the hull surface. Both a conventional, the DIRECT and hybrid algorithms were employed and from the results, the hybrid provided the most dense and robust Pareto frontier.

An application of model-based systems engineering in ship design optimization for the concept design of an Offshore Supply vessel is examined by (Corrigan, et al., 2018) and aims at the optimization of shipboard powertrain arrangements. The method architecture is based on three

distinctive stages: First is the selection of power system alternatives done by a dedicated tool containing a library of systems, second is the Assessment of the vessel operability performance with regards to equipment failures and required repairs and maintenance activities after a systems criticality assessment is done. Lastly, the Third is the assessment of the Life Cycle Cost of each design entailing CAPEX, failure costs, maintenance costs, mobilization, penalty as well as fuel costs. The optimization target afterwards is the minimization of the LCC. The First tool uses an interesting systems architecture for building functional blocks of machinery and assessing the performance of each one as well as communication with other systems.

2.3. Set-Based Ship Design and Application of Networks Engineering

In accordance with (Singer, et al., 2009), Set-Based design is a convergent design method for tackling complex engineering design problems. SBD requires the creation of broad sets of design parameters that are used to define trade-off information as it relates to the design. These sets are developed concurrently and gradually narrowed with increasing information fidelity. The SBD aims at discarding infeasible or dominated designs and delays the decision-making for later design stages when more information and feedback are available. In this way, reiterations and modifications in later stages of the design process are reduced. Furthermore, the design responds better to uncertainty due to the range of values for the design parameters. (Hannapel, 2012) developed a multi-disciplinary optimization algorithm based on the principles of set-based design whereas the design variables in the system optimization statement are not the design variables but the variables which define the sets. For this reason, scaling of the design variables is necessary the accurate performance of the optimization algorithm.

In the system-level optimization of their algorithm (Hannapel, 2012) also adopt a flexible approach in constraints, when a marginal violation of a constraint can yield to a significant improvement of an objective function. This is in turn applied to the optimization of a tanker with the parametric hull being developed in MaxSurf, with the calm water resistance being evaluated by the approximate power prediction formula of Holtrop and Mennen (Holtrop & Mennen, 1982), (Holtrop, 1984), while the manoeuvring and seakeeping characteristics being derived from surrogate models that have been developed. The challenge in the approach of (Hannapel, 2012) is that it cannot easily integrate synchronous simulations of several subsystems of each design, and therefore evolutionary algorithms such as NSGAI or MOSA cannot be applied leading to a significant drop in the efficiency of the algorithm.

Also, within the context of Set-Based Design (Goodrum, et al., 2018) proposed a novel method for investigating different design tools and how they behave in a complete design framework. The method enables the mapping of variables to disciplines organically through the structure of the network itself and enables the disciplines to be uncovered without their previous definition. The authors effectively apply information theory to a network by conducting a random walk that visits all nodes at least once. Huffman codes are used to assign each node a binary bit string the length of which is proportional to the frequency of visits. With this method, authors can effectively partition graphs into communities. This method has been applied for the design of a containership utilizing standard tools from the library of software developed by the University of Michigan. Most of them are empirical methods and formulae widely known in the literature (e.g. Holtrop and Mennen approximate power method) and are available in different language

codes (Fortran, C++ etc), Excel spreadsheets etc. Based on this a community grouping was done which was coincident with the principles of “classic” Naval Architecture disciplines. In the second stage, the hierarchical network structure is examined, providing valuable information about the flow of information between different design communities, the variable dependencies as well as the level of fidelity of each independent tool (higher number of inputs and thus higher flow of information). This leads to a very effective mapping of the design spaces, easier and faster exploration of trade-offs and contradicting requirements and enables the evaluation of each design tool structure and alignment with the design goal.

Yuan and Singer (Yuan & Singer, 2018) introduce fuzzy logic models to analyse the potential performance of ship designs within a set-based design environment. For each design variable, the design performance is assessed by a fuzzy logic controller and afterwards is subject to defuzzification creating a crisp output based on multiple fired fuzzy rules and their clipped output membership function. The result is a joint preference curve for each design variable. Such an approach can highlight the sensitivity of the optimization problem and indicate optimal solutions. Its application in the design optimization of a high-speed yacht with a very extended design space is due to the big range of each design variable which in this case are the principal dimensions and hull form particulars. The optimization goals are stability, resistance and arrangements which can be considered contradicting. Despite the efficiency of this method in simple applications, in more complex applications with a high number of design variables and objectives its robustness is not proven. Furthermore, the authors are not specific on the analytical engineering model used for the calculations, the fidelity as well as the geometrical core.

(Shields, et al., n.d.) focus on understanding the interdependent design relationship between logical architecture, physical architecture, and physical system solutions with a scalable and stochastic network method. Their approach formalizes the previous network-based distributed system re-representations. Their proposed “Logical-Physical Architecture Translation” algorithm generates routing through the geometric relationships of the vessel’s physical architecture that satisfy the system connectivity relationships in the logical architecture. Initially, nodes are defined corresponding to components and then the shortest paths between the nodes are generated with the shortest path algorithm. The routing from the shortest paths is randomly then selected from the list. This is a noticeable difference from existing distributed system design methods as it breaks away from template-based architectures based on existing best practices and thoughts stochastic generation of distributed systems physical solutions a better exploration of the design space occurs. The generated ensembles of physical solutions are then evaluated to find the probabilistic density of the physical solution between structural zones. Extensions to the routing density analysis include route weightings based on estimated component load, density by a number of systems connectivity and localized complexity calculation. However, this application is limited only to the arrangement’s connection of a vessel, which for naval applications might be vital, however, it is of minor importance for commercial vessels. Furthermore, there is no actual geometric core with a geometric surface of the vessel and numerical approaches to calculations reducing the fidelity of the solutions provided when benchmarked against numerical simulation results of the actual proposed arrangements.

Similarly, in (Shields, et al., 2015) the network study of iteration in ship design is altered to enable the analysis of cyclic networks with the use of Path Influence and applied to the Sen Bulker

problem (Sen & Yang, 1998). Due to the low complexity of the problem and the absence of both a geometrical core as well as analytical computations on the latter, the value of expanding such methodologies on a larger scale, and detailed design problems is uncertain. The more practical application of Network Science in Ship Design is examined by (Killaars, et al., 2015) examining the preliminary design of a motor yacht and an arctic drillship.

In (Le Nena, et al., 2019), the idea of using a Systems Architecture and Requirements management tool (SAR tool) has been developed to adapt systems engineering methods from the aerospace in the ship design process within the HOLISHIP EU-funded research project. A tool has been therefore developed that allows the user/designer to map components and their interfaces, group components to form higher-level assembly entities and propagate interface properties automatically. From this visualized approach, the system's architecture can be efficiently mapped with the use of circuits (networks and functional chains). Users can specify the components that participate in specific functional chains and easily identify potential sources of failure of the functional chain. The architecture of the SAR tool is organized around a message queue service. Each time a model, scenario or requirement is changed, then the domain-specific tool sends a message to the message queue. This in turn triggers the Design Simulation platform (in this instance CAESES®) to update and feed with additional simulations and relevant data.

Smith et al. (Smith, et al., 2018), examine the use of the Functional Resonance Analysis Method (FRAM) to monitor the functional dynamics of each performance and understand the processes that produce the measurement that can be obtained. In FRAM after several observations for a certain physical model are available then functional resonance can be produced and used to organize information, understand operational practices and evaluate practical performance. Their proposed methodology has been used to populate data from 3 different ship designs operating regularly in ice conditions and use them for the assessment of the propulsion and drivetrain plant for future design decisions. The lack of decomposing however the hull, propellers and machinery plants can lead to underestimations and false interpretations of a design. Furthermore, no filtering of data with regard to their reliability is performed. Based on this -under its current application, it is not considered a reliable tool for state-of-the-art assessments.

2.4. Ship Design Optimization Under Uncertainty

Uncertainty is often considered a lack of knowledge that may introduce risks to the outcome and execution of a process. A discussion about the challenges of defining uncertainty can be found in (Lassahn, 1985). (Noor, 2005), classified the quantification of uncertainty into three categories: probabilistic analysis, fuzzy set approaches and set-theoretical approaches.

Within the state of the art of uncertainty analysis in engineering design, it is interesting to note the work of (Fusi, et al., 2019) who have contributed an alternative formulation for design under uncertainty based on targeting the maximization of both the mean value and the minimum performance. Three methods are used for computing the minimum with the Polynomial Chaos expansion being the most promising and effective one. The method has proven effective in selecting only the designs with higher means performance from the front obtained with the classical mean robust approach and at the same time finding new designs with minimum values that would normally not be discovered under existing formulations.

The polynomial representation of model uncertainty in dynamical systems is studied by Vasile (Vasile, 2019) by capturing their unmodelled components through a hierarchical polynomial expansion in the state space. Also on the state of the art in uncertainty modelling, (Clarich & Russo, 2019) examine the SS-ANOVA regression applied directly to uncertainties variables as well as a methodology based on the stepwise regression methodology applied to Polynomial Chaos terms used for uncertainty quantification within the context of Robust Design Optimization. The new proposed approach is with aeronautical test cases, namely the (RAE 2822 airfoil for specified conditions with 13 uncertainties).

The marine environment is by definition an intrinsically stochastic environment concerning the weather, wave, wind, current and many other conditions the ships may be subject to. This creates an additional change during the preliminary design stage, which is tackled in the literature by the design under uncertainty approaches. The ship as an engineering system, however, may be subject to more types of uncertainty including but not limited to the following:

- Market Uncertainty: Uncertainty of Fuel Price, Uncertainty of Revenue, Freight Rate uncertainty, Financial Markets (lending) uncertainty, Regulatory uncertainty.
- Method Uncertainty: Calm Resistance and Power Uncertainty, Added Resistance Uncertainty, Weight and Displacement Estimation Uncertainty, and Structural Integrity Uncertainty.
- Environmental Uncertainties: Wind, Wave, Swell, Sea Temperature, Sea Current, Ice thickness Uncertainty

The above categorization can be also found together with the need for modelling the uncertainty of all levels and at all stages through the concept of Robust and Reliable Engineering discussed by (Erikstad & Rehn, 2015). In their paper, the state of the art on handling uncertainty in maritime systems is presented and furthermore, different methods of simulation market uncertainty are discussed and evaluated along with decision support tools in that direction (financial options, real options theory etc). To this extent, the handling of complexities throughout the Ship Design Process is discussed in (Gaspar, et al., 2012).

The effects of uncertainty during all stages of Ship Design as well as its implications in Optimization studies have been explored several times in the literature. In the doctoral thesis of (Hannapel, 2012) , (Hannapel & Vlahopoulos, 2010), two methods of Uncertainty modelling for ship design optimization are assessed, that robust optimization and reliability-based optimization. In reliability-based design, the effects of uncertainty in design variables and parameters on the constraints are considered. The optimal solution, in this case, will be calculated within a prescribed level of confidence with the purpose of the reliability analysis being the assessment of the probability that a design satisfies the constraints.

On the other hand, in robust design optimization, the effects of uncertainty in design variables and parameters on the objective functions are considered. The goal is that the optimal designs on a Pareto front maintain their dominance over other variants under the presence of uncertainty. Both methods are applied for the multi-objective optimization of a bulk carrier based on the existing literature case study of the Sen and Yang model (Sen & Yang, 1998), targeting the minimization of the lightship, maximization of annual cargo and minimization of transportation cost. The design variables are the principal dimensions and design speed, while 9 different

constraints are applied. As this is a typical case study in the literature, no geometric core is available, making it only a numerical optimization problem with the analytical model being based solely on empirical formulae. Originally a “deterministic” optimization run is conducted without considering any uncertainty whatsoever, the result of which is used as the baseline for the next runs. Uncertainty is introduced on the design speed and the result of the Lightship Weight Estimation in the form of error modelling, and the optimization problem is solved both by means of reliability analysis as well as robust optimization. From the results table, it is evident that in both cases the new dominant variant’s performance with regards to the objective functions has been degraded when compared to the deterministic solution. Additionally, the reliable optimum breadth slightly exceeds the width of Panama Canal's old locks which wasn’t considered as a constraint, however, poses limitations to the feasibility of the solution. The robust optimization performed after the reliability analysis gives a feasible solution, which interestingly has the same parameter value for the draft as the deterministic optimum.

An example of reliability-based design use of uncertainties in a Ship Design Multi-Disciplinary Optimization model is that of (Good, 2006). In this study, uncertainty is modelled as a third objective utilizing the “confidence of success” calculation for combining multiple sources of uncertainty by the mean value method. The confidence of success calculation will in return derive the probability of each design variant satisfying all design constraints and meeting performance objectives. This method was applied in turn for the multi-objective optimization of a US Navy surface combatant model (DDG 51) with genetic algorithms as the design generation engine and with two sources of uncertainty: bare hull resistance and total weight estimation.

Another example of reliability-based design in the literature is that of (Kalyanmoy, et al., 2015), where the introduced uncertainties simplified the ship design problem (McKesson, 2014) with no hull surface modelling, being relied only on regression formulae for the interdependencies between dimensions and characteristics. The variables are DWT, beam and speed and an NSGA II algorithm is used for the design variants generation within MATLAB. All these three design variables have been considered to be uncertain with a Gaussian distribution with a standard deviation proportional to 5% of their values. A detailed sensitivity analysis of the results illustrates several trends in the designs. However, as the hull surface, cargo hold arrangements, propeller design, engine matching and other design aspects are neglected from the study, the sensitivity analysis presented is considered of low fidelity with trends that in general are logical but might be distorted in more realistic ship models.

Two-stage stochastic programming for robust ship design optimization under uncertainty has been developed by (Diez & Peri, 2010), (Diez, et al., 2010). The first stage parameters are those that must be decided before the actual realization of the uncertain parameter. The second stage variables are related to corrective measures or recourses (operational-level decisions) against the onset of uncertain conditions. In the case of ship design, the first stage parameters are the principal dimensions, while the second stage could be the operating speed or retrofitted devices. The method has been applied for the optimization of the conceptual design of a bulk carrier, with the design variables being the principal dimensions and operating speed, while the uncertainties used for the fuel oil price, port handling rate (in tons/day) and the length of the round trip. Interestingly, when examining the length of the round trip the variation of the result between the

deterministic, single-stage stochastic and two-stage stochastic approach is coincident, indicating a very low sensitivity of the model in such uncertainty.

An important and comprehensive application of design under uncertainty is that of (Campana, et al., 2015), where a Reliability-Based Robust Design Optimization framework is developed for the design optimization of a high-speed catamaran. As the formulation framework is both reliable and robust, both the constraints and the objective function are defined as stochastic variables. Interestingly, the design space dimensionality is reduced by using a Karhunen-Loeve Expansion (KLE) which is namely a tool for reducing complexity by selecting a reduced number of design variables and at the same time, giving the guarantee that a desired maximum geometrical variance is maintained. Furthermore, results are provided by KLE without the need for computing the objective functions, enabling the authors to have a sensitivity analysis beforehand and focus on the optimization run accordingly. The optimization tool employed was a derivative-free algorithm, using deterministic particle swarm optimization principles. A dynamic Radial Basis Function (RBF) has been used as a surrogate model for the assessment of the vessel's motions, the stochastic wave frequency as well as the RMS transfer functions. The application of this optimization toolbox has been for the case of the high-speed Delft catamaran considering a realistic stochastic ocean environment by introducing the Probability Distribution Functions produced for the North Pacific area in the framework. Irregular wave numerical simulations (URANS) calculating the mean resistance in waves as well as the motion-related constraints for 5 sea states and 10 different speeds are the basis for creating the dynamic RBFs. The operational speed distribution is assumed to be uniform from 20% to 100% of the design speed. The design optimization is based on the KLE reduced design space, stochastic regular wave models, sequential surrogate model training and multi-objective extension of particle swarm optimization. Initial training and two refinements are used for a total of 120 designs at a cost of 1.5 million CPU hours. The selected design achieves a 10% reduction in the added resistance due to waves and a nearly 6% increase in operability. From the comparison of the result to the original hull, it is evident that the shape is quite unconventional and post-optimization validation of the results (especially concerning calm water resistance) is necessary.

Similar work can be also found in (Diez, et al., 2010) where the (joint) probability density function of the operating scenarios is taken as a design requirement and the expectation of the relevant merit factors is assessed during the optimization task minimization problem. A particle swarm optimization algorithm is employed for the optimization of the keel fin of a sailing yacht which is a hydro-elastic problem as the heavy ballast bulb of the keel generates a bending moment which together with the hydrodynamic loads induces an elastic displacement which is significant. The uncertainties apart from the environmental weather modelling include a probabilistic sailing scenario with regards to the cruise speed, heel and yaw angles.

In (Bergstrom, et al., 2015), the ice formation in the Northern Sea and ice height uncertainty are modelled and inserted in a MATLAB tool that is used for the simulation of the entire arctic LNG transport system determining the optimal vessel size for maximizing reliability and minimizing cost. It should be noted, however, that as this is a transport system simulation the detailed engineering of the hull, hydrodynamics and all other ship systems is omitted.

A stochastic design methodology to account for uncertainties in the early ship design process has been examined by Plessas and Papanikolaou (Plessas & Papanikolaou, 2015). The probability

distribution function of the Fuel Oil Price has been integrated within the Required Freight Rate calculation, accounting for market uncertainties. The optimization is applied for the case of a Post Panamax bulk carrier using the Sequential Quadratic Programming algorithm of MATLAB first on a deterministic approach and afterwards on a stochastic basis. Results indicate that dominant variants of the stochastic design optimization, are shorter in length and breadth and with a higher block coefficient. This can be interpreted by the penalization of the higher total resistance of larger vessels which has a detrimental effect on higher fuel oil prices, while the block coefficient is increased to compensate for the loss of cargo. However, the effect of this higher block coefficient on the hull form and its resistance is not taken into account.

This study has been subsequently expanded by Plessas et al. (Plessas, et al., 2018). A pre-defined operational scenario for the ship's operation in calm seas and representative weather conditions is used as a decision support tool in the early design stage. The uncertainties of the fuel oil price and freight rate are modelled and empirical models for the ship's performance in terms of resistance (Holtrop and Mennen methodology), added resistance in waves (Liu et al methodology) as well as added resistance due to wind (Blenderman model) are utilized. The optimization is targeted through systematic, exhaustive variation alternative hull/engine/propeller setups. The handling of uncertainties is achieved with the Monte Carlo method by evaluating the probability of a negative Net Present Value (NPV) of the investment (vessel acquisition), with the minimization of the latter "failure probability" being the optimization objective. The weather uncertainties of the route, including sea currents, are not considered nor any variation is made on local hull form characteristics and cargo tank arrangement parameters. Furthermore, the methodology focuses on solving a predefined route with a "static approach" to the self-propulsion equilibrium, not considering the engine loading limitations (torque limiters) and specific responses.

A decision support tool for the configuration of the optimal engine and propeller for a VLCC tanker is presented by (Hiekata, et al., 2015). A comprehensive model for simulating the propulsion plant performance coupled with the hull and propeller under a self-propulsion state is integrated, while uncertainties are introduced with regard to the oil price under a market projection model, using a Monte Carlo simulation. A linear regression model is used for the correlation of the average spot oil price to the Worldscale Flat Rate (WS) for tankers for the trade route examined.

An alternative approach to tackling the method uncertainty (apart from error modelling from existing vessel data) would be of optimizing the margins used in the design process. (Meyer, 2002), propose such an approach for the weight estimation of a naval vessel. Similar numerical methods to handle approximate values and relationships as well as to define design margins applied for the case of a bulk carrier can be also found in (MacCallum & Duffy, 1989).

Interestingly, no existing method considers the uncertainty of the acquisition and disposal costs both of which play a pivotal role for the RFR as well as other econometric values such as the Internal Rate of Return and Net Present Value. Furthermore, the charter market volatility and its effect on a vessel's profitability is rarely addressed. With the exception of the state-of-the-art hydrodynamic optimization studies mentioned above (Campana, et al., 2015), uncertainty considerations are usually included in simpler models with little or no geometric core and lower-fidelity calculations aiming at the generation of very large numbers of variants.

2.5. Holistic Ship Design and Optimization

Holism, originating from the Greek word from ὅλος (meaning all, entire, total), is the philosophical notion that all the properties of a given system (biological, chemical, social, economic, mental, linguistic, etc.) cannot be determined or explained by the sum of its component parts alone. Instead, the system as a “whole” determines in an important way how the parts behave. Aristotle in *Metaphysics* (H-6, 1045a8–10) (Aristotle & Ross, 1981) examines the problem of the unity of definition and offers a new solution based on the concepts of potentiality and actuality. He begins by pointing out that the things whose unity he is trying to explain are those “which have several parts and in which the totality is not, as it were, a mere heap, but the whole is something besides the parts”. Although the concept of holism was pervasive, the term holism, as an academic terminology, was introduced by the South African statesman Jan Smuts in his 1926 book, *Holism and Evolution* (Smuts, 1927) which defined holism as “*The tendency in nature to form wholes that are greater than the sum of the parts through creative evolution.*”

From a historical view, the various generations of ship design optimization models that entail holistic approaches as well as their historical evolution have been recorded by Nowacki (Nowacki, 2019). According to this analysis, the pivotal point for the growth in terms of scope and depth of the ship design and lifecycle analysis in the 1960s, with four distinctive models. Originally synthesis models appeared such as these in (Murphy, et al., 1965), (Mandel & Leopold, 1966), (Nowacki, et al., 1970) and (Söding & Poulsen, 1974) among others. Synthesis models had principal dimensions, size and speed as design variables (in most cases not inherently linked to a geometric core) with a few constraints and the optimization target being solely economic criteria (RFR, LCC, NPC etc). The design engines utilized in these models were gradient-based and direct search methods primarily. At the beginning of the 2000s, the first Risk-Based design optimization models such as (Papanikolaou, et al., 2010) and (Vassalos, 2009), appeared with applications on RoPax and cruise vessels as well as tankers. These methods targeted the safety (primarily) and economics criteria as well as that of environmental performance with design variables that apart from the principal dimensions included also the vessel’s geometry (parametric geometry core) with multiple constraints and design engines expanded also to Pareto Optimization tools, graphical visualization techniques and utility functions. In parallel, in the early 2010s Multi-Objective models (e.g. (Papanikolaou, et al., 2010b)) also appear with similar characteristics as the Risk-Based but expanded with a focus also on economic performance and with a more global approach. The introduction of Holistic Ship Design Optimization, which is the core and basic notion and principle of the present Thesis, appears in 2010 as introduced in the keynote paper (Papanikolaou, 2010). In this paper, the generic ship design optimization problem is defined and presented in its holistic nature. The typical process flow of computational methodologies for performing all the necessary computations included in the different design aspects is also defined. Typical holistic optimization examples are afterwards presented including the hull form optimization of high-speed vessels with respect to powering and wash as well as the Optimization of Ro-Ro passenger ships for enhanced safety and efficiency. After a decade of development, in Papanikolaou (Papanikolaou, 2019), the holistic ship design optimization is defined as the “mathematical understanding of exhaustive multi-objective and multi-constrained optimization procedures with *least reduction* of the entire real design problem”. The optimization

in holistic ship design is considered in Papanikolaou (Papanikolaou, 2019) as the design space exploration through variation using Multi-Objective optimization engines (most notably genetic algorithms) and the Pareto-optimal design identification and selection with the use of a utility functions technique. This technique is the basis for the optimization of large scale, non-linear design space problems with several criteria and requirements (that are often contradicting). This technique has been realized in Papanikolaou (Papanikolaou, 2019) in a number of instances and within the different design and optimization packages such as NAPA[®], CAESES[®] and modeFRONTIER[®]. The applications range from hull form optimization of twin-hull vessels and wave-piercing high-speed vessels focusing on the least calm water resistance and seakeeping performance (Papanikolaou, et al., 1996), (Papanikolaou & Daphnias, 1998) to logistics-based optimization of ship design for RoPAX ferries (Brent, et al., 2006), many studies on Risk-Based optimization of oil tankers (Papanikolaou, et al., 2011), parametric optimization of RoPAX ferries and cruise ships with a focus on damaged stability (Zaraphonitis, et al., 2013) & (Zaraphonitis, et al., 2012), parametric optimization of containerships focusing on efficiency and minimum ballast water requirements (Koepeke, et al., 2014) as well as parametric optimization of various ships types for minimizing the attained EEDI and optimal manoeuvring characteristics (Zaraphonitis, et al., 2016).

A notable example to be further elaborated as the current state-of-the-art in Holistic Ship Design is that of Risk-Based design and holistic optimization of tanker design. The publication of (Papanikolaou, et al., 2010), is a product of the TANKOPT research program which was the first out of a generation that aimed at the systematic, Risk-Based Optimization of AFRAMAX tankers (Papanikolaou, et al., 2007), with emphasis on the cargo-carrying capacity, steel weight and accidental oil outflow. A software developed by NTUA-SDL integrates the following packages: NAPA[™], a naval architectural software, POSEIDON[®], a structural design and analysis software developed by GL and modeFRONTIER[®], a general optimization program. The design optimization objectives include the maximization of the cargo capacity, the minimization of the accidental oil outflow parameter (MARPOL Annex I Regulation 23) and the minimization of the structural steel weight in the cargo area while maintaining the IACS Common Structural Rules requirements. From the publication's figures, it is concluded that «6X3 flat» Pareto designs dominate all the other, while there are several Pareto fronts with significantly better oil outflow and cargo volume performance than the reference design used. The multi-criteria decision-making problem is tackled by using utility functions to represent all three design objectives with the respective weights first being taken equal and then following different scenarios for their distribution. The same design concept and computational methodology has been further refined and evolved in (Sames, et al., 2011) and (Papanikolaou, et al., 2011), which is a product of the BEST+ research project, with the hull form modelling and methodology software being developed in Computer-Aided Engineering software CAESES[®] (then Friendship Framework[®]) software. Furthermore, the optimization engines offered by CAESES[®] have been used instead of the integration of the modeFRONTIER[®] software. The optimization is based on developed parametric models for the hull form, hull layout and hull structure. The optimum design with respect to the cost of transport was used as a starting point for the final hydrodynamic optimization of the aft body, addressing the quality of the wake field and propulsive efficiency as objectives. The oil outflow index is 9% lower than required by MARPOL, the EEDI is 16% lower

than the current reference line and the cost of transport is 7% lower compared to a reference design.

The above work is also expanded under a different scope in Nikolopoulos (Nikolopoulos, 2012), where the same computational framework is further refined based on updated parent twin skeg hull data and the case study of an innovative AFRAMAX tanker is studied.

Applications of holistic ship design optimization principles applied for container vessels by using a fully parametric hull surface modelled in CAESES® coupled with NAPA for compartmentation can be found in the studies of (Priftis, et al., 2018) as well as the previous studies of (Soulтанias, 2014), (Koutroukis, et al., 2013) and (Nikolopoulos, et al., 2014). The subject model was originally developed for the parametric design and optimization of a novel containership with an ellipsoidal midship section in Koutroukis (Koutroukis, 2012) and is based on the same principle of parametric design and optimization as the tanker optimization studies previously presented.

The HOLISHIP research project achieved a substantial advance of ship design through an integrated design software platform considering all ship design aspects. The key steps and updates are described in (Marzi, 2019). A new synthesis concept applied in the design process is considered in the form of a global control system allowing the flow of information from one system or design discipline others actuating the respective changes and updates and ensuring compliance with all the relative constraints. This platform has been realized in the CAESES® software environment which tightly combines Computer-Aided Design (CAD) and Process Integration and Design Optimization (PIDO). The platform as depicted by (Harries & Abt, 2019), is based on 5 distinct capabilities: Variable Geometry, Pre-Processing, Simulation, Post-Processing and Optimization and assessment, making it a good candidate for providing a basis for both holistic ship design studies due to its integration capabilities as well as simulation-driven design and optimization. Within HOLISHIP the CAESES® integrations are task-specific as any integration can start loosely and grow in stages with the increasing complexity of the system. The CAD functionality is retained within CAESES, a watertight tri-mesh of the hull is then transmitted to the HSVA *FreSco*⁺ code for the viscous flow simulation and total resistance and power estimation. The seakeeping behaviour is assessed by the NTUA code NEWDRIFT+, while intact and damaged stability by NAPA®. Other integrations include the steel structure modelling by the BV code MARS2000® as well as some low-level cost computations within CAESES®. The modelling and data management in CAESES® is done with an object-oriented view, allowing the attribution of values to parameters without set commands and constraints.

Another HOLISHIP project application can be found in (Harries, et al., n.d.) The holistic platform developed hosts tools from several disciplines including (among others) the Main dimensioning, lines and body plan development, hydrostatics, floodable length and freeboard, arrangements, structure, resistance and powering, lightship weight, capacities trim and stability, damage stability and cost estimates. For the coupling of tools, a novel approach has been used where rather than presenting the entire set of options that expert tools usually provide, technical APPs (short for applications) are configured such that a meaningful sub-set is made available for dedicated use by a wider audience, making the model preparation less time consuming and more efficient. In addition to technical APPs, the usage of surrogate models for the computationally intensive parts of the model is accelerating the design optimization procedure.

Surrogate models are derived from simulation tools that can run from CAESES separately and upfront to be subsequently replaced by a suitable response surface with a variety of methods such as Artificial Neural Networks, polynomial regression and Kriging. Most notably in their publication, surrogate models are used for calm water resistance prediction using RANS simulation results of the nu-Shallo and FreSCo+ codes of HSVA for the viscous, frictional and wave-making resistance and the added resistance prediction in waves using the NTUA Newdrift code. The application of this platform is intended for the design optimization of a RoPAX ship for short-sea voyages. CAESES is used for the hybrid modelling of the parametric ship surface with the shape being controlled with key parameters that are meaningful in the concept and pre-contract design stages. A NAPA model of the watertight subdivision of the parent vessel parametrized to enable variation is used for the stability and subdivision calculations, as well as all arrangements modelling and the preliminary calculation of the lightship weight. Surrogate models are also used here for the creation of non-linear regression models for predicting the SOLAS 2009 Attained Subdivision index. For the optimization stage, a compiler was introduced to convert a set of design equations, functions and calculation results into a non-linear optimization problem. Several optimization studies are conducted, beginning with a design space exploration using SOBOL, NSGAII and TSearch single objective algorithms with different objectives at each stage focusing on the maximization of the transport capacity and minimization of EEDI. In the above approach, the simulation for the power prediction is focused only on two design speeds and doesn't take into account the actual speed profile of the vessel. Furthermore, the uncertainty is not modelled either in terms of operating conditions, prevailing weather or economic environment but only the prediction error of the methods employed. This paper and relevant research are further elaborated by (Marzi, et al., n.d.), utilizing the same platform and setup but with additional optimization runs both using a Design-Of-Experiment (DoE) with the Sobol algorithm as well as with formal, global optimization runs with the NSGAII algorithm.

An interesting application of holistic ship theory in the ship design process is that of the optimization in the earlier, pre-contract ship design stage, commonly known as the tendering process as described in (Zaraphonitis, et al., 2019). The tool adaptation in the large scale, global optimization of a ROPAX ferry is studied.

A vital aspect of any holistic platform is that of the Life Cycle Design assessment of a vessel. The methods for such assessments are presented in (Maggioncalda, et al., 2019). In this context, a Lifecycle Costing (LCC) and Lifecycle Assessment module are developed. The costing methods can be either analogous estimation, parametric or bottom-up estimation depending on the available data. The KPIs selected in that study for the cost assessment are comprised of the Building Cost derived from Cost Estimation Relationships (CERs), CAPEX based on building cost (and not acquisition cost as done in real financial shipping valuations), OPEX, Maintenance and Repair costs, Average Annual costs in the form of a regression formula, RFR, NPV, Average annual Benefits, EBITDA and Return on Investment Capital (ROIC). Furthermore, environmental KPIs such as emissions (NO_x, SO_x, and PM), the IMO EEDI and cumulative energy demand are used. Although the above constitute a thorough approach it is rather a superficial one given that the hull degradation due to biological fouling is not taken into account in the lifecycle costs assessment, equipment degradation due to ageing, the Dry Docking and Special Survey costs are also neglected and furthermore all CAPEX are based on approximated Building costs instead of

acquisition cost. Such an approach cannot depict the volatile market conditions and thus the robustness of the produced/assessed designs is not properly evaluated.

The virtual prototyping and vessel simulations within a holistic ship design framework are discussed by (Flikkema, et al., 2019). The existing literature and industry gap according to this publication is the platform for information exchange between the different simulation tools (calm water, seakeeping, manoeuvring, structural etc). To cover this, a “Remote Component Environment (RCE)” is proposed which creates distributed workflow solutions even between servers of different companies collaborating on a common project. The RCE nodes exchange information based on Common Parametric Aircraft Configuration (CPACS) XML scheme. Their target is to adapt the latter within the EU HOLISHIP project for use in the marine environment. Within this direction, a concept testing demonstrator named HOLISPEC is being developed. For the demonstration case, a hydrodynamic manoeuvring behaviour high-fidelity model is coupled with a resistance and propulsion medium-fidelity model, a high-fidelity steering gear response mode, a medium-fidelity main propulsion engine model and a high-fidelity bridge simulator. Very interestingly, within such an environment the vessel’s operation can be simulated with a reasonable fidelity for the purpose of design verification and expanded also to optimization. However, such an expansion to design studies, although feasible is not presented or planned in their paper other than the planned development of virtual vessel sea trials. Additionally, lifecycle and uncertainty considerations are not taken into account.

Based on the above, one could argue that the Holistic Ship Design optimization is the expansion of “Design for X” into multiple dimensions for all critical systems and aspects of the vessel’s design. Rather interestingly, a common gap of all ship design models aimed at lifecycle assessment is the lack of the simulation of the vessel’s operation under real operating conditions. The gap remains not well studied in the literature with only specific attempts focusing on the simulation tool itself rather than its integration and effect on Ship Design.

2.6. Application of Simulation Methods in Ship Design

Within the direction of simulation in early ship design, (Tillig, et al., n.d.) propose a generic ship energy systems model that can predict the ship’s energy consumption during different operational conditions. The model proposed is intended either for the early ship design process with little data input or for the operational analysis of an existing vessel where an assessment of system modifications or other improvements is the purpose with a considerable number of available data for input. The model is divided into static and dynamic parts. The static includes the wetted surface, wind resistance, calm water resistance, propeller curves calculations along with engine data while the dynamic part utilizes the output of the static part for simulation in the time domain. The simulation part also includes the method from the assessment of the added resistance which is a very simple approximation using the ITTC method for wave heights smaller than 2m and the wind resistance with Blenderman’s formula which is considered outdated for modern commercial designs. An important part of the simulation model is the “cruise control”, namely the control of the speed and RPM when in a seaway with four options, target speed, target average speed, fixed throttle and target power. Although a quite smart approach from onboard experience only a constant RPM approach should be followed as the accelerations and constant RPM fluctuation due to environmental conditions for other options will have a negative impact

both on fuel consumption (due to acceleration effects) as well as engine fatigue and increased maintenance which are not depicted by the method. For the dynamic operational analysis, an artificial Atlantic route of 3000 nm was used with an assumption on the wave height and wind loads. The weather was kept constant but the speed profile was varied to four different settings. However, no uncertainty either in terms of weather or speed was modelled and the speed setpoints were arbitrarily set not being a product of actual operational profile analysis. The constant speed approach was the only technically feasible part of the model used. No information is given and assessed for auxiliaries such as diesel generators, boilers and auxiliaries. Furthermore, the time allocated for manoeuvring, cargo handling and cargo-related activities (COW, stripping purging, gas-free etc) is not taken into account. The design optimization undertaken is very simple, with two approaches followed one under a constant displacement and one with a fixed block coefficient, both of which are important variables for the early design optimization. The lightship model prediction is based on assumptions from the simplest empirical methods. Furthermore, there is no sensitivity regarding the changing engine model (1 cylinder more for some optimization variants) as well as changing ship dimensions. Lastly, a fixed sea margin approach is followed for the Main Engine instead of applying a probabilistic approach. Overall (Tillig, et al., n.d.) propose a very novel method for integrating simulation in the early ship design process, which however lacks depth in several subcomponents models, has no uncertainty modelling and the data used are arbitrarily assumed and does not a result of actual operating data or relative analysis.

This simulation tool is further elaborated in Tillig and Ringsberg (Tillig & Ringsberg, 2018) and applied for the assessment of the potential savings of sail-assisted vessels (e.g. utilizing Flettner Rotors).

In their paper (Ferrante, et al., n.d.), present the addition of a tool providing simulation capability for the early naval ship design. More specifically, they developed Smart Ship Systems Design (S3D) to work as a plug-in for the US Navy Leading Edge Architecture for Prototyping System (LEAPS) tools used in the early design stage of naval ships of the US Navy. The S3D is a collaborative environment allowing the interoperability of multiple simulation tools while it allows depicting concurrently information exchange between all the different shipboard systems during preliminary ship design and the variations in the various arrangement the latter means. It includes analytical, modelling and visualization tools that provide a common vision for the product under design across disciplines. Furthermore, it includes a database of product information and an expanding library of component models that can be used to assemble complex power, cooling and mechanical system models. The key to the system is the concurrent and collaborative nature of the tool and its ability for supporting distributed and eventually parallel simulations executed. As result, when an engineer makes modifications to the design all essential information is propagated to all users currently connected to the S3D environment allowing the entire team to work together in real-time and directly see the impact changes to the design have on the performance of all ship systems. This makes it an ideal tool for the detailed, rather than preliminary design stage and especially for complex applications such as Naval ship design. Furthermore, the simulation is tangible with regards to the information exchange between different systems and real-time updates rather than the simulation of the vessel's operation over its lifecycle under actual conditions.

The paper of Alwan (Alwan, n.d.), discusses the use of a simulation-based ship design framework to support early design decisions. An event-based simulation model is utilized in order to reduce the simulation cost using an event-based operational profile instead of time-domain simulation of vessel operation, using discrete event simulation for analysing system performance. The method starts with a set of possible solutions for the vessel's main dimensions, hull-form and machinery. Weather data is extracted from coordinates along the routes using the metocean model which produces probability distribution functions of weather patterns. The calm water resistance is calculated using the potential flow solver XPAN of Shipflow for predicting the wave pattern and the ITTC 1957 method for the frictional resistance. The added resistance is evaluated using the Gerritsma & Beukelman's method or Faltinsen's pressure integration method after solving the seakeeping motions problem with ShipX software using strip theory. The propeller is a Wageningen series propeller while the engine behaviour is simulated with a theoretical Mean Value Model adapted for Marine Engine applications. However, there are no applications of the methodology mentioned, there is no mention of the geometric core and parametric hull model utilized (if any) as well as the scope of the optimization that can be undertaken, such as range of design variables, constraints as well as the relative results.

A quasi-static discrete-event simulation model to replicate and assess the voyage of a general cargo vessel is proposed by (Sandvik, et al., 2018). The methodology follows the route of a parent vessel from which "real-time" data of 15-minute intervals have been obtained for one specific voyage. The approach is under a constant speed policy under the assumption of additional power to maintain ordered speed. The added resistance is calculated by using quadratic transfer functions by pressure integration method on the linear frequency domain strip theory seakeeping program ShipX, while the hindcast data from ECMWF ERA 50 catalogue are used for replicating environmental conditions. Results indicate an overestimation of the added resistance and considerable underestimation of the fuel consumption as the simulation module uses the reference shop tests of the vessel for the consumption calculation. When taking into account that the guaranteed SFOC in the shipbuilding specification and Shop Test SFOC curve have a 5-10% deviation from the actual measured onboard during sea trials one can fully justify the 30% deviations identified on an existing vessel. Additionally, (Sandvik, et al., 2018) don't take into account the new self-propulsion equilibrium the vessel reaches when in a seaway.

Within this scope, (Hassani, et al., 2016) study the virtual prototyping of an offshore supply vessel, where a digital twin is being produced capable of providing numerical simulation results regarding the hull resistance, dynamic positioning as well as the propulsion plant including the propeller, engines, and bow and stern thrusters. The simulation results indicate that the Dynamic Positioning Controller module can be further improved. The philosophy of such an approach is useful for integrating it within the preliminary design stage.

A relatively accurate vessel operational simulation tool is proposed by (Lorkowski, et al., 2018). Their approach is a goal-based application that under proper statistical modelling as well as data from high-fidelity computations and experiments is applied for the operating speed optimization for a RoPAX ferry. An interesting aspect of their approach is the use of probability density functions (PDF) in order to handle uncertainties with regards to various operating parameters of the vessel such as Displacement, Speed as well as prevailing environmental conditions. The simulation model accurately depicts all modes of resistance, including added resistance due to

wind (derived from wind tunnel tests) and added resistance due to waves derived from strip theory with the Faltinsen short wave correction formula. The shallow water effect as well as the fin stabilizer and rudder resistance are assessed from available experimental data of the parent vessel. A tangent search algorithm is used as the optimizer of the optimization problem, while the Life Cycle performance of the vessel at the selected speed is assessed by the LCPA tool. What is not taken into account during this analysis is the hull – propeller – engine coupling and interaction with regards to the position of each selected speed at the engine loading diagram as well as the effect of fouling on the lifecycle performance assessed.

Another simulation tool that can be also used within a design framework can be found in (Lu, et al., 2015) which is used within the context of optimal vessel routing. The model developed utilizes the Holtrop and Mennen method (Holtrop & Mennen, 1982) for the calculation of the calm water resistance and the Kwon method (Kwon, 2008) for predicting the speed loss of a displacement type ship due to added resistance in irregular waves and wind. The Kwon method has been modified by creating unique direction reduction coefficients and ship form coefficients for each specific ship type and size examined based on onboard measurements as recorded in Vessel Noon Reports. The correlation of the finalized vessel speed (considering the speed loss due to waves) with the required engine power is done through the speed power curve from the Sea Trials of each specific vessel. This might be valid as an approach when examining the performance of existing vessels however cannot be used within design frameworks as the hull-propeller interaction and the new operating point of the propeller in the self-propulsion equilibrium are not considered. A grid system on the map is also set up in order to identify the number of legs and stages of each voyage simulated each one determines with specific voyage data. The key performance indicator used for the assessment of the vessel's performance is the Energy Efficiency Operating Index (EEOI) as calculated from simulated data. The code has been applied for the case of a Suezmax and an Aframax oil tanker. The average difference of the calculated EEOI from simulation versus the equivalent EEOI calculated from actual data is around 5% and 7% for the case of the Suezmax and Aframax tankers respectively. At a second stage, the Authors attempt to correlate this EEOI prediction error to the hull roughness degradation due to biological fouling as well as the degradation of the Main Engine condition resulting in increased fuel consumption. Although the trend shows a distinctive linear correlation between the months after dry-docking and the prediction error in the relevant plot, it should be noted that the calibration undertaken for the Kwon method possibly distorts this kind of correlation. Furthermore, the hull fouling prediction should be also examined together with the propeller-delivered power which in this case is not possible.

2.7. Application of Surrogate Models in Ship Design

Surrogate models, more commonly referred to as response surface models, metamodels or emulators are mathematical formulations that mimic the behaviour of a given high-fidelity simulation model allowing the extrapolation and assessment of simulation results with different input with a significantly lower computational cost. They are constructed using a data-driven, bottom-up approach with common types of models being response surfaces, Kriging surfaces, Gradient-Enhanced Kriging (GEK) models (Bouhlef & Martins, 2019), radial basis functions,

support vector machines (Loshchilov, et al., 2010), space mapping and artificial neural networks depending on each application. Surrogate models are nowadays commonly used for shape optimization and general optimization studies where high-fidelity simulation results are necessary as depicted in (Chen, et al., 2015), (Peri & Tinti, 2012) as well as (Demo, et al., 2018). Another common application is the aerodynamic design of airfoils as can be found in the literature by (Umetani & Bickel, 2018), (Li, et al., 2018), (Yondo, et al., 2019), (Iuliano & Quagliarella, 2019) and (Cinquegrana & Iuliano, 2019).

A simplified example of the use of surrogate models for the optimization of hull forms within the early ship design stages is proposed by (Yan & Huang, n.d.). In their paper, they propose a method that utilizes a parametric NURBS hull model developed in NAPA for the Series 60 hull and coupled with a hydrodynamic and optimization module. The Radial Basis Function (RBF) is used for the generation of the 6 in total surrogate models (3 optimization cases at 2 different design speeds each) while for the optimization an artificial bee colony algorithm is used. The optimization problem on its own is highly constrained neither allowing any principal dimensions change nor any decrease in the displacement resulting in changes only in the local hullform parameters and the use (or not) of a bulbous bow. In case of inaccurate results, a simplified CFD (potential flow code) or RANS code are utilized in terms of the total resistance calculation. However, from the cross-validation of the surrogate models developed, good agreement is observed between the surrogate model solution for the total resistance versus the results of a simplified CFD calculation. However, for cases of ships with bulbous bows from the presented authors' diagrams, the scatter and standard deviation is higher but nonetheless acceptable for the scope of preliminary studies.

Another very good example of the use of surrogate models in ship design is contributed by (Guerrero, et al., n.d.). In their paper, they examine the optimization of the design of a vessel's bulbous bow with regards to resistance minimization with the use of surrogate models based on results of viscous flow RANS computations in OpenFOAM with $k-\omega$ SST turbulence model setup and the solver being validated against model test results for the parent hull. A "single input" parametrical model of the hull geometry defined by fixed global dimensions and characteristics is used with shape variation being limited only to local shape manipulation and variation with the use of Radial Base Functions (RBF). Control of surface C2 continuity is limited and the hull surface is of basic geometry.

What is significant in the research of (Guerrero, et al., n.d.) is the systematic approach they propose for the generation of surrogate models that will be used for interpolating results of analytical data. A sampling plan that covers the predefined design space in a uniform way is necessary. Based on the sampling plan points high fidelity simulations are conducted to create a pool of analytical results. The surrogate is then validated by performing a high-fidelity computation on a point that doesn't belong in the original sampling plan points and comparing the computation versus the interpolation results. The basis of this validation the surrogate model can be further trained and prediction errors estimated. For their study the Kriging interpolation method requiring due to the presence of numerical noise the use of derivative-free methods for optimization. For the optimization, the Dakota toolbox was used enabling users to have access to any optimization method available. The optimization target is the minimization of the total resistance of the vessel by alteration of the bulbous bow shape. Within this context the assumption

of fixed Trim (no dynamic sinkage taken into account) is made, the assessment is performed for only one operating point (one Froude Number) and only two design variables for the bulbous bow. For global and local minima, the reduction of the resistance is at the level of 7% with an accuracy of 2%. However, there are cases where there is a reduction of resistance at the region of 5% with a percentage error of 7%. Such solutions are a result of non-linear phenomena according to the authors. In addition to subject runs, the surrogate model was improved with the addition of new data points from high fidelity calculations (CFD in this case). From illustrations of the resulting dominant variants, the optimization algorithm pushed for a very slender bulbous bow with construction limitations.

An interesting application of surrogate models for calm water and seakeeping prediction in the early ship design stage is proposed by (Couser, et al., n.d.). A general hull-form of a mega-yacht was taken as the design basis without appendages. The model was parameterized in CAESES so that the geometry could be manipulated by a small number of free variables of the n-dimensional design space investigated. The bare hull resistance (no propulsion calculations) was calculated by potential flow theory within the SHIPFLOW package which is tightly integrated into CAESES, however similar studies with RANSE have been also made. The vessel motions due to waves were predicted using SEAKEEPER, a linear strip theory method for two scenarios (zero speed, and ahead speed of 16kts). The Hydrostatic Stability criteria were assessed by HYDRMAX and basis on the Large Commercial Yacht Code requirements. All external software used (SHIPFLOW, SEAKEEPER, HYDRMAX) are tightly integrated within the CAESES platform. The design space was investigated using a "Design of Experiments" approach to populate the domain with variants. The n-dimensional design space (in the present application 9-dimensional) was then captured by the use of n-dimensional response surfaces fitted using a Kriging approach. With the response surface generated, the interpolation can be instantaneous and with the use of iso-surfaces and iso-curves, the designer can depict all the sensitivities as well as correlations of the different design variables with objectives within the design space for future use.

The use of response surfaces has been studied also by (Harries & Abt, 2019). The design space investigation comprises 3 main tasks: the definition of a suitable parametric model to generate feasible design variants from a few key parameters, the numerical analysis of the vessel with simulation tools and the automation of vessel design variation, analysis and post-processing. The parametric hull is generated from Friendship Framework, SHIPFLOW performs calm water resistance prediction and Seakeeper the seakeeping and stability calculations. The test case for which the response surfaces were generated was a megayacht hull with twin screw and bulbous bow, without including the appendages in the model. The variant generation was done with the Sobol algorithm producing approximately 200 variants. In a meta-model, n-dimensional response surfaces with Kriging's approach were generated. After the generation the practically instantaneous interpolation and thus calm water and seakeeping prediction is possible. In the same study, correlation plots were also generated which can be used as design guidelines.

Other applications of surrogate models in marine design can be found in Ship Structural analysis within the study of (Prebeg, et al., 2018), utilizing a full quadratic response surface model to interpolate the results of internal energy absorbed by a ship structure during collision resulting from analytical FEM calculations.

2.8. Application of Big Data in Ship Design

Big Data refer to the amount, latency (time to store or access data) and structure of the data available to be analysed. As there is pressure for the digitalization of shipping operations and management, the amount of data from monitoring onboard sensors is increasing continuously. (Nakamura, 2015), propose a structure for the use of Big Data Centres by classifications societies, providing feedback to shipowners, shipyards, designers as well as equipment manufacturers. The use of Big Data for shipping operations and management is discussed by (Belanger, et al., 2018). They examine the challenges of sensor technology and data harvesting onboard commercial vessels as well as examples of the typical data sources onboard, how they can be used, their entity relationships as well as methods of data processing.

Within the design field, an interesting application of digital twin technology and harness of big data was presented by (Bekker, 2018) during the 2018 IMDC. A polar supply and research vessel to be deployed in arctic areas is used as the testbed for the application, with a wide array of full-scale measurements utilizing high fidelity sensors such as camera footage, ice cameras, accelerometers, strain gauges etc as well as AIS data. The parameters will assess MSIs, Human Responses to wave slamming, vessel rigid body motions, flexural modes, ice loads on both hull and propellers as well as environmental conditions. The project at the time of the writing is under implementation, so no data or analysis is yet ready.

An example of the application of statistical methods to onboard data for power prediction is examined by (Manderbacka & Haranen, 2018) with the fitting of a non-linear regression model to high-density onboard measured data. The independent variables of the model chosen are engine RPM, rudder angle, draft and trim as well as environmental conditions such as weather and swell conditions, shallow water and seawater temperature. The hull fouling is included in their model as an effect of time by adding the time variable into the set of independent variables. The effect of fouling can be therefore assessed as a conditional expectation of the propulsion power and speed through water for different time stamps assuming all other independent variables remain constant. Their model is trained each time new data are received and the marginal effect of all independent variables on the model response. Each dependent variable is modelled by a Generalized Additive Model with most terms are set to being polynomial functions, while the time-dependent term is a smoothing spline. The regularization is done by a cross-validation technique aiming at the minimization of the Mean Squared Error of the model prediction over the testing data. The model is applied to a fleet of two VLCC tanker sister ships. By keeping all independent variables constant and monitoring the trend of one, the effect of wind, swell and cross swell can be independently assessed as well as the hull fouling effect. From the visualized data results appear to be rational.

The reliability and accuracy of the ship performance extrapolation are discussed by (Bose & Molloy, 2009) and can be used as a reference when benchmarking big data against model tests, sea trials and onboard measurements. Similarly, the uncertainties entailed in ship performance monitoring are investigated by (Aldous, et al., 2015) where a time-domain algorithm used to simulate the ship's operational profile and performance trends are utilized in order to propagate the errors through Monte Carlo simulations. A "Guide to the expression of Uncertainty in Method (GUM)" framework approach is used for identifying the sources of uncertainty and classifying them, assigning probability distribution and their parameters and propagating the errors through

linearized models, concluding the output distribution of the result and report on overall uncertainty. The actual power is used to define the underlying ship performance with the assumptions of displacement (time in ballast and laden voyages respectively), environmental conditions (wind and waves), as well as time-dependent degradation of the hull and machinery (linear time-dependent assumption). The average actual power/speed/draught are estimated by averaging frequency, and the measured power is recorded by taking also into account the instrument uncertainties. The expected power is then reverse calculated with the addition of model uncertainty in random samples assigned from the assigned pdfs. The power difference is then assessed and done repeatedly in order to define the parameters, mean and standard error of the probability distribution function of power increase. A comprehensive tree is constructed for analysing all the different sources of uncertainty in ship performance monitoring ranging from model uncertainty, human error in measurements, instrument uncertainty as well as sampling error. A sensitivity analysis is then conducted with interesting results indicating that the highest sensitivity index lies in the precision of speed measurement, model and draught measurement precision.

A novel approach to handling big data originated from onboard measurements can be found in (Tsitsilonis & Theotokatos, 2018) which is also used in parts of the subject Thesis. Their proposed methodology is systematically addressing the vessel's main energy management by integrating a number of state-of-the-art tools in five distinct phases with each of the phases having several stages. The first phase is that of Data Collection which is comprised of the collection of the Required Monitored Parameters (RMPs) onboard either on a Noon Report or Automatic Continuous Logging basis along with the establishment of baseline data and acquisition of miscellaneous other data for gaining insight in the Main Engine operation. The second phase is the preliminary analysis of the data acquired being done in two steps: first the identification of missing RMPs and secondly the correction of RMPs in accordance with ISO standards and maker guidelines. The third phase and most important is the data analysis in four stages. Statistical analysis is firstly employed using an empirical formula for determining the data corresponding to steady-state operation under the assumption of a 5% slope of load variation in order to avoid transient phenomena of engine and propeller acceleration. Based on this the engine power and engine speed data are split into smaller data set on a per-voyage basis fitting propeller curve function for each data set. The fit follows the well-known propeller law with minimum R^2 values as acceptance criteria and for rendering the propeller curve function manipulation easier the propeller law is linearized by its transformation to a first-order polynomial by considering the natural logarithms of the two-equation components. The Most Frequent Occurring (MFO) propeller curve functions can now be formulated by considering the integral and distance parameters. These are treated as random variables and their PDFs are approximated by a Gaussian Kernel Density Estimation (KDE). In case the difference between two adjacent MFO propeller curves is lower than 5% of the MCR of the Main Engine then the two data sets are merged and a single MFO propeller is fitted. The categorization of the engine power and engine speed to subsets each corresponding to the respective MFO propeller curves leads to establishing the Most Frequent Occurring main engine loads. The quality of fit is assessed by the mean and standard deviation of the quality of the fit vector. The next stage of this phase includes the quality assessment of the RMPs corresponding to the steady-state engine operation (except engine RPM),

the indices of the engine power data corresponding to each MFO propeller curve, the sensors uncertainties and the load where the engine auxiliary blowers are activated/de-activated. After that, the air mass flow rate (through modelling of the turbocharger compressor) is predicted as well as the input data for the energy and exergy analyses. The fourth phase and fifth phase phases include the Energy and Exergy analyses and Energy-saving initiatives assessment which are outside the scope of the current literature survey. However, the first three phases of data analysis, filtering and smoothening are considered a basis for extracting value from big data derived from onboard automatic real-time measurements and their editing into best fits that can be used for producing PDFs for the operational profile simulation as discussed in later chapters.

2.9. Research Gaps

From the above review the following gaps in contemporary literature and research have been identified:

- Real-Time Simulation

The use of real-time dynamic simulation of the vessel responses considering actual wind, waves, currents have been considered. However, such approaches as previously explained follow are “decoupled” from the propeller and Main Engine. More specifically, the actual operating point of the propeller and shift of self-propulsion equilibrium and advance coefficient are not considered in applications that try to introduce voyage simulation in Ship Design Optimization. Furthermore, the codes are static and don’t follow an approach of voyage legs and dynamic conditions but instead use a more static calculation.

- Use of actual operating data in the design process.

In all the presented literature and current State-of-the-art research presented in Chapter 2, there is no consideration of the actual operating speed. Instead, all current research focuses on the use of either a nominal speed (typically at the Nominal Continuous Rating (NCR) of the Main Engine) or a range of adjacent speeds close to the latter. The analysis of actual, “in-voyage” speeds that depend on the leg of the voyage and derived from a form of systematic, statistical analysis haven’t been found in the literature for Ship Design Optimization studies.

- Introduction of a wider uncertainty considerations.

While the uncertainty of fuel pricing has been introduced before, the uncertainty of the freight rate market itself, as well as the uncertainty of the operating speed values and real-time weather coupled to trade route geographical location hasn’t been previously examined.

- Lifecycle and vessel ageing considerations.

Throughout the literature, the vessel’s condition during the optimization studies is considered as “new”, namely corresponding to the nominal condition upon delivery from the Shipbuilders. In the herein presented Research Work the deterioration of the hull condition (roughness), the Lifecycle Cargo Hold paint condition, wastage and maintenance costs (lifecycle OPEX and Dry Docking Costs) have been modelled based on actual data from Shipowners.

- Model Based on a large collection of Construction Data from actual vessels.

The majority of the Ship Design methodologies in the literature are either based on “one-off” case studies of specialist purpose vessels or systematic hull series (e.g. KVLCC2 etc) and baseline vessels that are quite different from the typical commercial vessels (bulkers, tankers, containerships) that dominate the current Global Fleet. Furthermore, naturally, there is no feedback from actual construction drawings to further enhance the level of detail of the model.

This is typically a direction where research on the generation of Digital Twin models is aimed at, however, this is out of the context of this study.

2.10. Contribution to the Area of Research

Based on the above literature survey conducted on the fields of Ship Design Optimization, the herein PhD Thesis topic is on the development and applications of a Ship Design Optimization Methodology that is expanding existing Holistic Ship Design Optimization platforms by the following novel additions, not previously and adequately studied in the literature, as well as their combination:

- Simulation of Vessel's Operation in the Preliminary Design Stage

A quasi-dynamic and a steady-state algorithm are developed for the hourly and minute-by-minute simulation of the vessel's operation for the entire lifecycle based on trade routes and prior analysis of the target vessel operational profile. The codes are validated against actual data acquired from onboard measurements.

- Development of a NEW Holtrop Model and embedding it in the RHODA Calm Water Resistance Module

Actual onboard data along with model test results are used for the calibration of the Holtrop and Mennen Approximate Power method and its integration in the RHODA Calm Water Resistance Module.

- Use of Big Data

Real-time data that have been automatically logged on 30-second intervals for a fleet of sistership parent vessels over a period of 2 years has been matched with high-accuracy weather data for the respective coordinates and analysed. The data are used to create actual voyages scenarios and the statistical analysis of the data provides a measure of the weather conditions uncertainty as well as a base for producing hybrid surrogate models for added resistance.

- Lifecycle considerations

Lifecycle costs such as OPEX, Drydocking and CAPEX costs based on actual operating data from listed shipping companies are parametrized and used for the economic analysis. Furthermore, a novel fouling model able to capture the increase of hull roughness has been developed for quantifying the corresponding added resistance as a function of the Docking Cycle state (years from last dock) and integrated in the simulation code accordingly.

- Robust Ship Design under Multi-Layered Uncertainty

The Design methodology introduces uncertainty in three distinct layers:

1. Environmental and Operating Uncertainty: Probability distribution functions of the prevailing weather conditions (wave, wind, currents) are used in the simulation process, as well as uncertainty regarding the operating speed based on onboard real-time data.
2. Market Uncertainty: The newbuilding acquisition price, the charter rate, profitability, fuel pricing as well as disposal price are modelled in a probabilistic way by the use of cumulative probability distribution functions based on actual market data from 1990 to 2015.
3. Method Uncertainty: The errors and uncertainty of methods used are also considered.

Chapter 3 : A Robust Holistic Optimization Ship Design Approach (RHODA)

The herein presented research work is using the principles of Holistic Ship Theory as defined previously in Chapter 2 with most notable the publication of (Papanikolaou, 2019) in order to derive a Methodology that can be employed for the preliminary design of common commercial vessels (Bulk Carriers, Tankers, Gas Carriers, Containerships etc.), the global optimization studies of concerned vessels as well as the assessment of different technologies, emission abatement measures and operational measures via its simulation module. The target of the methodology is the appropriate early design space exploration by the shipyard and the potential shipowner as well as the establishment of an early-stage simulation tool that with the use of well-established and robust methods can accurately predict the vessel-system responses that are necessary for the evaluation and life-cycle decision making by Owners, Shipyards, Policy Makers and Classification.

The need for a comprehensive, common, concurrent and tightly integrated approach has led the Author to decide to develop the Methodology within the CAESES® CAD/CAE software platform with minimal external software integrations. The big data that have been used for the development of the Digital Twin Model within CAESES have been developed with the use of MATLAB® and the IBM SPSS® with statistical and Machine Learning methods.

The workflow and structure of the proposed Methodology are realized in a design environment structured in accordance with Figure [4]. The process boxes in colour blue correspond to modules of the RHODA design environment that is existing, well defined in literature and available to a user (also in CAESES®). The process boxes in green colour correspond to modules that use methodologies, formulations and equations that are original research work and contributions made under the prism of the herein presented PhD thesis, while orange colour boxes are processes that have used empirical methods from the literature and calibrated them systematically to match available data from drawings. A “helicopter overview” of the process, origins and content of each process module of RHODA is summarized under Table 2.

In Chapter 4 that follows the RHODA processes that utilize existing or variations of existing methods are described and laid down. In Chapter 5, the RHODA processes that utilize Original Research work produced under the current PhD and their validation work are presented.

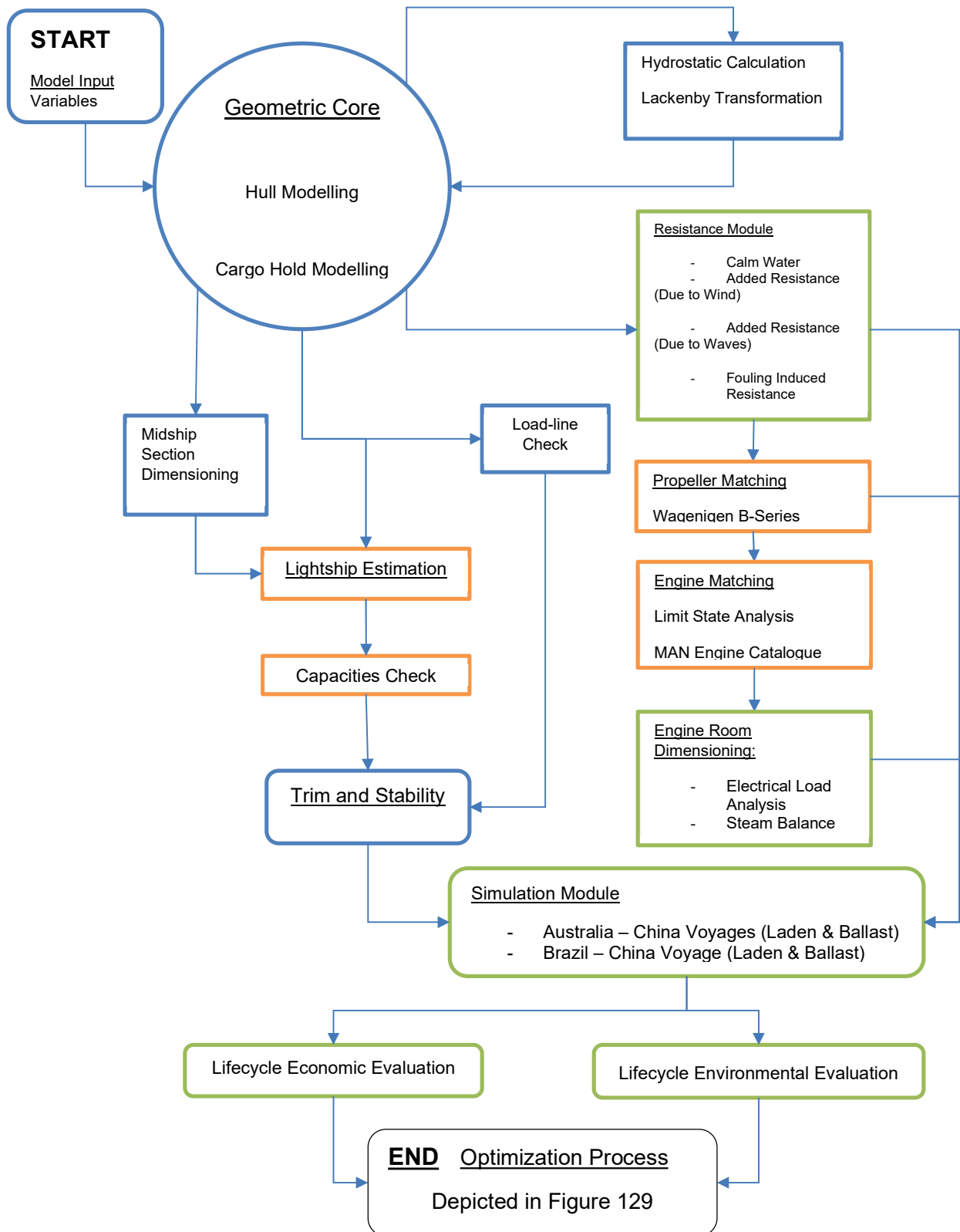


Figure 4: Workflow and structure of proposed methodology in the design environment

RHODA Process	Classification	Methodology
Geometric Core (Hull & Cargo Holds)	Existing Methods/Tools	CAESES ® design environment and Lackenby Transformation for CB determination
Hull Hydrostatics	Existing Methods/Tools	Standard hydrostatic computation setup in CAESES ®
Loadline Check	Existing Methods/Tools	International Loadline Convention 1966
Midship Section	Existing Methods/Tools	Classification Rules (IACS Common Structural Rules)
Lightship Estimation	Calibrated Method with Drawing and Ship Data <i>(digital twin principles)</i>	Schneekluth method calibrated with actual weights shipyard data in newbuilding stage. (Papanikolaou, 2014)
Capacities Check	Calibrated Method with Drawing and Ship Data <i>(digital twin principles)</i>	Various Ship Design literature formulations calibrated with actual weights from parent vessel (Papanikolaou, 2014)
Trim & Stability	Existing Methods/Tools	Standard loading conditions
Calm Water Resistance	Original Research Method	Modified Holtrop and Mennen Method (Nikolopoulos & Boulougouris, 2019)
Added Resistance due to Waves	Existing Methods/Tools <i>benchmarked and validated with Computational Methods.</i>	Liu method and modified Liu method for arbitrary wave directions (Liu, et al., 2016) (Liu, et al., 2020) First application of Liu method for arbitrary wave directions in the Ship Design literature

Added Resistance due to Wind	Existing Methods/Tools	Fujiwara empirical method under the provisions of ISO 15016 for sea trial corrections (Fujiwara, et al., 2005) (ISO15016:2015, 2015)
Added Resistance due to Fouling	Existing Methods/Tools	Townsin method with fouling development profile. (Townsin, 2003)
Propeller Matching	Calibrated Method with Drawing and Ship Data <i>(digital twin principles)</i>	Wageningen method with propeller self-equilibrium and adapted propulsion coefficients from modified Holtrop (Bernitsas, et al., 1981)
Main Engine Matching	Original Research Method	Matching with MAN Marine Engine program with simulation-based Limit State approach instead of Sea Margin
Engine Room Dimensioning	Calibrated Method with Drawing and Ship Data <i>(digital twin principles)</i>	“SMCR-Parametric” Engine Room dimensioning for electrical load analysis and steam balance.
Simulation Module	Original Research Method	Voyage Simulation tool developed for quasi-dynamic vessel response prediction validated from onboard high-frequency data.
Lifecycle Economic Evaluation	Original Research Method	Lifecycle based evaluation (LC method) from voyage simulation results.
Lifecycle Environmental Evaluation	Original Research Method	Lifecycle based evaluation (LC method) from voyage simulation results.

Table 2: Helicopter Overview of Methods used for RHODA processes

Chapter 4: Existing Methods Utilized in RHODA

In the present Chapter 4, the methods, equations and formulae there is a detailed description of the use of RHODA processes where known, established and available in the literature methods have been deployed with no adjustment or a calibration for fitting the purpose and design space examined in the case studies (low Froude number, full hull vessels). The methods can be used as is (e.g Liu method for added resistance) or adapted to fit the case study with the use of “Digital Twin approaches” where data acquired from drawings and construction documents of the Parent vessel in the case study are used for calibrating the results of known methods.

4.1. Geometrical Core and Variation

One of the basic prerequisites of ship design optimization is that of the variation of the vessel’s hull and arrangements. To do that a geometric core is necessary which can be realized with Ship Hull parametric models. Such models have been introduced and developed to capture the essence of functional surfaces while allowing the necessary freedom for individual design. Representative work in this area can be found in (Harries, 1998), (Harries & Nowacki, 1999), (Abt, et al., 2009), (Birk & Harries, 2000), (Abt, et al., 2003). In general, parametric approaches can be subdivided into Partially parametric and Fully parametric. As highlighted by (Harries & Nowacki, 1999), in computer-aided ship hull design (CASHD) the prime objective of the hull definition process is to develop a geometric description of the hull form such that:

1. All relevant physical and geometrical characteristics – i.e., form parameters like displacement, the centre of buoyancy, waterplane area, the centre of flotation, angle of the entrance of the design waterline etc. – are met and
2. An acceptable shape quality – often expressed by fairness – is achieved.

(Harries, 1998) developed a new geometric modelling system, which is completely based on form parameter design and called the FRIENDSHIP Modeler (later Friendship Framework ® and at the time of writing CAESSES ®) (Abt & Harries, 2007), with the modelling process being subdivided into three consecutive steps:

1. Parametric design of a suitable set of longitudinal basic curves.
2. Parametric modelling of a sufficient set of design sections derived from the basic curves.
3. Generation of a small set of surfaces that interpolate the design sections.

The general assumption within his approach is that the shape of a ship’s hull can be uniquely defined by a set of form parameters. The selected set of form parameters, therefore, determines which geometry can be generated and which geometry lies outside of the scope of the chosen mathematical model. The descriptors are flexible enough to incorporate new parameters as they appear to be needed. Three levels of form parameters shall be distinguished: Principal Parameters, Basic Curve Parameters which contain all design details for modelling the basic curves and therefore define the hull shape and Sectional parameters which are derived from the basic curves, representing the input to the process of generating design sections.

The set of form parameters that are considered for modelling a single planar curve is a generic set of purely geometric parameters which can be easily interpreted and thus specified. They can be positional, differential and integral parameters through which the shape of a curve can be directly controlled. The positional parameters are the points at the beginning and the end of the curve. The differential parameters include information on the tangent angle as well as the curvature both at the beginning and at the end of the curve. Lastly, the integral parameters are the area between the curve and the axis as well as the centroid of the latter area. From the curve generation point of view, the modelling of a basic curve is the same task as modelling a design section. The generic set of basic curves is comprised of twelve longitudinal, planar curves with curves of primary and secondary importance. Of primary importance are the following: Sectional Area Curve (SAC), Design Waterline (DWL), Flat of Side curve (FOS), Flat of Bottom curve (FOB), Centre Plane curve (CPC), Deck (DEC). The sectional area curve SAC furnishes the first integral form parameter for a design section. The curves DWL, CPC, FOS, FOB, and DEC all constitute purely positional form parameters. Differential and integral form parameters are given in the set of secondary basic curves and contain additional information on the sectional character of the hull. They provide details such as data on the tangent angle and curvature at the centre plane curve (or the Flat of the Bottom). The design waterline DWL and centre plane curve CPC are the only mandatory input, while all the other basic curves are optional. In general, all basic curves are comprised of three areas: a curved portion for the run, a straight part in the middle and again a curved portion for the entrance, though the parallel part might vanish (for cases of slender hulls).

In the same work by (Harries, 1998) , (Harries & Abt, 1998) a new method for the parametric design of B-spline curves applying fairness criteria is also developed. The modelling process is treated as an optimization problem¹ where curve fairness criteria constitute the objective function while form parameters are viewed as equality constraints. The vertices of the B-spline curve are free variables of this optimization problem. Form parameters are either known a-priori as design requirements or can be provided intuitively. They can also be refined from the «natural» values they assume in the optimization. The non-linear equation system created is solved by means of the Newton-Raphson method. In comparison to interactive B-Spline modelling, the relationship between input and output is reversed: The designer specifies the intended shape and the system computes the position of the vertices such that the designer's specifications are met. The modelling technique is, therefore, problem-oriented rather than manipulation-oriented. Furthermore, (Harries, 1998) and (Harries & Nowacki, 1999) developed a special surface type called Meta-Surface. An arbitrarily oriented cross-section of the surface is topologically described in a feature definition. Parameterized curves for the distribution of the section's input parameters along the surface can be created and linked to the feature definition through an entity called Curve Engine. Via the Curve Engine sections are generated at arbitrary positions within the range of basic curves, based on the template stored in the feature. The Metasurface then uses this Curve Engine in a specified range. Since the shape of each surface cross-section is known, a complete

mathematical description of the surface is obtained without the need for interpolation. Smooth basic curves and sections yield a smooth surface without any further manual fairing. What is more, this surface description is then completely dependent on parameters, making it well suited for systematic variation.

State-of-the-art methods for the hull form variation with the minimum user interface can be found in the literature in the works of (Ang, et al., 2018) , (Ichinose & Tahara, 2018), and (Kostas, et al., 2015).

The modelling strategy employed for the methodology in CAESES is consisted of modelling a fully parametric surface using the integration capabilities of the software previously described in three distinctive meta-surfaces: the aft body, the midship (parallel) section and the forebody. For each surface, there is a complete set of longitudinal basic curves, sectional curves and interpolating surfaces. A set of functions, controlling surface curvatures and tangents is also defined from each meta-model.

The three distinctive Meta-Surfaces are joined by the use of common boundary curves on their adjacent areas, generating a complete initial hull surface. The hydrostatic properties of the generated hull surface are assessed utilizing an integrated hydrostatic computation in CAESES to define the displacement volume, LCB, KB and C_b of the hull in accordance with the dimensions and variables originally set by the user. As the block coefficient, C_b is one hull form optimization variables, control of the latter (and thus of the displacement) is required. This is ensured by the use of the Generalized Lackenby transformation (Lackenby, 1950) which is employed to derive the desired C_p (C_b) and LCB values by shifting sections fore and aft respectively and modifying the hull's Sectional Area Curve (SAC).

More details about the parametric modelling employed for the present case studies can be found in Appendix I.

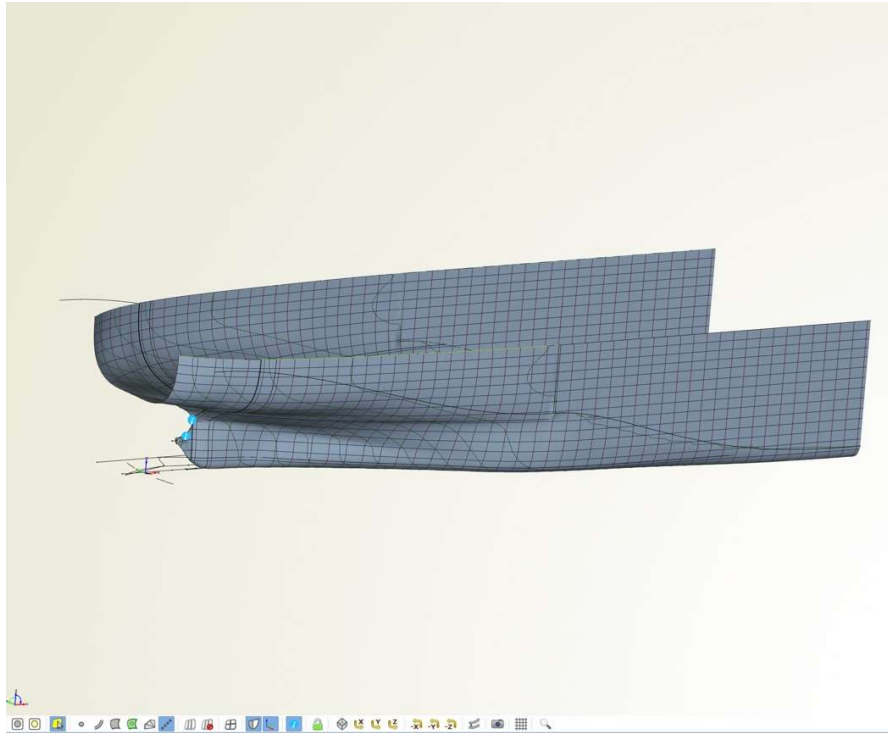


Figure 5: Aft Body Meta-Surface modelling in CAESES

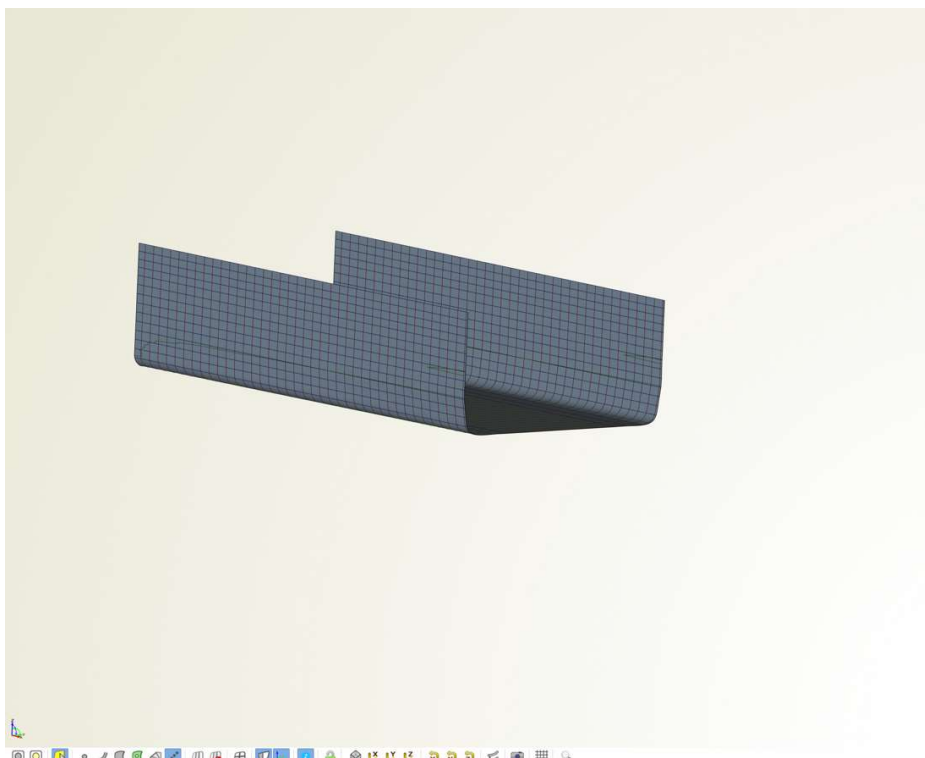


Figure 6: Midship Parallel Body Meta-Surface modelling in CAESES

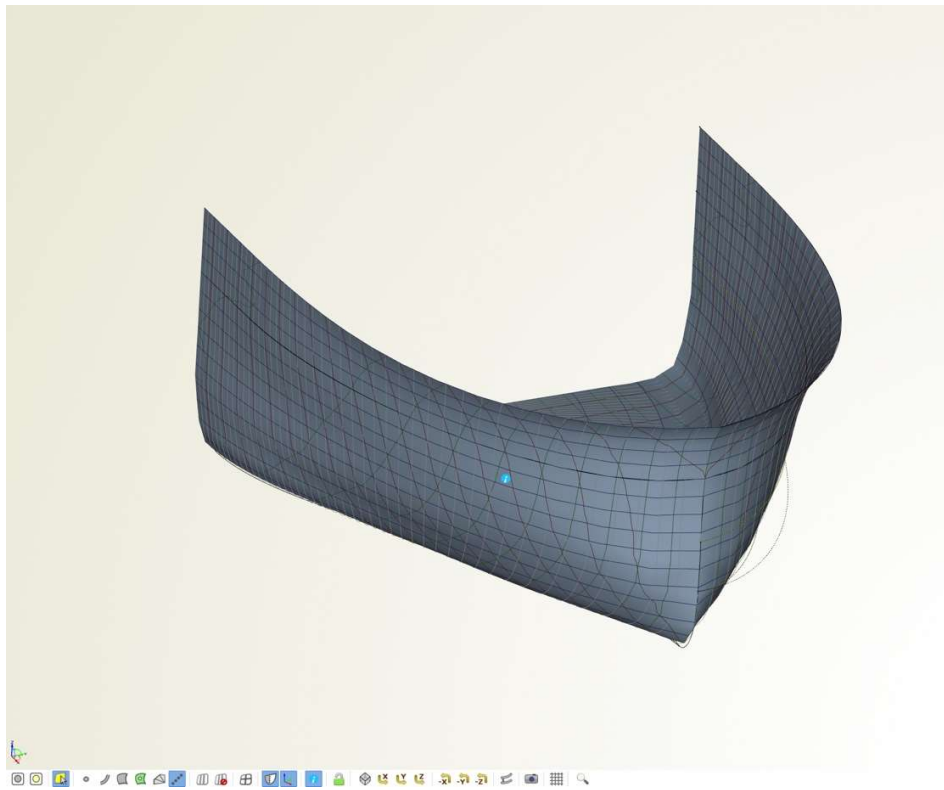


Figure 7: Forebody Meta-Surface modelling in CAESES

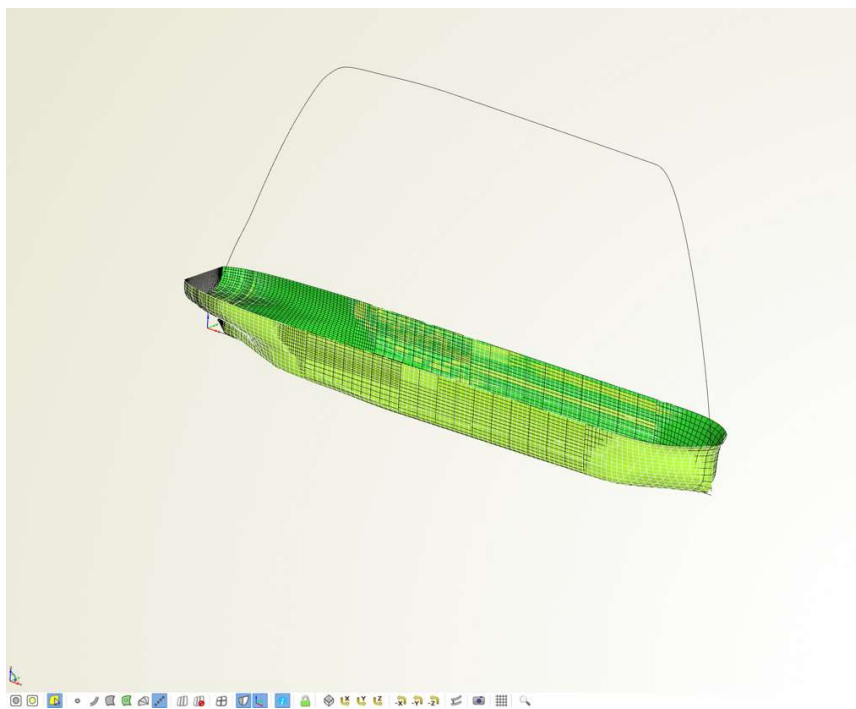


Figure 8: Hull and SAC after Lackenby Transformation

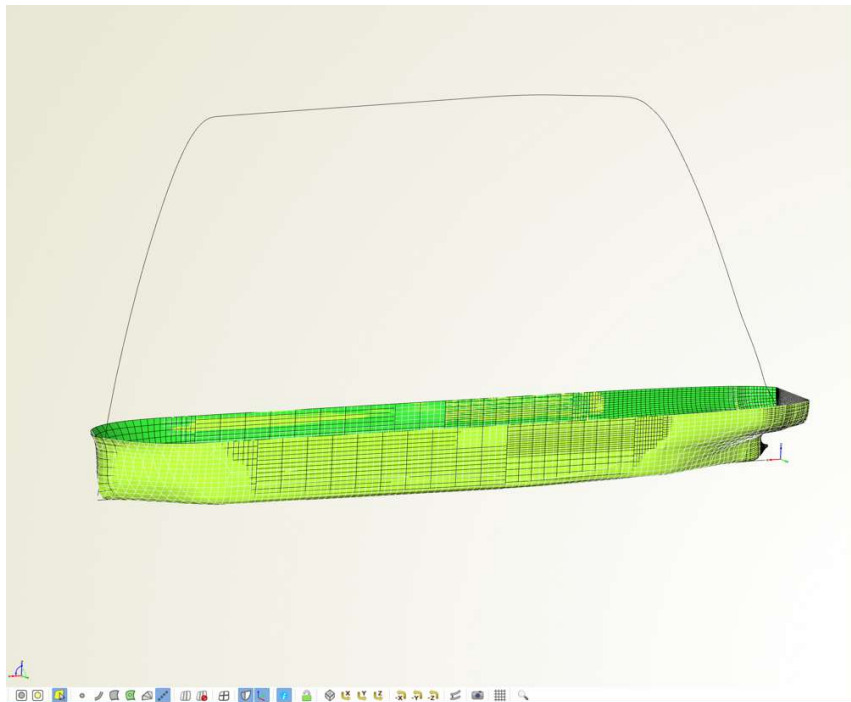


Figure 9: Hull and SAC after Lackenby Transformation

4.2. Cargo Hold Arrangement Modelling

The output surface from the Lackenby transformation described above is used as a basis for the generation of a group of parametric flat surfaces that constitute the vessel's compartmentation and cargo hold arrangement.

The same module also has capabilities for producing surfaces for double-hull vessels: either bulk carriers or Double Hull Crude Oil tankers built under IACS Harmonized CSR.

The capacity of each tank is calculated by creating offsets for each one of the tank surfaces and joining them together. For each offset group representing a cargo hold, a hydrostatic computation using the embedded capabilities of CAESES is performed giving the cargo hold volume, longitudinal and transverse moments as well the longitudinal, vertical and transverse centres of gravity. The total capacity is afterwards calculated along with the relevant centres of gravity. To improve further the calculation accuracy, a calibration factor derived from the parent hull arrangement is introduced. With this correction, the volume of structural frames is also approximately taken into account as well as a factor to derive with the Bale and Grain capacities.

4.3. Added Resistance in Seaways

4.3.1. Added Resistance in Waves

Several theoretical approaches for varying complexity and accuracy have been introduced in the past and numerically implemented/verified. The first far-field approach was introduced by (Maruo, 1957) in the late 50s. It was further elaborated by (Maruo, 1960) and (Joosen, 1966). The first near field, direct pressure integration appeared however the considered hydrodynamic pressure distribution was highly simplified (Boese, 1970). At about the same time the radiated energy approach of (Gerritsma & Beukelman, 1972) was introduced which is basically following the far-field approach of Maruo. (Strom-Tejsten, et al., 1973) did a thorough evaluation of all the above approaches to find large discrepancies between the numerical results from different theoretical approaches and relevant model experimental data. In his publication (Salvesen, 1974) investigated the added resistance by applying Gerritsma and Beukelman's method but using basic results of the STF seakeeping strip theory and found quite satisfactory results for the investigated ship hull forms. This is not surprising considering the superiority of the STF strip theory method for the prediction of ship motions over other methods at that time. An exact in the sense of potential theory near-field, direct pressure integration approach to the added resistance problem was introduced by (Faltinsen, et al., 1980) with good validation results. The observed deficiency of the approach in short waves was addressed by the introduction of a simplified added resistance estimation formula which models remarkably well the complicated interaction between the diffraction of waves and the steady flow around the ship. The same problem appears in exaggerated form with low speed, full hull forms with blunt bows (bulkers and tankers) for which (Ohkusu, 1985) proposed an improved approach. This method was further elaborated by (Iwashita & Ohkusu, 1992) who applied (Maruo, 1963) improved far-field formulation and the concept of Kochin functions, to obtain very good results for the added resistance of a fully submerged spheroid by use of a 3D pulsating and travelling source, Green function method. More recently using an enhanced unified theory (Kashiwagi, 2009) calculated the added resistance by a modified version of Maruo's approach with satisfactory results.

The first recall of a scientific formula for the prediction of the added resistance force in the short wave was Havelock's work for a formula that calculated the steady force acting on a fixed vertical circular cylinder in waves and later on Maruo's formula for the drift force acting on the ship in waves. (Fujii & Takahashi, 1975) were the first to propose a semi-empirical formula for the added resistance due to diffraction using Havelock's theory, which was afterwards revised by (Takahashi, 1988) based on revised experimental data. Faltinsen et al also developed an asymptotic formula for the added resistance on wall-sided hull forms in short waves as a by-product of their near field method for the calculation of the 2nd-order wave-induced forces and moment, namely by integrating the pressure over the hull surface using an approximate velocity potential near the bow. For full ships, the results based on this formula according to (Fujii & Takahashi, 1975) agree well with experimental data but for fine ship hulls there considerably large difference to experimental data. Further to this, some attempts by (Faltinsen, et al., 1980) were made to refine the formula but not with satisfactory results. In general, it should be noted that the complexity of the physical problem at hand in which viscous effects play a significant

role calls for the use of experimental data to fine-tune relevant semi-empirical coefficients. However such experimental data are scarce and pretty outdated. A more detailed review of methods for added resistance in waves estimation can be found in (Perez Arribas, 2007).

Method	Computational Requirements	Pre and Post Processing	Prediction Accuracy in Head Waves	Prediction Accuracy in Beam Seas	Prediction Accuracy in Following Seas
Empirical Formulae	Low	Zero	Mid	Low	Low
Rankine Panel Methods	Mid	Mid	High	High	Mid
RANS Methods	High	High	High	High	High

Table 3: Taxonomy and Overview of Different Added Resistance Estimation Approaches

The most notable empirical methods currently available in the literature include the empirical method of (Kwon, 2008) which is in turn based on the older publication of (Townsin & Kwon, 1983). In subject work, approximate weather formulae have been developed based on the Series 60 parent hull forms. The total resistance increase both in regular and irregular waves has been assessed to the total effect of waves with the use of the ITTC spectrum and a linear spectrum method, while the wind resistance has been assessed by the van Berlekom method (Van Berlekom, et al., 1975). The weather effect is not calculated in the form of resistance (kN) but in the form of a percentage of speed loss, ignoring the self-propulsion equilibrium and the propulsor’s performance in the seaway. The speed reduction percentage formulae are a function of the Beaufort Number. A correction factor for the operating speed in the form of a non-linear regression of the Froude number as well as the correction direction of waves as a function of the BN number are introduced. The method shows good agreement with experimental basis data up to a Beaufort number of 5, but above that, it consistently overestimates the speed loss. Furthermore, the method cannot be applied to the case of containerships and as in most empirical methodologies, the added resistance calculation of new hull forms deviating from the method basis/series exhibits considerable discrepancies.

In (Van Den Boom, et al., 2008), the Joint Industry Project for Sea Trials Analysis (STA-JIP) proposed two new methodologies for the assessment of the added resistance to be used in turn for corrections and analysis of full-scale measurements obtained during Sea Trials. The methods of Fuji, Nakamura, Townsin and Jinkine have been benchmarked against seakeeping model tests in regular and irregular waves with large discrepancies observed. Two new methods have been developed, based on the methodology of (Jinkine & Ferdinante, 1974) using model test results of the MARIN model basin database named STAWAVE1 and STAWAVE2 calculating the added

resistance due to reflection and both due to reflection and wave motion respectively (Grin, 2012). The STAWAVE1 methodology has been developed for mild waves acting on large vessels with a high surge speed, taking into account only the wave reflection component of added resistance based on the length of the bow section of the ship, wave height and direction. The STAWAVE2 method, on the other hand, has been developed for swell conditions and long waves taking also into account wave-induced motions with wave period, height and direction as input. For correction purposes, however, both methods are limited to the 45-degree envelope of bow waves not taking into account beam, quartering and following seas. The hull form shape is not taken into account with the methods being targeted for the analysis of speed trials instead of preliminary design studies. They have suggested methods in the relevant recommendations of the International Towing Tank Conference, (ITTC, 2014) and the ISO 15016 standard for sea trial corrections (ISO15016:2015, 2015).

In (Liu & Papanikolaou, 2015), a new approximate formula for the fast calculation is proposed for the case of head waves of short wavelength that can be easily programmed in the preliminary design stage based on the asymptotic formula developed by (Faltinsen, et al., 1980) by approximating the draft, flare angle and bluntness coefficients. The new formula is validated against experimental data illustrating good agreement, especially for low Froude number, and full hull forms. In the same study, the approach of (Jinkine & Ferdinante, 1974) (followed also in STAWAVE2 as described above) is revisited by extending the applicable range of speeds, adjusting the amplitude factor and introducing an additional term for short waves leading to a flatter curve in the transition region. For higher speeds and slender hull forms with a higher radius of gyration, the adjusted method illustrates higher fidelity than originally. The new formula has been also tested for the estimation of added resistance in irregular waves showing a very good agreement with experimental data. Furthermore, it is interesting to observe that the formula fits experimental data much better and with an increased sensitivity when compared with the STAWAVE2 method. In (Liu, et al., 2015) the short wave formula examined above is also extended for the case of quartering and beam waves. A further refinement, with the use of a ship draft correction coefficient which better accounts for wave pressure decay with ship's draft can be found in (Liu, et al., 2016). With the exception of the (Liu, et al., 2015) publication all such methods are limited to the case of head waves. Furthermore, such methods work with accuracy for full hulls with vertical wall sides, while for the case of finer hulls the accuracy is quite low. Lastly, the hull form sensitivity of such methods is relatively limited, however, for the cases of preliminary ship design, it can be considered adequate. It should be also noted that the accuracy of the method in the following seas is low, as the hydrodynamic flow phenomena on the stern areas are complex when in seaways and cannot be predicted by such methods. In these cases, a panel code that uses potential flow theory for estimating motions and solving the seakeeping problem around the vessels hull or a RANS code is required.

The advance and constant increase of available computational power gives ground for RANS methods for solving the seakeeping problem and calculating the added resistance in waves to be further developed. However, the computational cost continues to be a bottleneck and is forbidden for use in extensive optimization studies in any use other than that of the validation of Panel Methods used. For this reason, these are considered outside of the scope of the current Thesis.

The reader can refer for further reading however to the publications of (Kim, et al., n.d.), (Ley, et al., n.d.), (Söding, et al., n.d.), (Schmode, et al., n.d.).

For the purpose of the present Thesis, the method of (Liu, et al., 2016) has been chosen as the basis empirical formula employed in the estimation of the added resistance in waves of the generated variants. The use of the formula is limited for the case of head waves and is based on the best fitting of available experimental data for different types of hull forms. The formula has been simplified to the extent of using only the main ship particulars and fundamental wave characteristics for the estimation of the ship's added resistance.

The formula takes the below form:

$$\mathbf{R}_{AW} = \mathbf{R}_{AWR} + \mathbf{R}_{AWM} \quad (1)$$

Where:

$$\mathbf{R}_{AWR} = \frac{2.25}{2} \rho g B \zeta_a^2 a_d \sin^2 E \left(1 + 5 \sqrt{\frac{L_{pp}}{\lambda} Fn} \right) \left(\frac{0.87}{C_B} \right)^{1+4\sqrt{Fn}} \quad (2)$$

$$\mathbf{R}_{AWM} = 4\rho g \zeta_a^2 B^2 / L_{pp} \bar{\omega}^{b_1} \exp\left[\frac{b_1}{a_1}(1 - \bar{\omega}^{a_1})\right] a_1 a_2 \quad (3)$$

$$E = \text{atan}\left(\frac{B}{2L_E}\right) \quad (4)$$

$$a_1 = 60.3 * C_b^{1.34} * \left(\frac{0.87}{C_b}\right)^{1+Fn} \quad (5)$$

$$a_2 = \begin{cases} 0.0072 + 0.1676 * Fn & \text{for } Fn < 0.12 \\ Fn^{1.5} * \exp(-3.5 * Fn) & \text{for } Fn \geq 0.12 \end{cases} \quad (6)$$

$$\bar{\omega} = \begin{cases} \frac{\sqrt{\frac{L_{pp}}{g}} * \sqrt{\frac{k_{yy}}{L_{pp}}} * 0.05^{0.143}}{1.17} * \omega & \text{for } Fn < 0.05 \\ \frac{\sqrt{\frac{L_{pp}}{g}} * \sqrt{\frac{k_{yy}}{L_{pp}}} * Fn^{0.143}}{1.17} * \omega & \text{for } Fn \geq 0.05 \end{cases} \quad (7)$$

$$a_T = 1 - e^{-2kT} \quad (8)$$

For $C_b < 0.75$

$$b_1 = \begin{cases} 11.0 & \text{for } \bar{\omega} < 1 \\ -8.5 & \text{elsewhere} \end{cases} \quad (9)$$

$$d_1 = \begin{cases} 14.0 & \text{for } \bar{\omega} < 1 \\ -566 * \left(\frac{L_{pp}}{B}\right)^{-2.66} * 6 & \text{elsewhere} \end{cases} \quad (10)$$

While for $C_b \geq 0.75$

$$b_1 = \begin{cases} 11.0 & \text{for } \bar{\omega} < 1 \\ -8.5 & \text{elsewhere} \end{cases} \quad (11)$$

$$d_1 = \begin{cases} 566 * \left(\frac{L_{pp}}{B}\right)^{-2.66} & \text{for } \bar{\omega} < 1 \\ -566 * \left(\frac{L_{pp}}{B}\right)^{-2.66} * 6 & \text{elsewhere} \end{cases} \quad (12)$$

The above described method has been further expanded in (Liu & Papanikolaou, 2020) to predict the added resistance in arbitrary headings as well as refine its approach with regards to the effect of the hull slenderness (as expressed by the block coefficient) and trim angle.

With the introduction of the arbitrary wave heading consideration the formula is evolved to the below expression:

$$R_{AWM} = 4\rho g \zeta_a^2 \frac{B^2}{L_{pp}} a_1 a_2 a_3 \bar{\omega}^{b_1} \exp\left[\frac{b_1}{d_1}(1 - \bar{\omega}^{d_1})\right] \quad (13)$$

Where:

$$\bar{\omega} = 2.142^3 \sqrt{k_{yy}} \sqrt{\frac{L_{pp}}{\lambda}} \left[1 - \frac{0.111}{C_b} \left(\ln \frac{B}{T_{max}} - \ln 2.75\right)\right] \left(\frac{C_b}{0.65}\right)^{0.17} \left[(-1.377Fn^2 + 1.157Fn)|\cos a| + \frac{0.618(13 + \cos 2a)}{14}\right] \quad (14)$$

$$a_1 = \begin{cases} 60.3 * C_b^{1.34} * (4k_{yy})^2 \left(\frac{0.87}{C_b}\right)^{-(1+Fn)*\cos a} \left(\ln \frac{B}{T_{max}}\right)^{-1} \frac{(1-2\cos a)}{3} & \text{for } \frac{\pi}{2} \leq a < \pi \\ \text{interpolation between beam and following wave cases} & \text{for } 0 < a < \frac{\pi}{2} \\ f(U, V_g) & \text{for } a = 0 \end{cases} \quad (15)$$

a_2 remains the same as previously defined in eq. 6

$$a_3 = 1.0 + 28.7 \operatorname{atan} \frac{|T_a - T_f|}{L_{pp}} \quad (16)$$

b_1 remains as previously defined in eq. 11.

$$d_1 = \begin{cases} 566 * \left(\frac{L_{pp}}{B}\right)^{-2.66} & \text{for } \bar{\omega} < 1 \\ -566 * \left(\frac{L_{pp}}{B}\right)^{-2.66} * \left(4 - \frac{125 \operatorname{atan}|T_a - T_f|}{L_{pp}}\right) & \text{elsewhere} \end{cases} \quad (17)$$

The added resistance due to wave diffraction/ radiation has also evolved to a more complex expression:

$$R_{AWR} = \sum_{i=1}^4 R_{AWR}^i \quad (18)$$

Where:

When $E_1 \leq a \leq \pi$

$$R_{AWR}^1 = \frac{2.25}{4} \rho g B \zeta_a^2 a_T \left\{ \sin^2(E_1 - a) + \frac{2\omega_0 U}{g} [\cos E_1 \cos(E_1 - a) - \cos a] \right\} \left(\frac{0.87}{C_B} \right)^{(1+4\sqrt{Fn})f(a)} \quad (19)$$

When $\pi - E_1 \leq a \leq \pi$

$$R_{AWR}^2 = \frac{2.25}{4} \rho g B \zeta_a^2 a_T \left\{ \sin^2(E_1 + a) + \frac{2\omega_0 U}{g} [\cos E_1 \cos(E_1 + a) - \cos a] \right\} \left(\frac{0.87}{C_B} \right)^{(1+4\sqrt{Fn})f(a)} \quad (20)$$

When $0 \leq a \leq \pi - E_2$

$$R_{AWR}^3 = -\frac{2.25}{4} \rho g B \zeta_a^2 a_T \left\{ \sin^2(E_2 + a) + \frac{2\omega_0 U}{g} [\cos E_2 \cos(E_2 + a) - \cos a] \right\} \quad (21)$$

When $0 \leq a \leq E_2$

$$R_{AWR}^4 = -\frac{2.25}{4} \rho g B \zeta_a^2 a_T \left\{ \sin^2(E_2 - a) + \frac{2\omega_0 U}{g} [\cos E_2 \cos(E_2 - a) - \cos a] \right\} \quad (22)$$

ω_0 is the incident wave frequency

$$f(a) = \begin{cases} -\cos a & \text{for } \pi - E_1 \leq a \leq \pi \\ 0 & \text{for } a < \pi - E_1 \end{cases} \quad (23)$$

$$a_{T^*} = \begin{cases} 1 - \exp\left(-4\pi\left(\frac{T^*}{\lambda} - \frac{T^*}{2.5L_{pp}}\right)\right) & \text{for } \frac{\lambda}{L_{pp}} \leq 2.5 \\ 0 & \text{for } \frac{\lambda}{L_{pp}} > 2.5 \end{cases} \quad (24)$$

With:

$$T^* = \begin{cases} T_{max} & \text{for the } S_1 \text{ and } S_2 \text{ segments} \\ \begin{cases} \frac{T_{max}(4+\sqrt{|\cos a|})}{5} & \text{if } C_b \leq 0.75 \\ \frac{T_{max}(4+\sqrt{|\cos a|})}{3} & \text{if } C_b > 0.75 \end{cases} & \text{for the } S_3 \text{ and } S_4 \text{ segments} \end{cases} \quad (25)$$

In addition to the above formulations, in (Liu & Papanikolaou, 2020) the method is validated with experimental results from seakeeping model tests at various Froude Number velocities and for hulls of different block coefficients.

The application of added resistance empirical formulae in the herein presented methodology started with the application of the KWON (Kwon, 2008) and STAWAVE2 (Van Den Boom, et al., 2008) methodologies respectively in the first versions of the simulation framework and early publication works (Nikolopoulos & Boulougouris, 2015), (Nikolopoulos, et al., 2016). After 2017,

the method of Liu and Papanikolaou formula in its original format (Liu, et al., 2016) has been used for optimization runs and corresponding publications (Nikolopoulos & Boulougouris, 2018) and (Nikolopoulos & Boulougouris, 2020).

In addition to the above work, the modelled parent vessel hull surface has been exported from CAESES® to MAXSURF® for post-processing and then in Bentley Motions® software. Subject software is a potential flow theory panel code for solving the seakeeping problem, calculating added mass, vessel motions and estimating the vessel’s added resistance in waves. Either strip theory or panels can be used for the surface approximation by the Bentley Motions and for the purpose of the herein presented research Strip theory has been selected. Using the parent hull surface, several runs in each loading condition (design, scantling, ballast etc) have been conducted for a wide range of weather conditions as per Table 4 creating a sufficient result pool for the parent vessel.

Wave Headings	Vessel Advance Speed	Sea State /Spectrum / Wave Height/ T_p/T_s
0°	7 kn	SS3 / JONSWAP /0.88m/7.494s/5.906s
45°	8 kn	SS4 / JONSWAP /1.88m/8.791s/6.928s
90°	9 kn	SS5 / JONSWAP /3.25m/9.692s/7.638s
135°	10 kn	SS6 / JONSWAP /5.0m/12.392s/9.766s
180°	11 kn	SS7 / JONSWAP /7.50m/14.998s/11.819s
	12 kn	SS8 / JONSWAP /11.50m/16.393s/12.918s
	13 kn	Rogue / JONSWAP /14.0m/20.004s/16.786s
	14 kn	
	15 kn	
	16 kn	

Table 4: Environmental Conditions Setup for Parent vessel added resistance calculations.

The runs have been conducted both for panels as well as with strip theory. For the case of strip theory, transom sterns were selected and the seakeeping problem has been solved with the methods of Salvesen, Geritsma and Beukelman (I&II) and Havelock for all cases for comparative purposes.

The added resistance results have been subsequently comparatively assessed with the equivalent results of the new (Liu & Papanikolaou, 2020) for validation purposes prior to entering the method in the simulation framework. In view of this, 3 distinctive advancing speeds were selected from the entire possible operational envelope of the low-speed commercial vessels. The speeds chosen were low at 8 knots, a medium speed of 12 knots (the most frequently occurring speed for such vessels) and a high speed of 16 knots. The comparison was conducted at both Ballast and Laden Conditions and at wave incident angles of 180° (head waves), 135°, 90° (beam seas), 45° (quartering seas) and 0° (following seas) as seen in the below Table 5.

	Laden	Ballast
Draft (meters)	18.5 (fore and aft)	Fore: 7.938 / Aft: 9.0
Speed (knots)	8, 12, 16	8, 12, 16
Heading (degrees)	180°, 135°, 90°, 45°, 0°	180°, 135°, 90°, 45°, 0°

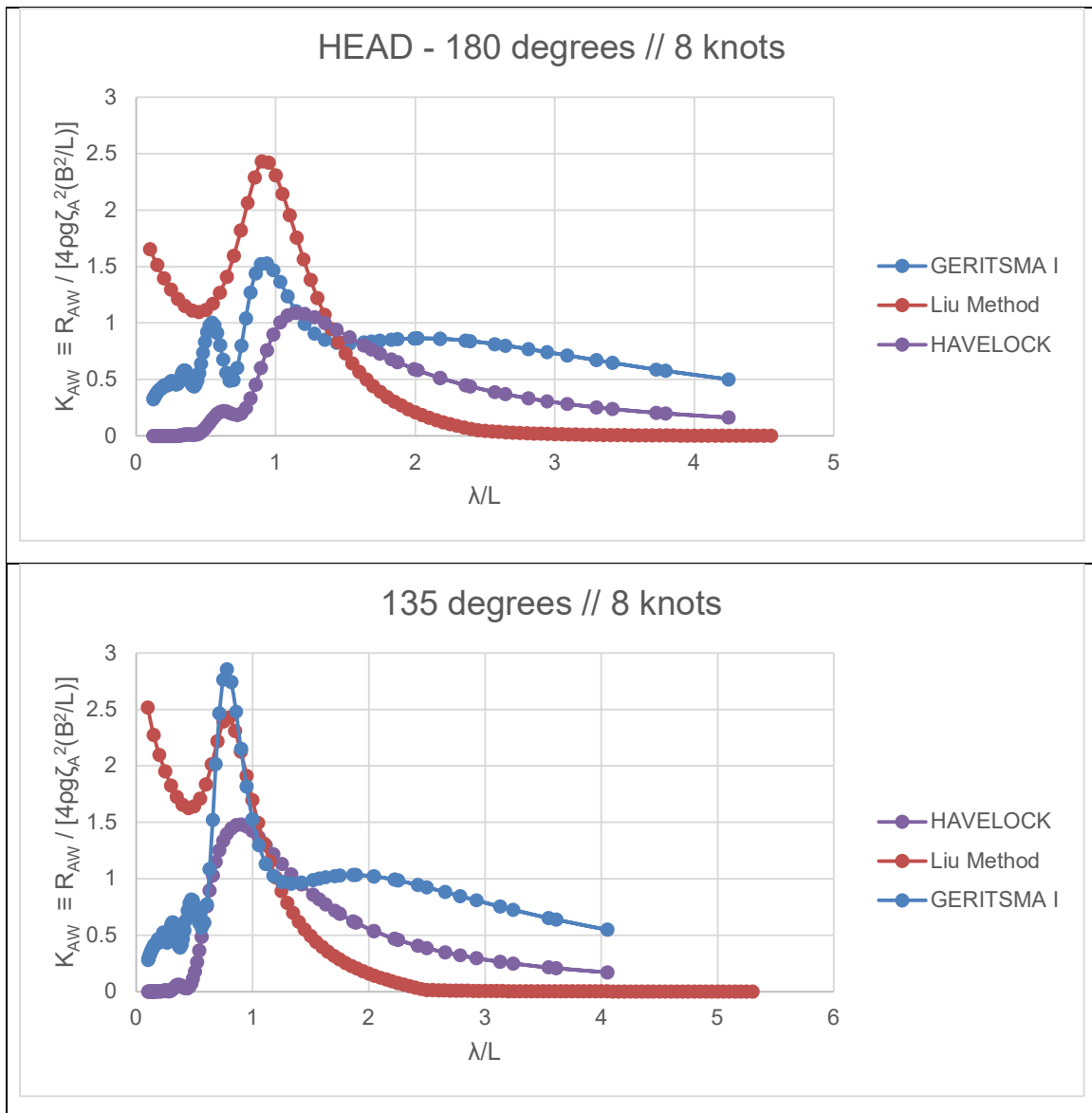
Table 5: Conditions examined in Liu Methodology Comparison to Panel Code Results

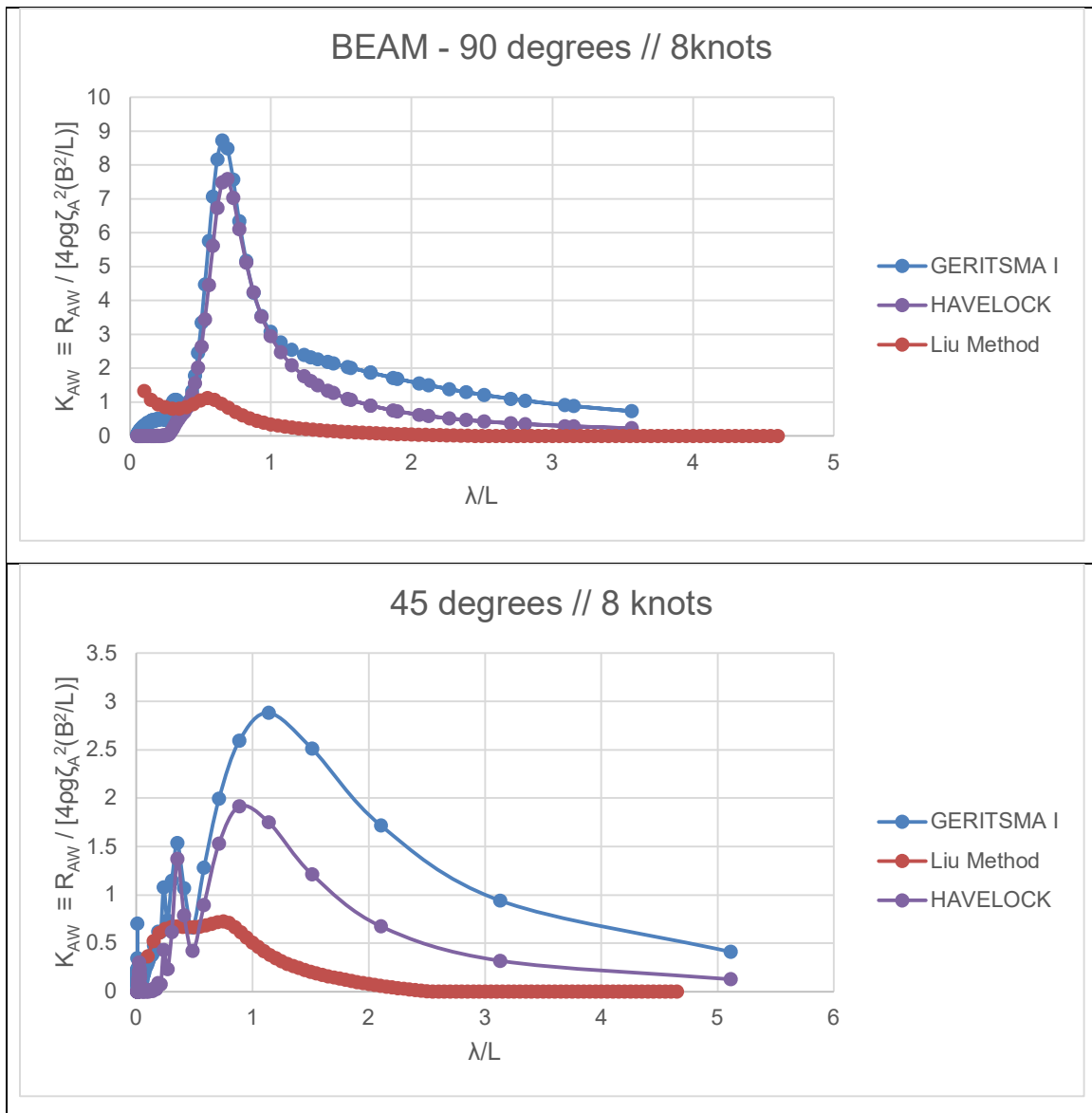
In the figures that follow, the improved empirical method Liu previously presented is compared to the results of potential flow theory runs.

4.3.1.1. Added Resistance Methods Benchmarking - Laden Condition – Advance Speed 8 knots

From Figure 10 presenting results for the Laden Condition at 8 knots advance speed for all wave directions the following clear observations are withdrawn:

1. The peak added resistance is observed roughly at the same position of the wave spectrum corresponding to a wave length of about λ/L_{bp} of 0.8-1.2 for all methods (Liu and potential flow theory) for all wave directions except following seas. For the case of the following seas (0° degrees), the added resistance predicted by the Liu method has an earlier peak at λ/L_{bp} of 0.7 instead of the 1.0-1.1 of the other methods.
2. For head seas (180° degrees) , the Liu method is more conservative compared to potential flow theory results for short waves while for longer waves the predicted added resistance of Liu is smaller than the potential flow theory results.
3. A similar trend is observed for 45° degrees wave heading, with the exception that peak added resistance is almost identical between Liu and potential flow theory results.
4. For the rest of the wave directions (90° , 135° , 180° degrees) the added resistance predicted by the Liu method is significantly smaller than potential flow results across the entire wave length spectrum.





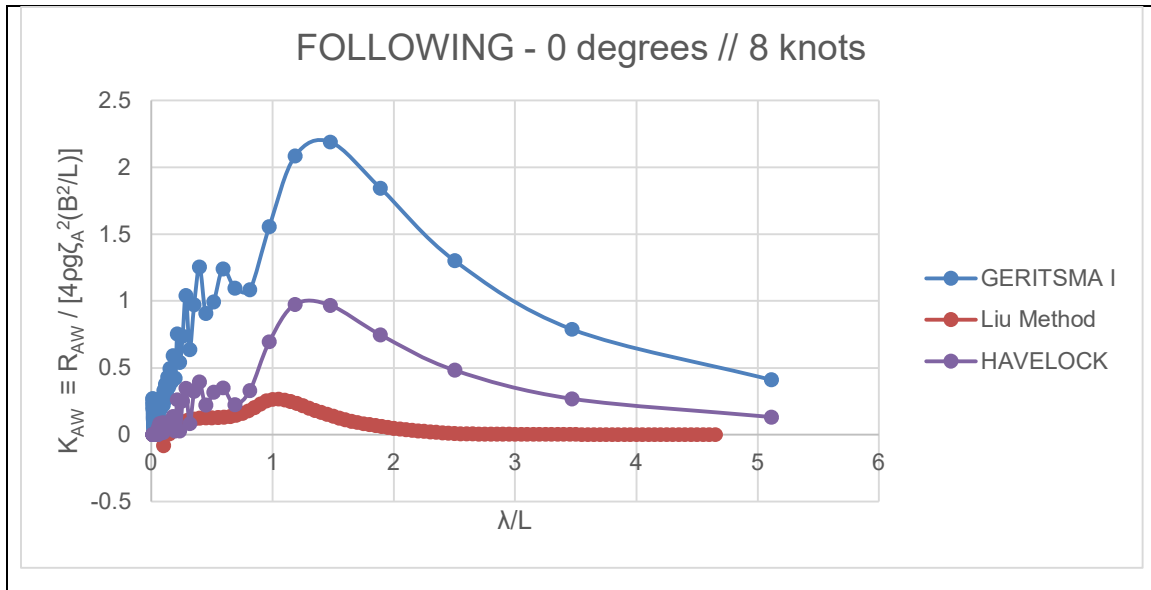
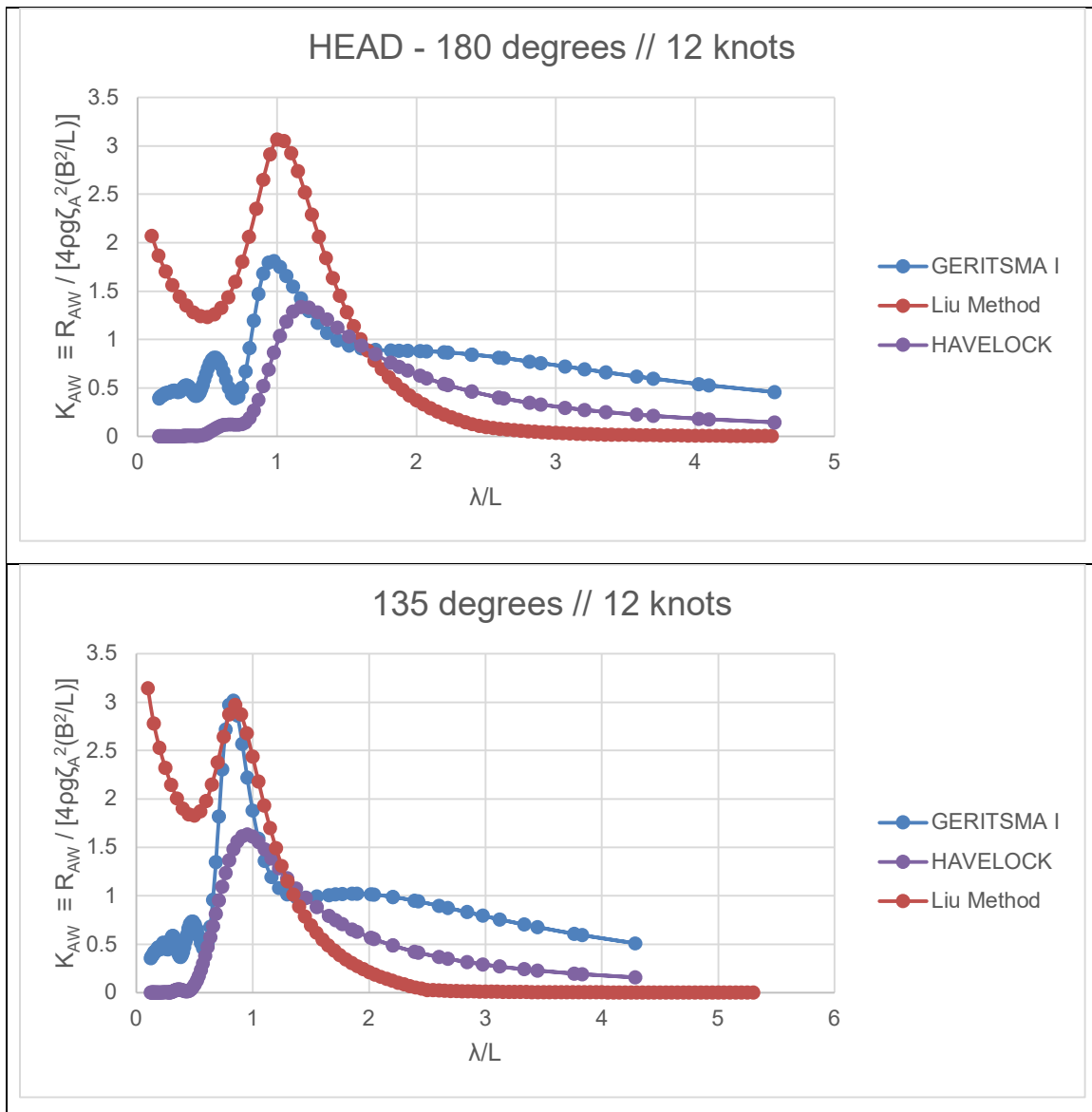


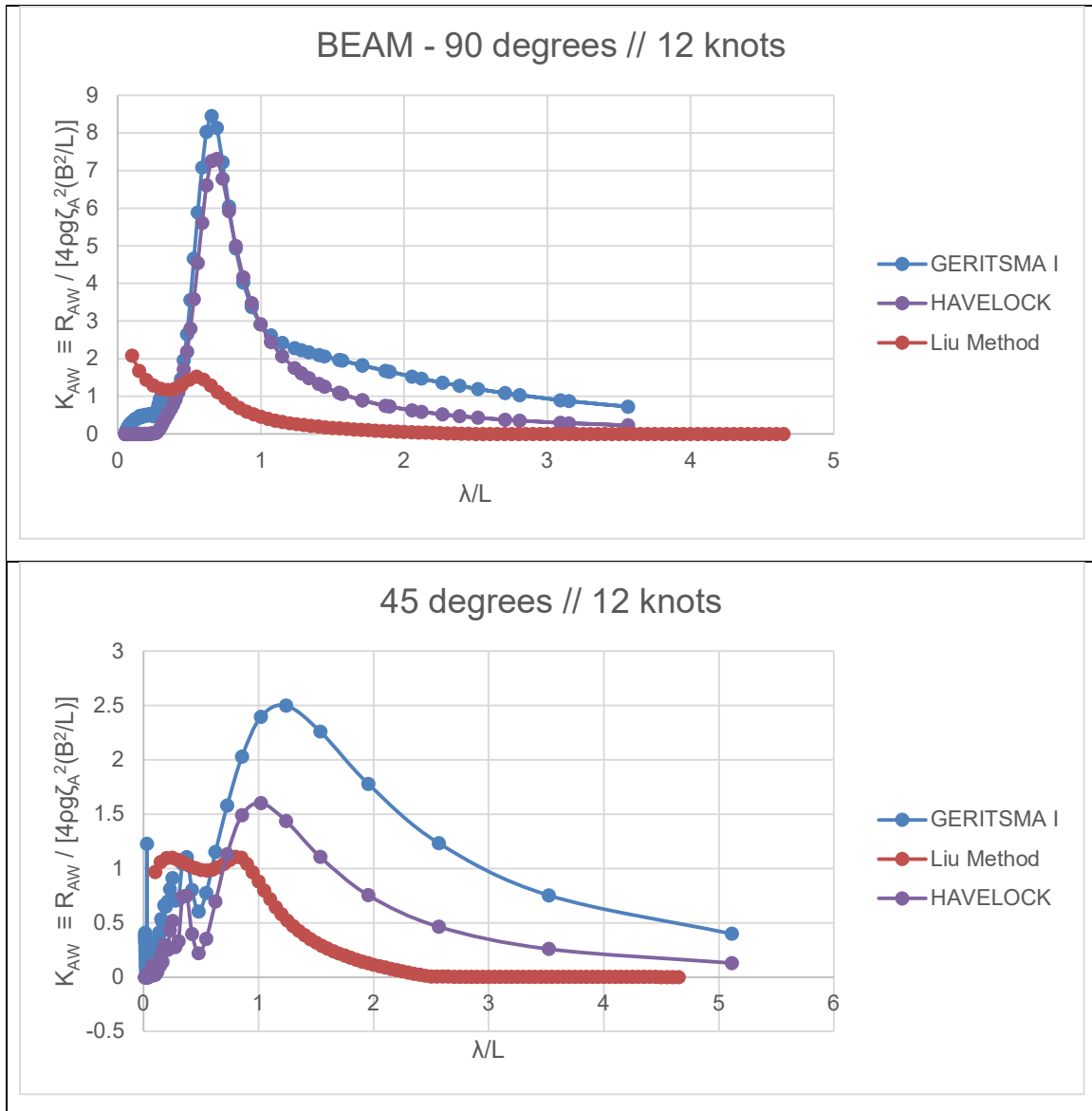
Figure 10: Non-Dimensional Added Resistance Comparison Liu vs. Strip Theory Results // Laden Condition at 8 Knots Advance Speed

4.3.1.2. Added Resistance Methods Benchmarking - Laden Condition – Advance Speed 12knots

From Figure 11 presenting results for the Laden Condition at 12 knots advance speed for all wave directions the following observations are withdrawn:

1. Head Seas (both 180° and 135° degrees) have the same behaviour and sensitivities as in the case of 8 knots advance speed.
2. For the case 45° the results of the Liu method continue to be lower than potential flow results but with a considerably smaller difference than in the previous speed.
3. For the case of following seas, interestingly the added resistance due to waves is negative for short wave lengths and considerably smaller for the rest of the range. Cases of negative added resistance have been observed also in the original publication (Liu & Papanikolaou, 2020) and validated with experimental data.





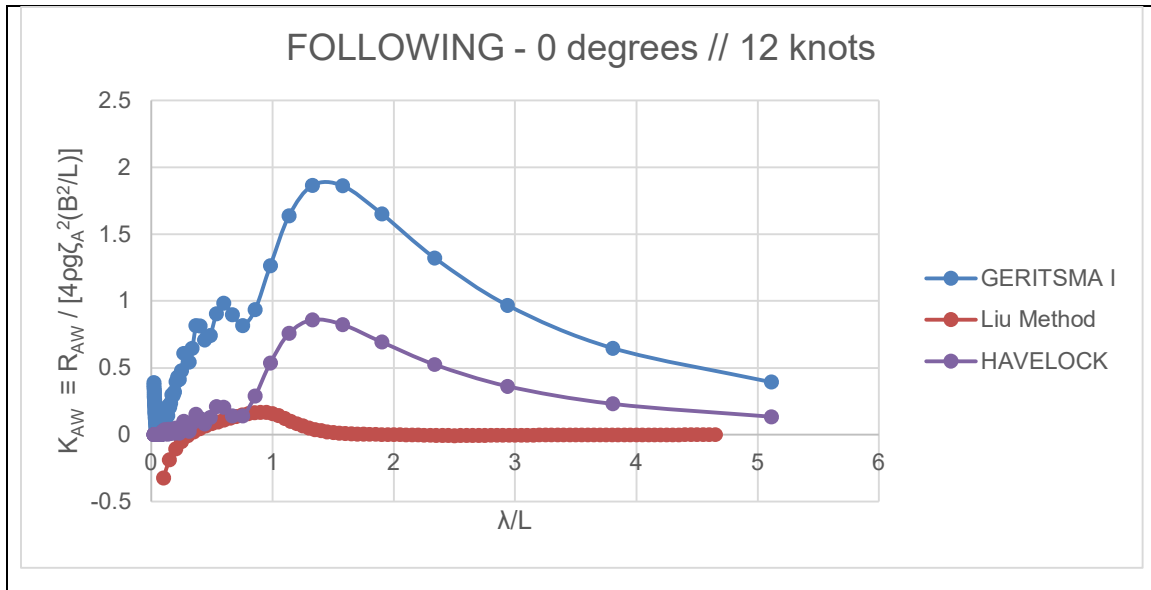
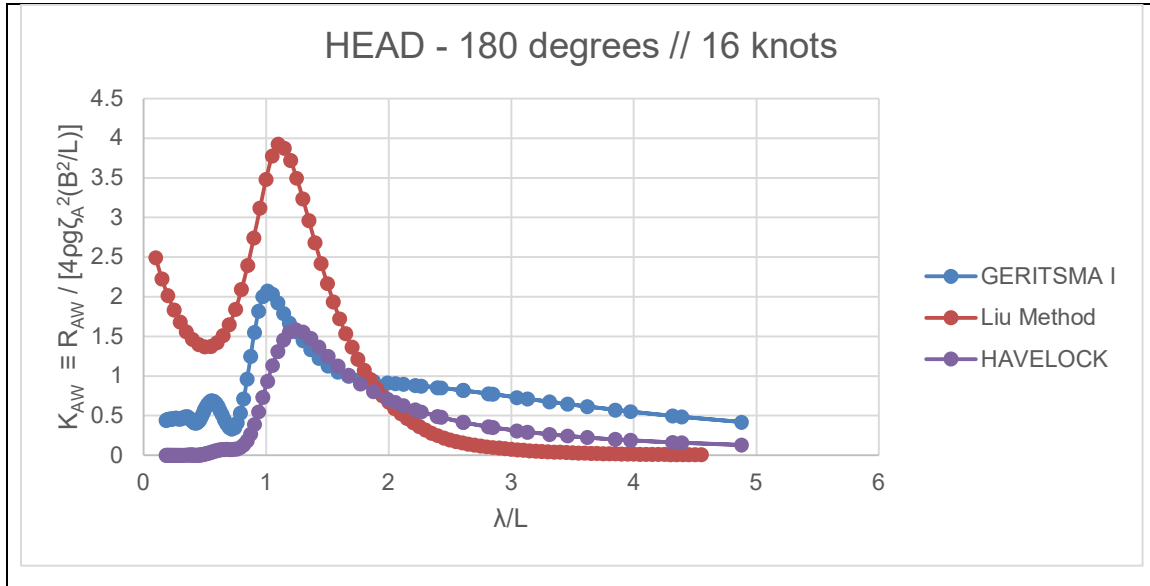


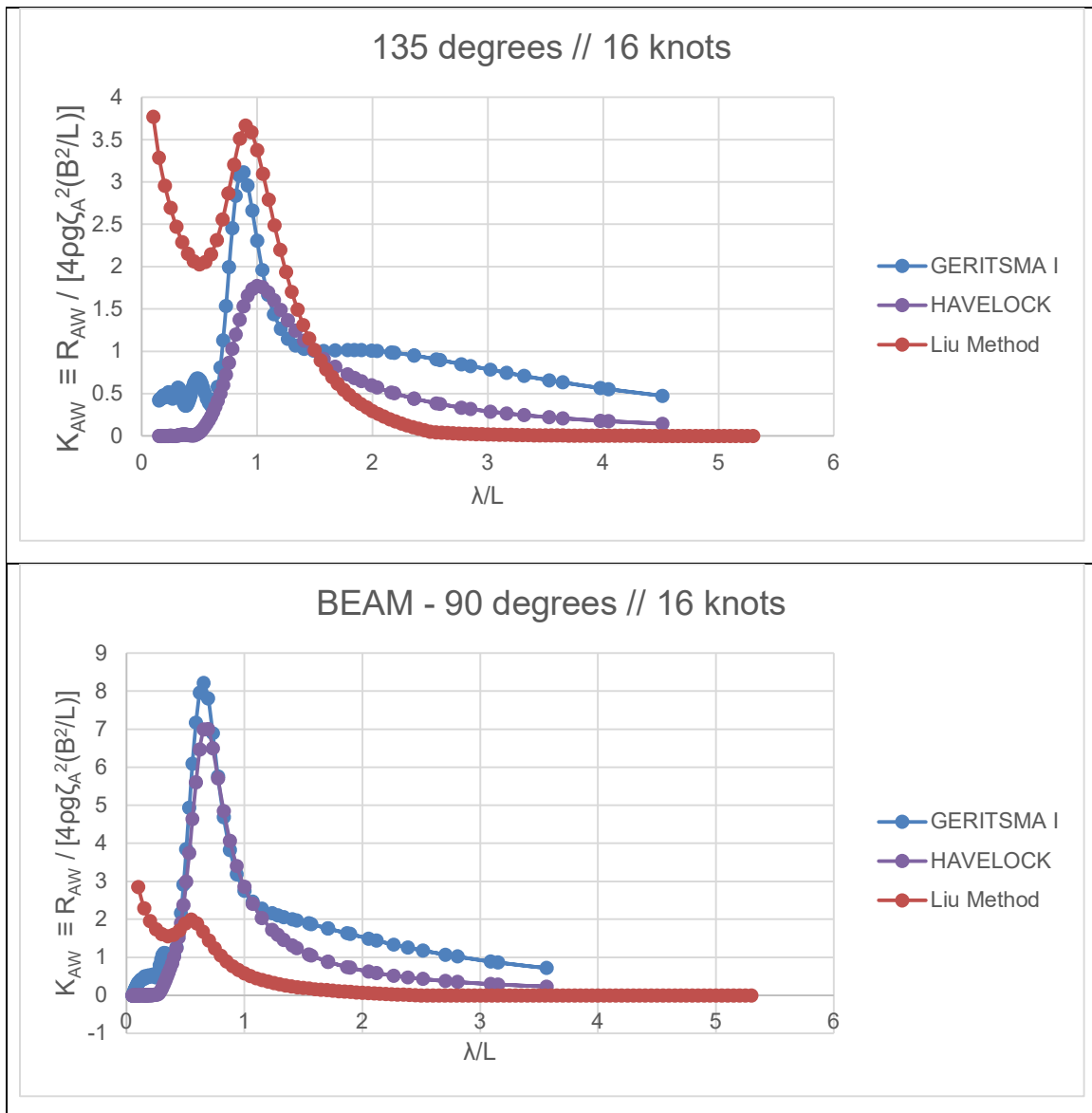
Figure 11: Non-Dimensional Added Resistance Comparison Liu vs. Strip Theory Results // Laden Condition at 12 Knots Advance Speed

4.3.1.3. Added Resistance Methods Benchmarking - Laden Condition – Advance Speed 16 knots

From Figure 12 presenting results for the Laden Condition at 16 knots advance speed for all wave directions the following observations are withdrawn:

1. For Head seas (180° degrees), the peak added resistance derived from the method of Liu is considerably higher and as per the previous advance speeds is lower for longer wave lengths. It should be observed at this point however, that by increasing speed the difference increases as well.
2. For 135° degrees wave direction, the peak added resistance is almost identical and remains similar for a wide area of the spectrum. It should be also noticed that for short wave lengths, the added resistance calculated by Liu is significantly higher than the potential flow results.
3. For beam seas (90°), the added resistance predicted by the Liu method is significantly lower throughout the spectrum.
4. For quartering seas (45°), the added resistance is similar for all short wavelengths. The peak added resistance is observed at a smaller λ/L while at longer wavelengths it is significantly smaller than the potential flow results.
5. For following seas (0°), the added resistance calculated by Liu is comparatively higher than in lower advance speeds. However, for the entire spectrum, the value of non-dimensional added resistance remains lower than the potential flow results.





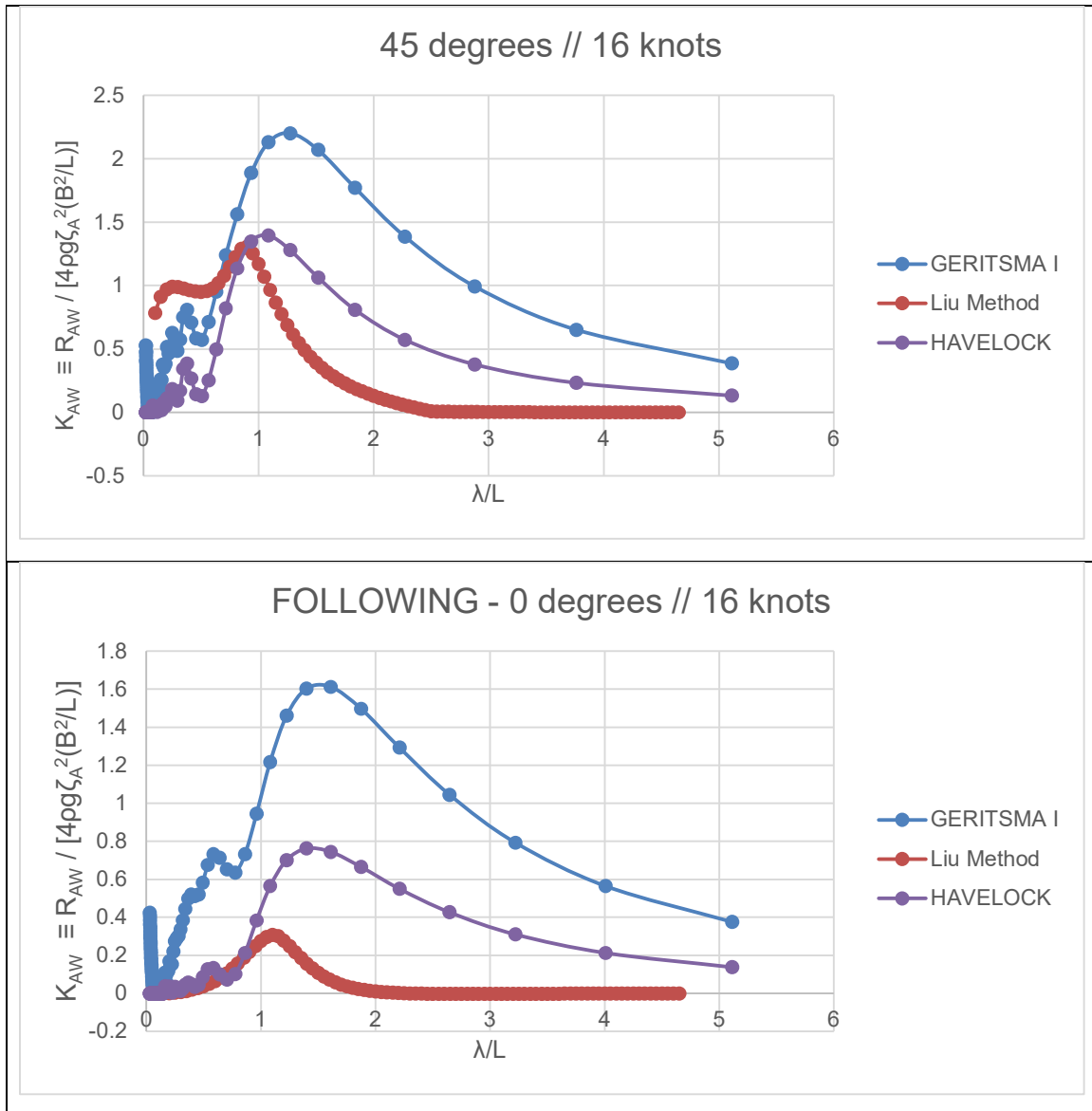
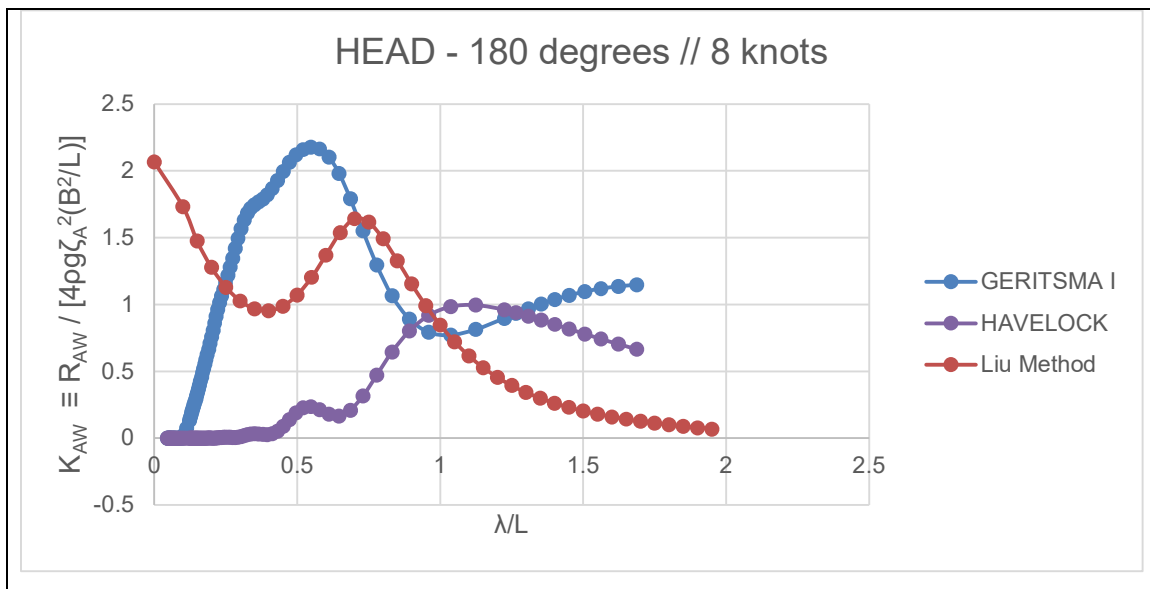


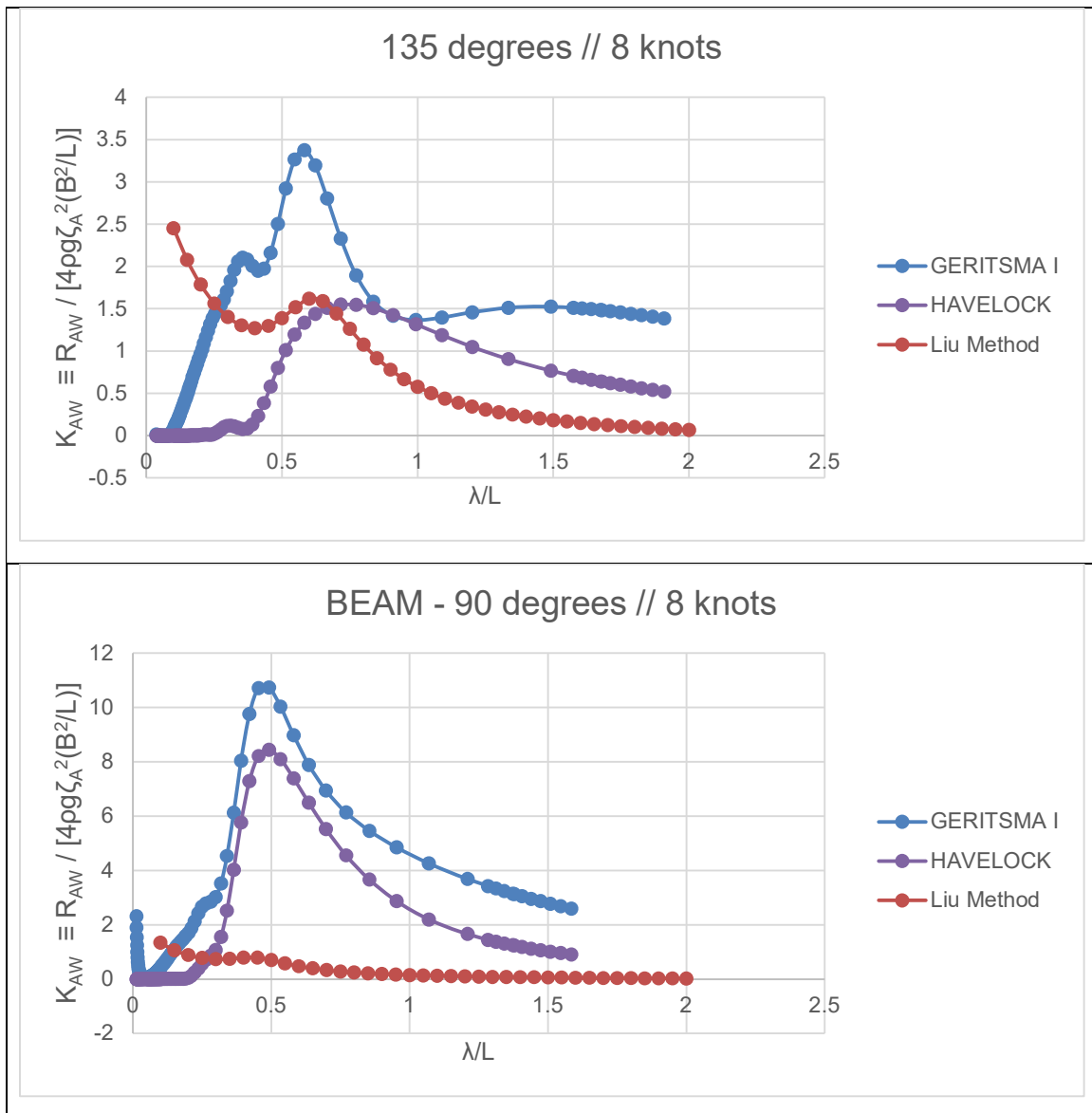
Figure 12: Non-Dimensional Added Resistance Comparison Liu vs. Strip Theory Results // Laden Condition at 16 Knots Advance Speed

4.3.1.4. Added Resistance Methods Benchmarking – Ballast Condition – Advance Speed 8 knots

From Figure 13 presenting results for the Ballast Condition at 8 knots advance speed for all wave directions the following conclusion can be drawn:

1. For all wave directions the Liu Methodology is less conservative than the strip theory code results with a smaller calculated added resistance in waves for medium and long waves.
2. Similarly, to the laden condition comparison, the Liu method provides a higher estimation of the added resistance for short waves due to its specific formulation described in the previous paragraph.
3. For head waves the peak added resistance predicted by Gerritsma is at lower λ/L than the one predicted by Liu method and Havelock has a peak resistance at higher wave lengths.
4. For 135° wave lengths, the peak added resistance is coincident for all methods in terms of wavelength.
5. For the following and quartering seas, a very low prediction of the Liu Method has been observed for this particular advance speed.





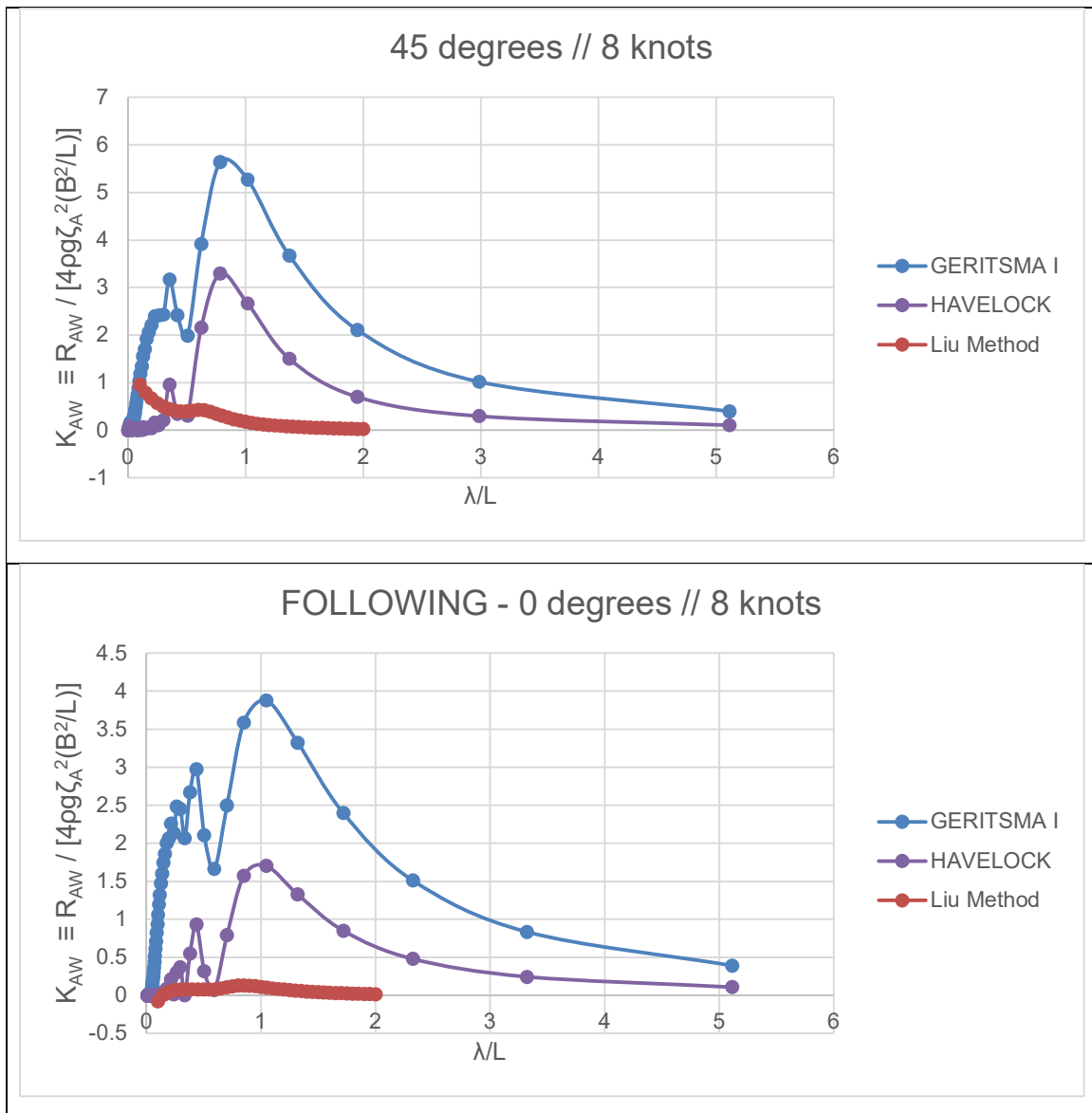
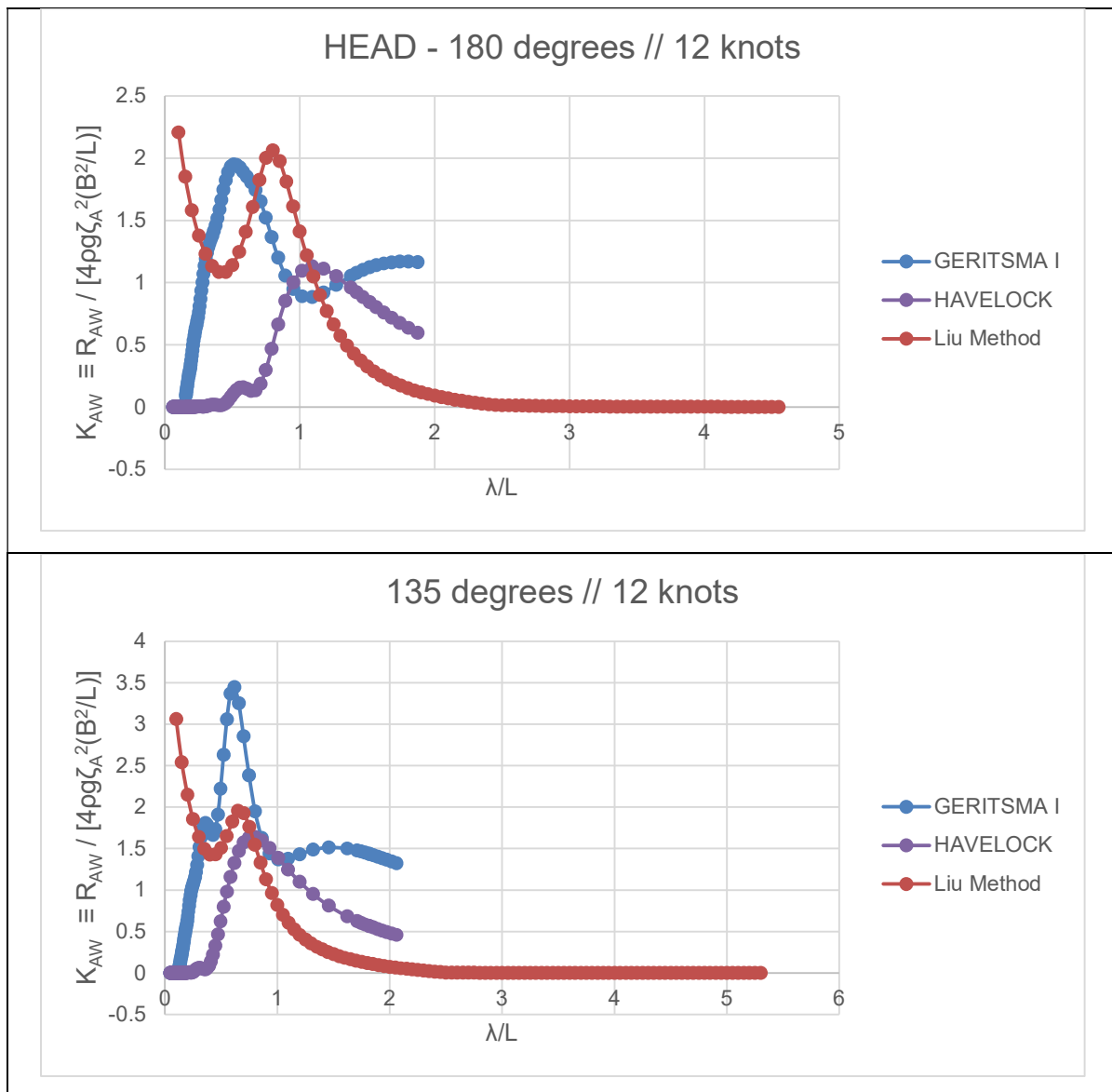


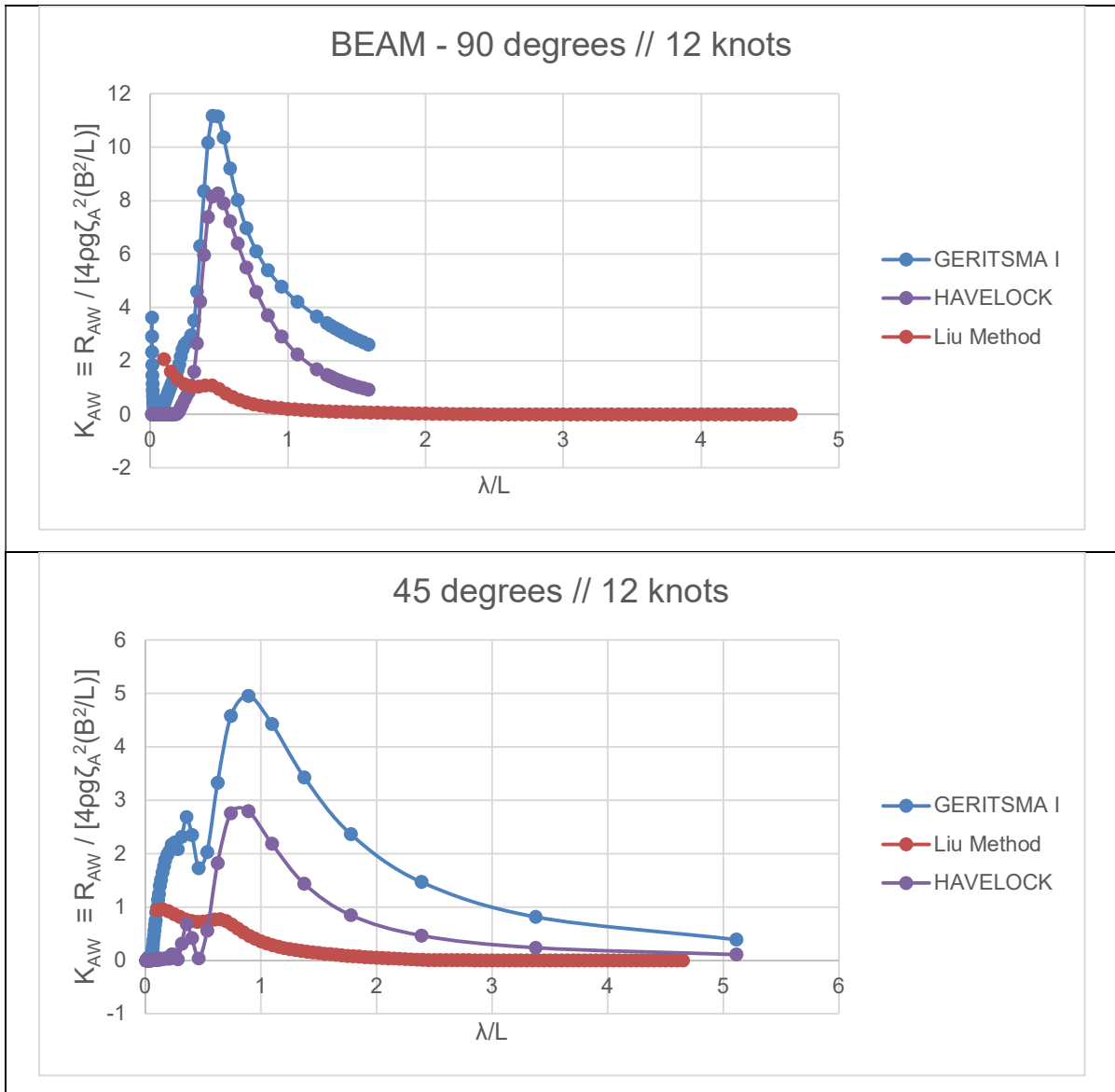
Figure 13: Non-Dimensional Added Resistance Comparison Liu vs. Strip Theory Results // Ballast Condition at 8 Knots Advance Speed

4.3.1.5. Added Resistance Methods Benchmarking – Ballast Condition – Advance Speed 12 knots

From Figure 14 presenting results for the Ballast Condition at 12 knots advance speed for all wave directions the following observations are withdrawn:

1. For the Head seas and 135 degrees wave angle, in short and medium waves the prediction of Liu method is very close to the one of the Strip Theory code results. For longer waves as in all other cases the Liu Method predicts an overall lower resistance figure.
2. The trend observed at the 8 knots advance speed with regards to the added resistance in beam, quartering and following seas remain with a significantly lower prediction for all wave lengths.





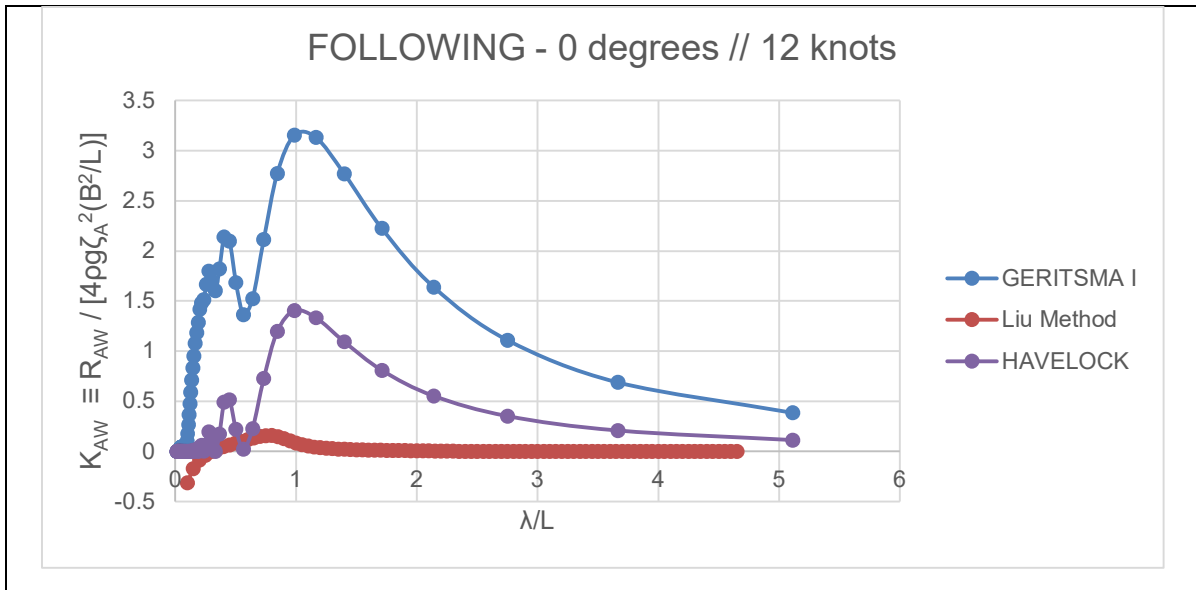
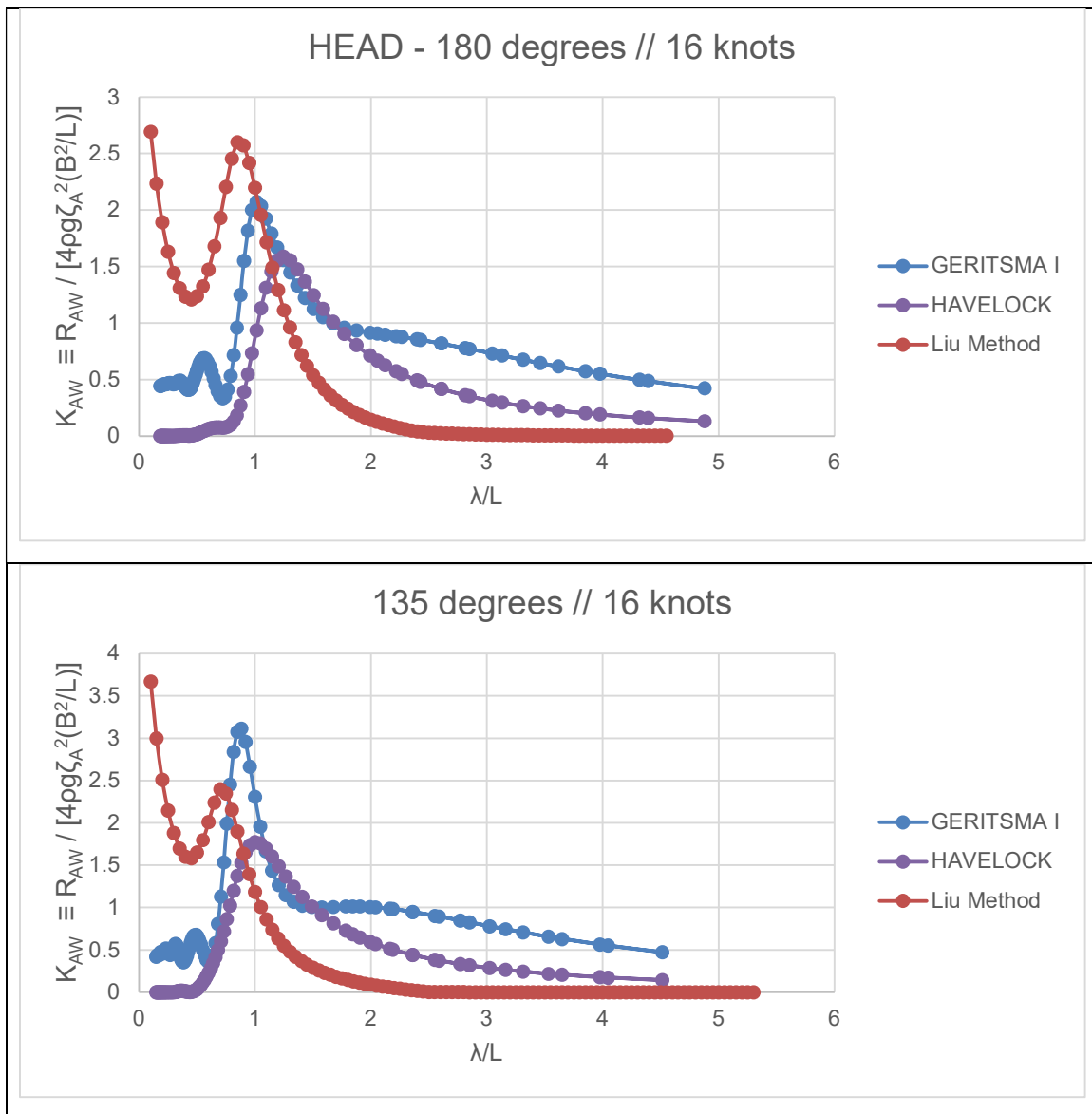


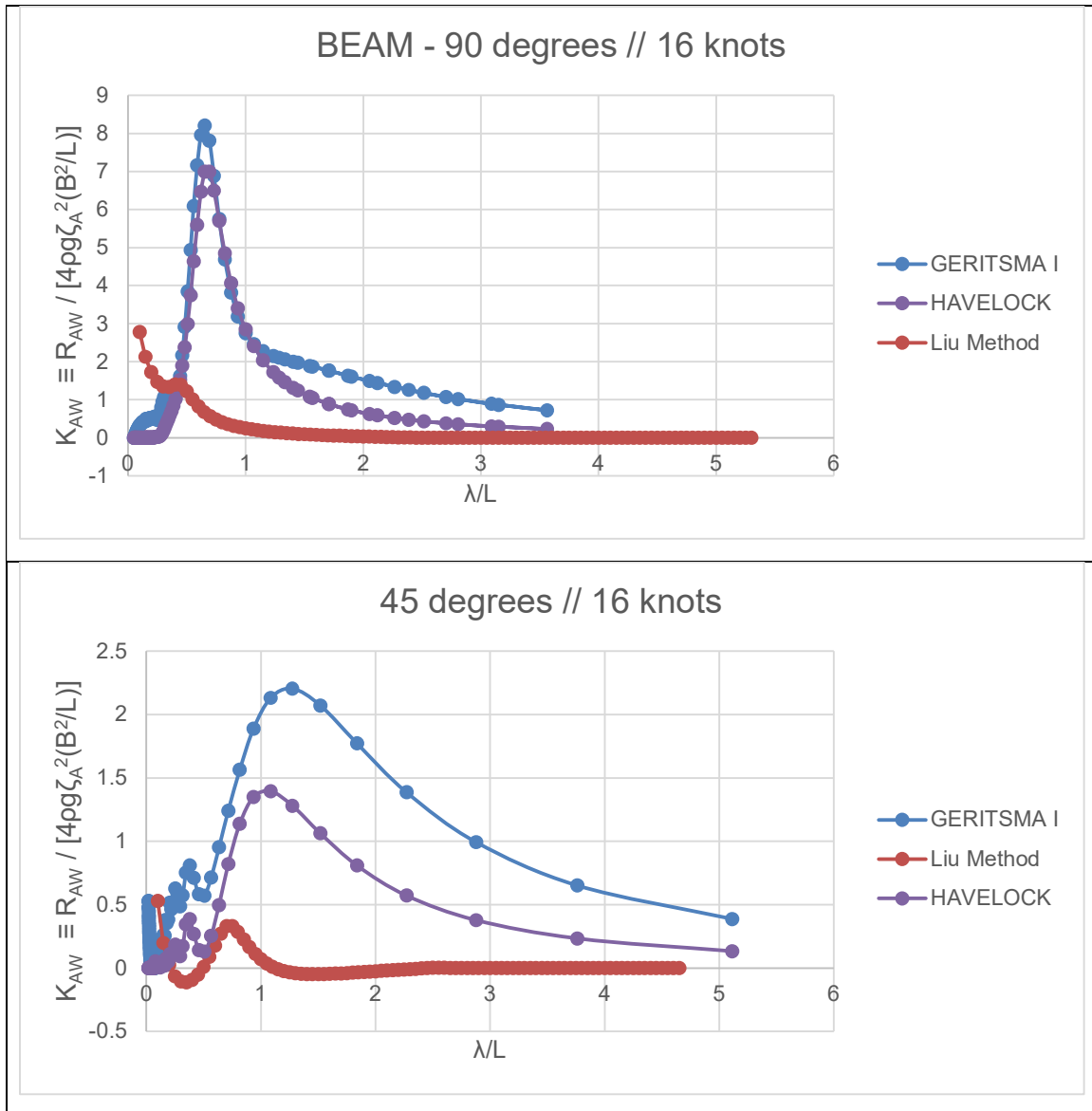
Figure 14: Non-Dimensional Added Resistance Comparison Liu vs. Strip Theory Results // Ballast Condition at 12 Knots Advance Speed

4.3.1.6. Added Resistance Methods Benchmarking – Ballast Condition – Advance Speed 16 knots

From Figure 15 presenting results for the Ballast Condition at 16 knots advance speed for all wave directions the following observations are drawn:

1. In contrast to previous runs, for head waves the Liu method yields an added resistance higher than the other methods up to wavelengths that are 1.5 times the length of the vessel. After this wavelength the other methods estimate a higher added resistance.
2. The peak added resistance is observed at the same wavelength all wave directions, except the following seas where it is observed at slightly smaller wavelengths.
3. Similarly, to the laden condition results, for the beam, quartering and following seas the added resistance calculated by the Liu method is significantly smaller than the panel code results.





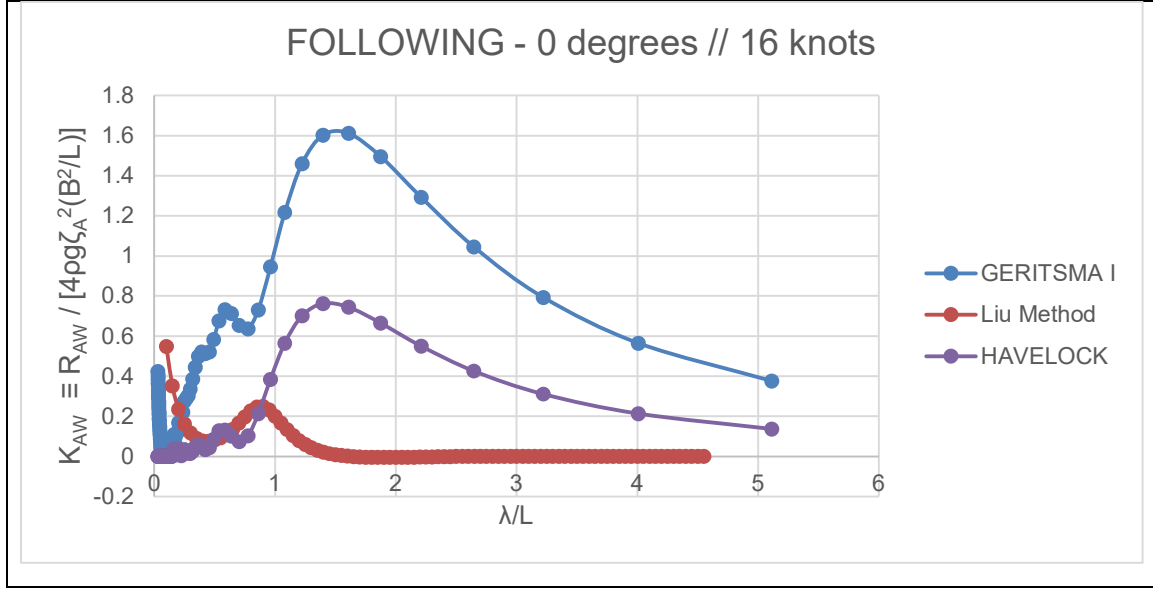


Figure 15: Non-Dimensional Added Resistance Comparison Liu vs. Strip Theory Code Results // Ballast Condition at 16 Knots Advance Speed

4.3.1.7. Conclusions on Added Resistance Methods

From the above analysis it is concluded that the Liu Method for calculating added resistance in arbitrary wave direction complies with the detail and sensitivity level required at the Preliminary Design Level (IMO Level 2 and Level 3 Calculation basis). As it is based on empirical formulae corresponding thus to minimal computational requirements it has been decided to use it as the predominant calculation method for Added Resistance in Waves and has been integrated into the Voyage Simulation environment of the herein presented methodology with the form of Spectral calculation using the JONSWAP spectrum following the formulation described in (Liu, et al., 2020):

$$R_{AW}(T_S, H_S, \alpha, V_{TW}) = 2 \int_0^{2\pi} \int_0^\infty \frac{R_{AW}(\omega, \alpha, V_{TW})}{\zeta_A^2} S_f(\omega, H_S) G(\alpha) d\omega d\alpha \quad (26)$$

Where G is the angular distribution function and the frequency spectrum is assumed to take the approximate form of the JONSWAP spectrum for a given significant wave height H_s and Peak period T_p :

$$S(H_S, T_p, \gamma) = \frac{\alpha^* H_S^2 \omega^{-5}}{\omega_p^{-4}} \exp\left[-\frac{5}{4} \left(\frac{\omega}{\omega_p}\right)^{-4}\right] \gamma \exp\left[\frac{-(\omega - \omega_p)^2}{2\sigma^2 \omega_p^2}\right] \quad (27)$$

With α^* being: $\alpha^* = \frac{0.0624}{0.23 + 0.0336 \cdot \frac{1.85}{(1.9 + \gamma)}}$ and $\gamma = 3.3$. If γ is reduced to 1.0 the JONSWAP spectrum is reduced to the modified Pierson-Moskowitz type spectrum. The angular distribution factor defined in (Liu, et al., 2020) a cosine-power type formula is applied:

$$G(\alpha) = \begin{cases} \frac{2^{2s} \Gamma^2(s+1)}{\pi \Gamma(2s+1)} \cos(\theta - \alpha)^{2s}, & |\theta - \alpha| < \pi/2 \\ 0, & \text{otherwise} \end{cases} \quad (28)$$

With s being the directional spreading parameter, Γ being the Gamma function and θ the primary wave direction.

4.3.2. Added Resistance due to Wind

The second important component of added resistance of a vessel in an actual seaway is the resistance induced by the wind forces acting on the vessel's superstructures and freeboard area, resulting in loss of speed, resistance as well as drifting and increased rudder angle for manoeuvring to the intended course.

The generalized approach for estimating the added resistance due to the enacting wind forces on the vessel's surfaces is from the below equation (ISO15016:2015, 2015):

$$R_{AA} = 0.5 * \rho_A * C_{AA}(\psi_{WRef}) * A_{XV} * V_{WRef}^2 - 0.5 * \rho_A * C_{AA}(0) * A_{XV} * V_G^2 \quad (29)$$

Where:

- ρ_A : mass density of air in kilograms per cubic meter
- C_{AA} : Wind Resistance coefficient, with $C_{AA}(0)$ being the Wind Resistance coefficient in head winds
- A_{XV} : Transverse Projected area above the waterline, including superstructures in square meters
- ψ_{WRef} : Relative wind direction at the reference height in degrees
- V_{WRef} : Relative wind velocity at the reference height in meters per second
- V_G : Measured ship's speed over ground in meters per second

Important work done for the estimation of added resistance due to wind can be found in (Isherwood, 1973) and (Blenderman, 1993).

The wind resistance coefficients can be derived either from model tests in a wind tunnel, databases of similar ship types or with the use of statistical regression formulae concerning wind resistance coefficients of various ship types (Fujiwara, et al., 2005).

The case of wind resistance coefficients derived from model tests is not considered applicable for the context of the herein presented research. Data sets of wind resistance coefficients have been developed by STA-JIP (Sea Trials Analysis JIP, 2006) with data available for VLCC tankers, LNG carriers, ferries, Pure Car Carriers (PCCs) and containerships. Such data are useful and easily applicable; however such data should be used cautiously as the statistical is quite small and applicable for certain windage profiles. In case the profile in question is outside this selected one, then there is a risk of improper estimation of the wind resistance coefficient. Furthermore, the sensitivities of the wind resistance coefficients with regards to a specific windage profile are not depicted at all.

For this reason, the Wind Resistance coefficient estimation method chosen for the present methodology design and simulation modules is the regression formulae developed by Fujiwara

(Fujiwara, et al., 2005) which is also a method favoured in the prevailing (ISO15016:2015, 2015) intended for sea trial data analysis of Newbuilding vessels. Fujiwara's method is considered reliable, robust, and accurate as the formula contains sensitivities and correlations with the hull and deckhouses geometry (via the use of projected surfaces).

The developed regression formula of Fujiwara takes the below formulation:

$$C_{AA}(\psi_{WR}) = C_{LF} * \cos(\psi_{WR}) + C_{XLI} * \left(\sin(\psi_{WR}) - \frac{1}{2} * \sin(\psi_{WR}) * \cos^2(\psi_{WR}) \right) * \sin(\psi_{WR}) * \cos(\psi_{WR}) + C_{ALF} * \sin(\psi_{WR}) * \cos^3(\psi_{WR}) \quad (30)$$

With the following expressions developed for individual components of the wind resistance coefficients:

For $0 \leq \psi_{WR} < 90 \text{ deg}$

$$C_{LF} = \beta_{10} + \beta_{11} * \frac{A_{LV}}{L_{OA} * B} + \beta_{12} * \frac{C_{MC}}{L_{OA}} \quad (31)$$

$$C_{XLI} = \delta_{10} + \delta_{11} * \frac{A_{LV}}{L_{OA} * H_{BR}} + \delta_{12} * \frac{A_{XV}}{B * H_{BR}} \quad (32)$$

$$C_{ALF} = \varepsilon_{10} + \varepsilon_{11} * \frac{A_{OD}}{A_{LV}} + \varepsilon_{12} * \frac{B}{L_{OA}} \quad (33)$$

For $90 < \psi_{WR} \leq 180 \text{ deg}$

$$C_{LF} = \beta_{20} + \beta_{21} * \frac{B}{L_{OA}} + \beta_{22} * \frac{H_C}{L_{OA}} + \beta_{23} * \frac{A_{OD}}{L_{OA}^2} + \beta_{24} * \frac{A_{XV}}{B^2} \quad (34)$$

$$C_{XLI} = \delta_{20} + \delta_{21} * \frac{A_{LV}}{L_{OA} * H_{BR}} + \delta_{22} * \frac{A_{XV}}{A_{LV}} + \delta_{23} * \frac{B}{L_{OA}} + \delta_{24} * \frac{A_{XV}}{B * H_{BR}} \quad (35)$$

$$C_{ALF} = \varepsilon_{20} + \varepsilon_{21} * \frac{A_{OD}}{A_{LV}} \quad (36)$$

And for the case of $\psi_{WR} = 90 \text{ deg}$

$$C_{AA}(90) = \frac{1}{2} * \{C_{AA}(90 - \mu) + C_{AA}(90 + \mu)\} \quad (37)$$

With:

$C_{AA}(\psi_{WR})$:	Wind Resistance coefficient for a given wind angle
ψ_{WR} :	Relative Wind Direction in degrees
L_{OA} :	Ship's Length Over All in meters
B :	Ship's Breadth in meters
A_{OD} :	Lateral Projected Area of superstructures above upper deck in square meters
A_{XV} :	Transverse Projected Area above the waterline, including superstructures in square meters

- A_{LV} : Lateral Projected Area above the waterline including superstructures in square meters
- C_{MC} : Horizontal distance from midship section to the centre of the lateral projected area where, positive is forward of the midship, in meters.
- H_{BR} : Height of top of the superstructure in meters.
- H_C : Height from waterline to centre of the lateral projected area in meters.
- μ : Smoothing range in degrees.

The coefficients β_{ij} , δ_{ij} , ε_{ij} can be found in tabular format in (Fujiwara, et al., 2005), (ISO15016:2015, 2015). The inputs and coordinate system used in the above described method are depicted in the Figure 16 below:

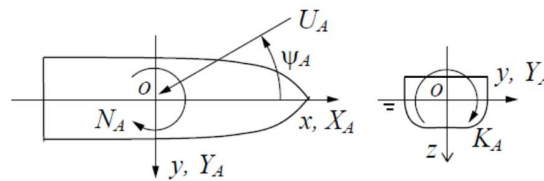


Fig. 1 Coordinate system.

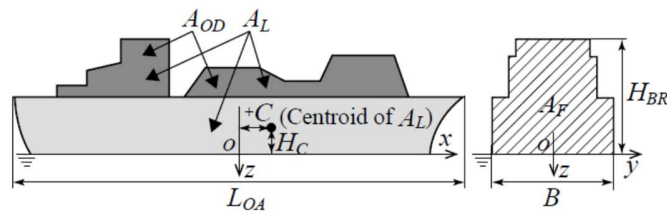


Figure 16: Coordinate system and input used in Fujiwara empirical formula for the estimation of added resistance due to wind (Fujiwara, et al., 2005).

4.3.3. Added Resistance due to Fouling

The effect of resistance due to fouling has been well documented in the works of Townsin. It is evident that for ships in service this resistance (and the relevant consumption) can be significant and affect significantly the performance of the hull and the propeller. Especially in limit state conditions where the vessel is subject to adverse wind, wave and current conditions, the absence or presence of fouling is a key factor in the assessment of any involuntary loss of speed. To date, the effect of fouling has not been considered in the early ship design process other than implementing the 15% offset margin on the main engine. However, with the use of the herein proposed methodology, the fouling can be more accurately depicted and its effect alter several design parameters with foremost being hull, engine and propeller matching.

For this simulation framework focusing on a fast and early ship design approach, the model of Townsin has been chosen for estimated the added resistance of each design due to fouling. More specifically, the following formula is employed (Townsin, 2003):

$$\frac{\Delta R}{R} = \frac{\Delta C_F}{C_T} = 0.044 * [(k_2/L)^{1/3} - (k_1/L)^{1/3}] \quad (38)$$

With k_2 and k_1 being the current and previous hull roughness respectively. The hull roughness increase on an annual basis is also estimated from (Townsin, 2003) which starts from an average and continues at an exponential rate.

Furthermore, in order to further enhance the lifecycle considerations, the dry-docking recoating is taken into account in the 5, 10, 15, 20 and 25-year interval with a reduction of the roughness to a level 10% higher than the previous coating system (e.g. roughness in 5 years is 10% higher than the newbuilding value, roughness in 10 years is 10% than the 5-year value etc.). The starting roughness value at the delivery stage of the vessel is assumed to be an average value of 97.5 microns (average of minimum reading of 75 μ and maximum reading of 120 μ). The roughness increase can be also observed in Figure 17.

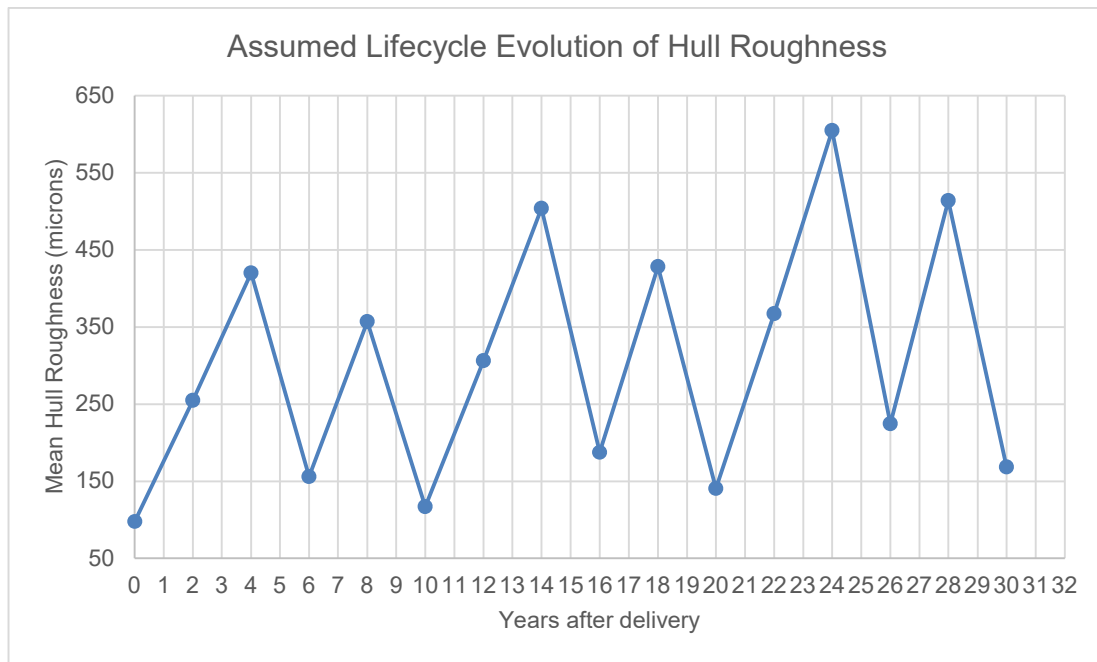


Figure 17: Assumed Roughness Increase as a function of Dry-Docking and Special Survey Cycles

The power increase corresponding to the above resistance increase is approximated by the following formula (Townsin, 2003):

$$1 + \frac{\Delta P}{P} = \frac{1 + \Delta R/R}{1 + \Delta \eta/\eta} \quad (39)$$

With the increase in the propeller open water efficiency being:

$$\frac{1}{1+\Delta\eta/\eta} = 0.30 * \left(1 + \frac{\Delta R}{R}\right) + 0.70 \quad (40)$$

4.4.Propulsion

In the propulsion module of the methodology, the generated hull with the calm water resistance characteristics (Effective Horsepower) estimated is matched with a propeller in order to be derived with the Delivered, Shaft Horsepower.

This coupling of hull and propeller is done through the well-known equation:

$$P_S = P_E * \frac{1-t}{1-w} * \eta_0 * \eta_R * \eta_S \quad (41)$$

Where:

P_E : Effective Horsepower as estimated from Calm Water Resistance Module (3.2.3)

P_S : Shaft Horsepower

w : Wake Fraction

t : Thrust Deduction

η_R : Relative Rotative Efficiency

η_0 : Propeller Open Water Efficiency

η_S : Shafting System Efficiency

4.4.1. Wake Fraction Estimation

Originally and for many applications of the methodology, the wake fraction has been estimated using the calibrated formulas of *Holtrop* (equations with calibrated coefficients L58-64 and B61-67), *Schneekluth* (equations with calibrated coefficients L65-67 and B68-70), *Kruger* (equations with calibrated coefficients L68-69 and B71-72), *Hecksher* (equations with calibrated coefficients L70-71 and B73-74) and *Troost* (equations with calibrated coefficients L72-73 and B75-76). As discussed in paragraph 5.1, subject calibrated coefficients have an improved accuracy compared to original ones. However, using the same pool of model test results that have been used for the Holtrop and propulsion coefficients calibration a new “digital-twin” expression has been generated to encompass the speed (Froude Number) sensitivity of the propulsion coefficients which is not depicted in any of the above formulas. The method selected to generate such a formulation is non-linear regression through the relevant command of the IBM SPSS® toolkit. The generalized equation has the following form:

$$w = a * C_b^a + b * Fn^b \quad (42)$$

Where:

C_b : is the ship’s block coefficient at the given draft.

F_n : is the Froude number at the given operating speed.

One can clearly notice that the equation's first part is the same as in all other empirical formulations, however, the second part has a non-linear component of the Froude number. As the results pool has been separated laden (design and scantling) and ballast (heavy and light) drafts and for the sake of better fitting and accuracy, two different expressions have been generated, one corresponding to each loading condition with the below finalized result:

$$w = \begin{cases} 0.227 * C_b^{-1.699} + 84.146 * F_n^{4.693} & \text{for Laden Conditions} \\ 0.357 * C_b^{-0.582} - 0.149 * F_n^{0.504} & \text{for Ballast Conditions} \end{cases} \quad (43)$$

4.4.2. Thrust Deduction Estimation

Similarly to the wake fraction, for many applications of the methodology, the thrust deduction coefficient has been estimated using the calibrated formulas of *Holtrop* (equations with calibrated coefficients L54-57 and B57-60). Again for this coefficient, by using the same pool of model test results that have been used for the Holtrop and propulsion coefficients calibration, a new "digital-twin" expression has been generated to encompass the speed (Froude Number) sensitivity of the propulsion coefficients which is not depicted in any of the above formulas. The method selected to generate such a formulation is non-linear regression through the relevant command of the IBM SPSS® toolkit. The generalized equation has the following form:

$$t = A * C_b^a + B * F_n^b * + C * D_{prop}^c \quad (44)$$

Where:

C_b : is the ship's block coefficient at the given draft.

F_n : is the Froude number at the given operating speed.

D_{prop} : is the propeller diameter in meters

As the results pool has been separated laden (design and scantling) and ballast (heavy and light) drafts and for the sake of better fitting and accuracy, two different expressions have been generated, one corresponding to each loading condition with the below finalized result:

$$t = \begin{cases} -37.014 * C_p^{47.36} + 0.048 * F_n^{-0.057} + 0.095 * (D_{prop})^{0.183} & \text{for Laden Conditions} \\ -0.531 * C_p^{15.354} - 1.632 * F_n^{0.007} * + 1.686 * (D_{prop})^{0.037} & \text{for Ballast Conditions} \end{cases} \quad (45)$$

4.4.3. Relative Rotative Efficiency Estimation

The relative rotative efficiency coefficient is estimated using the formulas with calibrated coefficients L50-53 and B53-56 generated from the Holtrop Calibration process described in

paragraph 5.1. As the estimation accuracy for this coefficient is excellent and there is little to no sensitivity to the operating speed (Froude number), no further expressions have been generated for this.

4.4.4. *Shafting System Efficiency Estimation.*

As the vessel type(s) herein examined have standardized shafting systems of direct-driven propellers with an intermediate shaft, intermediate bearing and tailshaft, the shafting system efficiency is typical 0.97-0.98 depending on the maker of the stern tube bearings and the length of the shafting system. For this reason, the shafting system of the parent vessel of 0.97 was selected as the standard for the studies. However, this may require revision in case the method is expanded to containership applications where the shafting length, number of shafts and number of bearings is considerably bigger.

4.4.5. *Propeller Open Water Efficiency Estimation*

The propeller efficiency estimation requires the modelling of the propeller as well as the estimation of its operating point. An approach could be to model a custom propeller in CAESES® geometrically. However, to define the operating point in terms of its advance coefficient (J), operating revolutions and speed, numerical open-water sea trials should be conducted. As the meshing generation (with sliding meshes to capture the revolution properly) is quite challenging, time-consuming and with a big computing power demand, this approach wasn't considered.

Instead, the propeller is assumed geometrically as a disc for all geometrical operations in CAESES®, while for all simulations and computations a series propeller is used instead. The most common and widely spread propeller series for large commercial vessels are the Wageningen B-Series (Lammeren, et al., 1969), (Oosterveld & van Oossanen, 1975) as they are the most extended with about 120 model propellers examined having from two to seven blades and big range of expanded area ratios as well as pitch ratios.

The Wageningen polynomials together with the complete K_t and K_q curves have been programmed in a feature within CAESES® as found in (Bernitsas, et al., 1981) and all polynomials developed in a dedicated database. By entering the following data, the user can generate the K_t and K_q curves as well as all open water characteristics of the defined and selected propeller:

1. Reynolds number where the propeller is operating
2. Expanded Area Ratio $\frac{A_E}{A_0}$
3. Pitch over Diameter Ratio P/D
4. Number of Blades Z

The above three together with the propeller Diameter are used as the design variables of the propeller and consequently each vessel variant during the optimization studies.

The following three codes have been developed in the design and simulation framework within CAESES® to derive the propeller characteristics:

1. “B-Series J”:

This feature code contains the Wageningen polynomials and generates K_t and K_Q curves for a defined propeller as described above. The code input is the following:

- i. Propeller Characteristics: Expanded Area Ratio $\frac{A_E}{A_0}$, Pitch Ratio P/D , Number of Blades Z , Propeller Diameter.
- ii. Reynolds number, Re
- iii. Revolutions (can be entered also in series for curve generation).
- iv. Advance Coefficient, J

The code output is the K_t and K_Q coefficients as well as the propeller open water efficiency. The feature can be used iteratively to generate the entire K_t and K_Q curves or called independently to give as an output single values for the propeller selection.

2. “RPM”:

This feature code utilizes the output data of the B-Series J code for determining the operating point of a defined propeller for a hull with given characteristics. The following data are used as input:

- i. Operating Speed, V_S in meters per second
- ii. Reynolds number, Re
- iii. Propeller Characteristics: Expanded Area Ratio $\frac{A_E}{A_0}$, Pitch Ratio P/D , Number of Blades Z , Propeller Diameter.
- iv. Revolutions in RPS (starting value prior iterations used).
- v. Sea Water Density, ρ_{SW}
- vi. Hull Total Resistance, R_t
- vii. Bollard Pull (if any), F
- viii. Thrust Deduction t ,
- ix. Wake w

Following iterations of the advance coefficient and RPM, the code returns as an output the finalized K_t , K_Q , open water efficiency η_0 as well as the final, “balance” propeller operating point (RPM and J).

3. *Propsel*

This feature code is for selecting and matching a propeller to the generated hull. It has the same input as the RPM code with the addition of the operating speed range to be examined, the starting advance coefficient J , the vessel’s speed-resistance curve, the vessel’s dimensions, the relative rotative efficiency η_R , and shaft efficiency η_S .

The code effectively calls for every speed-resistance point of the RPM code and afterwards solves the self-propulsion equilibrium described above to derive the delivered power and total propulsive efficiency. The code output in turn is the Speed – Delivered Power (P_D) and Speed – RPM curve (propeller curve) of the vessel. The curve is a B-Spline

interpolating 10 distinctive calculation points that are defined by the user as described above.

The communication and flowchart between the various features of the propeller selection module of the methodology are also identified in Figure [30].

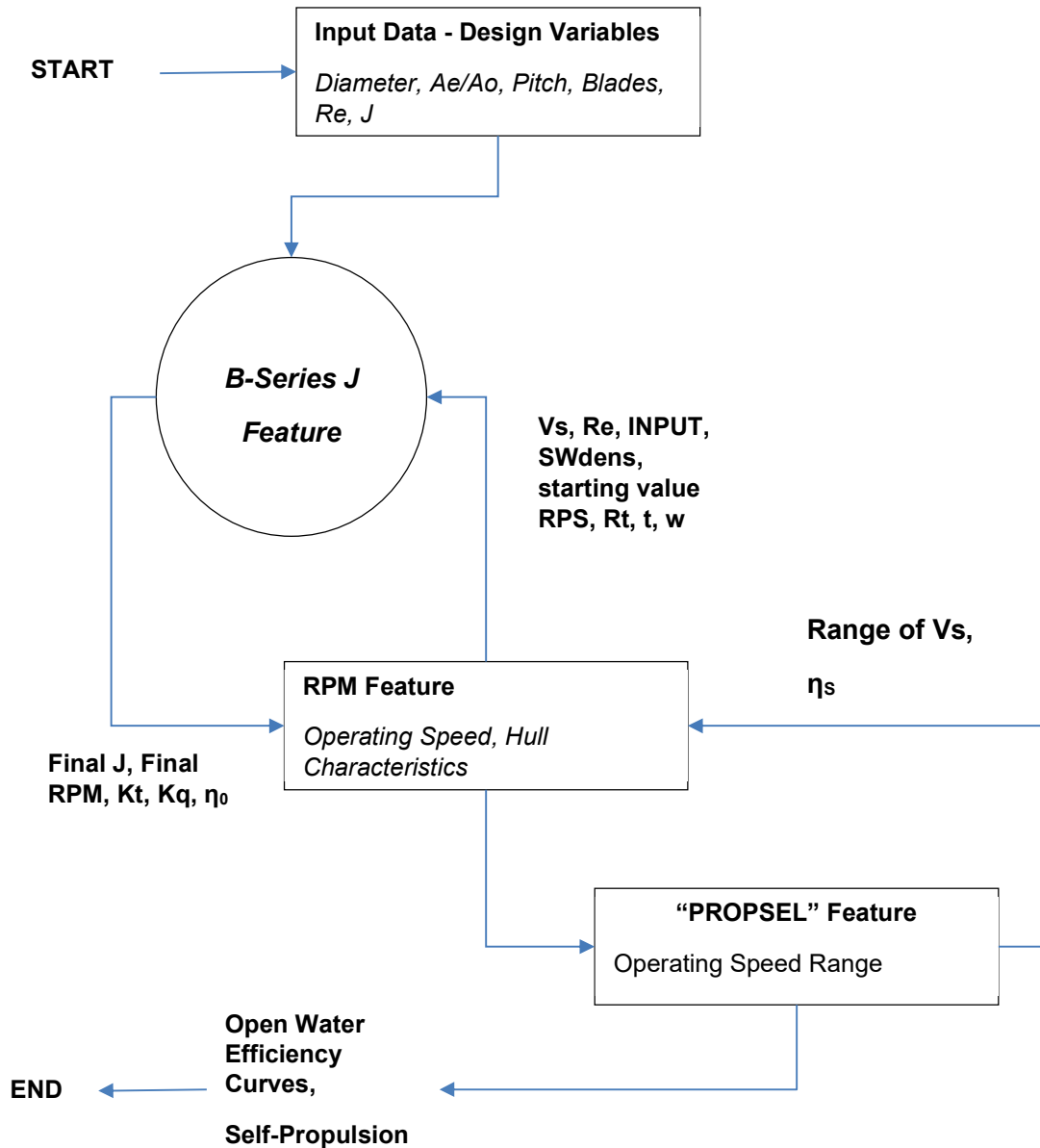


Figure 18: Flowchart of propeller calculation and propeller design selection

4.5. Electrical Load Analysis and Diesel Generators Sizing

For each design variant, given that the Main Engine has been selected and tuned in the Engine Selection module, the electrical balance and sizing of generators are followed. Given that for most ship types herein examined (bulk carriers, containerships) the Engine Room equipment and ancillaries size, capacity and thus electrical power heavily depend on the Main Engine output. An exception is the case of Tankers for which the electrical power requirements also depend on Auxiliary Boilers, the number and type of ballast pumps (steam or electrically driven), as well the cargo handling system (in case of FRAMO deep well pump installation). Lastly, for all vessel types, the installation of Ballast Water Treatment Systems (BWTS) imposes an additional load which in the case of electrolysis-based systems is considerable, especially in peak capacities and low salinity levels.

For the current methodology and the preliminary design of the vessel, the approach considered can be regarded as a “digital twin” method. The parent vessel electrical load analysis is analysed with all consumers being non-dimensionalised with the Main Engine’s SMCR for each of the prescribed operating conditions (Table 6). The consumer ratios can be safely considered as constant between the parent vessel and design variants. The electrical load analysis prescribed operating conditions follow the format of the respective analysis of the parent vessel:

1. Normal Sea Going (Continuous and Intermittent Loads)
2. Normal Sea Going in Ballast Condition (Continuous and Intermittent Loads)
3. Manoeuvring (Continuous and Intermittent Loads)
4. Loading with BWTS (Continuous and Intermittent Loads)
5. Unloading with BWTS (Continuous and Intermittent Loads)
6. Port / Anchorage (Continuous and Intermittent Loads)
7. Emergency (Continuous and Intermittent Loads)

Furthermore, with regards to the Ballast Water Treatment System, the latter is assumed to be of electrolysis type following the parent vessel. Initially, the required capacity of each ballast pump is calculated assuming that the vessel should be able to de-ballast its entire capacity for a given time (usually assumed 24-48 hours) by the user. For a given ballast pump capacity, a BWTS capacity is matched, and the relevant power requirements are assessed. The factor of 0.4 is used for the intermittent loads pursuant to the load calculations of the parent vessel building yard.

For estimating the alternator an additional margin of 10% is used, while an electrical efficiency of 0.85 is applied for estimating the required diesel generator engine power, assuming 3 sets of generators as per standard shipbuilding practice.

The SFOC curves of the generators are matched from the corresponding model capacities of the MAN and YANMAR catalogues depending on engine rating.

	Normal Sea Going		Manoeuvring		Loading/Unloading		Port	
	C.L	I.L	C.L	I.L	C.L	I.L	C.L	I.L
Machinery	0.025443	0.00506	0.03325	0.01660	0.07738	0.01660	0.01103	0.00688
Deck Equipment	0.02155	0.00026	0.01658	0.00860	0.00045	0.01200	0.00045	0.00209
Galley Equipment	0	0.00242	0	0.00242	0	0.00242	0	0.00242
Air Conditioning and Refrigeration Plant	0.00845	0.00025	0.00704	0.00025	0.00719	0.00025	0.00719	0.00025
Electrical Equipment	0.00276	0	0.00294	0	0.00295	0	0.00268	0

Table 6: Non-dimensionalised (with M/E SMCR) electrical load analysis from the parent vessel

4.6.Steam Balance and Composite Boiler Load

Similarly, to the case of the electrical balance, the steam balance of the vessel follows a “digital-twin” approach. For the case of bulk carriers that is herein examined, the onboard steam is required for the applications of fuel tank heating (whether a bunker or settling/service tanks) and Engine Room auxiliaries. For this application, the steam consumption (in kg/h) is non-dimensionalised by the fuel tank capacity (calculated in intact stability module) as seen in Table 7. For tanker applications, however, this is applicable only for the seagoing conditions as in the loading and discharging conditions the steam consumption curves of the Cargo and Ballast Pump steam turbines are modelled accordingly.

It should be noted that given the sensitivity in ambient weather conditions, the steam balance is considered for the winter and summer seasons respectively as per standard shipbuilding practice.

Tank Heating <i>Non dimensionalised by tank capacity</i>	ISO Condition	Winter Condition	Tropical Condition	Winter Port Condition
No.3 HFO (P)	0.21238	0.30551	0	0
No.3 HFO (S)	0.04141	0.13177	0	0.13177
No.1 HFO Service	0.40490	0.41308	0.37268	0.41308
No.1 HFO Settling	1.38241	1.39059	1.36196	1.39059
FO Sludge Tank	0.33249	0.49622	0	0.24937
FO Drain Tank	0.42424	0.81818	0	0
FO Overflow Tank	0	0	0	0

LO Sump Tank	0	0	0	0.056818
LO Sludge Tank	0.24623	0.31658	0	0.316583
Waste Oil Tank	0.70703	1.28125	0	1.28125
Engine Room Machinery <i>Non-dimensionalised by M/E SMCR</i>	ISO Condition	Winter Condition	Tropical Condition	Winter Port Condition
M/E FO Heaters	0.01282	0.01282	0.01282	0
D/Gs FO Heaters	0.00279	0.00279	0.00279	0.00279
FO Purifier Heaters	0.01270	0.01270	0.01270	0.01270
M/E LO Purifier Heater	0.00698	0.00698	0.00698	0
D/Gs LO Purifier Heater	0.00254	0.00254	0.00254	0.00254
M/E Jacket Water Preheater	0	0	0	0.01778
E/R General Service	0.00158	0.00158	0.00158	0.00158
Steam Tracing	0	0.00476	0	0.00952
HVAC	0	0.02571	0	0.02571
Calorifier	0.00457	0.00762	0.00228	0.00762
Sea Chests	0	0.00095	0	0

Table 7: Non-dimensionalised steam balance of parent vessel used here. All original steam consumptions were in kg/hCh

4.7. Lightship Weight Estimation

The lightship weight calculation is the next computation after the dimensioning of the Main Engine and Engine Room. The lightship weight estimations follow the traditional ship theory categorization into the 3 following weight categories (main):

1. Steel Weight
2. Machinery Weight
3. Outfitting Weight

For the basic design stage, typically analytical computations and a bill of materials are used, while in the preliminary stage various well-established empirical formulae and semi-analytical methods (e.g. Schneekluth method) are employed. In this study, a “hybrid” approach similar to previous sections is followed where empirical methods are calibrated based on either digital twin data or statistical databases.

4.7.1. Steel Weight

During the initial design stages, and the selection of optimal main dimensions, it is necessary to identify the effect of the change of the principal dimensions of a reference ship on the structural steel weight. Thus, at first, an accurate calculation of the steel weight of the reference ship is necessary. This can be done by modelling the entire hull structure in the design environment, modelling all major structural members (frames, bulkheads, longitudinal stiffeners, floors, girders etc) and assessing their strength and thickness based on current Class Rules (for the case of bulk carriers and tankers IACS Harmonized Common Structural Rules). This however on one hand requires the integration of a structural design software containing Class rules in the main design software and increased computing power on the other hand. Such integrations, apart from being rarely applied (Sames, et al., 2011) exhibit robustness issues and can work better in optimization applications where the variable range is relatively narrow.

Another approach, which has the degree of accuracy required in the preliminary design stage is the Schneekluth’s Lightship Weight Method (Papanikolaou, 2014). The method is a semi-analytical method developed for bulk carriers with hatch covers but expanded into several ship types. The method doesn’t include the weight of superstructures and deckhouses which is in turn calculated with the semi-analytical method of Müller and Kostner (Papanikolaou, 2014).

The steel weight estimation is based on the calculation of the total volume underneath the main deck of the vessel (including the additional volume due to sheer, camber and hatch coamings) corrected in the form of regression as per the below formula:

$$W'_{ST} = \nabla_U * C'_{ST} * \left[1 + 0.033 * \left(\frac{L}{D} - 12\right)\right] * \left[1 + 0.06 * \left(n - \frac{D}{D_0}\right)\right] * \left[1 + 0.05 * \left(1.85 - \frac{B}{D}\right)\right] * \left[1 + 0.2 * \left(\frac{T}{D} - 0.85\right)\right] * [0.92 + (1 - C_{BD})^2] * [1 + 0.75 * C_{BD} * (C_M - 0.98)] \quad (46)$$

Where $D_0 = 4m$ and $\frac{L}{D} \geq 9$ and C'_{ST} is a volume coefficient (ton/m³) that follows a range on the ship type.

This method has been herein further improved by using the actual construction data of the parent vessel. As the author has supervised the construction of the parent vessel at a prominent shipbuilding yard in China, all structural drawings along with construction drawings were available. Interestingly, as per the yard's safety practices, the steel weight of each shipbuilding block is calculated in advance to make the necessary rigging calculations for transportation from the block fabrication areas to the hull erection area next to the dry dock. All block weights have been thus collected and analysed to derive the exact weight of the entire steel structure (including outfitting).

Following this, a T-Search algorithm was employed to vary the values of the statistical coefficients and constants of subject methodology with the objective of the minimization of the difference between the actual and calculated values for the steel weight. The result was accuracy of 0.3% which is more than acceptable within the scope of basic/preliminary design. A different approach for increasing the accuracy and developed previously by the Author (Nikolopoulos, 2012) is a "zonal approach" of the hull areas to the cargo area, fore and aft end areas, respectively. The cargo area is calculated with the use of a response surface developed from a structural model while the fore and aft end weights are approximated as the residual weight from semi-analytical cubical methods like this of Schneekluth.

4.7.1.1. Machinery Weight

The machinery weight calculation is considered herein as the average of two methods: the Watson-Gilfillan formula and the calculation based on the Main Engines weight respectively.

1. The Watson-Gilfillan formula (Papanikolaou, 2014) is the following expression:

$$W_m = C_{md} * Pb^{0.89} \quad (47)$$

2. The other approach is to approximate the machinery weight based on the Main Engine weight as the latter is the largest component and its size affects all other engine room equipment:

$$W_m = W_{engine} + 0.72 * CSR^{0.77} , \text{ with the Main Engine weight being available from the Engine selection module database developed (paragraph 3.2.6) and the CSR being the continuous service rating of the engine (not to be confused with the SMCR).}$$

The two results are averaged to balance out any extreme differences.

4.7.1.2. Outfitting Weight

The outfitting weight is given that the outfittings of commercial vessels like bulk carriers, tankers and containerships are heavily correlated with the vessel's size are calculated with the use of a simplified empirical regression formula of the following expression (Papanikolaou, 2014):

$$W_{OT} = k_{OT} * L * B \quad (48)$$

With k_{OT} being a constant depending on ship type (default range of 0.17-0.8 t/m² for large bulk carriers).

4.7.2. Total Lightship Weight

The total lightship weight can be thus estimated as the sum of the steel, machinery, and outfitting weights. In order to validate the changes and calibrations (especially for the part of the steel

weight adaptation of Schneekluth’s method), the method calculation results have been compared with the actual lightship weights for a database of 34 large bulk carriers (larger than Panamax) that the Author has compiled (Table 8).

Vessel	Loa	Lpp	B	D	Ts	CB Ts	CM Ts	Engine	LW	Wst Schneekluth	Wm Watson Gilfillan	Wot	Wls calc	Wls real	Diff LS %
	[m]	[m]	[m]	[m]	[m]	[-]	[-]	[kW]	[t]	[t]	[t]	[t]			
VSL01 - PARENT	299.98	294	50.00	25	18.50	0.853	0.992	17494	26119	20413	1663	4043	26119	26119	0.0
VSL02	300	295.5	50.00	25	18.43	0.853	0.992	15250	28947	20401	1469	4043	25913	28947	11.7
VSL03	292.00	288.40	45.00	24.55	18.18	0.859	0.992	15860	24660	17838	1522	3542	22901	24660	7.7
VSL04	291.98	283.8	45.00	24.7	18.23	0.865	0.998	18660	24996	17997	1762	3541	23301	24996	7.3
VSL05	288.93	280.80	45.00	24.70	18.17	0.858	0.998	18630	21811	17577	1760	3504	22841	21811	4.5
VSL06	288.90	280.80	45.00	24.70	18.17	0.858	0.998	18630	21905	17569	1760	3504	22833	21905	4.1
VSL07	292	283	45.00	24.75	18.20	0.863	0.993	18660	26109	17898	1762	3542	23202	26109	12.5
VSL08	292.00	282.00	45.00	24.80	18.32	0.837	0.998	16860	24780	17571	1608	3542	22721	24780	9.1
VSL09	289.00	279.00	45.00	24.40	17.98	0.860	0.992	16860	21364	17525	1608	3505	22639	21364	5.6
VSL10	288.97	279.00	45.00	24	17.96	0.859	0.998	16860	21786	17583	1608	3505	22697	21786	4.0
VSL11	289.00	279.00	45.00	24.50	18.12	0.847	0.998	16860	23743	17432	1608	3505	22546	23743	5.3
VSL12	288.93	280	45.00	23.8	17.62	0.845	0.998	16107	21018	17337	1543	3504	22385	21018	6.1
VSL13	288.00	278.00	45.00	24	17.71	0.845	0.998	15886	21020	17249	1524	3493	22267	21020	5.6
VSL14	288.97	278.00	44.98	24	17.65	0.846	0.998	17091	21472	17347	1628	3503	22478	21472	4.5
VSL15	288.15	277.45	44.00	23.9	17.63	0.853	0.998	14710	23954	17021	1422	3417	21860	23954	9.6
VSL16	239.99	236.00	38.00	19.95	14.48	0.852	0.998	12700	14835	10645	1246	2458	14348	14835	3.4
VSL17	229.00	219.90	36.50	19.9	14.14	0.861	0.992	10300	13027	9521	1031	2253	12805	13027	1.7
VSL18	228.99	222.00	32.26	19.9	14.43	0.885	0.997	9800	10806	8733	986	1991	11710	10806	7.7
VSL19	228.99	222.00	32.26	19.9	14.43	0.885	0.997	11000	10978	8733	1094	1991	11818	10978	7.1
VSL20	228.99	222.00	32.26	19.9	14.43	0.885	0.997	9800	10999	8733	986	1991	11710	10999	6.1
VSL21	228.99	222.00	32.26	20.03	14.43	0.885	0.997	9800	11161	8737	986	1991	11714	11161	4.7
VSL22	228.99	222.00	32.26	20.03	14.43	0.885	0.997	9800	11206	8737	986	1991	11714	11206	4.3
VSL23	228.99	222.00	32.26	20.03	14.43	0.885	0.997	9800	11182	8737	986	1991	11714	11182	4.5
VSL24	228.99	222.00	32.26	20.03	14.43	0.885	0.997	9800	11186	8737	986	1991	11714	11186	4.5
VSL25	228.99	222.00	32.26	20.03	14.43	0.885	0.997	9800	11535	8737	986	1991	11714	11535	1.5
VSL26	228.99	222.00	32.26	20.03	14.43	0.885	0.997	9800	11559	8737	986	1991	11714	11559	1.3
VSL27	229.00	223.50	32.26	20.2	14.47	0.895	0.998	10260	14098	8820	1028	1991	11839	14098	19.1
VSL28	229.00	226.15	32.36	20	14.48	0.880	0.994	8880	12578	8716	902	1997	11615	12578	8.3
VSL29	225.00	217.00	32.26	19.3	14.03	0.860	0.992	9350	10151	8236	945	1956	11137	10151	8.9

VSL30	225.00	217.00	32.26	19.3	14.03	0.862	0.997	8830	10194	8276	897	1956	11130	10194	8.4
VSL31	225.00	218.00	32.20	19.2	13.82	0.870	0.993	8826	10061	8266	897	1953	11116	10061	9.5
VSL32	225.00	216.00	32.26	19.2	13.87	0.839	0.997	8628	9448	8108	879	1956	10944	9448	13.7
VSL33	225.00	216.00	32.26	19.2	13.87	0.839	0.997	8877	9495	8108	902	1956	10967	9495	13.4
VSL34	224.94	217.00	32.20	18.74	13.55	0.851	0.997	10223	10165	8106	1024	1952	11083	10165	8.3

Table 8: Database used for lightship weight estimation calibration

It should be noted that all vessels are gearless bulk carriers. The finalized coefficients after calibration take the form in equations 49 to 51. It should be noted that the calibration has been conducted with the use of a T-Search solver in Microsoft Excel™ having as variables the original constants of the Schneekluth methodology and optimizer target the minimization of average prediction error for all database vessels.

1. Steel Weight with Schneekluth's Method:

$$W'_{ST} = \nabla_U * C'_{ST} * \left[1 + 0.03380175 * \left(\frac{L}{D} - 13.176\right)\right] * \left[1 + 0.06 * \left(n - \frac{D}{D_0}\right)\right] * \left[1 + 0.05801716 * \left(1.7679434 - \frac{B}{D}\right)\right] * \left[1 + 0.27840088 * \left(\frac{T}{D} - 0.948001\right)\right] * [0.88079956 + (1 - C_{BD})^2] * [1 + 0.69496928 * C_{BD} * (C_M - 0.98)] \quad (49)$$

2. Outfitting Weight

$$W_{OT} = 0.26952941 * L * B \quad (50)$$

3. Machinery Weight:

$$W_m = 0.24751198 * P b^{0.89} \quad (51)$$

The lightship weight is increased over time due to the accumulation of fuel sludge, mud in ballast tanks, spares and stores etc. However, this effect is considered negligible and can be incorporated by a very small adjustment in the deadweight constants value as done by Chief Officers during loading conditions calculations. In view of this, no such considerations are herein considered. It should be also noted that as per current Class Rules, even in the case of retrofits such as BWTS and Exhaust Gas Cleaning Systems (EGCS / Scrubbers) installations the re-calculation of the lightship weight is omitted as the total change is less than 2% of the total weight (United States Coastguard, 2016)

4.7.3. Deadweight Analysis

For a given lightship and the subtraction of the latter from the displacement at the design draft the deadweight is derived which is decomposed to the following sub-groups of weights:

1. Consumables
 - a. Fuel (VLSFO and LSMGO)
 - b. Lube Oil
 - c. Stores and Supplies
2. Crew and Effects

- a. Crew (30 people)
 - b. Fresh Water
3. Deadweight Constant
- a. Constant of 654.5 tons as per parent vessel analysis.

The above are estimated for a range of 25,000 nautical miles which is typical requirements in Shipbuilding Specifications for vessels of the examined size and type and a complement of 30 crew members (for stores and freshwater estimations). Furthermore, the exact quantities in both the “DEPARTURE” and “ARRIVAL” conditions are considered with the arrival quantities assumed to be either 10% of the departure quantities or the results of actual consumption measurement (in the simulation module). The relevant centres of gravity are also calculated. The result is that the total payload capacity in tons is estimated. Based on the cargo holds volumetric capacity that is calculated in paragraph 4.2, the minimum cargo density is calculated and assessed as a constraint in the optimization process.

4.8. Hydrostatics, Trim, Stability and Loadline

The hydrostatics in the herein presented methodology are focused on three areas:

1. Initial Hull Form Hydrostatics Assessment
2. Trim and Stability Calculations for Intact Condition
3. Loadline and Freeboard Calculations.

For the commercial vessels that are herein examined (bulkers and tankers) the damaged stability is not a critical path aspect of the study as all such vessels have an inherent very good performance. The survivability of a vessel however is of a much higher importance for the designer in the cases of passenger and naval vessels. For the case of container vessels for which the loading conditions are critical and quite challenging due to the frequent port of calls, a separate module has been developed by the Author in CAESSES® in (Koutroukis, et al., 2013), (Nikolopoulos, et al., 2014) for the loading condition analysis and optimal loading of container vessels with a focus on the updated weather criterion in the IMO Intact Stability code.

The first stage of hydrostatic calculations takes place at the initiation of each design variant as per methodology workflow (Figure [4]), where the initial hull surface hydrostatic properties are calculated using the embedded hydrostatic computations of CAESSES®. The properties calculated include but are not limited to Displacement Volume, Centre of Buoyancy (LCB, VCB, TCB), Moments of Inertia, Wetted Surface, Waterline Area, Centre of Floatation (LCF, VCF, TCF) etc. The calculation is performed in two steps:

1. Calculation of Origin Hull (generated based on input design variables) and determination of C_b and LCB .
2. Calculation of Transformed Hull, where the hydrostatic properties of the Lackenby transformed hull surface (to match the desired C_b and LCB are computed.

The second stage of hydrostatic calculations is performed in the Trim and Stability Module. In this module, the trim and stability calculations for a set of prescribed loading condition is done where the trim, GM and weather criterion are checked in accordance with the IMO Intact Stability Code (International Maritime Organization (IMO), 2008). The following common prescribed loading conditions (Table 9):

Condition I.D	Loading Condition
L-SC-DEP	Full Load Departure – Scantling Draft
L-SC-ARR	Full Load Arrival – Scantling Draft
L-DE-DEP	Full Load Departure – Design Draft
L-DE-ARR	Full Load Arrival – Design Draft
L-PAR-DEP	Partial Load Departure – Pig Iron Loading
L-PAR-ARR	Partial Load Arrival – Pig Iron Loading
BAL-DEP	Light Ballast Departure
BAL-ARR	Light Ballast Arrival

Table 9: Loading Conditions examined in Stability Module.

An important aspect of the stability calculations is the input used for the centres of gravity of the different weight groups.

1. The centre of gravity of the cargo holds is determined from the capacity calculation done in the respective module for each cargo hold.
2. Lightship Weight
Both the longitudinal and vertical centre of gravity for the lightship weight is done for each respective weight category independently (Steel, Machinery, Outfitting) with the total lightship LC and VCG being derived from the torque equation. The independent weight categories centres of gravity are derived either from each methodology (e.g. from Schneekluth method for steel weight), empirical values (e.g. for outfitting weight) or from the vessel's arrangement (e.g. volumetric centre of Engine Room space for machinery weight).
3. The centre of gravity for the consumables (Fuels, Lubes, Stores, Crew etc) using the same non-dimensional ratios of the parent vessel for the respective categories, with LCG being non-dimensionalised with length and VCG by depth.

The third stage of hydrostatic calculations is the calculation of the Load Line, minimum freeboard and minimum bow height in accordance with the IMO International Convention on Loadlines of 1966 (International Maritime Organization (IMO), 1966). This is done with an embedded feature in CAESES that with minimum input does the necessary calculations. The loadline and minimum freeboard are used also as a constraint in the Design Optimization studies.

Chapter 5: Original Research and Developed Methodologies deployed in RHODA

In present Chapter that follows, there is a detailed presentation of the RHODA processes where original research has been applied in terms of novel methods, equations and tools. The main novelties in terms of method are comprised by the revamping and redefinition of the Holtrop and Mennen equations and methods for the estimation of Calm Water Resistance and powering, the development of a simulation-based limit state tool for matching of the hull and propeller with the Main Engine and dimensioning of the latter as well as the development of a Voyage Simulation tool with Lifecycle post-processing that is the core, basis and main novelty of current research work and main characteristic of the present RHODA. Another novel work aspect is that the voyage simulation tool results are validated with the use of actual, high-frequency onboard acquired data (“Big Data”).

5.1. Calm Water Resistance Estimation.

Traditionally and commercially the most accurate and established method for verifying and determining the calm water resistance and powering of a vessel is through towing tank model tests. The calm water resistance can be assessed with many different methods, ranging from hull series, empirical formulae to potential flow theory, RANS Methods of either Model or Full Scale. The latest developments in Computational methods in Marine Hydrodynamics are identified in the Specialist Committee on CFD in Marine Hydrodynamics of the International Towing Tank Symposium (ITTC) and can be found in the relevant report (I.T.T.C, 2014). The Table 10 gives an overview and comparison of different approaches for estimating the calm-water resistance of a vessel.

Method	Cost	Computational Requirements	Pre and Post Processing	Prediction Accuracy Effective Horse Power	Prediction Accuracy Delivered Horsepower
Systematic Series	Low	Low	Zero	*Only for hulls belonging to the series	*Only for hulls belonging to the series
Empirical Formulae	Low	Low	Zero	Mid	Low

RANS Methods Model Scale	Mid	Mid	Mid	High	High
RANS Methods Full Scale	Mid-High	High	High	High	High
Towing Tank Model Test	High	N/A	N/A	High	High

Table 10: Taxonomy of methods for estimating Calm Water resistance.

As the herein presented methodology is focused on the preliminary design optimization of commercial vessels, the towing tank model tests and full-scale RANS methods are not considered applicable within this research scope. RANS model scale models can be integrated into such a design framework as discussed in the literature survey, however, the usual, large number of design variants assessed in the early design explorations makes the use of surrogate models based on an adequately populated result pool necessary. Systematic series are also not applicable as will narrow significantly the hull shape and dimension variations to the applicability range of the series.

Empirical series on the other hand, despite their middle-level accuracy, have the advantage of practicably negligible requirements for computing power (can be easily done with a pocket calculator or excel worksheet).

From the various empirical methods available, the Holtrop and Mennen method (Holtrop & Mennen, 1982), (Holtrop, 1984) is currently considered one of the most accurate and efficient methods for the estimation of the resistance and propulsion power requirements of conventional mono-hull vessels at the initial stages of the design. The method equations for the various resistance components that derive from the statistical analysis and regression of a database with a large number of model test results. It was developed in the early 1970s by Jan Holtrop and Frits Mennen when they were working in the MARIN Research Centre and towing tank. They focused on developing a modern way to perform data analysis with a focus on the extrapolation of model tests. Initially, the method was designed for internal purposes so MARIN could make more accurate predictions. The two started with the system analysis and then re-analysed the model tests and the full-scale trials. The target was to have a component-wise prediction method that would show the difference between the model and full scale to serve the extrapolation of the model experiments (MARIN, 2010).

What makes the subject method an ideal candidate for design applications is that the total resistance is accurately decomposed in the various resistance components (frictional resistance, wave-making resistance, form resistance (viscous pressure), resistance due to bulbous bow and resistance due to transom stern). Furthermore, the model to full-scale correlation is accurately approached with a relevant formula. For applications where the range of design parameters is

large and subject to change, the methodology can provide good accuracy, correct trends and variant ranking in terms of resistance. However, for reasons of clarity the following restrictions should be noted:

1. The Holtrop methodology is based on the regression analysis of 334 ship models but within a range of dimension ratios (L/B, B/T, T/L, Cb, Cp, Cwp etc) (Holtrop, 1984). Although the range of applicability is significant and all typical vessel ratios are covered sufficiently, in cases of new designs where their ratios are close to the margins of the ones studied by Holtrop, a drop in the accuracy must be taken into account.
2. For non-conventional hull forms and all vessels having hull geometries significantly different from the original database used the accuracy of the subject methodology is limited. Additionally, for vessels fitted with hydrodynamic improvement energy devices (commonly referred to as Energy Saving Devices) that significantly affect various flow phenomena at the stern of such vessels the prediction error is increased as such cases are not included in the original database used by Holtrop and Mennen.

Following the development of the methodology and a second publication from Holtrop and Mennen (Holtrop, 1984) on its updated coefficients, its use is very widespread both in a plethora of initial design applications but also in ship operation and performance simulation modules with some recent examples in (Lu, et al., 2015) , (Mao, et al., 2016), (Vettor & Guedes Soares, 2016) and (Cichowicz, et al., 2015).

Due to this applicability and method's popularity, it has been decided to follow a hybrid approach, using the Holtrop and Mennen approach in a “digital twin” context (Nikolopoulos & Boulougouris, 2019). The multi-objective genetic algorithm NSGAI (Deb, et al., 2002) that is integrated into CAESES® has been used to statistically calibrate and redefine the constants of the Holtrop and Mennen methodology by using a large pool of results from model tests of actual commercial vessels that have “full” hull forms (large Cb coefficients) and operate at relatively low Froude numbers.

A database was built comprised of model test results of different vessels at multiple drafts and several speeds. The vessels collected are existing, modern “Eco-Type” vessels built after 2013 of full hull form (bulkers and tankers) that represent modern ship design trends. Their principal characteristics which were used as input for the Holtrop powering prediction are shown in Table 11:

Principal Particular	VSL01	VSL02	VSL03	VSL04	VSL05	VSL06	VSL07
Vessel Type	KVLCC2	VLCC	Newcastlemax	Capesize	Capesize	Ultramax	Ultramax
Lwl (m)	335	322	298.61	291	292	198	200
Lbp (m)	334	328	294	286	288	195	195
B (m)	61	60	50	45	45	32.26	32
Draft (m)	20.8	21.6	18.5	18.3	18.15	12.9	11.3
Displacement (m3)	343176.4	333410.3			202174.2	68864	61000
Cb	0.8098	0.7989	0.837	0.845	0.8595	0.8486	0.86
LCB (%)	0.035 fwd	0.03188	0.02368	0.0175	-0.0162	-0.0159	0.0285

Bulbous Bow transverse Area (m²)	100	123.9	100	100	00	10	63.053
Centre of bulbous bow transverse area (m)	7.5	11	7.5	7.5	6	5	6
Cm	0.998	0.998	0.998	0.997	0.9981	0.9981	0.9953
Transom Transverse Area (m²)	30	30	30	30	30	30	30
Cstern	0	0	0	0	0	0	0
Wetted Surface (m²)	29629.27	28226.2			20959.7	10196.8	9706
Cp	0.8114	0.8005	0.8538	0.8538	0.8538	0.8538	0.864

Table 11: Particulars of vessels examined

From Table 11 we can observe that the vessel model test database that serves as the calibration basis is made of full hull forms of bulk carriers and tankers including also vessels that were able to transit the old Panama Canal (PANAMAX beam dimension) resulting in adjustments of their length to beam ratio.

5.1.1. Initial Assessment Of Holtrop and Mennen Power Estimation Accuracy

Firstly, the Effective and Delivered Horsepower (EHP and SHP) has been calculated using Holtrop and Mennen’s method and compared to the model tests separately in Laden and Ballast Drafts. From the initial comparison, it is interesting to observe that in the Laden Condition the deviation of the method estimated values from the model test results is relatively small and increases in magnitude by increasing speed as seen from Figure 19, Figure 20, Figure 21, Figure 22.

With regards to the EHP prediction of Laden Conditions, interestingly for 5 out of 11 cases (45.5%) Holtrop and Mennen underestimate the resistance for the entire speed range ranging from 1% to 16%. For the other 5 cases, in low Froude numbers, Holtrop and Mennen overestimate the resistance by a maximum of 10% in the lowest respective speeds but by increasing Fn the relative overestimation is linearly decreasing up to a Froude number in the range of 0.12 to 0.17 (depending on each vessel case) where there is a transition to underestimation of the resistance by Holtrop and Mennen, while in even higher speeds this can be up to maximum 5%. The trend of the linear increase of the underestimation percentage by increasing speed is still very strong and evident as in the previous cases. For the KVLCC2 Case (VSL01), it is interesting to comment that at the very low Froude numbers of approximately 0.002 the Holtrop and Mennen method is underestimating the resistance while at 0.04 it marginally overestimates it. The overestimation percentage is increasing by increasing the Froude number up to a maximum of 15% at 0.055. From this Froude number, the overestimation percentage is decreasing up to 0.13 where it is practically zero. When compared to the other vessel cases of the herein study, this peculiar behaviour at low speeds up to 0.06 Froude number, according to the Authors’ understanding, can be attributed to the overestimation of various resistance components such as the influence of the bulbous bow,

the viscous pressure and the wave resistance. Unfortunately, the other vessel cases studied herein did not include tests at such low Froude numbers during their model testing, to see the behaviour of different hulls and geometries at low Froude numbers.

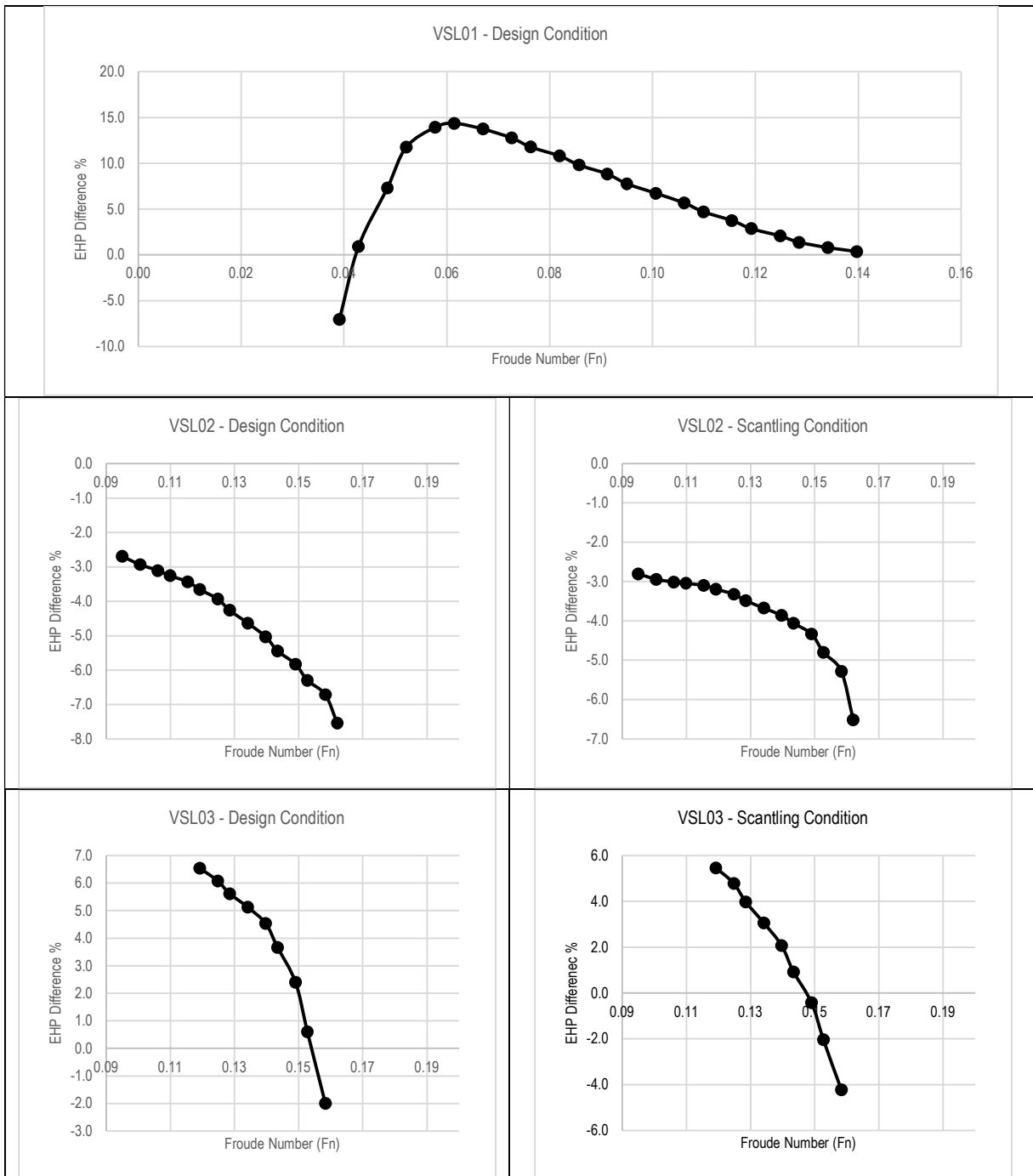
The strong correlation of the deviation of calculated SHP to the model test results in Laden Conditions with the Froude number is still evident. However, for the case of SHP it is non-linear (in contrast to the case of EHP), illustrating a logarithmic trend for VSL03, 04, 05, 06 and 07 while for vessel VSL02 it is additionally fluctuating. For 4 out of 10 total cases (40%), there is an underestimation of the SHP for the entire Froude number range which increases with increasing Froude numbers. The underestimation ranges from 1% at lower speeds to a maximum of 10% at higher speeds (15 knots). For 6 cases (60%) there is an overestimation of a maximum of 17% at low Froude numbers which is decreasing by increasing Fn up to the range of 0.135 to 0.175 Fn from which point there is an underestimation of the SHP increasing with the increase of the Froude number.

In contrast to the Laden conditions, in the ballast condition for all vessels, a significant underestimation of a higher relative magnitude is evident for both the EHP and SHP. Similarly, to the laden condition, the underestimation percentage of EHP is increasing almost linearly with the increase of the Froude number from about 20% at the lower range up to about 50% at the high range. The only nonlinear increase is for the case of VSL04, VSL05 and at High Froude numbers of VSL03 where a slight parabola is observed. The steepness of the curve is vessel dependent but for all cases, similarities can be observed.

On the other hand, the deviation of the estimated SHP from the model tests is similar to the EHP estimation error but on a smaller magnitude ranging from 10% at small Froude numbers up to 40% at high Froude numbers (close to 0.175). The trend of increasing under prediction by increasing speed is the same as in the case of the EHP.

From the above analysis, we can herein consider that the Holtrop and Mennen methodology is quite accurate for the EHP prediction but lacks accuracy in the SHP prediction as well as in the Ballast Conditions EHP and SHP prediction (off-design condition). Furthermore, the evident correlation between Froude number (thus vessel's speed) and inaccuracy according to the Authors' perception can be attributed to the different flow development and phenomena which cannot be captured by an empirical method. The trends are very consistent thus underlining the resulting robustness.

A Novel Methodology for Robust, Holistic, Simulation-Based Ship Design Optimization



A Novel Methodology for Robust, Holistic, Simulation-Based Ship Design Optimization

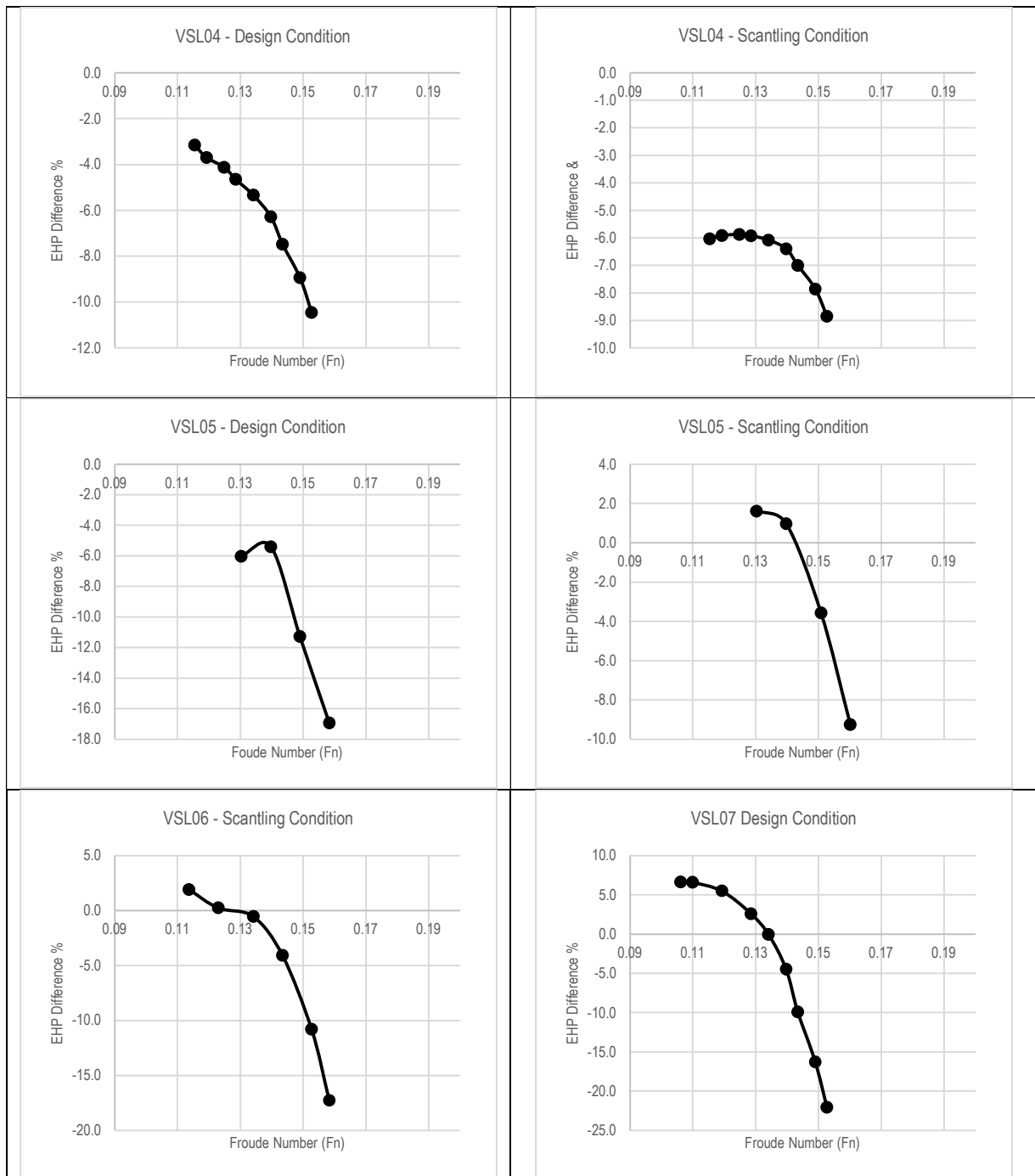
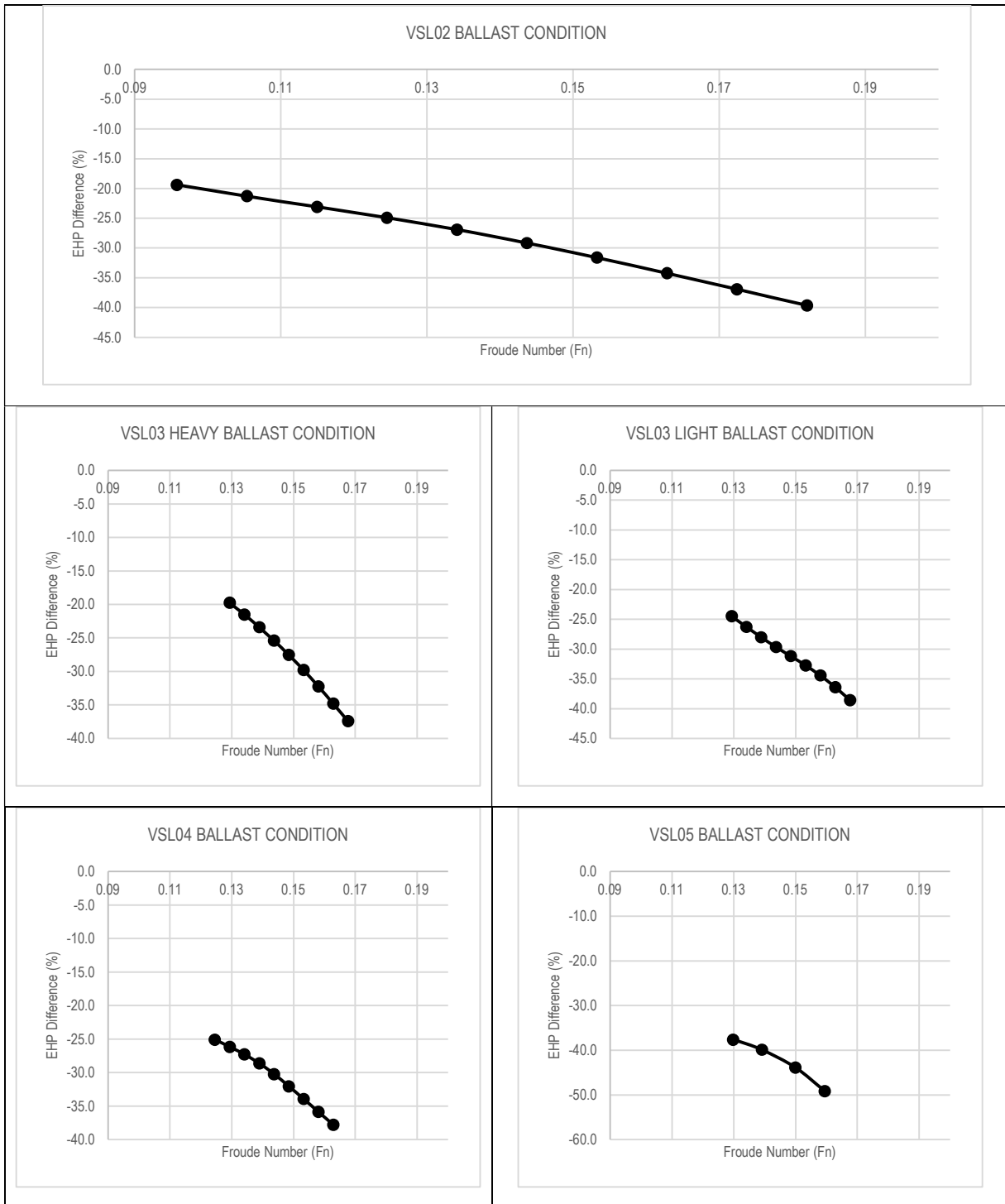


Figure 19: Distribution of the EHP difference (%) over different speeds – LADEN Condition

A Novel Methodology for Robust, Holistic, Simulation-Based Ship Design Optimization



A Novel Methodology for Robust, Holistic, Simulation-Based Ship Design Optimization

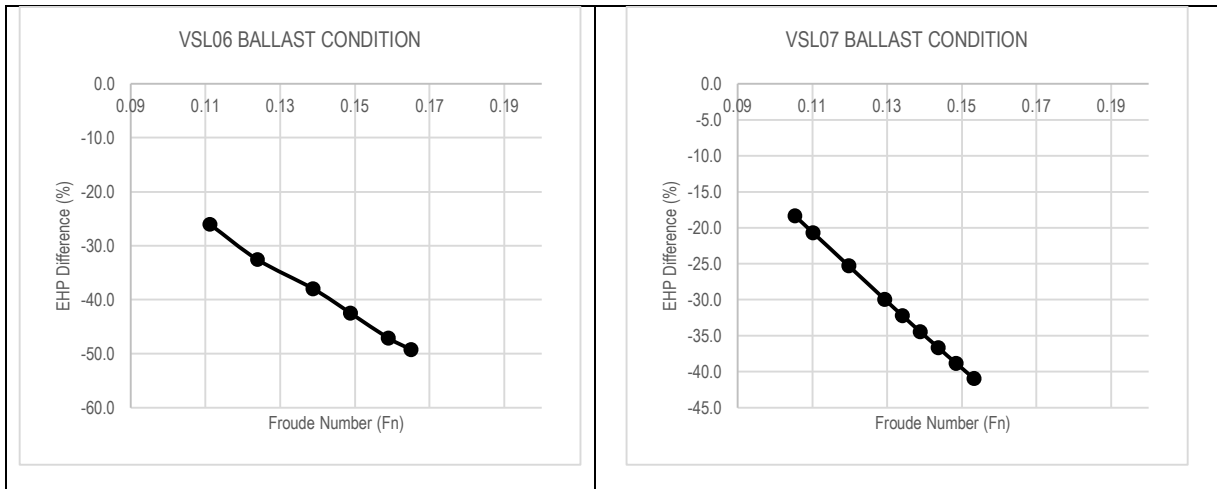
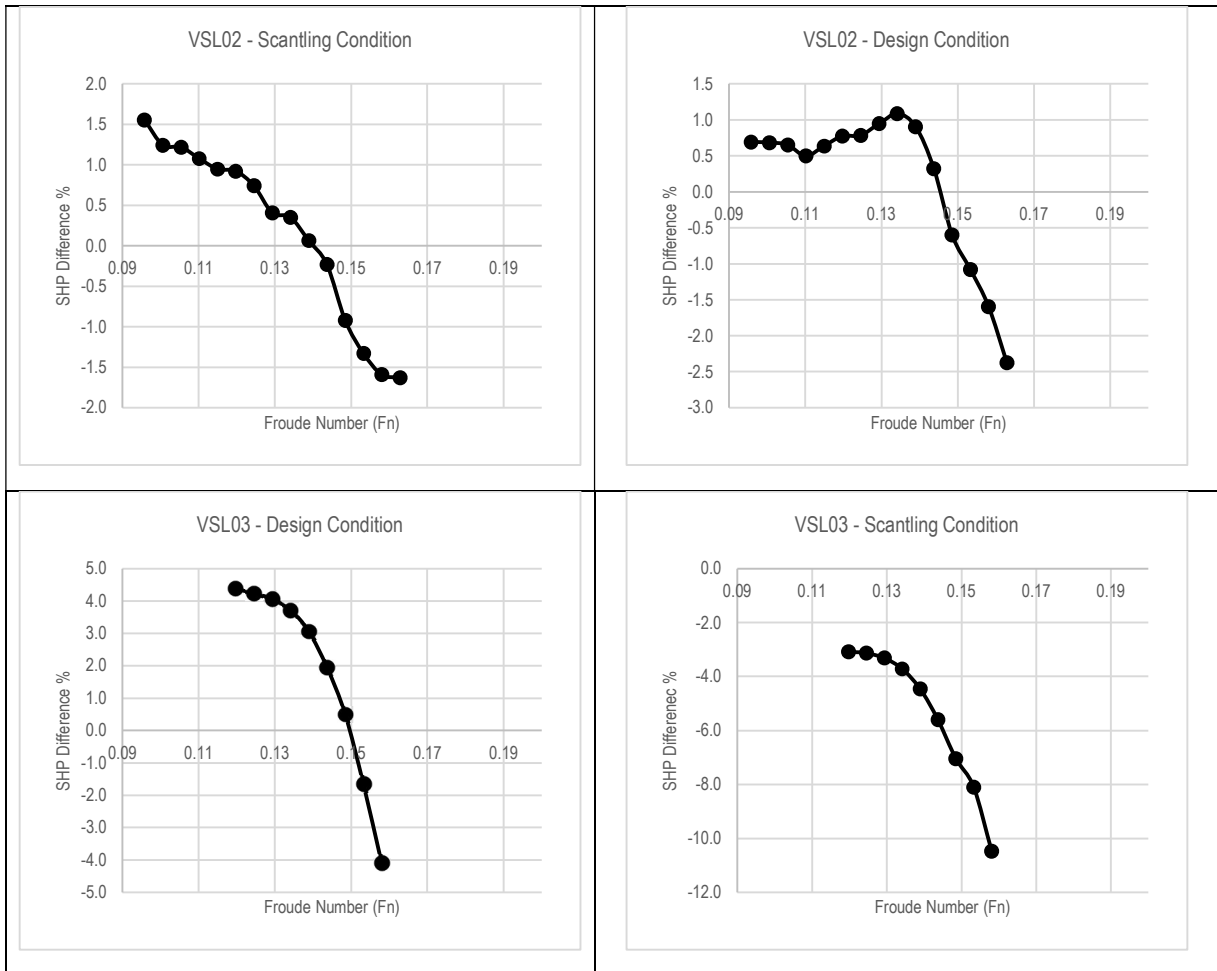


Figure 20: Distribution of the EHP difference (%) over different speeds – BALLAST Condition



A Novel Methodology for Robust, Holistic, Simulation-Based Ship Design Optimization

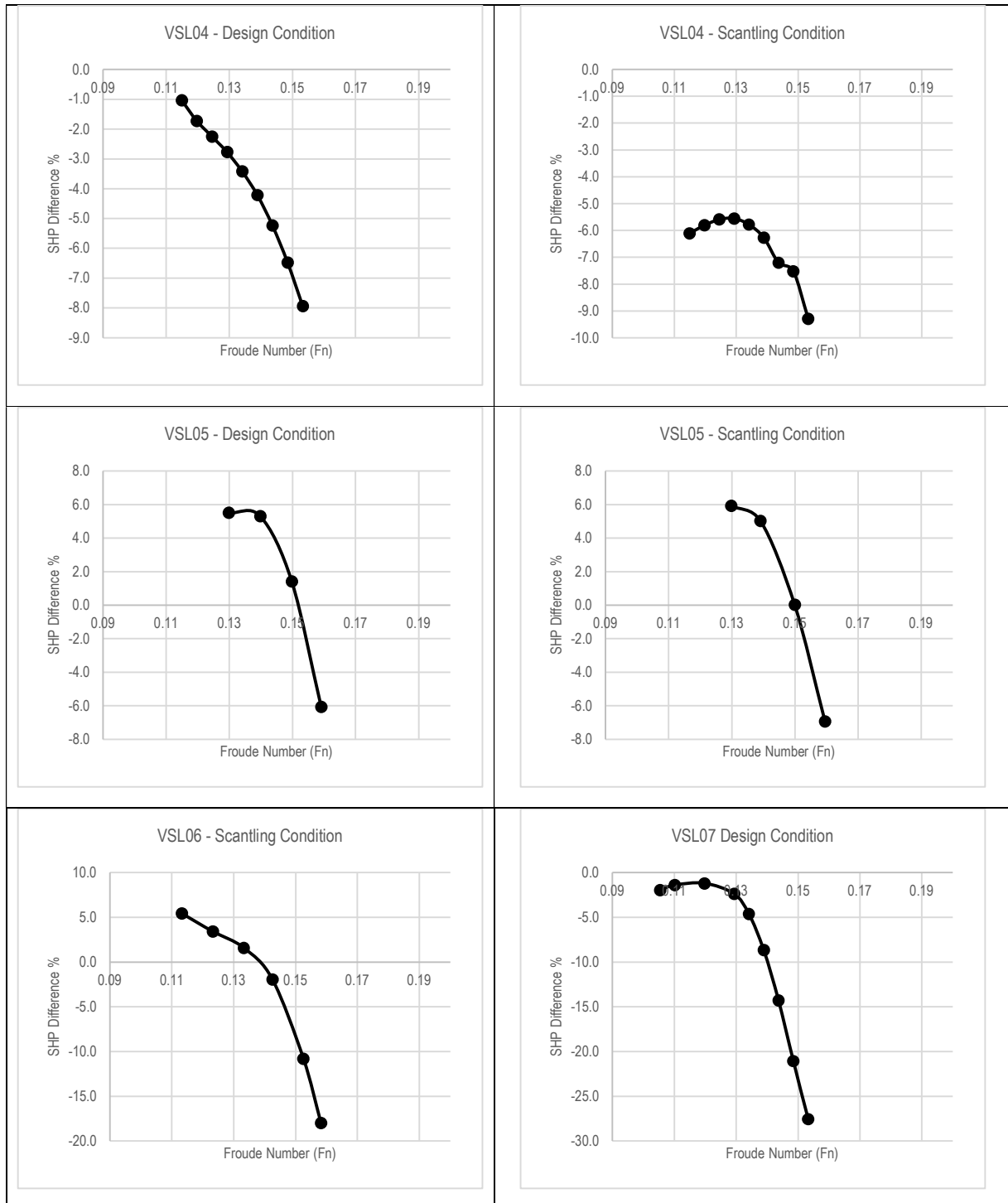
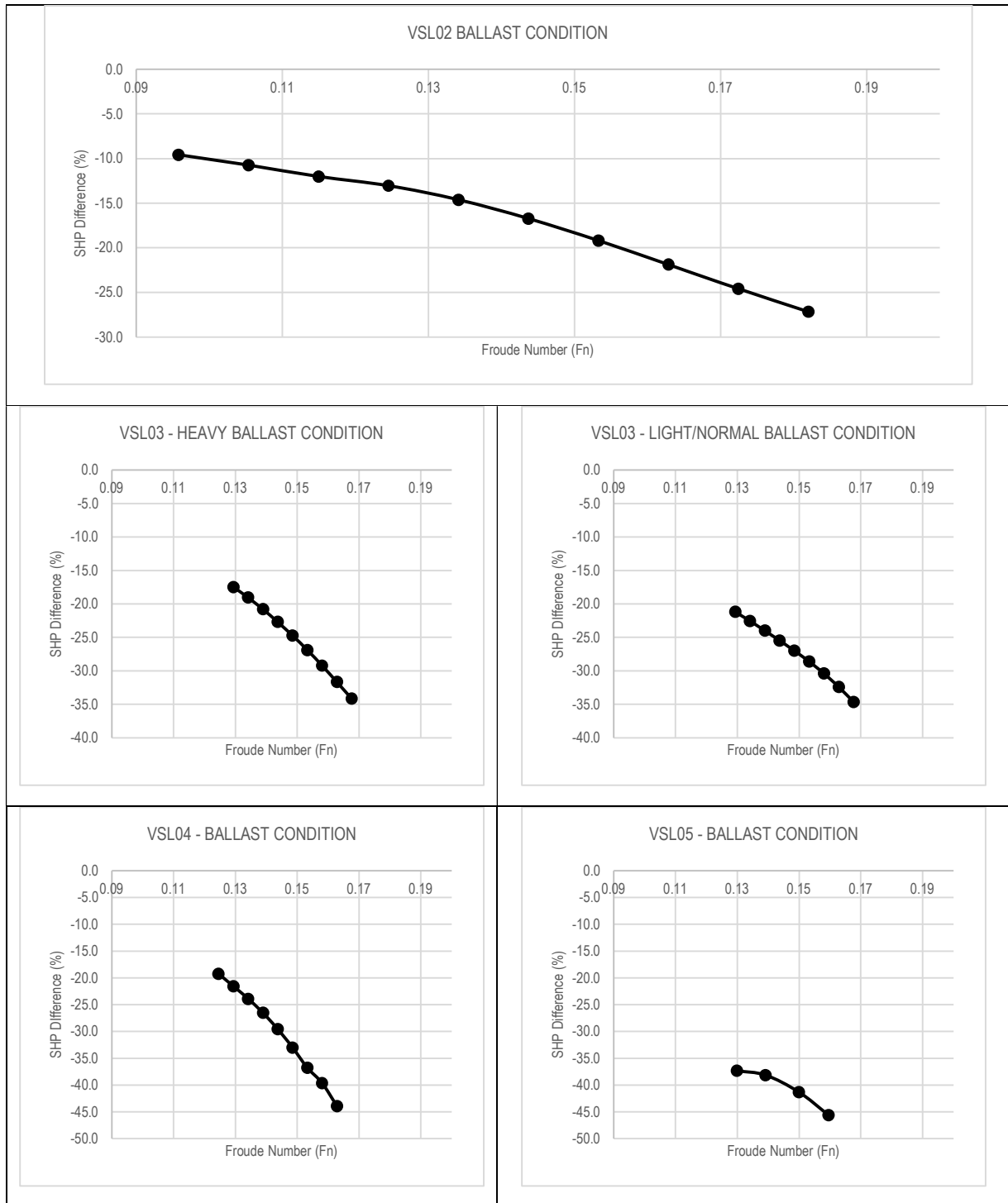


Figure 21: Shaft Power prediction error (%) distribution over different speeds – LADEN Condition

A Novel Methodology for Robust, Holistic, Simulation-Based Ship Design Optimization



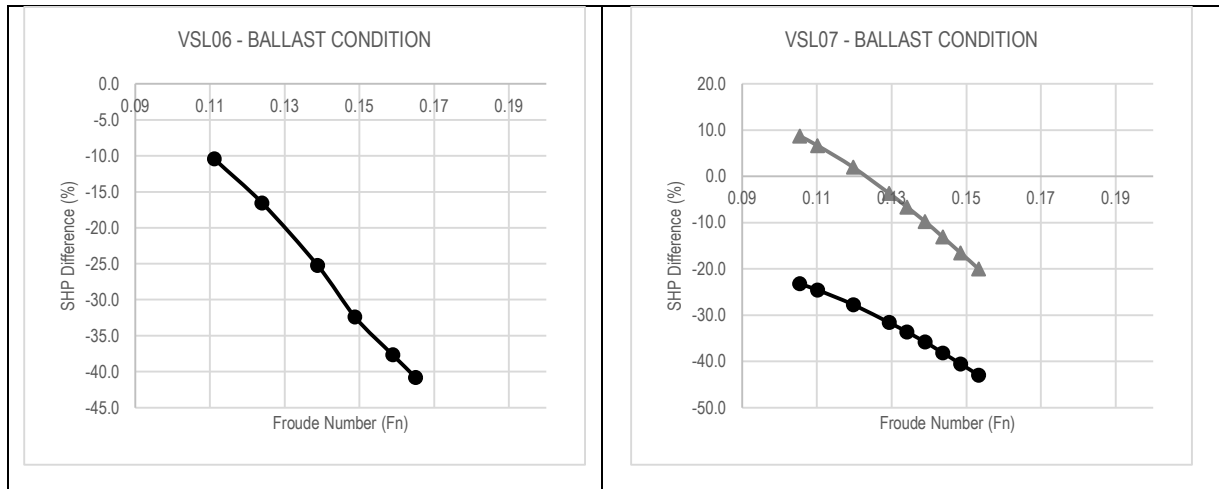


Figure 22: Shaft Power prediction error (%) distribution over different speeds – BALLAST Condition

5.1.2. Statistical Calibration Process.

An iterative, multi-staged evolutionary approach was followed afterwards for the calibration of the methodology by the control and variation of its original coefficients and constants, with each stage being treated as a typical optimization problem as depicted in Figure 23. The number of variants per calibration stage (1000-2000 depending on the run) has been chosen based on the code performance and speed criteria. The number of population of each generation, has been chosen to be large (100) in order to ensure proper solution space exploration per generation (quantified and verified in Design Of Experiment DoE runs) and the number of generations of 10 has been chosen with the criterion of ensuring adequate convergence of the NSGAI code.

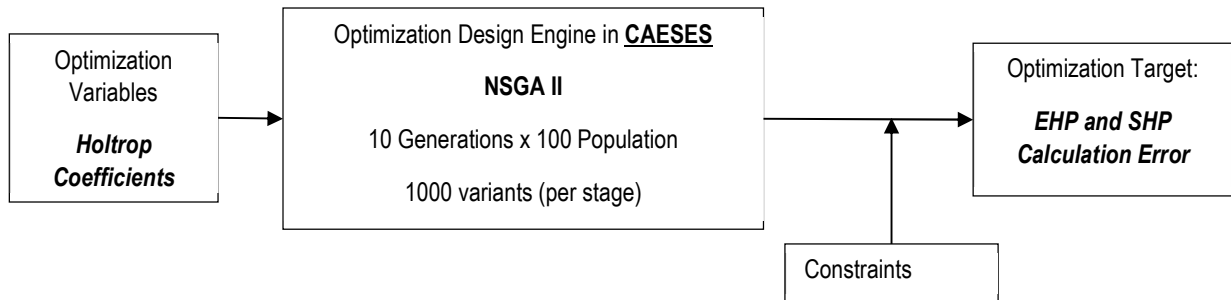


Figure 23: Generalized optimization problem workflow

As in every optimization problem, the following components were considered:

- a. Optimization Variables
 - b. Design Engine
 - c. Optimization Target
 - d. Design Constraints
- a. Optimization Variables

The variables of this problem were the selected constants and coefficients for each formula of each resistance component as formulated in the original Holtrop publication. The methodology was parametrically programmed in Excel that was controlled by CAESSES® using a COM integration. The constants became the variables of the new problem. The selected variables for the optimization can be summarized in Table 12 for the laden condition and Table 13 for the ballast condition respectively.

Calibration Variables – LADEN (Design and Scantling) Condition				
No.	Constant in Holtrop Formula	Value in Original Holtrop Publication	Value Calibration Minimum	Value Calibration Maximum
Wave Making Resistance				
L-1	$c_1 = 2223105 * c_7^{3.78613} * \left(\frac{T}{B}\right)^{1.07961} * (90 - i_E)^{-1.37565}$	2223105	2200000	2300000
L-2	$c_1 = 2223105 * c_7^{3.78613} * \left(\frac{T}{B}\right)^{1.07961} * (90 - i_E)^{-1.37565}$	3.78613	2.0	4.70
L-3	$c_1 = 2223105 * c_7^{3.78613} * \left(\frac{T}{B}\right)^{1.07961} * (90 - i_E)^{-1.37565}$	1.07961	0.6	1.30
L-4	$c_1 = 2223105 * c_7^{3.78613} * \left(\frac{T}{B}\right)^{1.07961} * (90 - i_E)^{-1.37565}$	-1.37565	-2.0	-0.80
L-5	$c_2 = \exp(-1.89 * \sqrt{c_3})$	-1.89	-3.0	-0.9
L-6	$c_3 = \frac{0.56 * A_{BT}^{1.5}}{B * T * (0.31 * \sqrt{A_{BT}} + T_F - h_B)}$	0.56	0.20	0.90
L-7	$c_3 = \frac{0.56 * A_{BT}^{1.5}}{B * T * (0.31 * \sqrt{A_{BT}} + T_F - h_B)}$	0.31	0.01	0.80
L-8	$c_3 = \frac{0.56 * A_{BT}^{1.5}}{B * T * (0.31 * \sqrt{A_{BT}} + T_F - h_B)}$	1.5	1.20	3.0
L-9	$c_5 = 1 - 0.8 * \frac{A_T}{B * T * C_M}$	0.8	0.20	1.50
L-10	$c_{15} = -1.69385 + c_{15_{new}} * \frac{L^3}{V}$	-1.69385	-2.0	-1.10
L-11	$c_{15} = -1.69385 + c_{15_{new}} * \frac{L^3}{V}$	$c_{15_{new}} = 0$	$c_{15_{new}} = -1$	$c_{15_{new}} = 2$
L-12	$m_1 = 0.0140407 * \frac{L}{T} - 1.75254 * \frac{1}{\sqrt[3]{L}} + 4.79323 * \frac{B}{L} - c_{16}$	0.0140407	0.005	0.10
L-13	$m_1 = 0.0140407 * \frac{L}{T} - 1.75254 * \frac{1}{\sqrt[3]{L}} + 4.79323 * \frac{B}{L} - c_{16}$	1.75254	1.10	2.50
L-14	$m_1 = 0.0140407 * \frac{L}{T} - 1.75254 * \frac{1}{\sqrt[3]{L}} + 4.79323 * \frac{B}{L} - c_{16}$	4.79323	3.70	5.70
L-15	$m_2 = c_{15} * C_p^2 * \exp(-0.1 * Fn^{-2})$	2	1.20	4.0
L-16	$m_2 = c_{15} * C_p^2 * \exp(-0.1 * Fn^{-2})$	-0.1	-0.50	-0.04
L-17	$m_2 = c_{15} * C_p^2 * \exp(-0.1 * Fn^{-2})$	-2	-4.0	-1.20
L-18	$c_{16} = 1.73014 - 0.7067 * C_P + c_{16_{new}} * C_P^2 + c_{16D_{new}} * C_P^3$	1.73014	1.20	2.50
L-19	$c_{16} = 1.73014 - 0.7067 * C_P + c_{16_{new}} * C_P^2 + c_{16D_{new}} * C_P^3$	0.7067	0.20	1.20

A Novel Methodology for Robust, Holistic, Simulation-Based Ship Design Optimization

L-20	$c_{16} = 1.73014 - 0.7067 * C_p + c_{16C_{new}} * C_p^2 + c_{16D_{new}} * C_p^3$	$c_{16C_{new}} = 0$	$c_{16C_{new}} = -2$	$c_{16C_{new}} = 2$
L-21	$c_{16} = 1.73014 - 0.7067 * C_p + c_{16C_{new}} * C_p^2 + c_{16D_{new}} * C_p^3$	$c_{16D_{new}} = 0$	$c_{16C_{new}} = -2$	$c_{16C_{new}} = 2$
L-22	$\lambda = 1.446 * C_p - 0.03 * \frac{L}{B} + c_{new}$	1.446	0.60	2.0
L-23	$\lambda = 1.446 * C_p - 0.03 * \frac{L}{B} + c_{new}$	0.03	0.01	0.10
L-24	$\lambda = 1.446 * C_p - 0.03 * \frac{L}{B} + c_{new}$	0	-2	2
L-25	$d = -0.9$	-0.9	-1.50	-0.30
L-26	$R_w = c_1 * c_2 * c_5 * \nabla * \rho * g * \exp\{m_1 * Fn^d + m_2 * \cos(\lambda * Fn^{-2})\}$	-2	0	1
Frictional Resistance - Form Factor				
L-27	$c_{12} = (T/L)^{0.2228446}$	0.2228446	0.05	0.80
L-28	$(1 + k_1) = c_{13} * \left\{ 0.93 + c_{12} * \left(\frac{B}{L_R} \right)^{0.92497} * (0.95 - C_p)^{-0.521448} * (1 - C_p + 0.0225 * LCB)^{0.6906} \right\}$	0.92497	0.40	1.50
L-29	$(1 + k_1) = c_{13} * \left\{ 0.93 + c_{12} * \left(\frac{B}{L_R} \right)^{0.92497} * (0.95 - C_p)^{-0.521448} * (1 - C_p + 0.0225 * LCB)^{0.6906} \right\}$	-0.521448	-0.90	-0.10
L-30	$(1 + k_1) = c_{13} * \left\{ 0.93 + c_{12} * \left(\frac{B}{L_R} \right)^{0.92497} * (0.95 - C_p)^{-0.521448} * (1 - C_p + 0.0225 * LCB)^{0.6906} \right\}$	0.6906	0.6906	1.50
L-31	$c_{13} = 1 + 0.003 * C_{stern}$	0	-3	3
Resistance due to Bulbous Bow				
L-32	$P_B = \frac{0.56 * \sqrt{A_{BT}}}{T_F - 1.5 * h_B}$	0.56	0.10	1.0
L-33	$R_B = \frac{0.11 * \exp(-3 * P_B^{-2}) * Fni^3 * A_{BT}^{1.5} * \rho * g}{1 + Fni^2}$	0.11	0.05	0.30
L-34	$R_B = \frac{0.11 * \exp(-3 * P_B^{-2}) * Fni^3 * A_{BT}^{1.5} * \rho * g}{1 + Fni^2}$	-3	-5.0	-1.50
L-35	$R_B = \frac{0.11 * \exp(-3 * P_B^{-2}) * Fni^3 * A_{BT}^{1.5} * \rho * g}{1 + Fni^2}$	2	1.2	4
L-36	$R_B = \frac{0.11 * \exp(-3 * P_B^{-2}) * Fni^3 * A_{BT}^{1.5} * \rho * g}{1 + Fni^2}$	3	1.5	4.0
L-37	$R_B = \frac{0.11 * \exp(-3 * P_B^{-2}) * Fni^3 * A_{BT}^{1.5} * \rho * g}{1 + Fni^2}$	1.5	1.20	3.0
L-38	$R_B = \frac{0.11 * \exp(-3 * P_B^{-2}) * Fni^3 * A_{BT}^{1.5} * \rho * g}{1 + Fni^2}$	2	1.50	4.50

A Novel Methodology for Robust, Holistic, Simulation-Based Ship Design Optimization

L-39	$Fni = \frac{v}{\sqrt{g * (T_F - h_B - 0.25 * \sqrt{A_{BT}}) + 0.15 * v^2}}$	2	1.50	4.50
Resistance due to Transom Immersion				
L-40	$c_6 = 0.2 * (1 - 0.2 * Fn_T)$	0.2	0.01	0.30
Model Ship Correlation				
L-41	$C_A = 0.006 * (L + 100)^{-0.16} - 0.00205 + 0.003 * \sqrt{\frac{L}{7.5}} * C_B^4 * c_2 * (0.04 - c_4) + c_{Anew} * Fn^{c_{Bnew}}$	0.006	0.001	0.10
L-42	$C_A = 0.006 * (L + 100)^{-0.16} - 0.00205 + 0.003 * \sqrt{\frac{L}{7.5}} * C_B^4 * c_2 * (0.04 - c_4) + c_{Anew} * Fn^{c_{Bnew}}$	-0.16	-0.50	-0.01
L-43	$C_A = 0.006 * (L + 100)^{-0.16} - 0.00205 + 0.003 * \sqrt{\frac{L}{7.5}} * C_B^4 * c_2 * (0.04 - c_4) + c_{Anew} * Fn^{c_{Bnew}}$	-0.00205	-0.10	-0.0001
L-44	$C_A = 0.006 * (L + 100)^{-0.16} - 0.00205 + 0.003 * \sqrt{\frac{L}{7.5}} * C_B^4 * c_2 * (0.04 - c_4) + c_{Anew} * Fn^{c_{Bnew}}$	0.003	0.001	0.10
L-45	$C_A = 0.006 * (L + 100)^{-0.16} - 0.00205 + 0.003 * \sqrt{\frac{L}{7.5}} * C_B^4 * c_2 * (0.04 - c_4) + c_{Anew} * Fn^{c_{Bnew}}$	7.5	3.0	10.0
L-46	$C_A = 0.006 * (L + 100)^{-0.16} - 0.00205 + 0.003 * \sqrt{\frac{L}{7.5}} * C_B^4 * c_2 * (0.04 - c_4) + c_{Anew} * Fn^{c_{Bnew}}$	4	2.0	6.0
L-47	$C_A = 0.006 * (L + 100)^{-0.16} - 0.00205 + 0.003 * \sqrt{\frac{L}{7.5}} * C_B^4 * c_2 * (0.04 - c_4) + c_{Anew} * Fn^{c_{Bnew}}$	-	-	-
L-48	$C_A = 0.006 * (L + 100)^{-0.16} - 0.00205 + 0.003 * \sqrt{\frac{L}{7.5}} * C_B^4 * c_2 * (0.04 - c_4) + c_{Anew} * Fn^{c_{Bnew}}$	$c_{Anew} = 0$	$c_{Anew} = -2$	$c_{Anew} = 2$
L-49	$C_A = 0.006 * (L + 100)^{-0.16} - 0.00205 + 0.003 * \sqrt{\frac{L}{7.5}} * C_B^4 * c_2 * (0.04 - c_4) + c_{Anew} * Fn^{c_{Bnew}}$	$c_{Bnew} = 0$	$c_{Bnew} = -2$	$c_{Bnew} = 2$
Propulsion Factors				
L-50	$\eta_R = 0.9922 - 0.05908 * \frac{A_E}{A_0} + 0.07424 * (C_P - 0.0225 * lcb)$	0.9922	-	-
L-51	$\eta_R = 0.9922 - 0.05908 * \frac{A_E}{A_0} + 0.07424 * (C_P - 0.0225 * lcb)$	0.05908	-	-
L-52	$\eta_R = 0.9922 - 0.05908 * \frac{A_E}{A_0} + 0.07424 * (C_P - 0.0225 * lcb)$	0.07424	-	-
L-53	$\eta_R = 0.9922 - 0.05908 * \frac{A_E}{A_0} + 0.07424 * (C_P - 0.0225 * lcb)$	0.0225	-	-
L-54	$t_{HOLTROP} = 0.001979 * \frac{L}{B * (1 - C_P)} + 1.0585 * \frac{B}{L} - 0.00524 - 0.1418 * \frac{D^2}{B * T}$	0.001979	0.0001	0.1
L-55	$t_{HOLTROP} = 0.001979 * \frac{L}{B * (1 - C_P)} + 1.0585 * \frac{B}{L} - 0.00524 - 0.1418 * \frac{D^2}{B * T}$	1.0585	0.4	1.9

A Novel Methodology for Robust, Holistic, Simulation-Based Ship Design Optimization

L-56	$t_{HOLTROP} = 0.001979 * \frac{L}{B * (1 - C_P)} + 1.0585 * \frac{B}{L} - 0.00524 - 0.1418 * \frac{D^2}{B * T}$	-0.00524	-0.02	-0.001
L-57	$t_{HOLTROP} = 0.001979 * \frac{L}{B * (1 - C_P)} + 1.0585 * \frac{B}{L} - 0.00524 - 0.1418 * \frac{D^2}{B * T}$	-0.1418	-0.3	-0.01
L-58	$W_{HOLTROP} = c_9 * C_V * \frac{L}{T_A} * \left(0.0661875 + 1.21756 * c_{11} * \frac{C_V}{(1 - C_{P1})} \right) + 0.24558$ $* \sqrt{\frac{B}{L * (1 - C_{P1})} - \frac{0.09726}{0.95 - C_P} + \frac{0.11434}{0.95 - C_B}} + 0.75 * C_{Stern}$ $* C_V + 0.002 * C_{Stern}$	0.0661875	-	-
L-59	$W_{HOLTROP} = c_9 * C_V * \frac{L}{T_A} * \left(0.0661875 + 1.21756 * c_{11} * \frac{C_V}{(1 - C_{P1})} \right) + 0.24558$ $* \sqrt{\frac{B}{L * (1 - C_{P1})} - \frac{0.09726}{0.95 - C_P} + \frac{0.11434}{0.95 - C_B}} + 0.75 * C_{Stern}$ $* C_V + 0.002 * C_{Stern}$	1.21756	-	-
L-60	$W_{HOLTROP} = c_9 * C_V * \frac{L}{T_A} * \left(0.0661875 + 1.21756 * c_{11} * \frac{C_V}{(1 - C_{P1})} \right) + 0.24558$ $* \sqrt{\frac{B}{L * (1 - C_{P1})} - \frac{0.09726}{0.95 - C_P} + \frac{0.11434}{0.95 - C_B}} + 0.75 * C_{Stern}$ $* C_V + 0.002 * C_{Stern}$	0.24558	-	-
L-61	$W_{HOLTROP} = c_9 * C_V * \frac{L}{T_A} * \left(0.0661875 + 1.21756 * c_{11} * \frac{C_V}{(1 - C_{P1})} \right) + 0.24558$ $* \sqrt{\frac{B}{L * (1 - C_{P1})} - \frac{0.09726}{0.95 - C_P} + \frac{0.11434}{0.95 - C_B}} + 0.75 * C_{Stern}$ $* C_V + 0.002 * C_{Stern}$	0.09726	-	-
L-62	$W_{HOLTROP} = c_9 * C_V * \frac{L}{T_A} * \left(0.0661875 + 1.21756 * c_{11} * \frac{C_V}{(1 - C_{P1})} \right) + 0.24558$ $* \sqrt{\frac{B}{L * (1 - C_{P1})} - \frac{0.09726}{0.95 - C_P} + \frac{0.11434}{0.95 - C_B}} + 0.75 * C_{Stern}$ $* C_V + 0.002 * C_{Stern}$	0.11434	-	-
L-63	$c_{11} = 0.0833333 * \left(\frac{T_A}{D} \right)^3 + 1.33333$	0.0833333	-	-
L-64	$c_{11} = 0.0833333 * \left(\frac{T_A}{D} \right)^3 + 1.33333$	1.3333	-	-
L-65	$W_{SCHNEEKLUTH} = 0.5 * C_P * \frac{1.6}{1 + \frac{D}{T}} * \frac{16}{10 + \frac{L}{B}}$	0.5	0.1	0.9
L-66	$W_{SCHNEEKLUTH} = 0.5 * C_P * \frac{1.6}{1 + \frac{D}{T}} * \frac{16}{10 + \frac{L}{B}}$	1.6	0.1	3
L-67	$W_{SCHNEEKLUTH} = 0.5 * C_P * \frac{1.6}{1 + \frac{D}{T}} * \frac{16}{10 + \frac{L}{B}}$	16	8	20
L-68	$W_{KRUGER} = 0.75 * C_B - 0.24$	0.75	0.5	1.5
L-69	$W_{KRUGER} = 0.75 * C_B - 0.24$	0.24	0.1	0.5
L-70	$W_{HECKSCHER} = 0.7 * C_P - 0.18$	0.7	0.25	1.5

A Novel Methodology for Robust, Holistic, Simulation-Based Ship Design Optimization

L-71	$W_{HECKSCHER} = 0.7 * C_p - \mathbf{0.18}$	-0.18	-0.3	0.3
L-72	$W_{TROOST} = \mathbf{0.25} + 2.5 * (C_B - 0.6)^2$	0.25	0.1	0.4
L-73	$W_{TROOST} = 0.25 + \mathbf{2.5} * (C_B - 0.6)^2$	2.5	0.1	4

Table 12: Holtrop Constants used as variables in optimization problem and their respective value range – LADEN CONDITION.

Calibration Variables – BALLAST Condition				
No.	Constant in Holtrop Formula	Value in Original Holtrop Publication	Value Calibration Minimum	Value Calibration Maximum
Wave Making Resistance				
B-1	$c_1 = \mathbf{2223105} * c_7^{3.78613} * \left(\frac{T}{B}\right)^{1.07961} * (90 - i_E)^{-1.37565}$	2223105	2100000	2250000
B-2	$c_1 = 2223105 * c_7^{\mathbf{3.78613}} * \left(\frac{T}{B}\right)^{1.07961} * (90 - i_E)^{-1.37565}$	3.78613	3.6	3.8
B-3	$c_1 = 2223105 * c_7^{3.78613} * \left(\frac{T}{B}\right)^{\mathbf{1.07961}} * (90 - i_E)^{-1.37565}$	1.07961	1.0	1.2
B-4	$c_1 = 2223105 * c_7^{3.78613} * \left(\frac{T}{B}\right)^{1.07961} * (90 - i_E)^{\mathbf{-1.37565}}$	-1.37565	-1.5	-1.0
B-5	$c_2 = \exp(\mathbf{-1.89} * \sqrt{c_3})$	-1.89	-2.5	-1.5
B-6	$c_3 = \frac{\mathbf{0.56} * A_{BT}^{1.5}}{B * T * (0.31 * \sqrt{A_{BT}} + T_F - h_B)}$	0.56	0.40	0.60
B-7	$c_3 = \frac{0.56 * A_{BT}^{1.5}}{B * T * (\mathbf{0.31} * \sqrt{A_{BT}} + T_F - h_B)}$	0.31	0.20	0.40
B-8	$c_3 = \frac{0.56 * A_{BT}^{\mathbf{1.5}}}{B * T * (0.31 * \sqrt{A_{BT}} + T_F - h_B)}$	1.5	1.2	3
B-9	$c_5 = 1 - \mathbf{0.8} * \frac{A_T}{B * T * C_M}$	0.8	0.7	0.9
B-10	$c_{15} = \mathbf{-1.69385} + c_{15_{new}} * \frac{L^3}{V}$	-1.69385	-1.80	-1.50
B-11	$c_{15} = -1.69385 + \mathbf{c_{15_{new}}} * \frac{L^3}{V}$	$c_{15_{new}} = 0$	$c_{15_{new}} = -1$	$c_{15_{new}} = 3$
B-12	$m_1 = \mathbf{0.0140407} * \frac{L}{T} - 1.75254 * \frac{1}{\sqrt[3]{V}} + 4.79323 * \frac{B}{L} - c_{16}$	0.0140407	0.01	0.02
B-13	$m_1 = 0.0140407 * \frac{L}{T} - \mathbf{1.75254} * \frac{1}{\sqrt[3]{V}} + 4.79323 * \frac{B}{L} - c_{16}$	1.75254	1.60	1.90
B-14	$m_1 = 0.0140407 * \frac{L}{T} - 1.75254 * \frac{1}{\sqrt[3]{V}} + \mathbf{4.79323} * \frac{B}{L} - c_{16}$	4.79323	4.60	4.90
B-15	$m_2 = c_{15} * C_p^2 * \exp(-0.1 * Fn^{-2})$	2	1.2	3
B-16	$m_2 = c_{15} * C_p^2 * \exp(\mathbf{-0.1} * Fn^{-2})$	-0.1	-0.8	-0.01
B-17	$m_2 = c_{15} * C_p^2 * \exp(-0.1 * Fn^{-2})$	-2	-3.5	-1.5
B-18	$c_{16} = \mathbf{8.07981} * C_p - 13.8673 * C_p^2 + 6.984388 * C_p^3$	8.07981	4.0	12.0
B-19	$c_{16} = 8.07981 * C_p - \mathbf{13.8673} * C_p^2 + 6.984388 * C_p^3$	-13.8673	-25.0	-10.0
B-20	$c_{16} = 8.07981 * C_p - 13.8673 * C_p^2 + \mathbf{6.984388} * C_p^3$	6.984388	3.0	11.0

A Novel Methodology for Robust, Holistic, Simulation-Based Ship Design Optimization

B-21	$c_{16} = 8.07981 * C_p - 13.8673 * C_p^2 + 6.984388 * C_p^3$	1	0.9	1.6
B-22	$c_{16} = 8.07981 * C_p - 13.8673 * C_p^2 + 6.984388 * C_p^3$	2	1.8	2.9
B-23	$c_{16} = 8.07981 * C_p - 13.8673 * C_p^2 + 6.984388 * C_p^3$	3	2.6	3.5
B-24	$\lambda = 1.446 * C_p - 0.03 * \frac{L}{B} + c_{new}$	1.446	1.40	1.50
B-25	$\lambda = 1.446 * C_p - 0.03 * \frac{L}{B} + c_{new}$	0.03	0.001	1.0
B-26	$\lambda = 1.446 * C_p - 0.03 * \frac{L}{B} + c_{new}$	0	-2.0	2.0
B-27	$d = -0.9$	-0.9	-2.0	-0.1
B-28	$R_w = c_1 * c_2 * c_5 * \nabla * \rho * g * \exp\{m_1 * Fn^d + m_2 * \cos(\lambda * Fn^{-2})\}$	-2	-3.0	1.50
Frictional Resistance - Form Factor				
B-29	$c_{12} = 48.20 * \left(\frac{T}{L} - 0.02\right)^{2.078} + 0.479948$	48.20	25.0	60.0
B-30	$c_{12} = 48.20 * \left(\frac{T}{L} - 0.02\right)^{2.078} + 0.479948$	2.078	0.50	4.0
B-31	$c_{12} = 48.20 * \left(\frac{T}{L} - 0.02\right)^{2.078} + 0.479948$	0.479948	0.35	0.60
B-32	$(1 + k_1) = c_{13} * \left\{ 0.93 + c_{12} * \left(\frac{B}{L_R}\right)^{0.92497} * (0.95 - C_p)^{-0.521448} * (1 - C_p + 0.0225 * LCB)^{0.6906} \right\}$	0.92497	0.30	1.50
B-33	$(1 + k_1) = c_{13} * \left\{ 0.93 + c_{12} * \left(\frac{B}{L_R}\right)^{0.92497} * (0.95 - C_p)^{-0.521448} * (1 - C_p + 0.0225 * LCB)^{0.6906} \right\}$	-0.521448	-3.0	-1.50
B-34	$(1 + k_1) = c_{13} * \left\{ 0.93 + c_{12} * \left(\frac{B}{L_R}\right)^{0.92497} * (0.95 - C_p)^{-0.521448} * (1 - C_p + 0.0225 * LCB)^{0.6906} \right\}$	0.6906	0.20	0.90
B-35	$c_{13} = 1 + 0.003 * C_{stern}$	0.003	0.001	0.70
B-36	$c_{13} = 1 + 0.003 * C_{stern}$	0	0.10	2.0
Resistance due to Bulbous Bow				
B-37	$P_B = \frac{0.56 * \sqrt{A_{BT}}}{T_F - 1.5 * h_B}$	0.56	0.10	0.90
B-38	$R_B = \frac{0.11 * \exp(-3 * P_B^{-2}) * Fni^3 * A_{BT}^{1.5} * \rho * g}{1 + Fni^2}$	0.11	0.01	0.30
B-39	$R_B = \frac{0.11 * \exp(-3 * P_B^{-2}) * Fni^3 * A_{BT}^{1.5} * \rho * g}{1 + Fni^2}$	-3	-5.0	-1.0
B-40	$R_B = \frac{0.11 * \exp(-3 * P_B^{-2}) * Fni^3 * A_{BT}^{1.5} * \rho * g}{1 + Fni^2}$	2	-3.0	-1.50
B-41	$R_B = \frac{0.11 * \exp(-3 * P_B^{-2}) * Fni^3 * A_{BT}^{1.5} * \rho * g}{1 + Fni^2}$	3	1.80	4.0
B-42	$R_B = \frac{0.11 * \exp(-3 * P_B^{-2}) * Fni^3 * A_{BT}^{1.5} * \rho * g}{1 + Fni^2}$	1.5	1.2	3.0

A Novel Methodology for Robust, Holistic, Simulation-Based Ship Design Optimization

B-43	$R_B = \frac{0.11 * \exp(-3 * P_B^{-2}) * Fni^3 * A_{BT}^{1.5} * \rho * g}{1 + Fni^2}$	2	1.60	2.60
B-44	$Fni = \frac{v}{\sqrt{g * (T_F - h_B - 0.25 * \sqrt{A_{BT}}) + 0.15 * v^2}}$	2	1.40	2.60
Resistance due to Transom Immersion				
B-45	$c_6 = 0.2 * (1 - 0.2 * Fn_T)$	0.2	0.01	2.0
Model Ship Correlation				
B-46	$C_A = 0.006 * (L + 100)^{-0.16} - 0.00205 + 0.003 * \sqrt{\frac{L}{7.5}} * C_B^4 * c_2 * (0.04 - c_4) + C_{Anew} * Fn^{c_{Bnew}}$	0.006	0.001	0.50
B-47	$C_A = 0.006 * (L + 100)^{-0.16} - 0.00205 + 0.003 * \sqrt{\frac{L}{7.5}} * C_B^4 * c_2 * (0.04 - c_4) + C_{Anew} * Fn^{c_{Bnew}}$	-0.16	-0.50	-0.01
B-48	$C_A = 0.006 * (L + 100)^{-0.16} - 0.00205 + 0.003 * \sqrt{\frac{L}{7.5}} * C_B^4 * c_2 * (0.04 - c_4) + C_{Anew} * Fn^{c_{Bnew}}$	-0.00205	-0.06	-0.10
B-49	$C_A = 0.006 * (L + 100)^{-0.16} - 0.00205 + 0.003 * \sqrt{\frac{L}{7.5}} * C_B^4 * c_2 * (0.04 - c_4) + C_{Anew} * Fn^{c_{Bnew}}$	0.003	0.001	0.10
B-50	$C_A = 0.006 * (L + 100)^{-0.16} - 0.00205 + 0.003 * \sqrt{\frac{L}{7.5}} * C_B^4 * c_2 * (0.04 - c_4) + C_{Anew} * Fn^{c_{Bnew}}$	7.5	6.0	11.0
B-51	$C_A = 0.006 * (L + 100)^{-0.16} - 0.00205 + 0.003 * \sqrt{\frac{L}{7.5}} * C_B^4 * c_2 * (0.04 - c_4) + C_{Anew} * Fn^{c_{Bnew}}$	0.04	-	-
B-52	$C_A = 0.006 * (L + 100)^{-0.16} - 0.00205 + 0.003 * \sqrt{\frac{L}{7.5}} * C_B^4 * c_2 * (0.04 - c_4) + C_{Anew} * Fn^{c_{Bnew}}$	$c_{Anew} = 0$	$c_{Anew} = 0.20$	$c_{Anew} = 1.20$
B-53	$C_A = 0.006 * (L + 100)^{-0.16} - 0.00205 + 0.003 * \sqrt{\frac{L}{7.5}} * C_B^4 * c_2 * (0.04 - c_4) + C_{Anew} * Fn^{c_{Bnew}}$	$c_{Bnew} = 0$	$c_{Bnew} = -1.0$	$c_{Bnew} = 1.0$
B-54	$c_4 = c_{4new} * \frac{T_F}{L}$	$c_{4new} = 1$	$c_{4new} = 0.01$	$c_{4new} = 5$
Propulsion Factors				
B-53	$\eta_R = 0.9922 - 0.05908 * \frac{A_E}{A_0} + 0.07424 * (C_P - 0.0225 * lcb)$	0.9922	-	-
B-54	$\eta_R = 0.9922 - 0.05908 * \frac{A_E}{A_0} + 0.07424 * (C_P - 0.0225 * lcb)$	0.05908	-	-
B-55	$\eta_R = 0.9922 - 0.05908 * \frac{A_E}{A_0} + 0.07424 * (C_P - 0.0225 * lcb)$	0.07424	-	-
B-56	$\eta_R = 0.9922 - 0.05908 * \frac{A_E}{A_0} + 0.07424 * (C_P - 0.0225 * lcb)$	0.0225	-	-
B-57	$t_{HOLTROP} = 0.001979 * \frac{L}{B * (1 - C_P)} + 1.0585 * \frac{B}{L} - 0.00524 - 0.1418 * \frac{D^2}{B * T}$	0.001979	0.0001	0.9

A Novel Methodology for Robust, Holistic, Simulation-Based Ship Design Optimization

B-58	$t_{HOLTROP} = 0.001979 * \frac{L}{B * (1 - C_p)} + 1.0585 * \frac{B}{L} - 0.00524 - 0.1418 * \frac{D^2}{B * T}$	1.0585	0.5	2.5
B-59	$t_{HOLTROP} = 0.001979 * \frac{L}{B * (1 - C_p)} + 1.0585 * \frac{B}{L} - 0.00524 - 0.1418 * \frac{D^2}{B * T}$	-0.00524	-0.1	-10 ⁻⁵
B-60	$t_{HOLTROP} = 0.001979 * \frac{L}{B * (1 - C_p)} + 1.0585 * \frac{B}{L} - 0.00524 - 0.1418 * \frac{D^2}{B * T}$	-0.1418	0.0001	0.9
B-61	$W_{HOLTROP} = c_9 * C_V * \frac{L}{T_A} * \left(0.0661875 + 1.21756 * c_{11} * \frac{C_V}{(1 - C_{p1})} \right) + 0.24558$ $* \sqrt{\frac{B}{L * (1 - C_{p1})} - \frac{0.09726}{0.95 - C_p} + \frac{0.11434}{0.95 - C_B}} + 0.75 * C_{Stern}$ $* C_V + 0.002 * C_{Stern}$	0.0661875	-	-
B-62	$W_{HOLTROP} = c_9 * C_V * \frac{L}{T_A} * \left(0.0661875 + 1.21756 * c_{11} * \frac{C_V}{(1 - C_{p1})} \right) + 0.24558$ $* \sqrt{\frac{B}{L * (1 - C_{p1})} - \frac{0.09726}{0.95 - C_p} + \frac{0.11434}{0.95 - C_B}} + 0.75 * C_{Stern}$ $* C_V + 0.002 * C_{Stern}$	1.21756	-	-
B-63	$W_{HOLTROP} = c_9 * C_V * \frac{L}{T_A} * \left(0.0661875 + 1.21756 * c_{11} * \frac{C_V}{(1 - C_{p1})} \right) + 0.24558$ $* \sqrt{\frac{B}{L * (1 - C_{p1})} - \frac{0.09726}{0.95 - C_p} + \frac{0.11434}{0.95 - C_B}} + 0.75 * C_{Stern}$ $* C_V + 0.002 * C_{Stern}$	0.24558	-	-
B-64	$W_{HOLTROP} = c_9 * C_V * \frac{L}{T_A} * \left(0.0661875 + 1.21756 * c_{11} * \frac{C_V}{(1 - C_{p1})} \right) + 0.24558$ $* \sqrt{\frac{B}{L * (1 - C_{p1})} - \frac{0.09726}{0.95 - C_p} + \frac{0.11434}{0.95 - C_B}} + 0.75 * C_{Stern}$ $* C_V + 0.002 * C_{Stern}$	0.09726	-	-
B-65	$W_{HOLTROP} = c_9 * C_V * \frac{L}{T_A} * \left(0.0661875 + 1.21756 * c_{11} * \frac{C_V}{(1 - C_{p1})} \right) + 0.24558$ $* \sqrt{\frac{B}{L * (1 - C_{p1})} - \frac{0.09726}{0.95 - C_p} + \frac{0.11434}{0.95 - C_B}} + 0.75 * C_{Stern}$ $* C_V + 0.002 * C_{Stern}$	0.11434	-	-
B-66	$c_{11} = 0.0833333 * \left(\frac{T_A}{D} \right)^3 + 1.33333$	0.0833333	-	-
B-67	$c_{11} = 0.0833333 * \left(\frac{T_A}{D} \right)^3 + 1.33333$	1.3333	-	-
B-68	$W_{SCHNEEKLUTH} = 0.5 * C_p * \frac{1.6}{1 + \frac{D}{T}} * \frac{16}{10 + \frac{L}{B}}$	0.5	0.1	0.9
B-69	$W_{SCHNEEKLUTH} = 0.5 * C_p * \frac{1.6}{1 + \frac{D}{T}} * \frac{16}{10 + \frac{L}{B}}$	1.6	0.5	2.5
B-70	$W_{SCHNEEKLUTH} = 0.5 * C_p * \frac{1.6}{1 + \frac{D}{T}} * \frac{16}{10 + \frac{L}{B}}$	16	6	25
B-71	$W_{KRUGER} = 0.75 * C_B - 0.24$	0.75	0.4	0.9

B-72	$w_{KRUGER} = 0.75 * C_B - 0.24$	0.24	0.05	0.5
B-73	$w_{HECKSCHER} = 0.7 * C_P - 0.18$	0.7	0.2	0.9
B-74	$w_{HECKSCHER} = 0.7 * C_P - 0.18$	-0.18	-0.40	-0.01
B-75	$w_{TROOST} = 0.25 + 2.5 * (C_B - 0.6)^2$	0.25	0.1	0.4
B-76	$w_{TROOST} = 0.25 + 2.5 * (C_B - 0.6)^2$	2.5	0.1	4

Table 13: Holtrop Constants used as variables in optimization problem and their respective value range – BALLAST CONDITION.

For each vessel case, the difference between the Holtrop prediction and the respective model test result for each speed run (basis on the model tests) is calculated and its minimization is set as the target of the optimization run. The difference is dependent on the calibration stage and can either be the difference in the Effective Power or the difference in the propulsion factors, namely the thrust deduction, relative rotative efficiency and wake field fraction respectively. It should be pointed out that the absolute value (i.e., unsigned magnitude) of the differences was used instead of the signed difference since using the latter might lead to results with larger overall errors if the positive and negative differences cancel each other.

b. Design Engine

The design engine applied can be either the NSGA II (Non-dominating Sorting Genetic Algorithm) (Deb, et al., 2002) or the MOSA (Multi-Objective Simulation Annealing) (Ulungu, et al., July 1999) algorithms.

These algorithms are fully integrated and available in the CAESSES® software. The setup was done using a simple COM integration for the communication with the Excel working file containing the Holtrop methodology data and calculations, with the input values being the new variable values for the Holtrop coefficients and the output is the deviation of the EHP and SHP from model test results.

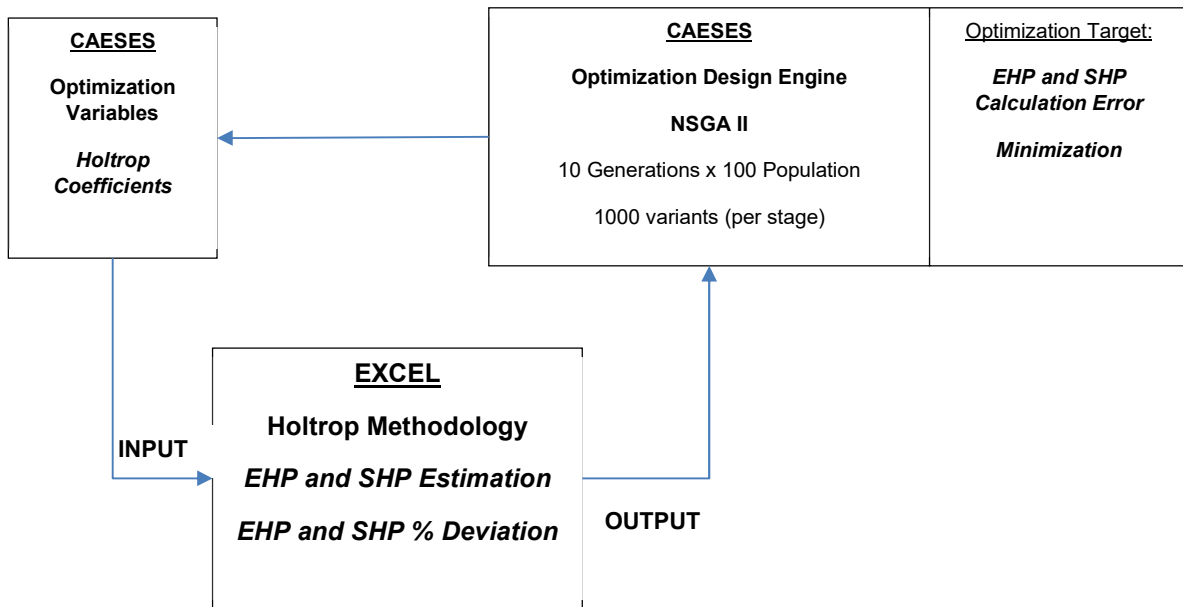


Figure 24: Specific Optimization Problem and Design Engine Setup

c. Constraints

The only constraint set was an upper limit on the optimization target, which is rejecting effectively combinations of the coefficients resulting in an average EHP and average SHP difference (depending on the calibration stage) greater than 15%. This was done to put a restriction and since this is an evolutionary algorithm push the latter to converge to the target.

As previously mentioned, the calibration study is a multi-staged one, to separate the different optimization targets (Figure 25).

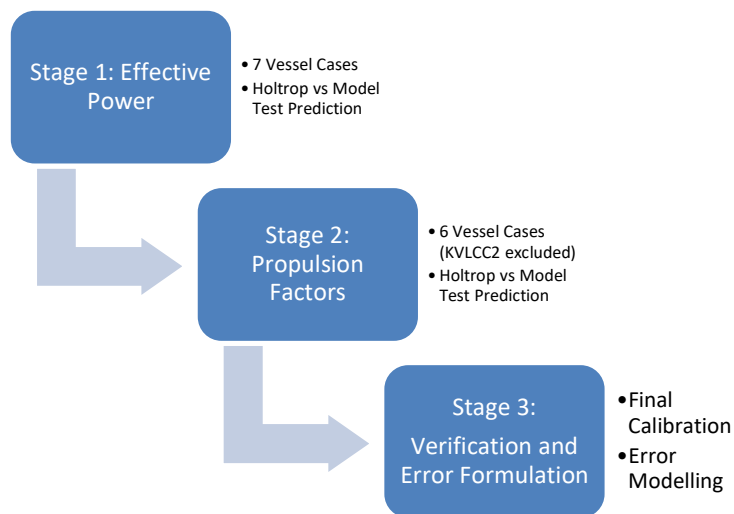


Figure 25: Stages and tools employed for each one

5.1.3. Stage 1: Effective Horsepower Coefficients Calibration

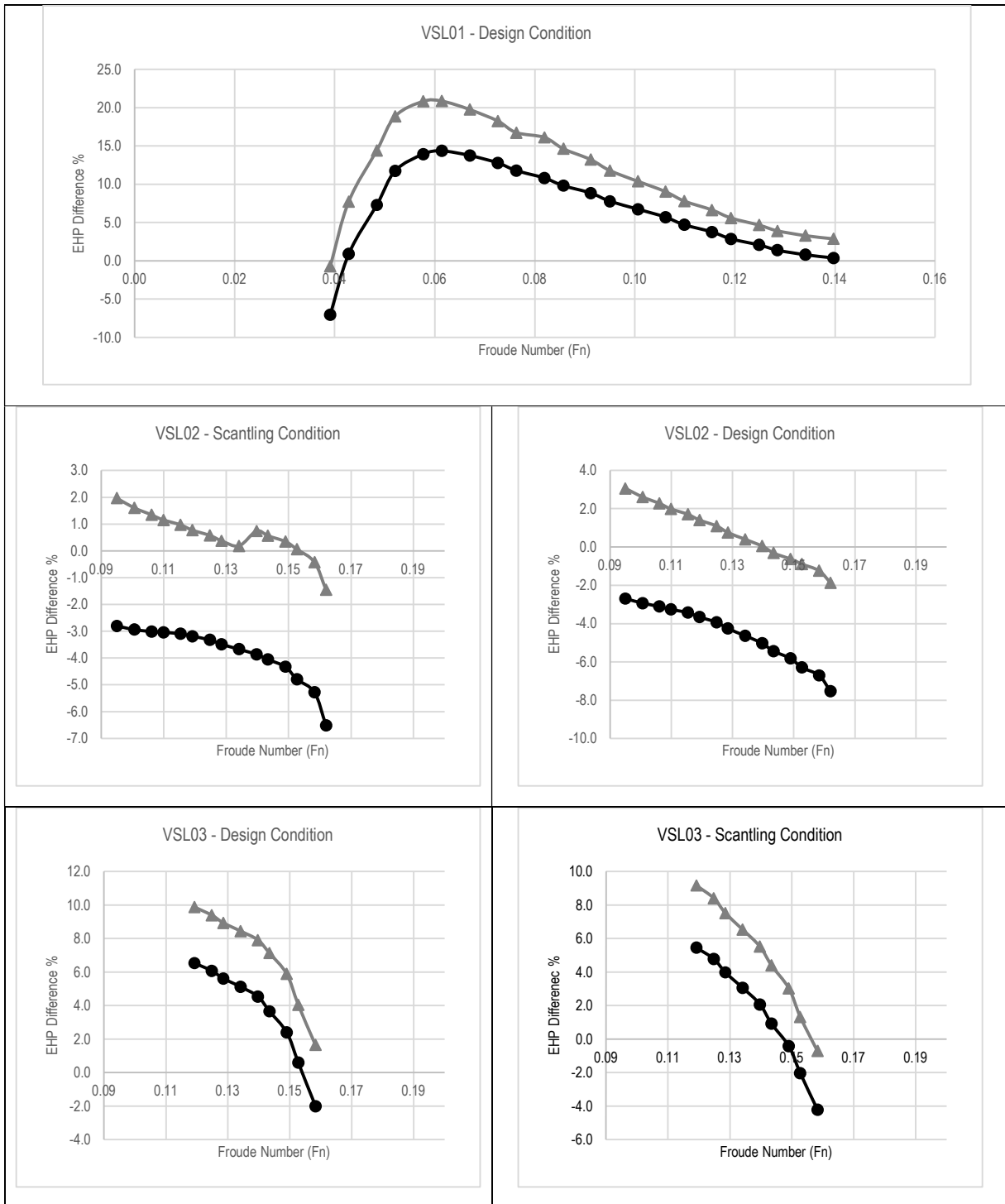
The first calibration stage is for the bare hull resistance and power requirement. The parameters that underwent systematic variation were from 1 to 49 for Laden Conditions and 1 to 54 for Ballast Conditions are depicted in Table 12 and Table 13 with the same range of variance. The variation engine employed was the NSGA II algorithm in the CAESES platform with a chosen set of 10 generations of variants with each generation having 100 variants population thus resulting in 1000 variants, in other words, 1000 combinations of the 49 parameters.

For this stage, the optimization target was set to be the absolute value of the percentage of the difference between the Effective Horsepower (EHP-kW) between the model test estimation and each "Holtrop variant" prediction, with the minimum being the desired merit. This was done for all 7 vessel cases in all speed-power points of each model test, resulting in 111 differences calculated at the points referred to as "calibration points". Furthermore, for the ease of the selection process, the average value of the differences of the calibration points per vessel was calculated as it can assist in the sorting of the best variants during post-processing. Within this spirit, the average value for the methodology in total (as the average of the averages of absolute differences) was calculated to serve also as a constraint. This constraint imposed was set as having not more than 15% of average deviations.

The optimization was on a chain basis for 3 optimization loops, meaning that the best variant from the first run was set as the initial solution for the 2nd and the best variant from the 2nd run was set as the initial solution for the 3rd run. This was done as the initial solution/state is critical for evolutionary algorithms such as the NSGAI contributing to more efficient convergence as well as a better final solution.

The results were sorted and a combination was selected from the lowest average absolute difference basis. The resulting values improved the Effective Power curves prediction error as can be seen from the below Figure 26 and Figure 27. In all the below graphs the grey, triangle marker curve represents the error distribution after calibration while the black, circle marker curve the error distribution corresponding to the original coefficients of the method. From the results, it is evident that the simulation had an obvious positive effect as in all vessel cases the prediction has been improved given the fact that all EHP differences have been reduced, while all the trends in terms of deviation over speed have been accurately maintained. In fact, if one observes the form of the curves it is evident that the calibrated curves are in fact "translations" of the original publication curves towards the x-axis.

A Novel Methodology for Robust, Holistic, Simulation-Based Ship Design Optimization



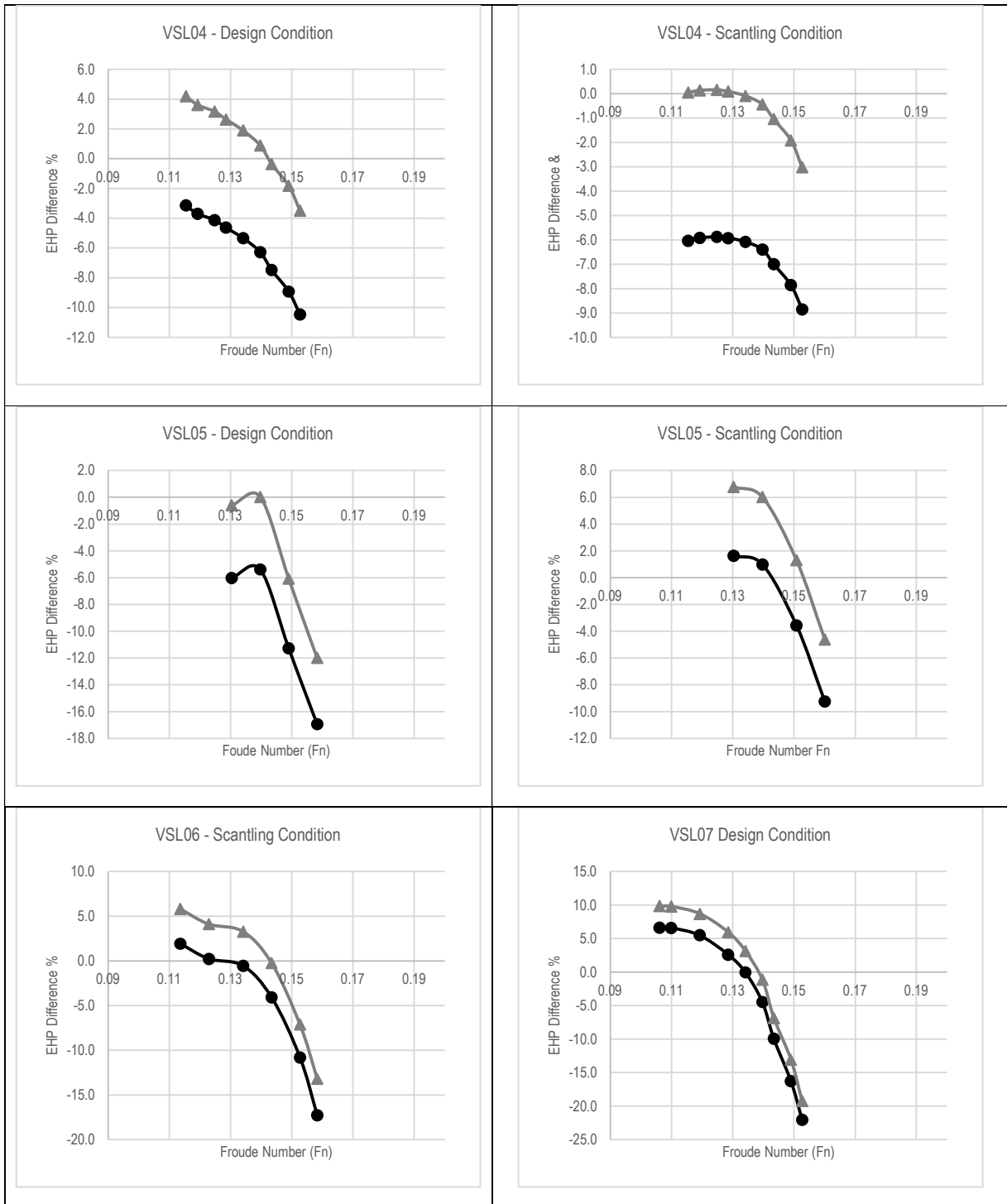


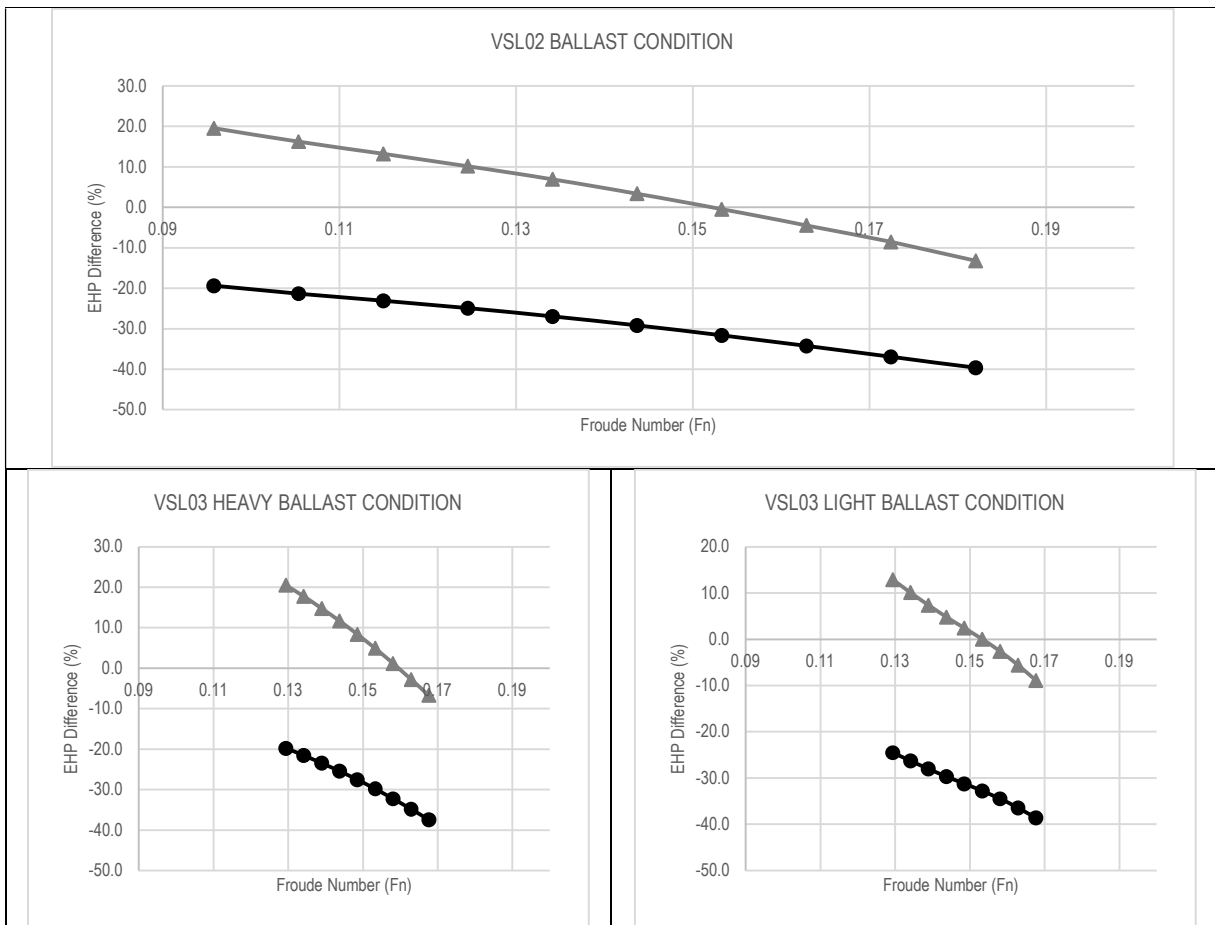
Figure 26: Distribution of EHP difference over speeds – LADEN Condition

Figure 26 depicts the distribution of the EHP difference over different speeds for the Laden Conditions for each vessel. The following interesting observations arise:

1. For 1 out of 11 cases (VSL03 – Design Condition), the translation of the deviation distribution was such that for the entire Froude number range there is an overestimation

of the resistance which however is decreasing (on a 3rd power basis) by increasing speed following the same trend as the equivalent curve before the calibration. The maximum overestimation is -10% but by increasing the Froude number it is reduced to almost 0.5%.

2. Another interesting case would be that of VSL05 Design Condition, where for low speeds there is an underestimation which is decreasing by increasing curves starting from 1% at low Froude numbers and up to a minimum of -2% overestimation and then sharply passes again to the underestimating region with the underestimation increasing sharply by increasing Froude numbers up to a maximum of 13%.
3. For 8 out of 11 cases, the effect of the apparent translation of the deviation distribution curve is that there is an overestimation at low speeds of a maximum -10% which is decreased steeply by increasing speed up to a transition speed within the range of 0.125 to 0.175 Froude number from which point there is a transit to the underestimation area with a steep increase of underestimation by increasing speed up to a maximum 20% underestimation.



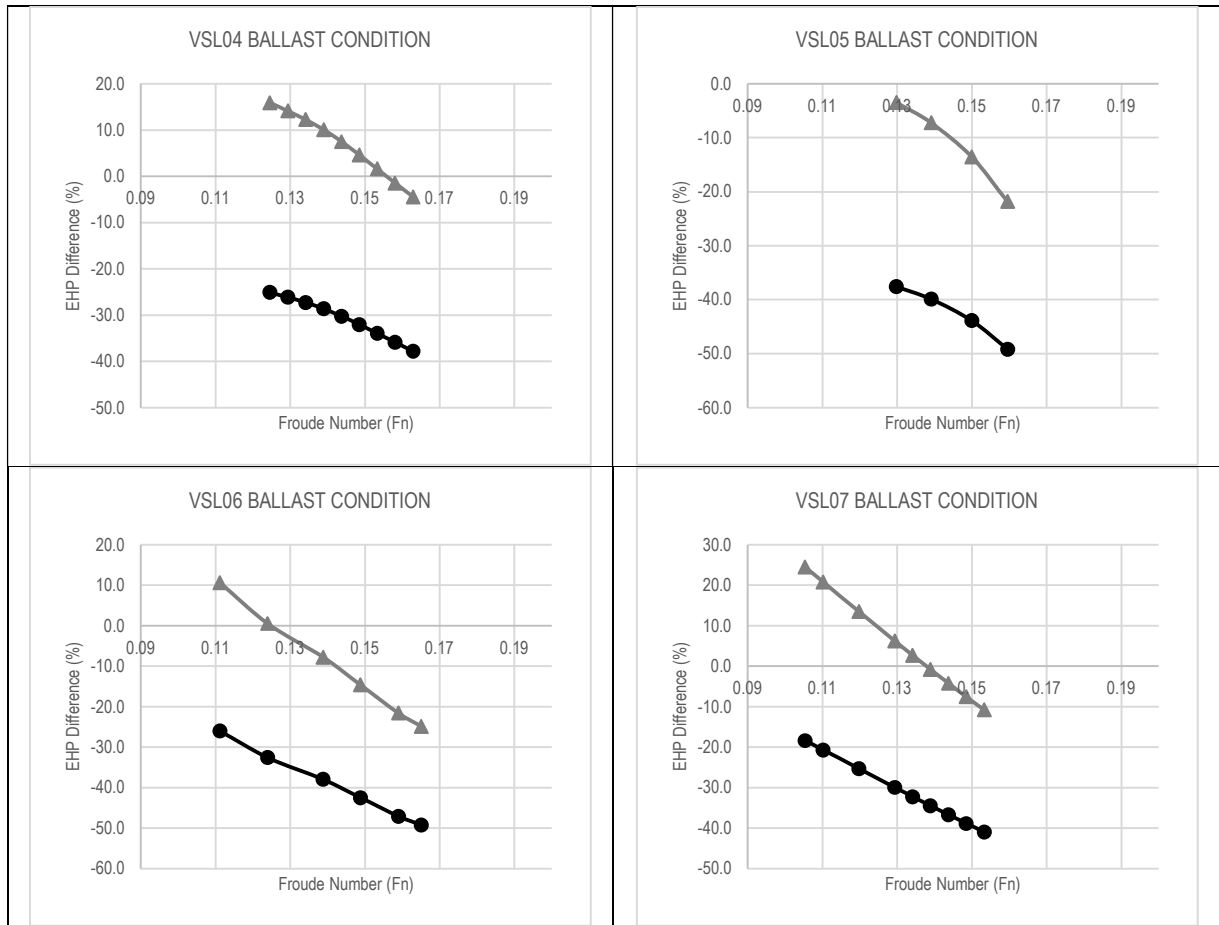


Figure 27: Distribution of EHP difference over different speeds – BALLAST Condition

Figure 27 depicts the distribution of the EHP difference over different speeds for the Ballast Conditions. The following interesting observations arise:

1. For 1 out of 7 cases (VSL05), the deviation distribution is located at the underestimating region for all Froude numbers, starting from a minimum of 2% at low Froude numbers which are increasing on a power rate by increasing speed and up to a maximum of 20% at high Froude numbers.
2. For the rest 6 out of 7 cases, due to the translation of the error distribution curve, an overestimation at low speeds is observed which is decreasing by increasing speed and at a transition speed of the region of 0.15 Froude number changes to the underestimation region which is increasing by increasing speed up to a maximum of 20%.
3. For all cases and since the same trends of the curves before the calibration are kept the correlation between deviation and speed is very close to being linear and with a high steepness, which is in contrast to the Laden Condition which follows a 2nd-3rd power fit correlation.

Table 14 and Table 15 summarize the EHP difference between the Holtrop Prediction and the model test results prior to and after the calibration for Laden and Ballast Conditions respectively. For the Laden conditions (both design and scantling) the improvement over all seems marginal as the deviation decreased from 5.7% to 4.7% in terms of absolute deviation. If one looks however at the nominal deviation of the “translation” observed in the deviation graphs and described above, it has improved from an average underestimation of 1.4% to an overestimation of -1.9% which is preferable in ship design studies to have a safer design margin for sizing the propulsion plant. For the laden conditions, one can also observe that despite an improvement of the prediction in some vessels of the herein presented study database is very distinct (VSL02, VSL03, VSL04, VSL05), for other vessels’ in the same database and the same selected optimization variant the prediction error is higher when compared to the respective error corresponding to the original Holtrop coefficients. This highlights the sensitivity of the method which is expected given the already low level of prediction error (%) for the original Holtrop coefficients in the laden conditions.

In the Ballast conditions, the average absolute deviation was reduced from 31.8% to 9.78% which makes it a considerable improvement that constitutes the basis for the next Stage 2 calibration for the Delivered Horse Power (SHP).

STAGE 1 CALIBRATION RESULTS - LADEN CONDITIONS				
Vessel	Average Error (%) EHP After Calibration	Average Absolute Error (%) EHP After Calibration	Average Error (%) EHP Original Holtrop Coefficients	Average Absolute Error (%) EHP Original Holtrop Coefficients
VSL01 - Design Condition	-11.206	11.272	-6.593	7.234
VSL02 - Scantling - Low Speed	-0.584	0.835	3.826	3.826
VSL02 - Design - Low Speed	-0.695	1.353	4.583	4.583
VSL03 - Design Condition	-7.035	7.035	-3.620	4.063
VSL03 - Scantling Condition	-5.025	5.183	-1.514	2.992
VSL04 - Design Condition	-1.194	2.454	6.008	6.008
VSL04 - Scantling Condition	0.675	0.770	6.658	6.658
VSL05 - Design Condition	4.668	4.677	9.908	9.908
VSL05 - Scantling Condition	-2.361	4.678	2.553	3.852
VSL06 - Scantling Condition	1.222	5.627	5.088	5.807
VSL07 - Design Condition	0.309	8.638	3.498	8.229
ENTIRE DATABASE	-1.930	4.775	2.763	5.742

Table 14: EHP Deviation from Model Tests Prior and After Stage 1 Calibration – LADEN CONDITIONS

STAGE 1 CALIBRATION RESULTS - BALLAST CONDITIONS			
Vessel	Average Error (%) EHP - NSGA11-885	Average Absolute Error (%) EHP - NSGA11-885	Average Error (%) EHP - Original Holtrop Coefficients
VSL02 – Ballast Condition	-4.269	9.604	28.725
VSL03 - Heavy Ballast Condition	-7.765	9.863	27.989
VSL03 -Light Ballast Condition	-2.298	6.086	31.310
VSL04 - Ballast Condition	-6.692	7.999	30.769
VSL05 - Ballast Condition	11.517	11.517	37.813
VSL06 - Ballast Condition	9.609	13.330	40.913
7VSL07 - Ballast Condition	-4.933	10.119	30.823
ENTIRE DATABASE	-0.690	9.788	32.620

Table 15: EHP Deviation from Model Tests Prior and After Stage 1 Calibration – BALLAST CONDITION

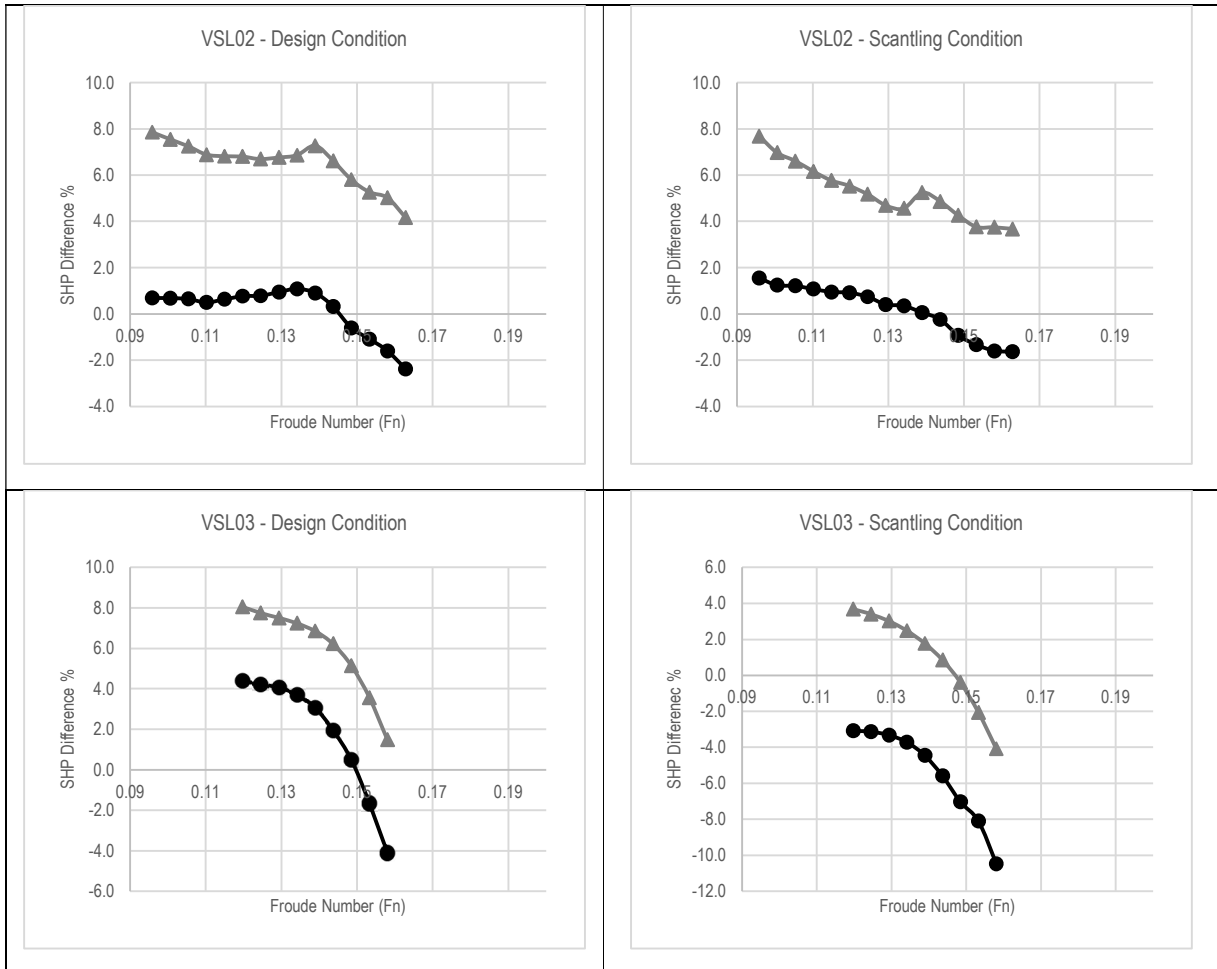
5.1.4. Stage 2: Delivered Horsepower Coefficients

The same simulation runs for the minimization of the Effective Horsepower (EHP) prediction error, and run also for the minimization of the Delivered/Shaft Horsepower (SHP) error. For mitigating the bare hull resistance to the self-propulsion state, the propeller open water characteristics were used from one hand, and empirical formulae for the wake fraction, thrust deduction and relative rotative efficiency coefficients. The coefficients of the formulae used for the estimation of the latter were the optimization variables, while the SHP prediction error minimization was the optimization target.

In Figure 28 the SHP deviation distribution over different speeds is depicted for the Laden Conditions with the below interesting observations:

1. For 5 out of 10 cases an overestimation of the SHP for the entire range of Froude numbers is observed from a maximum of 20% at the low Froude number range and up to 4% at the high range, indicating the same trend of increasing underestimation by increasing Froude number. The reason for the high overestimation at the low speeds, in this case, is the translation of the original curve to lower overestimating regions to attain an average close to zero deviation.
2. For 4 out of 10 cases while at the lower Froude number range there is an overestimation of up to 15% at higher Froude numbers that transcends to the underestimation region at a transition Froude number ranging from 0.125 to 0.175 depending on each vessel case, while the underestimation at the highest speeds is maximum 15%.
3. An interesting case out of the above 5 mentioned, is VSL07 where up to 0.16 Froude number the overestimation is practically constant at 5% and then drops rapidly, transits to the underestimating region, increasing linearly and steeply by increasing speed with a maximum underestimation of 30%.

- For 1 out of 10 cases there is only underestimation for all Froude numbers having the same trend as with the original case however translated to a much lower level of error. This can be seen from an underestimation of 1% at low Froude numbers and up to a maximum of 3% at higher. Interestingly for this case (VSL04 Scantling Condition) the difference from 12 to 14 knots is almost constant at 1% and changes rapidly from 0.135 to 0.15 Froude number with an almost linear increase by increasing speed.



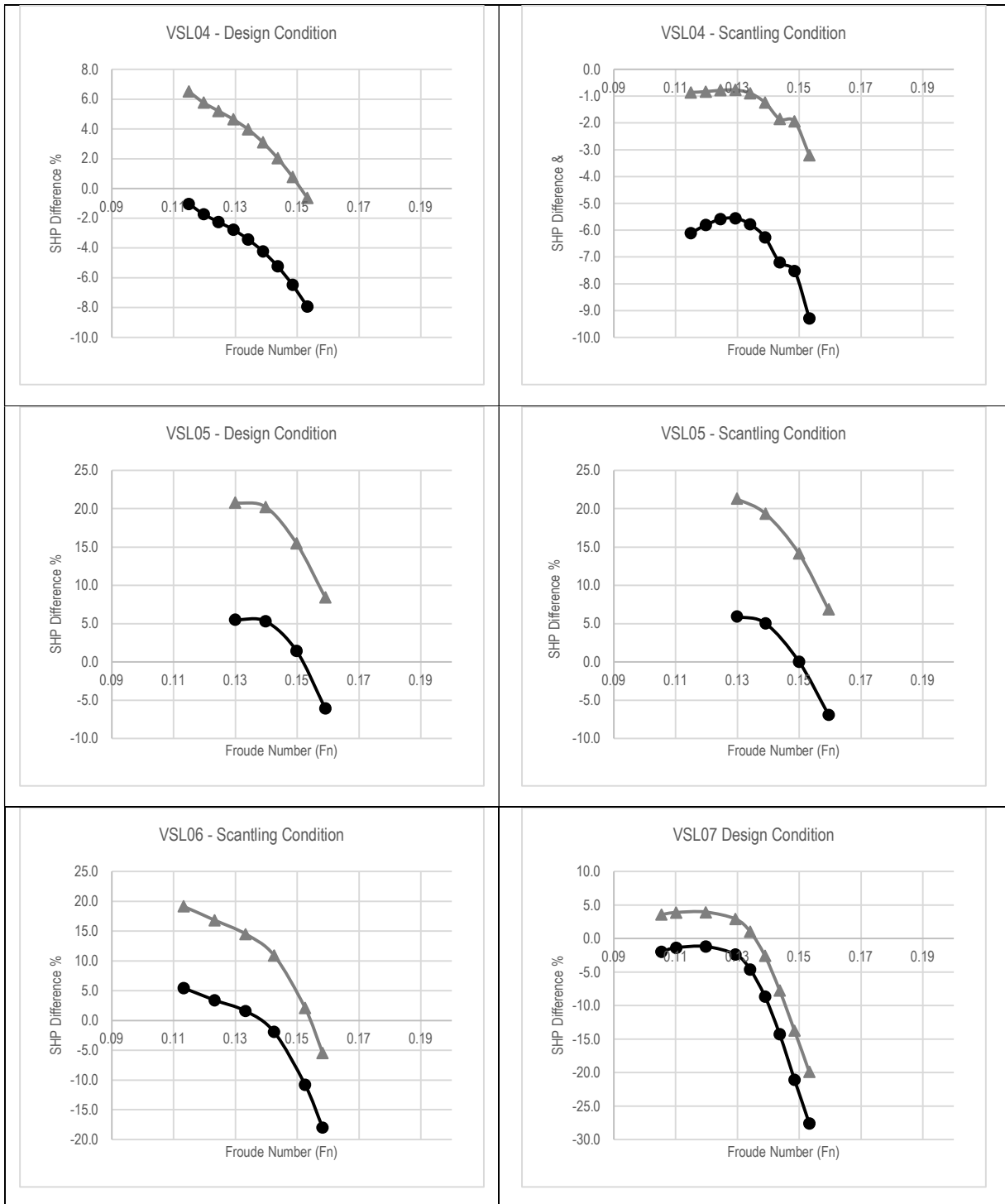
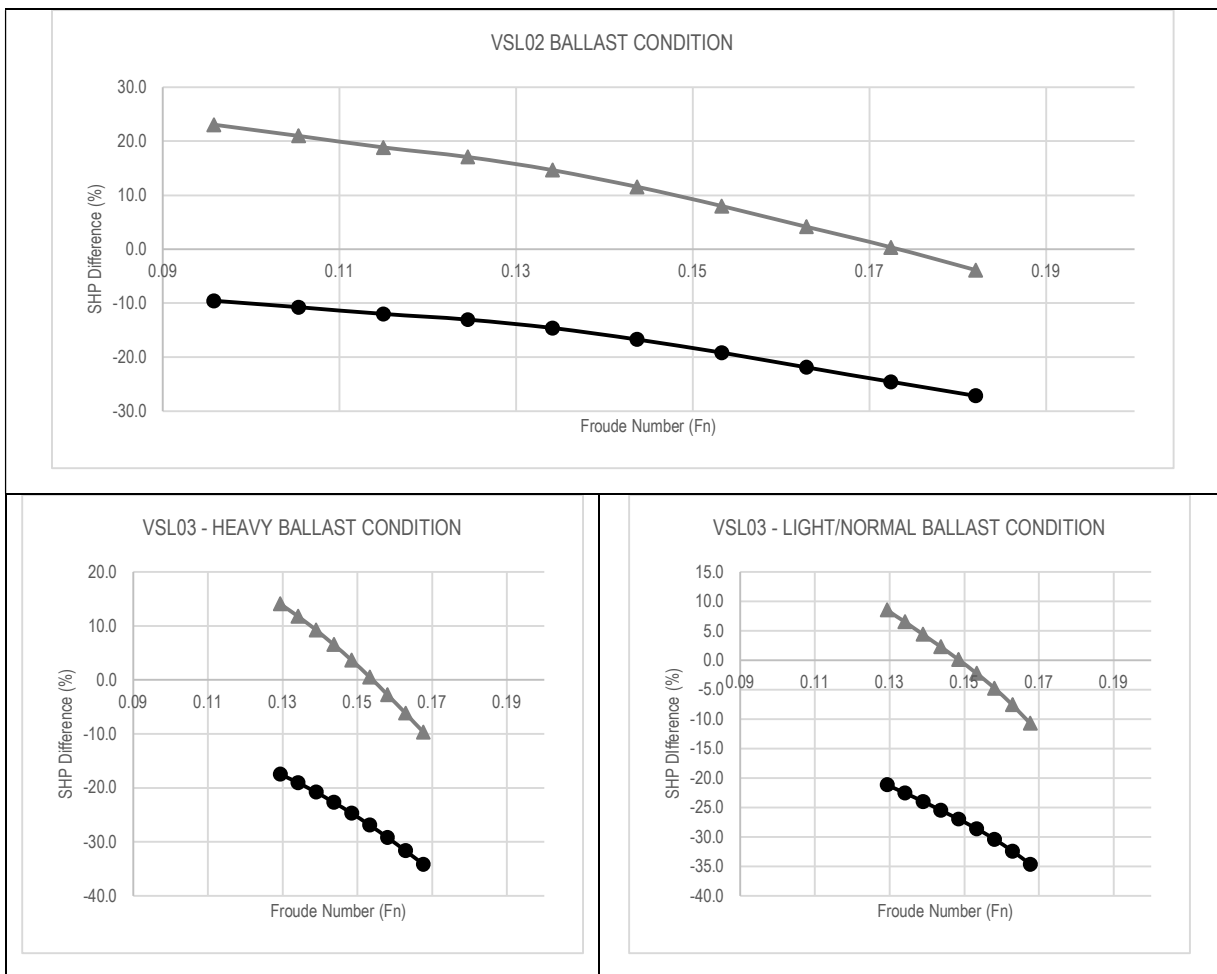


Figure 28: Deviation of SHP over different speeds – LADEN Condition

Figure 29 depicts the SHP deviation distribution over different speeds for the Ballast Conditions with the below observations:

1. For 1 out of 7 cases (VSL05 ballast condition), the methodology underestimates the required power for the entire Froude number range with the latter descending by increasing speed and having the same trend as before the calibration.
2. For the rest 6 out of 7 cases, there is an overestimation of the required power at low speeds of a maximum of 25% which by increasing speeds linearly decreases and at a Froude number at the region 0.15 (depending on each vessel) there is a transition to the underestimation region. The underestimation also increases linearly by increasing speed up to a maximum of 15%.



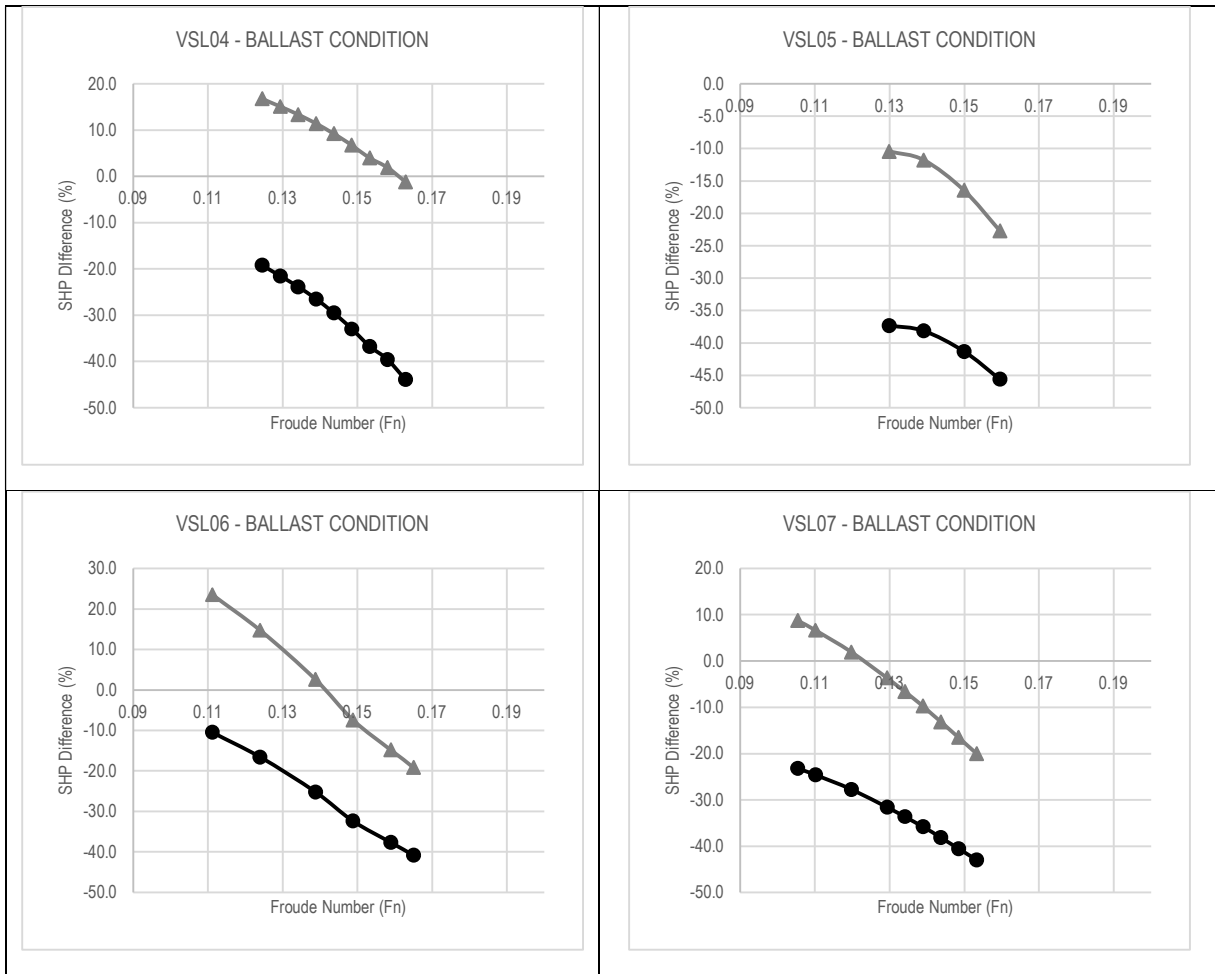


Figure 29: Deviation of SHP over different speeds – BALLAST Condition

In Table 16 (for the Laden conditions) and Table 17 (for the Ballast conditions) the deviation of the predicted required Delivered Horsepower (SHP) prior to the calibration (original Holtrop coefficients) and after the calibration, when compared to the model test prediction is depicted. The average absolute error (%) has been significantly reduced from 28.68% to 10.3% for the Ballast Conditions. For the Laden Conditions, however, the average absolute error (%) increased marginally from 4.59 % to 7.49%. The reason for this is the already small prediction error. By trying to improve such a small error the sensitivity is at a level that can improve the prediction accuracy for some cases and deteriorate for others. A typical example is VSL02 for which the prediction error decrease increased from 0.95% to 5 % while in the meantime and the same combination of variables the prediction error of VSL02, for VSL04, decreased from 6.57 % to 1.37%.

In addition to the above, it should also be noted, that when looking at the average deviation (not absolute) this has been an average underestimation of 1.74% prior to the calibration which has been changed to an average overestimation of -4.65% which leads to a safer margin for predictions at the preliminary ship design stages.

Lastly, all the individual components have improved accuracy, thus the herein proposed calibrated methodology depicts more accurately the sensitivities of the methodology in main dimensions and design characteristics for all the resistance sub-components which is very useful for preliminary ship design studies.

Vessel	SHP Average Error (%) After Stage 2 Calibration	SHP Average Absolute Error (%) After Stage 2 Calibration	SHP Average Error (%) Prior Stage 2 Calibration	SHP Average Absolute Error (%) Prior Stage 2 Calibration
VSL02 - Scantling Condition	5.250	5.250	0.188	0.948
VSL02 - Design Condition	6.510	6.510	0.156	0.908
VSL03 - Design Condition	5.977	5.977	1.793	3.073
VSL03 - Scantling Condition	0.959	2.4151	-5.434	5.434
VSL04 - Design Condition	3.482	3.625	-3.898	3.898
VSL04 - Scantling Condition	-1.373	1.373	-6.571	6.571
VSL05 - Design Condition	16.221	16.221	1.533	4.572
VSL05 - Scantling Condition	15.408	15.408	1.008	4.472
VSL06 - Scantling Condition	9.682	11.496	-3.375	6.855
VSL07 - Design Condition	-3.170	6.594	-9.227	9.227
ENTIRE DATABASE	5.894	7.487	-2.382	4.596

Table 16: Average Deviation of the Delivered Horsepower (%) per vessel – LADEN Condition

Vessel	SHP Average Error (%) After Stage 2 Calibration	SHP Average Absolute Error (%) After Stage 2 Calibration	SHP Average Error (%) Prior Stage 2 Calibration	SHP Average Absolute Error (%) Prior Stage 2 Calibration
VSL02 - Ballast - Low Speed	11.467	12.240	-16.954	16.954
VSL03 - Heavy Ballast Condition	3.0225	7.154	-25.178	25.178
VSL03 -Light Ballast Condition	-0.3793	5.228	-27.354	27.354
VSL04 - Ballast Condition	8.577	8.843	-30.424	30.424
VSL05 - Ballast Condition	-15.331	15.331	-40.589	40.589
VSL06 - Ballast Condition	-0.081	13.709	-27.181	27.181
VSL07 - Ballast Condition	-5.820	9.668	-33.141	33.141
ENTIRE DATABASE	0.207	10.311	-28.689	28.689

Table 17: Average Deviation of the Delivered Horsepower (%) per vessel – BALLAST Condition

The below Table 18 summarizes, the finalized values chosen for the Holtrop constants in terms of resistance and propulsion power prediction formula following the two-stage optimization and calibration process.

No.	Value in Original Holtrop Publication LADEN	Value After Final Calibration LADEN	No.	Value in Original Holtrop Publication BALLAST	Value After Final Calibration BALLAST
-----	--	--	-----	--	--

A Novel Methodology for Robust, Holistic, Simulation-Based Ship Design Optimization

L-1	2223105	2242064.546	B-1	2223105	2207306.02
L-2	3.78613	2.965053788	B-2	3.78613	2.369306477
L-3	1.07961	0.987251087	B-3	1.07961	0.965964752
L-4	-1.37565	-1.248029297	B-4	-1.37565	-1.426852827
L-5	-1.89	-1.585484092	B-5	-1.89	-1.865680934
L-6	0.56	0.888603037	B-6	0.56	0.310946822
L-7	0.31	0.679055924	B-7	0.31	0.599398947
L-8	1.5	0.679055924	B-8	1.5	2.660425727
L-9	0.8	0.311482414	B-9	0.8	0.866790265
L-10	-1.69835	-1.968221561	B-10	-1.69835	-1.492373541
L-11	$c_{15_{new}} = 0$	1.215701534	B-11	$c_{15_{new}} = 0$	-0.3111146715
L-12	0.0140407	0.022718547	B-12	0.0140407	0.01282916
L-13	1.75254	1.420567636	B-13	1.75254	1.28395819
L-14	4.79323	5.681261921	B-14	4.79323	4.854474708
L-15	2	2.580880446	B-15	2	2.202572671
L-16	-0.1	-0.147266651	B-16	-0.1	-0.405693141
L-17	-2	-2.988265812	B-17	-2	1.654390784
L-18	1.73014	1.465613794	B-18	8.07981	7.892027161
L-19	0.7067	0.6426	B-19	-13.8673	-12.1206
L-20	$c_{16C_{new}} = 0$	1.516899	B-20	6.984388	9.3225
L-21	$c_{16D_{new}} = 0$	-0.340063	B-21	1	1.3920
L-22	1.446	1.815469596	B-22	2	2.8830
L-23	0.03	0.023458457	B-23	3	3.1013
L-24	0	0.318760967	B-24	1.446	2.238521401
L-25	-0.9	-1.202760357	B-25	0.03	0.4431
L-26	-2	-2.374135958	B-26	0	0.0587
L-27	0.2228446	0.377695125	B-27	-0.9	-0.3324
L-28	0.92497	0.668810559	B-28	-2	-1.8767
L-29	-0.521448	-0.623591974	B-29	48.2	28.87945373
L-30	0.6906	0.766962692	B-30	2.078	3.323125048
L-31	0	-2.825314717	B-31	0.479948	0.446070497
L-32	0.56	0.843195239	B-32	0.92497	0.613664454
L-33	0.11	0.095151446	B-33	-0.521448	-0.565916533
L-34	-3	-3.153574426	B-34	0.6906	0.532242313
L-35	2	3.251325246	B-35	0.003	0.01538851
L-36	3	2.339742123	B-36	0	1.952800793
L-37	1.5	1.458429847	B-37	0.56	0.354276341
L-38	2	2.337720302	B-38	0.11	0.067300832
L-39	2	3.939871824	B-39	-3	-3.752483406
L-40	0.2	0.223463188	B-40	2	-1.800297551
L-41	0.006	0.069377752	B-41	3	3.084248112
L-42	-0.16	-0.417208057	B-42	1.5	1.358590066
L-43	-0.00205	-0.034246056	B-43	2	1.663599603
L-44	0.003	0.125382971	B-44	2	1.456360723
L-45	7.5	3.736263066	B-45	0.2	0.885375296
L-46	4	4.217013809	B-46	0.006	0.223290471
L-47		0.036289769	B-47	-0.16	-0.092530251

A Novel Methodology for Robust, Holistic, Simulation-Based Ship Design Optimization

L-48	$c_{Anew} = 0$	2.948729686	B-48	-0.00205	0.082350805
L-49	$c_{Bnew} = 0$	0.013092241	B-49	0.003	0.095168963
L-50	0.9922	0.9922	B-50	7.5	6.146944381
L-51	0.05908	0.05908	B-51	0.04	0.478261311
L-52	0.07424	0.07424	B-52	$c_{Anew} = 0$	0.36520943
L-53	0.0225	0.0225	B-53	$c_{Bnew} = 0$	-0.673182269
L-54	0.001979	0.0001	B-54	$c_{4new} = 1$	3.186513619
L-55	1.0585	3	B-53	0.9922	0.9922
L-56	-0.00524	-0.107307217	B-54	0.05908	0.05908
L-57	-0.1418	-0.001	B-55	0.07424	0.07424
L-58	0.0661875	0.0661875	B-56	0.0225	0.0225
L-59	1.21756	1.21756	B-57	0.001979	0.00001
L-60	0.24558	0.24558	B-58	1.0585	1.403225943
L-61	0.09726	0.09726	B-59	-0.00524	-0.032286653
L-62	0.11434	0.11434	B-60	-0.1418	-0.01
L-63	0.08333333	0.08333333	B-61	0.0661875	0.0661875
L-64	1.3333	1.3333	B-62	1.21756	1.21756
L-65	0.5	0.432109375	B-63	0.24558	0.24558
L-66	1.6	1.325859375	B-64	0.09726	0.09726
L-67	16	15.72532144	B-65	0.11434	0.11434
L-68	0.75	0.662024983	B-66	0.08333333	0.08333333
L-69	0.24	0.176972156	B-67	1.3333	1.3333
L-70	0.7	0.316622043	B-68	0.5	0.5
L-71	-0.18	-0.101944784	B-69	1.6	1.6
L-72	0.25	0.25	B-70	16	16
L-73	2.5	2.5	B-71	0.75	0.820510639
			B-72	0.24	0.102842033
			B-73	0.7	0.431767617
			B-74	-0.18	-0.048268475
			B-75	0.25	0.252269833
			B-76	2.5	0.1

Table 18: Values of Holtrop coefficients after calibration for bare hull resistance

5.1.5. Stage 3: Verification and Error Formulation

Following the systematic calibration and for a given, final prediction error (%) per vessel per speed, the latter was examined to be modelled for corrections in new prediction applications. To do so, however, it is necessary to provide a formulation for the estimation of error distribution as a function of the examined vessel characteristics. This distribution was modelled utilizing a non-linear regression formula generated in the IBM SPSS Software, for the database used herein for calibration and the coefficients deriving from the Stage 2 calibration. The below equations can be used as a result:

A Novel Methodology for Robust, Holistic, Simulation-Based Ship Design Optimization

$$\begin{aligned} \text{Error}(\%)_{LADEN} &= 0.008 * L_{BP}^{-8.096} + 0.009 * B^{-1.346} + 0.006 * T_m^{-34.137} + 0.039 * C_B^{1100.918} - 0.014 * WS^{-4.877} \\ \text{Error}(\%)_{BAL} &= -1132.36 * L_{BP}^{-0.055} - 95.054 * B^{-0.275} + 911.906 * T_m^{-0.080} + 158.633 * C_B^{2.854} + 0.256 * WS^{0.457} \end{aligned} \quad (52)$$

Where:

L_{BP} : Length between perpendiculars

B : Breadth (moulded)

T_m : Midship Draft

C_B : Block Coefficient

WS : Wetted Surface

5.2. Main Engine Dimensioning

5.2.1. Introduction

Following the dimensioning and matching of the propeller for the hull and the determination of its operating point, the Propulsion Plant is dimensioned along with the Electrical Generation and Steam Generation Plant and Engine Room Ancillaries. Given that the methodology focuses on the design of low Froude number, high block coefficient commercial vessels (bulklers, tankers), as well as more slender vessels of medium Froude number such as containerships, the propulsion plants herein chosen, are directly driven, slow speed, two-stroke diesel engines of large bore and stroke dimensions. Please note that from the Author's previous work, the module is also expandable to twin 2-stroke engine and engine room installations, Diesel Electric and Dual Fuel Diesel Electric Installations (Nikolopoulos, 2012).

The originality of the research work is that the dimensioning of the Main Engine here is based on a "Limit State Approach". Conventionally, the Main Engine power is determined by the application of a "Sea Margin" of 15% on the delivered power and (in some cases in the industry) of a "Propeller RPM Margin" of 4-6% (based on the propeller selection). Such an approach has the inherent risk of incorrect dimensioning the M/E power and M/E RPM and matching incorrectly the engine to the chosen propeller. To avoid this an original Limit State approach has been developed during which the SMCR and corresponding RPM are selected in order to be able to serve a Limit State characterized by the below parameters (user defined):

1. Maximum service speed.
2. Sea State on JONSWAP spectrum
3. Wind Speed
4. Average Hull Roughness increase due to current.
5. Current velocity of head (adverse current).
6. "Derating Margin" for optimizing SFOC curves and maximum firing pressure.

A calculation using the above from the tools developed in the RHODA methodology returns as an output not just the Main Engine SMCR and corresponding RPM but also the engine model, turbocharger and auxiliaries required.

5.2.2. Developed Engine Dimensioning and Selection Module

The first development stage for this tool was the creation of a digital parametric engine catalogue. The Main Engine Program of MAN B&W (MAN, 2017) and the corresponding project guides (MAN, 2020), have been selected and the selection envelopes of all available engines above 700mm bore (S/G70 ME) have been parametrically defined in CAESSES by developing the relevant curves. This is done by using the RPM and Power range of the engine envelope which is defined by points L_1 , L_2 , L_3 and L_4 (Figure 30). Subsequently, for each engine the L1L3 and L2L4 lines are plotted in CAESSES with the use of a straight line. These lines correspond to engine design points with the same Mean Effective Pressure (MEP) that depending on the RPM setting corresponds to an output power per cylinder. It should be noted at this point that the output power is non-dimensionalised by the number of cylinders. The number of cylinders for the engines considered

has a small range (typically between 6-7), however, this number determines the main engine length and thus Engine Room length. To take this into consideration a constraint is introduced into the module that constrains the length of the engine based on the Engine Room bulkhead position design variable and thus available Engine Room space.

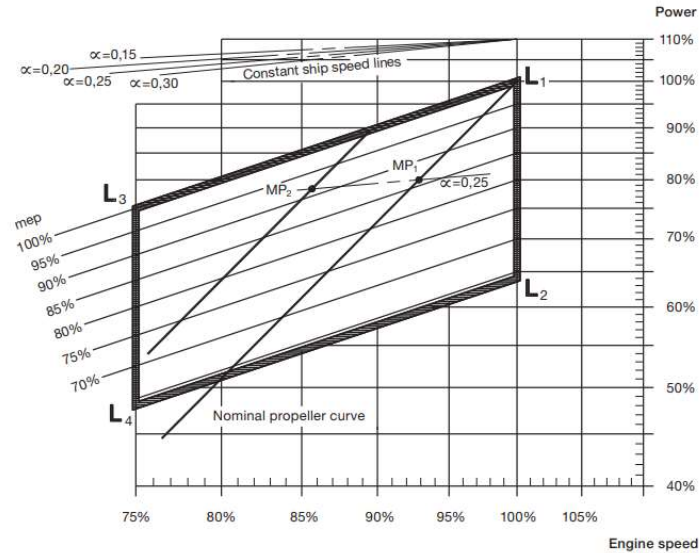


Figure 30: Engine Layout Envelope (MAN, 2020)

In addition to the L1L3 and L2L4 lines which are typically defined by MAN, intermediate iso-MEP lines are developed. The reason for the development of such lines is that the Specific Fuel Oil Consumption (SFOC in gr/kWh) is linearly dependent on the value of the MEP, meaning that along an iso-MEP curve the SFOC curve at different load points of the Main Engine (typically 50%, 75%, 100%) is constant. Thus, at any given arbitrary given point within the engine envelope (Figure 30), the SFOC curve can be approximated by linear interpolation between two iso-MEP curves. Subject calculations have been also validated with the use of the MAN CEAS® Engine Room Dimensioning tool that is freely available on the internet.

One of the disadvantages of using the Marine Engine Program is that the SFOC curve information that can be extracted from there is based on 50%, 75% and 100%. The SFOC curve generation based on these points is not sufficient as the extrapolation to lower loads from 50% is not entirely linear and thus at low loads, the SFOC information will be less accurate. In order to tackle this challenge, all available engine configurations as per Table 19 have been simulated with the MAN CEAS® Engine Room Dimensioning tool at the second stage of development of the parametric engine database. The important advantage of this approach is that the SFOC curve is generated from 10% to 100% of the Main Engine Load. Additionally, the steam production curves, exhaust temperature and urea consumption curves are generated.

Available Engine Models in Database:	G60/G70/G80/G90 ME-C 9.5 and ME-GI 9.5 (with 1.5% pilot).
Main Engine Loads:	10% to 100% of SMCR
Bore Size:	600 to 900 mm
Tuning Methods Available:	Part Load Optimization / Low Load Optimization
Tier III Compliance Technologies Available:	HPSCR, LPSCR, EGR, ecoEGR (for ME-GI engines)

Table 19: Engine Models Database

Lastly, as an industry known design practice and rule of thumb, it is preferably that the layout point on the engine envelope is chosen to be closer to the L2L4 line corresponding to bigger torque/MEP margins and smaller SFOC values. This is ensured by the addition of a “de-rating” constraint, which is in fact a margin of 10% from the L1L3 line. In case the layout point is closer than 10% to this line, the code automatically changes the examined engine by shifting to a larger bore model (e.g from G70-700mm bore to G80-800mm bore). It should also be noted that for reasons of efficiency, since the G-type engines are the predominantly available engines from MAN and they feature lower consumption and emissions, the older S-type engines haven’t been included. It should be noted that a typical 2-3 Euros /kW are considered for the increase of kW when moving from a smaller to a larger engine which is a typical value subject to negotiation during the discussion of the Shipbuilding contract and Specification. The user also has the option of selecting the following:

1. Main Engine Tuning Strategy
Selection between Part or Low Load Optimization
2. Tier III Compliance Technology:
Selection between High-Pressure Selective Catalytic Reaction (SCR), Low-Pressure SCR and Exhaust Gas Recirculation (EGR).
All engines within the engine selection library are Tier III compliant in accordance with the MARPOL Annex VI, Regulation 13 as amended by the IMO MEPC 66 requirement (International Maritime Organization (IMO), 2014)for ships built after the 1st of January 2016.
3. Dual Fuel Engine Application.
The equivalent ME-GI engines for methane (LNG) consumption have also been included in the database.

The Input for the Main Engine Selection Module is also illustrated in Table 20 and Figure 31.

Engine Type	ME-C or ME-GI
Required Power	Just input, separately calculated with a Goal-Based Approach
Required RPM	Propeller Design RPM from Propeller Selection Module
Sea Margin	User’s choice for sea margin application <i>(not used in goal-based approach)</i>

Propeller Margin	User's choice. Recommended value of 5-10% (MAN, 2015)
Derating Margin	User's choice. For optimization studies considered at the range of 0-5%.
Engine Tuning	Part Load Optimization / Low Load Optimization
Tier III Compliance Method	EGR/HPSCR/LPSCR/ecoEGR

Table 20: Inputs of Main Engine Selection Module

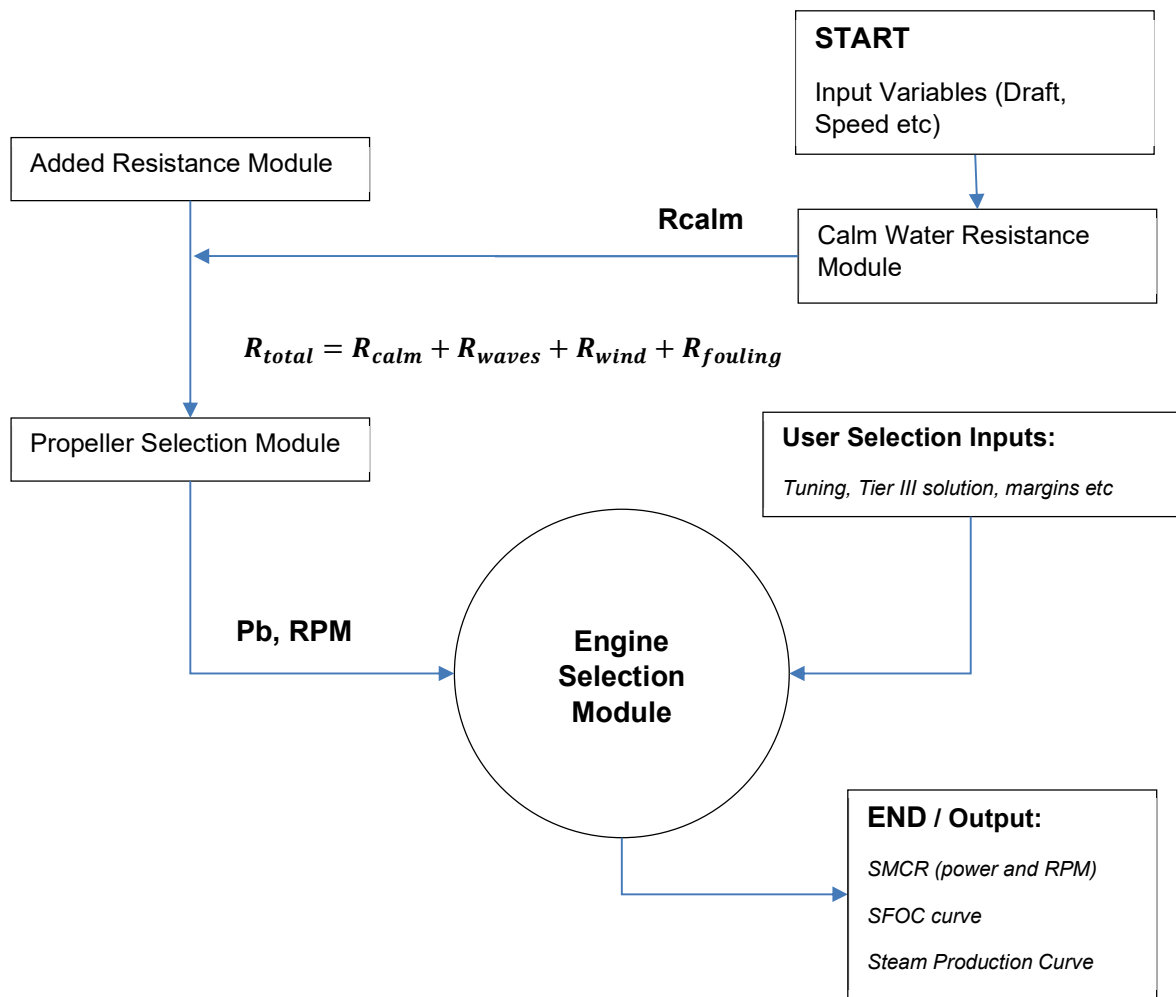


Figure 31: Flowchart of Engine Selection Procedure

An important point and functionality for the Engine Selection Module is the innovative way of matching and sizing the Engine. So far the matching and sizing of the engine were based on two imposed margins: A Sea Margin of 15% on the delivered power corresponding to the design speed for the scantling draft and the use of an RPM margin (light-running margin) for the RPM-power curve (propeller curve) of usually 3%. This is typically depicted in the majority of modern vessel Shipbuilding Specifications.

However, the application of simply two margins is not considered adequate, especially given the power and speed reductions that have been triggered by the IMO MEPC, as well as the inevitable design speed reductions undertaken by all major shipbuilders to attain allowable Energy Efficiency Design Index (EEDI) values. On the other hand, IMO also introduced the Minimum Propulsion Power Requirement in MEPC.232(65) (International Maritime Organization (IMO), 2013) aiming at eliminating under-powered vessels, the effects and efficiency of which are comparatively assessed with added resistance calculations in the case studies and application chapter.

Given the issues highlighted above, a goal-based approach without the use of margins is used here instead. The dimensioning strategy determines a limit state condition in which the vessel at any given moment when in service should be able to maintain the full design speed. The DHP corresponding to this limit state condition is the Specified Maximum Continuous Rating (SMCR) of the Main Engine of the design. The limit state condition is subject to the user's preference, as it is parametric and determined in the Engine Selection Module. A proposed limit state used herein is as per below:

1. Sea State 5 at head and beam seas (whichever is greater).
2. The adverse (head) current of 1.5 knots.
3. Roughness increases due to fouling corresponding to 4 years without cleaning (approximately 420 microns from the baseline of 150 microns as per ITTC recommendations).
4. Wind Corresponding to Sea State 5.

In addition to the above the following two margins for deriving with the final SMCR (Delivered power and revolutions):

1. RPM light running margin of 10% for the propeller curve, in compliance with MAN B&W recommendations (MAN, 2015).
2. An additional power margin of 5% is for derating the Main Engine to attain a better SFOC curve. This margin should not be confused with the 10% distance from the L1L3 line which is an internal constraint of the Engine Selection Module.

In addition to SFOC curves, curves of steam production from 20% to 100% are produced. These are used in turn as steam production curves in the operation simulation, to assess the potential load (if required) of the composite boiler to match the steam consumption requirements.

Diesel Generators

5.3. Lifecycle Voyages Simulation Environment

This module is an integrated code within the methodology that simulates the actual operating conditions of the vessel for its entire lifecycle

5.3.1. Voyage Definition

For the herein presented methodology, a Voyage is defined as the transit of a vessel under examination from an (Origin) Port to another (Destination) Port including any intermediate stoppages (e.g Singapore stoppages bunkering) and considering the time required for preparation for receipt of cargo (hold/tank cleaning operations). For reasons of methodology completeness over the entire lifecycle of the vessel, the operation of cargo loading and cargo discharging are considered as separate events but naturally included in the simulation module with modelling being focused on capturing the vessel responses and sensitivities of the electrical load , ballast pump and , if applicable, boilers (cargo handling plant).

Given the above definition of Voyage, the primary characterization of the latter is the loading condition of the vessel between the Origin and Destination and more specifically if the vessel is loaded with cargo (Laden Condition) or empty with ballast in the segregated respective tanks to maintain the required stability and propeller immersion requirements (Ballast Condition).

5.3.2. Use of Big Data for Voyage Simulation

One of the novel aspects of this methodology has been the use of big data and the statistical analysis of the latter with the IBM SPSS® toolkit for the creation of linear and non-linear regression formulas as well as probability distribution functions and descriptive statistical studies. The Big Data that are herein discussed are considered onboard real-time measurements for a fleet of vessels for key parameters including but not limited to Engine Room signals, Navigation Station signals etc. Big Data in the present study and methodology are also considered the market data as discussed in paragraph 3.3.6.

The onboard data are being collected from the data acquisition system, “Vessel Performance Monitoring System (VPMS)”. The Author has been a member of the team that has coordinated, planned and executed the configuration, installation and implementation of this system. The VPMS system collects and logs real-time data recorded on a 30-second basis. The 30-second recording entries are automatically averaged into 5-minute bundles that are accessible and transmitted 3 times per day ashore. The system signal processing flow chart can be seen in Figure 32. An indicative list of the tags that are being recorded is found in Table 21.

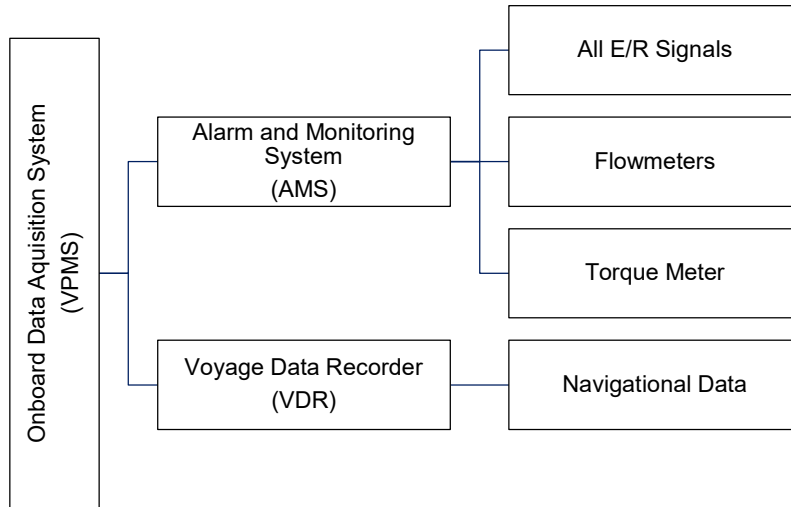


Figure 32: Process flow of the data acquisition system

Engine Room		Navigation Data
M/E RPM	M/E Shaft Power (torque meter)	Rudder Angle Indicator
M/E Rev. Counter	Cooling Water Temperature (inlet)	Rudder Rate of Turn
No.1 T/C RPM	Cooling Water Temperature (outlet)	Longitude Coordinates
No.2 T/C RPM	M/E and G/E FO Flow Inlet – Counter	Latitude Coordinates
Fuel Pump Index	G/E FO Flow Inlet – Counter	Speed Over Ground (GPS – SoG)
M/E RPM (torque meter)	G/E FO Flow Outlet – Counter	Heading (Gyro)
M/E Torque	FO Viscosity – M/E	Wind Direction (Anemometer)
FO Viscosity – G/E	FO Temperature – G/E Outlet	Wind Speed
FO Temperature – M/E Inlet	FO Service Tanks Temperature	Speed Through Water
FO Temperature – G/E Inlet	FO Settling Tanks Temperature	Speed Transverse Through Water
M/E Cylinder Exhaust Gas Temperatures	M/E Exhaust Gas Temperature – Before T/Cs	Water Depth
M/E Exhaust Gas Temperature – After T/Cs	Engine Room Temperature	Significant Wave Height - Wind (Weather Service)
M/E Scavenge Air Pressure	M/E Scavenge Air Temperature	Significant Wave Height – Swell (Weather Service)
Air Coolers Inlet and Outlet Air Temperature	No.1 G/E Power	Wind Wave Direction (Weather Service)
No.2 G/E Power	No.3 G/E Power	Swell Wave Direction (Weather Service)
M/E Thrust Pad, Stern Tube Bearing, Intermediate Bearing Temperatures		Ocean Current Velocity (Weather Service)
		Ocean Current Direction (Weather Service)
		Wind Velocity (Weather Service)
		Wind Direction (Weather Service)

Table 21: Summary of collected signals used for database generation.

It should be noted that weather information has been also extracted from a weather service provider at a later stage of the methodology developed in late 2019. The Data are satellite weather hindcast matched with the timestamp and coordinates of each line to include all the necessary information for the prevailing wave, wind and current conditions. The use of the weather data matched is further discussed and elaborated in Chapter 5.3.4 and 5.3.7 where a voyage is replicated based on these data to validate and test the simulation code in dynamic conditions. The VPMS system data have been extracted for a fleet of 5 Capesize and Newcastlemax bulk carriers operating at both the Brazil and Australia trade routes for a period of approximately 36 months. The data pool that has been collected is comprised of no less than 320,000 lines per vessel with an equal number of data points, corresponding a data pool of a total of 1.37GB size and 1,5 million recordings. All of the data has been handled through Microsoft Excel® spreadsheets for splitting into ballast and laden conditions respectively, filtering out erroneous readings as well as matching to sailing conditions (at sea, manoeuvring, discharging, at the port, loading, at anchor) and afterwards exported to the IBM SPSS® toolkit for statistical analysis. The procedure followed for the filtering of the erroneous data is similar to the one followed in the ISO19030 for performance and speed drop analysis (International Organization for Standardization (ISO), 2016) with the procedure depicted in Figure 33.

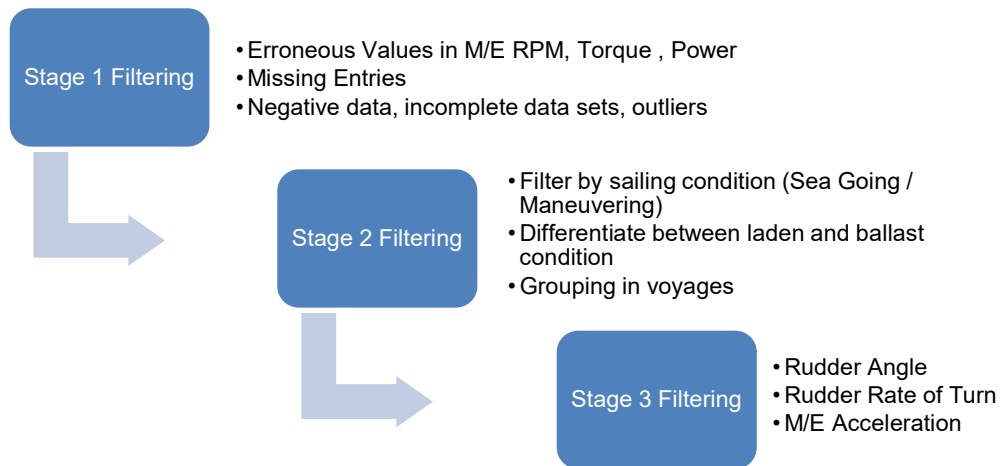


Figure 33: Filtering process for creating data pool

5.3.3. Input Data

For each one of the legs (given distance in nautical miles) the average speed and added resistance curves are input as well as the loading of the generators, the manoeuvring time. If the leg includes a discharging, loading or bunkering port the port stay in hours is also used. Based on this profile the voyage time, emissions, the energy required, associated costs together with the fuel costs are calculated on a much more accurate and realistic basis. Further details on input data are found in Table 22.

Operational Simulation Input Parameters	
General	
ISO corrected SFOC Curve	Speed Power Curve - Calm Water
Auxiliary Engines Power (kW)	SFOC curve for auxiliary Engines
Auxiliary Engine Load during Cargo Hold Cleaning (%)	Time for Cargo Hold Cleaning (hours)
Main Engine SMCR (kW)	Main Engine Load in Manoeuvring (%)
Cylinder Oil Feed Rate (normalized average) (gr/kWh)	Electrical Power Required during Normal Sea Going (kW)
Blowers Electrical Power (kW)	Required Electrical Power during Manoeuvring (kW)
Main Engine SFOC during Manoeuvring (gr/kWh)	Sulphur Content in Fuel (%)
Main Dimensions	
Length Overall (m)	Length Between Perpendiculars (m)
Breadth (m)	Voyage Draft (m)
Wind Profile	
Total Lateral Projected Area (m ²)	Total Transverse Projected Area (m ²)
Lateral Projected Area of Superstructures above deck (m ²)	Fujiwara Hc (m)
Height of Superstructures (m)	
Added Resistance	
Wave Length Probability Distribution Function Curve	Entrance Angle Length (m)
Roughness Increase due to fouling (microns/year)	
Propulsion	
Thrust Deduction Curve	Wake Fraction Curve
Propeller Diameter (m)	Expanded Area Ratio (m ²)
Number of Blades	Pitch over Diameter Ratio
Propeller Shaft Mechanical Efficiency	Relative Rotative Efficiency
Speed – RPM Curve	
Loading/Discharging Port	
Electrical Loads during Loading (kW)	Time in Loading/Discharging Port (hours)
Time for manoeuvring (hours)	
Sea Passage Leg	
Distance (nautical miles)	Average Transit Speed (knots)
Probability of Head Current	Probability of Astern Current
Low Current Velocity (knots)	Mid Current Velocity (knots)
High Current Velocity (knots)	
Sea Passage Leg – Singapore (additional)	
Manoeuvring Time (hours)	Electrical Load in Port (kW)

Port Stay for Bunkering (hours)	
---------------------------------	--

Table 22: Input Parameters of Seaways Simulation Module

5.3.4. Environmental Parameters Modelling

The most important input for the simulation module apart from the vessel’s characteristics is the modelling of the environmental parameters the candidate vessels will be exposed to when transiting the simulated voyages. The environmental conditions and weather effects are considered in the following three categories:

1. Sea Waves (wind origin) and Swell.
2. Wind
3. Currents

To model the environmental parameters a statistical approach has been followed depending on each parameter. The data populated that

5.3.4.1. Modelling of Wind Conditions

The modelling of the sea winds has been done in two stages depending on the availability of data throughout the code development. More specifically, at the first stage and until 2019, the onboard data acquired from the vessel’s anemometer have been gathered and statistically edited (Figure 34 , Figure 35). In the second stage and after 2020, the matched data from weather providers have been also used. For the sake of clarity and validation, the data from the anemometer for a specific voyage have been compared and correlated with the ones provided by the weather provider. Interestingly, there is a relatively wide scatter, however, their correlation is clearly linear. In case the data were to be used for applying corrections and comparing to a baseline, that would create a challenge. However, for their application in the simulation within the ship design scope of work this scatter has a smaller effect. The reason for this is that the point of concern for such an application is the generation of a (reliable) Probability Distribution Function. Within this scope, the two generated PDFs will be very similar since their cumulative probability, as well as the probability of occurrence, is almost identical due to their strongly linear correlation.

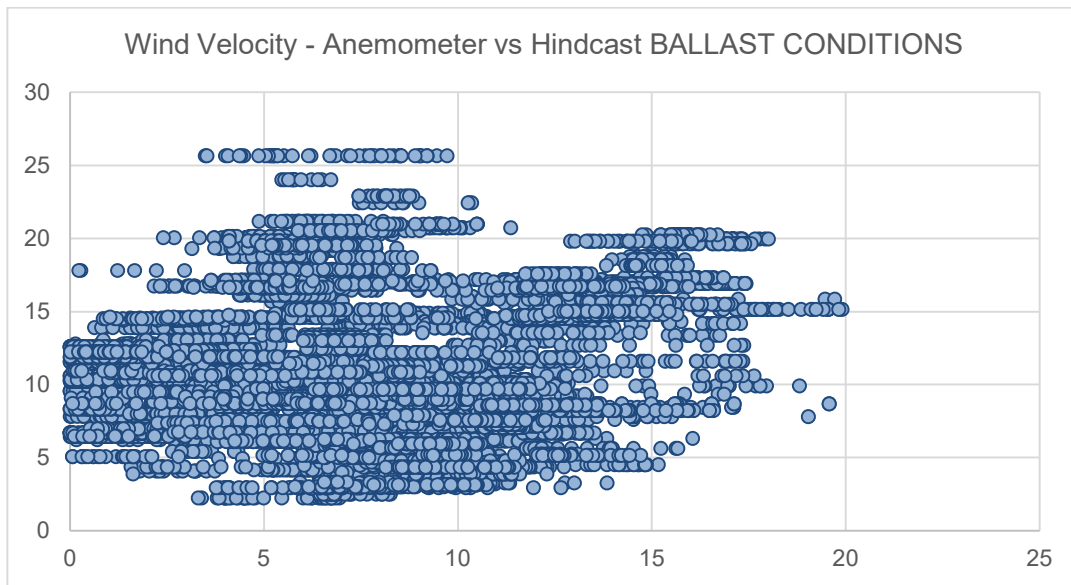


Figure 34: Correlation between Anemometer Readings and Matched Weather Data – BALLAST

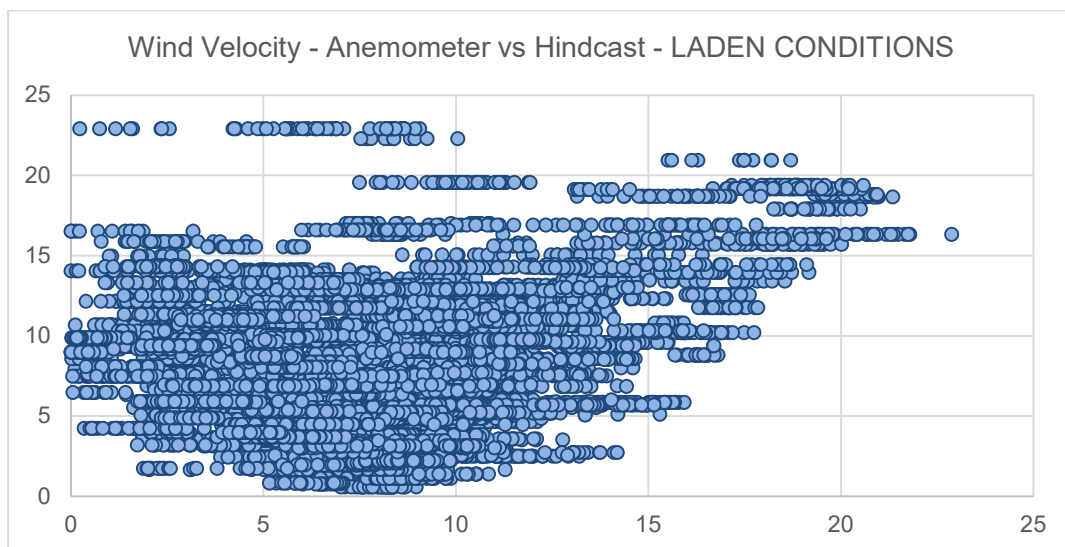


Figure 35: Correlation between Anemometer Readings and Matched Weather Data – LADEN

Furthermore, it should be added, that the matched data from weather providers are only applicable to the Australia to China route and not the Brazil route, so only the first has been updated accordingly.

Based on the anemometer readings, the data have been extracted for all routes and inserted in the IBM SPSS® toolkit. After running descriptive statistics and doing normality checks, the simulation module of SPSS was used to derive the probability distribution functions, for the wind velocity and wind direction. The results of the fitted PDF for the onboard data measurements can be seen in Table 23 with regards to wind direction and velocity and for the case of matched satellite data in Table 24 respectively. The histograms of the original/raw data as well as that of the simulated data are depicted in Figure 36 , Figure 37 , Figure 38 , Figure 39 for wind velocity and wind direction acquired from onboard measurements. From the other hand, Figure 40 to Figure 47 depict the histograms of the raw and simulated data for wind velocity and wind direction acquired for matched satellite weather data.

Variable	Probability Distribution Function
Wind Velocity <i>Mean:</i> 14.8238 <i>StDev:</i> 7.26268	Gamma Distribution Shape: 4.277 Scale: 0.289
Wind Direction <i>Mean:</i> 172.0549 <i>StDev:</i> 72.24666	Normal Distribution Mean: 170.461 Standard Deviation: 77.537

Table 23: Fitted Probability Distribution Functions for onboard data - Wind

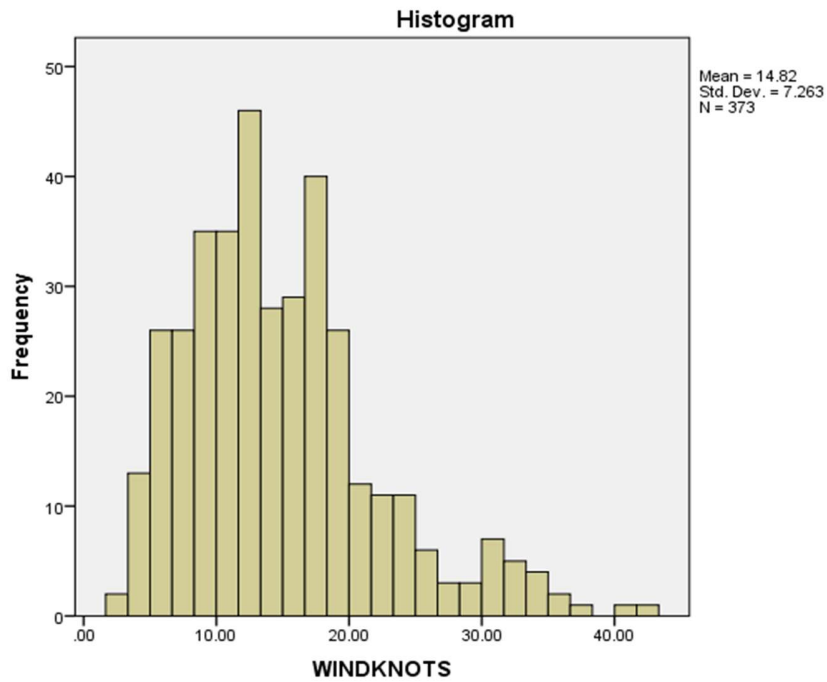


Figure 36: Histogram of the populated values for Wind Velocity – onboard data

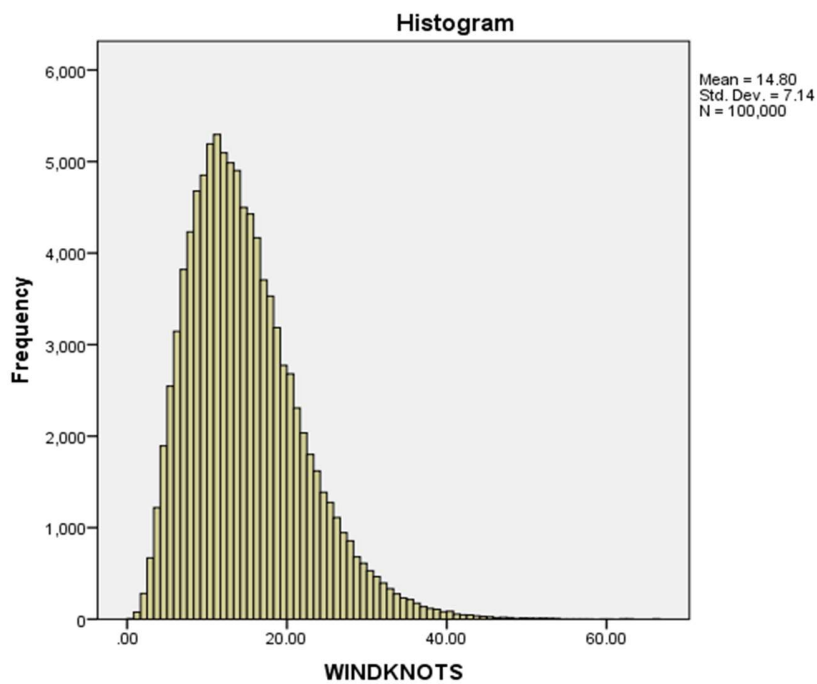


Figure 37: Histogram of Gamma PDF simulated data for Wind Velocity -onboard data

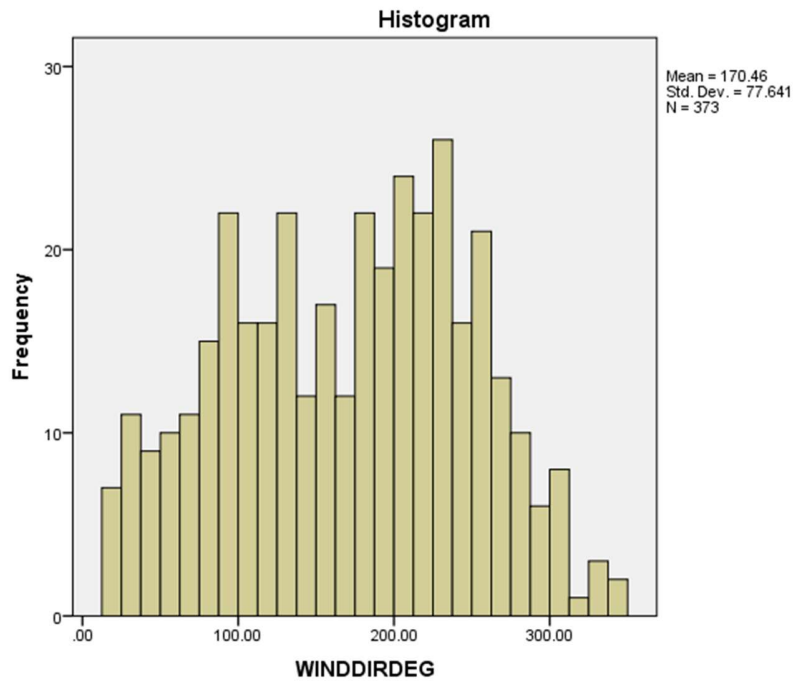


Figure 38: Histogram of the populated values for Wind Direction – onboard data

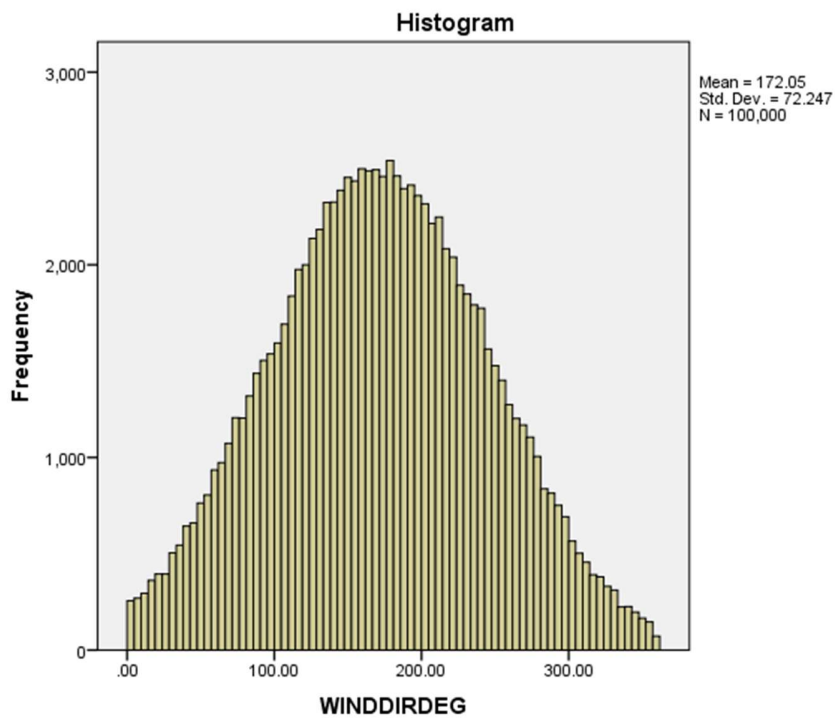


Figure 39: Histogram of Normal PDF simulated data for Wind Direction – onboard data

Variable	Probability Distribution Function
Wind Velocity – Laden Voyage <i>Mean: 4.463</i> <i>StDev: 2.182</i>	Weibull Distribution α : 5.037 β : 2.152 γ : 0.000
Wind Direction – Laden Voyage <i>Mean: 43.957</i> <i>StDev: 36.533</i>	Exponential Distribution Scale Parameter: 0.023
Wind Velocity – Ballast Voyage <i>Mean: 5.212</i> <i>StDev: 2.305</i>	Lognormal Distribution a: 4.697 b: 0.471
Wind Direction – Ballast Voyage <i>Mean: 42.569</i> <i>StDev: 42.014</i>	Exponential Distribution Scale Parameter: 0.023

Table 24: Fitted Probability Distribution Functions for matched satellite weather data

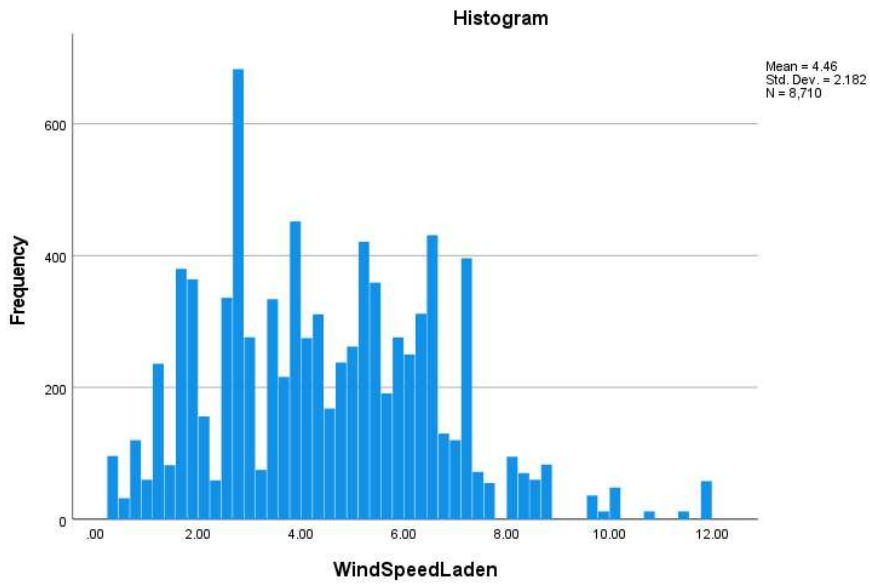


Figure 40: Histogram of the populated values for Wind Velocity LADEN – matched satellite data

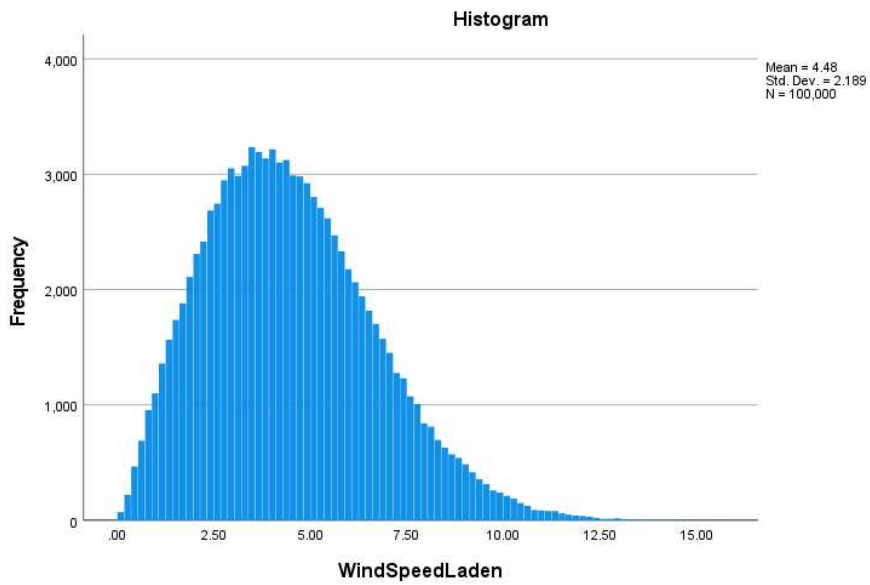


Figure 41: Histogram of Normal PDF simulated data for Wind Velocity LADEN – matched satellite data

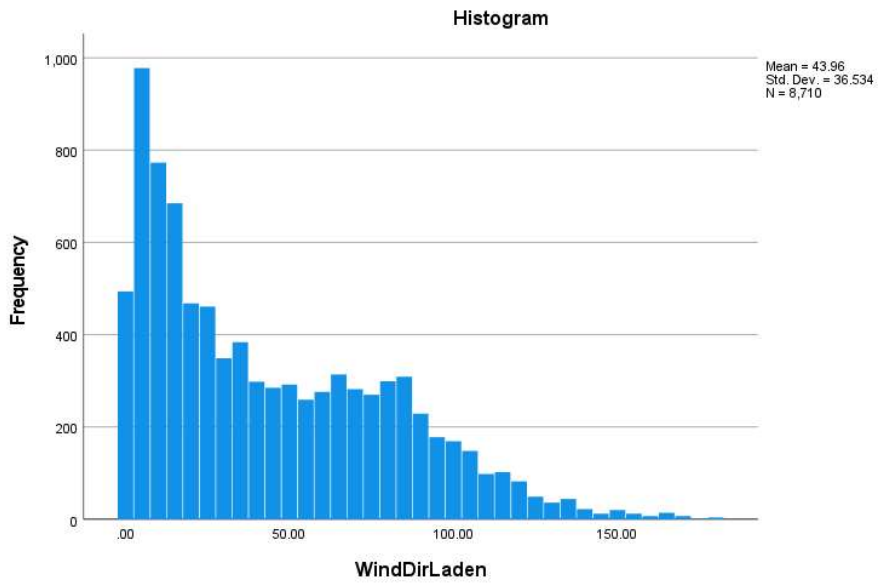


Figure 42: Histogram of the populated values for Wind Direction LADEN– matched satellite data

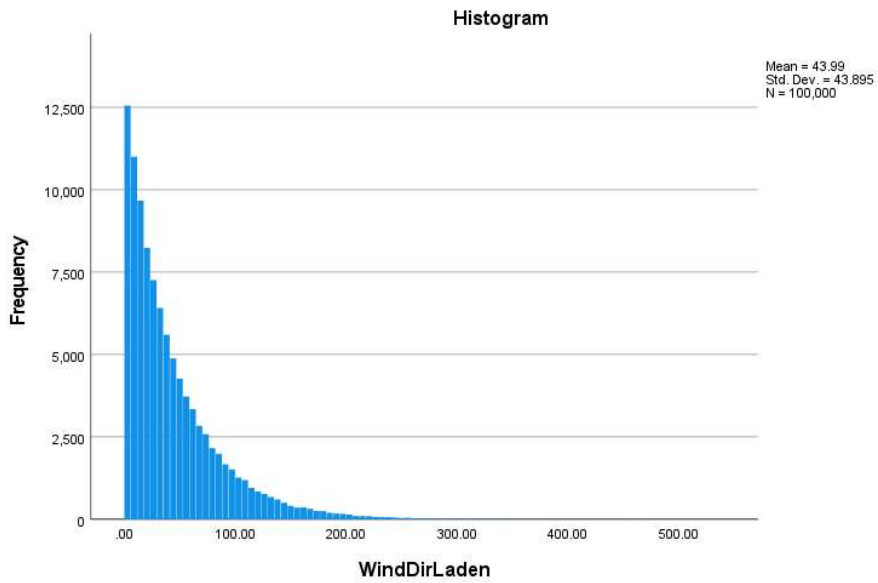


Figure 43: Histogram of Exponential PDF simulated data for Wind Direction LADEN – matched satellite data

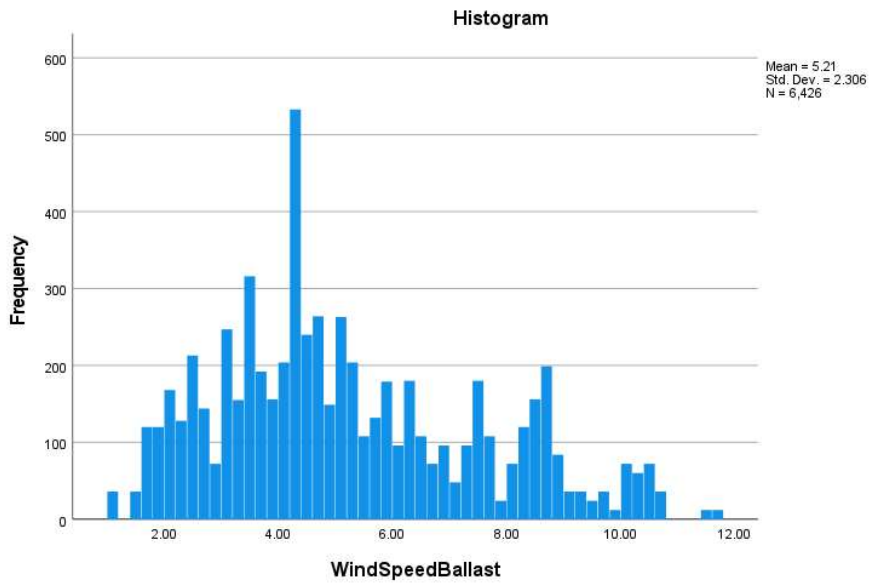


Figure 44: Histogram of the populated values for Wind Velocity BALLAST – matched satellite data

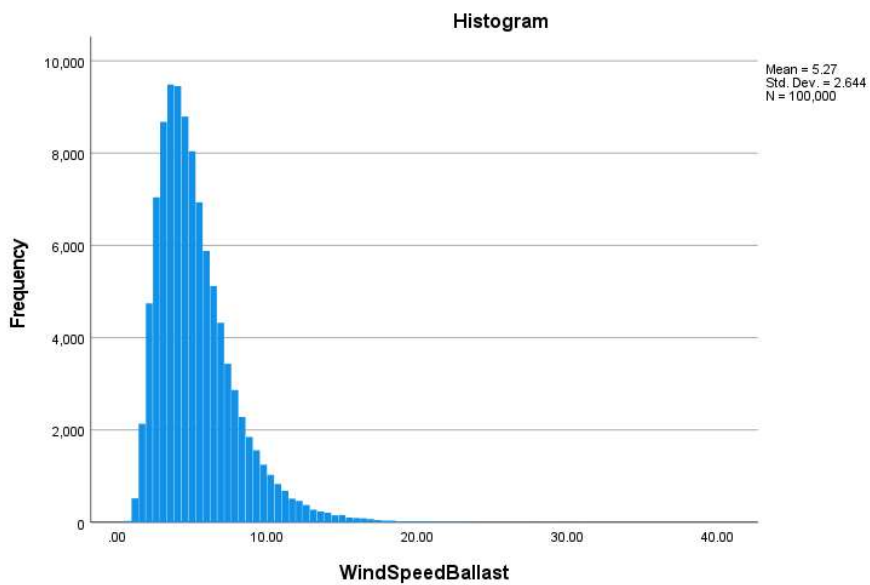


Figure 45: Histogram of Lognormal PDF simulated data for Wind Velocity BALLAST – matched satellite data

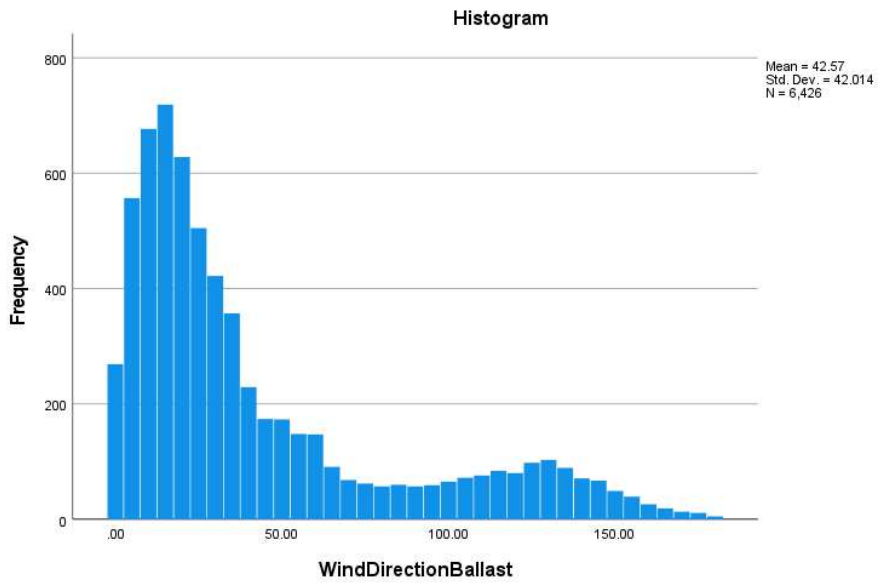


Figure 46: Histogram of the populated values for Wind Direction BALLAST – matched satellite data

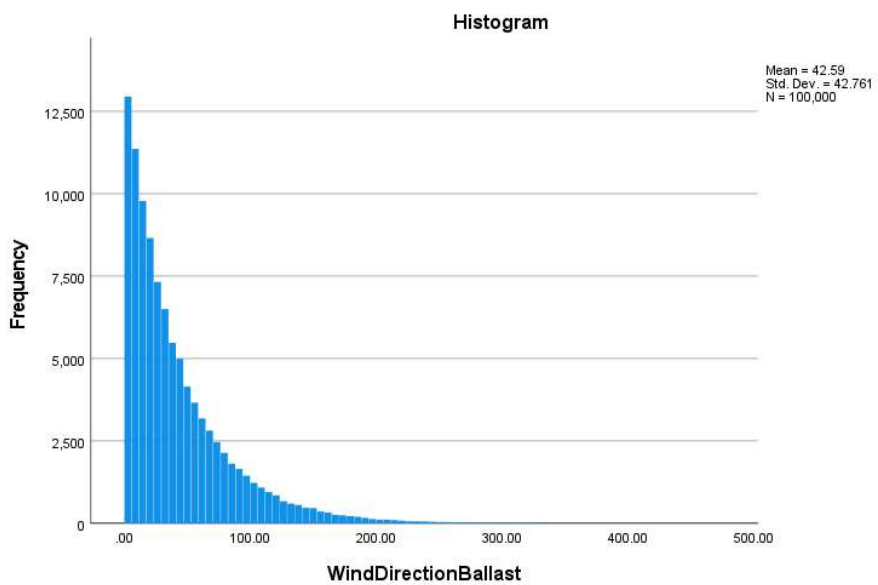


Figure 47: Histogram of Exponential PDF simulated data for Wind Direction BALLAST – matched satellite data

5.3.4.2. Modelling of Sea Currents

The sea currents have been modelled in the methodology using the same approach as the one previously described for the wind. The information for current velocity was available from noon reports (standardized report transmitted at 1200 Local Time each noon by a vessel) based on crew’s daily observations. As currents are localized and dynamic phenomena heavily correlated to the vessel’s heading, the dataset has been split into Laden and Ballast conditions for each of the trade routes. In a second stage, hindcast satellite data matched to the coordinates and timestamp were available by a weather provider. These data however were only available for the Australia trade route, thus only the latter was changed.

For both cases, the data have been processed in the IBM SPSS® first with descriptive statistics and normality checks on the populated data and then best fitting a PDF and simulating data using this input PDF. The results of the fitted PDFs for each case can be seen in Table 25 for crew observations data and Table 26 for matched satellite data respectively. The current velocity and direction histograms of the populated and simulated data can be identified from Figure 48 to Figure 57 for crew observations data and from Figure 58 to Figure 65 for matched satellite data respectively.

Variable	Probability Distribution Function
Current Velocity LADEN - Brazil <i>Mean:</i> 0.67 <i>StDev:</i> 1.606	Exponential Scale: 1.484
Current Velocity LADEN - Australia <i>Mean:</i> 0.67 <i>StDev:</i> 0.467	Normal Mean: 0.674 Standard Deviation: 0.465
Current Velocity BALLAST - Brazil <i>Mean:</i> 0.65 <i>StDev:</i> 2.114	Exponential Scale: 1.532
Current Velocity BALLAST - Australia <i>Mean:</i> 0.8987 <i>StDev:</i> 3.84136	Exponential Scale: 1.113
Current Direction <i>Mean:</i> 156.1678 <i>StDev:</i> 106.8679	Uniform Minimum: 0 Maximum 337.50

Table 25: Fitted Probability Distribution Functions for crew observations - Currents

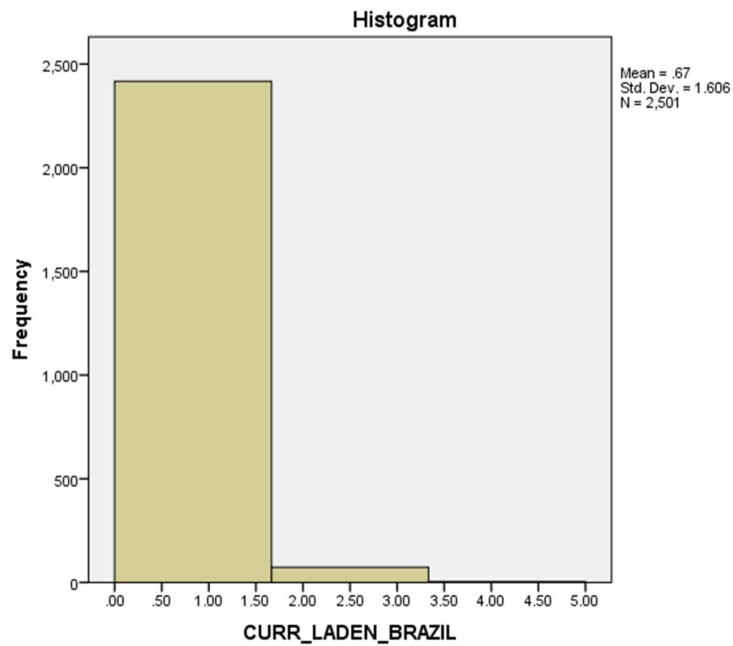


Figure 48: Histogram of the populated values for Current Velocity LADEN – Brazil Onboard data

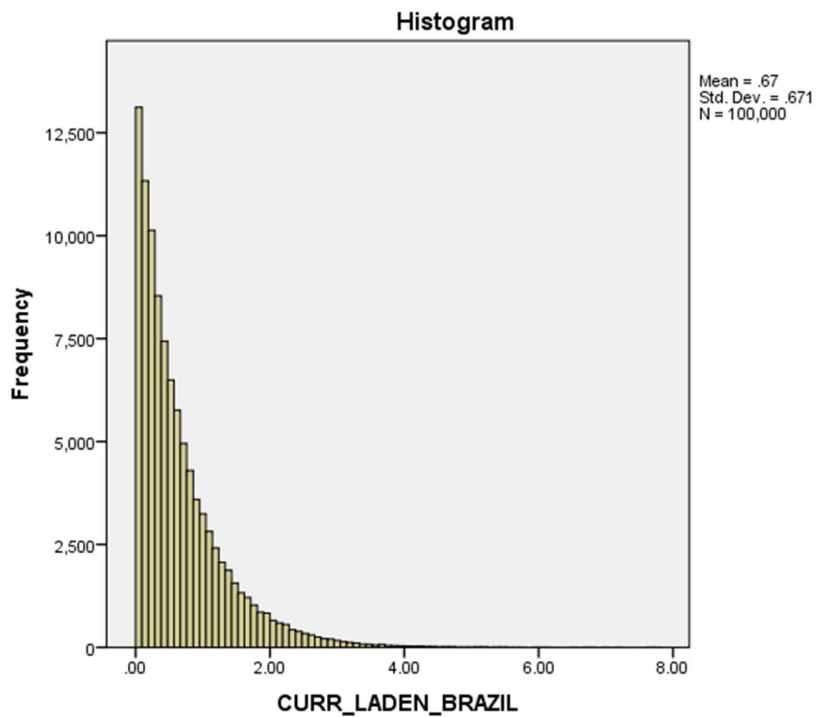


Figure 49: Histogram of Exponential PDF simulated data for Current Velocity LADEN -Brazil onboard data

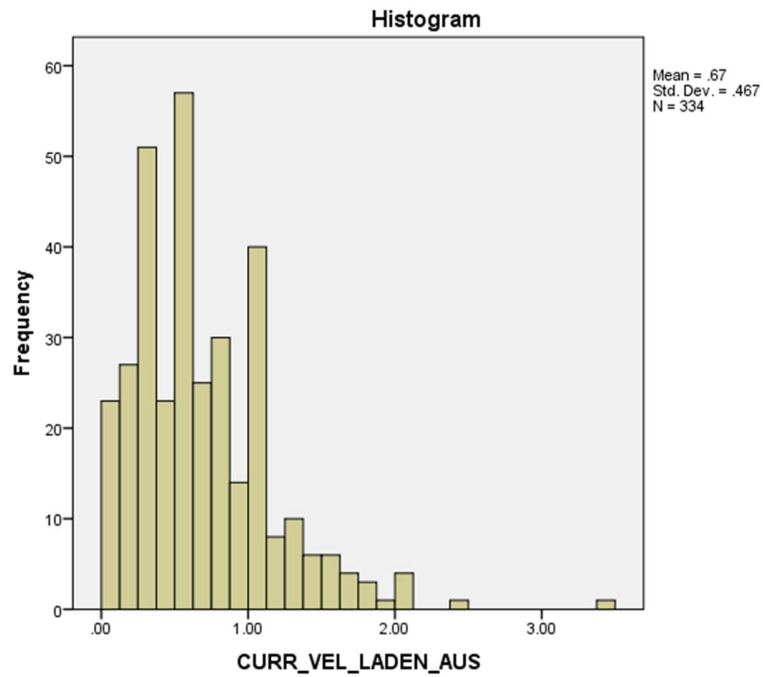


Figure 50: Histogram of the populated values for Current Velocity LADEN – Australia Onboard data

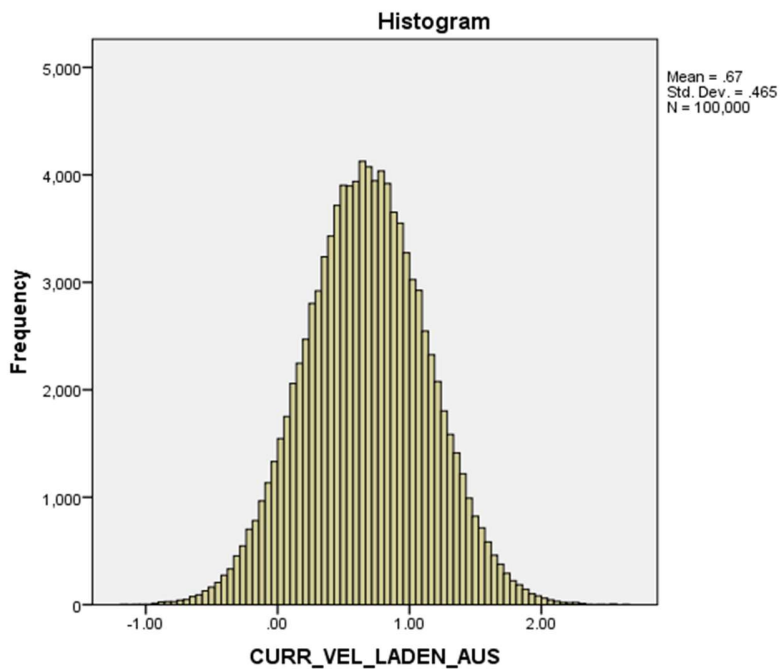


Figure 51: Histogram of Normal PDF simulated data for Current Velocity LADEN -Australia onboard data

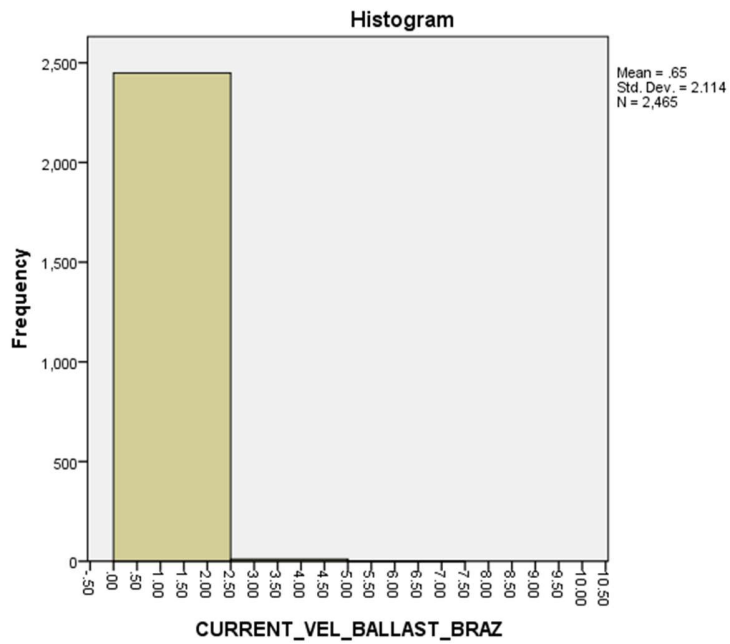


Figure 52: Histogram of the populated values for Current Velocity BALLAST – Brazil Onboard data

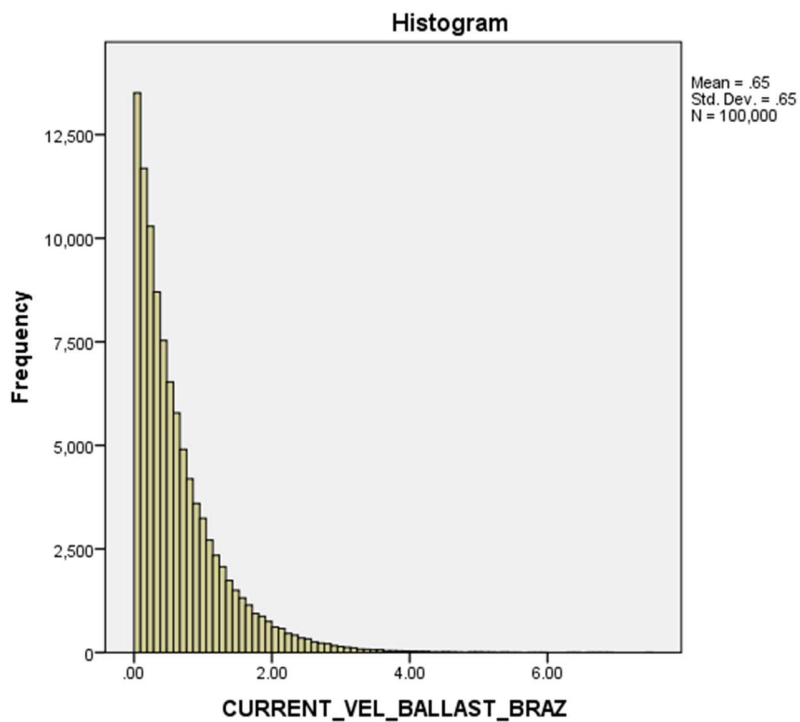


Figure 53: Histogram of Exponential PDF simulated data for Current Velocity BALLAST -Brazil onboard data

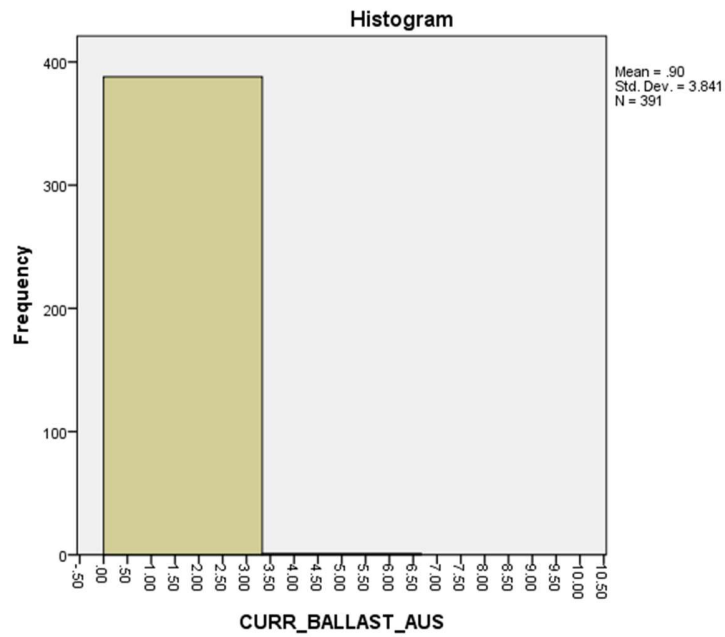


Figure 54: Histogram of the populated values for Current Velocity BALLAST – Australia Onboard data

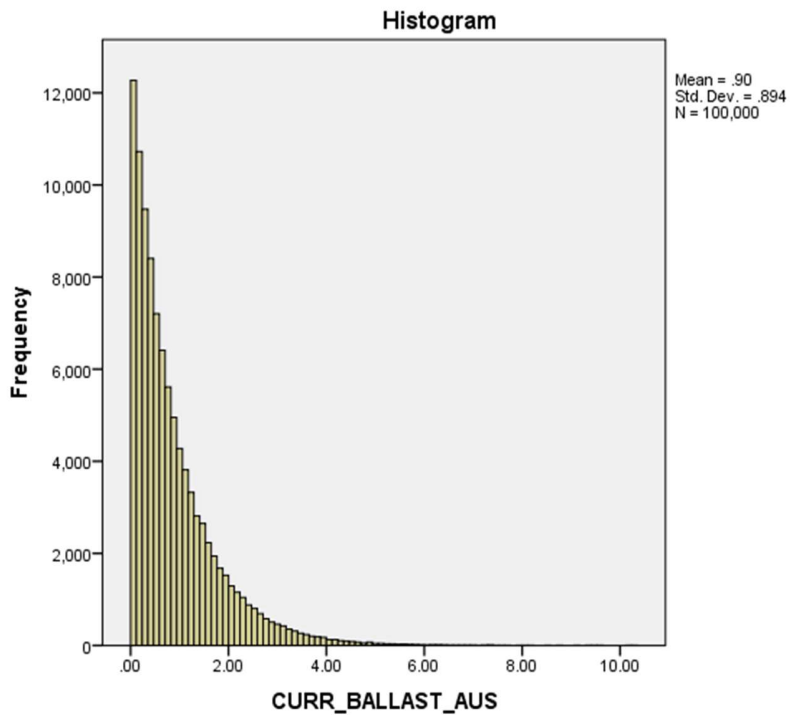


Figure 55: Histogram of Exponential PDF simulated data for Current Velocity BALLAST -Australia onboard data

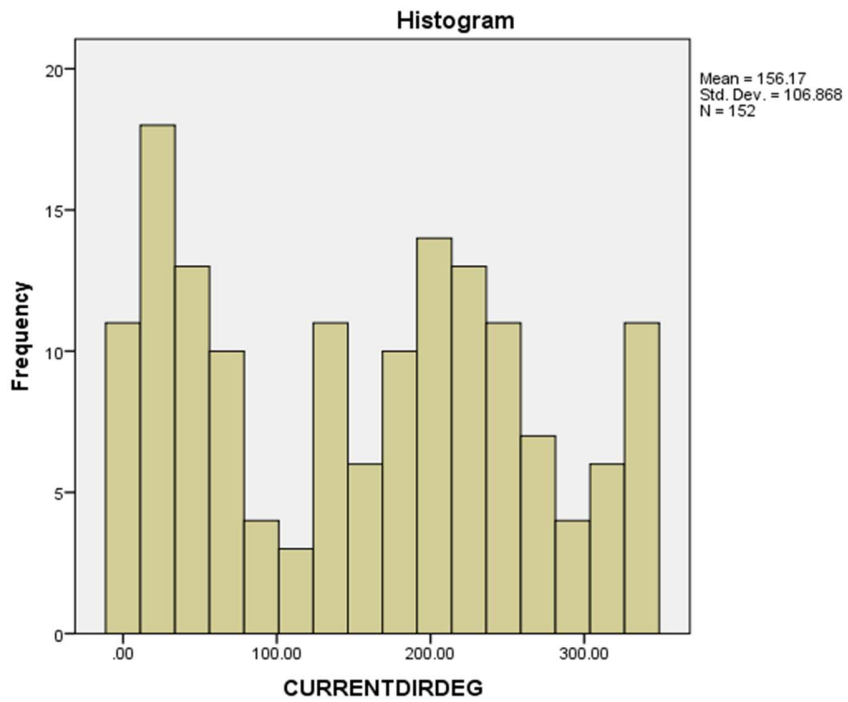


Figure 56: Histogram of the populated values for Current Direction – onboard data

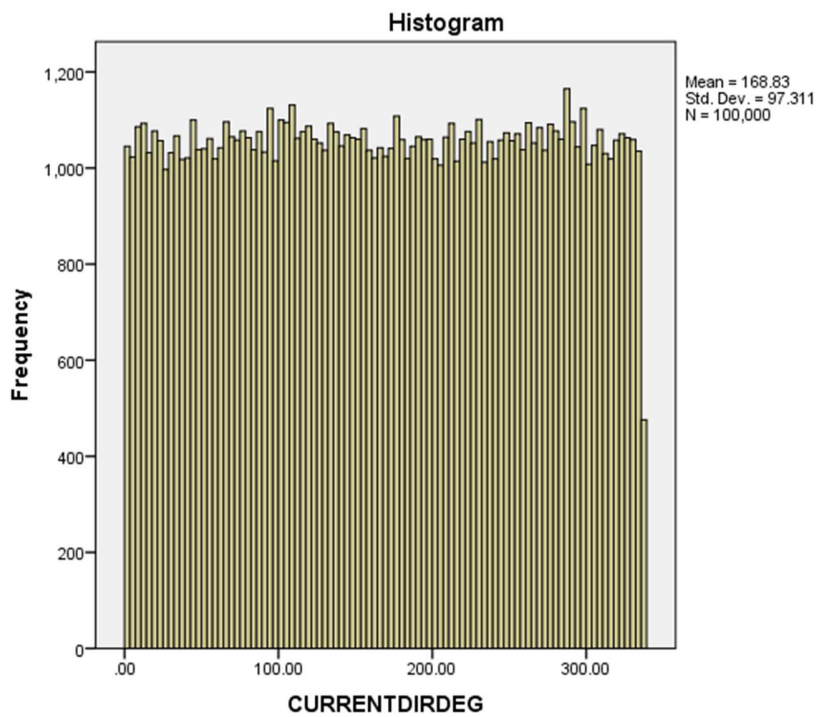


Figure 57: Histogram of Uniform PDF simulated data for Current Direction – onboard data

Variable	Probability Distribution Function
Current Velocity – Laden Voyages <i>Mean: 0.441</i> <i>StDev: 0.431</i>	Exponential Distribution Scale: 2.268
Current Direction – Laden Voyages <i>Mean: 0.691</i> <i>StDev: 9.426</i>	Normal Distribution Mean: 183.461 StDev: 95.815
Current Velocity – Ballast Voyages <i>Mean: 0.543</i> <i>StDev: 0.437</i>	Lognormal Distribution a: 0.402 b: 0.819
Current Direction – Ballast Voyages <i>Mean: 0.439</i> <i>StDev: 6.826</i>	Normal Distribution Mean: 195.128 Standard Deviation: 96.570

Table 26: Fitted Probability Distribution Functions for matched satellite data- Currents

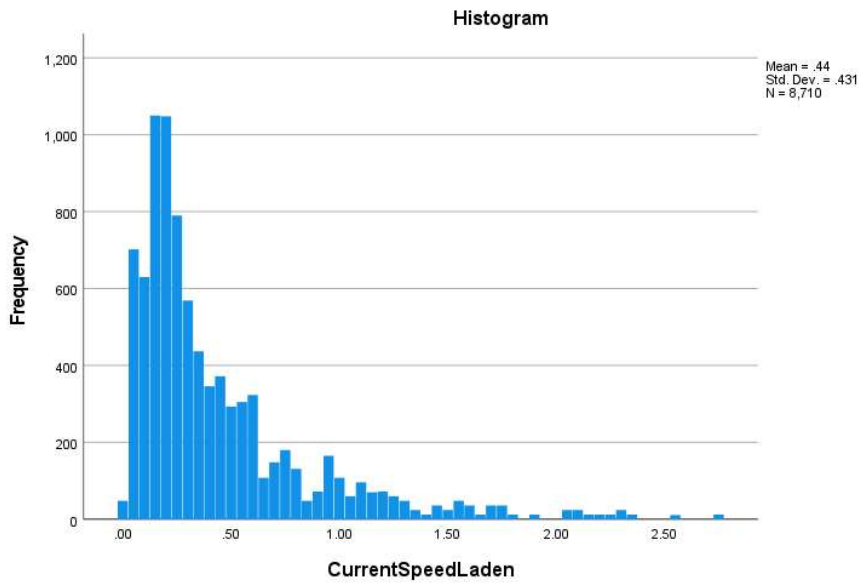


Figure 58: Histogram of the populated values for Current Velocity LADEN – matched satellite data

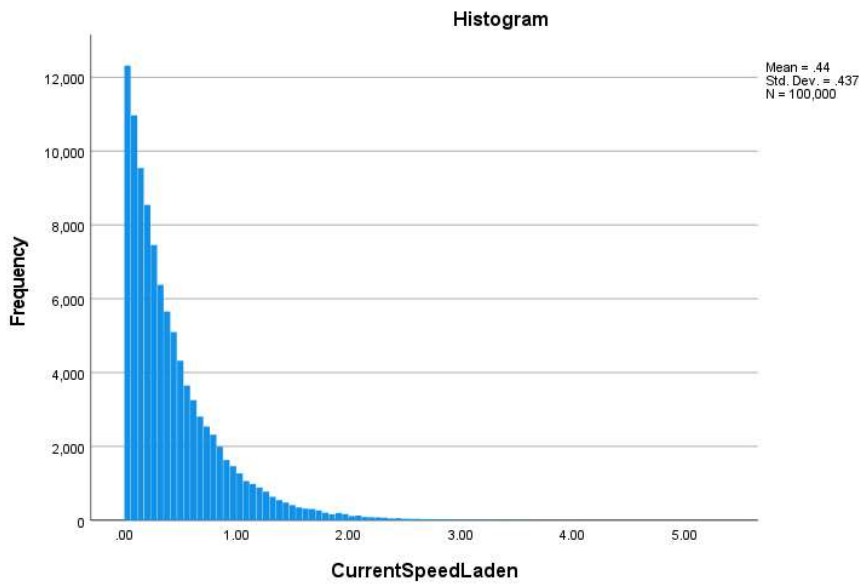


Figure 59: Histogram of Exponential PDF simulated data for Current Velocity LADEN – matched satellite data

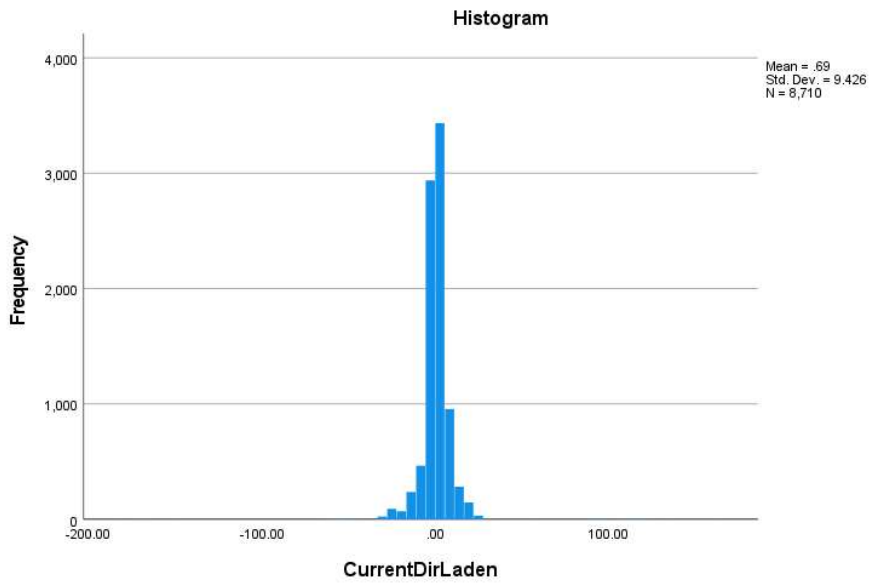


Figure 60: Histogram of populated values for Current Direction LADEN – matched satellite data

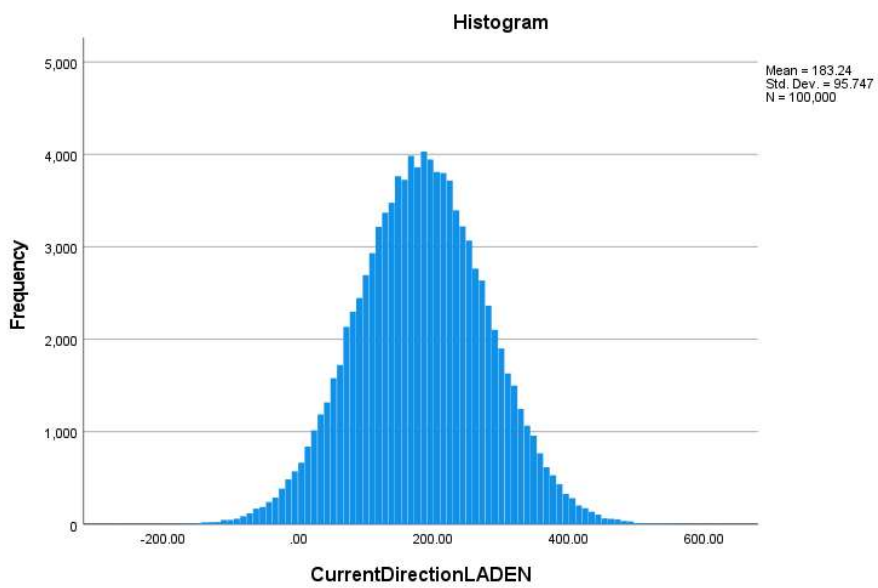


Figure 61: Histogram of Normal PDF simulated data for Current Direction LADEN – matched satellite data

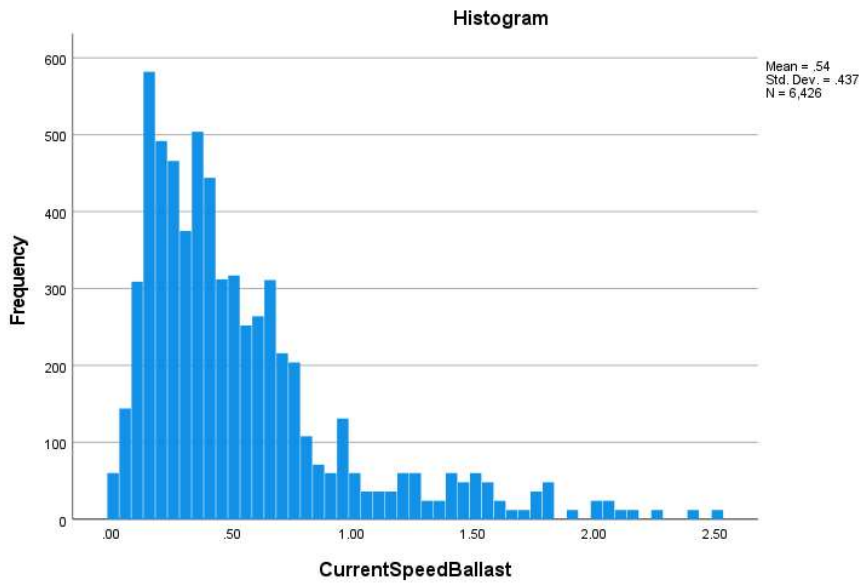


Figure 62: Histogram of the populated values for Current Velocity BALLAST – matched satellite data

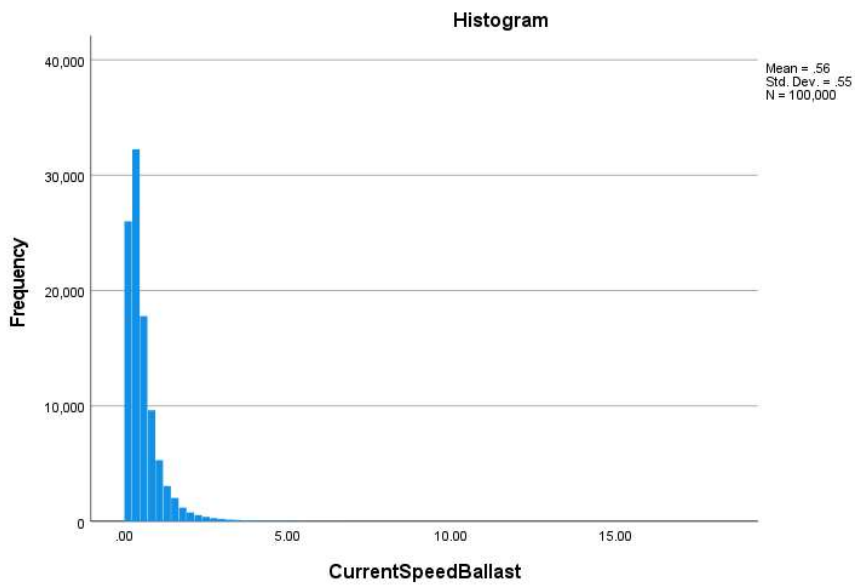


Figure 63: Histogram of Lognormal PDF simulated data for Current Velocity BALLAST – matched satellite data

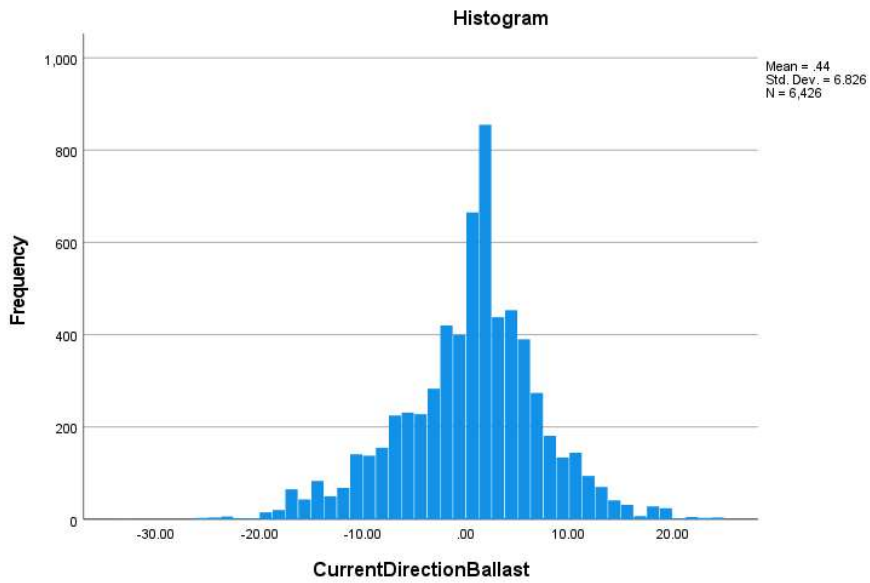


Figure 64: Histogram of the populated values for Current Direction BALLAST – matched satellite data

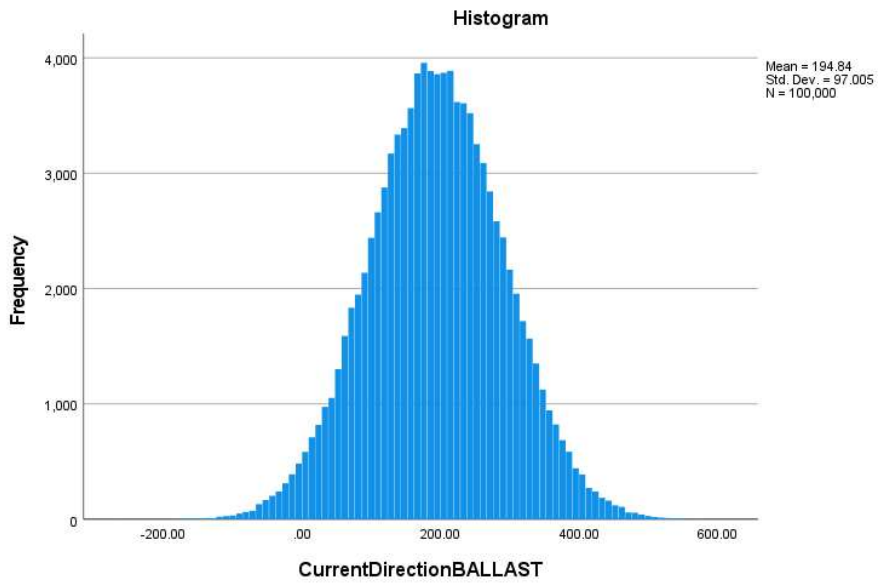


Figure 65: Histogram of Normal PDF simulated data for Current Direction BALLAST – matched satellite data

5.3.4.3. Modelling of Sea Waves

In a similar fashion to winds and currents, sea waves have been modelled with two different approaches: the one was as a product of onboard data and the second was with the use of long term wave statistics and matched weather data (depending on the application), both of them on a comparative basis.

A. Modelling from Available Onboard Data

The available onboard data were minimal, restricted to crew observations logged in noon reports which have been matched with the onboard data acquired basis on their timestamp. In order to have a more accurate and dynamic representation at the first stage of the development of the methodology, swell waves were omitted from our considerations focusing on wind waves. Afterwards, the observations have been matched with the wind velocity and wind direction data acquired from the anemometer. Since only wind-generated waves were assumed at this stage, the wave direction was assumed to be the same as the wind direction. The correlation of the wave height with the wind velocity is very distinctive as can be observed from Figure 66.

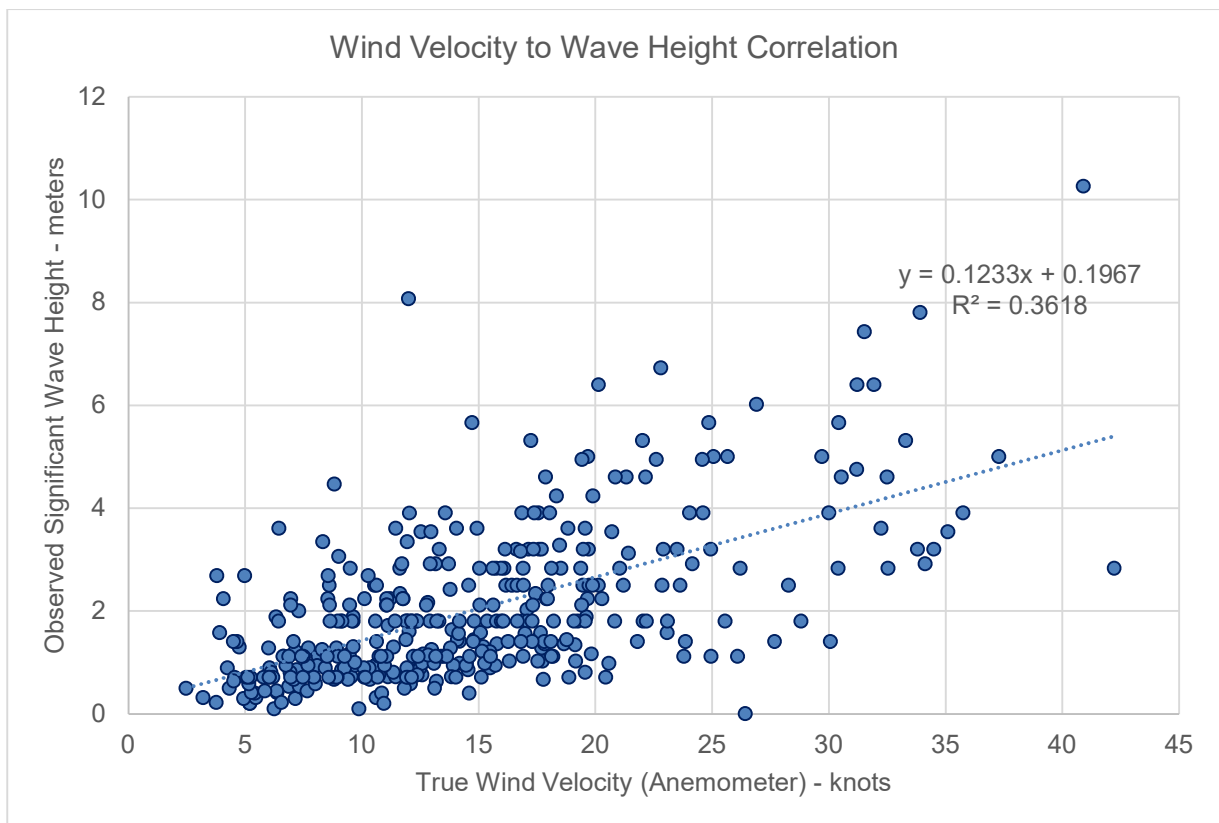


Figure 66: Correlation of Anemometer Wind Velocity vs. Crew Observed Wave Height

The relevant scatter data depicted in Figure 66, after being filtered for outliers, have been transferred to the IBM SPSS® database to run descriptive statistics. After the normality checks, two models have been created for the wave height expression one linear and one non-linear. As a result, the original wave model can be summarized as per below:

1. Wave Height:

- a. Linear Correlation to Wind Velocity:

$$Wave\ Height = 0.1233 * WindVelocity + 0.1967 \quad (53)$$

- b. Non-Linear Correlation to Wind Velocity:

$$WaveHeight = 0.161 * WindVelocity^{0.939} \quad (54)$$

- c. Probability Distribution Function: Taken the same as the corresponding wind velocity

An interesting observation is that the correlation created here is also quite similar to the correlation followed for the Beaufort Scale:

2. Wave Direction:

- a. Magnitude:

Taken the same as the Wind Direction

- b. Probability Distribution Function:

Taken the same as the corresponding wind direction.

B. Modelling from Matched Satellite Weather Data

At a second stage, as previously discussed for the rest of the environmental parameters, from late 2019, the timespan and coordinates of the onboard collected database has been matched with hindcast satellite data available from a weather provider. From these, the available wave data include the significant wave height, direction and modal period of the wind-generated waves as well as the swell. The use of such data has been focused on the generation of complete voyages in real time to validate on a dynamic basis the output of the simulation tool as described in paragraph 5.3.7.

C. Use of Long Term Wave Statistics

At a last stage and for the modelling of the waves within the design environment, for each individual leg based on the starting and ending coordinates one of the global areas in the below scattered area is matched (Figure 67). For each area of the worldwide map that has been matched with the individual leg routes, the parameters of long term statistics are available from the DNV-RP-C205 Recommended Practice on Environmental Conditions and Environmental Loads (DNV, October 2010).

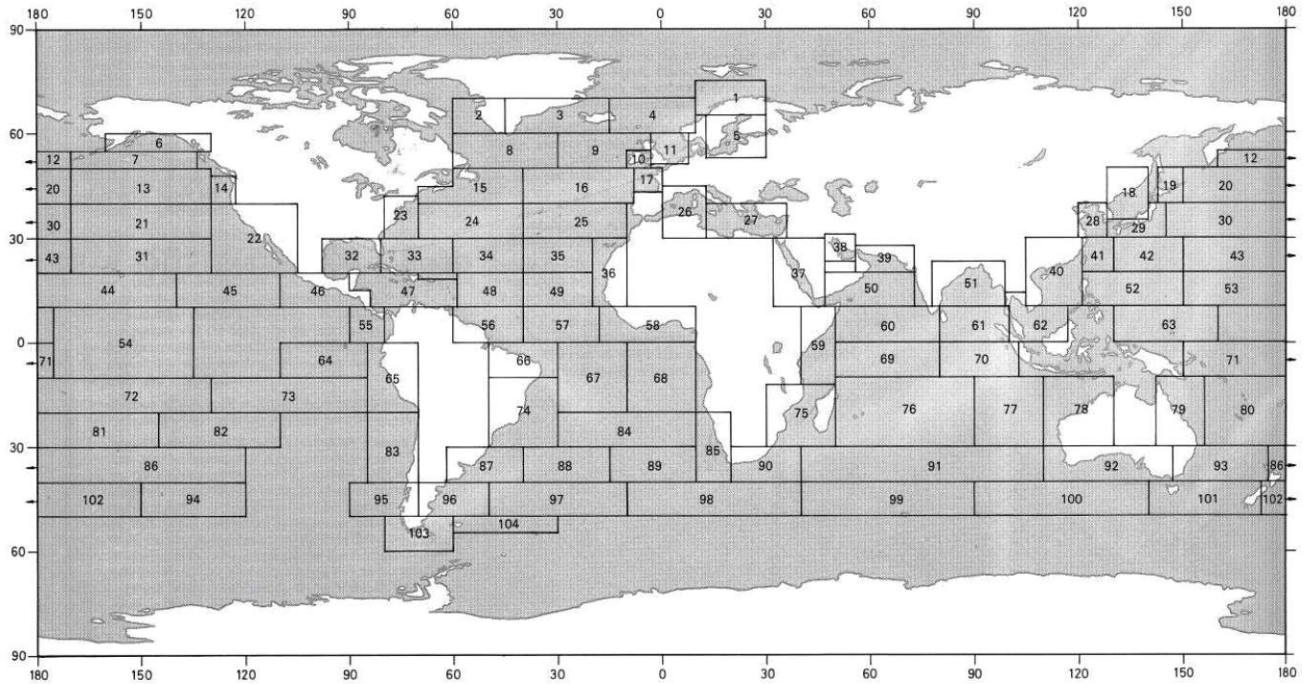


Figure 67: Scatter Diagram of Worldwide Sea Regions (DNV, October 2010)

For each of the above mentioned regions a Joint environmental model is recommended by DNV (DNV, October 2010). The reason is that for wave-induced loads and reliability analysis, joint environmental models provide more consistent treatment. Furthermore, the assessment of the relative importance of the various environmental variables during extreme load/response conditions and at failure such models have a better response.

For this application, a Conditional Modelling Approach (CMA) is followed as defined by (Britner-Gregersen & Haver, 1991), which uses a joint density function defined in terms of a marginal distribution and a series of conditional density functions. The significant wave height in such a model is defined by a 3-parameter Weibull probability density function:

$$f_H(h) = \frac{\beta_{H_S}}{\alpha_{H_S}} \left(\frac{h - \gamma_{H_S}}{\alpha_{H_S}} \right)^{\beta_{H_S} - 1} \exp \left\{ - \left(\frac{h - \gamma_{H_S}}{\alpha_{H_S}} \right)^{\beta_{H_S}} \right\} \quad (55)$$

While the zero-crossing wave period conditional on H_S is modelled by a log-normal distribution:

$$f_{Tz|H_S}(t|h) = \frac{1}{\sigma t \sqrt{2\pi}} \exp \left\{ - \frac{(\ln(t - \mu))^2}{2\sigma^2} \right\} \quad (56)$$

The distribution parameters of the mean and standard deviation are functions of the significant wave height as defined in :

$$\mu = E[\ln Tz] = \alpha_0 + \alpha_1 h^{\alpha_2} \quad (57)$$

$$\sigma = std[\ln Tz] = b_0 + b_1 e^{b_2 h} \quad (58)$$

The below Table 27 summarizes the environmental modelling considered for the herein presented methodology:

Methodology Global Environmental Model	
Wind – Onboard Data	1st Generation (2015-2019)
Data Source:	Onboard data acquired from vessel anemometer
Wind Velocity PDF:	Gamma Distribution Shape: 4.277 Scale: 0.289
Wind Direction PDF:	Normal Distribution Mean: 170.461 Standard Deviation: 77.537
Wind – Onboard Data	
	2nd Generation (2019-) Only Applicable for Australia Trade Route
Data Source:	Satellite weather hindcast data matched to timestamp and coordinates.
Wind Velocity PDF – Laden Condition:	Weibull Distribution α : 5.037 β : 2.152 γ : 0.000
Wind Velocity PDF – Ballast Condition:	Lognormal Distribution a: 4.697 b: 0.471
Wind Direction PDF – Laden Condition:	Exponential Distribution Scale Parameter: 0.023
Wind Direction PDF – Ballast Condition:	Exponential Distribution Scale Parameter: 0.023
Current – Onboard Data	
	1st Generation (2015-2019)
Data Source:	Crew Observation (Noon Reports)
Current Velocity PDF – Laden Condition Brazilian Trade:	Exponential Distribution Scale: 1.484
Current Velocity PDF – Laden Condition Australian Trade:	Normal Distribution Mean: 0.674 Standard Deviation: 0.465
Current Velocity PDF – Ballast Condition Brazilian Trade:	Exponential Distribution Scale: 1.532
Current Velocity PDF – Ballast Condition Australian Trade:	Exponential Distribution Scale: 1.113
Current Direction PDF:	Uniform Distribution Minimum: 0 Maximum 337.50

Current – Matched Satellite Weather Data	2nd Generation (2019-) Only Applicable for Australia Trade Route
Data Source:	Satellite weather hindcast data matched to timestamp and coordinates.
Current Velocity PDF – Laden Condition:	Exponential Distribution, Scale: 2.268
Current Velocity PDF – Ballast Condition:	Lognormal Distribution a: 0.402 b: 0.819
Current Direction PDF – Laden Condition:	Normal Distribution Mean: 183.461 StDev: 95.815
Current Direction PDF – Ballast Condition:	Normal Distribution Mean: 195.128 Standard Deviation: 96.570
Waves – Onboard Data Correlation <i>(wind waves only)</i>	
Data Source:	Onboard data acquired from vessel anemometer
Wave Height – Linear Correlation	$Wave\ Height = 0.1233 * WindVelocity + 0.1967$
Wave Height – Non-Linear Correlation	$WaveHeight = 0.161 * WindVelocity^{0.939}$
Wave Height PDF:	From transformation using the linear and non-linear correlations, assumed to be the same as the Wind Velocity PDF
Wave Direction PDF:	Assumed to be the same as the prevailing wind generating the waves
Zero Crossing PDF:	Assumed same as in Long Term Wave Statistics
Waves – Matched Satellite Weather Data <i>(wind waves and swell)</i>	
Data Source:	Satellite weather hindcast data matched to timestamp and coordinates.
Wave Height PDF – Laden Condition:	Weibull Distribution α : 1.528 β : 1.209 γ : 0.000
Wave Height PDF – Ballast Condition:	Weibull Distribution α : 1.974 β : 1.005 γ : 0.000
Wave Direction PDF:	Assumed to be the same as the prevailing wind generating the waves

Zero Crossing PDF:	Assumed same as in Long Term Wave Statistics
Waves – Long Term Wave Statistics (CMA Joint Environmental Model)	2nd Generation (2019-)
Data Source:	DNV Global Weather Statistics (DNV, October 2010)
Wave Height PDF:	Weibull Distribution $f_H(h) = \frac{\beta_{Hs}}{\alpha_{Hs}} \left(\frac{h - \gamma_{Hs}}{\alpha_{Hs}} \right)^{\beta_{Hs}-1} \exp \left\{ - \left(\frac{h - \gamma_{Hs}}{\alpha_{Hs}} \right)^{\beta_{Hs}} \right\}$ $\mu = E[\ln Tz] = \alpha_0 + \alpha_1 h^{\alpha_2}$ $\sigma = std[\ln Tz] = b_0 + b_1 e^{b_2 h}$
Wave Direction PDF:	Assumed same with satellite model,
Zero Crossing PDF:	$f_{Tz Hs}(t h) = \frac{1}{\sigma t \sqrt{2\pi}} \exp \left\{ - \frac{(\ln(t - \mu))^2}{2\sigma^2} \right\}$

Table 27: Global Environmental Model developed and considered

5.3.5. Simulation of the Vessel's Operation

The process flow of the vessel voyage simulation module of the RHODA is seen in Figure 68 and is described in the present paragraph.

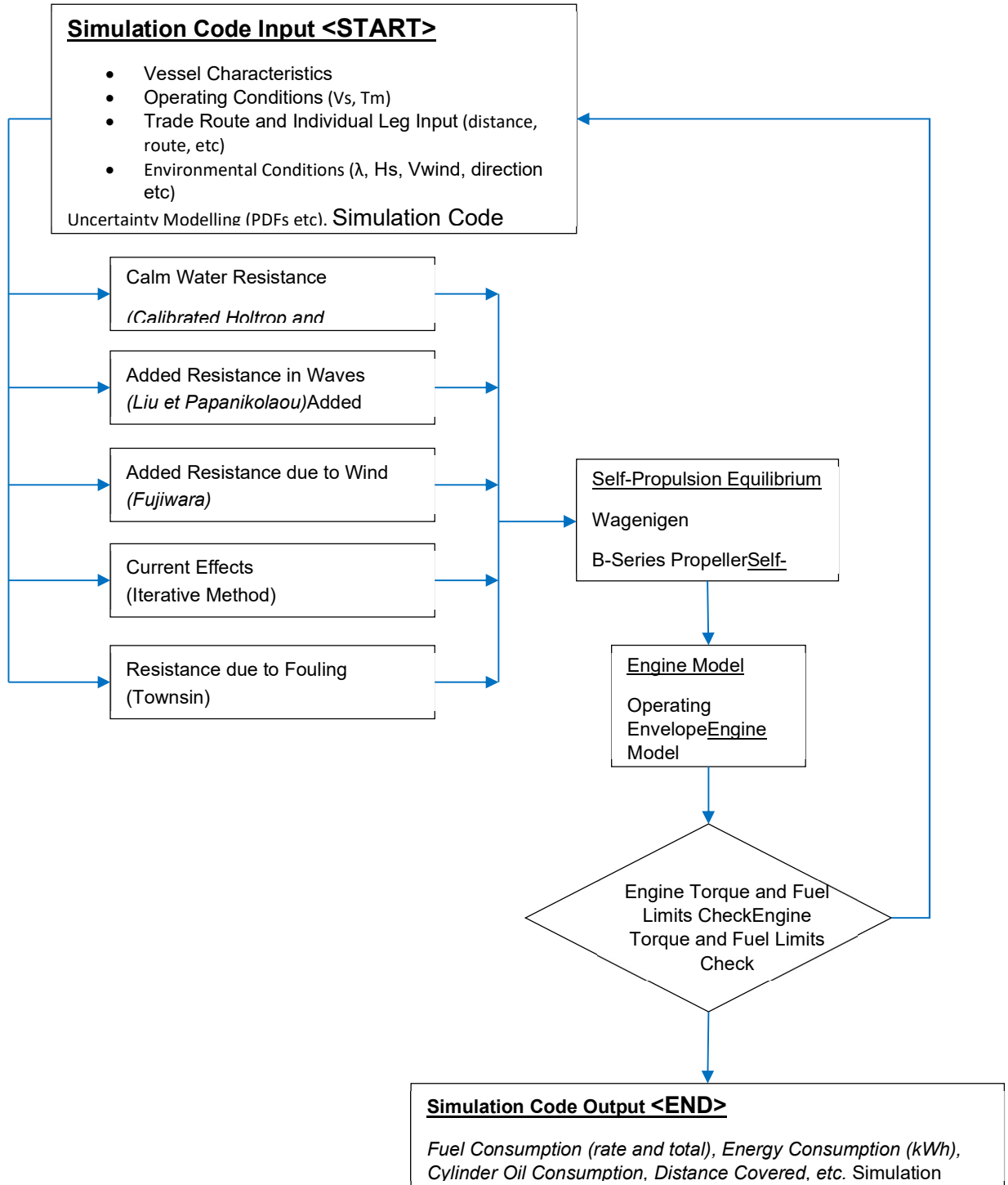


Figure 68: Process flow of integrated code for simulating vessel's responses and operation profile

5.3.5.1. Step 1: Speed Definition, Uncertainty and Current Effects

For each individual leg the operating (ordered) speed by the user is defined as an input in the simulation code. This is in turn corrected against the following uncertainty effects in order to be used for resistance and power calculations:

1. Effect of Current.

For each voyage leg, a low, medium and high current velocity are defined. The velocity amplitude is determined from the minimum, maximum and average speed from the onboard data. For each of the three current velocities, a probability of occurrence is then estimated using the log-normal probability distribution function that has been generated as described in paragraph 3.3.4.2. The speed through the water is then corrected for the astern and ahead current of these velocities on the basis of the effective vector of the current (longitudinal direction). The drift effect from the transverse current is not taken into account at this stage. The correction to the operating speed is positive for the cases of astern current and negative for ahead current. The ahead of and astern currents are considered for an “operating envelope” of ± 45 degrees both in the ahead and astern term, as the side currents will only yield deviation rather than speed loss.

2. Ordered Speed Uncertainty

For each fixed voyage of a vessel, a Charter Party Agreement (CPA) governs two or three different speeds in laden and ballast conditions and their corresponding consumptions. However, as per shipping operations modern practice, the actual transit speed ordered by Charterers is determined by the latter party based on weather data and their logistics support ashore. One can understand that there is a distinctive uncertainty on the contractual and actually ordered operating speed. This uncertainty is depicted here twofold: first an average actual speed value is estimated for each individual leg (and sub-leg) for a large fleet of Capesize and Newcastlemax vessels employed in the trade (with multiple different charterers included in the statistical sample). It should be noted that the statistical sample used here has been larger than the database of onboard data used for the environmental model. More specifically, a fleet of more than 30 vessels has been examined for the average leg speeds encountered and afterwards deployed in the simulation input. As done previously in the generation of the environmental model, the data have been split between Laden and Ballast conditions for the Australia and Brazil Trade Route respectively and populated in the IBM SPSS®. After the first stage normality tests and descriptive statistics, each variable has been fitted with a Probability Distribution Function (PDF) and simulated. The fitted probability distribution functions for the various speeds can be found in the below Table 28. The histograms of the populated and simulated data for both loading conditions in the Australia trade route can be found in Figure 69 to Figure 71. The corresponding histograms for the Brazil trade route can be found in Figures Figure 72 to Figure 76.

Variable	Probability Distribution Function
Operating Speed LADEN – Australia <i>Mean:</i> 10.7887 <i>StDev:</i> 1.44492	Normal Distribution Mean: 10.858 Standard Deviation: 1.120
Operating Speed LADEN – Brazil <i>Mean:</i> 10.5795 <i>StDev:</i> 1.55538	Normal Distribution Mean: 10.579 Standard Deviation: 1.558
Operating Speed BALLAST – Australia <i>Mean:</i> 10.8580 <i>StDev:</i> 1.12152	Normal Distribution Mean: 10.789 Standard Deviation: 1.443
Operating Speed BALLAST - Brazil <i>Mean:</i> 9.9485 <i>StDev:</i> 2.46279	Normal Distribution Mean: 9.949 Standard Deviation: 2.462

Table 28: Fitted Probability Distribution Functions for Operating Speeds in Simulation Model

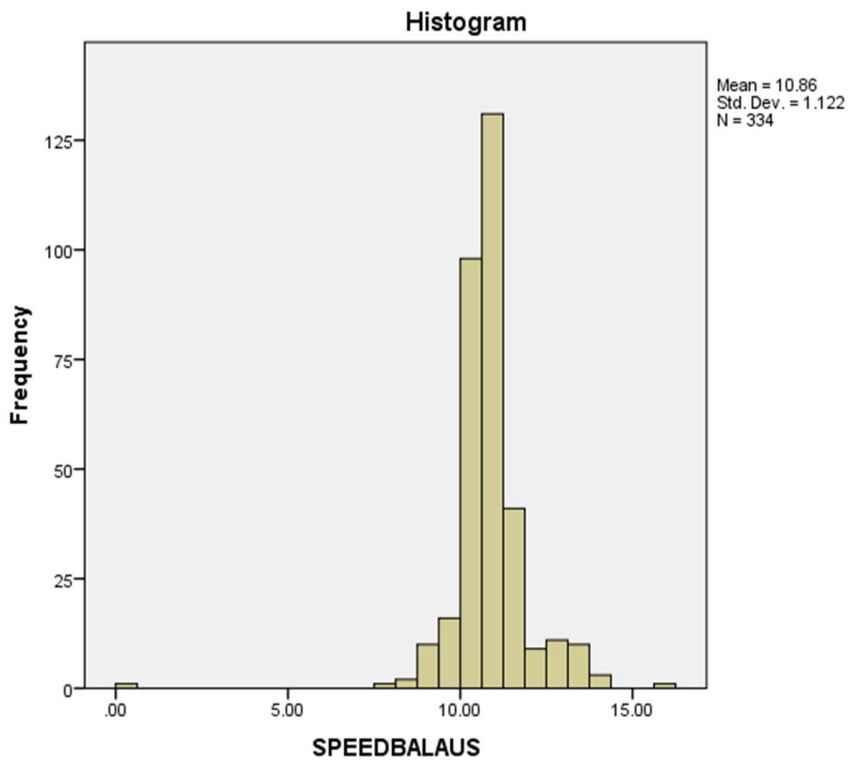


Figure 69: Histogram of the populated values for Operating Speed LADEN - Australia

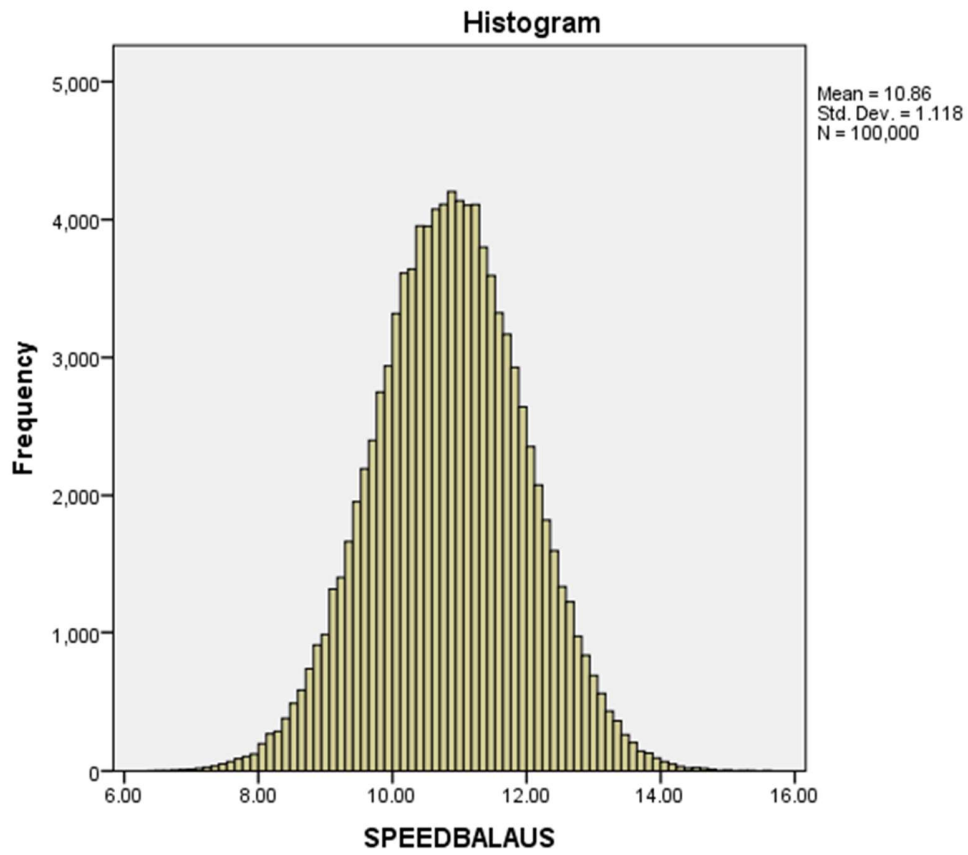


Figure 70: Histogram of Normal PDF simulated data for Operating Speed LADEN - Australia

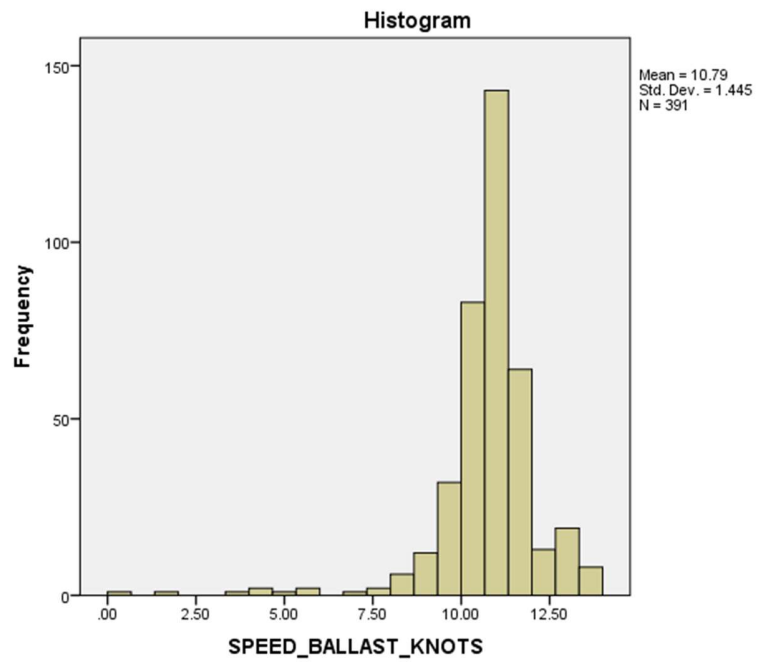


Figure 71: Histogram of the populated values for Operating Speed BALLAST - Australia

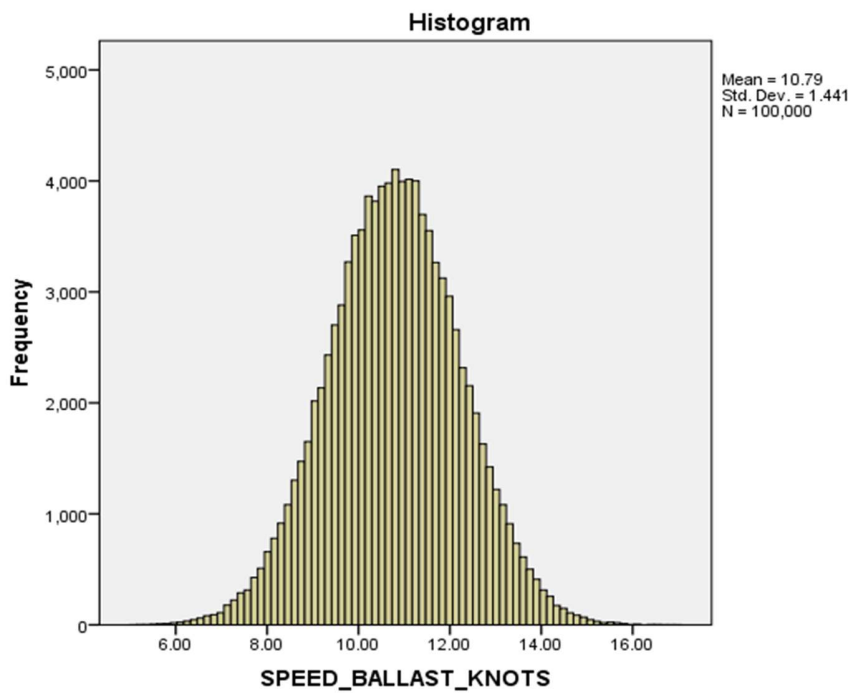


Figure 72: Histogram of Normal PDF simulated data for Operating Speed BALLAST - Australia

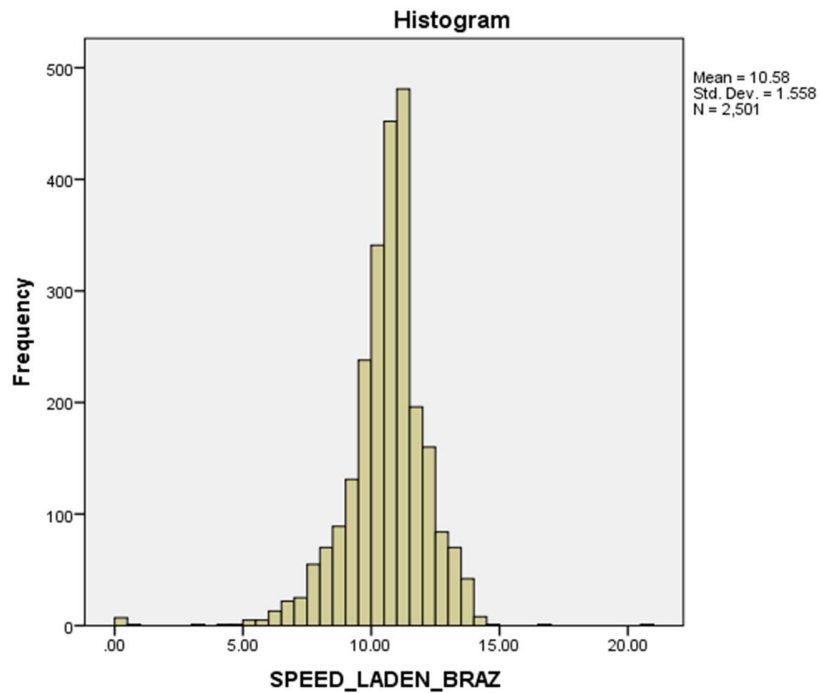


Figure 73: Histogram of the populated values for Operating Speed LADEN – Brazil

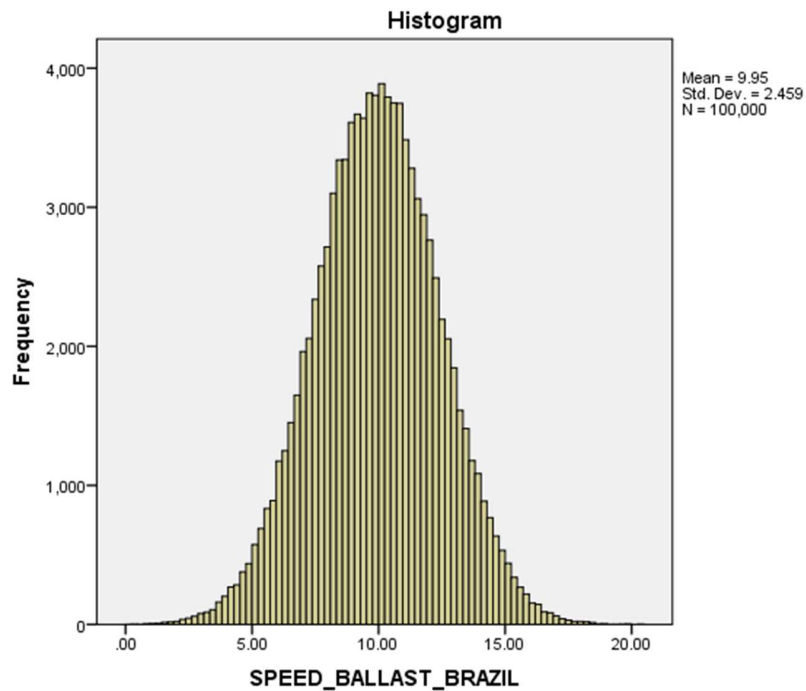


Figure 74: Histogram of Normal PDF simulated data for Operating Speed LADEN - Brazil

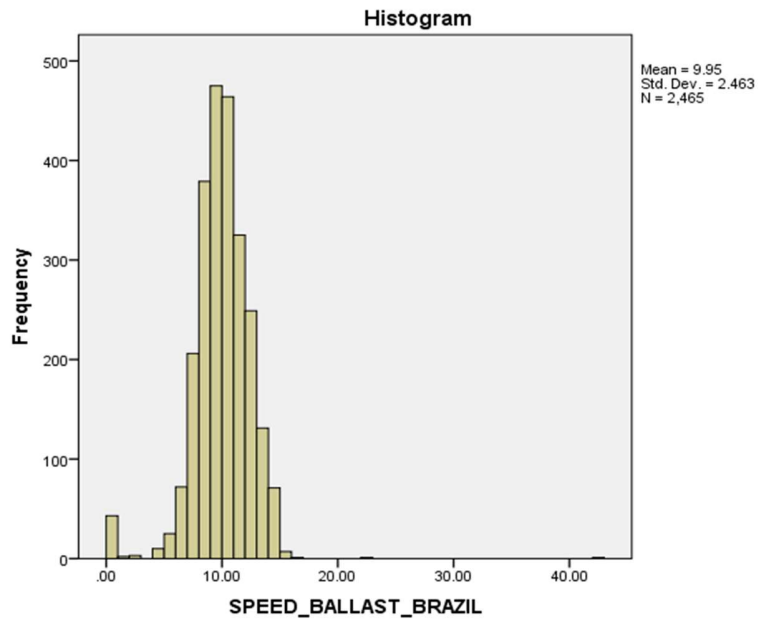


Figure 75: Histogram of the populated values for Operating Speed BALLAST – Brazil

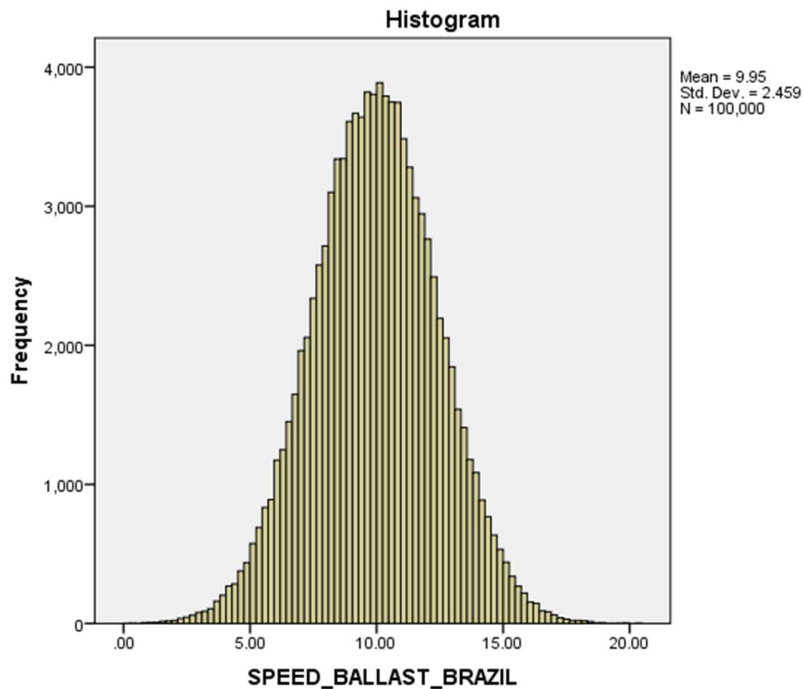


Figure 76: Histogram of Normal PDF simulated data for Operating Speed BALLAST - Brazil

For the final speed correction, a 20% margin of sailing above and below the average speed respectively is defined and the probability of occurrence of the extreme low and high operating speed values is estimated by the aforementioned operating speed PDFs. Given the probabilities of above and below margins are now known, the operating speed is finalized.

3. Involuntary Loss of Speed

Prior to using the speed as an input in the next modules (as per Figure []) flowchart, there is a loop function that used in order to take into account the involuntary loss of speed due to slow down of the Main Engine in case the powering requirements in the examined seaway exceed those of the torque/fuel, Mean Effective Pressure and SCMR limits of the specific engine envelope of each design variant examined.

From the above mentioned two corrections, the probabilistic ship speed is derived based on which both the calm water required delivered power is calculated as well as the added resistance and power calculations take place. Further to this extent, following the ship design optimization studies of the next chapter, a study on the optimization of the supply chain by variation of the sailing speed of each leg is also examined on a comparative basis with existing ship speed optimization studies.

5.3.5.2. Step 2: Calm Water Resistance Estimation

The calm water resistance for the final corrected speed is estimated by interpolating a polynomial curve that is generated for each design variant in the Calm Water Resistance Module (paragraph 3.2.3). The curve has been generated at 1-knot intervals from 7 to 17 knots for the ballast and laden conditions. This approach ensures even smaller computational requirements during the simulation stage with the bulk of the computational effort being focused during the design generation process.

5.3.5.3. Step 3: Added Resistance due to Fouling Estimation

The first of the added resistance components is that of the resistance attributed to the fouling of the hull and propeller. The added resistance due to biological fouling of the vessel's hull is estimated with the use of the model described in paragraph 3.2.4.3 and with the assumed curve of roughness increase for the vessel's lifecycle.

5.3.5.4. Step 4: Added Resistance due to Wind and Waves

For each leg stage and corresponding time step an "add-on" added resistance module is called from within the operational simulation module in order to calculate the added resistance.

The added resistance module has as input all the operational parameters and output the probabilistic value of the added resistance due to waves and added resistance due to wind.

1. Added Resistance Due to Wind:

The added resistance due to the wind is estimated using the same methodology as the one described in paragraph 3.2.4.2. The resistance due to wind is estimated for wind force from 1 to 9 BN in the Beaufort Scale at 1 BN intervals and for wind directions from 0° to 180° at intervals of 22.5 degrees. The developed code furthermore assumes that the effect of wind and waves is

symmetrical, therefore the added resistance for the 180° to 360° range is taken the same as its symmetrical counterparts already calculated. The probability of occurrence for the wind velocities and wind direction are estimated using the Environmental model described in paragraph 5.3.4, with the probability of occurrence for the wind direction being regarded as an independent variable (statistically) from the wind velocity.

Beaufort Scale	Wind Velocity (knots)
0	0
1	3
2	6
3	10
4	16
5	21
6	27
7	33
8	40
9	47

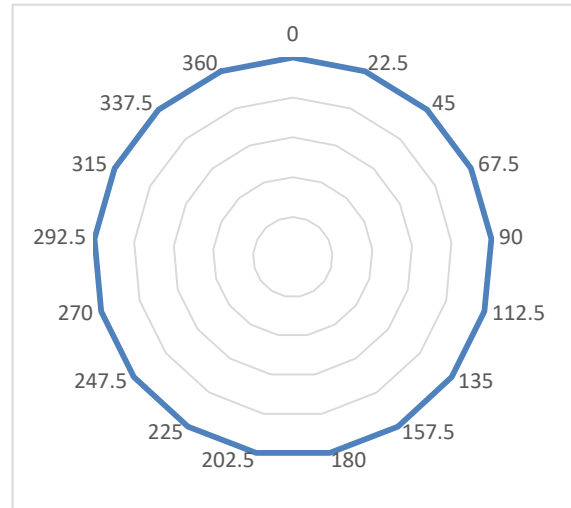


Figure 77: Wind Velocities and Directions used as input in Simulation Module

2. Added Resistance Due to Waves:

The added resistance due to waves is estimated using the hybrid surrogate model approach that has been previously discussed in paragraph 3.2.4.1 with the Liu methods (Liu, et al., 2016), (Liu & Papanikolaou, 2020) set as a basis. The wave characteristics that are used as an input in the above method are the following:

a. Significant Wave Height

As the significant wave height is the primary and most critical input for the wave-induced added resistance calculation the simulation tool uses a probabilistic method. Instead of using random values, or prescribed values of one executed voyage, the code runs the added resistance calculation for all the normally encountered wave heights depending on the prevailing Douglas Sea State as per below Table 29 in accordance with the North Atlantic normally encountered values. For each of the wave height and zero-crossing periods, the probability of occurrence is calculated by using the PDFs defined by long term wave statistics described in the Environmental Model in paragraph 5.3.4

Sea State	Wave Height (m)	Zero-Crossing Period (sec)
1	0.05	0
2	0.05	7.5
3	0.88	7.5
4	1.88	8.8
5	3.25	9.7
6	5.00	12.4
7	7.50	15.0
8	11.50	16.4
9	14.00	20.0

Table 29: Sea States considered for added resistance estimation in seaways

b. Wave Length and Wave Direction.

For the purpose of deriving with one figure for the added resistance in a typical, fully developed seaway, the herein proposed methodology employs a spectral approach as found in (Liu, et al., 2020). The RAO of the added resistance in regular waves in long-crested waves is expressed as:

$$\overline{R_{AW}}'(T_S, H_S, \alpha, V_{TW}) = 2 \int_0^\infty \frac{R_{AW}(\omega, \alpha, V_{TW})}{\zeta_A^2} S_f(\omega, H_S) d\omega \quad (59)$$

The mean added resistance in short-crested waves is calculated by a linear superimposition of the directional wave spectrum and the $R_{AW}(\omega, \alpha, V)$ as per below:

$$\overline{R_{AW}}'(T_S, H_S, \alpha, V_{TW}) = 2 \int_0^{2\pi} \int_0^\infty \frac{R_{AW}(\omega, \alpha, V_{TW})}{\zeta_A^2} S_f(\omega, H_S) G(a) d\omega \quad (60)$$

With G being the angular distribution function. The directional spectrum E describing the sea conditions is calculated as:

$$E = S_f(\omega, H_S) G(a) \quad (61)$$

The frequency spectrum is assumed to take the approximate form of the JONSWAP spectrum:

$$S(H_S, T_p, \gamma) = \frac{a^* H_S^2 \omega^{-5}}{\omega_p^{-4}} \exp\left[-\frac{5}{4} \left(\frac{\omega}{\omega_p}\right)^{-4}\right] \gamma \exp\left[\frac{-(\omega - \omega_p)^2}{2\sigma^2 \omega_p^2}\right] \quad (62)$$

With $a^* = \frac{0.0624}{0.23 + 0.0336\gamma - 0.185/(1.9 + \gamma)}$ and $\sigma = 0.07$ for $\omega \leq \omega_p$ while $\sigma = 0.09$ for $\omega > \omega_p$. For developing seaways, the wave energy spectrum normally used has a peak enhancement factor $\gamma = 3.3$. (Liu, et al., 2020) in the same paper introduce the use of the angular distribution function following the below cosine formulation:

$$G(a) = \begin{cases} \frac{2^{2s} \Gamma^2(2s+1)}{\pi \Gamma(2s+1)} \cos^{2s}(\theta - \alpha), & |\theta - \alpha| < \pi/2 \\ 0, & \text{otherwise} \end{cases} \quad (63)$$

5.3.5.5. Step 5: Total Resistance Estimation

The total resistance estimation is the summation of the calm water resistance for the actual speed examined and the various components of the added resistance:

$$R_{total} = R_{calm}(V_{corr}) + R_{wind} + R_{waves} + R_{fouling} \quad (64)$$

5.3.5.6. Step 6: Self Propulsion Equilibrium

With the total resistance now estimated, the self-propulsion equilibrium is established. As described in paragraph 3.2.5 the equilibrium equation is used as a basis:

$$P_S = P_E * \frac{1-t}{1-w} * \eta_0 * \eta_R * \eta_S \quad (65)$$

The thrust deduction t , wake fraction w and relative rotative efficiency η_R are inputs of the simulation module in the form of curves. The curves are part of the calm water resistance module (together with the calm water resistance curve). The shaft efficiency is considered as a constant of 0.97 as also described in paragraph 4.4. The challenging part is how to determine the new propeller operating point given the added resistance.

In order to do so, the *Propsel* code is called but with the updated resistance information in order to take into account the total resistance instead. After an iterative procedure from the initial solution (using the initial J and RPM as input), the *RPM* code gives feedback to the *Propsel* code about the new operating point regarding the advance coefficient, RPM and propeller efficiency. Given the other curves, the Delivered horsepower can be then calculated.

5.3.5.7. Step 7: Engine Torque and Fuel Limits Check

An important consideration that is not taken into account in the simulation codes currently existing in the literature is the existence of a constraint of the Delivered horsepower with regards to the engine operating envelope. The delivered power calculated in Step 6 of the simulation is the one required by the propeller, so in the next step, it is considered necessary to verify if the Main Engine can deliver this power at the RPM setting. For this reason, the corresponding Fuel/Torque Limit for a given RPM (Figure 78) for the specific engine envelope is compared to the required power. If the required power exceeds 98% of this limit then the speed is dropped by 1 knot and the calculation is repeated from Step 2.

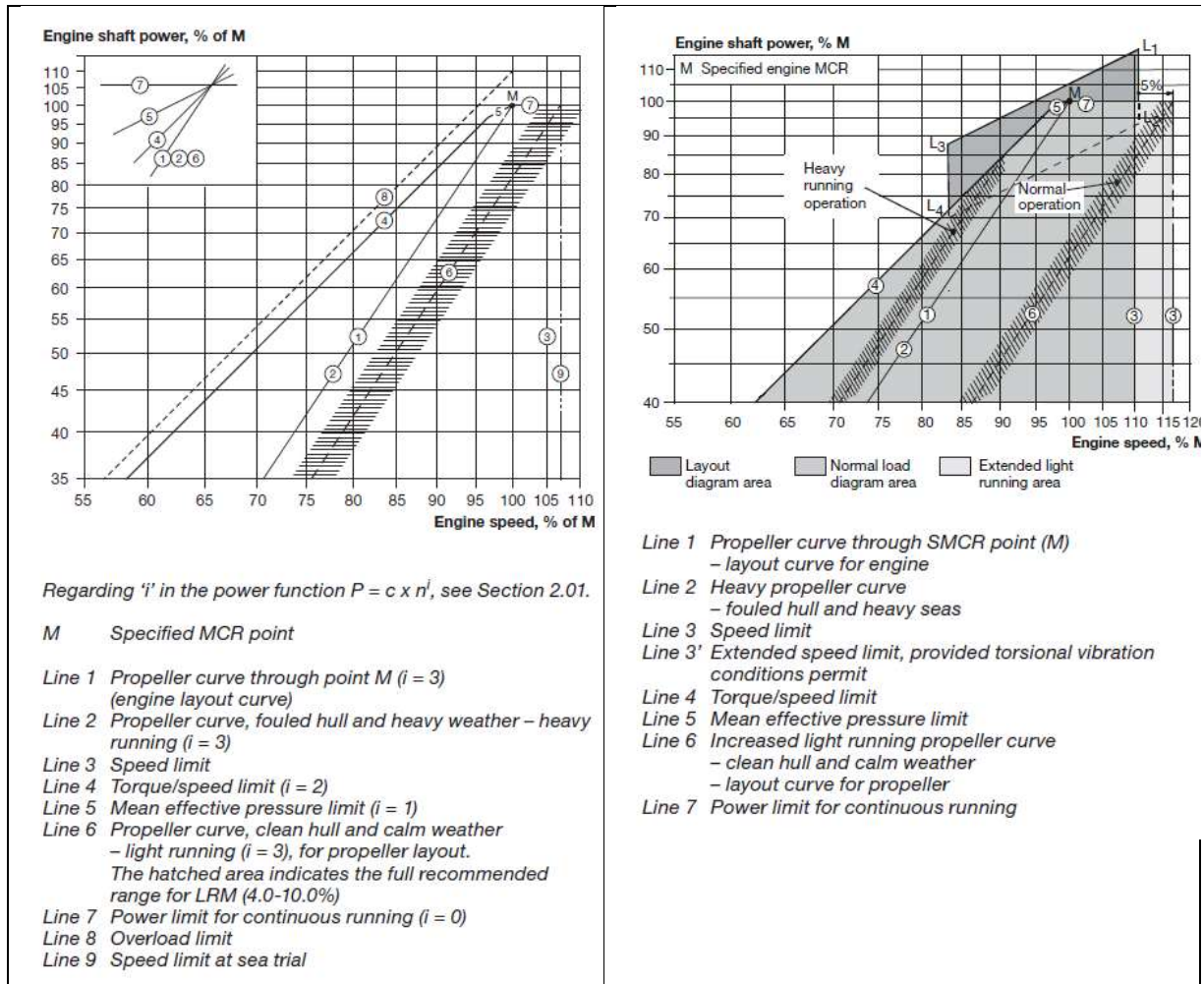


Figure 78: Engine Envelope of the 6G70ME-C engine (MAN, 2020).

5.3.5.8. Step 8: M/E and Auxiliaries Fuel and Energy Consumption Estimation

With the fuel and torque limits checked it is assured that the engine can operate at the Power and RPM (namely torque) requirements of the propeller.

The SFOC curve as extracted from the Main Engine Matching module (see paragraph 5.2) is interpolated for the power setting of each specific leg and the specific fuel consumption in gr/kWh is calculated. It is afterwards ISO corrected for the specified conditions (temperature and pressure) as well as the specified fuel used (with regards to its Low Calorific Value / LCV).

The auxiliary engines load is estimated based on the sailing condition and the Main Engine load. In case that the Main Engine Load is below 35% of the SMCR, then the Blowers electrical load is also added assuming their operation. Based on the final load, the number of operating generators is determined and the fuel oil consumption is calculated by interpolating the code input SFOC curve for the D/Gs.

The ambient temperature that is given as input is used with an "if" function to determine the relevant season and thus the estimated steam consumption, corresponding boiler steam production, boiler load and fuel consumption from the parametrized boiler performance curves.

The output data for each leg and the whole voyage respectively are indicated in the below Table 30.

No.	Simulation Code Outputs	Unit of Measure
1.	Main Engine Fuel Oil Consumption (per Leg)	Tons
2.	Main Engine Fuel Oil Consumption (Voyage)	Tons
3.	Auxiliary Engines Fuel Oil Consumption (per Leg)	Tons
4.	Auxiliary Engines Fuel Oil Consumption (Voyage)	Tons
5.	Boiler Engines Fuel Oil Consumption (per Leg)	Tons
6.	Boiler Engines Fuel Oil Consumption (Voyage)	Tons
7.	Total Fuel Consumption Onboard (per Leg)	Tons
8.	Total Fuel Consumption Onboard (Voyage)	Tons
9.	Cylinder Oil Consumption (per Leg)	Tons
10.	Cylinder Oil Consumption (Voyage)	Tons
11.	CO2 Emissions (per Leg)	Tons
12.	CO2 Emissions (Voyage)	Tons
13.	Main Engine Work (per Leg)	kWh
14.	Main Engine Work (Voyage)	kWh
15.	Auxiliary Engines Work (per Leg)	kWh
16.	Auxiliary Engines Work (Voyage)	kWh
17.	Total Voyage Transit Time	Hours
18.	Total Voyage Transit Time	Days
19.	Fuel Rate	Fuel Tons/ton*miles
20.	Main Engine Energy Consumption (Voyage)	MJ/ton*mile
21.	Auxiliary Engines Energy Consumption (Voyage)	MJ/ton*mile
22.	Total Energy Consumption (Voyage)	MJ/ton*mile

Table 30: Simulation Code Output Variables summary

5.3.6. Lifecycle Economic and Environmental Assessment.

With the operational life of the vessel being approximated and reproduced with detailed and specific voyages in a dynamic simulation environment as described in paragraph 3.3.5, their results can be in turn used in order a very realistic and robust assessment of its lifecycle economic and environmental performance to be conducted.

5.3.6.1. Lifecycle Economic Assessment by Market Rate Simulation

For the proposed lifecycle economic assessment, firstly the charter market of large bulk carriers is modelled based on historical data for the Time Charter Rate Equivalent (TCE), Acquisition and Disposal (scrapping/recycling) prices from 1990 to 2015 as extracted from Clarkson's Shipping Intelligence database (Clarksons Shipping Intelligence, 2015). The following data was extracted and edited for the years 1990 to 2015:

1. IFO 180 Price in USD/t
2. IFO 380 Price in USD/t
3. MGO bunker prices (Singapore) in USD/t
4. MDO bunker prices (Singapore) in USD/t
5. Capesize 176-180k DWT Newbuilding Prices in million USD
6. Capesize Scrap Value in million USD
7. Indian Sub-continent Demolition Prices in USD/LDT (light weight tons)
8. Far East Sub-continent Demolition Prices in USD/LDT (light weight tons)
9. Capesize Long Run Historical Earnings in USD/day
10. Capesize Fleet Development in Number of Vessels and Metric Tonnes DWT

The herein proposed methodology considers the economic assessment of each design variant by the following economic metrics and indicators:

1. Capital Expenditure (CAPEX) in U.S dollars per day.

The Capital Expenditure (CAPEX) are the costs regarding the acquisition, disposal and major upgrade or maintenance of an asset (i.e vessel) and are in turn typically comprised of the following:

- i. Acquisition and Residual (Disposal) Cost in million U.S dollars*

The acquisition cost can be either the price of acquiring a newbuild vessel as per the prevailing Shipbuilding Contract or the price paid for acquiring a second-hand vessel. For the purposes of the present research, it is assumed to be the cost of a newbuild vessel. Since this is a commercial market price it is subject to the supply and demand balance of newbuilding slots from Shipyards. Interestingly, it is quite common that the acquisition cost increases in high freight market conditions (commonly referred to as "super-cycles") due to the big demand in shipbuilding slots and turn decreases during low freight rate conditions. Such a correlation has been also examined in the extracted market data. It is therefore self-explanatory that a static, constant value for the asset acquisition price that has been previously followed in ship design optimization studies is a very crude assumption that however significantly affects the optimization target of Required Freight Rate. Interestingly, the uncertainty of the market acquisition price has never been

examined in the relevant ship design literature. For this particular reason, in the herein presented methodology a probabilistic approach is followed to adequately capture this sensitivity contributing to the overall robustness of the design optimization result. It should be noted that by robustness here we define the ability of a high-performing design variant to maintain its dominant performance in the optimization target under different design environment exogenous conditions.

The probabilistic modelling of the vessel acquisition price is done in three stages. The first stage, involves the definition of a lightship price ratio in USD per lightship ton. This has been modelled by deriving an average DWT and lightship per vessel using the Fleet DWT and deployment (number of vessels) for the 1990 to 2015 fleet on a per month basis from the Clarksons Shipping Intelligence Database (Clarksons Shipping Intelligence, 2015). The average lightship was cross-evaluated with the relevant results of empirical formulae and the database used for the digital twin lightship method described in paragraph 4.7. The acquisition price was calculated as Capesize Bulker Newbuilding Price as found in the created database from the Clarksons Shipping Intelligence database from 1990 to 2015 (Clarksons Shipping Intelligence, 2015). The reason for deploying such a price rate is the necessity to correlate the size of the vessel to the building and acquisition price, thus enhancing the sensitivity of our code to the dimension and volumetric variation of the design variants.

In a second stage, the new Newbuilding Price ratio (USD/lightship ton) has been correlated to the corresponding month Capesize Earnings in USD/day (Clarksons Shipping Intelligence, 2015). This was performed in the IBM SPSS® Statistical kit after running descriptive statistics and normality checks, resulting in the below non-linear regression expression:

$$NBprice = 157.335 * Earnings^{0.269} \quad (66)$$

The same approach has been followed for the expression of the Scrap value (disposal value), using the India/Bangladesh Demolition values from 1990 to 2015 from (Clarksons Shipping Intelligence, 2015):

$$Scrap_price = 25.648 * Earnings^{0.244} \quad (67)$$

In the third and last stage, the created models for the USD/ton lightship are used in order to calculate a tangible value for the acquisition and disposal price that can be used for estimating the metrics for the lifecycle economic assessment of each vessel (CAPEX and RFR). This is done with a probabilistic, weighted, approach. Three scenarios for earnings are defined: a high market with earnings of TCE 150,000 USD/day, a medium market with earnings of TCE 35,000 USD/day and a low market with earnings of TCE of 5,000 USD/day. The respective probability of occurrence was estimated using the Probability Distribution Function (PDF) for Capesize TCE Earnings for 1990 to 2015 modelled from the created database (Clarksons Shipping Intelligence, 2015). After the population of the data in IBM SPSS® these have been tested for normality and descriptive statistics. The histogram capturing the frequency of occurrence for the original dataset can be seen in

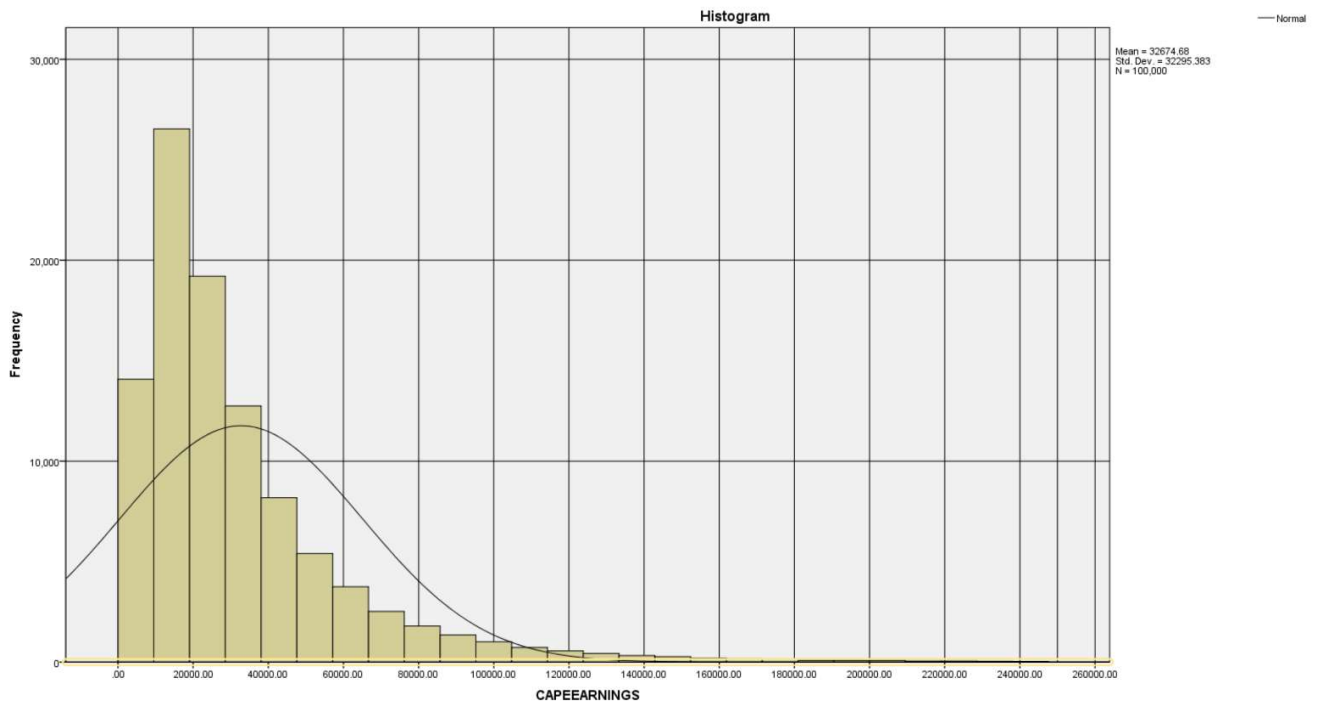


Figure 79. Consequently, for the original dataset, the best-fitted Probability Distribution to the populated data was the Lognormal PDF with the parameters shown in Table 31. The histogram with the frequency of occurrence for the simulated data from the generated PDF can be seen in Figure 80.

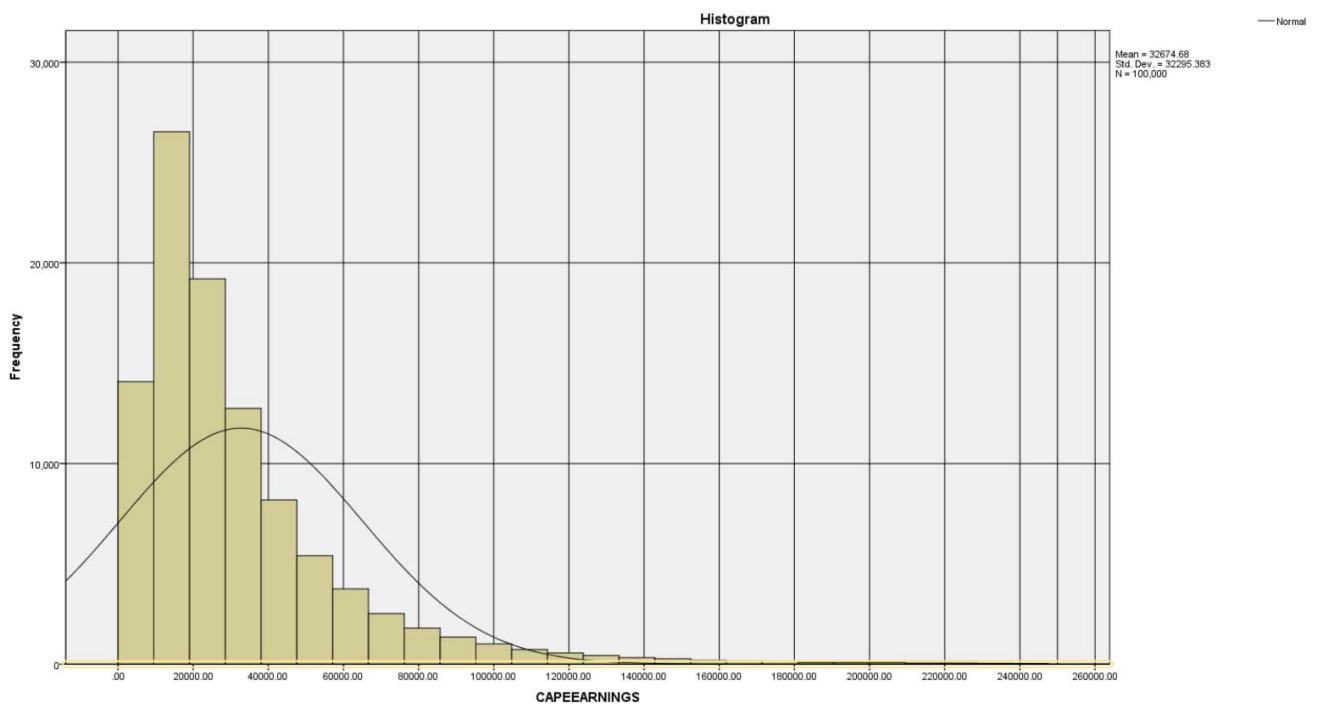


Figure 79: Histogram of the populated values for Capesize Earnings from 1990 to 2015.

Variable	Probability Distribution Function
Capesize Earnings 1990-2015 Mean: 32674.68 StDev: 32295.38	Lognormal a: 23194.93 b: 0.830

Table 31: Fitted Probability Distribution Function for TCE Earnings

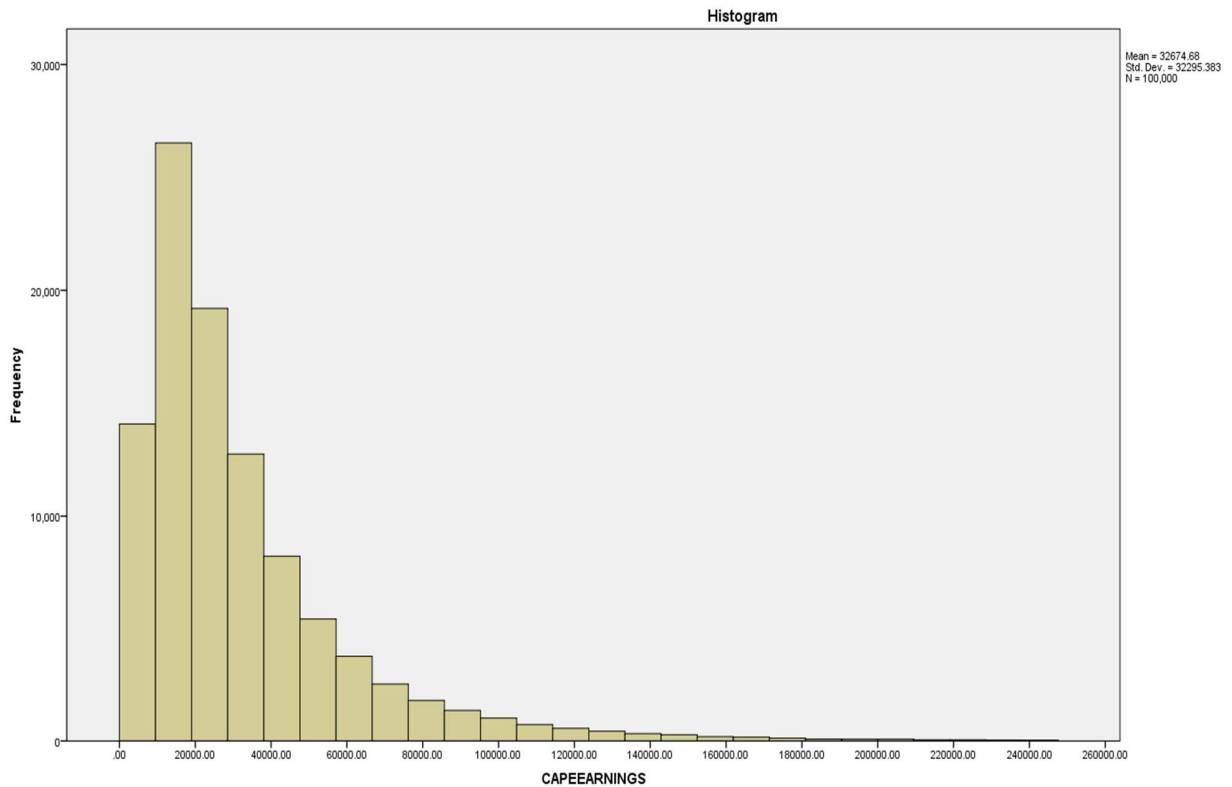


Figure 80: Histogram of lognormal PDF simulated data for TCE Earnings

The probabilistic value of newbuilding and scrap price can thus be assumed to be as per below:

$$NBprice = \frac{NBprice_{HIGH} * p(HIGH) + NBprice_{MID} * p(MID) + NBprice_{LOW} * p(LOW)}{p(HIGH) + p(MID) + p(LOW)} \quad (68)$$

$$Scrap_price = \frac{Scrap_price_{HIGH} * p(HIGH) + Scrap_price_{MID} * p(MID) + Scrap_price_{LOW} * p(LOW)}{p(HIGH) + p(MID) + p(LOW)} \quad (69)$$

Concluding, for both equations the value returned is USD/ton of lightship and serve as magnification factors for the acquisition and residual values of the vessel. Furthermore, the two last which are used for the CAPEX calculation, are also probabilistic by applying the same probabilities that are used for High, Mid and Low Earnings with the respective amounts introduced in the above-presented formulas. In this way, it can accurately depict the volatility of

the market and the response of each design variant as well as the effect of its dimensions on its lifecycle economic performance.

ii. *Costs of Dry Dockings and Upgrades in million U.S dollars*

The second component of CAPEX considered after the acquisition and disposal costs are the cost of Dry Docking and Upgrades. For the herein presented methodology, it is assumed that the vessel will be fitted from delivery with Ballast Water Treatment Systems and Tier III emission control systems, so the cost for upgrades is limited to maintenance and modification works done during Dry Dockings to upgrade the operational functionalities and efficiency of the vessel. The Dry Docking cost is primarily a function of the vessel’s age, size and engine type. For the case of bulk carriers we herein examine, an important cost is the one of cargo hold treatment in order to maintain cargo hold cleanliness and prevent corrosion in the structural arrangements of cargo holds. It should be noted that as per literature on wastage modelling (Bauk & Ivošević, 2010), (Garbatov & Guedes Soares, 2008) and (Garbatov & Guedes Soares, 2011), the milestone for the initiation of wastage and corrosion on ship structural members is the deterioration of the vessel’s coating and breakdown in the adjacent area. For this purpose, we herein assume that a prudent maintenance strategy in Dry Dockings is followed with blasting and recoating at each dry-docking for cargo holds as well as onboard maintenance. Additionally, renewals in tons are assumed for cargo hold tank top plating (normally not coated) and ballast tanks structural members after the 15th year of age of the vessel.

Given the above consideration, the Dry Docking costs of a fleet of 75 large bulk carriers from 2005 to 2015 have been populated, filtered and statistically edited. The Dry Docking costs are broken into different categories with regards to the relevant cost centres and functional components. Following that, non-linear regression formulae have been developed having the vessel’s size (DWT), age and Main Engine SMCR and Dry Docking days as independent variables in IBM SPSS®. The resulting model for Dry Docking cost is depicted in Table 32.

Group	Estimated Shipyard Cost	Expression
10	General Services	$GS = 0.002DWT^{1.387} + 1424.274 * Days^{0.954}$
20	Tank Cleaning	$TC = 3.7458 * 10^{-6}DWT^{1.676} + 363.835 * Days^{0.954}$
30	Staging	$S = 2600.568 + 0.078 * CHT + 0.147 * HCT + 0.113 * SW$
40	Dry Docking dues	$DDD = 2806 * DWT^{0.797}$
50	Dry Docking Works	$DDW = 433.344 * DWT^{0.354}$
60	Hull Treatment	$HT = 12.455 * DWT^{0.702} + 3680 * Age^{0.328}$
70	Cargo Hold Treatment	$CHT = 11.922 * DWT^{0.798}$
80	Ballast Tanks Treatment	0 (onboard maintenance assumed)
90	Hatch Cover, Cranes and Deck Treatment	$HCT = 3183.278 * Age^{0.6}$
100	Steel Works	$SW = 1.026 * 10^{-12}DWT^{-3.281} + 1.992 * Age^{3.684}$
110	Hatch Cover Works	$HCW = 8.456DWT^{0.644}$
120	Cranes and Grabs	0 (for gearless, large bulk carriers)
130	Outfitting, Safety and other Deck Works	$O = 4.716DWT^{0.737}$
140	Machinery	$MACH = 77.716MCR^{0.701}$
150	Electrical – Automation	$EL = 1322.795MCR^{0.250}$

160	Deck Piping	$DP = 895.971Age^{1.028}$
170	Machinery Piping	$MP = 111.655MCR^{0.539}$
180	Trials	0 (assumed to be done under own power after DD without tugs)
ADD	Shipyard Additional Quotation	$ADD = 82.911DWT^{0.552}$
Group	Estimated External/Vendor Cost	Expression
	Class	3,000
	Paints (Antifouling for 60-month protection)	$AFS = 324.353 * HT^{0.491}$
	Paints – Cargo Holds	$CHP = 42.219 * CHT^{0.573}$
	Paints – Main Deck	5,000
	Spares	$SPA = 7.622MCR + 4291 * Age - 39558.759$
	Stores	$STO = 56580DWT^{-0.042}$
	Lubricants	$LU = 0.283MCR^{1.156}$
	Forwarding	$FOR = 52.573SPA^{0.535}$
	Ultrasonic Gauging	$UT = 187.865Age^{1.497}$
	Services and Technicians	$SE = 21870.579Age^{0.488}$
	Superintendents	$SUPT = 2 * 180 * Days$
	Tickets	$TICK = 3039.912 + 0.317 * SUPT + 0.048 * SE$
	Crew Bonus	2500
	Agency Costs	$AG = 8.774Age^{2.084} + 1301.151DWT^{0.296}$

Table 32: Dry Docking Costs Model developed

In addition to the above, similarly to previous approaches in the herein presented methodology for the statistical generation of digital twins, a non-linear expression for the model’s error has been also developed in IBM SPSS®:

$$ERR = 54888 + 1.752Age + 4.404 * 10^{-5}TOTAL\ COST \quad (70)$$

2. Operational Expenditure (OPEX) in U.S dollars per day

Similarly to the CAPEX modelling, the OPEX is in turn comprised of the following cost categories. All categories in OPEX have been modelled from reported data of a stock exchange listed bulk carrier Ship Management company. The models have been generated by the use of the Simplex algorithm solver in Microsoft Excel ® and are depicted in Table 33 below.

OPEX Cost Category	Expression
Cost of Crew and Crew Victualing	$Crew = 1032679 * Crew\ Number$
Cost of Spares Supply	$Spares = 0.0559 * MCR$
Cost of Stores Supply	$Stores = 0.0023 * DWT$
Other Maintenance and Insurance Costs	$Others = 0.0056 * DWT$

Table 33: OPEX Model developed

3. Required Freight Rate (RFR) in U.S dollars per ton of cargo.

The Required Freight Rate (RFR) is the most common index used in Ship Design for assessing the economic performance of a candidate vessel. Assuming that the vessel operates in the spot market, the RFR is expressing the minimum amount of income in US dollars per ton of cargo transported in order for the vessel to have a breakeven between cash inflows and outflows taking into account the acquisition cost, the disposal cost and the vessel's depreciation. The mathematical expression of the latter would be the following:

$$RFR = \frac{Total\ Costs}{Round\ Trips * Cargo * Years} \quad (71)$$

Where:

Total Costs: the total costs for operating the vessel, discounted in Net Present Value on a per-year basis. The cost summation is as per below:

$$Total\ Costs = CAPEX + OPEX + Fuel\ Cost \quad (72)$$

Round Trips: the number of annual roundtrips for a given trade route (as per simulation module)

Cargo: the vessel's cargo intake (payload in tons)

Years: the number of operating years.

It can be observed that the Required Freight Rate in the total cost part, includes the vessel's fuel costs as it is based on the spot market assumption in which the fuel costs are on the potential shipowner's account.

As the price of fuel entails a great uncertainty it is commonly considered in ship design under uncertainty studies in the literature as discussed in Chapter 2 (Plessas, et al., 2018), (Priftis, et al., 2018). Similarly, in the herein presented methodology the fuel price uncertainty is captured by using a probability-weighted approach. In a first stage, probability distribution functions for the pricing in Singapore (common bunkering port) for the common marine fuel grades of IFO180, IFO380, MGO and MDO are generated using the populated data from the Clarksons Shipping Intelligence Database for years 1990 to 2015. The data have been populated in the IBM SPSS® software and statistically examined. The histograms with the frequency of occurrence of the various IFO180, IFO380 and MGO prices can be seen in Figure 81 to Figure 83.

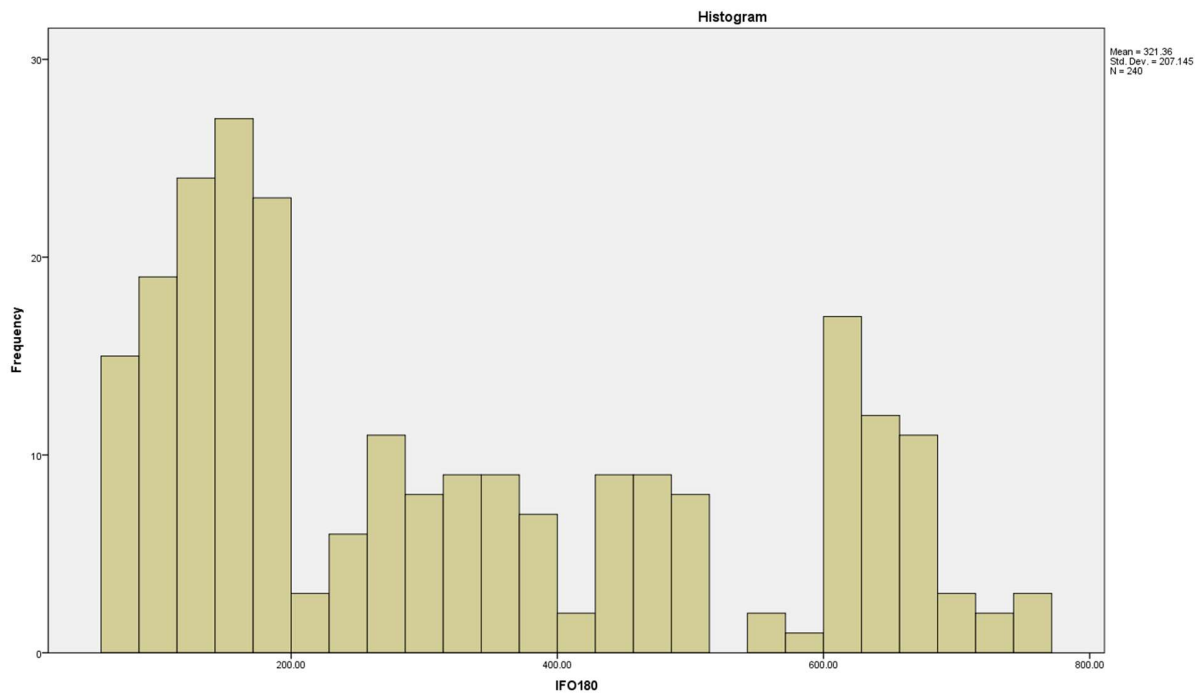


Figure 81: Histogram of the populated values for IFO180 prices from 1990 to 2015.

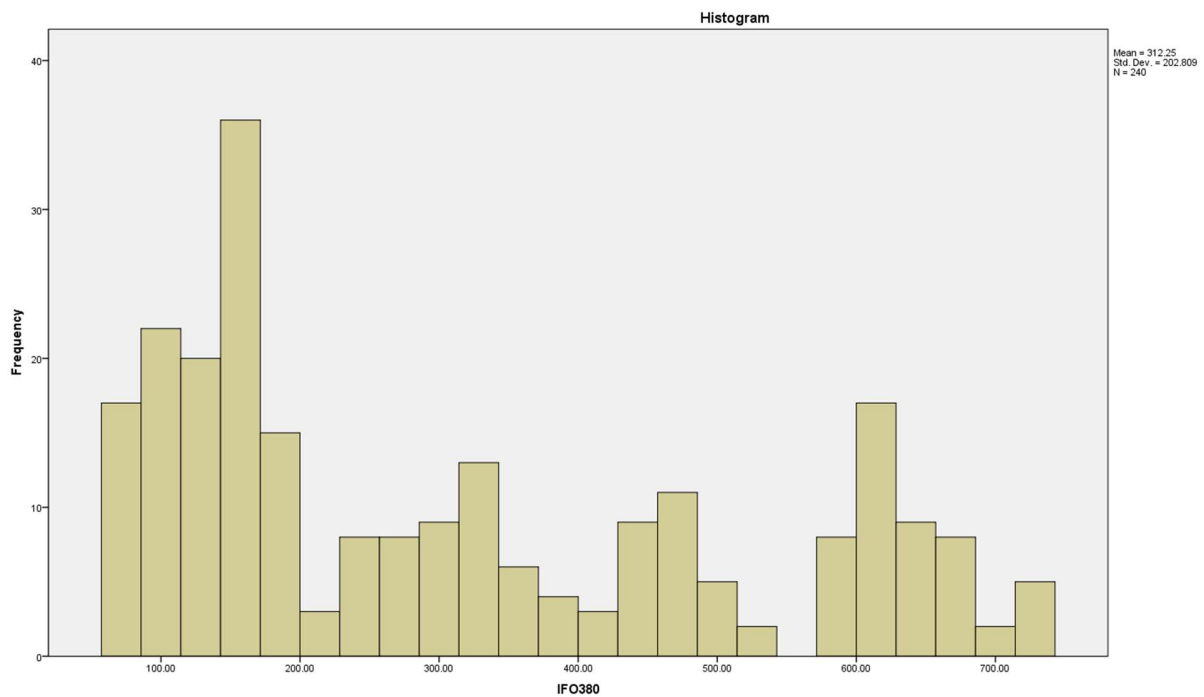


Figure 82: Histogram of the populated values for IFO380 prices from 1990 to 2015.

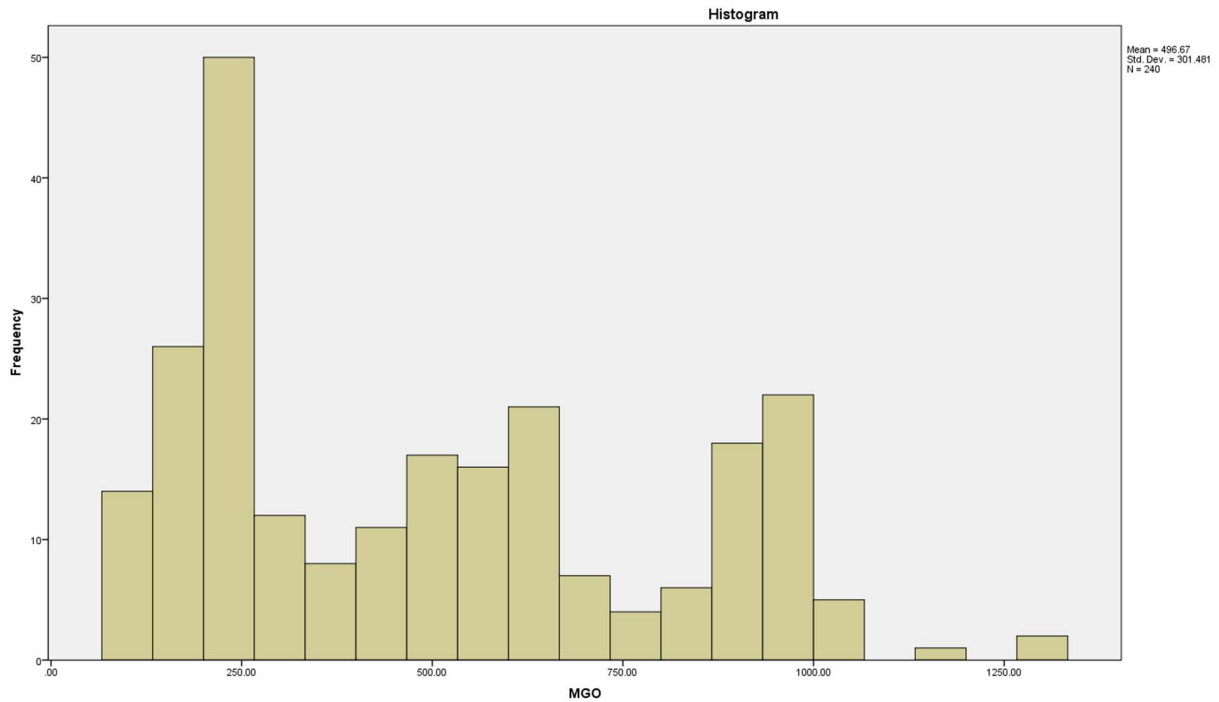


Figure 83: Histogram of the populated values for MGO prices from 1990 to 2015.

Following the database population, the normality checks and descriptive statistics running, the data have been fitted with the most appropriate Probability Distribution Functions in IBM SPSS®. These were in turn simulated in the simulation module. The PDFs are derived from data simulation in the IBM SPSS® as per below can be summarized in Table 34 and the new histograms of the PDFs used in the methodology can be found in

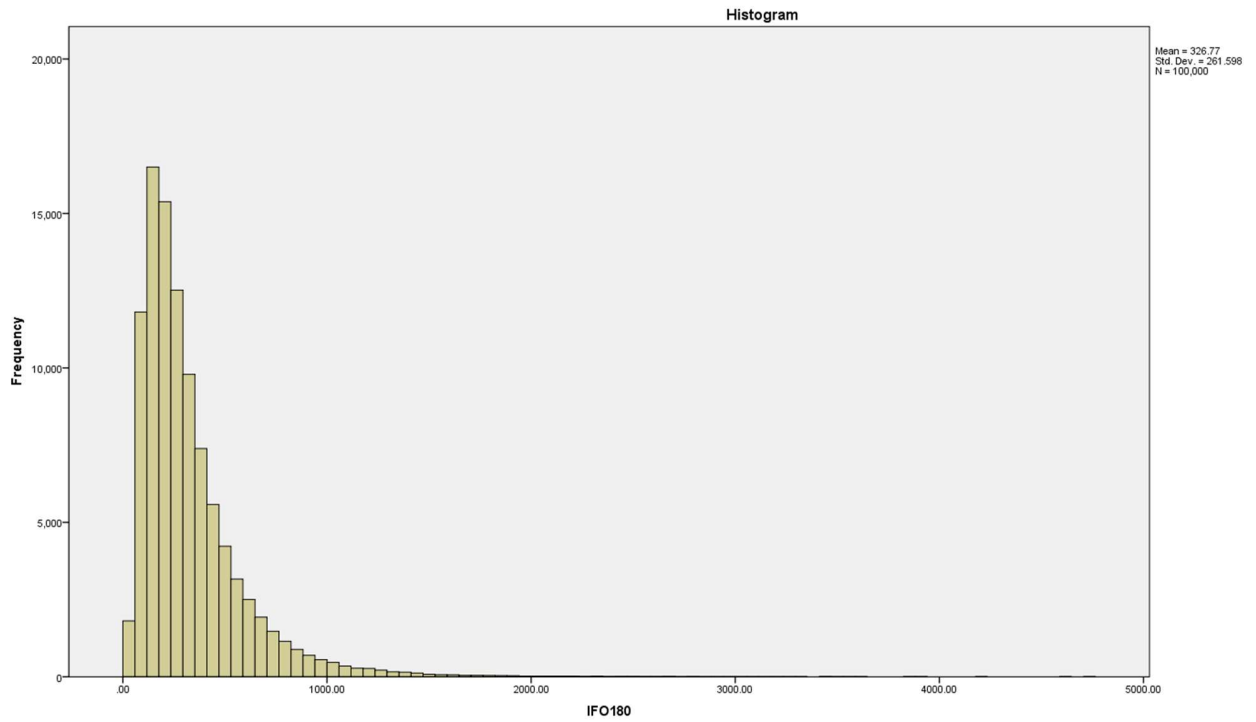


Figure 84 to

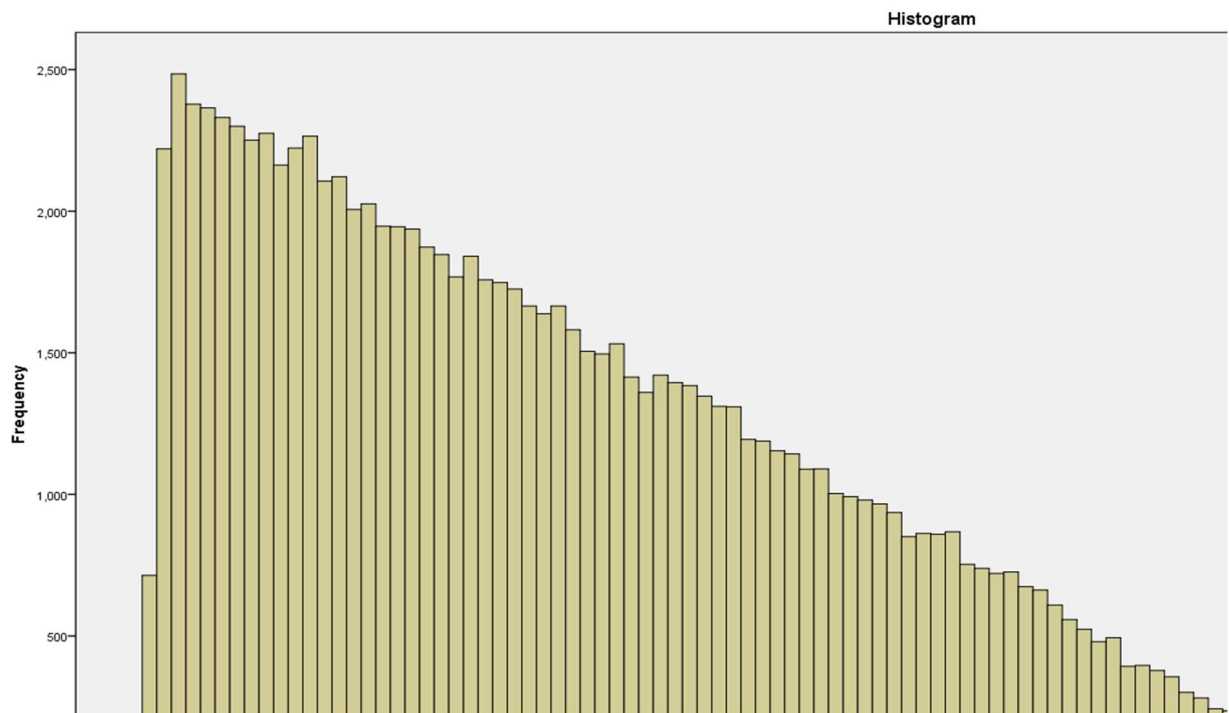


Figure 86.

Variable	Probability Distribution Function
IFO180 Price	Lognormal

<i>Mean:</i> 326.77 <i>StDev:</i> 261.598	a: 255.081 b: 0.705
IFO380 Price <i>Mean:</i> 317.66 <i>StDev:</i> 257.249	Lognormal a: 246.93 b: 0.711
Marine Gas Oil (MGO) Price <i>Mean:</i> 496.82 <i>StDev:</i> 273.059	Triangular Min: 101.25 Max: 1268.13 Mode: 120.65

Table 34: Fuel Cost Probability Functions developed and used

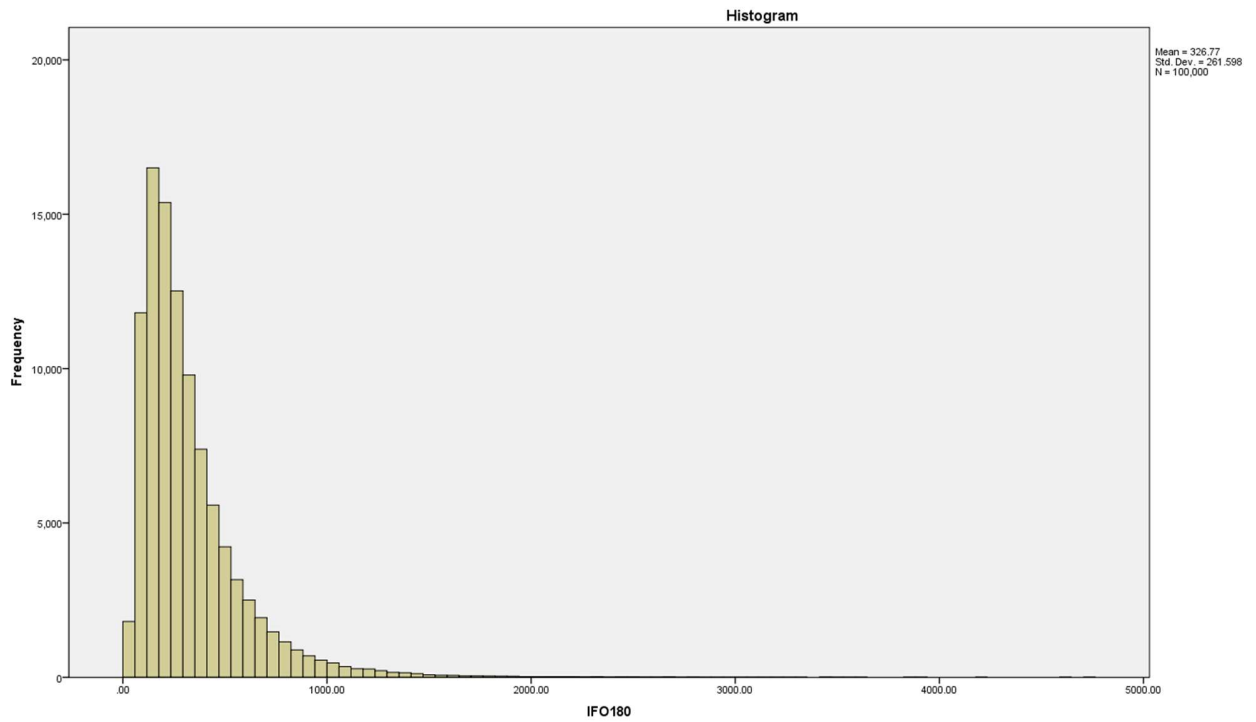


Figure 84: Histogram of lognormal PDF simulated data for IFO180

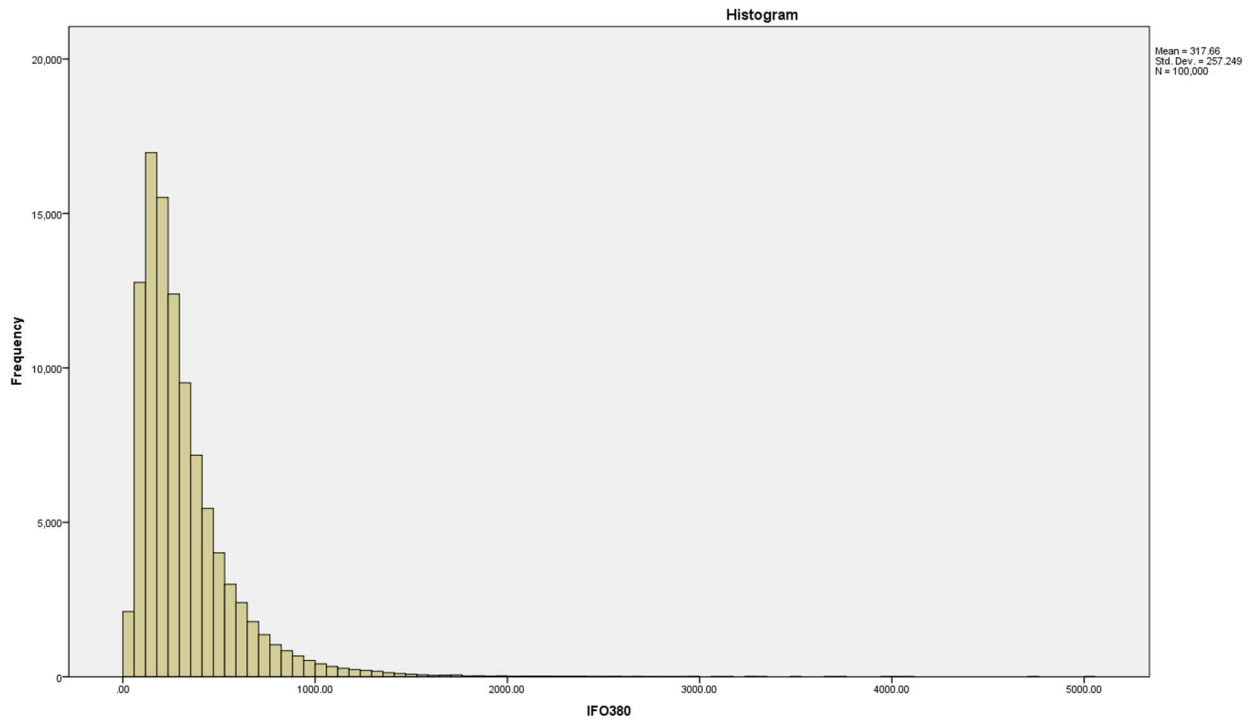


Figure 85: Histogram of lognormal PDF simulated data for IFO380

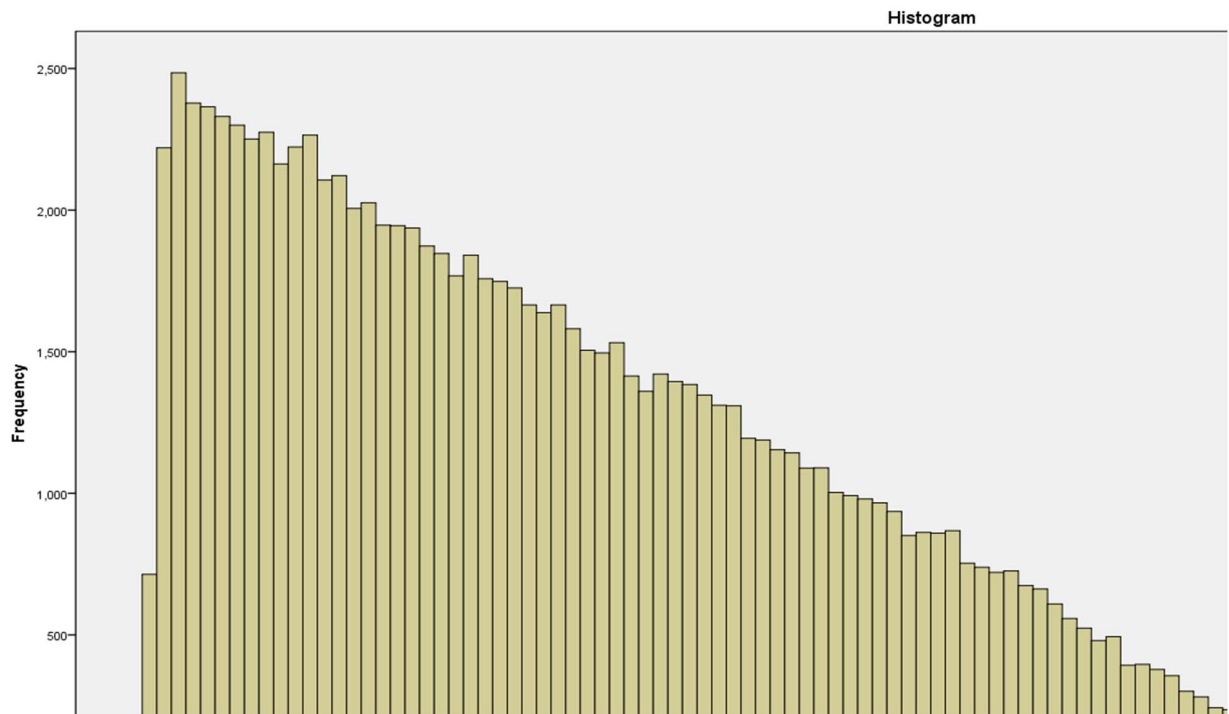


Figure 86: Histogram of lognormal PDF simulated data for MGO

At a second stage, given the above-mentioned PDFs and the total fuel consumption for a given trade route (Australia or Brazil as per paragraph 5.3.1) based on the simulation module output, the total fuel cost is estimated on a probabilistic basis. Three fuel prices are assumed: High at 1500 USD/ton (IFO380), Mid at 450 USD/ton (IFO380) and Low at 150 USD/ton (IFO380). The probability for each scenario is estimated and the corrected total cost is derived as a probabilistic summation:

$$Fuel\ Cost = \frac{Fuel\ Cost_{HIGH} * p(HIGH) + Fuel\ Cost_{MID} * p(MID) + Fuel\ Cost_{LOW} * p(LOW)}{p(HIGH) + p(MID) + p(LOW)} \quad (73)$$

4. Lifecycle Profitability in U.S dollars.

The market uncertainty is predominately expressed by the uncertainty of the vessel’s Earnings. For this particular reason and as for many stock-listed the profitability and cash inflows are of particular importance a lifecycle market simulation tool has been developed as per Figure 87. The actual freight rate market from 1990 to 2015 has been introduced and complemented by three new charter market scenarios that have been defined (Figure 87). The total profitability for each scenario is estimated for each vessel and further complement the RFR index.

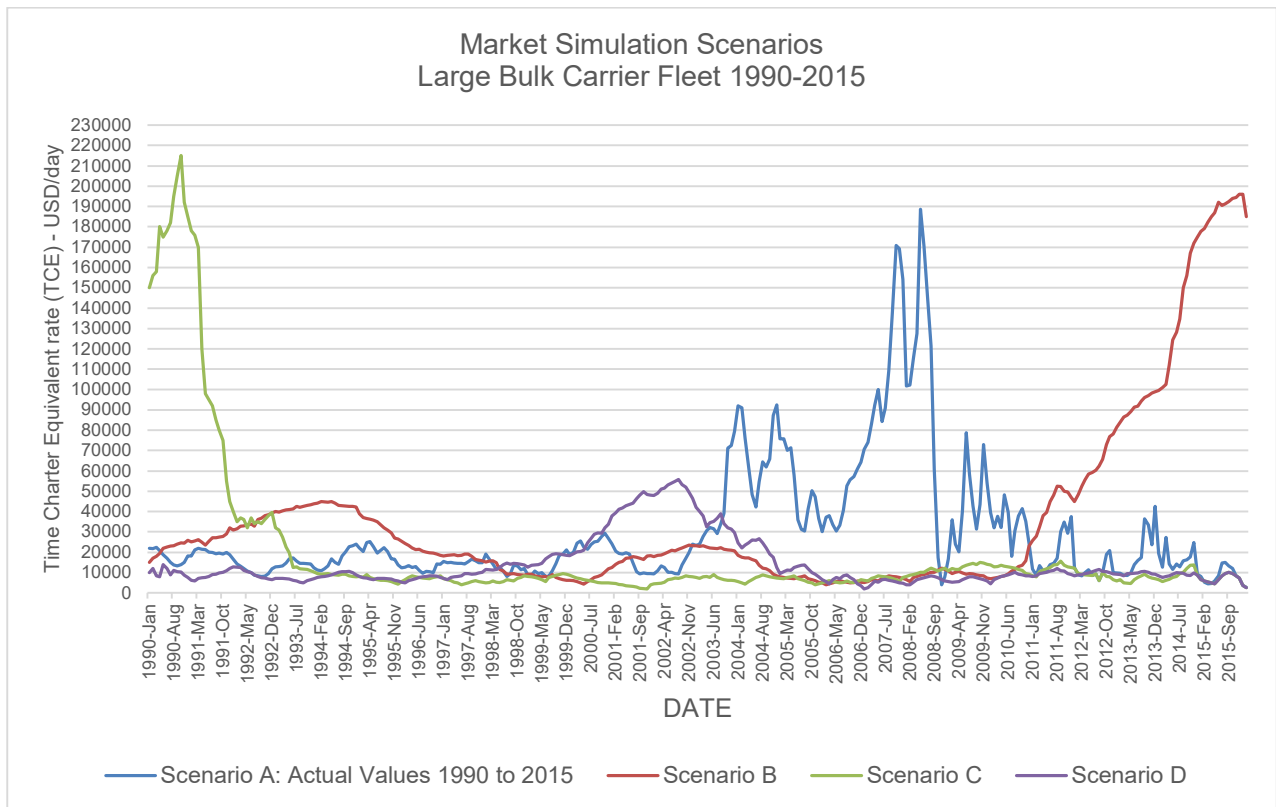


Figure 87: Market scenarios simulated for the vessel’s lifecycle

5. Required Freight Rate (RFR)

The Required Freight Rate constitutes a synthesis of all the above ship economical metrics, representing the breakeven and IRR of a vessel as an investment. The required freight rate is the hypothetical freight which will ensure a break-even for the hypothetical shipowner between the operating costs, capital costs and its income based on the annual voyages as well as collective cargo capacity and is expressed in USD per ton of cargo and can be formulated as per below:

$$RFR = \frac{OPEX+CAPEX+Fuel\ Costs}{Annual\ Cargo\ Volume} \quad (74)$$

The above is realized and mathematically programmed in the form of monetary flows and timeseries with positive flows being income and negative flows being expenses similar to the below Figure 88:

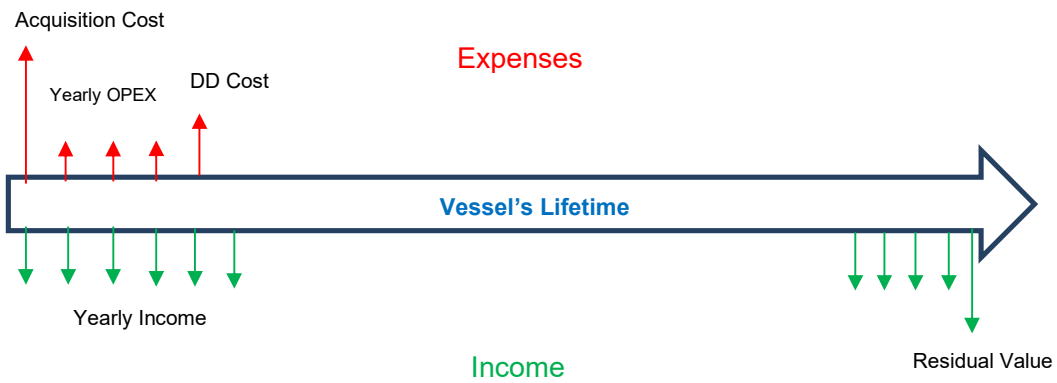


Figure 88: Monetary Flows over time modelled for RFR calculation

As the vessel's lifetime is a significant time (assumed 25 years for this instance), each monetary flow is referenced to year "0" which marks the vessel's delivery by use of the Net Present Value (NPV) formulation. All costs are modelled on an annual rate, in order to be able to have a common denominator with the annual costs and thus produce the RFR value. This metric is considered as the best representation of a vessel's economic performance in Ship Design Studies (Papanikolaou, 2010), (Papanikolaou, 2014), (Nikolopoulos, 2012) and is a centrepiece in all optimization studies being a core optimization target.

For optimization studies post-2019 and to further push for innovative ship designs, also a carbon taxation figure was added to the RFR formula:

$$RFR = \frac{OPEX+CAPEX+Fuel\ Costs+Carb\ Tax}{Annual\ Cargo\ Volume} \quad (75)$$

The Carbon Tax is calculated from the annual CO₂ emissions (derived from voyage simulation tools) multiplied by a CO₂ tax on USD/ton CO₂e that is given in three cases: low (50 USD/t), medium (100 USD/ton) and high (200 USD/ton). Given that Emission Trading Schemes (ETS) are not yet in place, an even weight distribution among the three values is assigned.

5.3.6.2. Lifecycle Environmental Assessment

The lifecycle environmental performance is based on translating the simulation module output into the following environmental indices:

1. Energy Efficiency Design Index (EEDI)

The Energy Efficiency Design Index (EEDI) has been made mandatory for new ships and the Ship Energy Efficiency Management Plan (SEEMP) for all ships in July 2011 during the IMO MEPC 62 session with the adoption of amendments to MARPOL Annex VI (International Maritime Organization (IMO), 2011). This was the first legally binding climate change treaty to be adopted since the Kyoto Protocol.

The principle of the EEDI is the calculation of required energy and subsequent CO₂ emissions of a vessel for a given design point with regards to operating speed, draft, capacity and engine rating on a transport work basis (ton*miles). The attained value is checked for compliance against a minimum energy efficiency level per capacity mile (e.g. tonne mile) for different ship type and size segments, derived from a baseline curve that is a function of the ship’s deadweight.

The reference levels of the baseline curves are to be tightened incrementally every five years.

The CO₂ reduction level (grams of CO₂ per tonne mile) is escalating starting from a 10% reduction for the EEDI Phase I and tightened every five years until 2025 and onwards when a 30% reduction is mandated for applicable ship types calculated from a reference line representing the average efficiency for ships built between 2000 and 2010. The required reduction levels are shown in Figure 89.

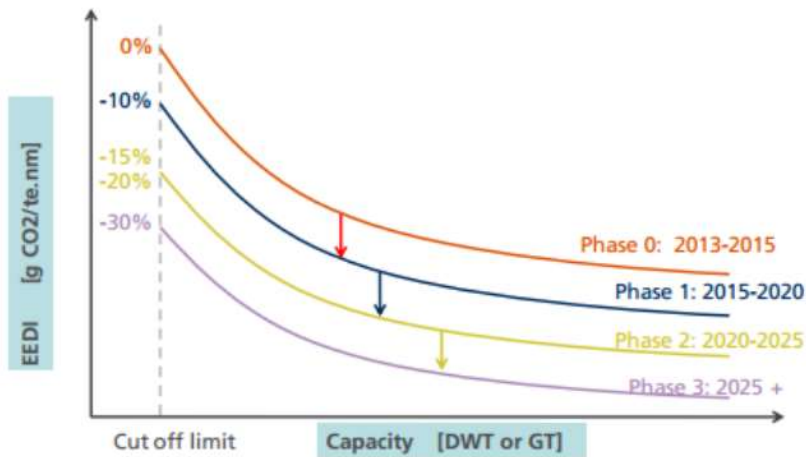


Figure 89: EEDI Phased Reduction (International Maritime Organization (IMO), 2016)

In the herein presented methodology, the Energy Efficiency Design Index (EEDI) is calculated according to the formula proposed in the IMO resolution MEPC.212(63), using the values of 70 % deadweight and 75% of the MCR of the engines and the corresponding reference speed:

$$\begin{aligned}
 EEDI = & \frac{\left(\prod_{j=1}^M f_j \right) \left(\sum_{i=1}^{nME} P_{ME(i)} * C_{FME(i)} * S_{FCME(i)} \right) + \left(P_{AE} * C_{FAE} * S_{FCAE} \right)}{f_i * Capacity * V_{ref} * f_w} + \\
 & \frac{\left\{ \left(\prod_{j=1}^M f_j * \sum_{i=1}^{nPTI} P_{PTI(i)} - \sum_{i=1}^{neff} f_{eff(i)} * P_{AE_{eff}(i)} \right) * C_{FAE} * S_{FCAE} \right\} - \left(\sum_{i=1}^{neff} f_{eff(i)} * P_{eff(i)} * C_{FME} * S_{FCME} \right)}{f_i * Capacity * V_{ref} * f_w} \quad (76)
 \end{aligned}$$

The minimization of this index is one of the primary targets of the conducted optimization. The engine power is directly related to the resistance of the hullform, while the deadweight is also related to both the hullform in terms of displacement and to the ship's lightship weight.

The baseline reference which also serves as an optimization constraint is as per below:

$$Reference\ EEDI_{bulk\ carrier} = 961.79 DWT^{0.477} \quad (77)$$

While the EEDI effectively creates a common index and baseline for energy efficiency the formulation and consideration of the latter are focused on only one design point with regards to the design speed, design draft and engine load neglecting the actual operation of the vessel both in terms of actual loading and powering as well as in terms of Main Engine performance and consumption. As most commercial vessels operate at "off-design" conditions and not at a single operating profile this index might not be representative of the actual environmental performance especially in the present context of robust, multi-disciplinary and multi-criteria optimization. In the herein presented Thesis and 205eviationoh work, a separate analysis is conducted with regards to the sensitivity of EEDI and its correlation with other vessel performance indices. However, the ultimate target is to assess the transport efficiency of each candidate vessel as a product of operational simulation with actual weather conditions using an Energy Efficiency Operational Index calculated from simulated voyages for each vessel candidate. This is, in turn, is set as one of the optimization targets of simulation drive optimization runs

2. Energy Efficiency Operational Index (EEOI)

The Ship Energy Efficiency Management Plan (SEEMP) establishes a mechanism to improve the energy efficiency of a ship in a cost-effective manner, providing an approach for shipping companies to manage ship and fleet efficiency performance over time. The instrument and main metric to do this is the Energy Efficiency Operational Indicator (EEOI).

The Energy Efficiency Operational Index (EEOI) is calculated in accordance with the provisions set by IMO MEPC.1/Circ.684 (International Maritime Organization (IMO), 2009) and defined as the ratio of the mass of CO₂ emitted per unit of actual transport work:

$$EEOI = \frac{M_{CO_2}}{Transport\ Work} \quad (78)$$

In the herein presented methodology the summed mass of emitted CO₂ from the vessel's operation is calculated within the simulation module for each respective trade route. Within the simulation module, the transported cargo and elapsed distance are also calculated. The EEOI is estimated for each trade route as well as for different scenarios of trade route patterns in the

vessel's lifecycle. The EEOI value minimization is one of the primary optimization targets. In addition to EEOI, a new index is also developed and assessed, expressing energy consumption in total Mega Joules per transport work $\frac{MJ}{ton \cdot mile}$.

Further analysis of the correlation between EEDI and EEOI is conducted at the end of Chapter 4 based on the optimization results.

5.3.7. Simulation Code Validation

A very important and last step prior to the deployment of the Voyage simulation code in the RHODA methodology and its application in Ship Design Optimization Studies is the validation, performance and sensitivity assessment of the latter. In more detail, the focus is on estimating the prediction accuracy of the Voyage Simulator in terms of delivered shaft power against actual data acquired onboard in accordance with the output “cleansed” data pool described in paragraph 3.3.2. The reason for having all focus on the shaft power is to reduce the number of different layers of uncertainty being inherent in the calculation. Such an example is the SFOC curve and value and their uncertainty, which despite the low magnitude of fluctuation of the latter it can introduce further deviations especially for data acquired from vessels of an older age and with questionable Main Engine performance.

The validation effort is split into two independent steps: the first concerning the data population, consolidation and packaging and the second on the replication of the Code in MATLAB and its benchmarking against big data.

5.3.7.1. Step 1: Data Population, Consolidation and Filtration

A data pool has been created from the Big Data acquired onboard as mentioned in paragraph 3.3.2. Subject data have been matched with completed voyages and synthetic data have been introduced to include additional information regarding voyage parameters not included (such as cargo type, cargo in tons, arrival and departure bunkers etc.). Following the population and consolidation of data in independent voyages a total of more than 50,000 lines of records have been gathered. The populated data have been afterwards checked for missing records or erroneous records (e.g unrealistic values for key variables) and then filtered specifically to correspond to steady-state seagoing conditions. In Table 35, the number of filters employed along with their corresponding ranges can be identified.

Measurement	Filter Variable Name	Filter Range
Speed Over Ground (knots)	SoG	>7 knots
Vessel's Operating Condition	STATUS	At Sea Excluded port, idle and manoeuvring conditions
Shaft Power	SHAFT_PWR	>10% SMCR
Rudder Angle (degrees)	Rudder_Angle_Indicator	-10 to + 10 degrees

Rudder Rate of Turn	RUDDER_ROT	-10 to +10 degrees/min
---------------------	------------	------------------------

Table 35: List of Filters applied for processing Populated Data

- The vessel’s operating condition was used in order to exclude

Upon completion of the filtration process, the resulting data pool has been reduced to 8710 lines of records for the Laden Voyages and 6426 lines of records for the Ballast Voyages.

5.3.7.2. Step 2: Code Replication in MATLAB™

The next step in the code validation process is the replication of the latter in an environment suitable for handling both the complex code with many subroutines itself and in the meantime capable of processing this large number of data which are input and benchmark vectors to the code and code output respectively. Although the data have been acquired in the form of Microsoft Excel™ spreadsheets, the handling of large number of formulae with many functions and several independent subroutines were not deemed suitable for this application. On the other hand, the use of CAESES™ can succeed in the desirable coding capabilities, however, the handling of such large volumes of data would be only possible through the customized integration of a coding and mathematical suite like MATLAB™ or Mathematica™ with an additional effort. In view of this, it was chosen to replicate the developed code of the design environment (CAESES™) in MATLAB™ and perform the entire validation study there.

A major and important note at this point is the philosophy of speed governance within the code. As the voyage simulation module is an elaborate high-frequency vessel powering assessment code and given that the main and heaviest correlated variable to the speed all power estimations have the latter as the main parameter. The differentiation point here however is how speed is ordered. On one hand, in current shipping operational practices, the vessel receives an ordered speed from charterers and the operation department of the shipping company and uses a constant RPM approach for attaining minimum speed (sometimes exceeding it). Although this a proven seamanship practice, there is some improvement that can be attained from this and the reader can further elaborate on Constant Speed voyage optimization solutions and equipment in the literature (LEAN MARINE, 2022). From the other hand, the developed code in CAESES uses the desired transit speed (Speed Over Ground / SoG and same as typical Charter Party Agreements for which more information is provided in the paragraph) as input and with a constant speed approach calculates the different RPM and Power Output from the vessel and its Main Engine. The code validation speed governance philosophy however has to balance between remaining as true as possible to the actual code and blending of formulae employed in the RHODA method and the matching of the ordered speed from the data is benchmarked against. For this particular reason, it has been chosen at this point to use a speed-centric calculation that however employs a

transformation of the ordered speed from the ordered RPM of the acquired data. The data are transformed using a reversed speed/ RPM curve from the sea trials of each concerned vessel to transform the ordered RPM to ordered speed which is latter processed in the same way as in the code itself.

5.3.7.3. Step 3: Results and Comparison with actual operating Data

Having the target to validate and define the accuracy as well as the sensitivity of the simulation code deployed in RHODA, the response of the replicated code in MATLAB™ in terms of estimated Delivered Shaft power (in kW), Speed Over Ground (SoG) and Speed Through Water (StW) using RPM as an input has been compared with the actual measurements of power (as obtained from the onboard torque meter) and Speed as obtained from the DGPS readings of SoG and Speed Log readings of StW.

The various voyages have been separated in segments to avoid overshoot values at the beginning and end of each one and problems of data non-continuity.

Voyage 1 – Laden Condition

From Figure 90 for Voyage 1 in Laden condition, it is evident that there is a very good agreement between the predicted power (orange timeline) and the recorded values (blue timeline). Power peaks are mostly accurately predicted showcasing also the good dynamic response of the code, while there is an overestimation for a period of recording which is attributed to incorrect capturing of the current speed. This is further supported when looking at the timeline of the power deviation (Figure 91) according to which only in one instance there is an underprediction of 25% while for the rest of the recorded time, all predictions are within a 5-10% margin of accuracy. The prediction accuracy of the SoG is also satisfactory as seen in Figure 92 with the blue timeline corresponding to the actual measurement, while the orange timeline represents the estimated values. In Figure 93 illustrating the distribution of deviation of estimated SoG some peak areas are identified as marked. Such areas are stoppages of the vessel that due to asynchronous data logging haven't been filtered out in the Step 2 process. The rest of the high deviations are attributed to distortions from the current velocity and direction.

Such deviations are better identified in Figure 94 depicting the estimated vs. actual StW. At this point, it should be stressed that the onboard measurement of Speed through water is done with the use of the Speed Log which is a device of low fidelity as due to its location on the vessel peaks it can produce incorrect readings caused by air bubbles trapped under the flat bottom areas. The same can be also seen from the distribution graph of Figure 95. When looking closer, however, it is evident that most of the deviations have an order of magnitude below 10%.

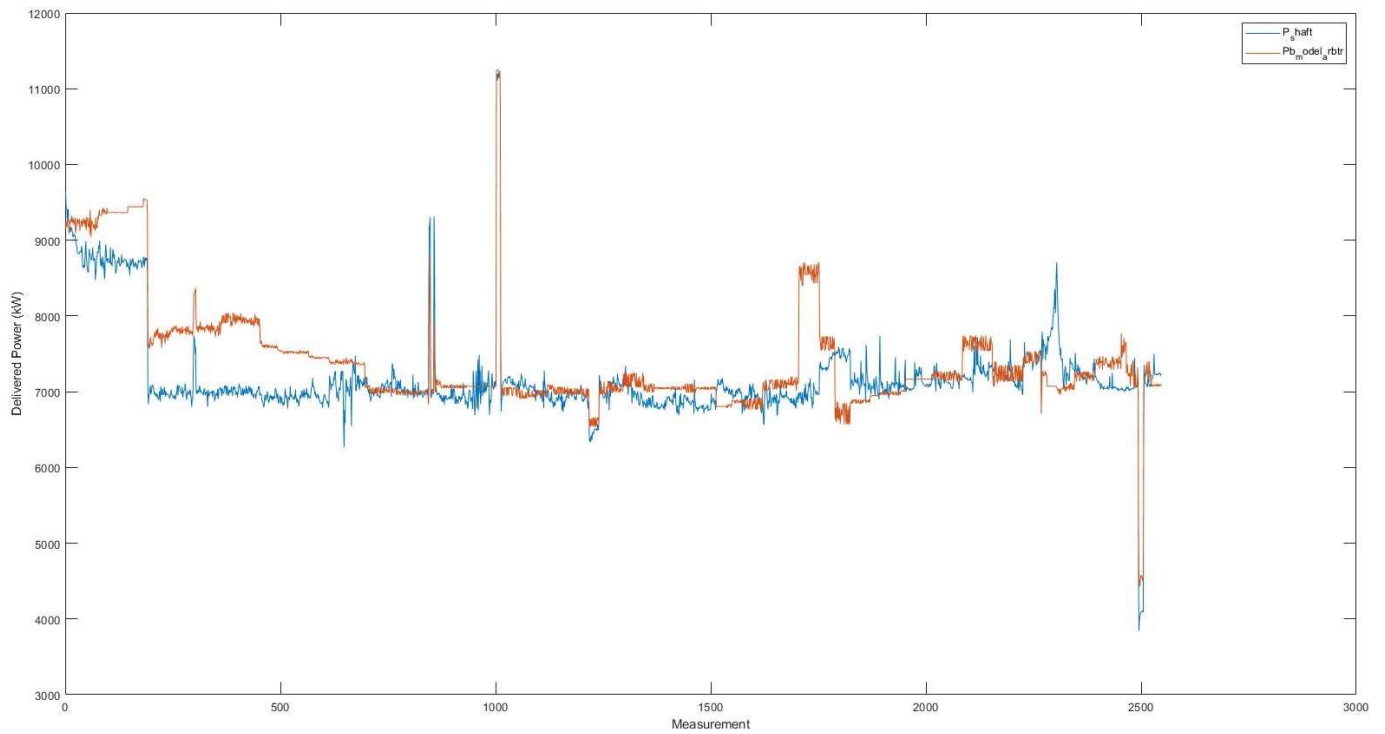


Figure 90: Timeline of Predicted vs. Actual Delivered Power (Pb in kW) – LADEN / VOYAGE 1

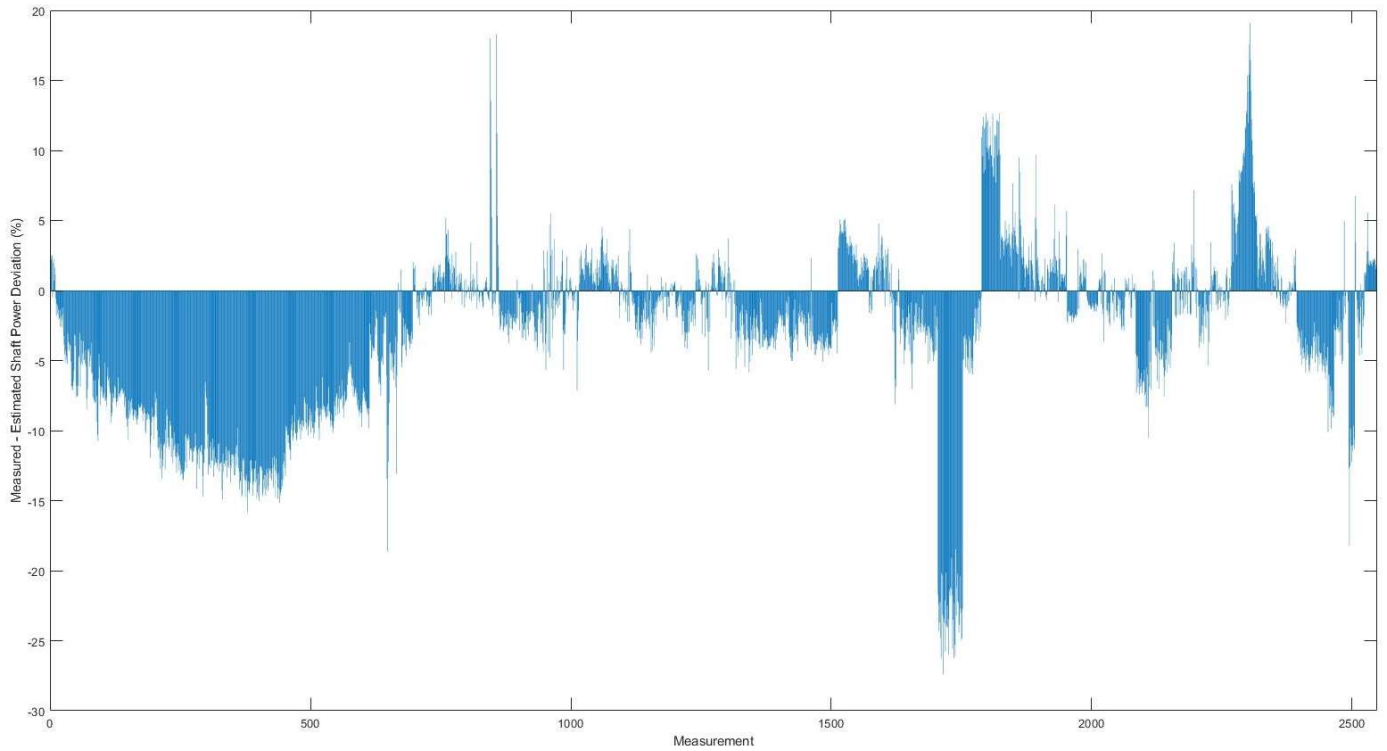


Figure 91: Timeline of Deviation of Estimated Shaft Power (%) – LADEN / VOYAGE 1

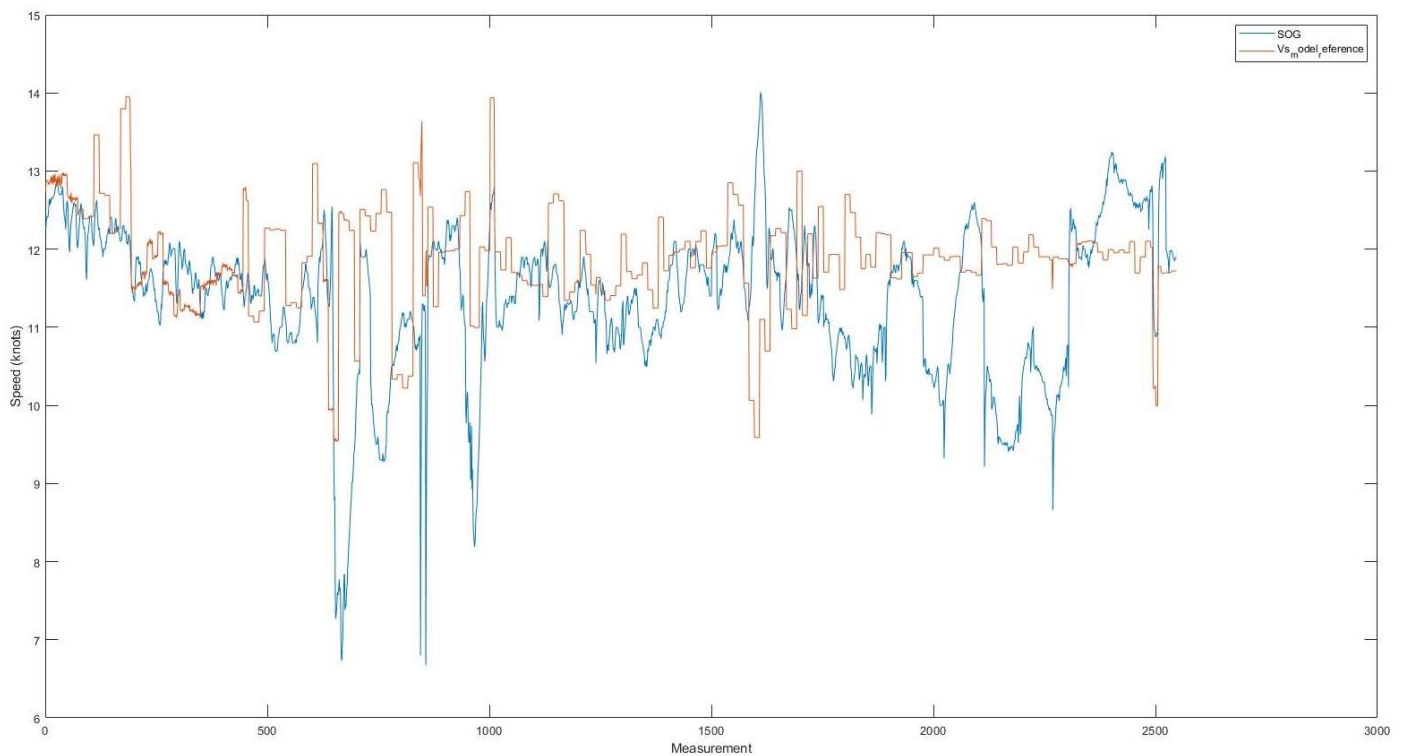


Figure 92: Timeline of Predicted vs. Actual Speed Over Ground (SOG in knots) – LADEN / VOYAGE 1

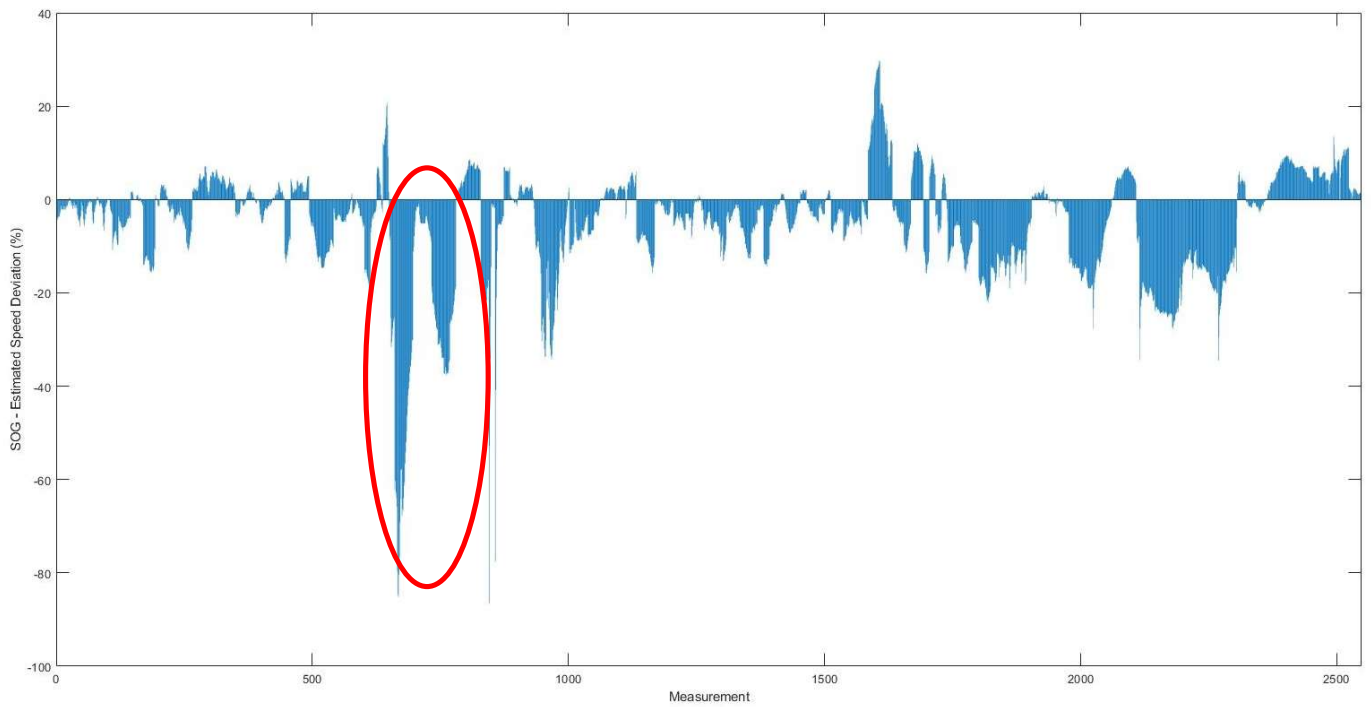


Figure 93: Timeline of SOG Estimation Deviation (%) – LADEN / VOYAGE 1

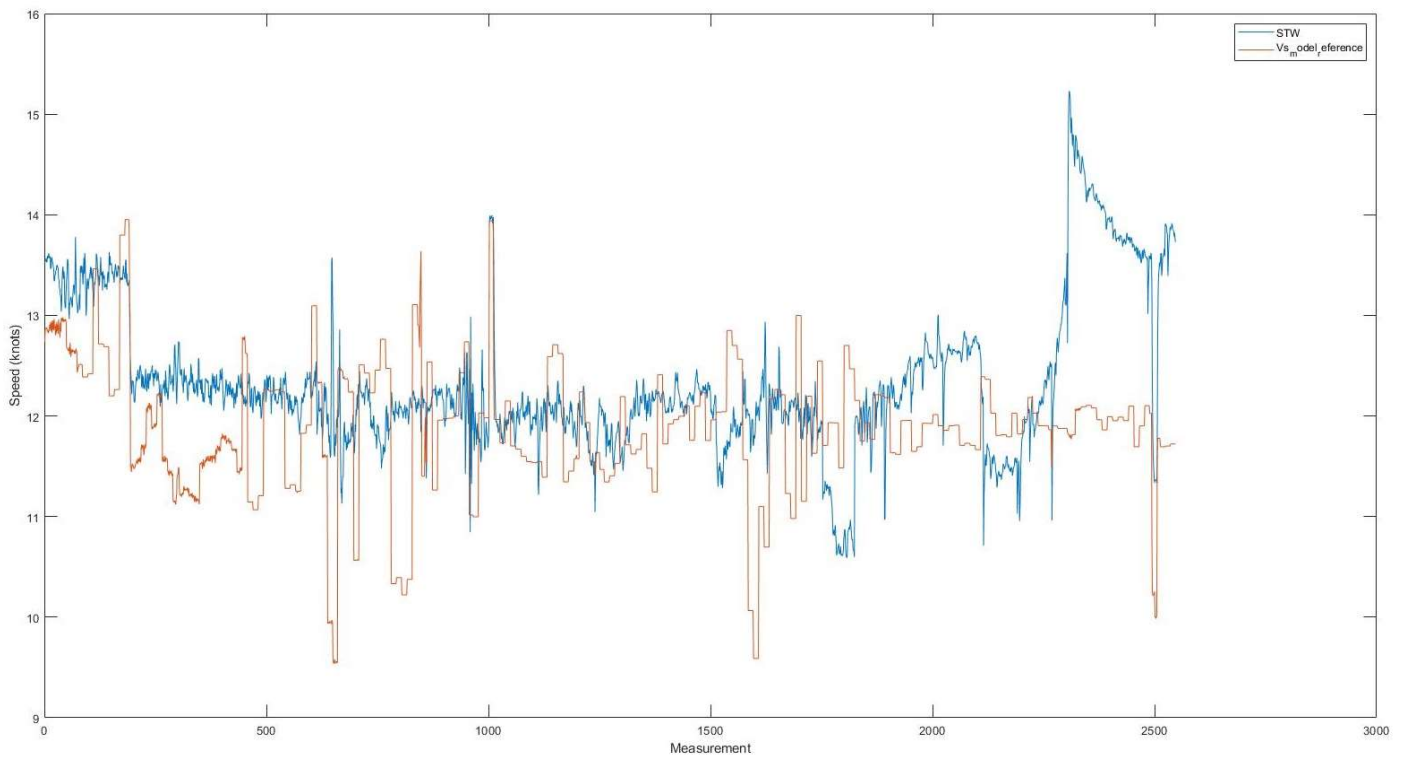


Figure 94: Timeline of Estimated vs. Actual Speed Through Water (STW in knots) – LADEN / VOYAGE 1

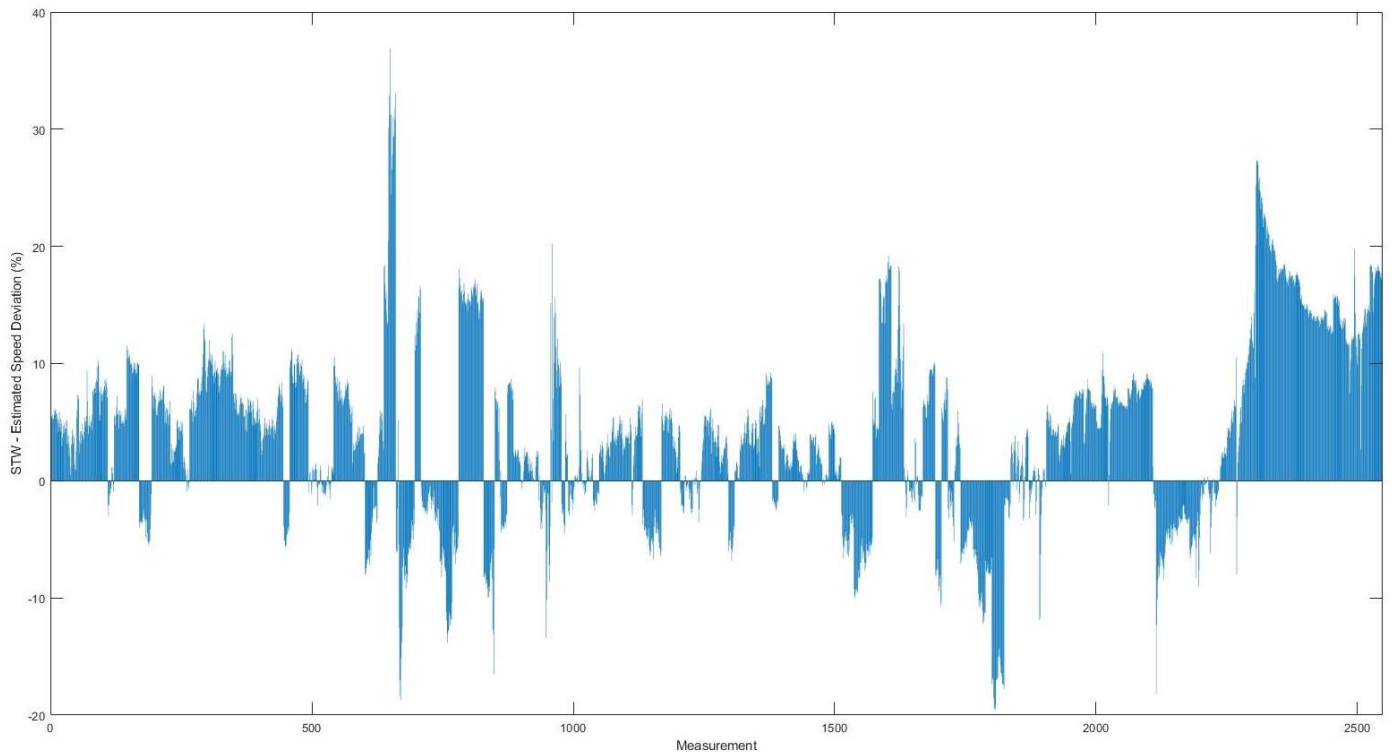


Figure 95: Timeline of STW Deviation (%) – LADEN / VOYAGE 1

Voyage 2 – Laden

From Figure 96 through Figure 101 the equivalent study can be identified for the 2nd laden voyage examined. An interesting observation for this case is that with regards to power prediction fidelity, an initial big deviation is identified. As the measurement of shaft power illustrates a peak that sharply decays, the attributed reason for such a deviation is the rapid acceleration of the engine. Acceleration phenomena typically distort the power readings when correlated to the corresponding RPM values. That is why their publication of (Tsitsilonis & Theotokatos, 2018) filter our acceleration phenomena using recommendations from engine builders on the rate of change of the Main Engine Power over time as a filter. If the timeline of the deviation is closely observed in Figure 97, apart from the first deviation peak, the rest of the timeline is kept at reasonable levels. To elaborate more on this, a frequency distribution graph (histogram in Figure 98) has been produced to understand the distribution of deviation for the given voyage. Interestingly, the most frequent readings are at 0-2% and the majority of the deviations are kept within the $\pm 5\%$ region. From Figure 99, the estimated SoG versus the actual is following similar patterns however is overestimated by the code as a general tendency, as witnessed also by the timeline of deviation Figure 100. Lastly, the estimation of Speed Through Water as seen in Figure 101 is considered to have a good fidelity and generally very similar trending with the exception

of a single drop of speed from actual measurements which is attributed to the momentary error of the Speed Log measurement.

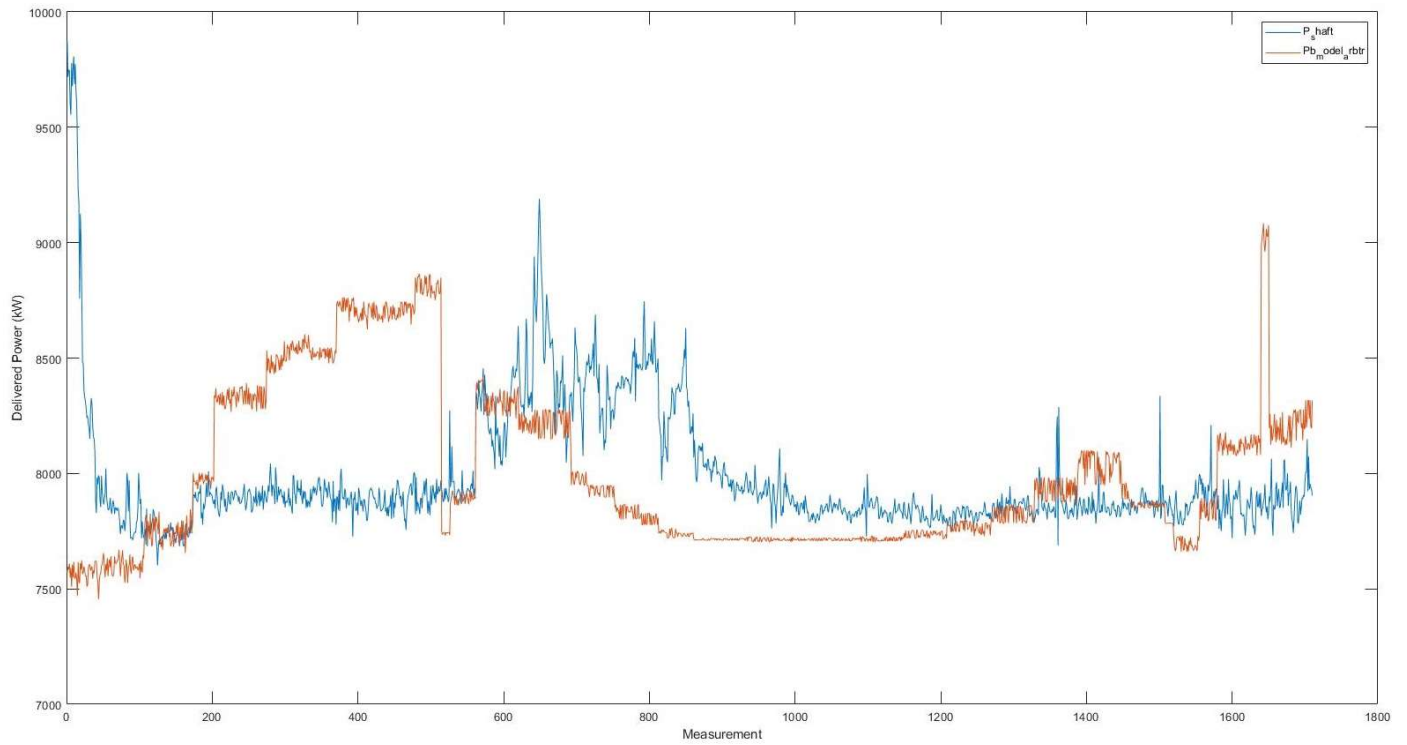


Figure 96: Timeline of Predicted vs. Actual Delivered Power (P_b in kW) – LADEN / VOYAGE 2

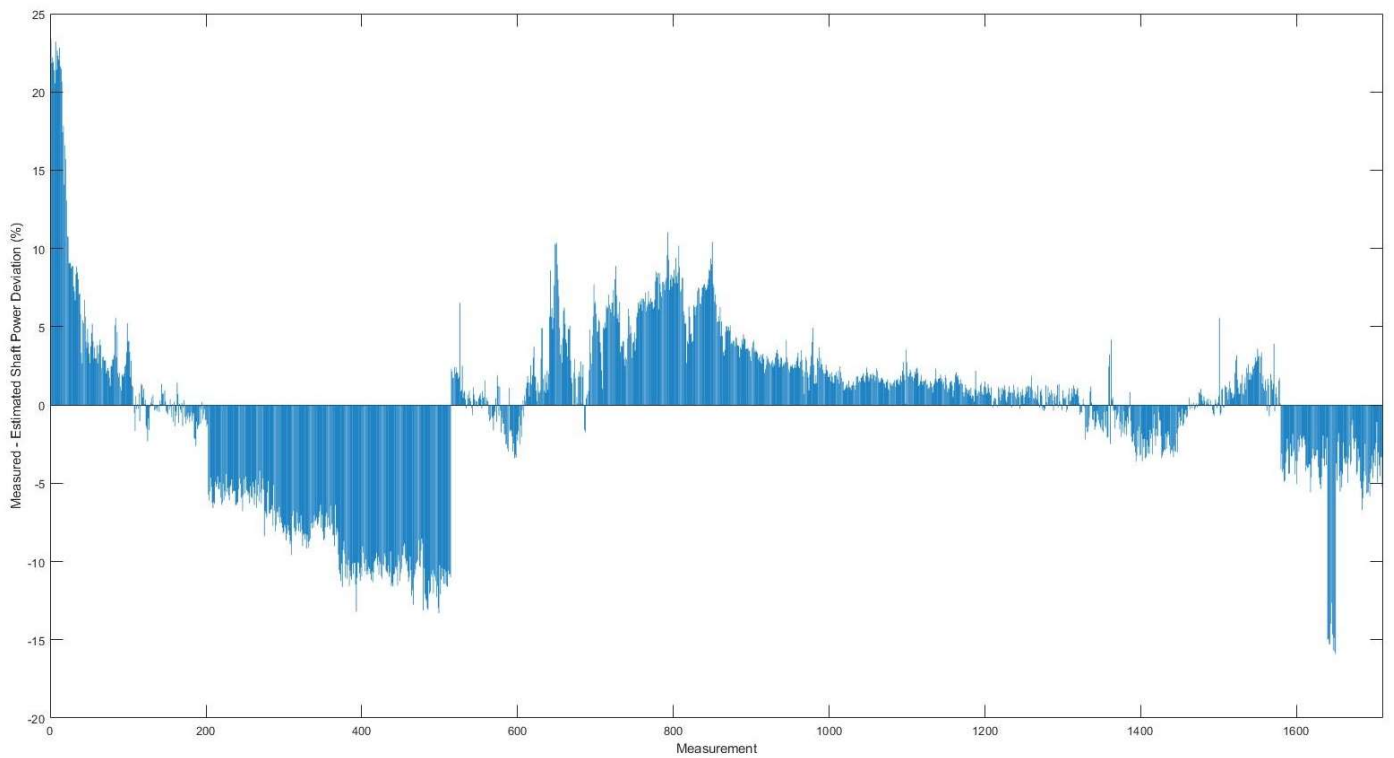


Figure 97: Timeline of Delivered Power Deviation (%) – LADEN / VOYAGE 2

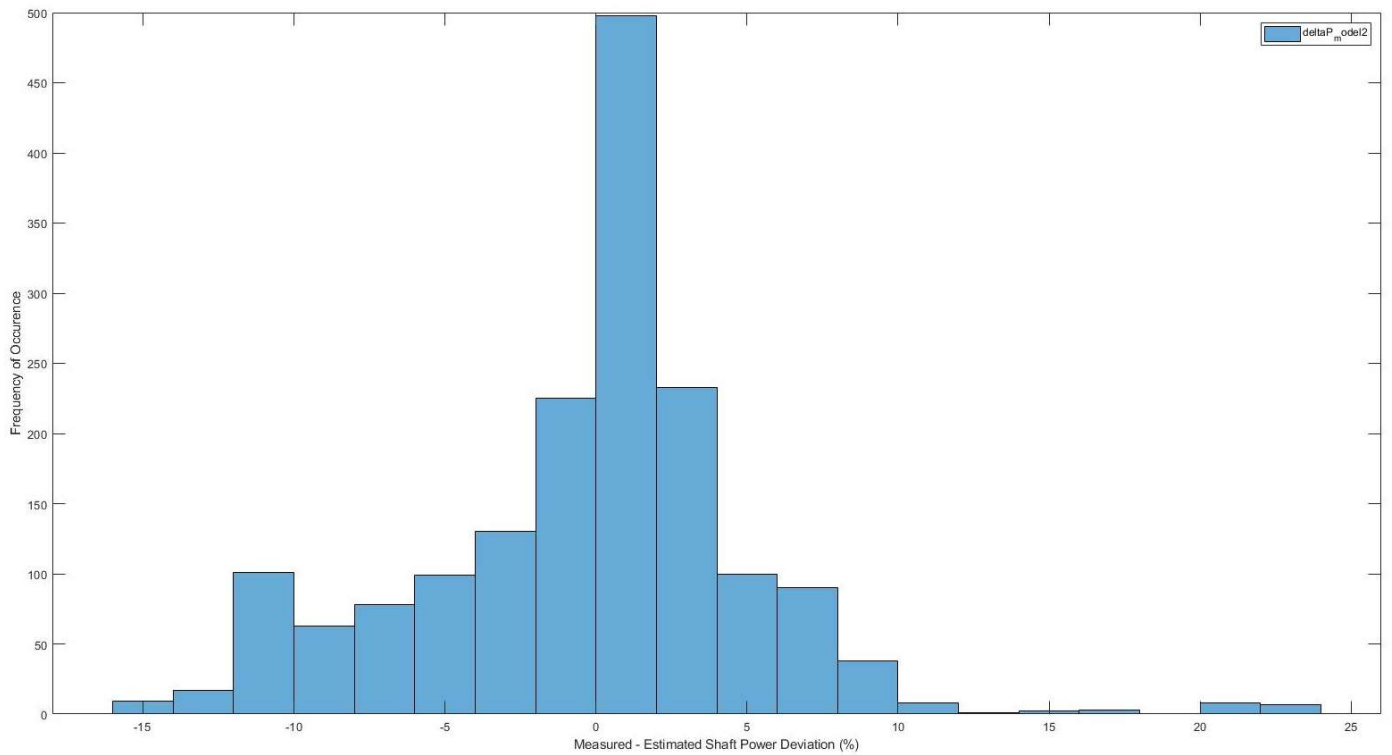


Figure 98: Frequency Distribution (Histogram) of Shaft Power Deviation – LADEN / VOYAGE 2

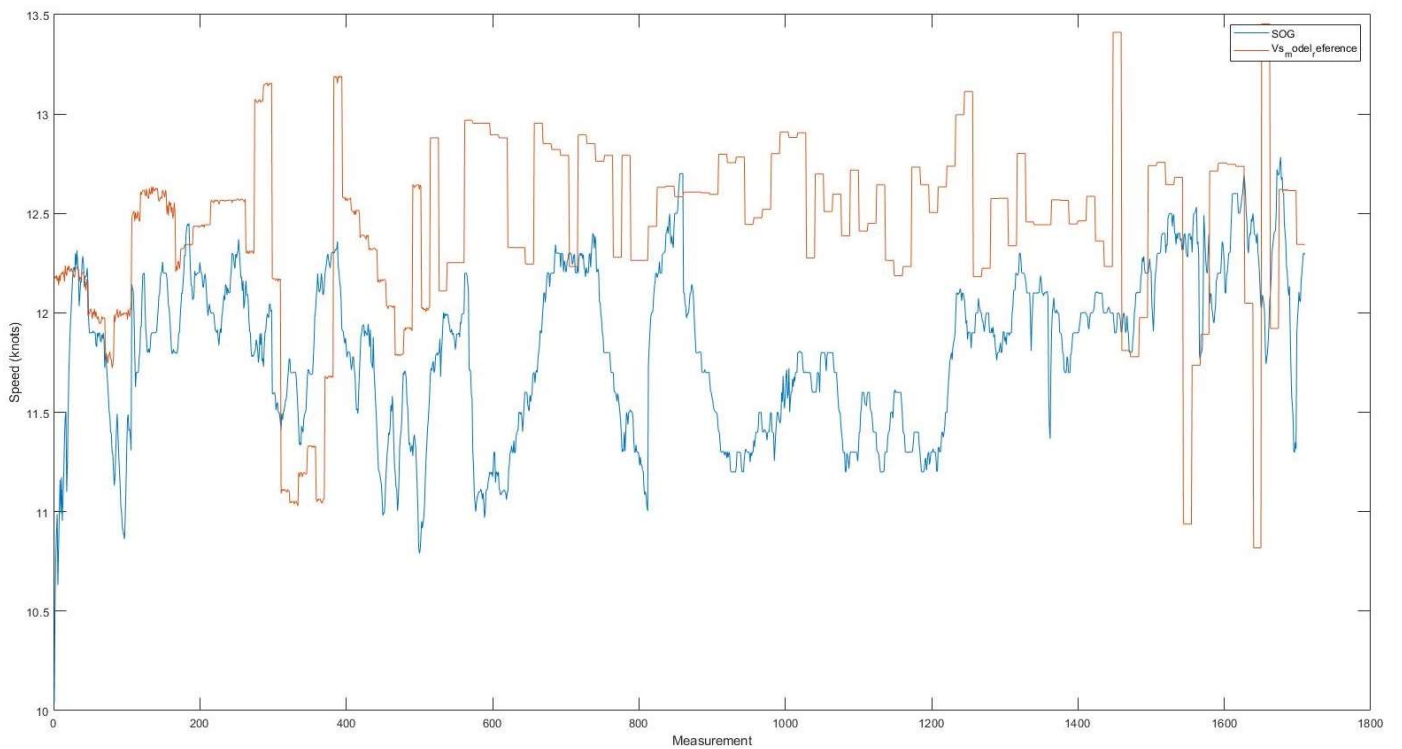


Figure 99: Timeline of Estimated vs. Actual Speed Over Ground (SOG in knots) – LADEN / VOYAGE 2

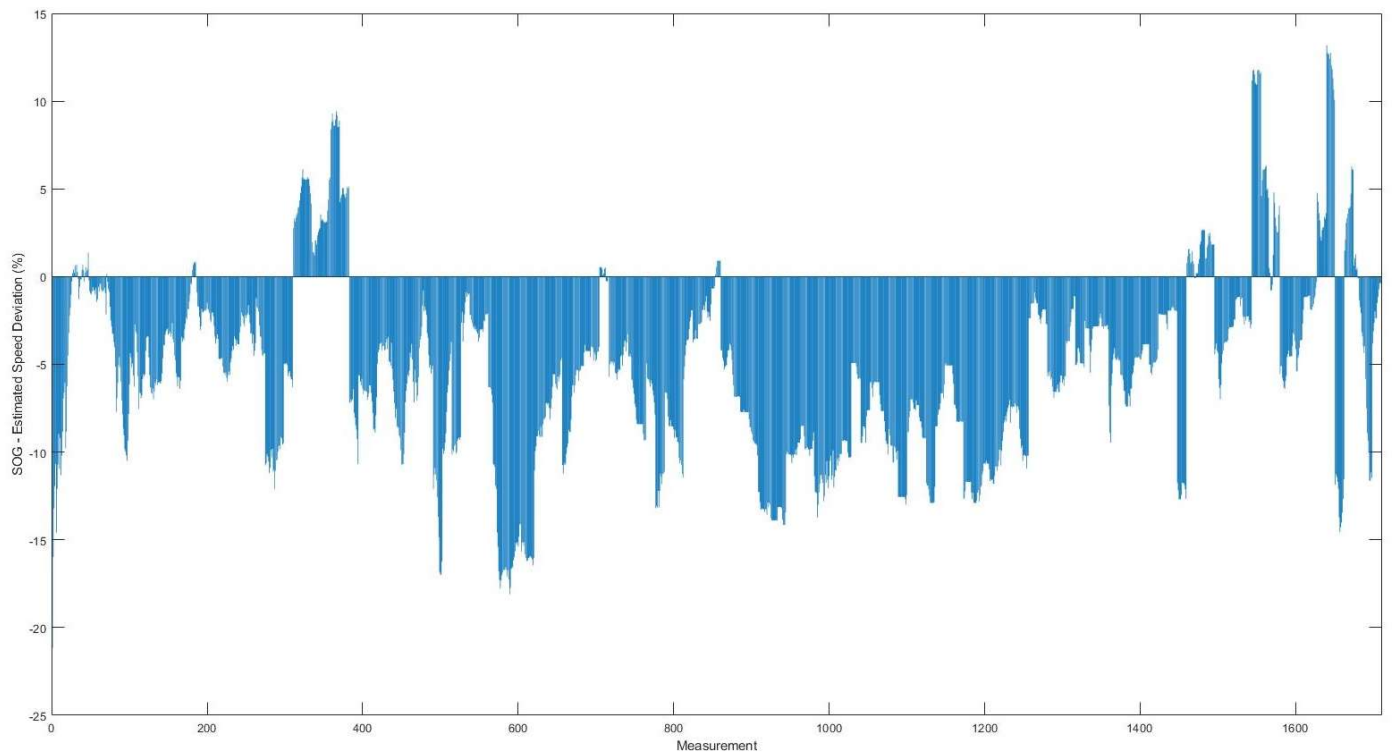


Figure 100: Timeline of Speed Over ground (SoG) Deviation (%) – LADEN / VOYAGE 2

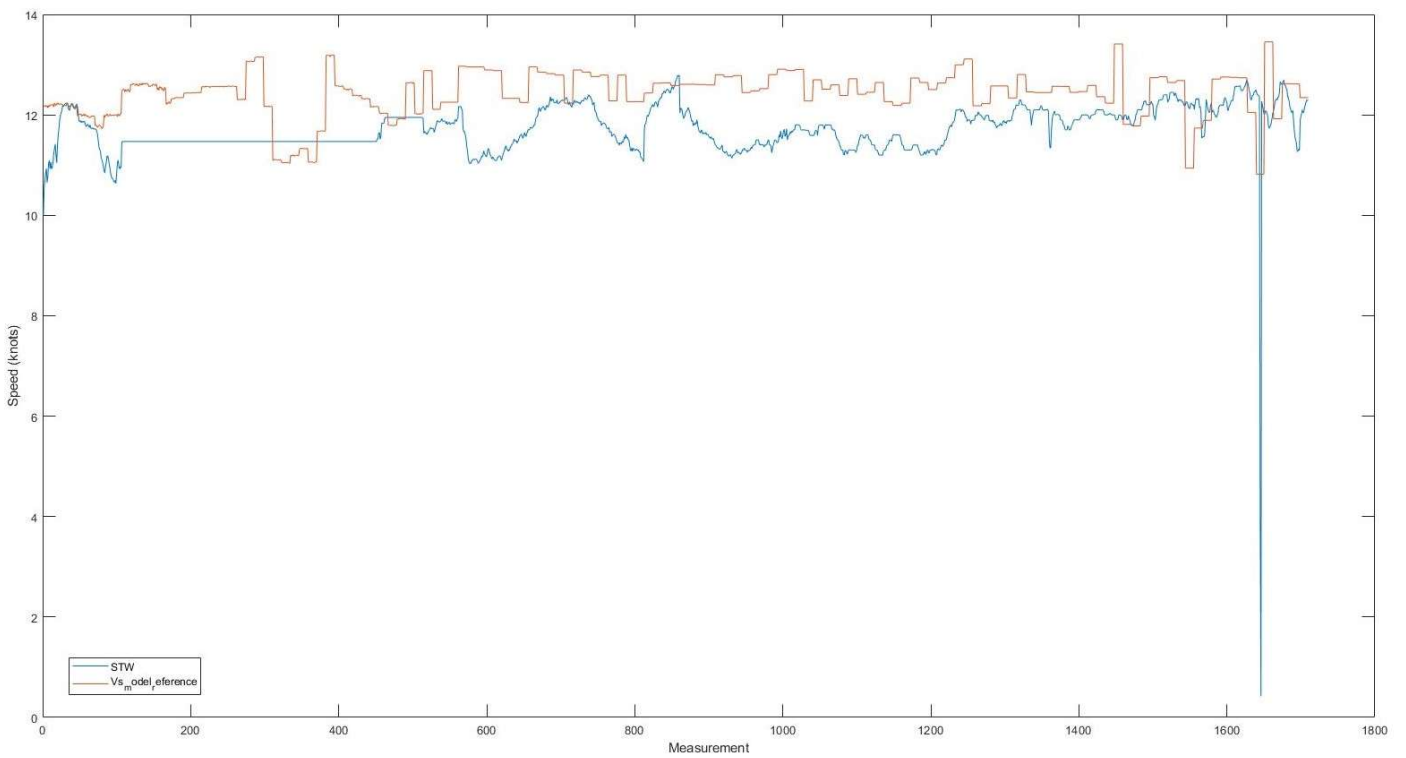


Figure 101: Timeline of Estimated vs. Actual Speed Through Water (STW in knots) – LADEN / VOYAGE 2

Voyage 1 – Ballast

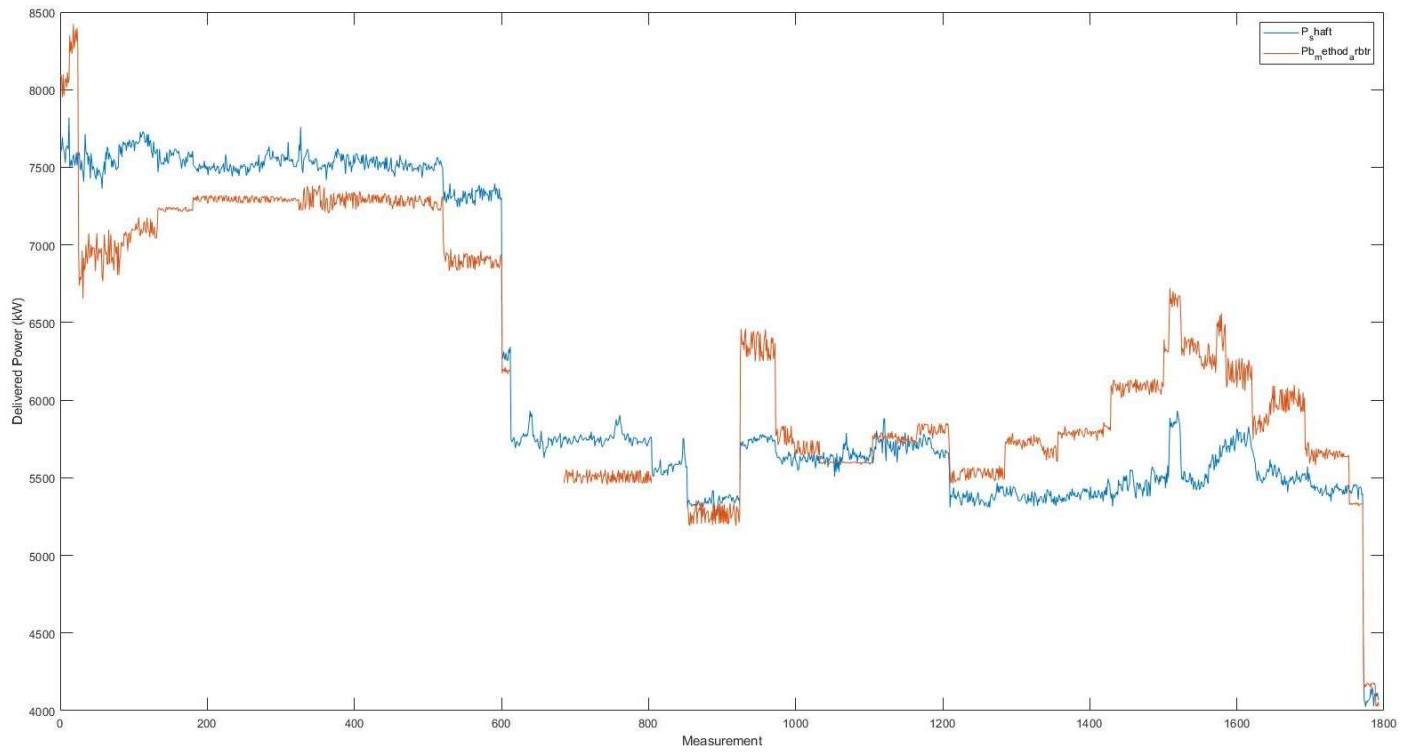


Figure 102: Timeline of Predicted vs. Actual Delivered Power (Pb in kW) – BALLAST / VOYAGE 1

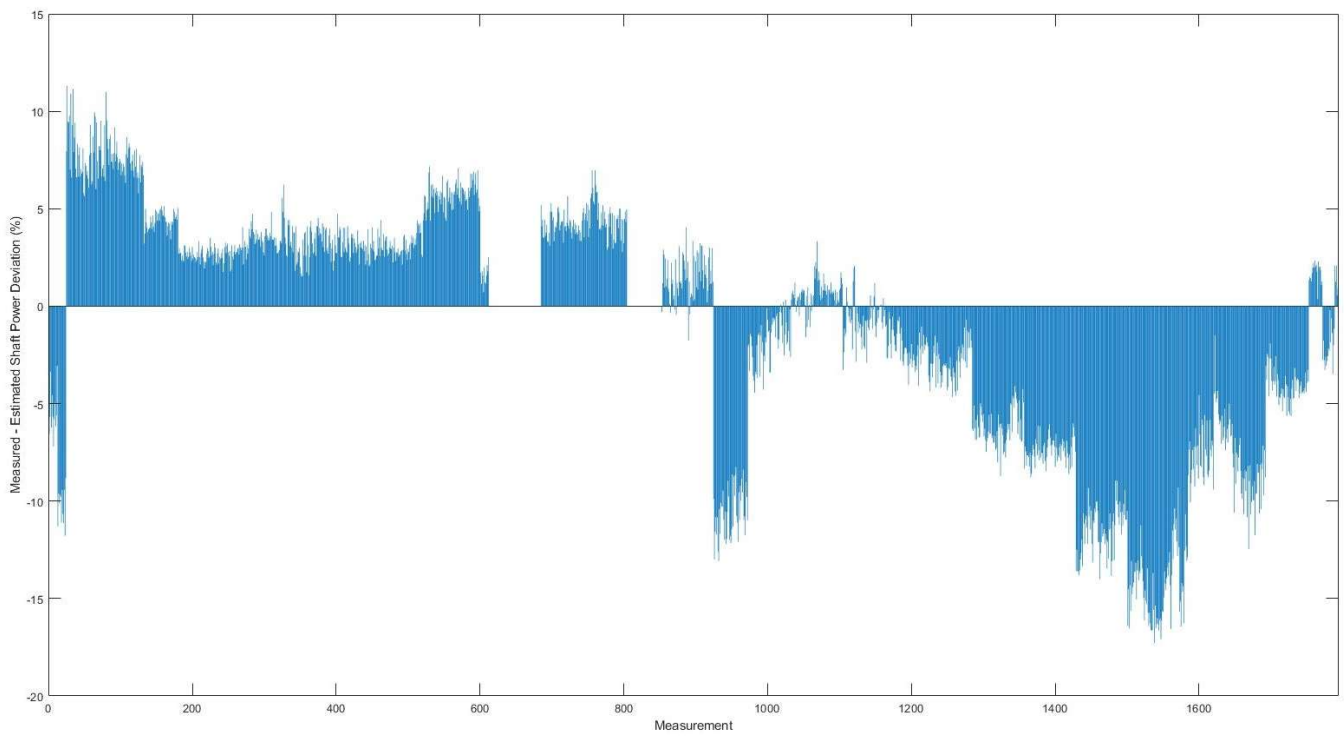


Figure 103: Timeline of Delivered Power Deviation (%) – BALLAST/ VOYAGE 1

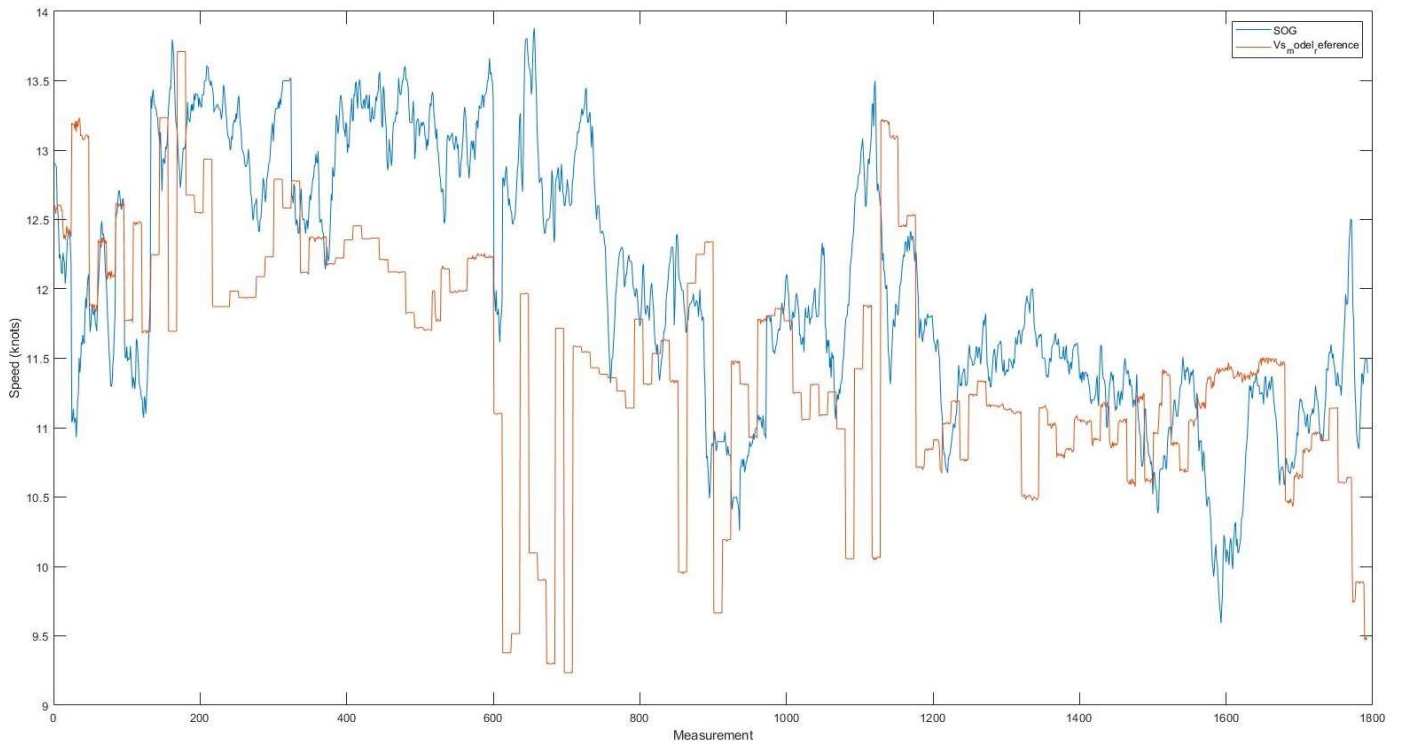


Figure 104: Timeline of Estimated vs. Actual Speed Over Ground (SoG in knots) – BALLAT / VOYAGE 1

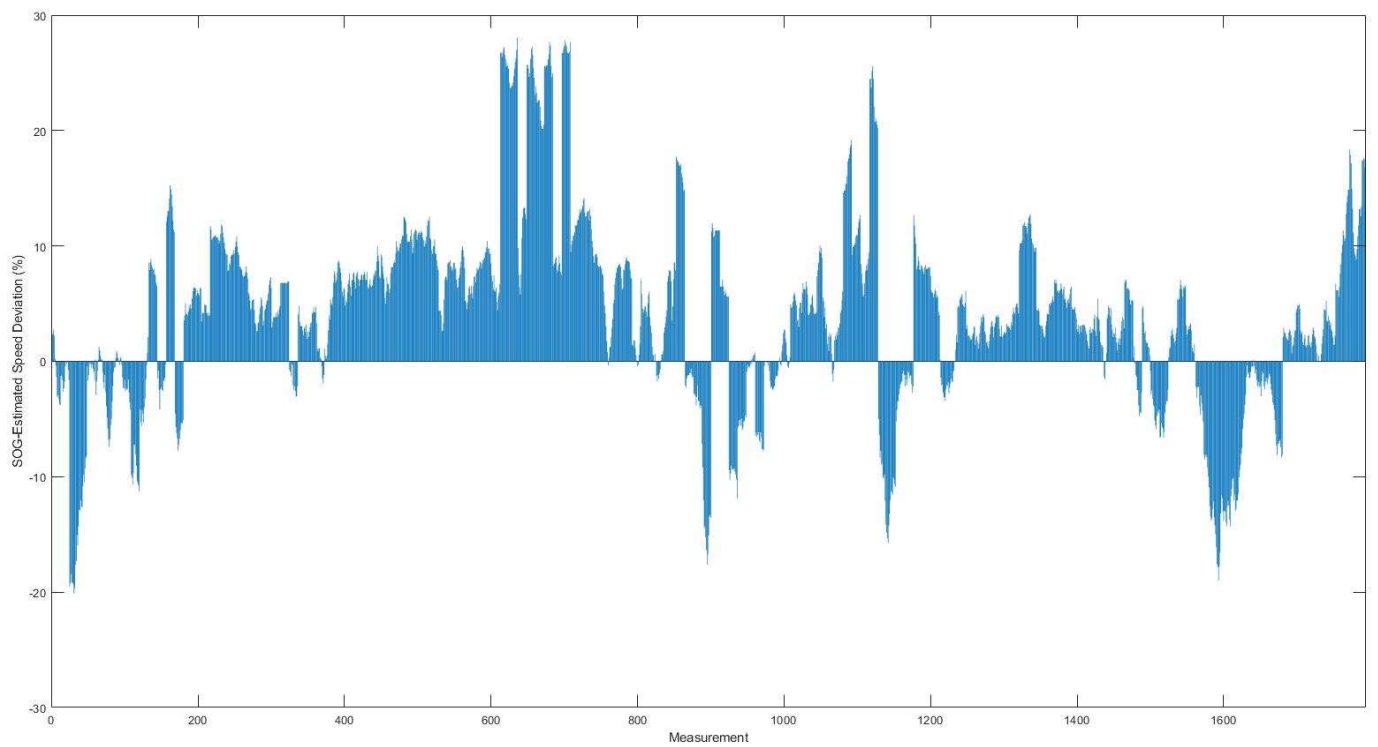


Figure 105: Timeline of Speed Over ground (SoG) Deviation (%) – BALLAST / VOYAGE 1

From Figure 102 to Figure 105, the results of the timelines of the data resulting from approximation/estimation using the RHODA simulation module versus the equivalent actual data are witnessed for Voyage 1 in Ballast condition. As it is evident the delivered power (Figure 102) has a strong agreement and all power peaks and fluctuations are well captured by synthetic data with the prediction falling at the $\pm 5\%$ of the actual value with few exceptions reaching 10% deviation (Figure 103). The prediction of Speed Over Ground (SoG) is also accurate but to a lesser extent as witnessed from the timelines of Figure 104 as well as the time evolution of the deviation between simulated and actual data. The main reasons for such deviations are the following:

1. Current direction and velocity of the matched satellite hindcast data is not the one actually witnessed by the ship's hull. The development of sea currents in general is very dynamic and can be fluctuating significantly within meters away from the ship's location and heading. That is also a reason for the absence of generalized joint probability distribution models per geographical area for this environmental parameter similar to the ones existing for wind and waves and used in the research successfully (DNV, October 2010).
2. The actual geometry of the waterline in ballast condition is harder to predict and thus gives accurate predictions for calm water resistance and propulsion factors than in laden condition.
3. The measured and logged values of the speed log might have an asynchronous logging with the data acquisition device onboard the ship.

Considering the above two points, the prediction especially with regards to the delivered power is considered acceptable.

Voyage 2 – Ballast

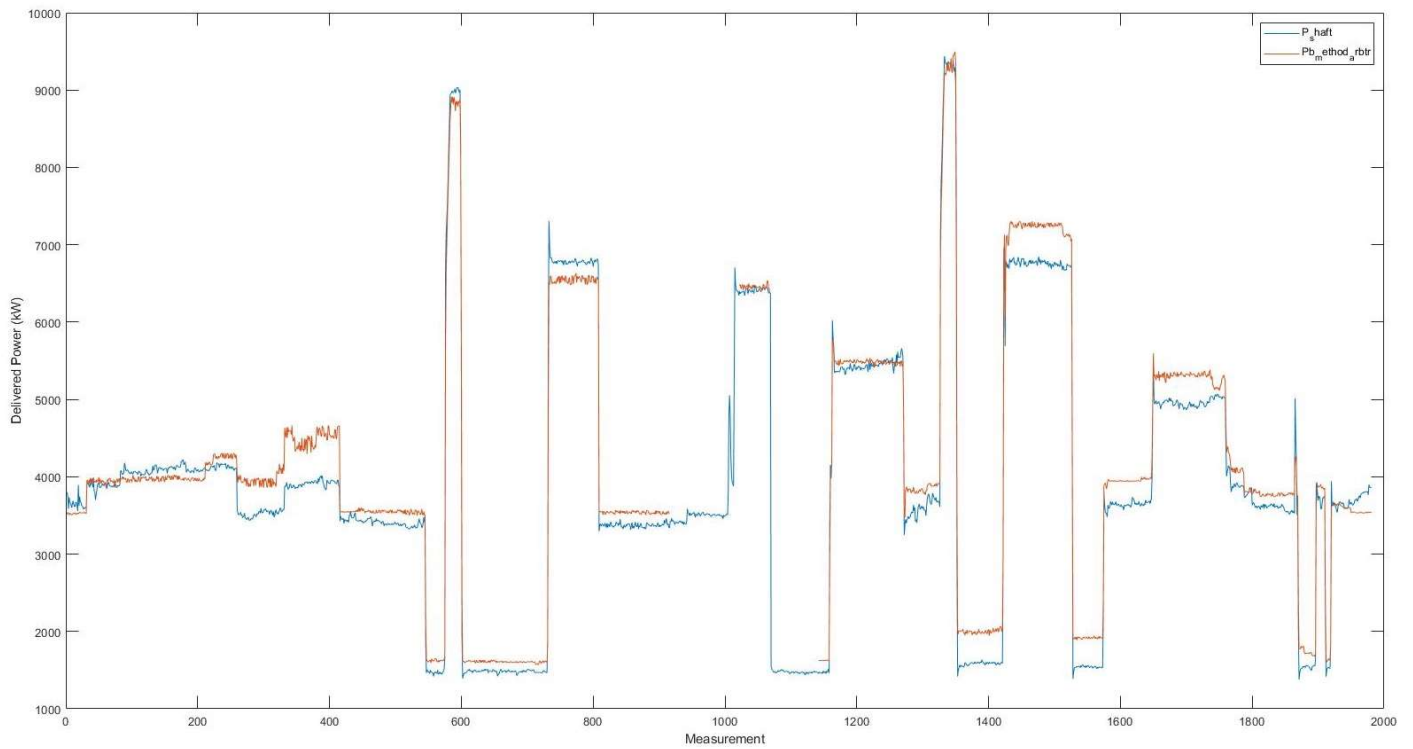


Figure 106: Timeline of Predicted vs. Actual Delivered Power (Pb in kW) – BALLAST / VOYAGE 2

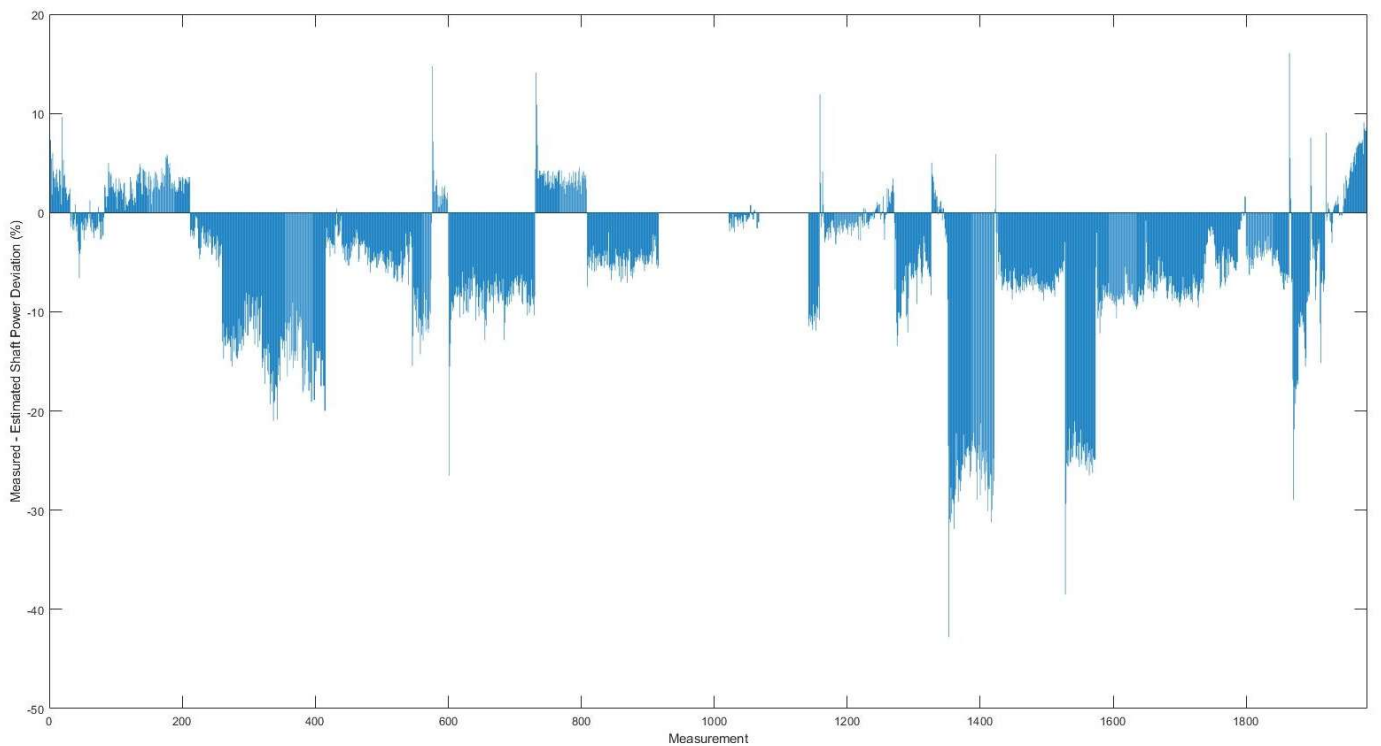


Figure 107: Timeline of Delivered Power Deviation (%) – BALLAST/ VOYAGE 2

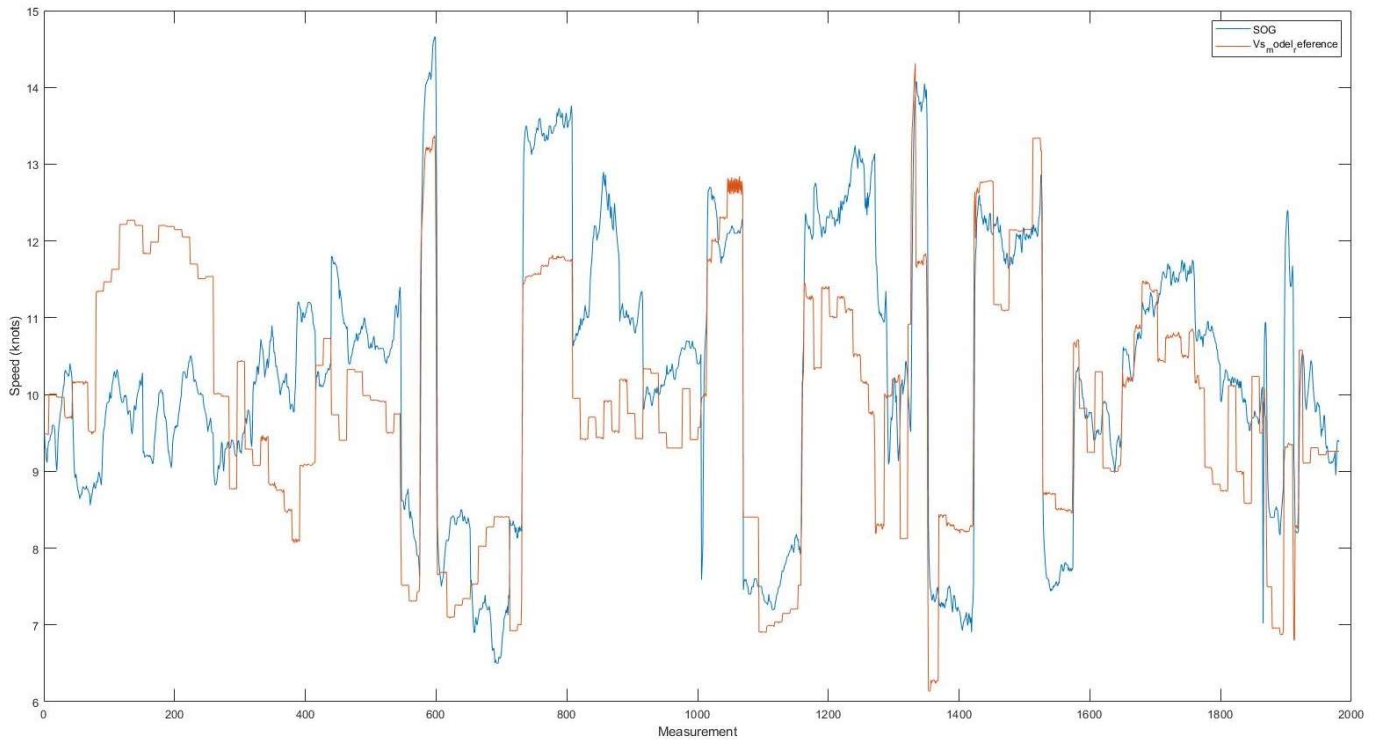


Figure 108: Timeline of Estimated vs. Actual Speed Over Ground (SoG in knots) – BALLAT / VOYAGE 2

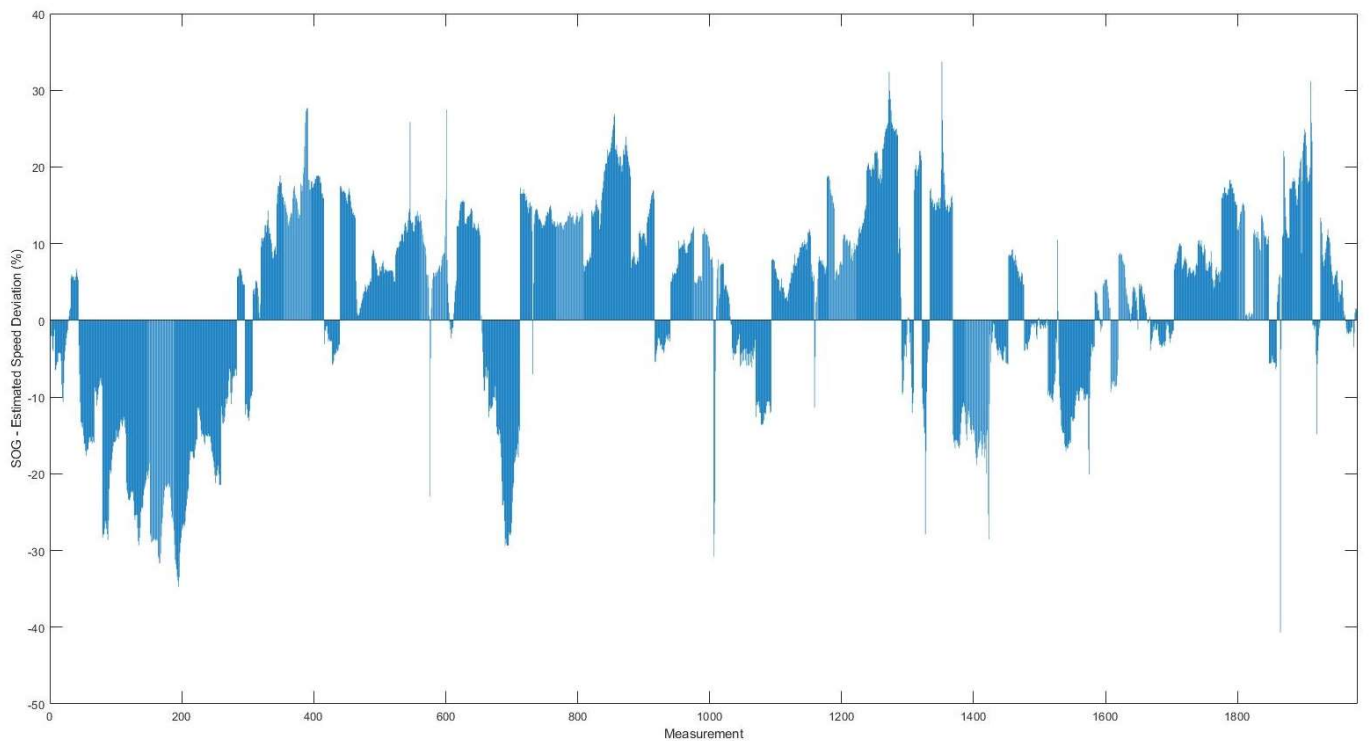


Figure 109: Timeline of Speed Over ground (SoG) Deviation (%) – BALLAST / VOYAGE 2

The pattern of the predictions observed in Ballast Voyage 1 is similar to the ones in Voyage 2 as per Figure 106 to Figure 109. The delivered power (Figure 106), has an even stronger agreement for this voyage with all simulated values falling very close to the actual respective ones. Again all power peaks and fluctuations are well captured by synthetic data with the prediction falling at the $\pm 5\%$ of the actual value with few exception reaching 15% deviation (Figure [108]). With the exception of the first 200 loggings in the timeline, the rest of the SoG predictions are also in very good agreement with actual data, an improvement compared to Voyage 1 predictions as seen in Figure 108. This is also confirmed in Figure 109, where after the first 200 loggings, the simulated data are very close to the actual with a maximum 10% underestimation (generally underestimated). The deviation of the first 200 loggings, is a typical case of improper matching of the satellite hindcast of the current direction and velocity as the speed figures are distorted and opposite to the actual with a 30% deviation.

Voyage 3 – Ballast

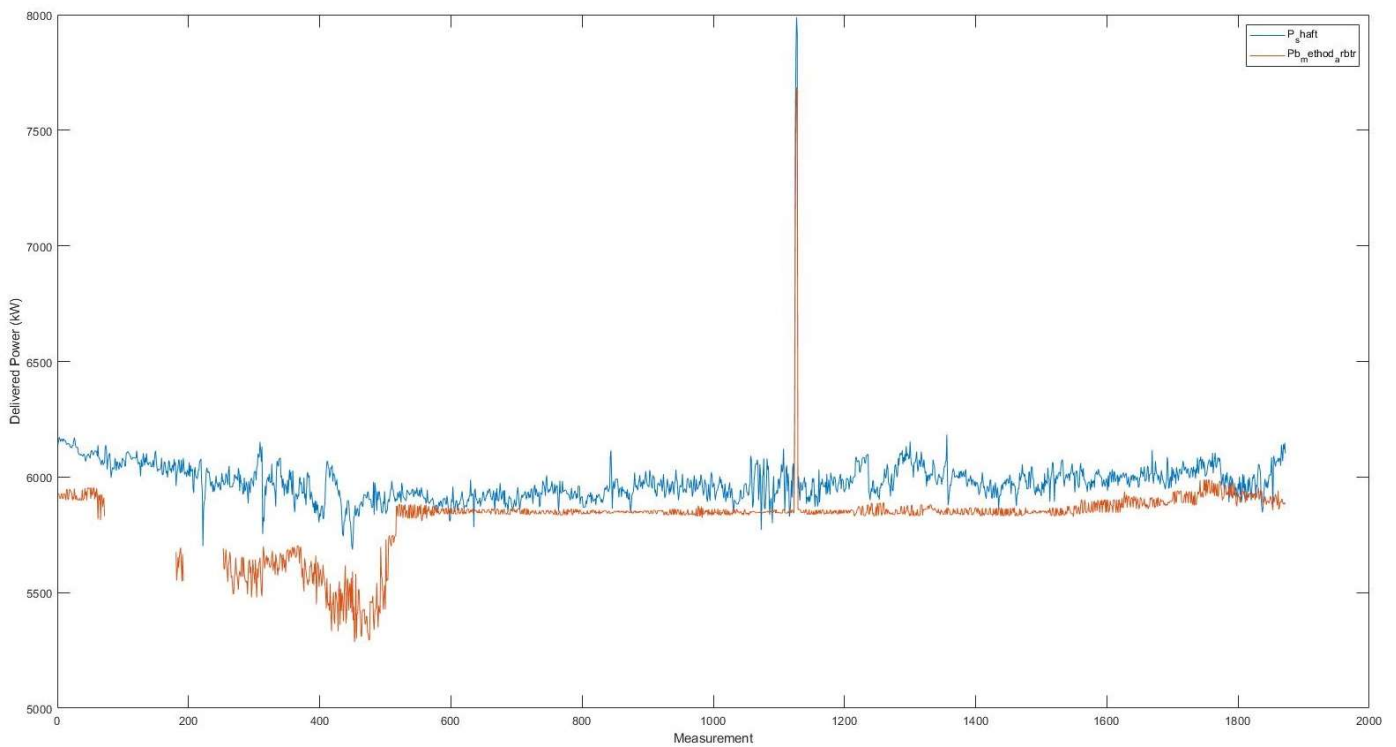


Figure 110: Timeline of Predicted vs. Actual Delivered Power (Pb in kW) – BALLAST / VOYAGE 3

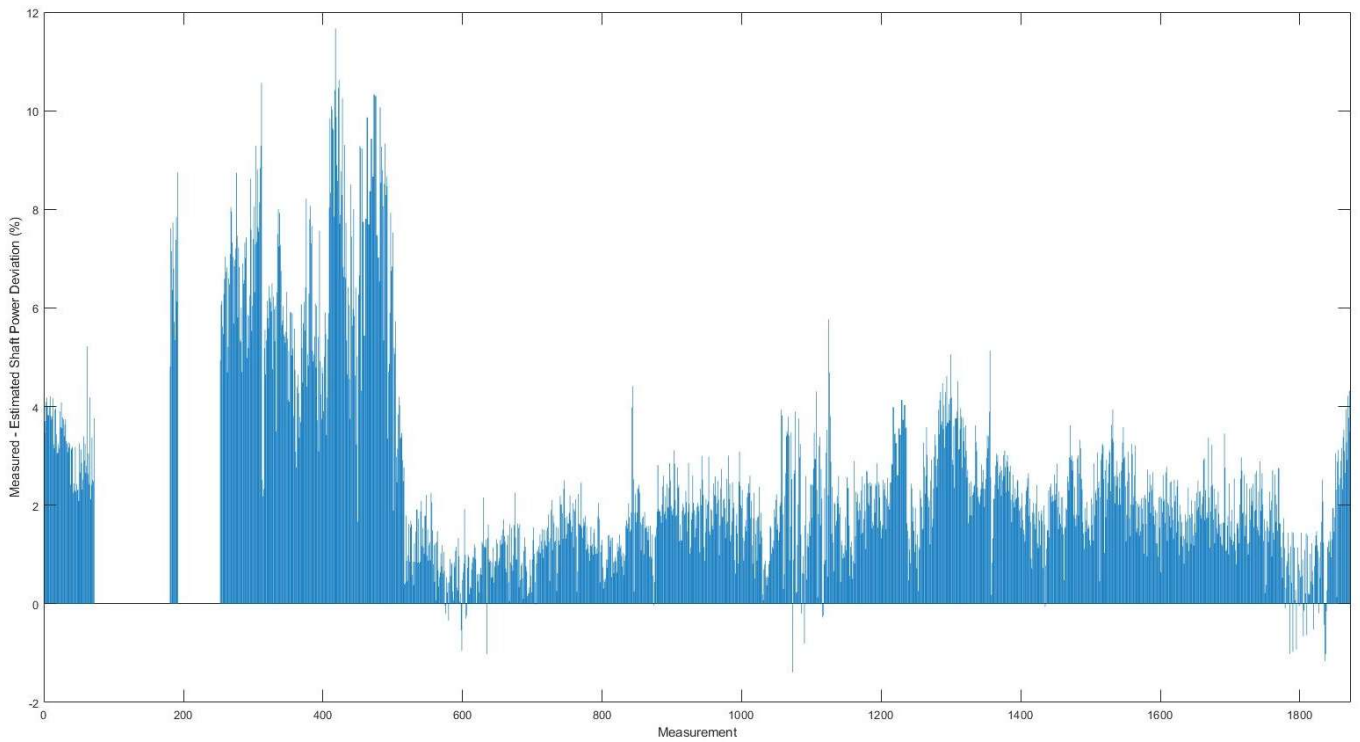


Figure 111: Timeline of Delivered Power Deviation (%) – BALLAST/ VOYAGE 3

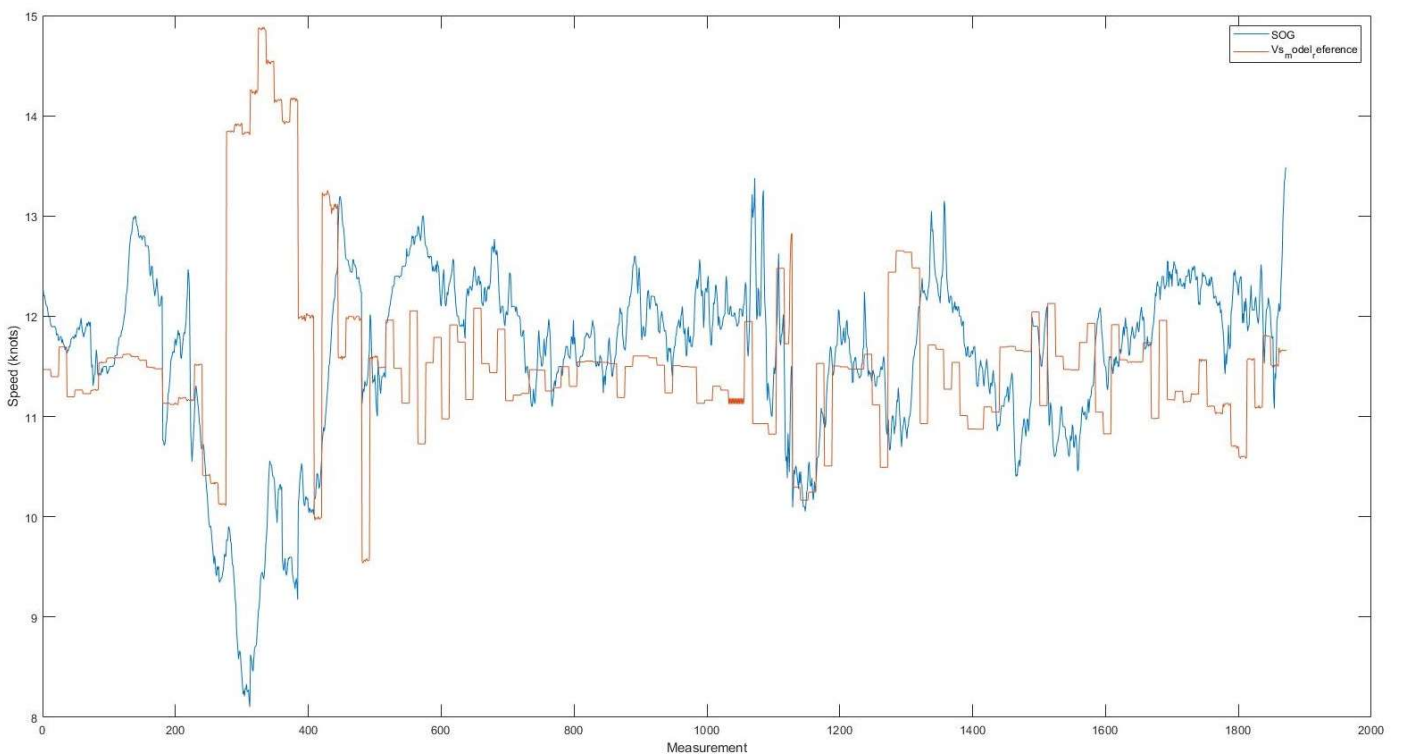


Figure 112: Timeline of Estimated vs. Actual Speed Over Ground (SoG in knots) – BALLAT / VOYAGE 3

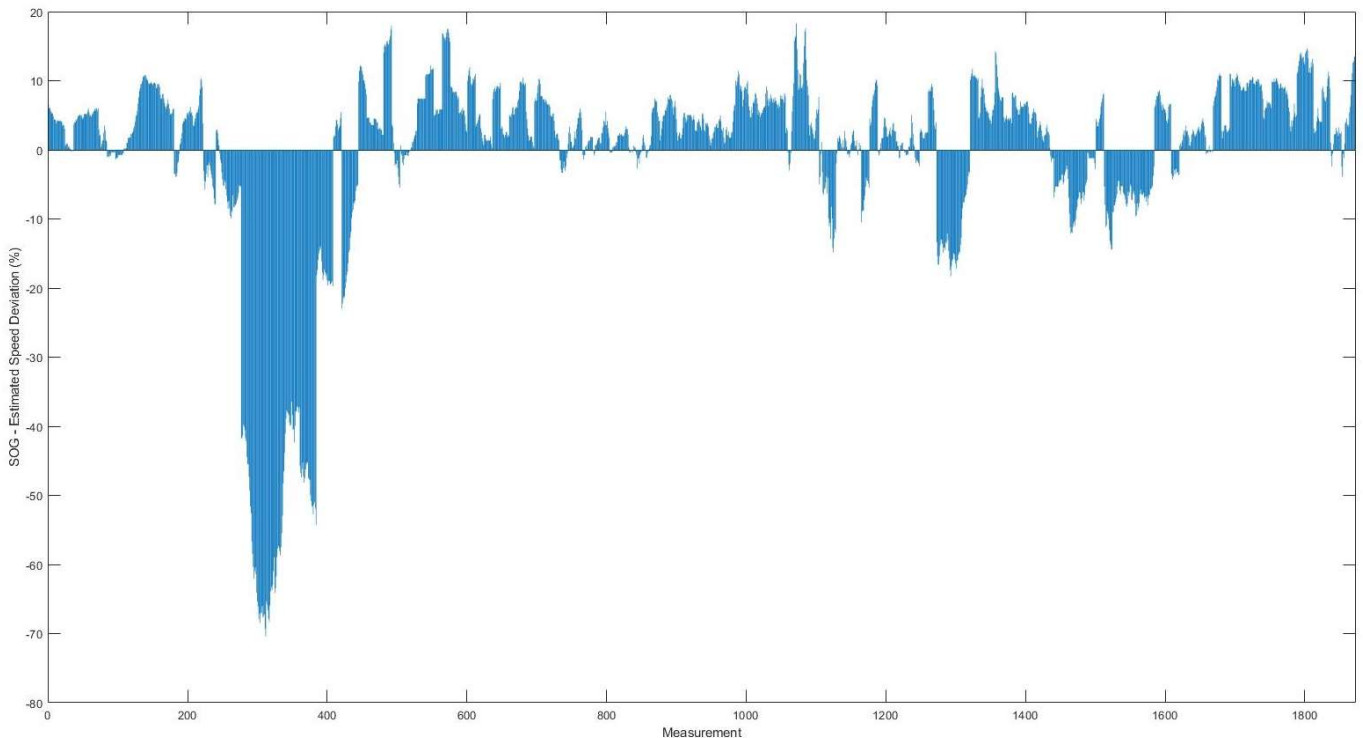


Figure 113: Timeline of Speed Over ground (SoG) Deviation (%) – BALLAST / VOYAGE 2

Lastly, the timelines of the simulated vs. actual results for Voyage 3 in Ballast condition are seen in Figure 110 to Figure 113. The delivered power simulated values have the same pattern with actual data (Figure 110) with the exception of a systematic underprediction. The power surge observed in the 1100th datapoint region observed from actual data is very accurately predicted by the simulation module as well. As a result, again the deviation of the predicted power is not more than 4% for the majority of the timeline showcasing the strong power estimation capabilities of the RHODA simulation tool. In terms of SoG prediction, with the exception of an incorrect prediction at the region of 300th loggings (same case as in 200th logging incorrect prediction for Voyage 2) there is also a good agreement (Figure 112) with all deviations falling in the range between 5% overprediction and 10% underprediction. The region around 300th loggings has a considerable deviation of 70% which is attributed to the following reasons:

1. Incorrect readings from speed log and GPS and incorrect logging of the latter.
2. Incorrect matching of current direction and velocity of the satellite hindcast data.

5.3.7.4. Conclusions for Simulation Code Validity

From the analysis conducted in Chapter 5.3.7 of the herein presented Thesis and its corresponding results the following conclusions can be withdrawn:

1. The simulation module that will be deployed within RHODA and the application of the latter in Ship Preliminary design optimization studies produces very strong predictions of the delivered power when compared to actual data harvested from high-frequency data acquisition devices on a fleet of vessels with the same design as the parent vessel for this study.
2. The RHODA simulation module also produces strong predictions for the Speed Over Ground and Speed Through Water when compared with actual fleet high-frequency data.
3. All power peaks, surges and generic power trends are captured by RHODA by a very big majority. Individual deviations during isolated and narrow timeline periods can be attributed to the following reasons:
 - a. Main Engine RPM fluctuation and engine acceleration phenomena are not filtered out in the data cleansing stage.
 - b. Vessel stoppages (short) are not being filtered out in the data cleansing stage.
 - c. Asynchronous data logging of the measuring instrument/sensor (in this case M/E torquemeters) with the data acquisition device onboard. This can happen due to different data harvesting frequencies between the sensor and the alarm monitoring system (AMS) of the vessel as well as between the AMS and the data acquisition device. In general, for this study, 30sec data have been used. As the data frequency is higher such asynchronous data logging events will be more frequent.
 - d. Accuracy of measuring sensors. Torque meters in general are accurate measuring devices that require annual calibration to retain their measuring fidelity. The issue with power meter readings has been also addressed in the ISO 15016 standard for sea trials where two measurement instruments are used (ISO15016:2015, 2015).
4. Issues with SoG and StW prediction are encountered more frequently, however from the distributions produced they are at an acceptable level. Such deviations can be attributed to the following reasons:
 - a. Low fidelity of measuring devices and especially the speed log, with measurements being affected by bubbles entrapment in the flat bottom region as well as development of slime in the sensor area.
 - b. Incorrect matching of satellite hindcast data and dynamic fluctuation of sea currents' direction and velocity.

- c. Other dynamic phenomena developed.
5. In general, since the timeline evolution trends are all captured by the RHODA simulation model, only systematic low-magnitude deviation issues are observed. These are not an issue since systematic prediction deviations will not influence or distort any ranking among optimization variants and members of the design cloud population and will be carried over as systematic errors acceptable within the preliminary and basic design stages.
6. The very accurately estimated delivered power is the primary basis of formulation of the energy demand and emissions. Speed plays also a very important, but secondary role during the formation of the efficiency rate as it is the basis for creating the energy rate (in ton-miles) and thus overall efficiency.
7. The synthetic data produced by RHODA are a very good approximation of the actual operating data and thus the simulation module of RHODA can produce very accurate results for the voyage result and deployed in optimization studies
8. From Chapter 3.3 that describes the simulation environment developed a key novelty of the Thesis is evident. There has been no such application of high-level of detail, comprehensive and accurate dynamic simulation systems in Ship Design Environments making the RHODA approach proposed a novel tool and method for future ship designs that due to exogenous factors require an examination of the entire vessel operation and lifecycle for producing efficient and economic designs.
9. The simulation approach can be also edited and adapted for use as a basis for future vessel performance assessment studies similar to the attempts made by (Liu, et al., 2020) and (Tsitsilonis & Theotokatos, 2018)

Chapter 6: Bulk Carrier Optimization Case Studies

When focusing on the dry bulk cargo transportation, the carriage of major bulk commodities, i.e. iron ore, coal and grain the iron ore and coal dominate this market. According to the United Nations UNCTAD Report (UNCTAD, 2017), in 2017 a record 1,364 million tons of iron ore and 1,142 million tons of coals have been transported by sea. The total dry bulk seaborne trade in 2017 totalled 4,827 million tons making iron ore and coal the dominant commodities with 28.3% and 23.7% of the total trade. The bilateral trade for the two major commodities is in fact very specific. On one hand, the Chinese economy poses a constant demand for iron (for construction) and coal (for energy). On the other hand, the major iron ore exporters are located in South America (primarily Brazil) and Australia, while coal production in order of mil tons is concentrated in Indonesia, Australia and Russia with 383, 301, and 314 mil tons respectively. The present paper focuses on vessels intended for this trade which can be grouped in the Capesize / Very Large Ore Carrier (VLOC) segment of the shipping market. The design of such (and all) bulk carriers in general for the past decade (2008-2018) focused on the increase of efficiency by two means: increase of cargo-carrying capacity and decrease of energy demands. In most cases the optimization, if any, is based on a single design point in terms of both speed and loading condition (draft and thus displacement) by the alternation of the local geometrical characteristics only.

6.1. Parent Vessel

A parent, baseline vessel is herein used as a primary source of reference as well as calibration for the methodology and all the formulas/computations applied in the latter. The vessel chosen for this study belongs to the relevant recent segment of Newcastlemax Bulkers and is a newly delivered vessel (2015). The baseline parametric geometry has been adapted to fit the hull form lines available. As previously mentioned, (Paragraph 5.1), the model test results of the subject vessel were used to calibrate and better adapt Holtrop statistical methodology for the prediction of powering along the entire speed-power curve. The principal particulars of the vessel can be found in the below Table 36:

Baseline Vessel Principal Particulars	
Length overall	299.98
Length between perpendiculars	294
Beam	50
Scantling Draft	18.5
Deck Height	25
Cb	0.8521
Main Engine Specified MCR (kW)	17494 @ 78.7 RPM / MAN B&W 6G70ME-C9.2
Deadweight (tons)	Abt 208,000
Lightship Weight (tons)	26,120
Cargo Hold Capacity (m ³)	224,712.1

Table 36: Baseline Vessel Principal Particulars

The parent vessel features a “full” hull with high Cb, corresponding to operations at low speeds (smaller than 0.1Fn), and featuring a long parallel midbody, almost symmetric to the middle section, transom stern and almost vertical stem profile with a minimized to zero bulbous bow overhang. However, fore-end sections have bulb characteristics. A small flair is applied for waterlines above the summer draft, while the Flat Bottom surface is relatively slender at the fore area and aft ends. The hull was imported into the design environment with the use of an “.iges” file. Using the parent hull non-parametric, deterministic surfaces as a template, a set of fully parametric surfaces were generated to match the parent hull using the integrated capabilities of the CAESES® platform and the tools included within the Geometric core of the methodologies.

The cargo hold arrangement (Figure 114 to Figure 116) is spatially defined first by the position of the Engine Room and Collision (fore) bulkhead, the frame spacing and the number of cargo holds. With these variables, the longitudinal compartmentation is defined. The arrangement of the cargo holds follows the typical compartmentation of single skin Bulk Carriers built under the IACS Harmonized Common Structural Rules (CSR) with a transverse system for structural design. Each cargo hold has a tank top defined by the double bottom height and the extent of the hopper areas. The hopper is defined by its width (running length) and angle starting from the tank top and terminating at the side shell. The hopper line is used as a generator for the parametric surface corresponding to the hopper plating, while the side shell surface uses the Lackenby surface information available. For each cargo hold, also a topside wing tank is arranged which is defined by the slopping plate. The slopping plate parametric surface is generated by a parametric straight line starting from the side shell and terminating at the hatch coaming opening. This line is defined by the topside tank width and topside tank height which are optimization variables. For each bulkhead position, an upper and lower stool is provided and defined parametrically.

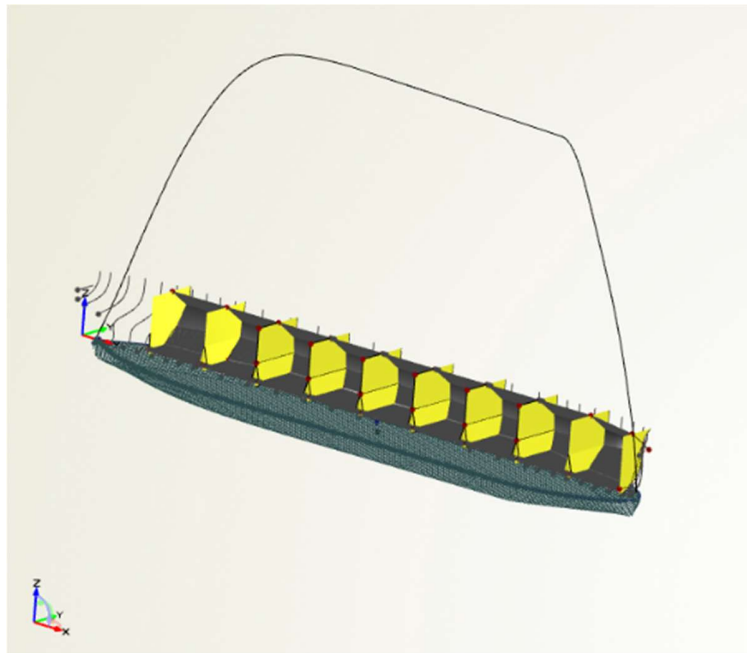


Figure 114: Parametric Cargo Hold Surfaces in CAESSES®

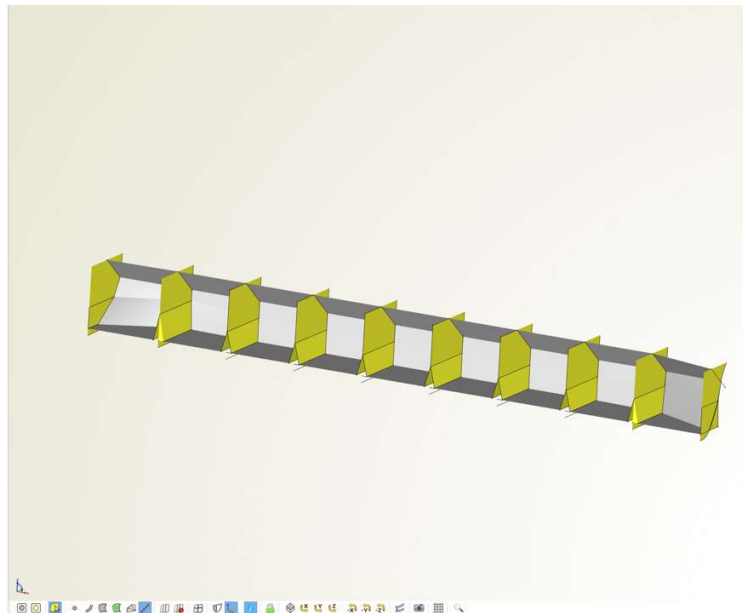


Figure 115: Parametric Cargo Hold Surfaces in CAESES®

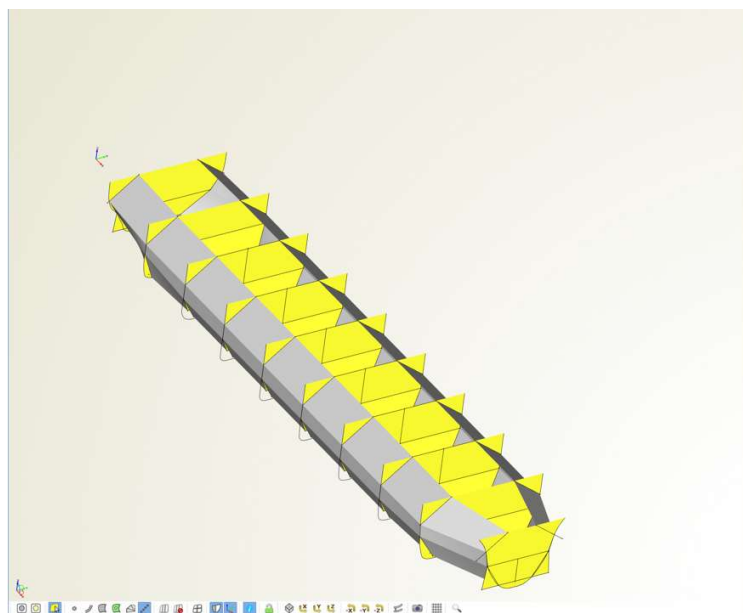


Figure 116: Parametric Cargo Hold Surfaces in CAESES®

6.2. Trade Routes Definition and Voyage Planning for Simulation

For the Bulk Carrier optimization case study, two trade routes are considered, the Brazil to China roundtrip and Australia to China roundtrip. Each voyage is split into legs depending on distinctive Seas and Oceans with each leg being comprised of equally distanced sub-legs. The leg distances and route planning have been plotted with the use of the “Distance Viewer” module of the ECOS® software used for voyage planning.

6.2.1. Brazil to China Roundtrip

Since the large bulk carrier trade is considered, the trip from Brazil to China fully loaded with iron ore and the ballast return trip have been analysed and can be parametrically simulated. In Figure 117 and Figure 118 one can identify the typical Capesize and VLOC sea passage and route between the ports of Tubarao and Ponta De Madeira where the Brazilian Ore company VALE has large export terminals and the Chinese port of Qingdao which is considered a large imports terminal for iron ore.

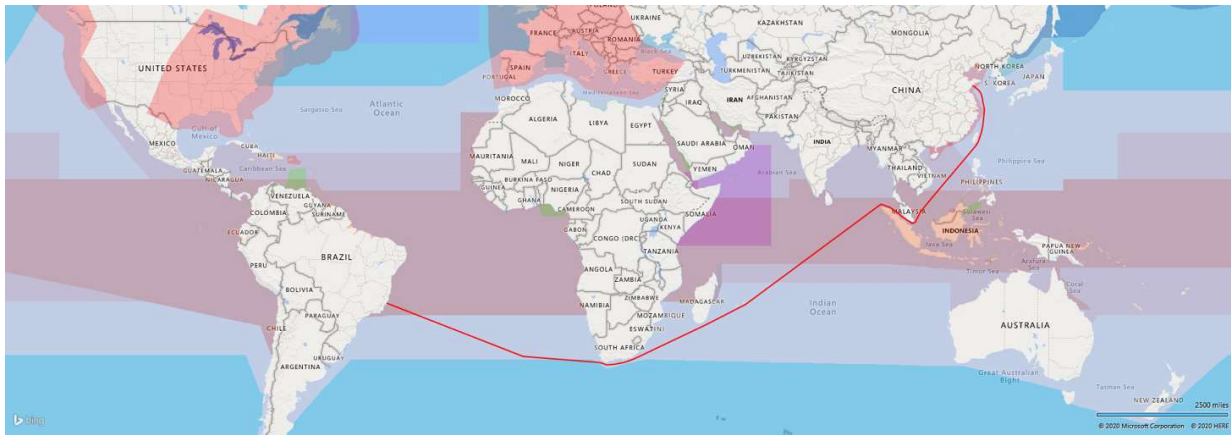


Figure 117: Tubarao to Qingdao Sea Passage (11,358 nautical miles)

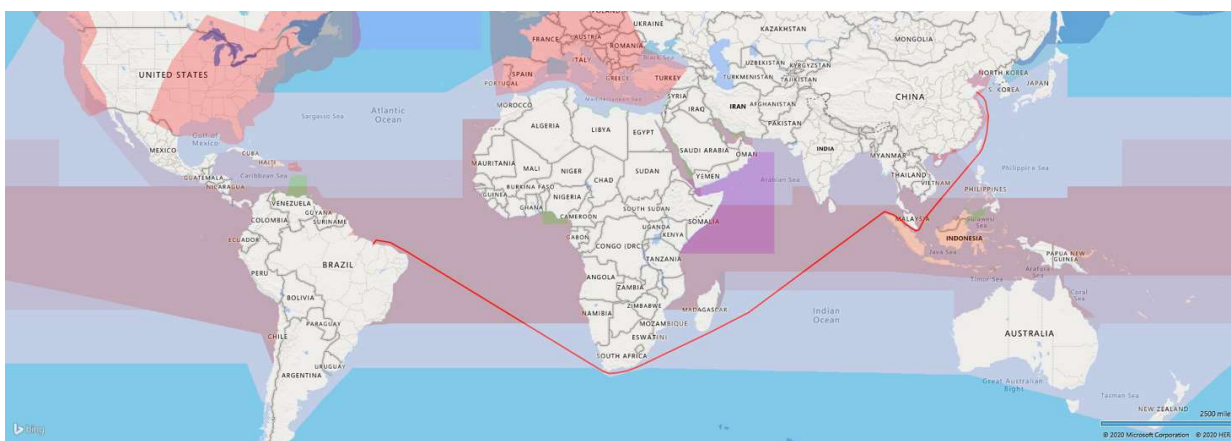


Figure 118: Ponta De Madeira to Qingdao Sea Passage (12,261 nautical miles)

For the generalized “Brazil to China” that is simulated in the present study, the scenario of loading in Tubarao, Brazil and discharging in Qingdao, China has been selected as it is the most frequently occurring ones. This is also the same as the “Route C3” defined in the Baltic Exchange BCI Index (Baltic Capesize Index) (BMTI, 2020). The total sea passage has been split into the following Voyage Legs:

1. Leg A: South Atlantic Passage

The first leg (Figure 119) is considered to be commenced from the loading port of Tubarao until the ship reaches the offshore area (OPL) outside of the Cape of Good Hope in South Africa, thus transiting the South Atlantic Ocean.

The total leg distance is 3,253 nautical miles and is split into four equally distanced sub-legs of 813.25 nautical miles each (A1, A2, A3, A4).

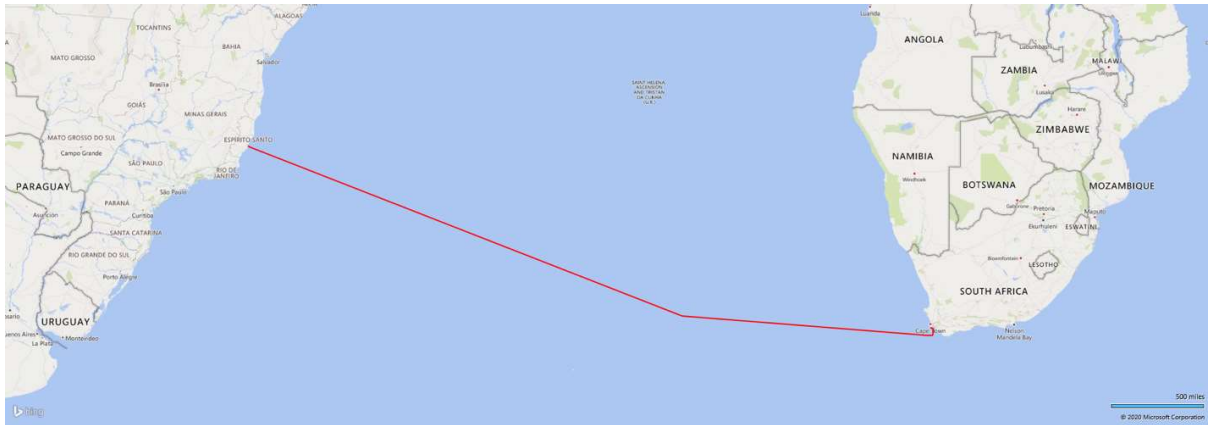


Figure 119: Leg A – South Atlantic Passage route

2. Leg B: Indian Ocean Passage

The second voyage leg (Figure 120) commences from the offshore area outside of the Cape of Good Hope until the ship reaches the entrance of the Malacca Straits.

The total leg distance is 5,517 nautical miles and is split into four equally distanced sub-legs of 1379.25 nautical miles each (B1, B2, B3, B4).

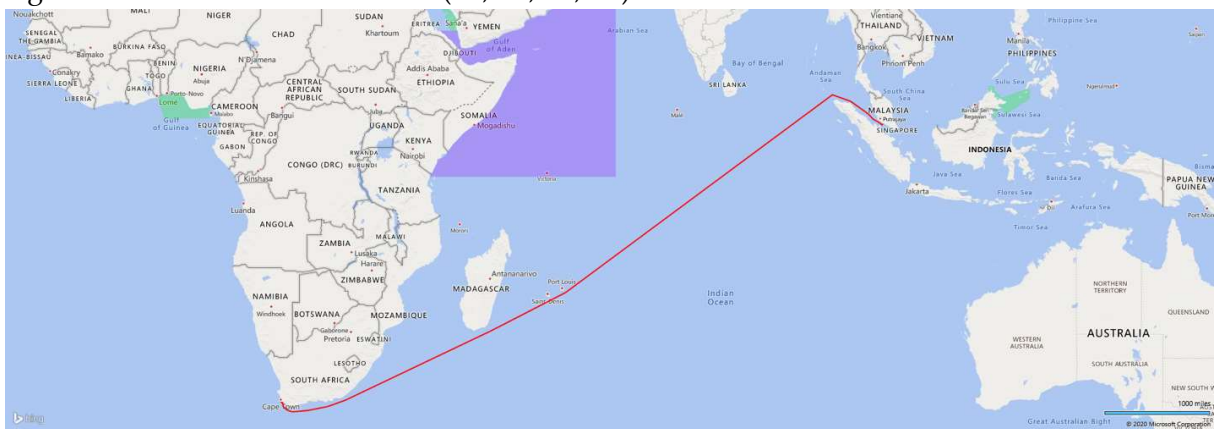


Figure 120: Leg B – Indian Ocean Passage

3. Leg C: Passage through Malacca and Singapore Straights.

The third leg (Figure 121) is the passage through the Singapore Straights. As this passage, is through an area of heavy marine traffic, constant course and RPM adjustment is a requirement. In view of this, for simulation purposes, this is considered as a “manoeuvring leg” of a total distance of 155 nautical miles. Furthermore, a stoppage for fuel and lube oil bunkering is assumed both for the laden and ballast legs as Singapore is a common bunkering area for such vessels due to the prevailing fuel pricing. The duration of the stay in Singapore is determined based on the pumping capability of a typical bunkering barge (300-400 tons/hour) for low sulphur IFO180 fuels and the typical capacities that are stemmed for such voyages basis on the vessel’s daily consumption.

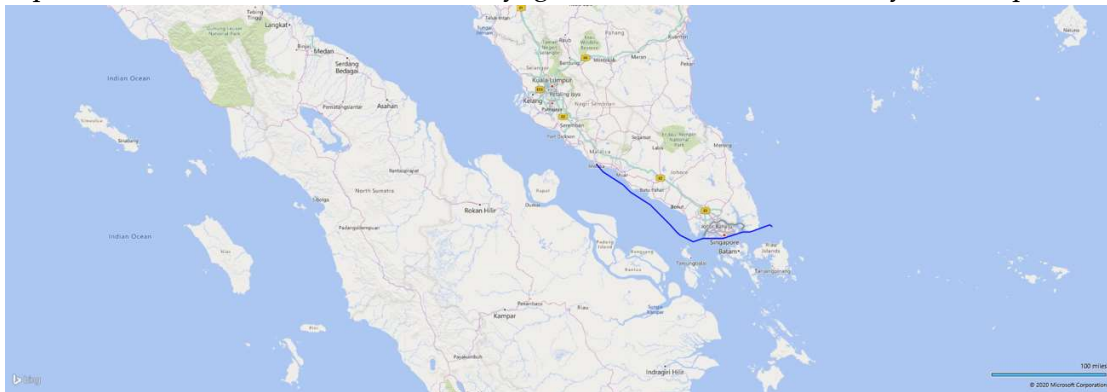


Figure 121: Leg C – Passage through Malacca and Singapore Straights

4. Leg D1 to D2: South China Sea and final approach to Qingdao

The fourth and final leg of the transit (Figure 122) is the passage from the exit of Singapore Straights to the discharging port of Qingdao. The passage from inside the Straights of Taiwan is excluded from the route planning since as per prudent maritime practice it is avoided due to high traffic and fishing trawlers activity. Instead, navigation around the island of Taiwan is preferred.

The total leg distance is 2,574 nautical miles and is split into two equally distanced sub-legs of 1,287 nautical miles each (D1, D2).

A Novel Methodology for Robust, Holistic, Simulation-Based Ship Design Optimization

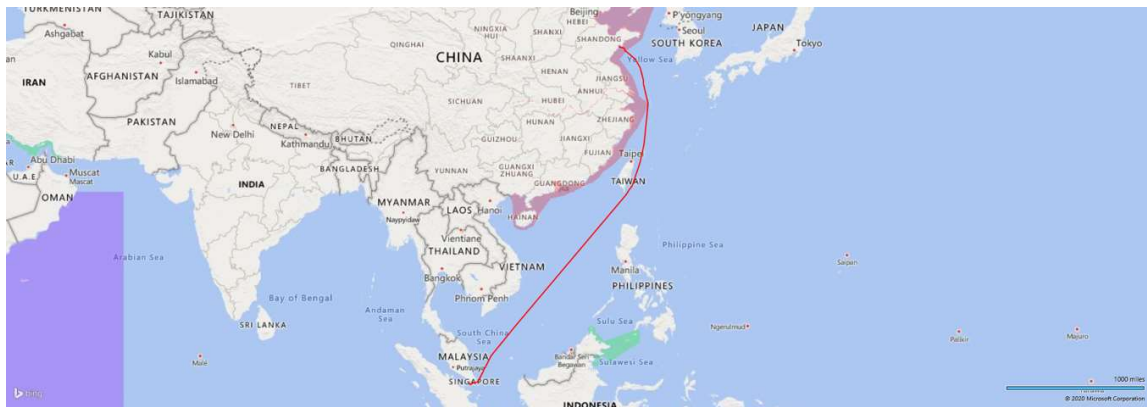


Figure 122: Leg D – Passage from Singapore Straights Eastern Exit to Qingdao

6.2.2. Australia to China Roundtrip

The second group of typical voyages where large bulk carriers are employed are voyages either from the port of Newcastle in South Australia carrying coal to Chinese ports (Figure 124) or from the Western Australian adjacent ports of Port Hedland and Port Walcott to Chinese ports (Figure 123).

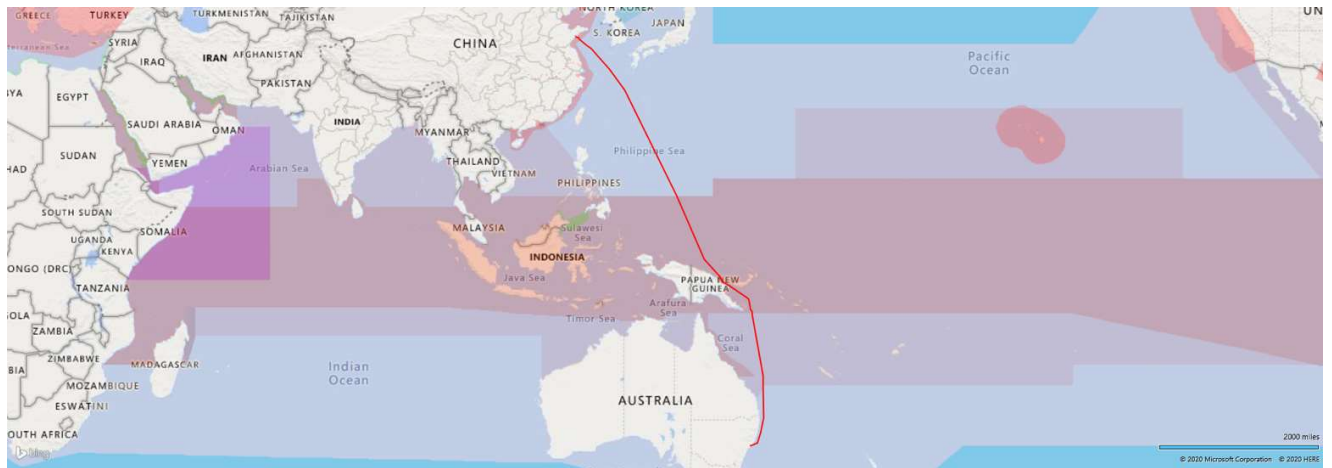


Figure 123: Newcastle (AU) to Qingdao Sea Passage (4,797 nm)

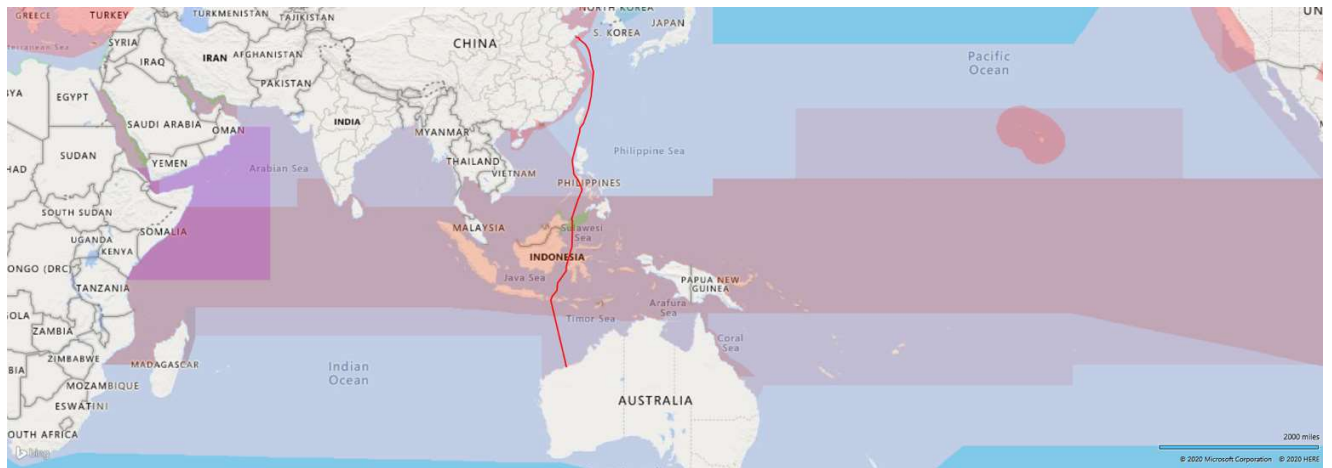


Figure 124: Port Hedland, Port Walcott to Qingdao Sea Passage (3,696 nm)

For the generalized “Australia to China” that is simulated in the present study, the scenario of loading in Port Hedland, Australia and discharging in Qingdao, China has been selected as it is the most frequently occurring one and furthermore it can accommodate not only Newcastlemax bulk carriers (208-210,000 DWT) but also VLOCs so it can be used for multiple ranges of dimensions and trade route and ship size assumptions. The same voyage is also reflected in “Route C5” defined in the Baltic Exchange BCI Index (Baltic Capesize Index) (BMTI, 2020). The total sea passage has been split into the following Voyage Legs:

1. Leg A: Port Hedland to Philippines Sea Passage

The first leg (Figure 125) is considered to be commenced from the loading port of Port Hedland (or Port Walcott) until the ship reaches the offshore area (OPL) outside of Manilla in the Philippines, thus transiting the Sulawesi and Sulu Seas.

The total leg distance is 2,240 nautical miles and is split into four equally distanced sub-legs of 560 nautical miles each (A1,A2,A3,A4).

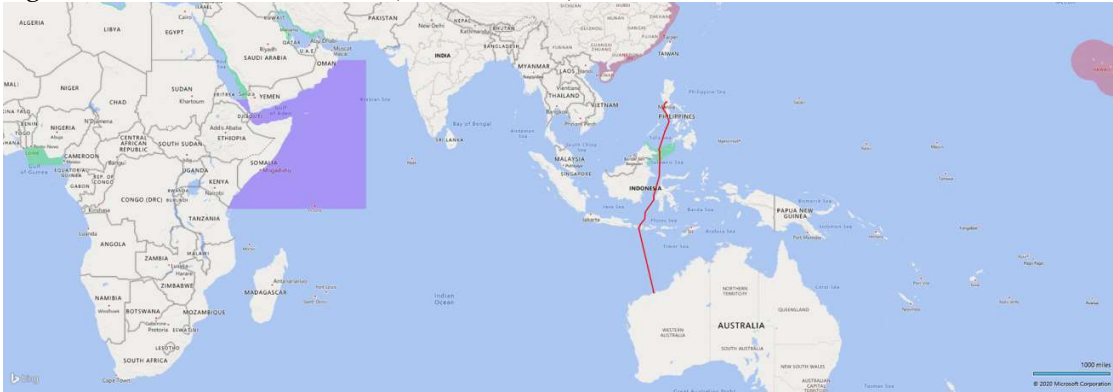


Figure 125: Leg A – Port Headland to Philippines Sea Passage

2. Leg B: Philippines to Qingdao Sea Passage

The second leg (Figure 126) commences from the offshore area outside of Manilla in the Philippines until the ship reaches the discharging port of Qingdao in China, thus transiting the South China Sea, avoiding (as mentioned in the previous paragraph) the Straights of Taiwan.

The total leg distance is 1456 nautical miles and is split into four equally distanced sub-legs of 364 nautical miles each (B1, B2, B3, B4).



Figure 126: Leg B – Philippines to Qingdao Sea Passage

3. Leg C: Qingdao to Singapore with a bunkering stop – BALLAST LEG ONLY

For the ballast return voyage from Qingdao to Port Hedland, a bunkering stop in Singapore is included in the voyage planning of the simulation (Figure 127).

The total leg length is 2,548 nautical miles and is split into two equally distanced legs of 1,274 nautical miles each (C1, C2).



Figure 127: Leg C – Qingdao to Singapore for bunkering (BALLAST LEG ONLY)

4. **Leg A: Singapore to Port Hedland – BALLAST LEG ONLY**

For the same ballast leg (Figure 128), the rest of the transit from Singapore IPL to Port Hedland is simulated.

The total leg length is 1,749 nautical miles and is split into two equally distanced legs of 874.5 nautical miles each (A1, A2).

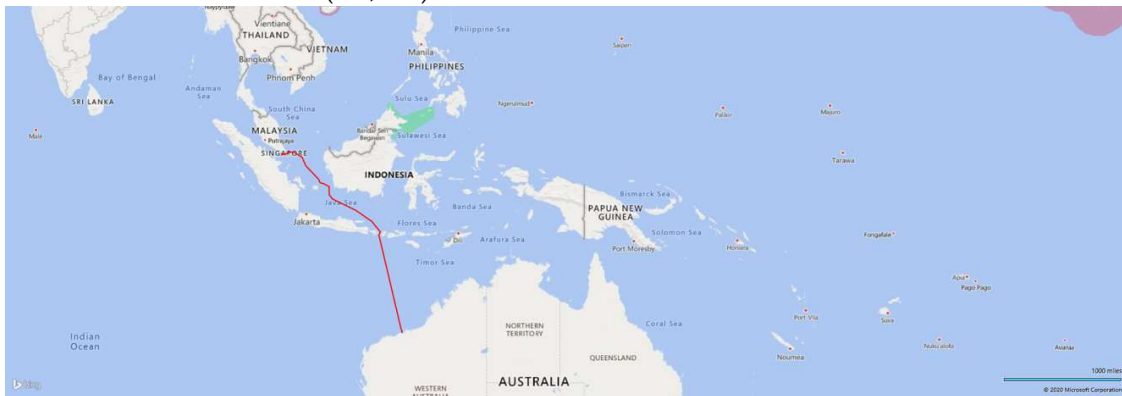


Figure 128: Leg A – Singapore IPL to Port Hedland (BALLAST LEG ONLY)

6.3. Optimization Problem Definition

6.3.1. Definition of the Optimization Problem and Workflow.

Optimization models typically represent problem choices as decision variables (in our case Design Variables) and seek values of those that minimize or maximize objective functions of the decision variables subject to constraints expressing the limits on possible decision choices. If one would like to formulate a mathematical representation of the above, it could be the following:

$$\text{Objective Function}^2: \quad \min f(x_i) \text{ or } \max f(x_i) \quad (79)$$

$$\text{Design Variable:} \quad \begin{bmatrix} x_1 \\ x_2 \\ x_3 \\ \dots \\ x_n \end{bmatrix} \quad i=1, \dots, n \quad (80)$$

$$\text{Design Variable Bounds:} \quad x_{i \min} \leq x_i \leq x_{i \max} \quad (81)$$

$$\text{Equality Constraints:} \quad g(x_i) = a \quad (82)$$

$$\text{Inequality Constraints} \quad b \leq h(x_i) \leq a \quad (83)$$

While the function giving the output figures from the input variables is the mathematical model of the physical process or system subject to optimization, an external engine is producing the variation mechanism in the form of a different combination of design variables. Such engines are called optimizers or Design Engines and depending on the variation technique followed belong to certain categories. When focusing on the Design Optimization of Engineering Systems and more specifically, complex marine structures and systems like commercial vessels one can refer to the flow process best described in (Papanikolaou, 2010), (Papanikolaou, et al., 2011) , (Nikolopoulos & Boulougouris, 2020). For the context of this study, the iterative optimization process followed herein can be graphically interpreted from the flow chart of Figure 129.

² Also known as optimization target or design/optimization merit.

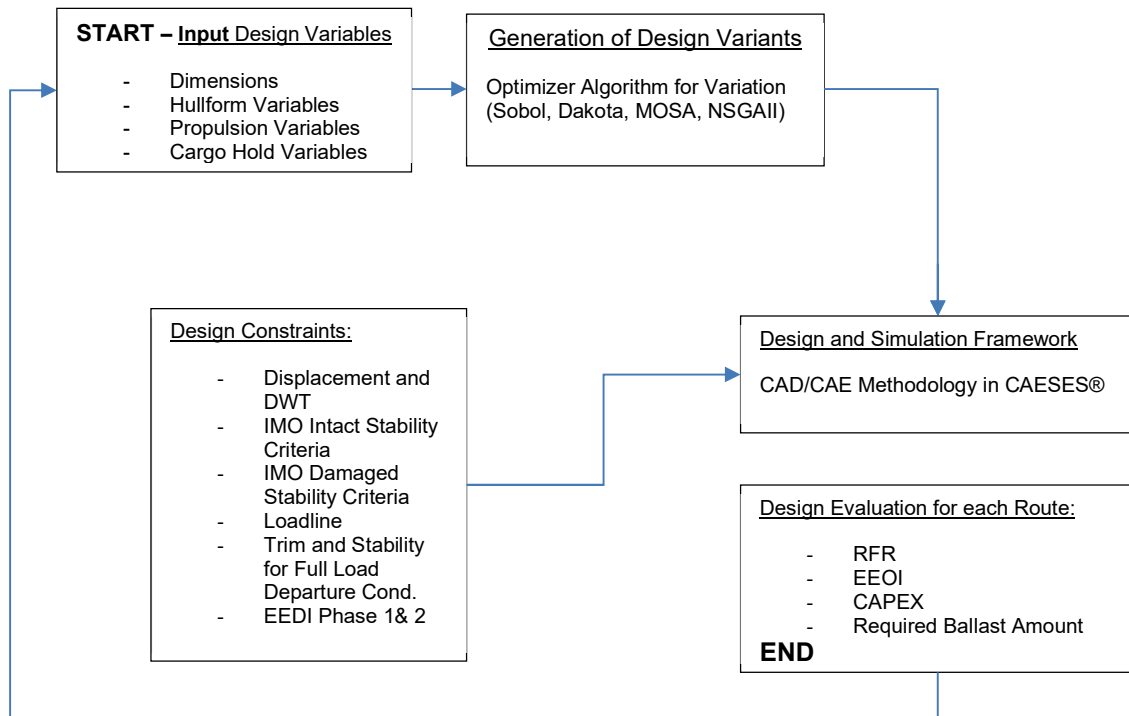


Figure 129: The optimization Loop applied.

For each iteration of the same loop, the design variables receive their input values from the «design engine» applied in the CAESES. The design engine can either be a random number generator or an optimization algorithm depending on the optimization stage. The applied values then trigger the generation of a new variant from the holistic, parametric model that utilizes the developed methodology for that matter.

After the variant generation, the Design Objectives, which are selected as the measures of merit of each variant are logged and assessed accordingly while in the meantime the Design Constraints imposed are checked for compliance. The Design constraints chosen for this application were the calculated values for Deadweight, Cargo Specific Gravity and the Stability Criteria of the 2008 Intact Stability Code. The size restrictions (in terms of vessel’s dimensions) were not used in constraints given the fact they were taken into account in the applied range of the Design Variables.

Prior to any formal optimization run, it is necessary to explore and fully understand both the design space (potential for improvement with given constraints) as well as the sensitivity of the methodology by a Design of Experiments procedure, using a system available random number generator that follows the Sobol sequence procedure (Sobol, 1976). The sensitivity analysis is a very important, preparatory step in which it is ensured that no major, unreasonable manipulations occur. In addition to that, it is important to see that the results are realistic both on a quantitative and qualitative basis, with the latter in need of particular attention since the design ranking and selection is the essence of optimization (the value of a favoured design is not important than the relationship with all the other produced designs).

6.3.2. Optimization Design Variables

From the below Table 37 and Table 38, one can identify the selected design variables of the subject optimization problem. The latter are in three categories; principal dimensions, hull form characteristics (Cb, LCB and Parallel Midbody) and cargo hold arrangement parameters. The more detailed design variables of the hull form arrangement for the detailed shape of the bulbous bow (if any), flair and stem shape as well as stern shape are going to be assessed in a separate optimization study with the use of integrated CFD codes.

ID	Design Variable	Lower Boundary	Upper Boundary
N_01	Length between Perpendiculars	275	300
N_02	Beam	45	50
N_03	Draft	17	22
N_04	Deck height	24	30
N_05	Hopper Height	7	10
N_06	Hopper Breadth (m)	3	6
N_07	Topside Height (m)	4	12
N_08	Topside Breadth (m)	6	15
N_09	Block Coefficient Cb	0.7	0.87
N_10	LCB (%Lbp)	0.505	0.525
N_11	Bilge Height (m)	2.4	7
N_12	Bilge Width (m)	2.4	8
N_13	Propeller Diameter (m)	8	10
N_14	Propeller Expanded Area Ratio	0.4	1
N_15	Propeller Pitch over Diameter	0.7	1.2
N_16	Propeller Number of Blades	4	5

Table 37: List and range of design variables of the optimization problem for Newcastlemax Studies.

ID	Design Variable	Lower Boundary	Upper Boundary
W_01	Length between Perpendiculars	275	340
W_02	Beam	45	65
W_03	Draft	17	22
W_04	Deck height	24	30
W_05	Hopper Height	6	12
W_06	Hopper Breadth (m)	3	6
W_07	Topside Height (m)	4	12
W_08	Topside Breadth (m)	6	15
W_09	Block Coefficient C_b	0.7	0.87
W_10	LCB (%Lbp)	0.505	0.525
W_11	Bilge Height (m)	2.4	7
W_12	Bilge Width (m)	2.4	7
W_13	Propeller Diameter (m)	8	10
W_14	Propeller Expanded Area Ratio	0.4	1
W_15	Propeller Pitch over Diameter	0.7	1.2
W_16	Propeller Number of Blades	4	5

Table 38: List and range of design variables of the optimization problem for WOZMAX Studies.

The range of each variable has been set considering the following:

1. Range and applicability of applied computational methods.
2. Robustness of the hull and cargo holds parametric surface with regards to geometrical merits such as surface smoothness, the feasibility of the hull surface, continuity, cargo holds structural and spatial limitations etc.
3. The upper and lower bounds decision especially for the Length, Breadth and Draft (to a lesser extent) were decided in order for the produced vessels to belong to the same vessel size category and thus produce a meaningful comparison basis. In this aspect, both two sub-categories are bulk carriers between 175,000 – 250,000 tons. However, since this range is considerable and in order to avoid distortion of the optimization process and results from extreme effects of scale economies, it was decided to treat two main subcategories:

The Newcastlemax size and VLOC size with the latter being an expansion of the first in order to demonstrate the improved optimization space and potential with slightly relaxed size boundaries.

6.3.3. Optimization Design Constraints

The optimization constraints can be summarized in the below Table 39:

ID	Constraint Name	Constraint
C-01	Cargo Capacity	>170,000 tons (5,000 warning distance)
C-02	Cargo Special Gravity	> 0.6 tons/m ³ (0.1 t/m ³ warning distance)
C-03	Freeboard Height	>Minimum Freeboard Height (Type B Ships of ILLC 1966)
C-04	SMCR	≥ 5000 kW
C-05	DWT Limit	< 280,000 tons (1,500 tons warning distance)
C-06	EEDI ³	< Maximum allowed EEDI Phase 2 (for given DWT)

Table 39: Inequality Constraints used in Optimization Runs

The reasons for choosing the above-mentioned inequality constraints are for either design feasibility or robustness of the results of the design generation code. More specifically:

1. Cargo Capacity (C-01) constraint is used to ensure that only realistic cargo hold arrangements will be produced. Indeed, there have been observed cases of unrealistically low cargo arrangement volumes given the examined size of the ship (e.g 100,000) which corresponded to combinations of cargo hold arrangement design variables that produced unfeasible arrangement structures triggering a “crushed geometrical surface and thus zero capacity for concerned holds. To ensure that only fully realized cargo hold arrangements will be used, this constraint was introduced.

³ Used only in Simulation Driven Optimization Runs where the EEOI is used instead as objective and EEDI is introduced as a constraint in order to further

2. Cargo Special Gravity (C-02) constraint, on the other hand, is used to ensure that the cargo hold arrangement size corresponds to a realistic density/special gravity at 98% loading. This has been extensively used in tanker optimization studies (Papanikolaou, et al., 2011), (Nikolopoulos, 2012) as the Authors have observed that in other optimization studies in the industry the cargo hold volumes were alarmingly high for the DWT at summer draft, indicating that the prospective design cannot load at 98% with a special gravity corresponding to a normal cargo and not violate the stability and loadline regulations.
3. The Freeboard Height (C-03) constraint is used as both the Draft and the Deck Height are used as design variables. The goal is to avoid combinations of the above two design variables that produce a freeboard height that violates the requirements of the International Loadline Convention of 1966 (International Maritime Organization (IMO), 1966) for Type "B" ships (open deck bulk carriers).
4. The Main Engine Specified Maximum Continuous Rating / SMCR (C-04) is set as a minimum to avoid the generation of unrealistic designs that might occur from errors in the resistance and propulsion modules of the methodology and give results with zero or empty resistance values (NaN).
5. The Deadweight DWT (C-05) is used to have an upper limit of size on all the produced design variants to avoid shifting to the next category of large vessels (VLOCs of 300-400,000 tons DWT).
6. The EEDI (C-06) is used as a constraint for simulation-driven studies where the EEOI is instead the optimization target. As any commercial ship design is obliged and has the constraint of EEDI so the generated designs have it as well. The user can choose which Phase EEDI is to be used (Phase 1, Phase 2, Phase 3).

It should be noted that depending on the application and ship type, other constraints can be used as well, such as stability ($GZ-\varphi$) characteristics for containership optimization (Koutroukis, et al., 2013), (Nikolopoulos, et al., 2014), (Soultanias, 2014).

6.3.4. Optimization Targets (Design Merits)

The parameters representing and quantifying the design merits that are the optimization targets are summarized (for various optimization runs) in the below Table 40:

I.D	Name	Applicable Optimization Runs
O-01	Required Freight Rate (Australia Trade)	Deterministic Optimization Runs Simulation Driven Runs (2016-2019) Simulation Driven Runs (2019-)
O-02	Required Freight Rate (Brazil Trade)	Deterministic Optimization Runs Simulation Driven Runs (2016-2019) Simulation Driven Runs (2019-)
O-03	EEDI	Deterministic Optimization Runs
O-04	EEOI	Simulation Driven Runs (2016-2019) Simulation Driven Runs (2019-)
O-05	Required Ballast Amount	Deterministic Optimization Runs Simulation Driven Runs (2016-2019) Simulation Driven Runs (2019-)
O-06	OPEX	Simulation Driven Runs (2016-2019)
O-07	CAPEX	Simulation Driven Runs (2016-2019)

Table 40: Overview of Optimization Targets throughout Optimization Studies

As can see the Required Freight Rate target is the central idea of the optimization runs and the most used objective. The RFR is differentiated for each trade route examined. However, following the completion of the deterministic runs and corresponding post-processing analysis it has been decided to keep one RFR value for each vessel type; the Australian Trade RFR for the Newcastlemax studies and the Brazilian Trade RFR for the WOZMAX studies. As already mentioned, EEDI is used as a deterministic metric of the energy efficiency of a design variant for the respective studies, while EEOI is the simulation-based equivalent metric. The details of the RFR calculation are discussed in paragraph 3.3.6.1.

The Required Ballast Amount is another optimization target. As in previous studies, this is the third core optimization target which is set in order to minimize the environmental footprint of the vessel on one hand and demonstrate that nearly zero-ballast ships can be developed with minimized Ballast Water Treatment infrastructure onboard.

In previous optimization studies ((Nikolopoulos & Boulougouris, 2018), (Nikolopoulos, et al., 2016), (Nikolopoulos & Boulougouris, 2020)), the merits of the Operational Expenditure (OPEX) and Capital Expenditure (CAPEX) were also set as optimization targets. However, from the results and discussion in subject published research as well as the fact that both OPEX and CAPEX are included in the RFR calculation, it was decided that these optimization targets wouldn't be further utilized in order to avoid polarization phenomena on the Pareto frontiers, distortion of the utility functions and the overall optimization path from an over-constraint problem with strongly correlated optimization targets

6.3.5. Optimization Studies Strategy

The optimization studies herein examined are separated into two pathways: Deterministic Studies and Simulation-Driven Studies (

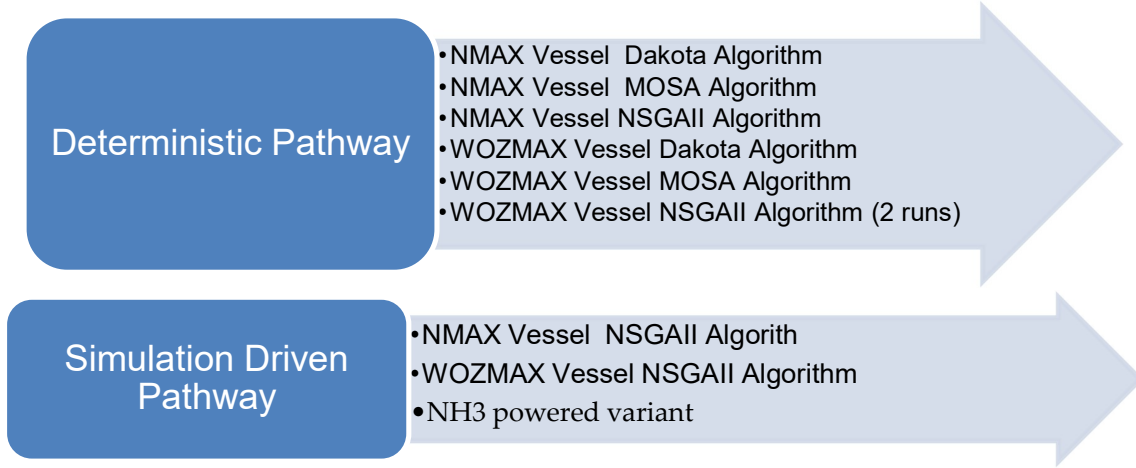


Figure 130:). The reason for conducting the first is to examine and highlight the value, differences and effect of the vessel’s operational simulation utilizing the developed Digital Twin on both the optimization method, procedure and most importantly on its results. Additionally, the robustness of the derived dominant variants and Pareto fronts can be further comparatively assessed against the equivalent Simulation pathway products.

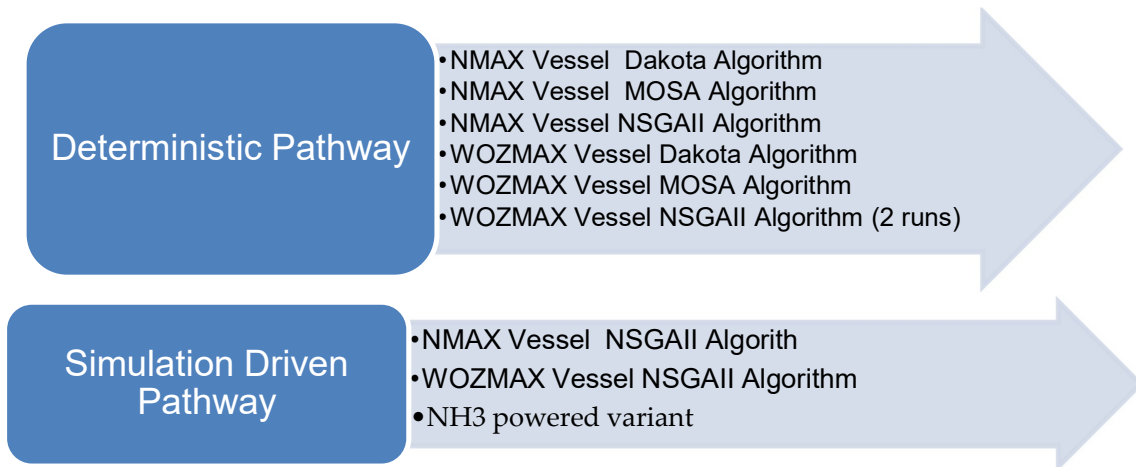


Figure 130: Optimization Pathways examined.

For improved reference and documentation purposes, the runs on the two simulation pathways have been recorded as per the taxonomy in Table 41: Taxonomy of optimization runs explored. Table 41.

Pathway	RUN ID	Vessel Type	Algorithm	Operational Simulation?	Market Uncertainty?	Design Population
Deterministic	Det_NMAX_01	Newcastlemax	Dakota	No	No	3000

Deterministic	Det_NMAX_02	Newcastlemax	MOSA	No	No	3000
Deterministic	Det_NMAX_03	Newcastlemax	NSGAI	No	No	3000
Deterministic	Det_WOZMAX_01	WOZMAX	Dakota	No	No	3000
Deterministic	Det_WOZMAX_02	WOZMAX	MOSA	No	No	3000
Deterministic	Det_WOZMAX_03	WOZMAX	NSGAI	No	No	3000
Deterministic	Det_WOZMAX_04 ⁴	WOZMAX	NSGAI	No	No	3000
Simulation Driven	Sim_NMAX_01	Newcastlemax	NSGAI	Yes	No	1500
Simulation Driven	Sim_NMAX_02	Newcastlemax	NSGAI	Yes	Yes	1500
Simulation Driven	Sim_WOZMAX_01	WOZMAX	NSGAI	Yes	No	1500
Simulation Driven	Sim_WOZMAX_02	WOZMAX	NSGAI	Yes	Yes	1500

Table 41: Taxonomy of optimization runs explored.

Furthermore, the original deterministic pathway, due to its computationally lighter setup serves as a basis for a comparative assessment of different approaches in optimization. CAESES™ offers the following design engines that can be used for parametric model variation and thus optimization:

- SOBOL

Original Publication: (Sobol, 1976)

This algorithm is used for Design of Experiment (DoE) studies to explore the boundaries of the design space and follows a quasi-random number generator approach to perform a uniform “filling” of a mathematically defined area/space with members of equal distances. It is not an optimization engine or tool but is used instead in the preliminary stages for sensitivity analysis and refinement of optimization objectives and variables. It is fully integrated and readily available as a “Design Engine” for variation in the design environment in use (CAESES™ CAE system).

- DAKOTA

Original Publication: (Adams, et al., 2009)

Dakota is a software and optimization toolkit package in Open C++ code that provides a flexible, extensible interface between simulation codes and iterative systems analysis methods which include:

⁴ Subject run conducted with the same variables as all previous deterministic runs (Det_WOZMAX_01~03) but with only one RFR, the one corresponding to the Brazilian Trade Route, set as an objective in order to “de-polarize” the Pareto fronts.

1. Optimization with gradient and non-gradient-based methods
2. Uncertainty quantification with sampling, reliability, stochastic expansion, and epistemic methods,
3. Sensitivity variance analysis with design of experiments and parameter study equations.

For the purposes of the currently presented research work, DAKOTA has been used both for sensitivity analysis and calibration studies as well as for formal optimization runs and its results were benchmarked against those of MOSA and NSGAI. It is fully integrated and readily available as a “Design Engine” for variation in the design environment in use (CAESES™ CAE system).

- MOSA (Multi-Objective Simulation Annealing)

Original Publication: (Ulungu, et al., July 1999)

The multi-objective simulation annealing algorithm has been developed to tackle with Multi-Objective Combinatorial Optimization problems by finding the Pareto set of solutions. The simulated annealing principles require that the feasible solution set is well structured. It is an iterative and evolutionary approach starting from an initial set of solutions with variants being populated by the decreasing of each of the design variables from their maximum value (like in the annealing process of metallurgy). MOSA in fact is a trajectory-based algorithm, where, in a first phase, diversified generation strategies are used to define candidate solutions at different stages of the search procedure. In a second phase, a reannealing process starting at low temperature is implemented to intensify the search based on the last solutions of the first phase.

It is fully integrated and readily available as a “Design Engine” for variation in the design environment in use (CAESES™ CAE system).

- NSGAI (Non-Sorting Genetic Algorithm II)

Original Publication: (Deb, et al., 2002)

The Non-Sorting Genetic Algorithm II is in fact a mathematical model of the function of biological evolution (Darwin, 1859) and biological trees. NSGA-II is one of the most popular multi-objective optimization algorithms with three special characteristics, fast non-dominated sorting approach, fast crowded distance estimation procedure and simple crowded comparison operator. The algorithm works in 6 steps: starting from population initialization (step 1), non-dominated sorting (step 2), crowding distance assessment (step 3), Selection of individuals carried out using a binary tournament selection (step 4), Genetic Operators using simulated binary crossover and polynomial mutation (step 5) and finally recommendation and selection (step 6).

It is fully integrated and readily available as a “Design Engine” for variation in the design environment in use (CAESES™ CAE system). Within the framework, the user is also able to change the parameters of the Genetic Operators (mutation and crossover probabilities).

The formal optimization runs involve the determination of the number of generations and the definition of the population of each generation to be explored. Then the generated designs are ranked according to several scenarios regarding the mentality of the decision-maker. One favoured design is picked to be the baseline design of the next optimization run, where the same procedure is followed. When it is evident that there is little more potential for improvement the best designs are picked using the same ranking principles with utility functions and are exported for analysis.

Both the SOBOL and NSGA II algorithms as well as a plethora of other variant generation and optimization algorithms are fully integrated and available within the CAESES.

The reasoning for examining two vessel types is that the parent vessel type of Newcastlemax bulk carrier has some strict size constraints (beam and length) in order to fit the port of Newcastle in Australia. However, after assessing the trading of ships in subject port with commercial operators as well as analysing AIS data, it was observed that large ore carriers tend not to be employed in charters that involve loading in Newcastle, but instead are preferred in ports of Western and Northern Australia (Port Walcott, Port Hedland etc.) leaving smaller sized vessels (eg Panamax and Kamsarmax gearless bulk carriers) to load coal from this area.

In view of this it was decided, using the same baseline to expand the range of all main dimension variables to the size of VLOCs (Very Large Ore Carriers) and the intermediate size of WOZMAX (West-Australia Max) designs which have emerged in recent years (Energy, 2017). By this expansion, apart from the better optimization opportunities and more comprehensive exploration of the design space, the robustness and adaptability of the herein-presented methodology and framework are validated.

6.3.6. Pareto Designs Ranking and Selection

One of the most critical steps during the optimization of any system is the selection and sorting of the dominant variants. For this reason, it is necessary to follow a rational, rather than an intuitive, approach in order to consider in an unbiased way all trade-offs that exist. One such method is the utility functions technique which is used on derived Pareto Frontiers for sorting and ranking of members of the design population. A Pareto Front is a set of nondominated solutions, being chosen as optimal, if no objective can be improved without sacrificing at least one other objective. On the other hand a solution x^* is referred to as dominated by another solution x if, and only if, x is equally good or better than x^* with respect to all objectives (Di Pierro, et al., 2009).

For the engineering problem herein examine the desirable merits of the generated designs are minimum EEOI, RFR and Required Ballast Amount.

Instead of using fixed weights for the set criteria in the evaluation of the variants, a utility function of the following formulation is rather assumed:

$$U = w_{EEOI} * u(EEOI) + w_{RFR} * u(RFR) + w_{CAPEX} * u(CAPEX) \quad (84)$$

The utility of each design variant with regards to the optimization targets is normalized by the best attained KPI valuation of each design population. The weights assigned for each respective KPI of each variant are a linear function of the distance of the attained utility value to the maximum utility value (under the normalization has a value of 1) of the design population. The design population is in turn ranked in descending order from the maximum to minimum attained utility as per equation (20). The top 10 most favourable designs are selected for each maximum weight scenario (Table 42) as dominant variants resulting in the identification and sorting of 40 designs with the best performance according to each utility scenario.

Maximum Objective Weight	U1	U2	U3	U4	U5 ⁵
RFR	1/3	0.3	0.2	0.5	1/3
EEDI // EEOI	1/3	0.3	0.2	0	1/3
Required Ballast Water Amount	1/3	0.4	0.6	0.5	1/3

Table 42: Weights used for the utility functions

In a second stage, the linear distribution of the utility weight for each design variant was altered due to observed polarized regions of the Pareto frontier. To facilitate a more comprehensive design exploration the use of a logarithmic distribution of weight for utility functions was introduced as a means to “de-polarize” local Pareto peaks and can explore the Pareto front for middle areas, despite considerable concessions made for one of the optimization merits (Figure 131). This was implemented on a testing and observation basis for deterministic optimization run Det_WOZMAX_04 (Table 41). to assess the evaluation, ranking and picking process with this algorithm prior to scaling up the implementation for simulation-driven runs (RUN IDs Sim_NMAX_01 ~ Sim_WOZMAX_02).

⁵ Logarithmic Weight Distribution Maximum Nominal Weights

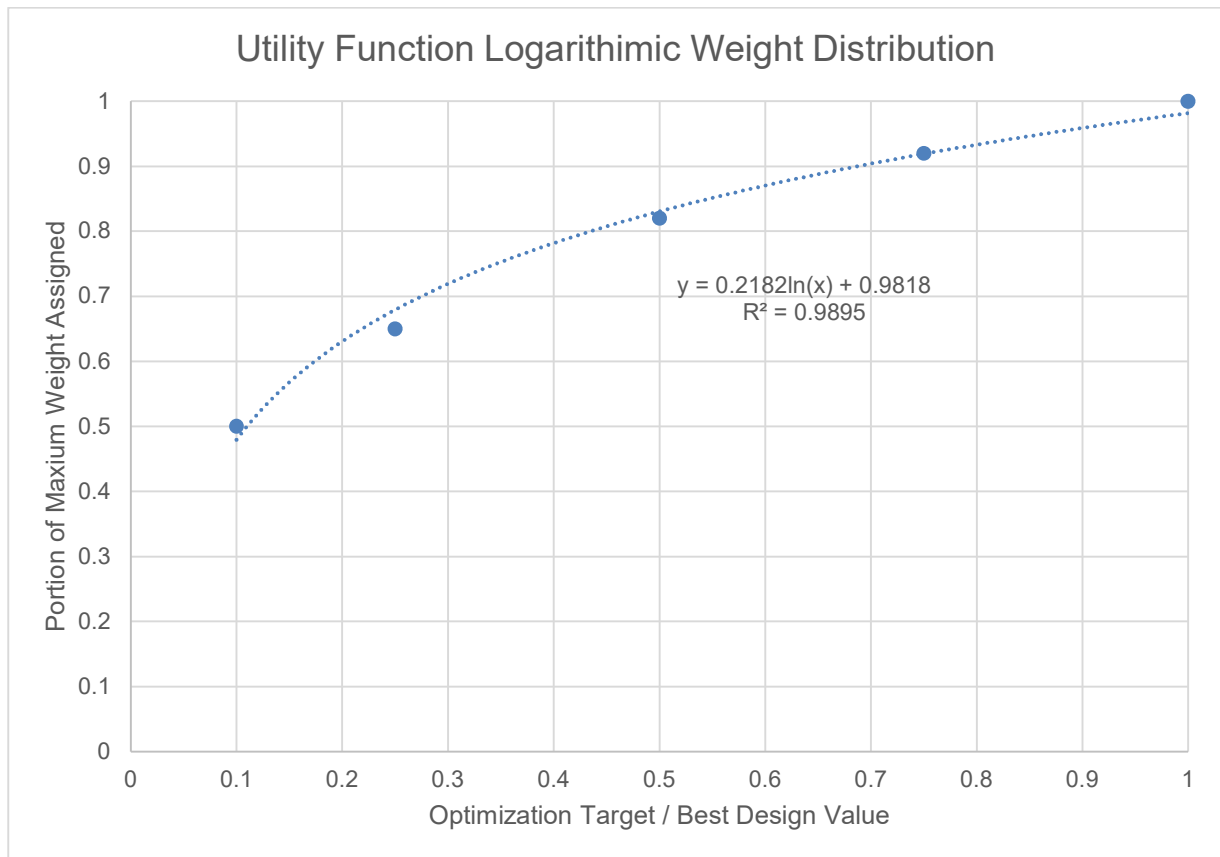


Figure 131: Assumed Logarithmic distribution for Utility Functions

6.4. Stage 1: Multi-Objective Optimization (Deterministic)

6.4.1. Optimization Problem Setup

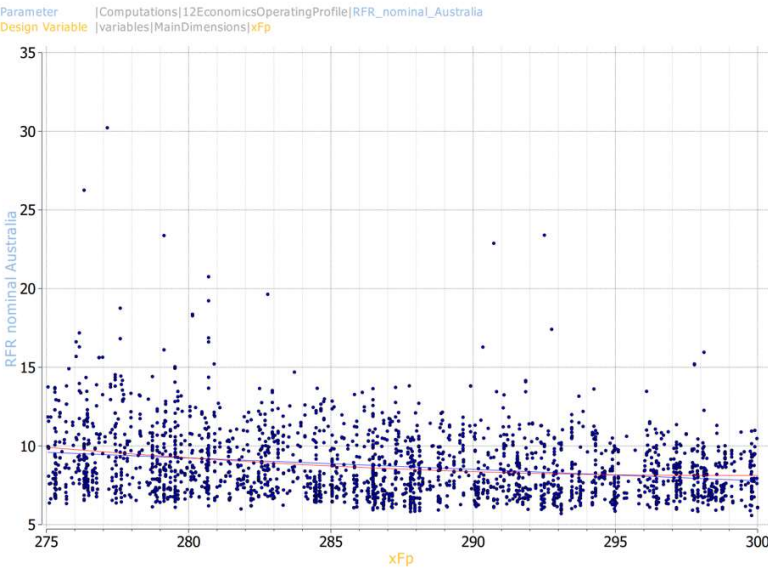
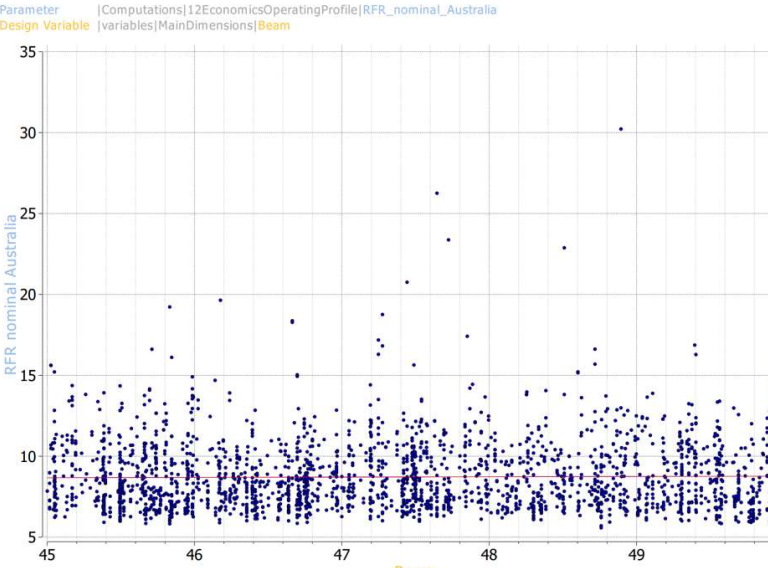
The optimization problem here is defined in paragraph 6.2. The focus and targets of deterministic runs are the following:

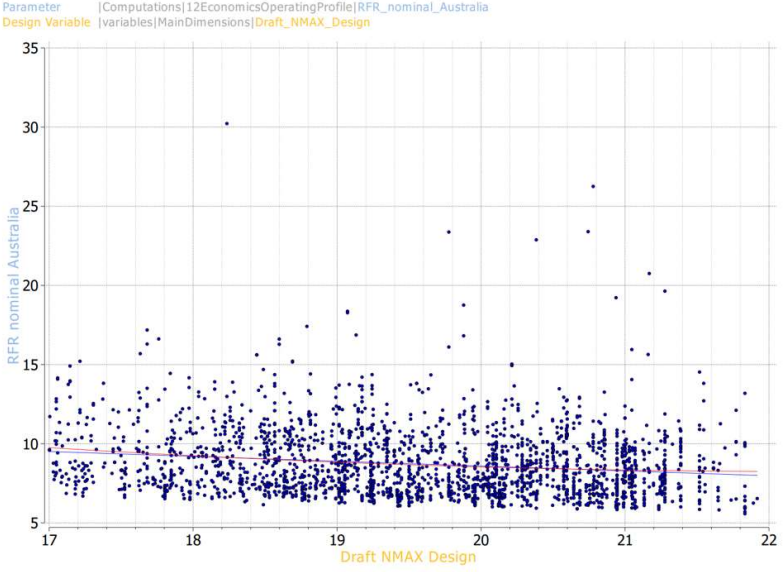
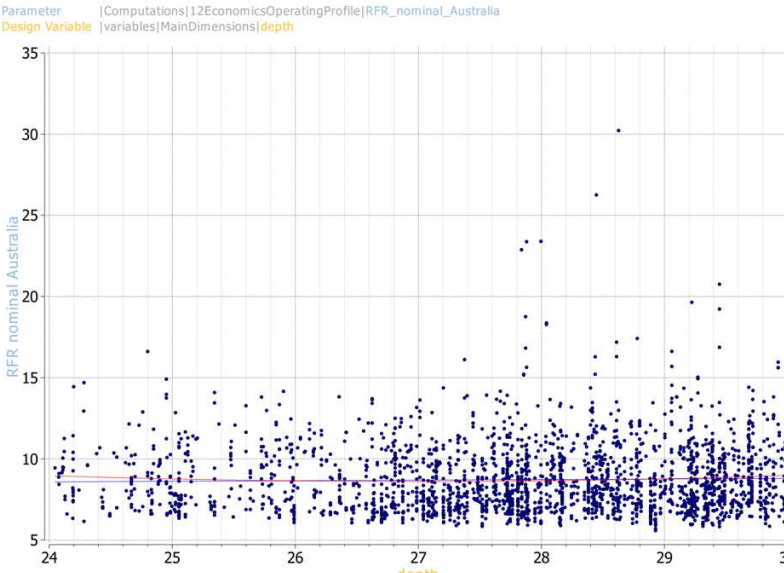
1. Design Space Exploration and Formal Optimization.
2. Comprehensive sensitivity analysis and targets behaviour analysis
3. Set a baseline on the limits of optimization and compare the results of each run with the equivalent results of runs conducted with Voyage Simulation enabled.
4. Compare the optimization efficiency and potential to voyage simulation optimization studies.
5. Compare different optimization engines and highlight the most promising ones.
6. Compare optimization results filter and sort variables and have a more robust framework for optimization.
7. Compare the use of linear vs. logarithmic weight distribution for the utility functions and its effect on design ranking and selection.

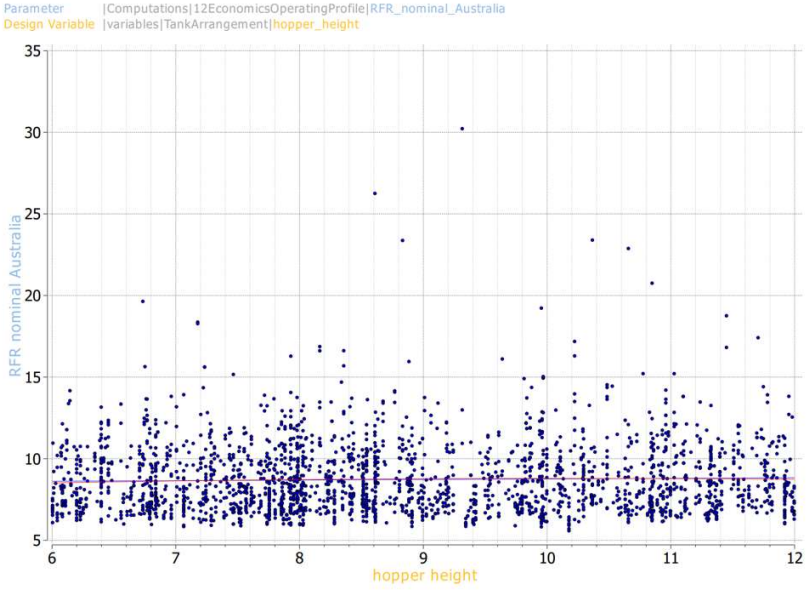
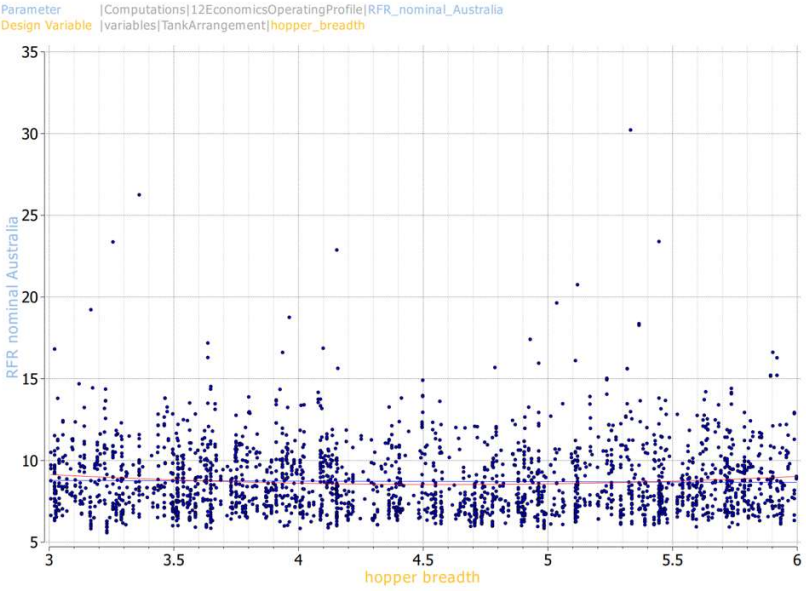
6.4.2. Sensitivity Analysis

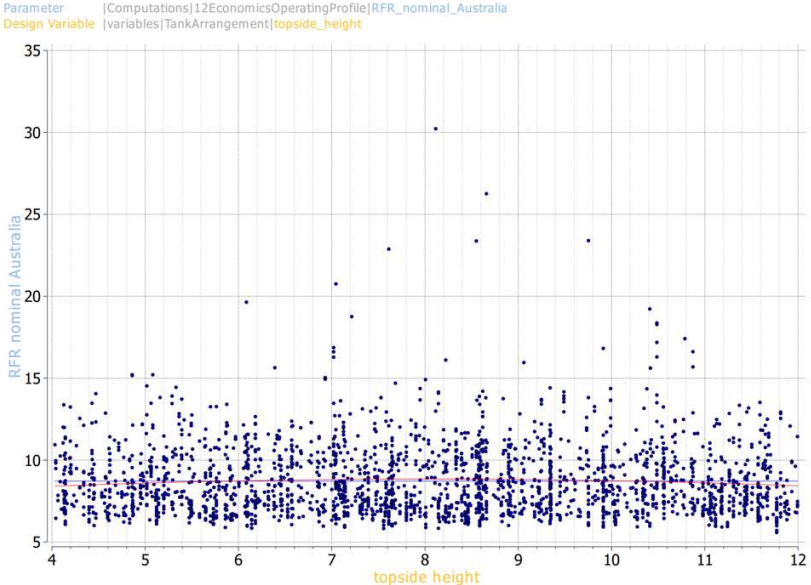
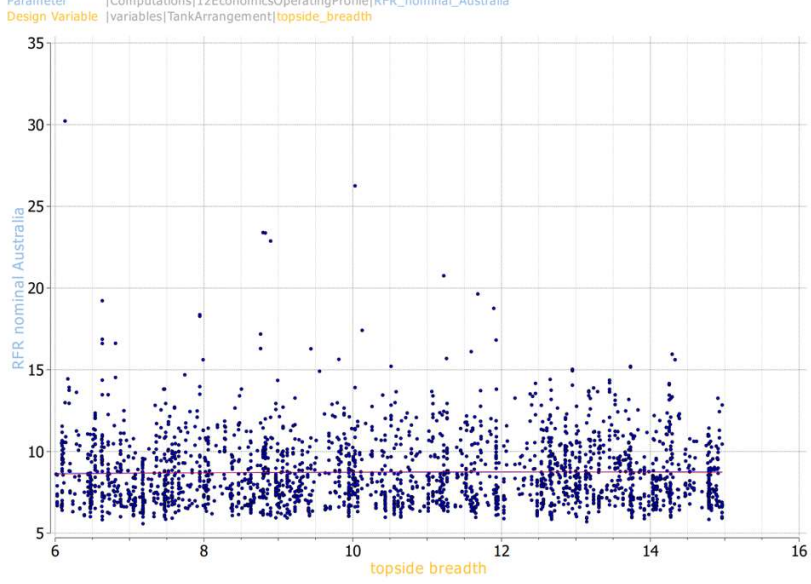
In Table 43 to Table 48 the effect of the design variables on each optimization objective can be identified for the Newcastlemax and WOZMAX case studies respectively. The detailed sensitivity scatter diagrams can be found as separate documents submitted with the Thesis Material in Appendix I. Some general observations that worth mentioning are the following:

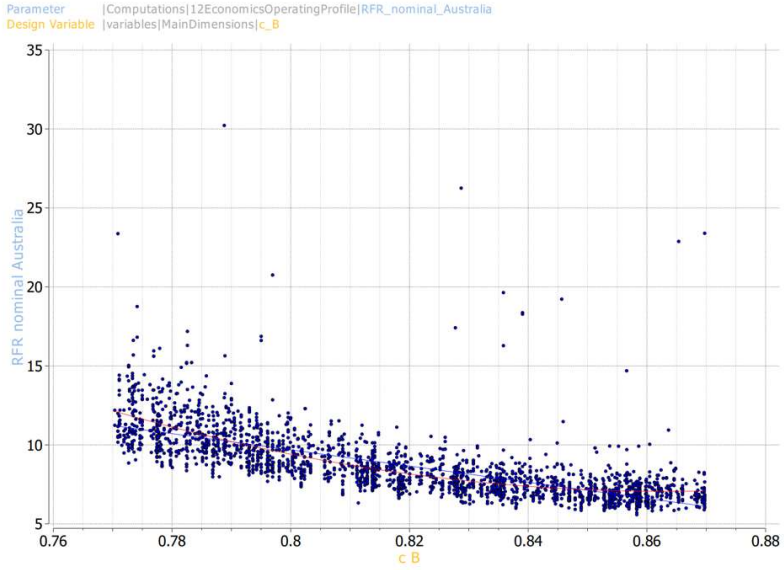
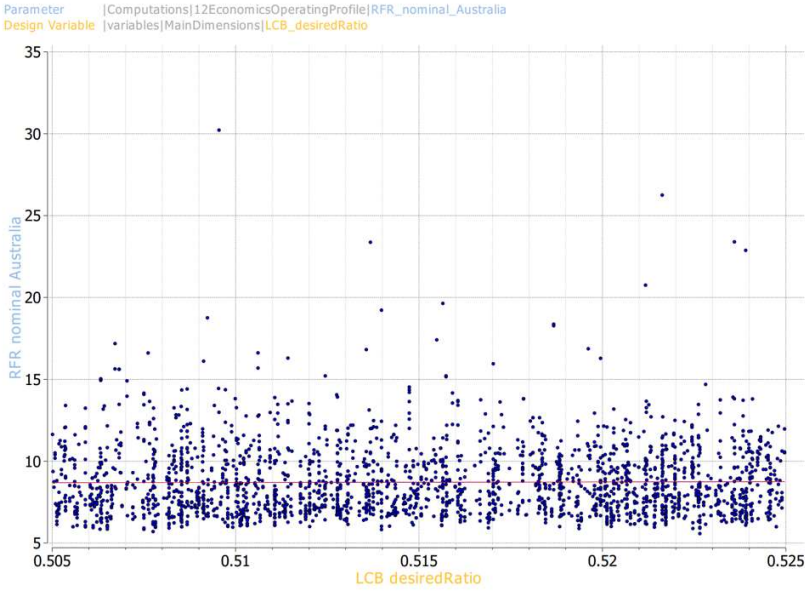
- Increasing vessel dimensions lead from one hand to decrease of the RFR and EEDI.
- From the other BW amount is sharply increasing.
- The antagonistic behaviour between the BW amount and the RFR/EEDI objectives is evident and requires strong multi-objective design generators combined with the robust platform of RHODA as will be seen in the next chapters.
- The Block coefficient is the parameter having the most intense effect on optimization objectives as it is the lead catalyst for hull shape formation.
- LCB appears to have small effect on optimization objectives but big importance in hull transformation in combination with C_b .
- An unexpected effect is that of the cargo hold parameters on the EEDI through increases on Cargo Capacity.
- Same patterns of sensitivity are observed between Newcastlemax and WOZMAX designs, despite the “release” of the design variables at higher range fields.
- The optimization constraints create a shift of design populations towards end ranges of variables, most notably in the case of design draft and deck height (bound to load line constraint).

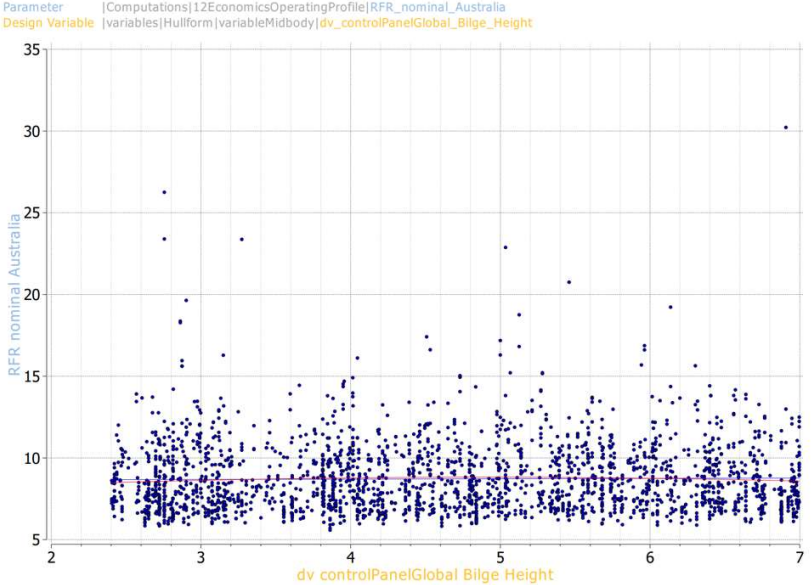
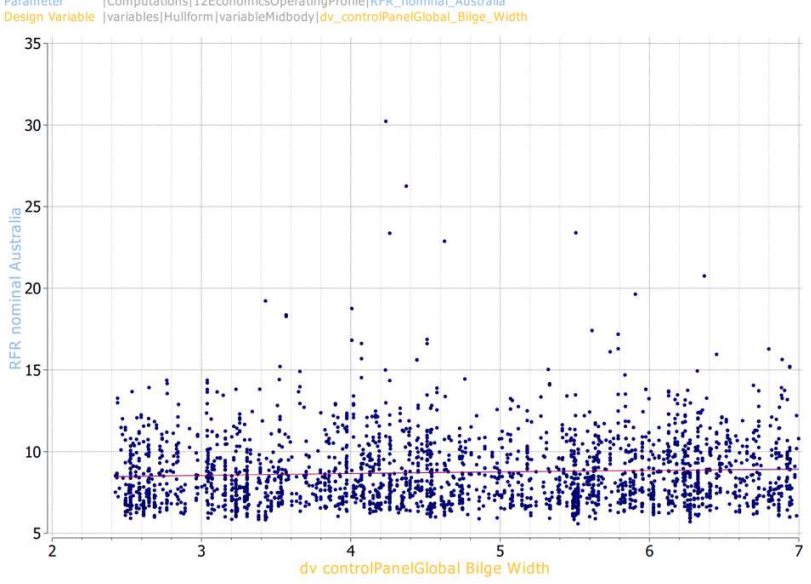
ID	Design Variable	Effect on RFR
N_01	Length between Perpendiculars	<p>High sensitivity of RFR in Length between perpendiculars: decrease of RFR by increasing length.</p>  <p>Parameter [Computations]12EconomicsOperatingProfile[RFR_nominal_Australia] Design Variable [variables]MainDimensions[xFp]</p>
N_02	Beam	<p>Uniform, no sensitivity by increasing or decreasing beam to RFR.</p>  <p>Parameter [Computations]12EconomicsOperatingProfile[RFR_nominal_Australia] Design Variable [variables]MainDimensions[Beam]</p>

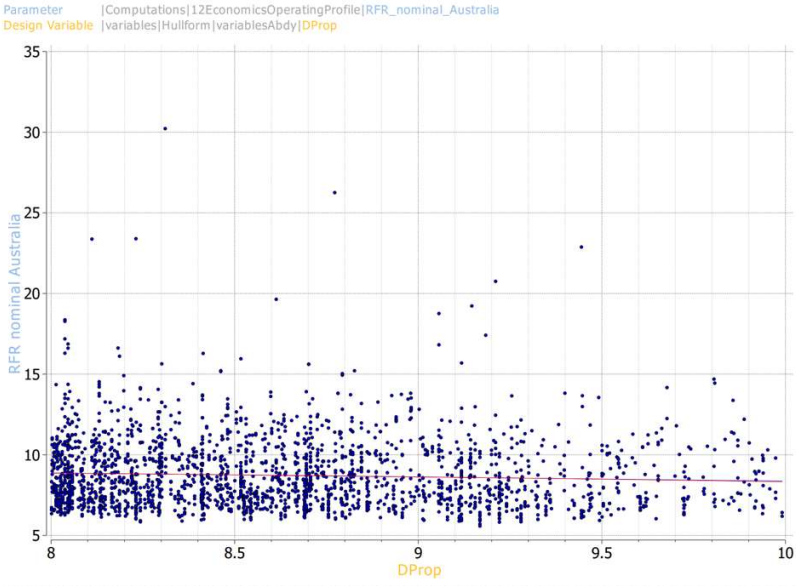
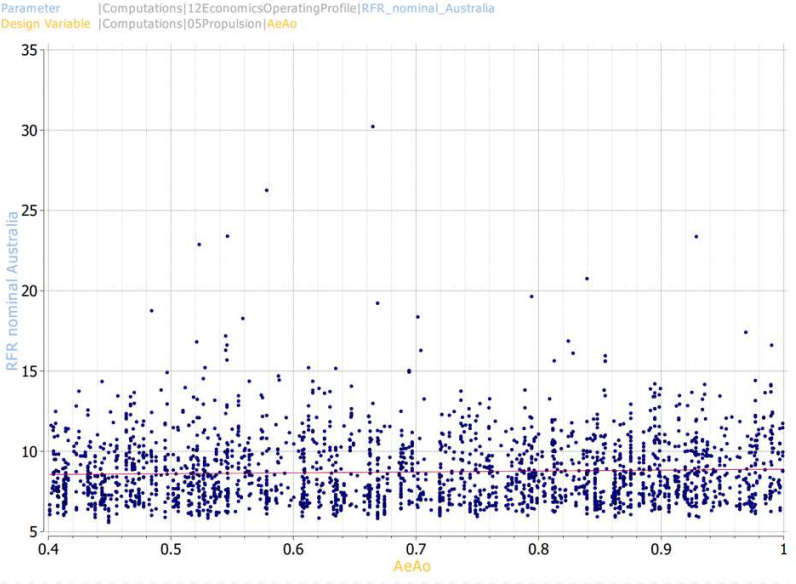
<p>N_03</p>	<p>Draft</p>	<p>By increasing draft, slight decrease on the RFR.</p>  <p>Parameter Computations 12EconomicsOperatingProfile RFR_nominal_Australia Design Variable variables MainDimensions Draft_NMAX_Design</p>
<p>N_04</p>	<p>Deck height</p>	<p>Slight decrease of RFR by increasing Deck height, majority of feasible designs concentrated in higher deck height values.</p>  <p>Parameter Computations 12EconomicsOperatingProfile RFR_nominal_Australia Design Variable variables MainDimensions depth</p>

<p>N_05</p>	<p>Hopper Height</p>	<p>Slight increase of RFR in 9.0m region of hopper height with lower values for extreme values.</p>  <p>Parameter [Computations]12EconomicsOperatingProfile RFR_nominal_Australia Design Variable [variables]TankArrangement hopper_height</p>
<p>N_06</p>	<p>Hopper Breadth (m)</p>	<p>Slight decrease of RFR in 4.5m region of hopper breadth with higher values for extreme values.</p>  <p>Parameter [Computations]12EconomicsOperatingProfile RFR_nominal_Australia Design Variable [variables]TankArrangement hopper_breadth</p>

<p>N_07</p>	<p>Topside Height (m)</p>	<p>Uniform distribution of designs, small sensitivity of RFR in Topside Height.</p>  <p>Parameter [Computations]12EconomicsOperatingProfile[RFR_nominal_Australia] Design Variable [variables]TankArrangement[topside_height]</p>
<p>N_08</p>	<p>Topside Breadth (m)</p>	<p>Uniform distribution of designs, small sensitivity of RFR in Topside Breadth.</p>  <p>Parameter [Computations]12EconomicsOperatingProfile[RFR_nominal_Australia] Design Variable [variables]TankArrangement[topside_breadth]</p>

<p>N_09</p>	<p>Block Coefficient Cb</p>	<p>High sensitivity, increasing Cb decreases the RFR up to 0.85 (then stable).</p>  <p>Parameter [Computations]12EconomicsOperatingProfile RFR_nominal_Australia Design Variable [variables]MainDimensions c_B</p>
<p>N_10</p>	<p>LCB (%Lbp)</p>	<p>Uniform distribution of designs, small sensitivity of RFR in LCB.</p>  <p>Parameter [Computations]12EconomicsOperatingProfile RFR_nominal_Australia Design Variable [variables]MainDimensions LCB_desiredRatio</p>

<p>N_11</p>	<p>Bilge Height (m)</p>	<p>Uniform distribution of designs, small sensitivity of RFR in Bilge Height</p>  <p>Parameter [Computations]12EconomicsOperatingProfile RFR_nominal_Australia Design Variable variables Hullform variableMidbody dv_controlPanelGlobal_Bilge_Height</p>
<p>N_12</p>	<p>Bilge Width (m)</p>	<p>Uniform distribution of designs, small sensitivity of RFR in Bilge Width</p>  <p>Parameter [Computations]12EconomicsOperatingProfile RFR_nominal_Australia Design Variable variables Hullform variableMidbody dv_controlPanelGlobal_Bilge_Width</p>

<p>N_13</p>	<p>Propeller Diameter (m)</p>	<p>Decrease of RFR by increasing propeller diameter, higher design population in lower diameters.</p> 
<p>N_14</p>	<p>Propeller Expanded Area Ratio</p>	<p>Uniform distribution with little sensitivity of RFR in Expanded Area Ratio.</p> 

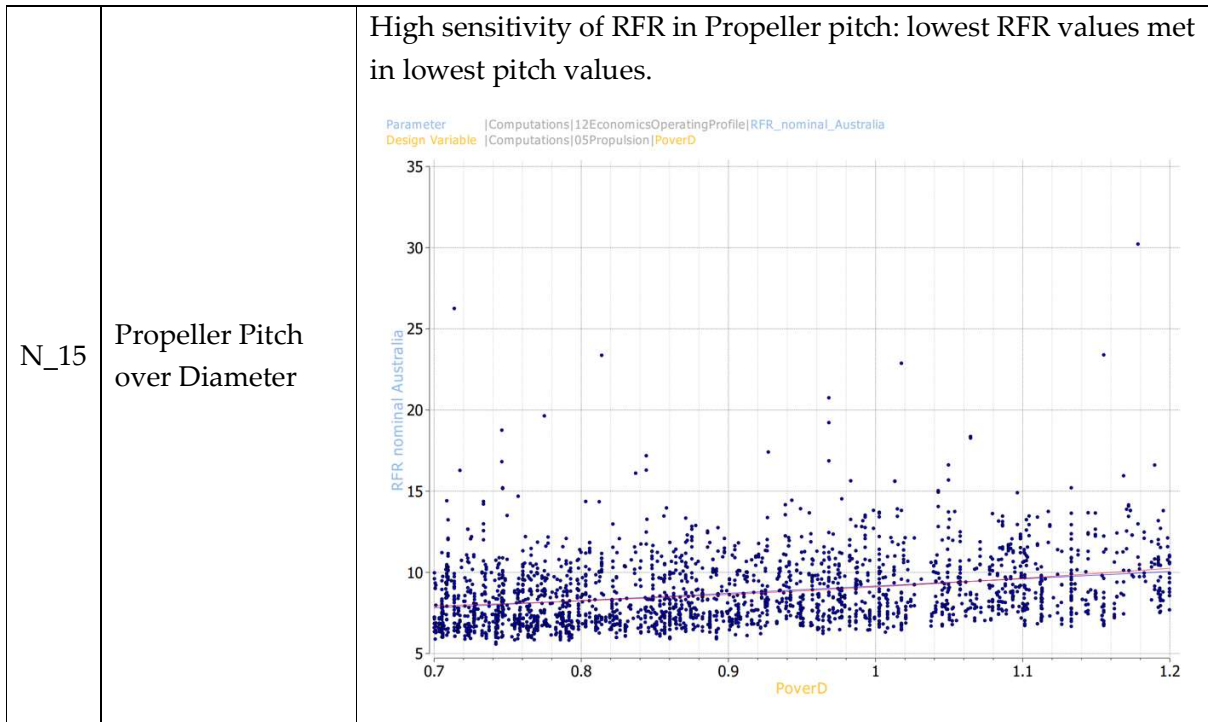
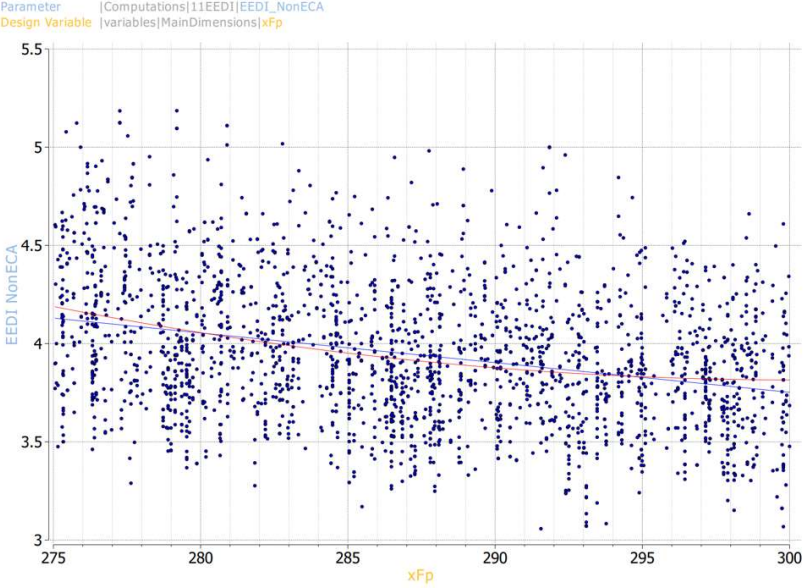
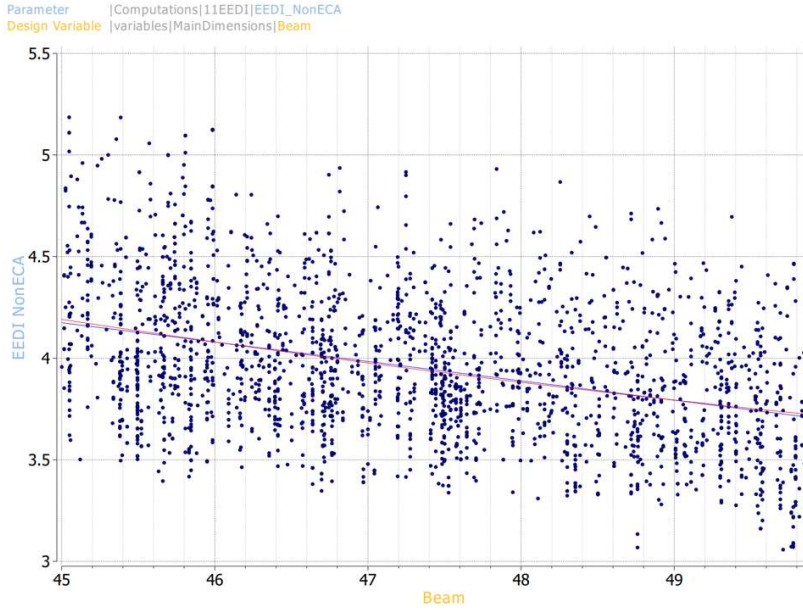
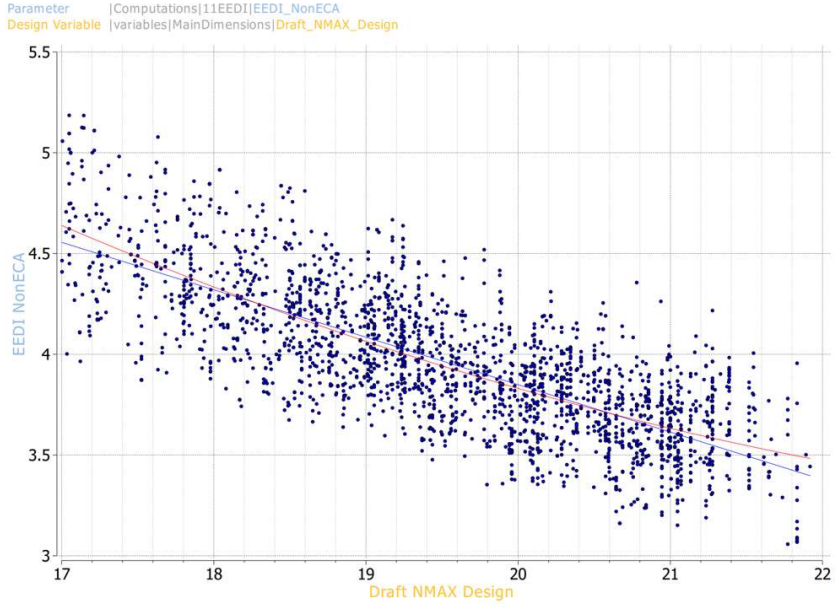
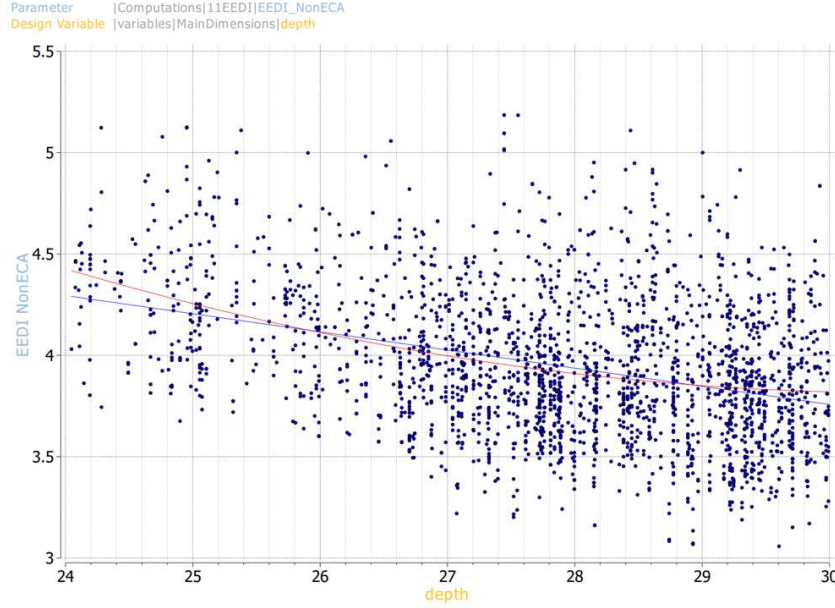
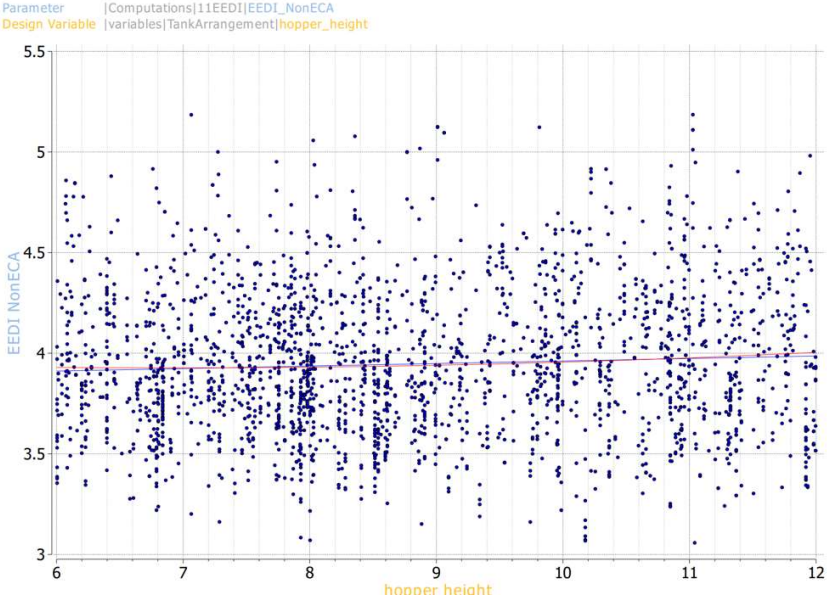
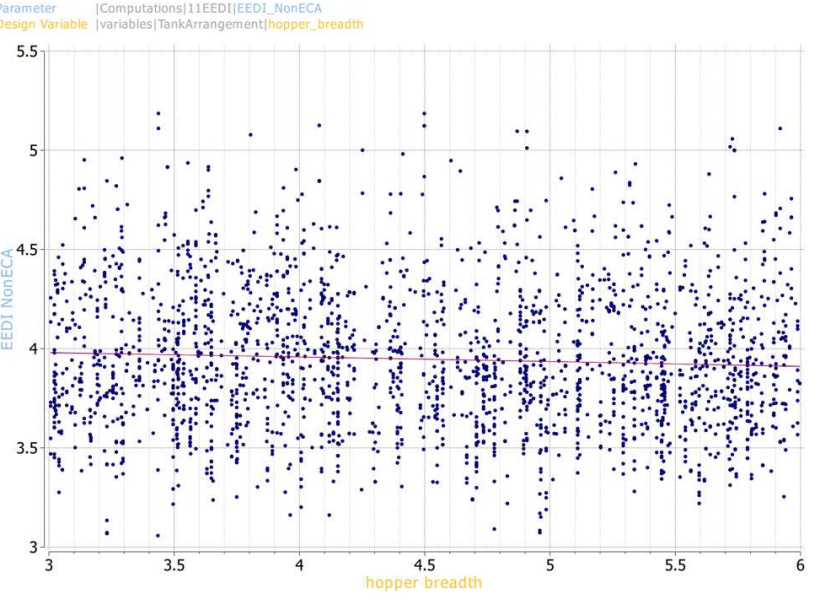
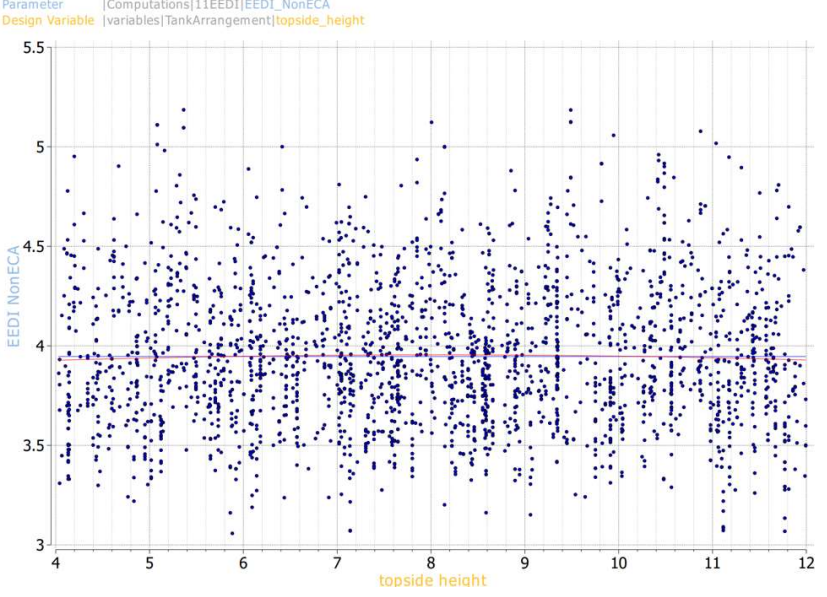
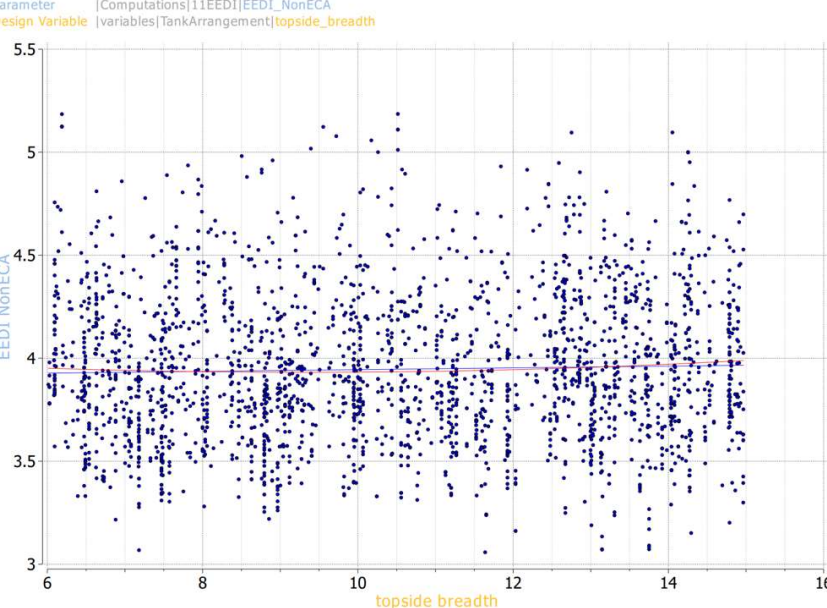


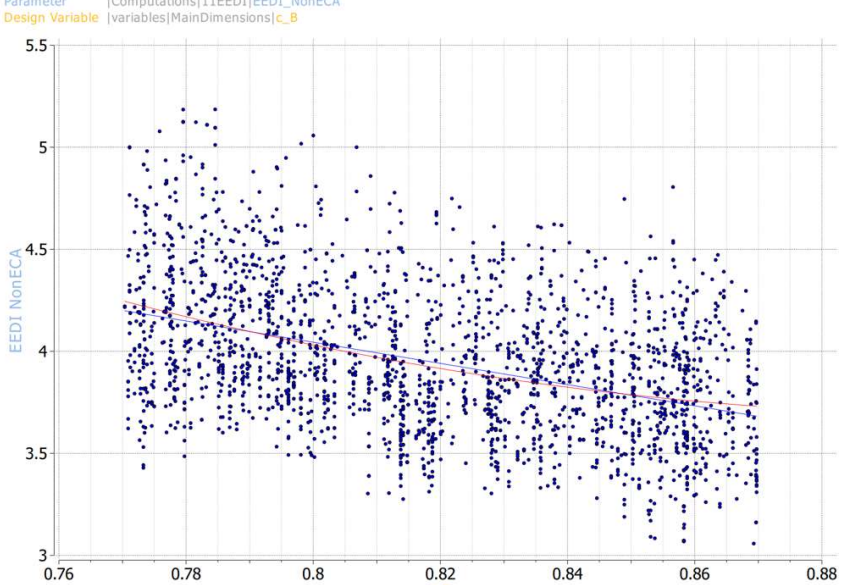
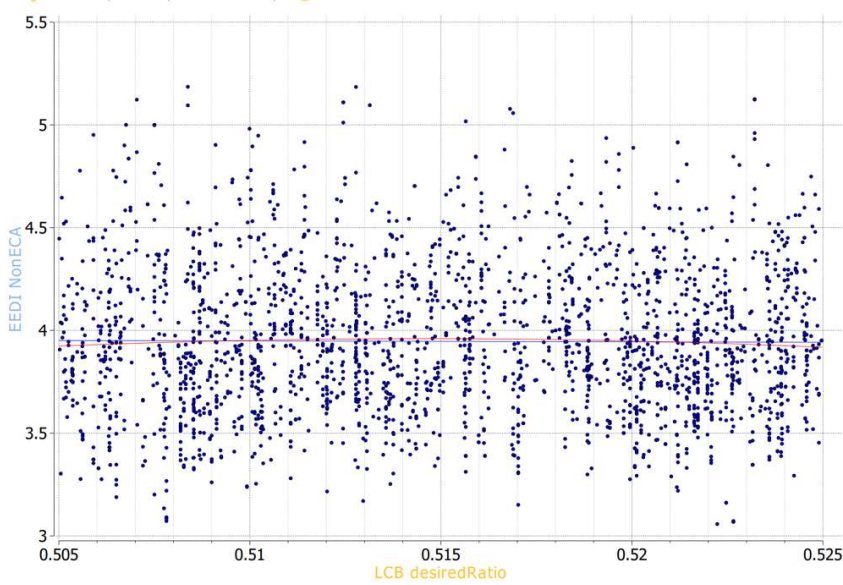
Table 43: RFR Sensitivity on Design Variables – Deterministic NEWCASTLEMAX Case Studies

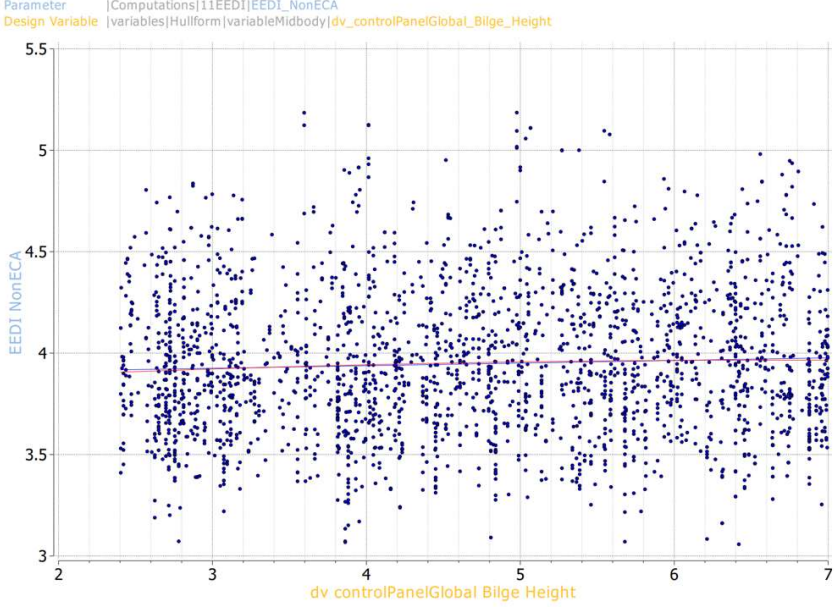
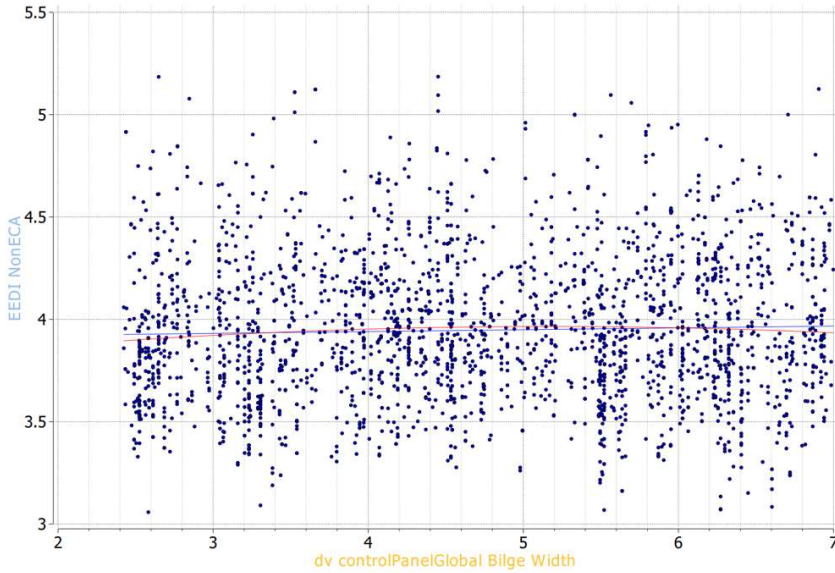
ID	Design Variable	Effect on EEDI
N_01	Length between Perpendiculars	<p>High sensitivity of EEDI in Lbp. EEDI decreases by increasing length. Higher scatter of designs.</p>  <p>The plot shows a dense cloud of blue data points with a downward-sloping trend line. The y-axis is labeled 'EEDI NonECA' and ranges from 3 to 5.5. The x-axis is labeled 'xFp' and ranges from 275 to 300. A legend at the top left identifies the parameter as 'EEDI_NonECA' and the design variable as 'xFp'.</p>
N_02	Beam	<p>High sensitivity of EEDI in Beam: EEDI decreases by increasing length.</p>  <p>The plot shows a dense cloud of blue data points with a downward-sloping trend line. The y-axis is labeled 'EEDI NonECA' and ranges from 3 to 5.5. The x-axis is labeled 'Beam' and ranges from 45 to 50. A legend at the top left identifies the parameter as 'EEDI_NonECA' and the design variable as 'Beam'.</p>

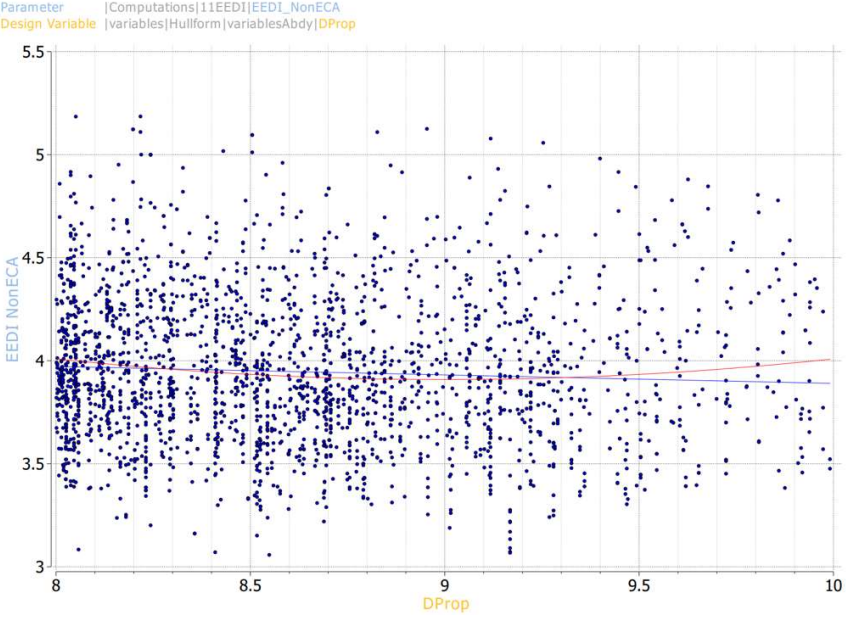
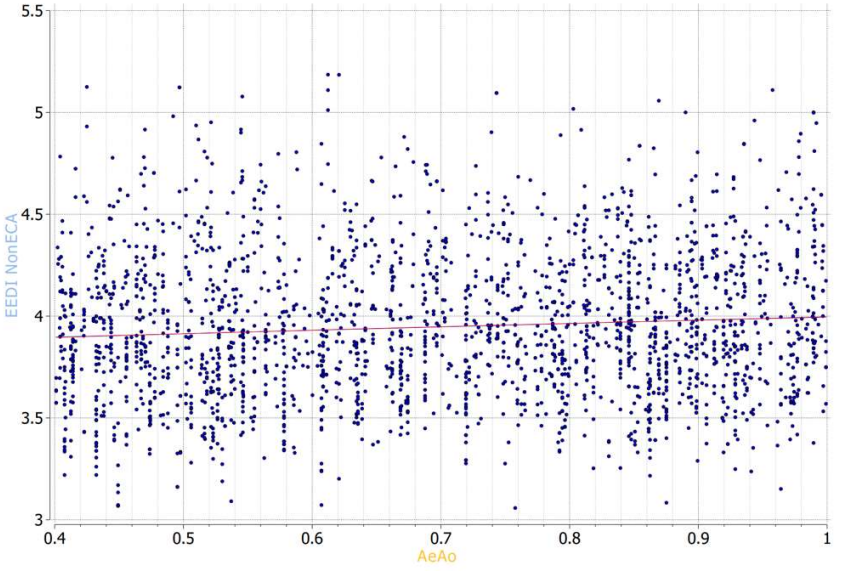
<p>N_03</p>	<p>Draft</p>	<p>High sensitivity of EEDI in Draft: EEDI decreases sharply by increasing draft.</p>  <p>Parameter Computations 11EEDI EEDI_NonECA Design Variable variables MainDimensions Draft_NMAX_Design</p>
<p>N_04</p>	<p>Deck height</p>	<p>High sensitivity of EEDI in Deck Height : EEDI decreases by increasing deck height. Scatter increases by increasing deck height and most of the design population is concentrated at higher values.</p>  <p>Parameter Computations 11EEDI EEDI_NonECA Design Variable variables MainDimensions depth</p>

<p>N_05</p>	<p>Hopper Height</p>	<p>Increase of Hopper Height leads to increase of EEDI (through cargo capacity and deadweight).</p>  <p>Parameter [Computations]11EEDI EEDI_NonECA Design Variable [variables]TankArrangement hopper_height</p>
<p>N_06</p>	<p>Hopper Breadth (m)</p>	<p>Increase of Hopper Breadth leads to decrease of EEDI (through cargo capacity and deadweight).</p>  <p>Parameter [Computations]11EEDI EEDI_NonECA Design Variable [variables]TankArrangement hopper_breadth</p>

<p>N_07</p>	<p>Topside Height (m)</p>	<p>EEDI sensitivity in topside height is low and close to zero</p>  <p>Parameter Computations 11EEDI EEDI_NonECA Design Variable variables TankArrangement topside_height</p>
<p>N_08</p>	<p>Topside Breadth (m)</p>	<p>EEDI sensitivity in topside breadth is low and close to zero</p>  <p>Parameter Computations 11EEDI EEDI_NonECA Design Variable variables TankArrangement topside_breadth</p>

<p>N_09</p>	<p>Block Coefficient Cb</p>	<p>High sensitivity of EEDI in Cb: EEDI decreases sharply by increasing the block coefficient.</p>  <p>Parameter Computations 11EEDI EEDI_NonECA Design Variable variables MainDimensions c_B</p>
<p>N_10</p>	<p>LCB (%Lbp)</p>	<p>Little sensitivity of EEDI in LCB position with uniform distribution of designs.</p>  <p>Parameter Computations 11EEDI EEDI_NonECA Design Variable variables MainDimensions LCB_desiredRatio</p>

<p>N_11</p>	<p>Bilge Height (m)</p>	<p>Slight sensitivity of EEDI in Bilge Height value: with increasing bilge height the EEDI slightly increases.</p>  <p>Parameter Computations 11EEDI EEDI_NonECA Design Variable variables Hullform variableMidbody dv_controlPanelGlobal_Bilge_Height</p>
<p>N_12</p>	<p>Bilge Width (m)</p>	<p>Little sensitivity of EEDI in bilge width.</p>  <p>Parameter Computations 11EEDI EEDI_NonECA Design Variable variables Hullform variableMidbody dv_controlPanelGlobal_Bilge_Width</p>

<p>N_13</p>	<p>Propeller Diameter (m)</p>	<p>EEDI has a low sensitivity in the change of propeller diameter, with lowest figures being observed for 9.0m diameter region propellers.</p>  <p>Parameter Computations 11EEDI EEDI_NonECA Design Variable variables Hullform variablesAbdy DProp</p>
<p>N_14</p>	<p>Propeller Expanded Area Ratio</p>	<p>Decreasing EEDI in propellers with lower expanded area ratios</p>  <p>Parameter Computations 11EEDI EEDI_NonECA Design Variable Computations 05Propulsion AeAo</p>

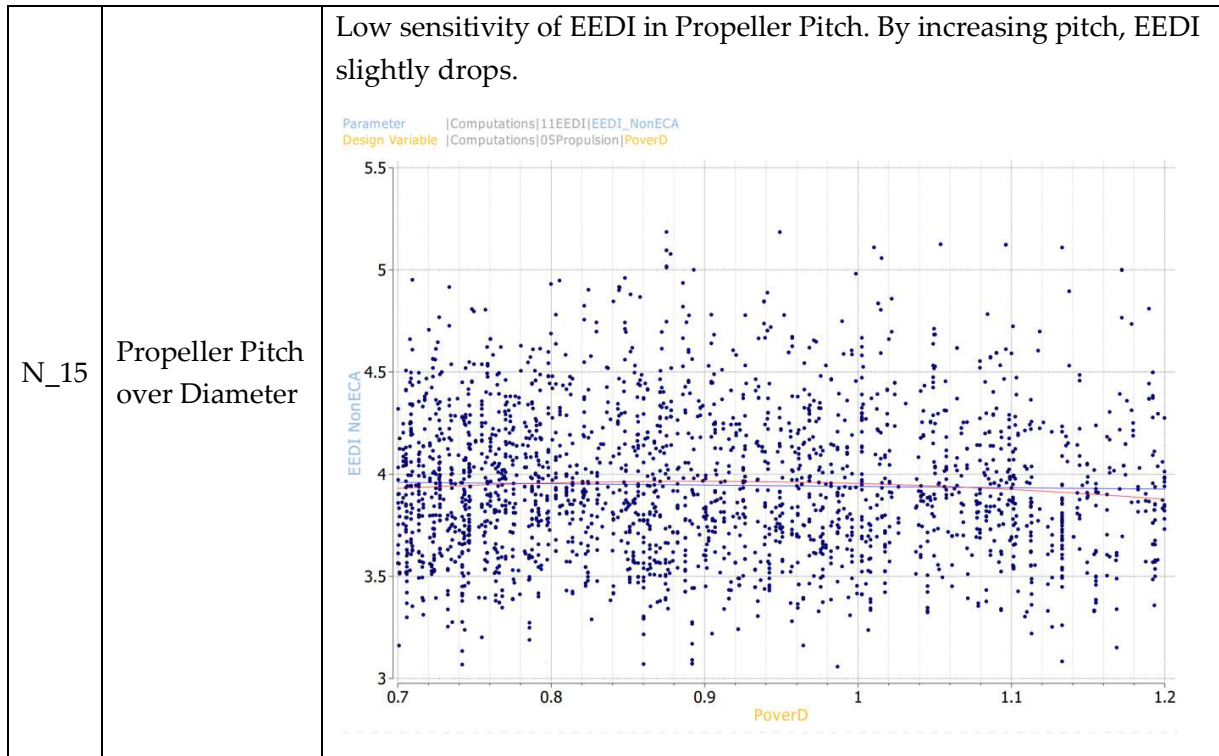
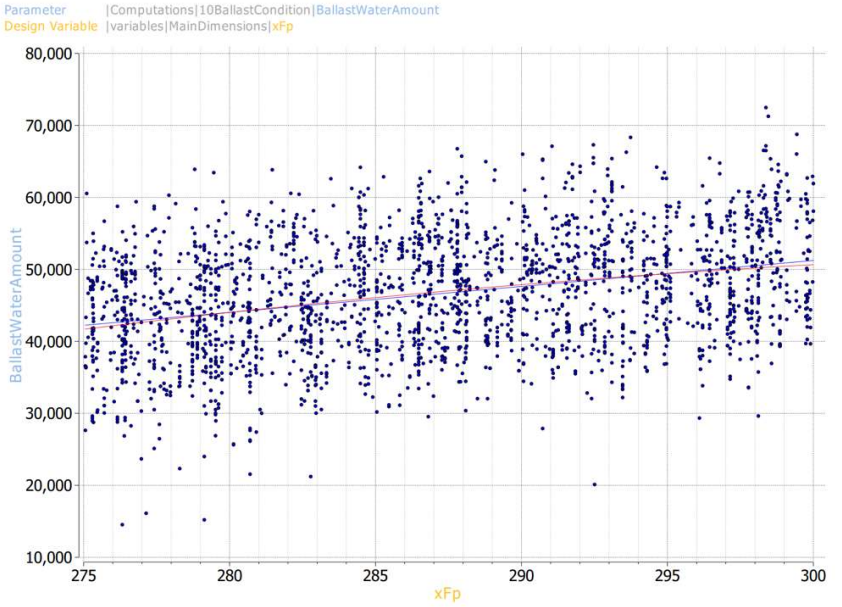
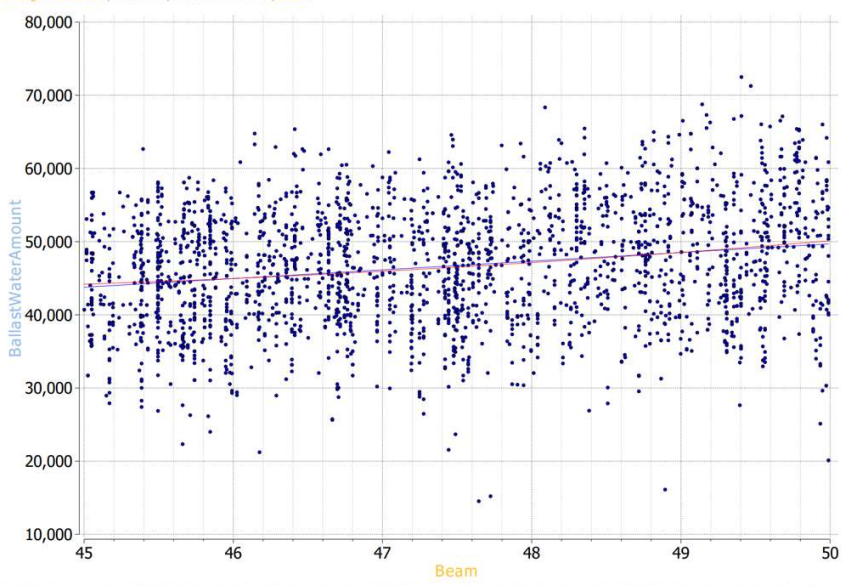
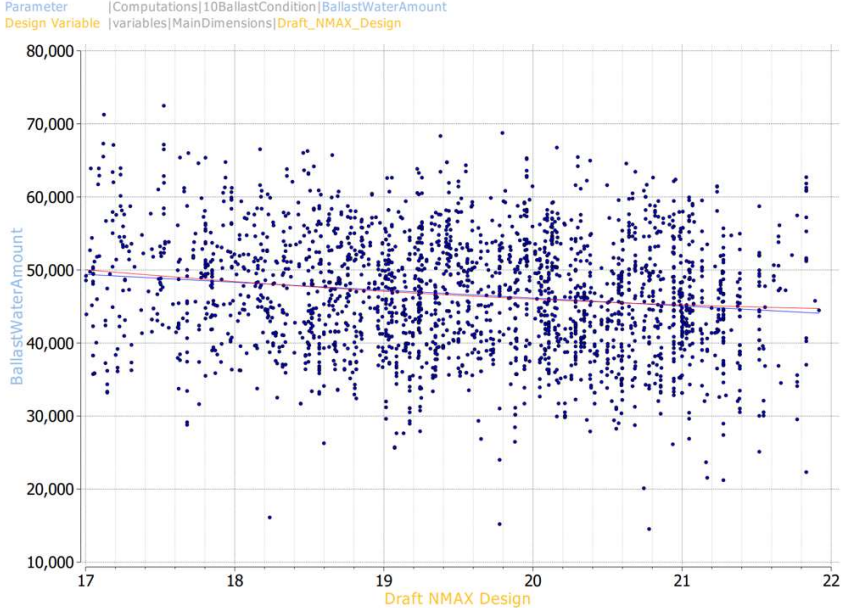
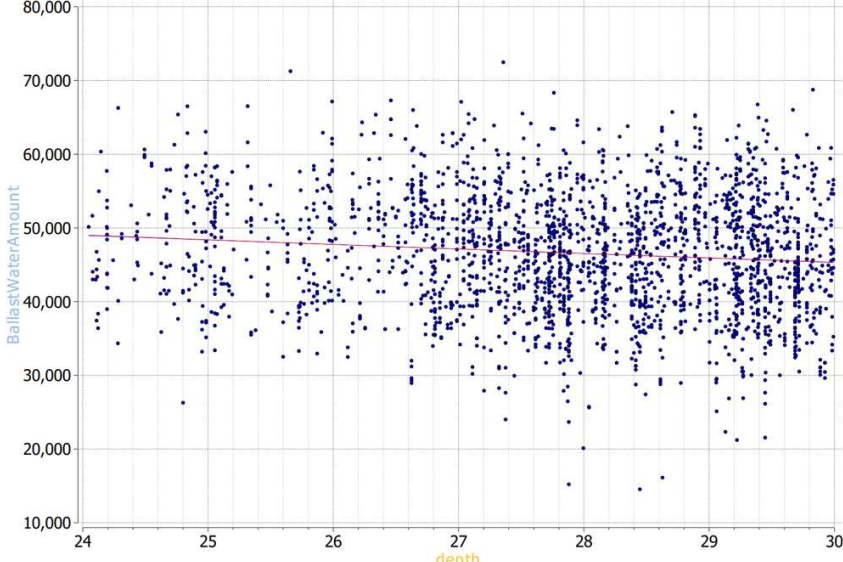
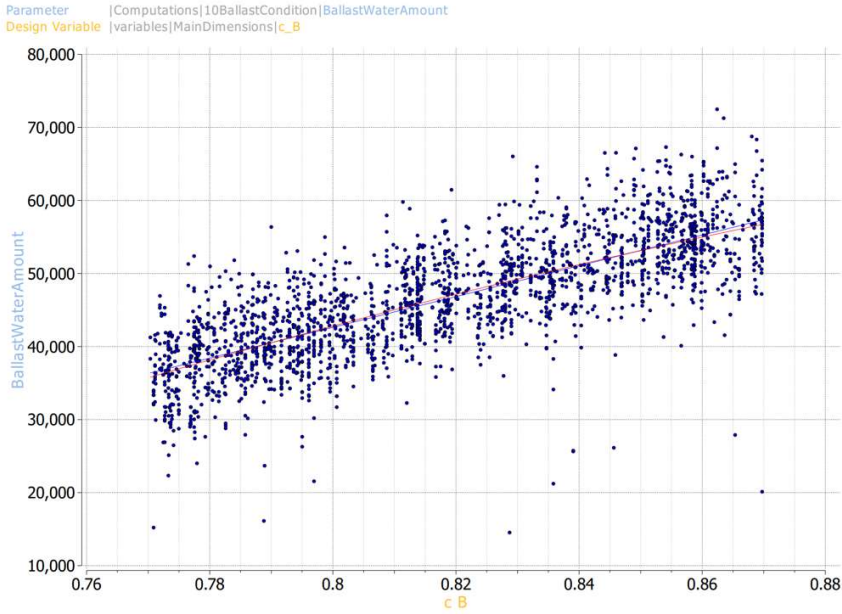
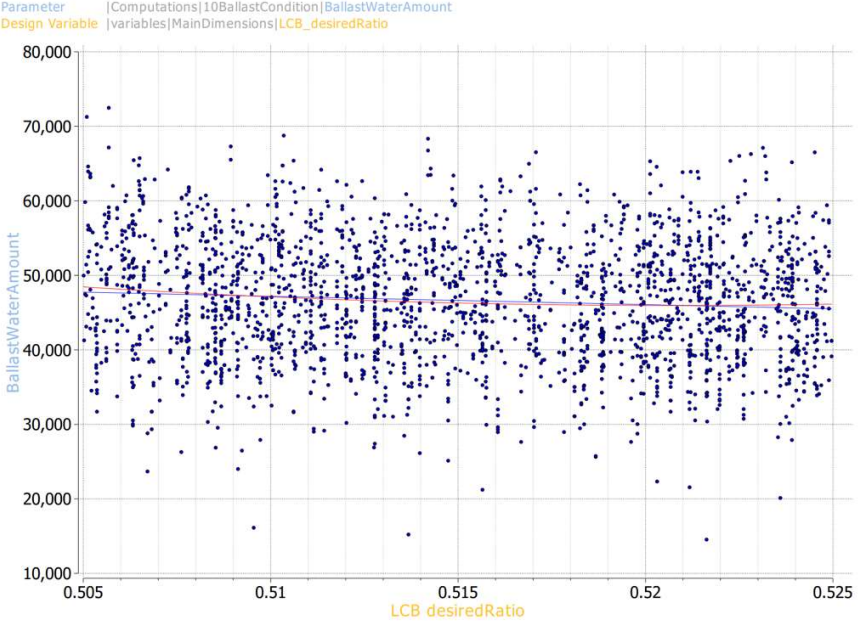
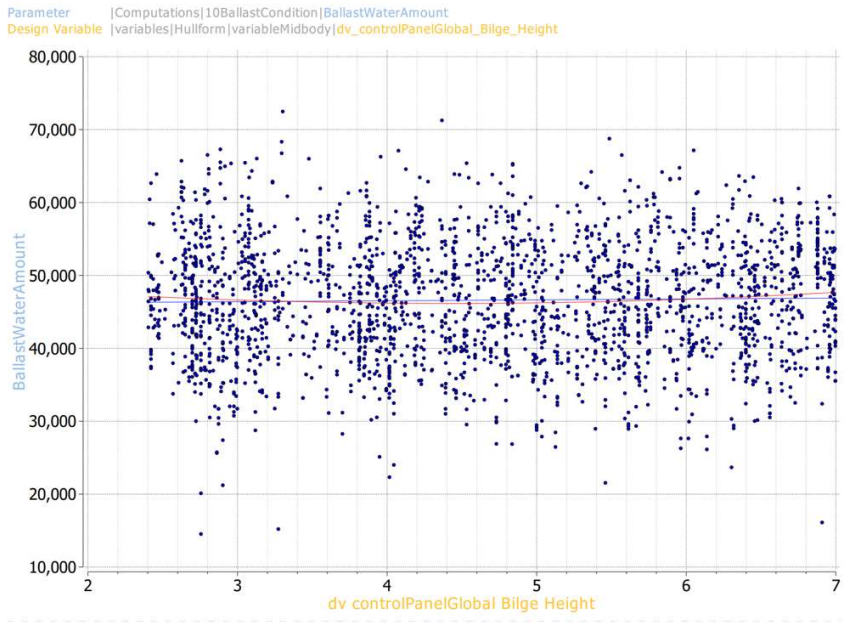


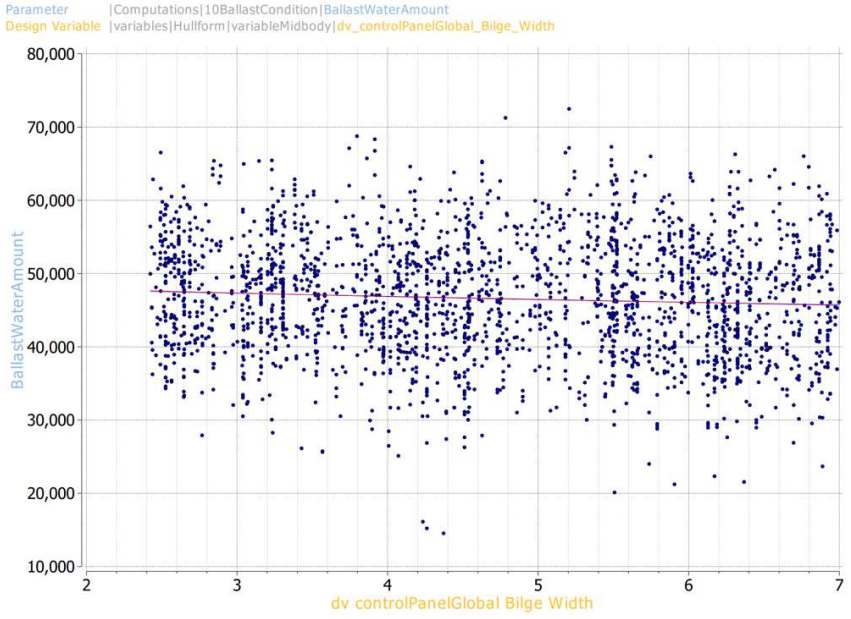
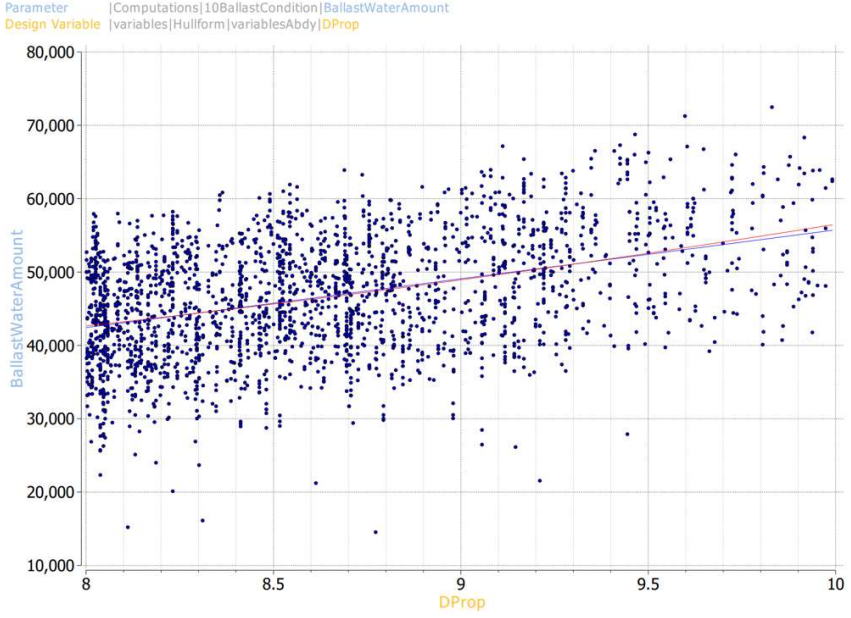
Table 44: EEDI Sensitivity on Design Variables – Deterministic NEWCASTLEMAX Case Studies

ID	Design Variable	Effect on Required Ballast Water Amount
N_01	Length between Perpendiculars	<p>High Sensitivity of BW Amount in Lbp: Increased by increasing length.</p>  <p>Parameter Computations 10BallastCondition BallastWaterAmount Design Variable variables MainDimensions xFp</p>
N_02	Beam	<p>Increased BW Amount by increasing beam.</p>  <p>Parameter Computations 10BallastCondition BallastWaterAmount Design Variable variables MainDimensions Beam</p>

<p>N_03</p>	<p>Draft</p>	<p>Low sensitivity of Ballast Water Amount in Deck Heigh: Increasing design draft leads to decreasing BW Amount</p>  <p>Parameter Computations 10BallastCondition BallastWaterAmount Design Variable variables MainDimensions Draft_NMAX_Design</p>
<p>N_04</p>	<p>Deck height</p>	<p>Increasing Deck Height leads to decreasing BW Amount</p>  <p>Parameter Computations 10BallastCondition BallastWaterAmount Design Variable variables MainDimensions depth</p>

N_05	Hopper Height	No sensitivity of BW Amount with this variable
N_06	Hopper Breadth (m)	No sensitivity of BW Amount with this variable
N_07	Topside Height (m)	No sensitivity of BW Amount with this variable
N_08	Topside Breadth (m)	No sensitivity of BW Amount with this variable
N_09	Block Coefficient Cb	<p>High Sensitivity of BW Amount in Cb. By increasing block coefficient there is a sharp increase of the BW Amount.</p>  <p>Parameter Computations 10BallastCondition BallastWaterAmount Design Variable variables MainDimensions c_B</p>

<p>N_10</p>	<p>LCB (%Lbp)</p>	<p>LCB has a positive effect on Ballast Water amount: by increasing the LCB % the required BW Amount slightly drops</p>  <p>Parameter Computations 10BallastCondition BallastWaterAmount Design Variable variables MainDimensions LCB_desiredRatio</p>
<p>N_11</p>	<p>Bilge Height (m)</p>	<p>Almost zero sensitivity of BW Amount to changes of the Bilge Height</p>  <p>Parameter Computations 10BallastCondition BallastWaterAmount Design Variable variables Hullform variableMidbody dv_controlPanelGlobal_Bilge_Height</p>

<p>N_12</p>	<p>Bilge Width (m)</p>	<p>Almost zero sensitivity of BW Amount to changes of the Bilge Width</p>  <p>Parameter Computations 10BallastCondition BallastWaterAmount Design Variable variables Hullform variableMidbody dv_controlPanelGlobal_Bilge_Width</p>
<p>N_13</p>	<p>Propeller Diameter (m)</p>	<p>High Sensitivity of BW Amount in Propeller Diameter: with increasing diameter , required BW Amount sharply increases (due to Aft Draft requirements)</p>  <p>Parameter Computations 10BallastCondition BallastWaterAmount Design Variable variables Hullform variablesAbdy DProp</p>

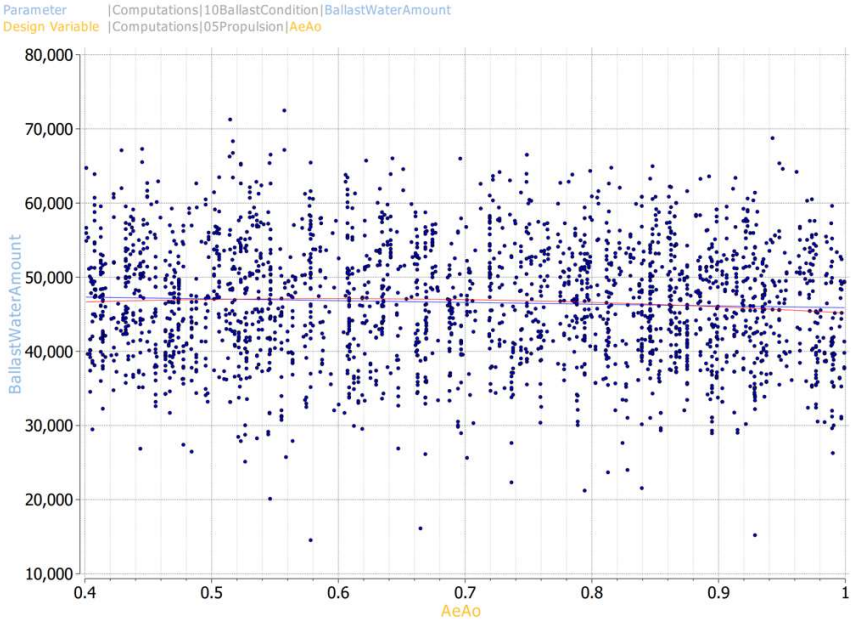
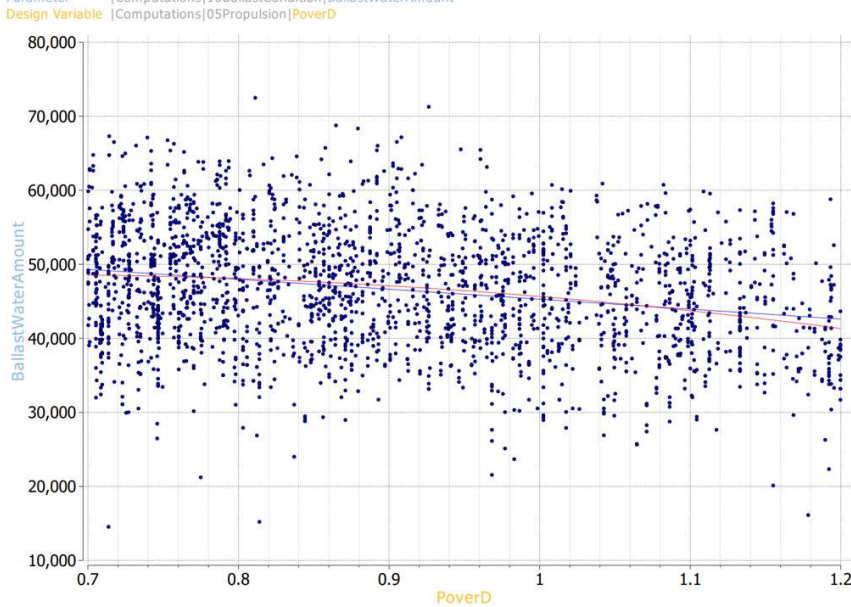
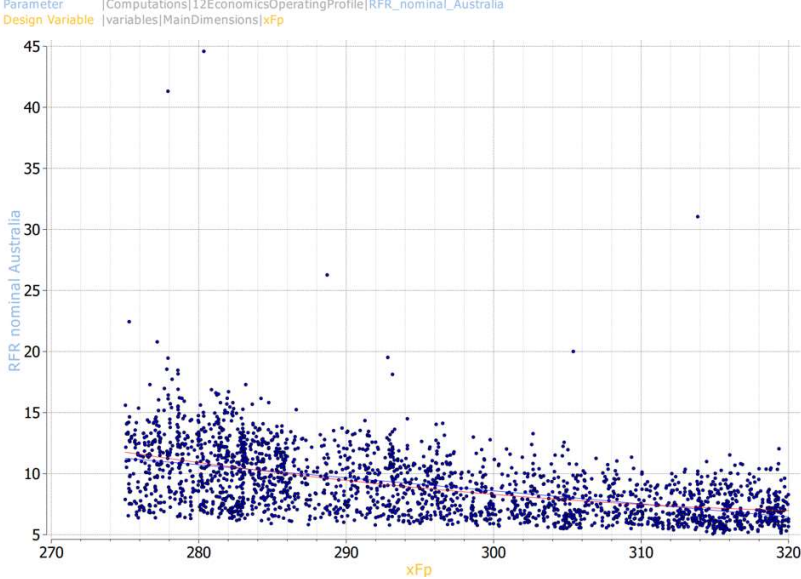
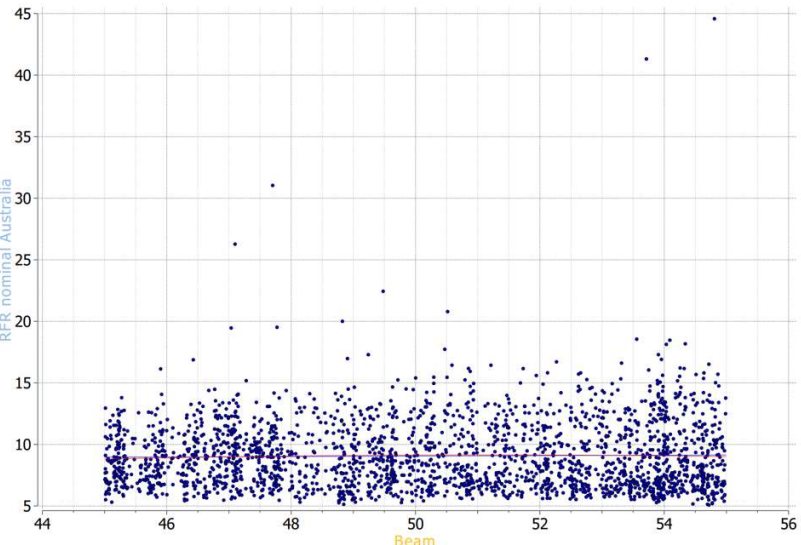
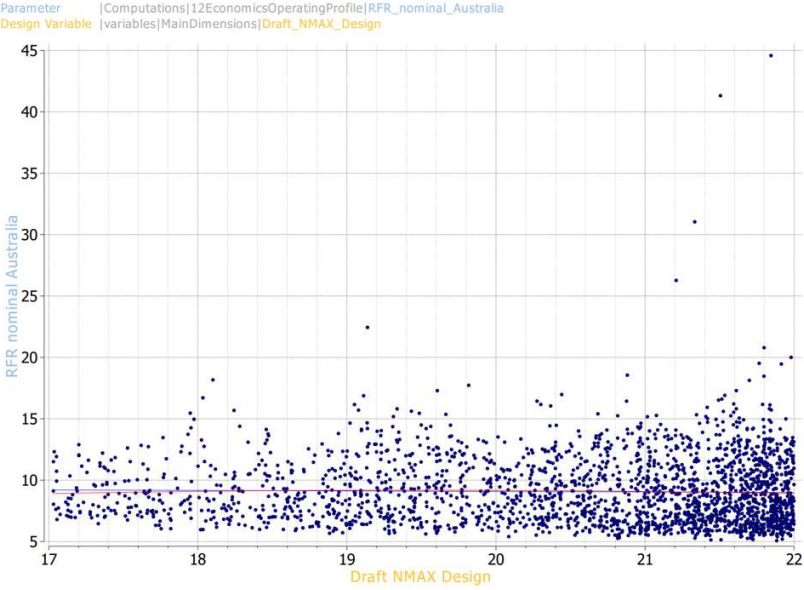
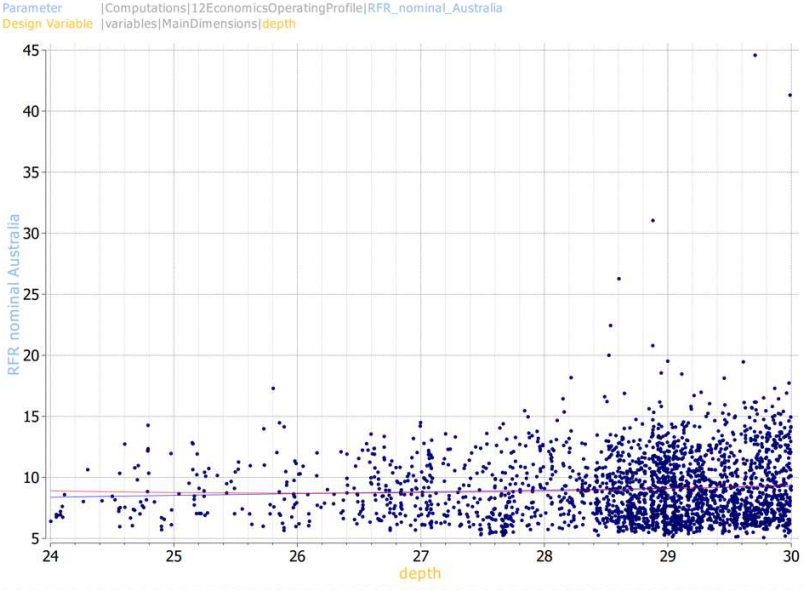
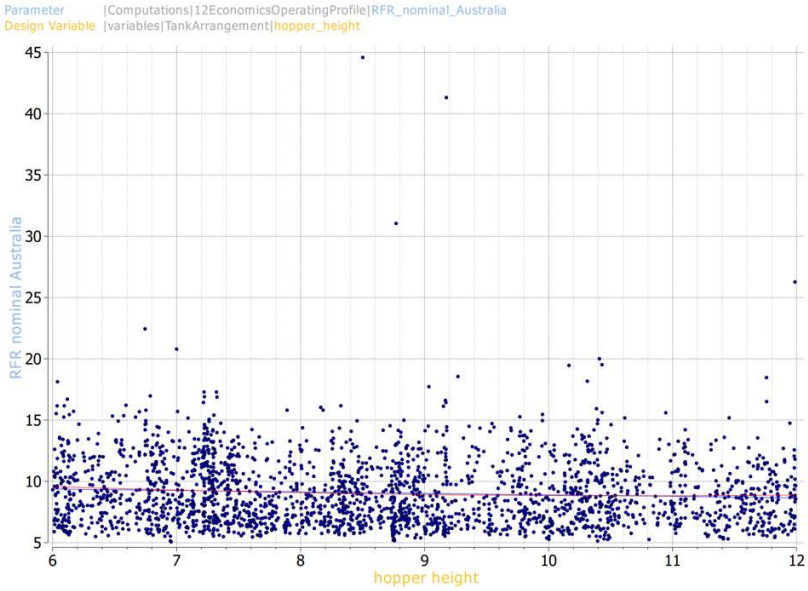
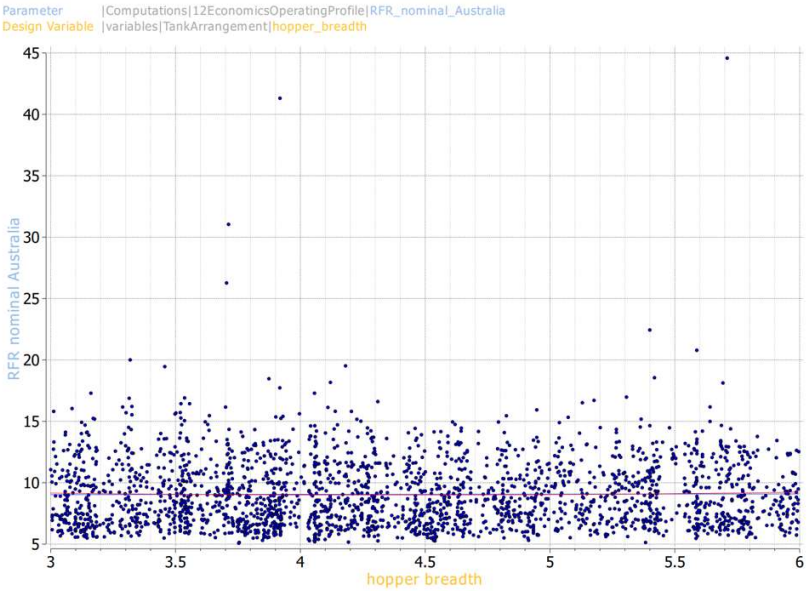
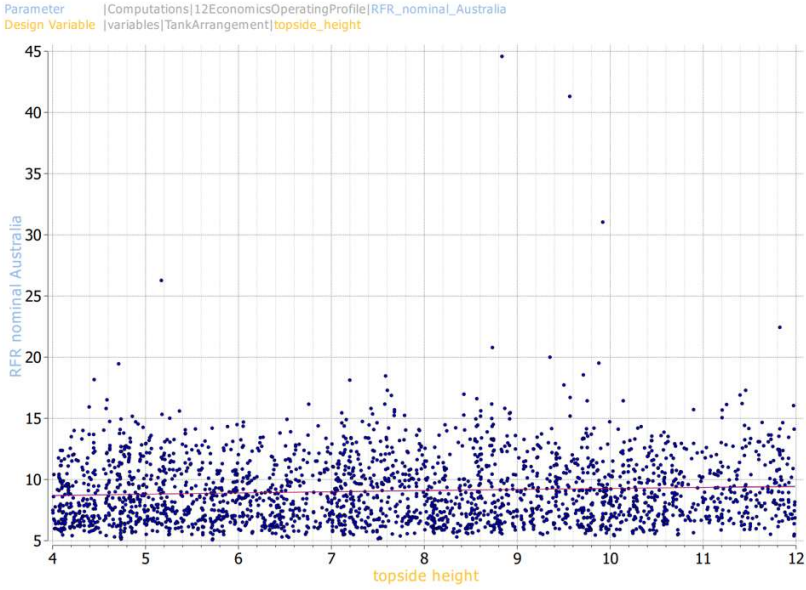
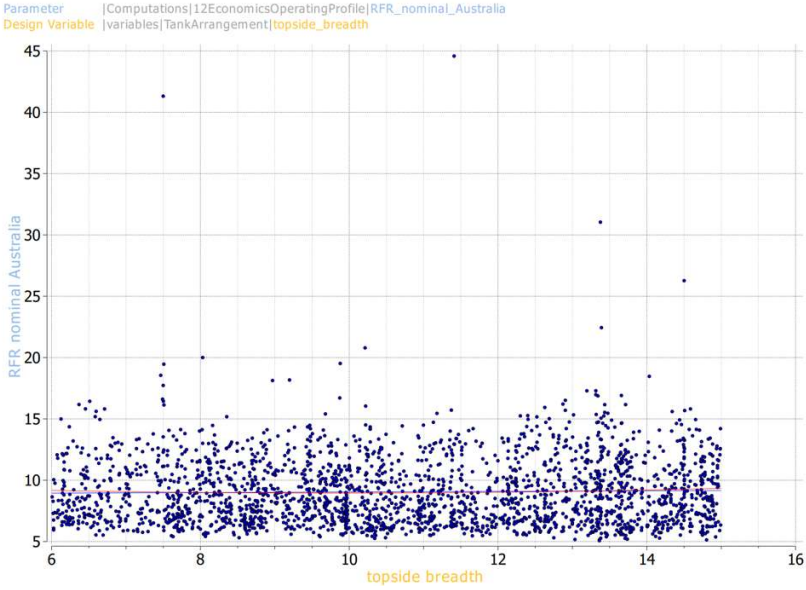
<p>N_14</p>	<p>Propeller Expanded Area Ratio</p>	<p>No sensitivity of BW Amount in Propeller Expanded Area Ratio</p> 
<p>N_15</p>	<p>Propeller Pitch over Diameter</p>	<p>High Sensitivity of BW Amount in Pitch: Increasing pitch leads to lower BW Amount (due to propeller diameter reduction)</p> 

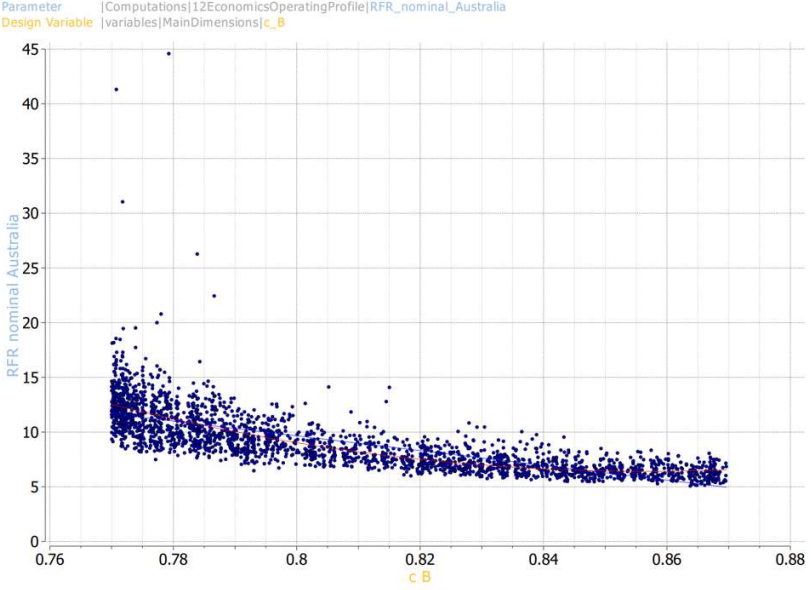
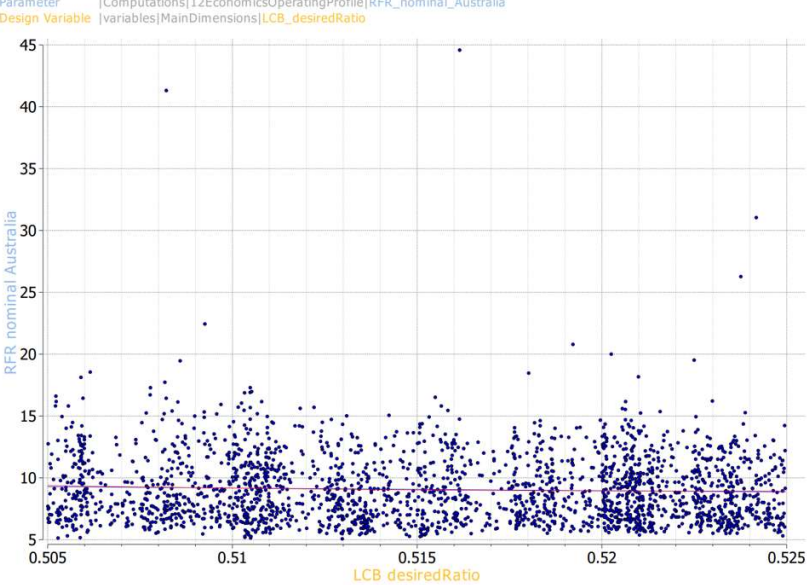
Table 45: BW Amount Sensitivity on Design Variables – Deterministic Newcastlemax Case Studies

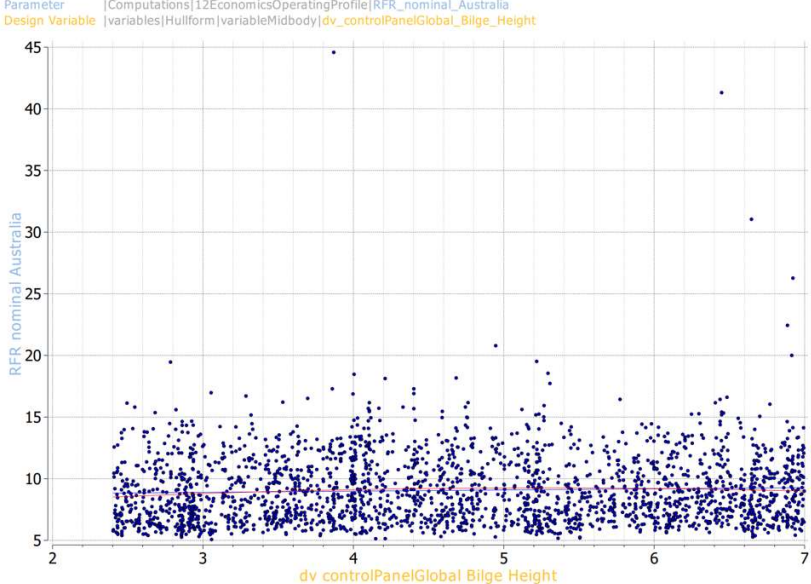
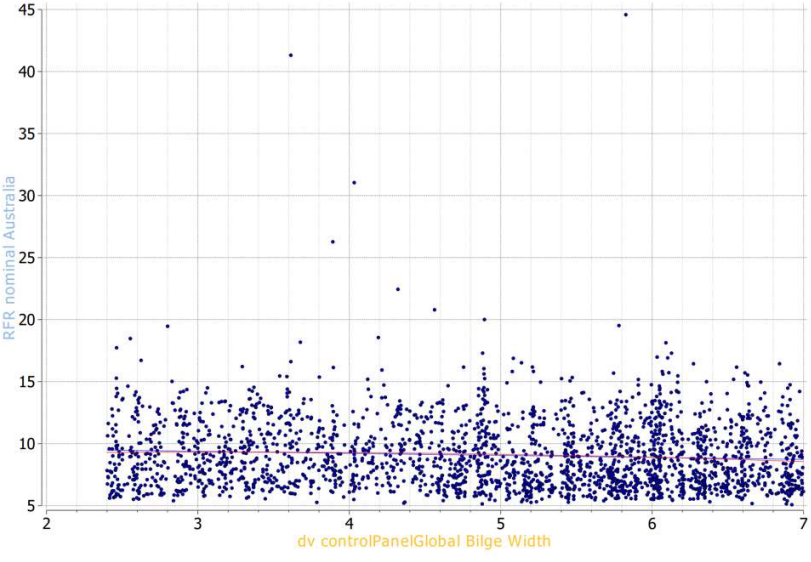
ID	Design Variable	Effect on RFR
N_01	Length between Perpendiculars	<p>High sensitivity of RFR in Length between perpendiculars: decrease of RFR by increasing length.</p> <p>Higher concentration and less scatter in regions of higher lengths</p> 
N_02	Beam	<p>Uniform, no sensitivity by increasing or decreasing beam to RFR.</p> 

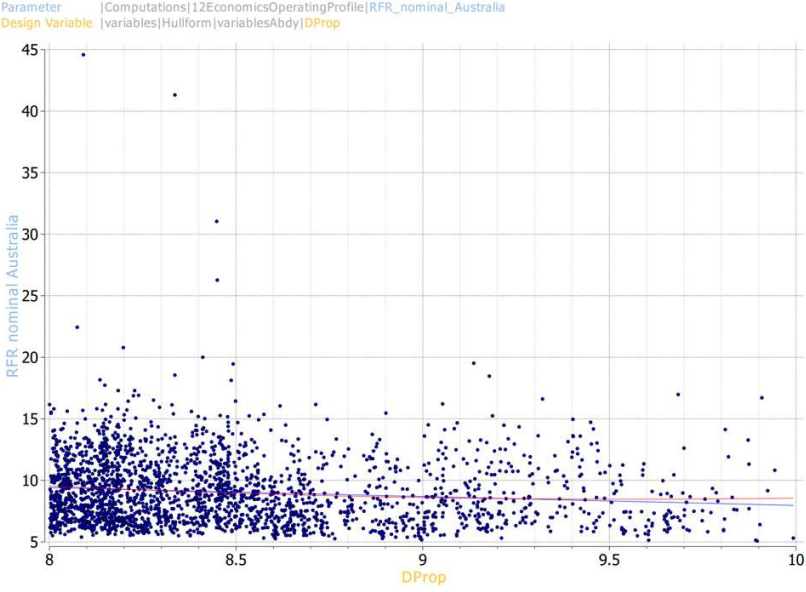
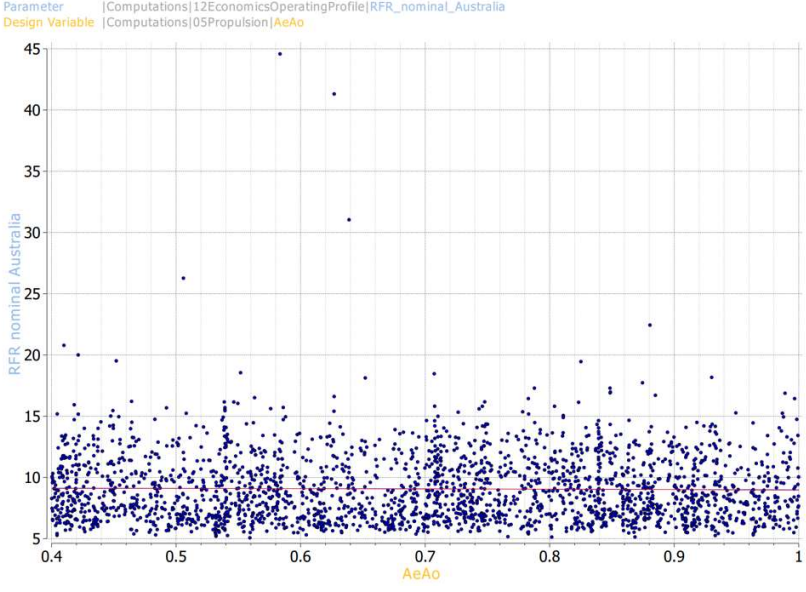
<p>N_03</p>	<p>Draft</p>	<p>Almost no sensitivity of RFR on changes of design draft. Slight decrease observed and higher concentration of feasible designs in higher deck height values</p>  <p>Parameter [Computations]12EconomicsOperatingProfile[RFR_nominal_Australia] Design Variable [variables]MainDimensions[Draft_NMAX_Design]</p>
<p>N_04</p>	<p>Deck height</p>	<p>Slight decrease of RFR by increasing Deck height, majority of feasible designs concentrated in higher deck height values (loadline constraint).</p>  <p>Parameter [Computations]12EconomicsOperatingProfile[RFR_nominal_Australia] Design Variable [variables]MainDimensions[depth]</p>

<p>N_05</p>	<p>Hopper Height</p>	<p>Slight increase of RFR in 9.0m region of hopper height with lower values for extreme values.</p>  <p>Parameter [Computations]12EconomicsOperatingProfile RFR_nominal_Australia Design Variable [variables]TankArrangement hopper_height</p>
<p>N_06</p>	<p>Hopper Breadth (m)</p>	<p>Uniform distribution of designs, zero sensitivity of RFR in Topside Height.</p>  <p>Parameter [Computations]12EconomicsOperatingProfile RFR_nominal_Australia Design Variable [variables]TankArrangement hopper_breadth</p>

<p>N_07</p>	<p>Topside Height (m)</p>	<p>Uniform distribution of designs, small sensitivity of RFR in Topside Height.</p>  <p>Parameter [Computations]12EconomicsOperatingProfile RFR_nominal_Australia Design Variable [variables]TankArrangement topside_height</p>
<p>N_08</p>	<p>Topside Breadth (m)</p>	<p>Uniform distribution of designs, small sensitivity of RFR in Topside Breadth.</p>  <p>Parameter [Computations]12EconomicsOperatingProfile RFR_nominal_Australia Design Variable [variables]TankArrangement topside_breadth</p>

<p>N_09</p>	<p>Block Coefficient Cb</p>	<p>High sensitivity, increasing Cb decreases the RFR constantly.</p> 
<p>N_10</p>	<p>LCB (%Lbp)</p>	<p>Uniform distribution of designs, zero sensitivity of RFR in LCB.</p> 

<p>N_11</p>	<p>Bilge Height (m)</p>	<p>Uniform distribution of designs, small sensitivity of RFR in Bilge Height</p>  <p>Parameter [Computations]12EconomicsOperatingProfile[RFR_nominal_Australia] Design Variable [variables]Hullform variableMidbody dv_controlPanelGlobal_Bilge_Height</p>
<p>N_12</p>	<p>Bilge Width (m)</p>	<p>Uniform distribution of designs, zero sensitivity of RFR in Bilge Width</p>  <p>Parameter [Computations]12EconomicsOperatingProfile[RFR_nominal_Australia] Design Variable [variables]Hullform variableMidbody dv_controlPanelGlobal_Bilge_Width</p>

<p>N_13</p>	<p>Propeller Diameter (m)</p>	<p>Decrease of RFR by increasing propeller diameter, higher design population in lower diameters, Smaller sensitivity compared to Newcastlemax designs</p>  <p>Parameter [Computations]12EconomicsOperatingProfile RFR_nominal_Australia Design Variable [variables]Hullform variablesAbdy DProp</p>
<p>N_14</p>	<p>Propeller Expanded Area Ratio</p>	<p>Uniform distribution with little sensitivity of RFR in Expanded Area Ratio.</p>  <p>Parameter [Computations]12EconomicsOperatingProfile RFR_nominal_Australia Design Variable [Computations]05Propulsion AeAo</p>

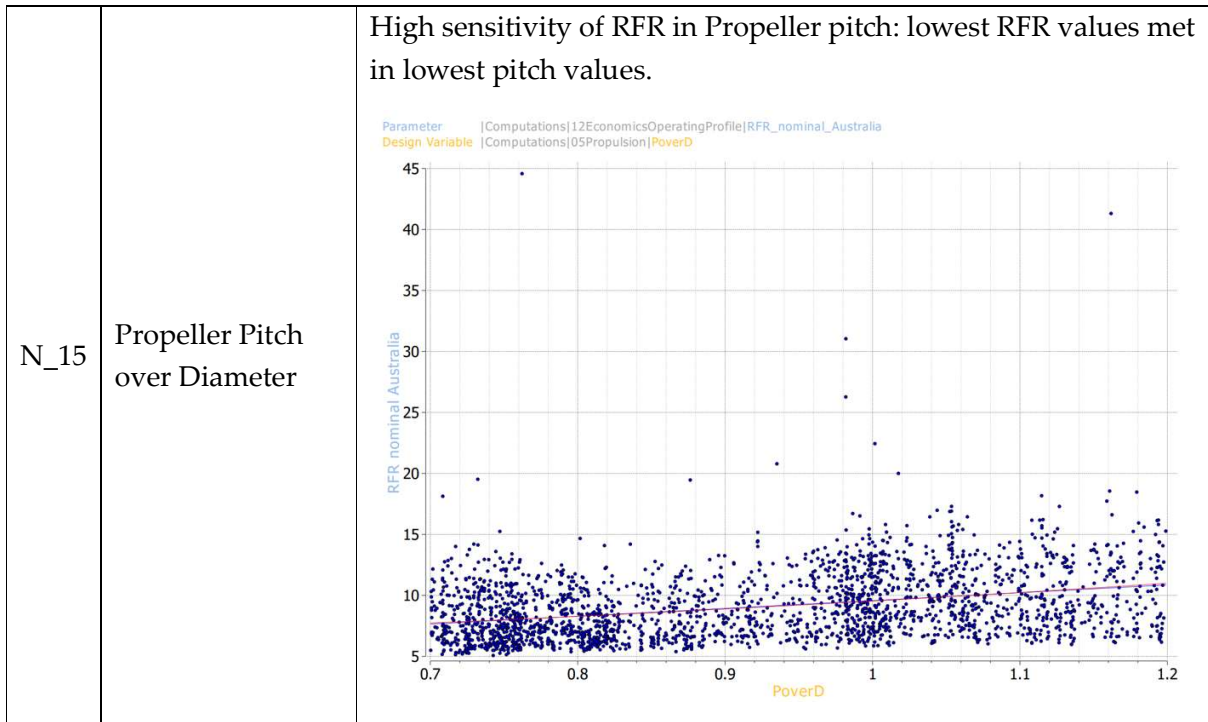
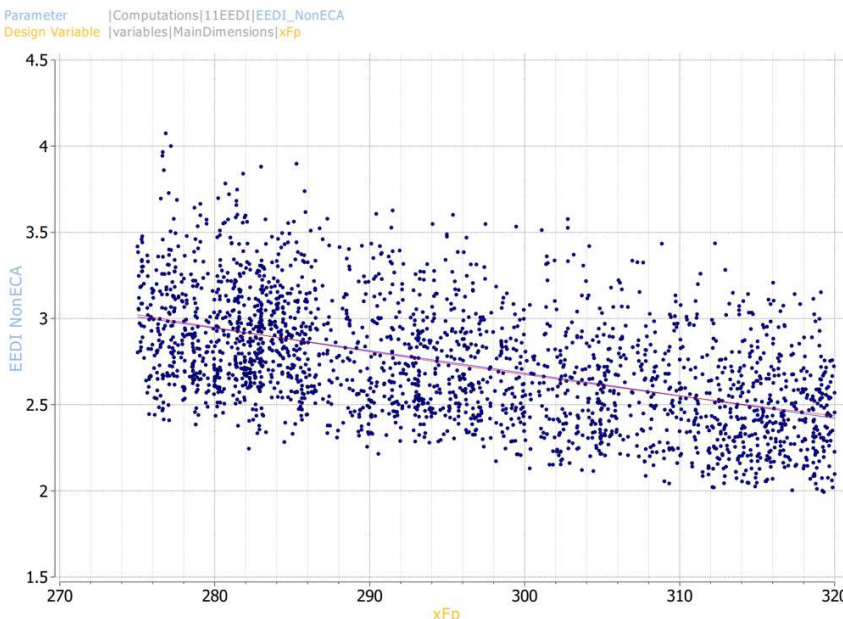
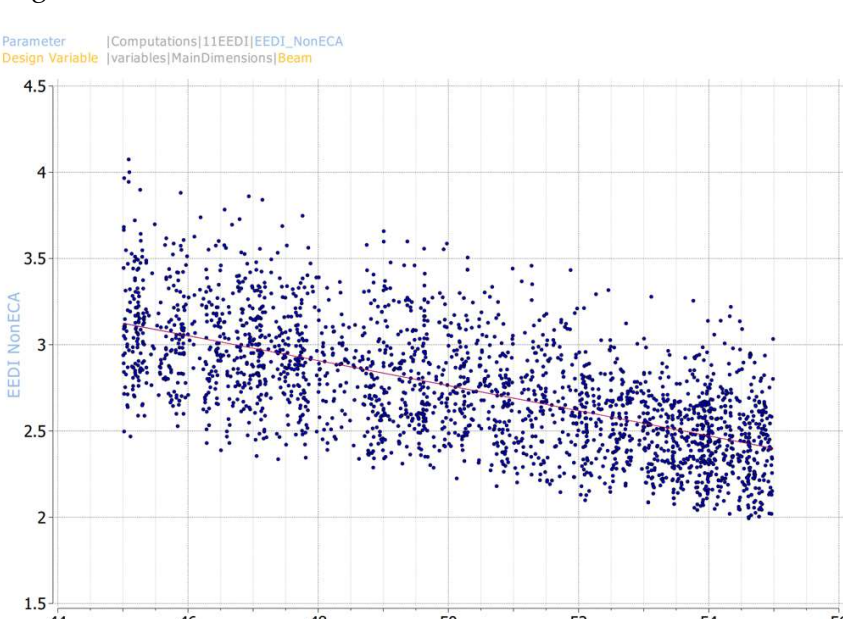
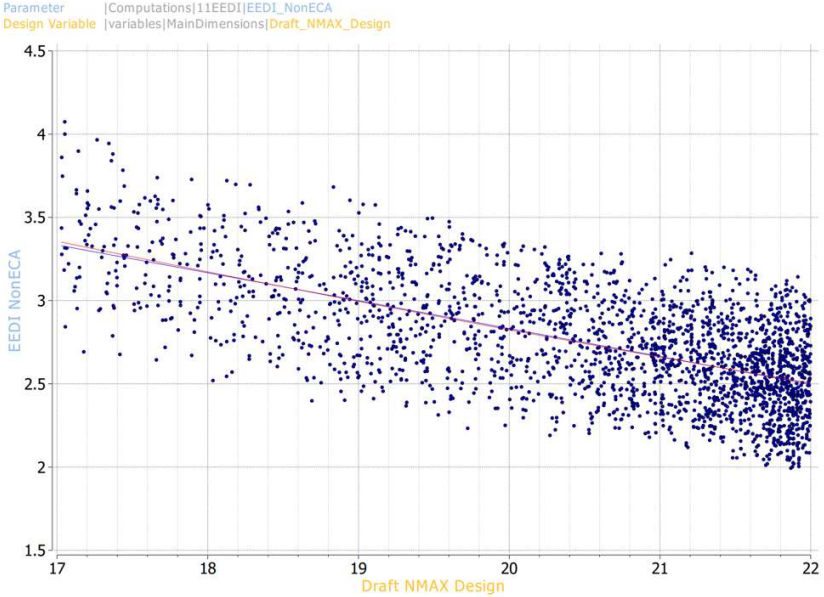
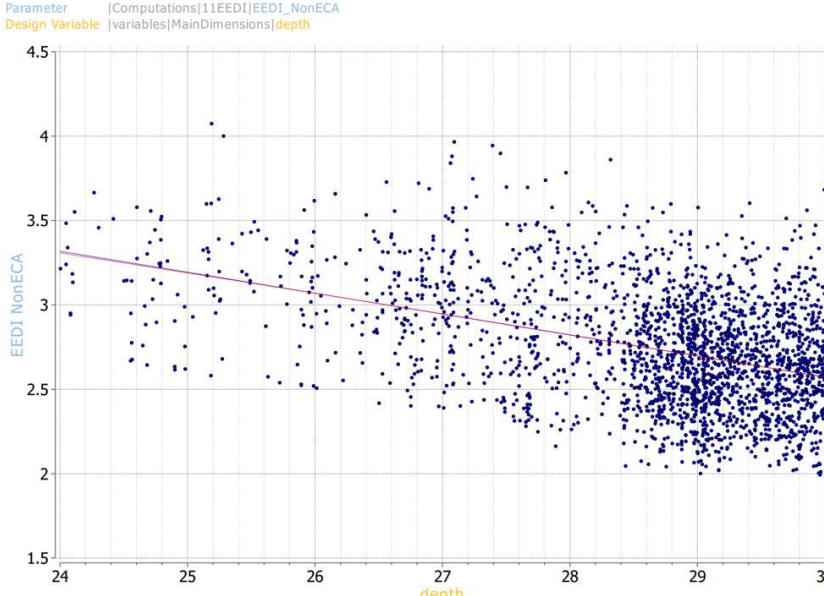
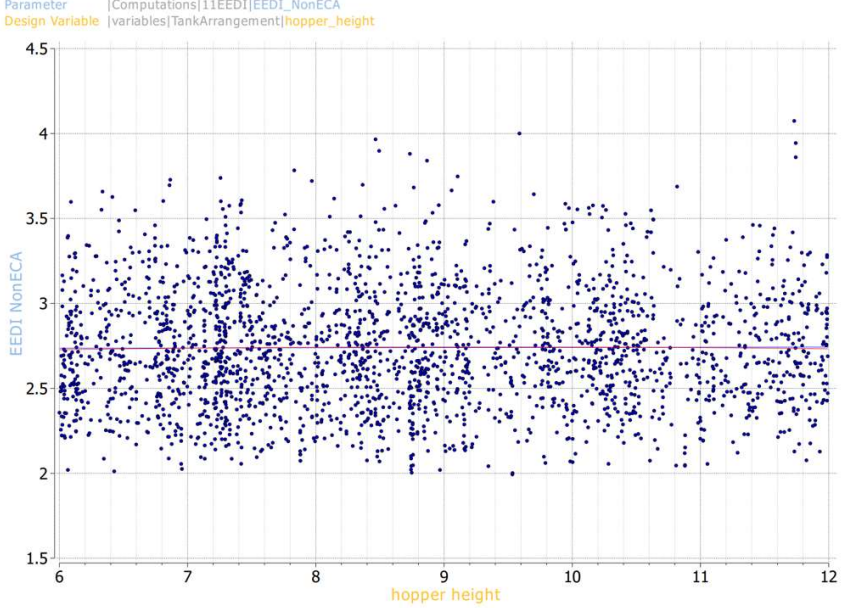
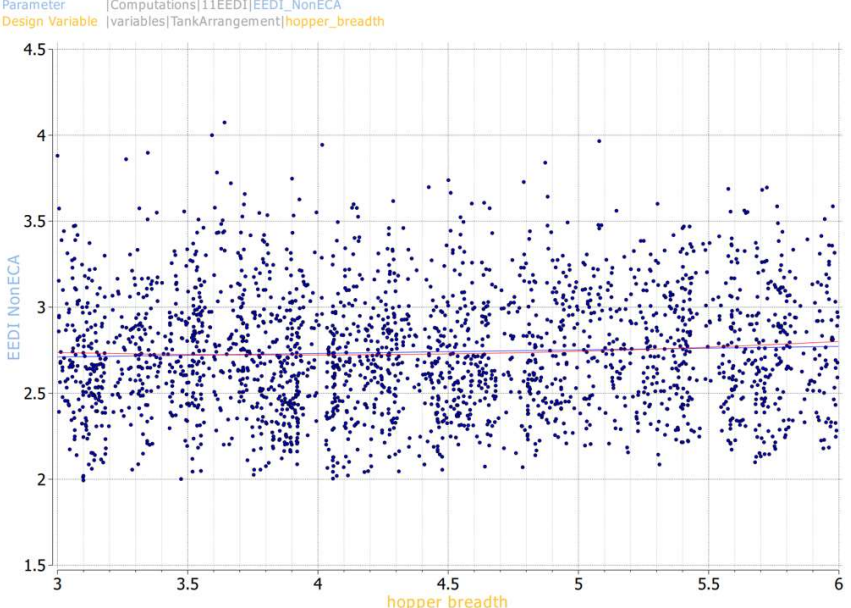
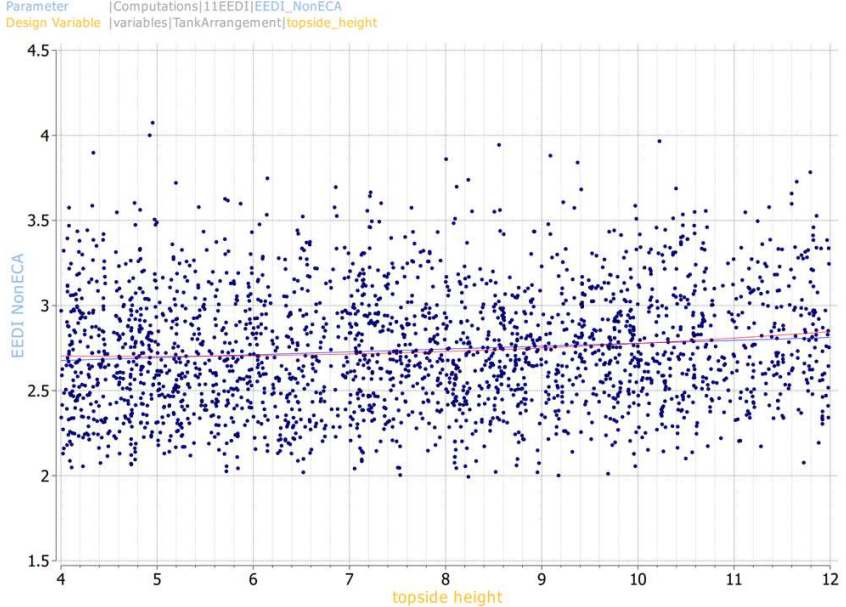
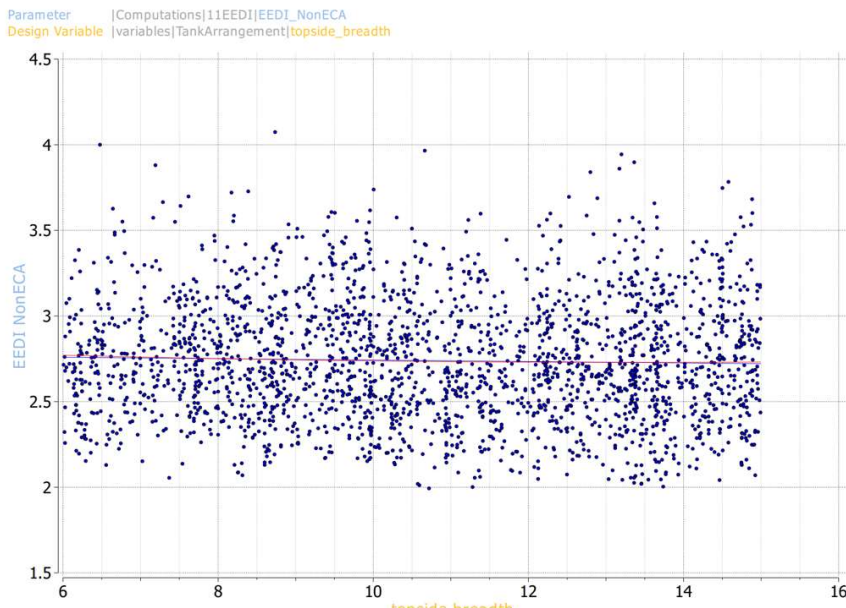


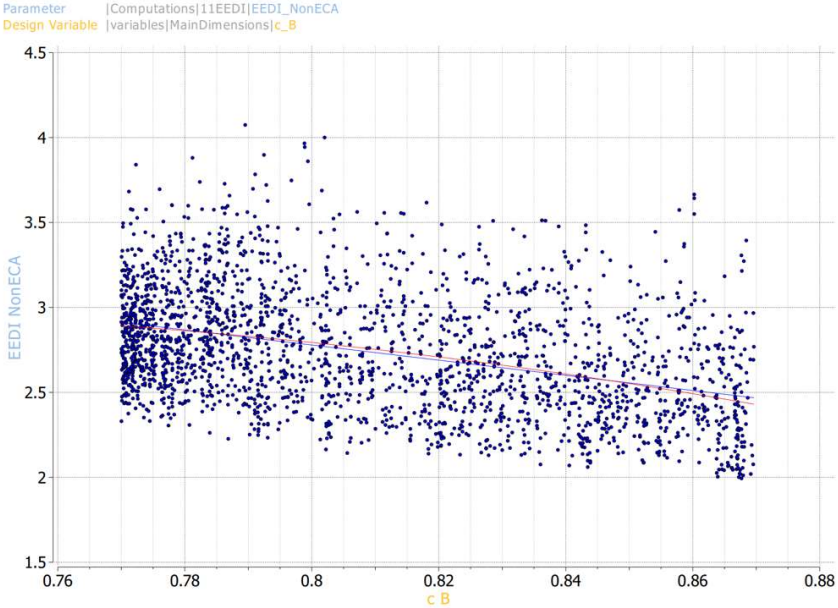
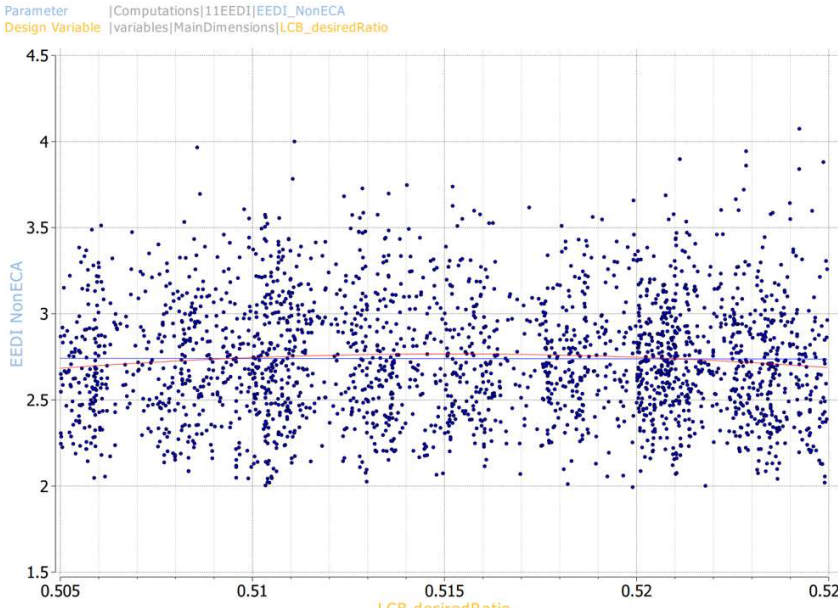
Table 46: RFR Sensitivity on Design Variables – Deterministic WOZMAX Case Studies

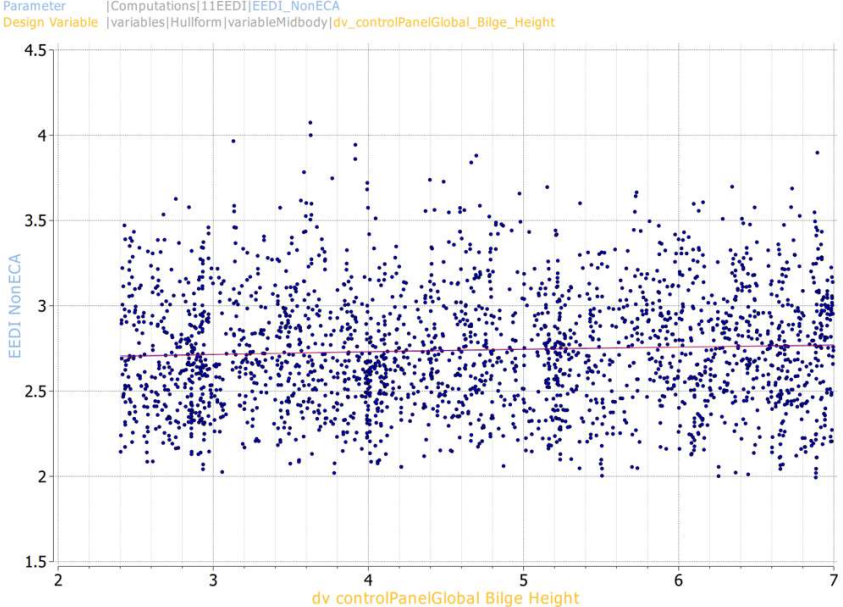
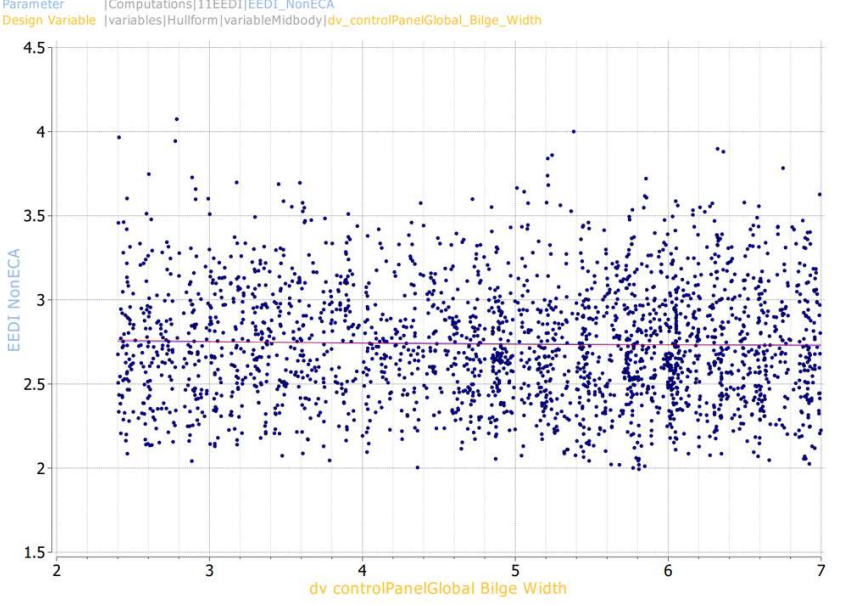
ID	Design Variable	Effect on EEDI
N_01	Length between Perpendiculars	<p>High sensitivity of EEDI in Lbp. EEDI decreases by increasing length.</p>  <p>Parameter [Computations]11EEDI[EEDI_NonECA] Design Variable [variables]MainDimensions xFp</p>
N_02	Beam	<p>High sensitivity of EEDI in Beam: EEDI decreases by increasing length.</p>  <p>Parameter [Computations]11EEDI[EEDI_NonECA] Design Variable [variables]MainDimensions Beam</p>

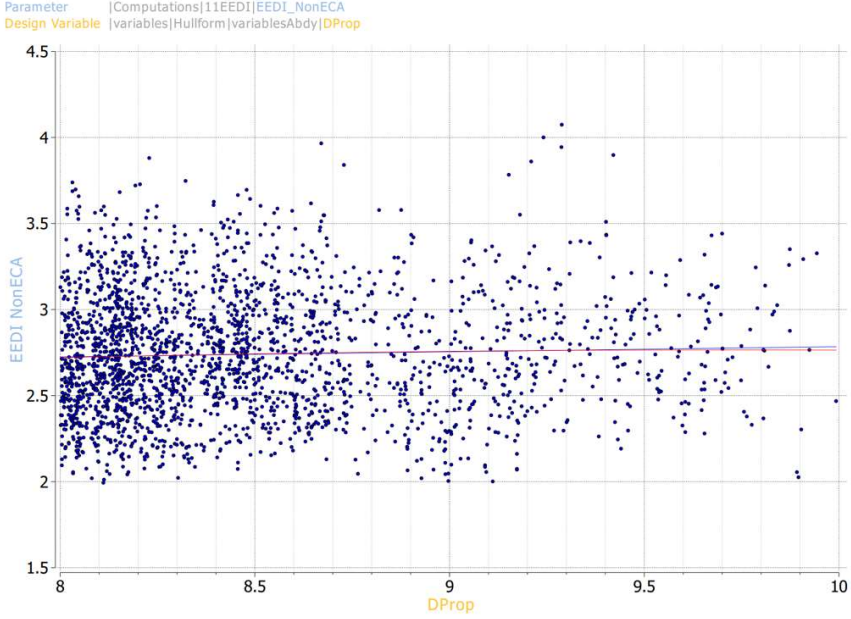
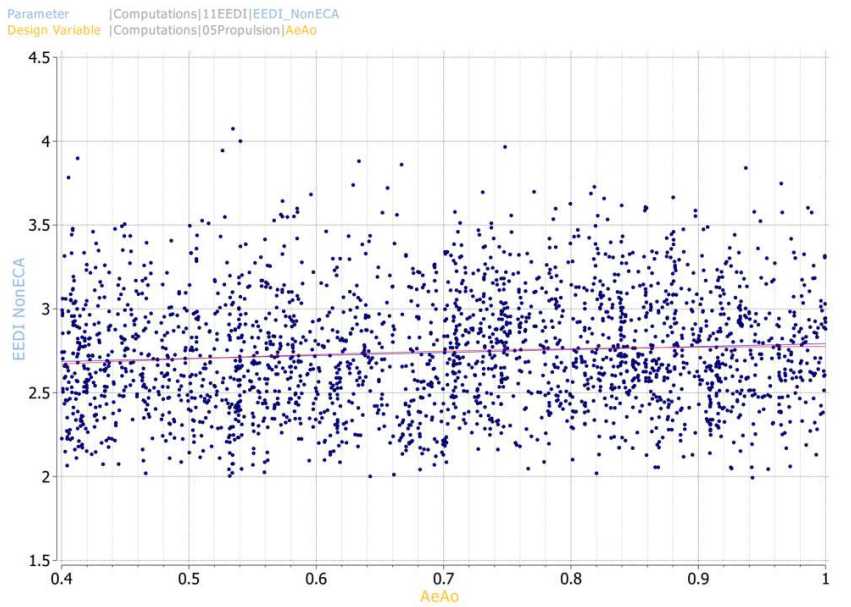
<p>N_03</p>	<p>Draft</p>	<p>High sensitivity of EEDI in Draft: EEDI decreases sharply by increasing draft</p> 
<p>N_04</p>	<p>Deck height</p>	<p>High sensitivity of EEDI in Deck Height : EEDI decreases by increasing deck height. Scatter increases by increasing deck height and most of the design population is concentrated at higher values (loadline constraint).</p> 

<p>N_05</p>	<p>Hopper Height</p>	<p>Increase of Hopper Height leads to increase of EEDI (through cargo capacity and deadweight).</p>  <p>Parameter Computations 11EEDI EEDI_NonECA Design Variable variables TankArrangement hopper_height</p>
<p>N_06</p>	<p>Hopper Breadth (m)</p>	<p>Increase of Hopper Breadth leads to decrease of EEDI (through cargo capacity and deadweight).</p>  <p>Parameter Computations 11EEDI EEDI_NonECA Design Variable variables TankArrangement hopper_breadth</p>

<p>N_07</p>	<p>Topside Height (m)</p>	<p>EEDI sensitivity in topside height is low and close to zero</p>  <p>Parameter Computations 11EEDI EEDI_NonECA Design Variable variables TankArrangement topside_height</p>
<p>N_08</p>	<p>Topside Breadth (m)</p>	<p>EEDI sensitivity in topside breadth is low and close to zero</p>  <p>Parameter Computations 11EEDI EEDI_NonECA Design Variable variables TankArrangement topside_breadth</p>

<p>N_09</p>	<p>Block Coefficient Cb</p>	<p>High sensitivity of EEDI in Cb: EEDI decreases sharply by increasing the block coefficient.</p>  <p>Parameter Computations 1 EEDI EEDI_NonECA Design Variable variables MainDimensions c_B</p>
<p>N_10</p>	<p>LCB (%Lbp)</p>	<p>Little to zero sensitivity of EEDI in LCB position with uniform distribution of designs.</p>  <p>Parameter Computations 1 EEDI EEDI_NonECA Design Variable variables MainDimensions LCB_desiredRatio</p>

<p>N_11</p>	<p>Bilge Height (m)</p>	<p>Slight sensitivity of EEDI in Bilge Height value: with increasing bilge height the EEDI slightly increases.</p>  <p>Parameter Computations 11EEDI EEDI_NonECA Design Variable variables Hullform variableMidbody dv_controlPanelGlobal_Bilge_Height</p>
<p>N_12</p>	<p>Bilge Width (m)</p>	<p>Little sensitivity of EEDI in bilge width.</p>  <p>Parameter Computations 11EEDI EEDI_NonECA Design Variable variables Hullform variableMidbody dv_controlPanelGlobal_Bilge_Width</p>

<p>N_13</p>	<p>Propeller Diameter (m)</p>	<p>EEDI has a low sensitivity in the change of propeller diameter, with lowest figures being observed for 9.0m diameter region propellers.</p>  <p>The scatter plot shows EEDI NonECA on the y-axis (ranging from 1.5 to 4.5) and DProp on the x-axis (ranging from 8 to 10). A dense cloud of blue data points is centered around a horizontal red line at approximately EEDI = 2.7. The distribution is relatively uniform across the diameter range, with a slight concentration of points between 8.5m and 9.5m.</p>
<p>N_14</p>	<p>Propeller Expanded Area Ratio</p>	<p>Decreasing EEDI in propellers with lower expanded area ratios</p>  <p>The scatter plot shows EEDI NonECA on the y-axis (ranging from 1.5 to 4.5) and AeAo on the x-axis (ranging from 0.4 to 1.0). A dense cloud of blue data points is centered around a horizontal red line at approximately EEDI = 2.7. There is a clear downward trend, with higher EEDI values (up to 4.0) concentrated at lower AeAo values (around 0.4-0.5) and lower EEDI values (down to 2.0) appearing at higher AeAo values (around 0.8-1.0).</p>

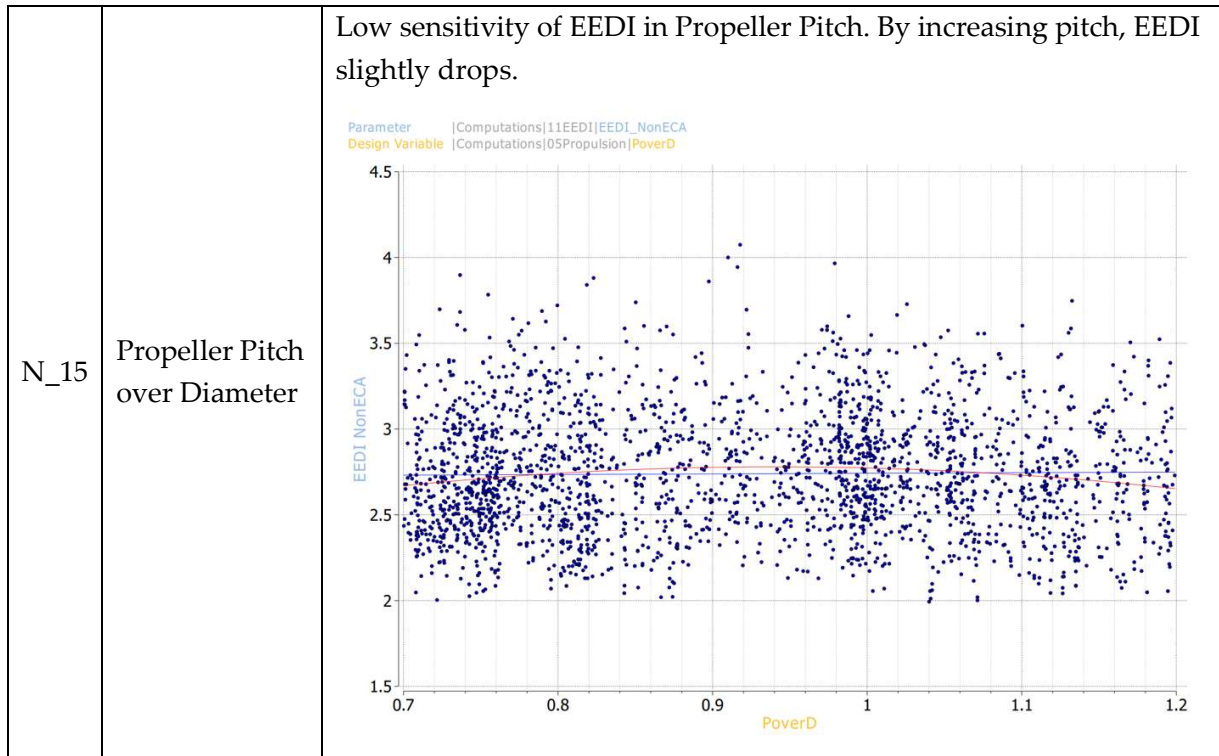
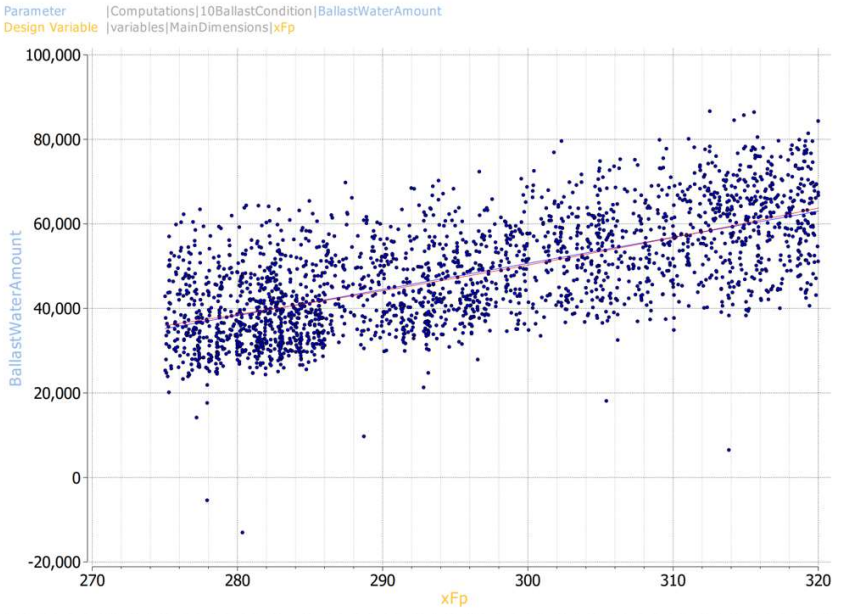
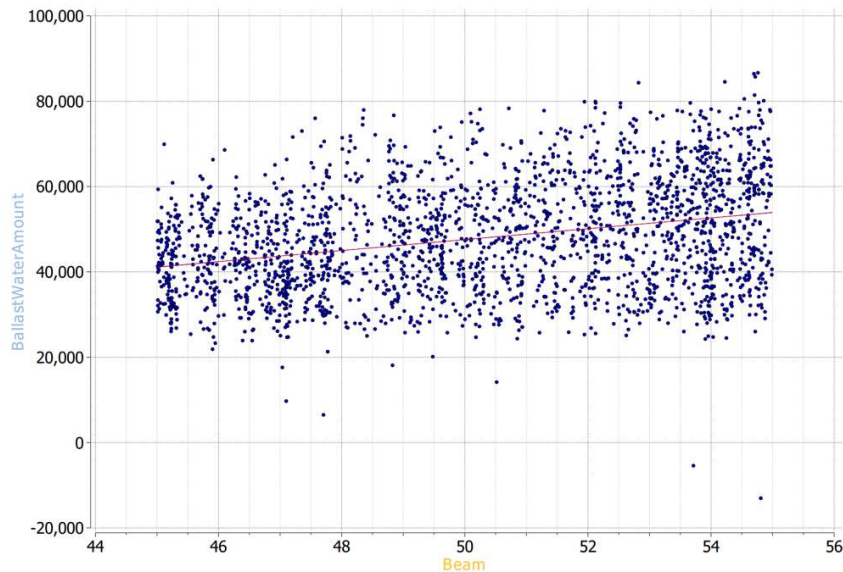
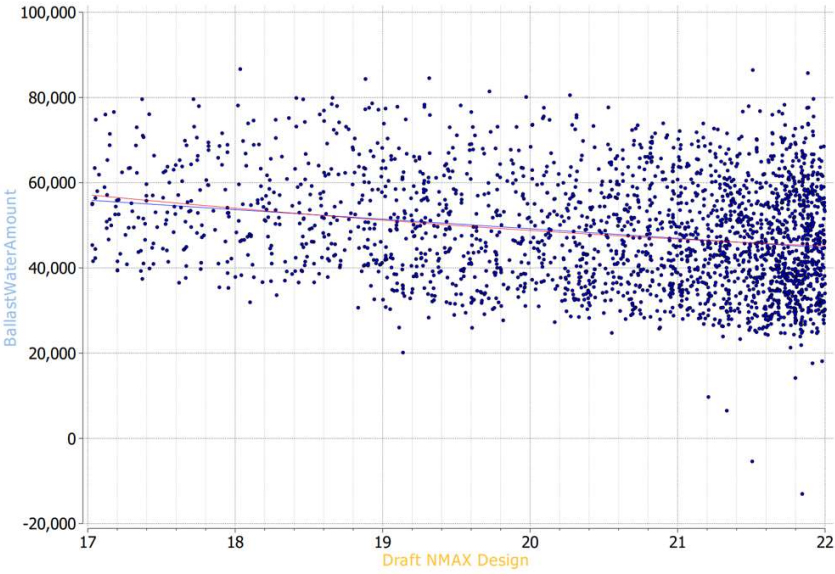
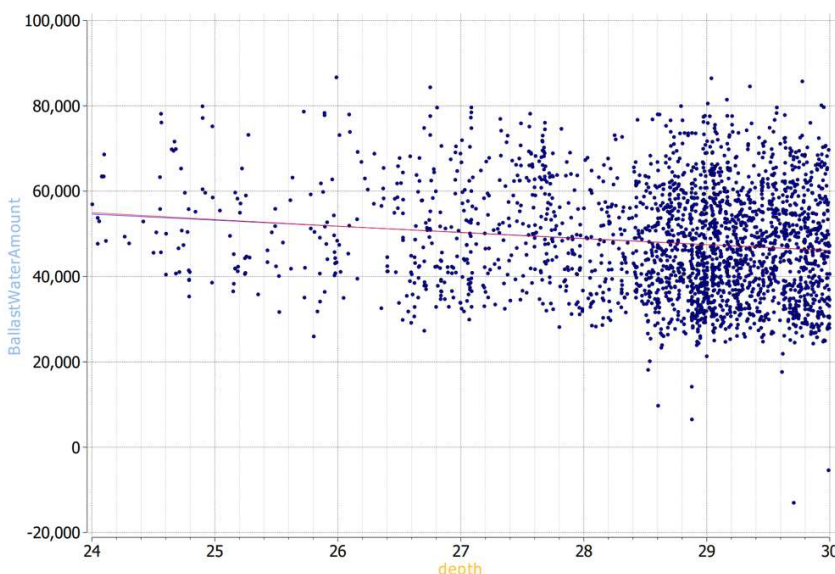
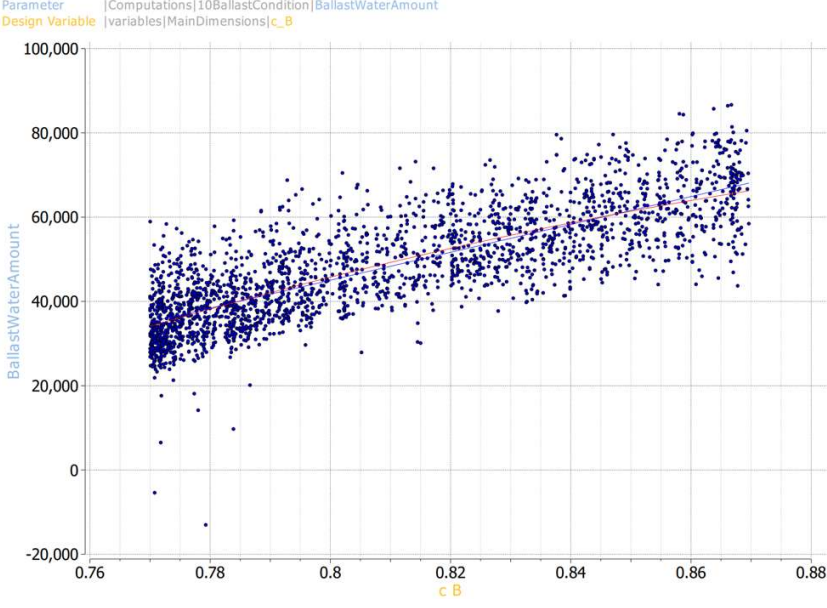


Table 47: EEDI Sensitivity on Design Variables – Deterministic WOZMAX Case Studies

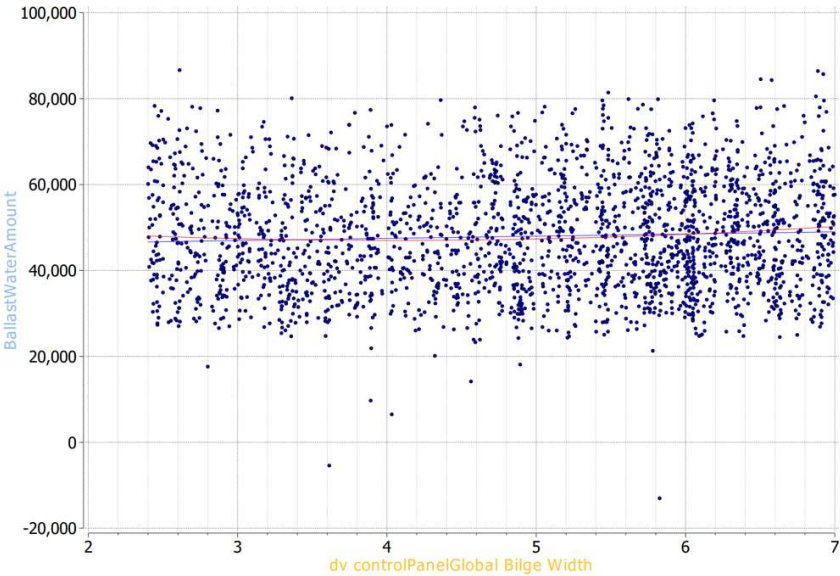
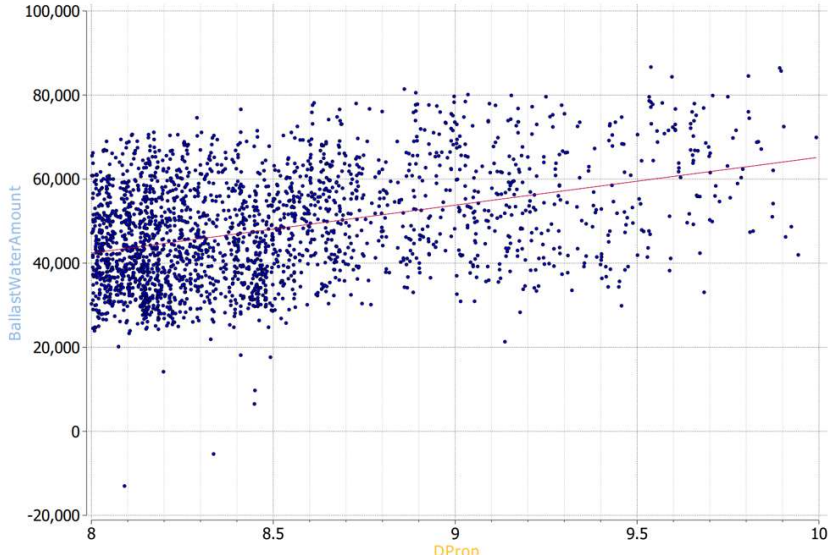
ID	Design Variable	Effect on Required Ballast Water Amount
N_01	Length between Perpendiculars	<p>High Sensitivity of BW Amount in Lbp: Increased by increasing length.</p> 
N_02	Beam	<p>Increased BW Amount by increasing beam.</p> 
N_03	Draft	<p>Low sensitivity of Ballast Water Amount in Deck Heigh: Increasing design draft leads to decreasing BW Amount</p>

A Novel Methodology for Robust, Holistic, Simulation-Based Ship Design Optimization

		<p>Parameter [Computations]10BallastCondition BallastWaterAmount Design Variable [variables]MainDimensions Draft_NMAX_Design</p> 
N_04	Deck height	<p>Increasing Deck Height leads to decreasing the BW Amount</p> <p>Parameter [Computations]10BallastCondition BallastWaterAmount Design Variable [variables]MainDimensions depth</p> 
N_05	Hopper Height	No sensitivity of BW Amount with this variable

N_06	Hopper Breadth (m)	No sensitivity of BW Amount with this variable
N_07	Topside Height (m)	No sensitivity of BW Amount with this variable
N_08	Topside Breadth (m)	No sensitivity of BW Amount with this variable
N_09	Block Coefficient Cb	<p>High Sensitivity of BW Amount in Cb. By increasing block coefficient there is a sharp increase of the BW Amount.</p>  <p>Parameter Computations 10BallastCondition BallastWaterAmount Design Variable variables MainDimensions c_B</p>
N_10	LCB (%Lbp)	LCB has a positive effect on Ballast Water amount: by increasing the LCB % the required BW Amount slightly drops

		<p>Parameter [Computations 10BallastCondition BallastWaterAmount Design Variable variables MainDimensions LCB_desiredRatio</p>
N_11	Bilge Height (m)	<p>Almost zero sensitivity of BW Amount to changes of the Bilge Height</p> <p>Parameter [Computations 10BallastCondition BallastWaterAmount Design Variable variables Hullform variableMidbody dv_controlPanelGlobal_Bilge_Height</p>
N_12	Bilge Width (m)	<p>Almost zero sensitivity of BW Amount to changes of the Bilge Width</p>

		<p>Parameter Computations 10BallastCondition BallastWaterAmount Design Variable variables Hullform variableMidbody dv_controlPanelGlobal_Bilge_Width</p> 
N_13	Propeller Diameter (m)	<p>High Sensitivity of BW Amount in Propeller Diameter: with increasing diameter , required BW Amount sharply increases (due to Aft Draft requirements)</p> <p>Parameter Computations 10BallastCondition BallastWaterAmount Design Variable variables Hullform variablesAbdy DProp</p> 
N_14	Propeller Expanded Area Ratio	No sensitivity of BW Amount in Propeller Expanded Area Ratio

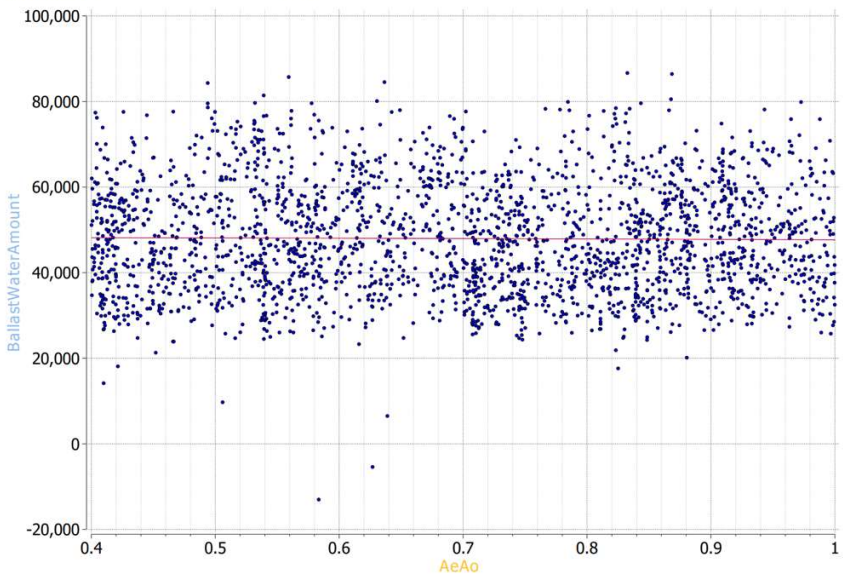
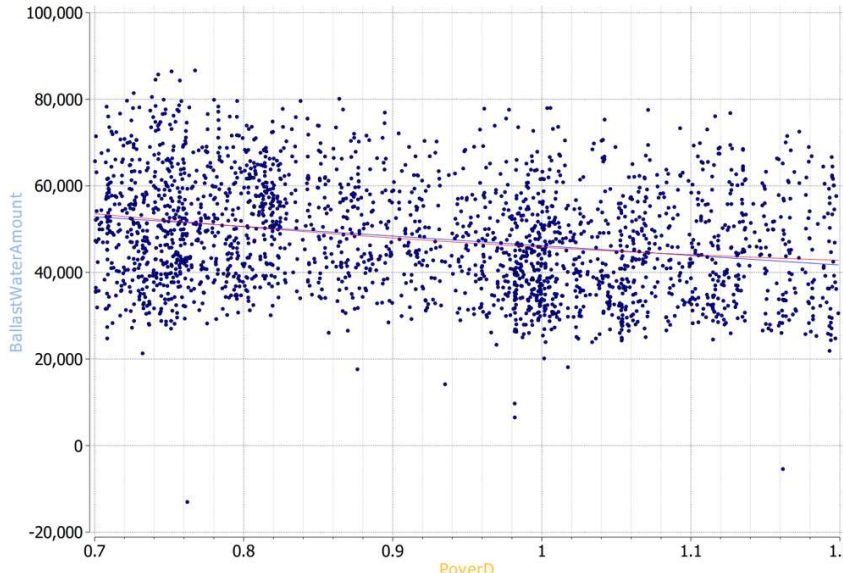
		<p>Parameter Computations 10BallastCondition BallastWaterAmount Design Variable Computations 05Propulsion AeAo</p> 
<p>N_15</p>	<p>Propeller Pitch over Diameter</p>	<p>High Sensitivity of BW Amount in Pitch: Increasing pitch leads to lower BW Amount (due to propeller diameter reduction)</p> <p>Parameter Computations 10BallastCondition BallastWaterAmount Design Variable Computations 05Propulsion PoverD</p> 

Table 48: BW Amount Sensitivity on Design Variables – Deterministic WOZMAX Case Studies

6.4.3. Optimization Results

6.4.3.1. Newcastlemax Design – Dakota Algorithm (ID: Det_NMAX_01)

For this optimization run (ID: Det_NMAX_01) a total number of 2409 viable designs were generated out of a total population of 3000 designs corresponding to 80.3% success rate.

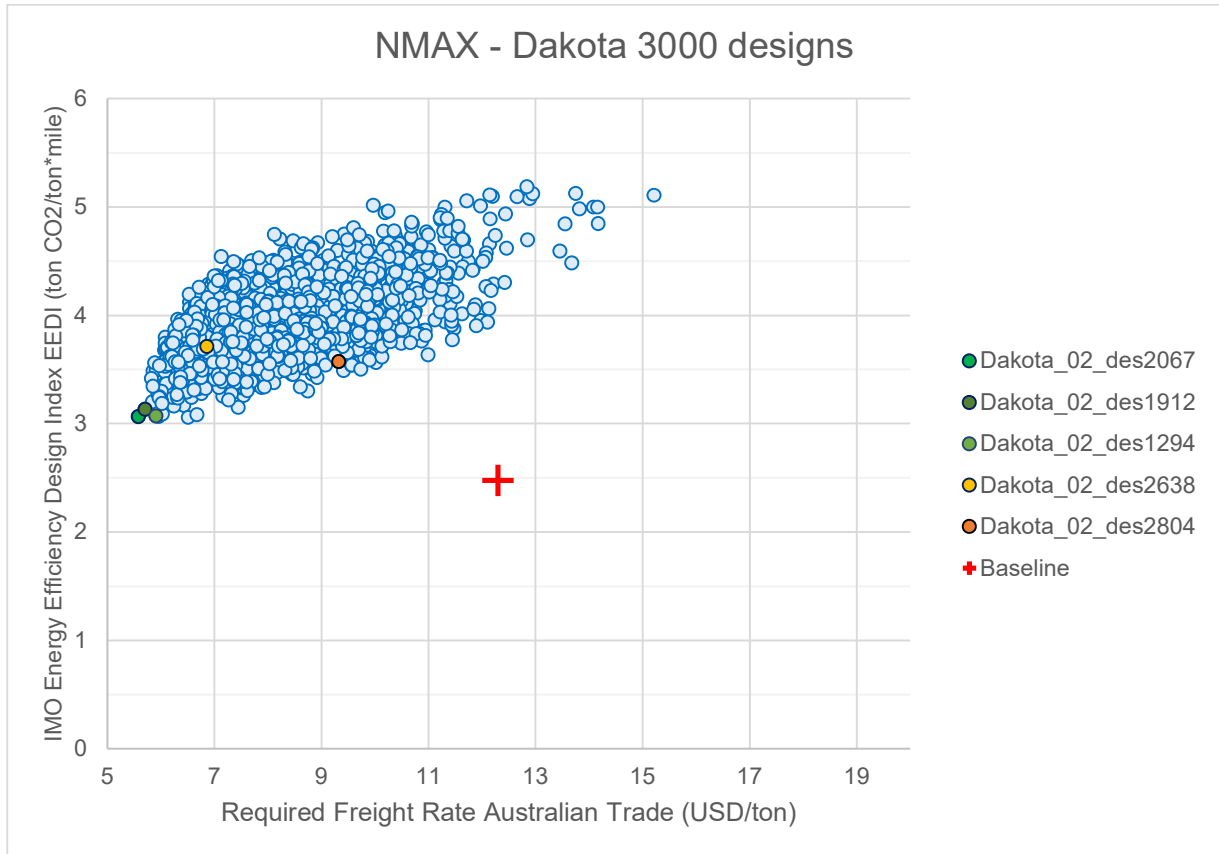


Figure 132: Det_NMAX_01 / EEDI vs. RFR Design Scatter Diagram with Baseline Vessel and Dominant Variants superimposed.

From the first deterministic run when looking at the scatter diagram between the RFR and EEDI objectives (Figure 132), a dense design cloud is observed with a strong linear correlation among the two. The width of the linear area represents the design range and uncertainty of the resulting design efficiency. Due such a strong linear correlation, the Pareto front is reduced to a concentrated peak of designs. Interestingly, the Baseline design dominates all designs in terms of EEDI performance with none being able to outperform the latter. As it will be presented in the next Paragraph, the use of EEDI as a constraint instead of objective will “guide” the algorithm towards pareto fronts with dominant variants with better EEDI values.

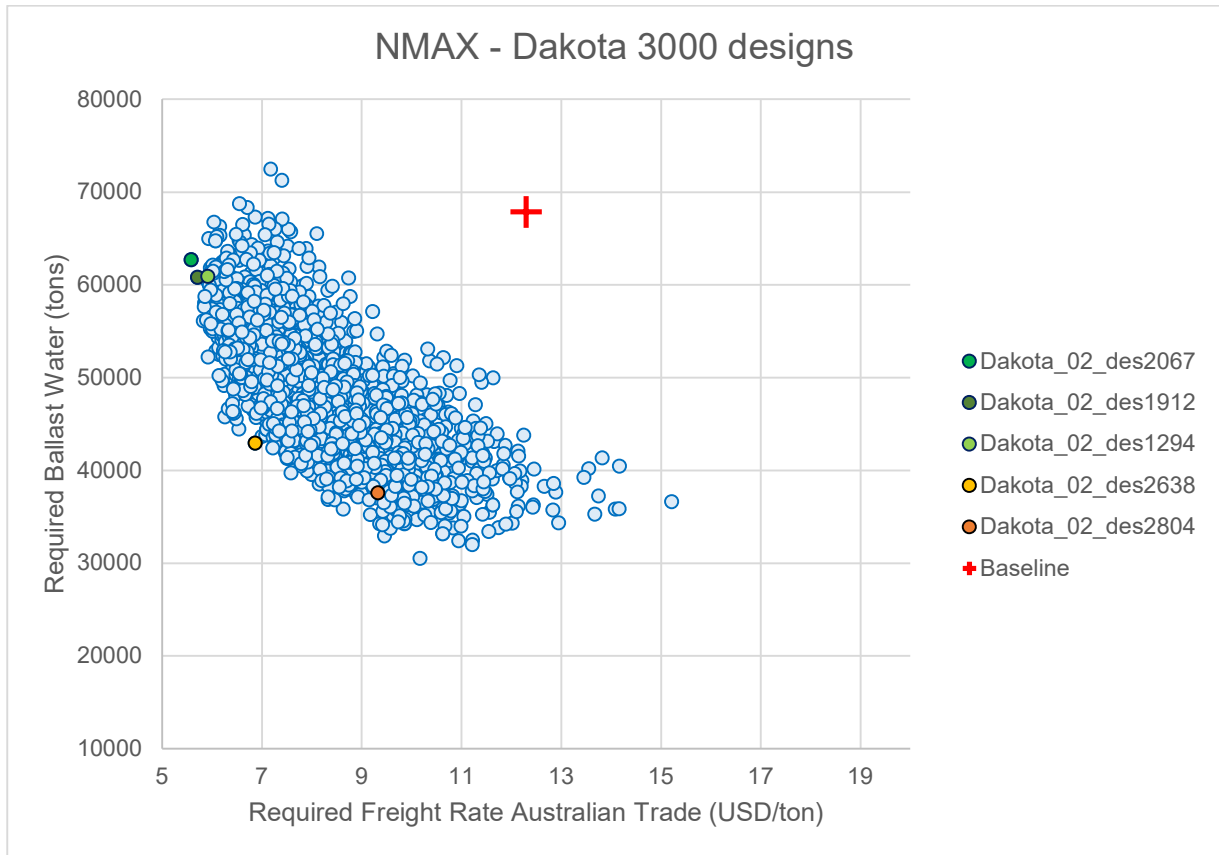


Figure 133: Det_NMAX_01 / Required Ballast Water vs. RFR Design Scatter Diagram with Baseline Vessel and Dominant Variants superimposed.

When looking at the relationship between the RFR (Australian Trade) and the Required Ballast Water amount (Figure 133) a strong Pareto front is emerged that is characterized by two distinctive areas: the area of full, larger vessels that feature an improved RFR and EEDI but require larger amounts of ballast water. The other area is characterized by smaller-sized vessels with considerably less amount of ballast required for each ship coming at the cost of EEDI and RFR. The regions of the middle of the Pareto arch that is formed are not easily peaked by the use of linear utility function due to the high magnitude and gravity of the pole of Area 1, given that two of the three optimization merits reach their local minima/optima. All designs have a considerable distance from the baseline, indicating the effect of optimization. For instance, for the same amount of ballast water required as the baseline, the RFR is improved by more than 50%.

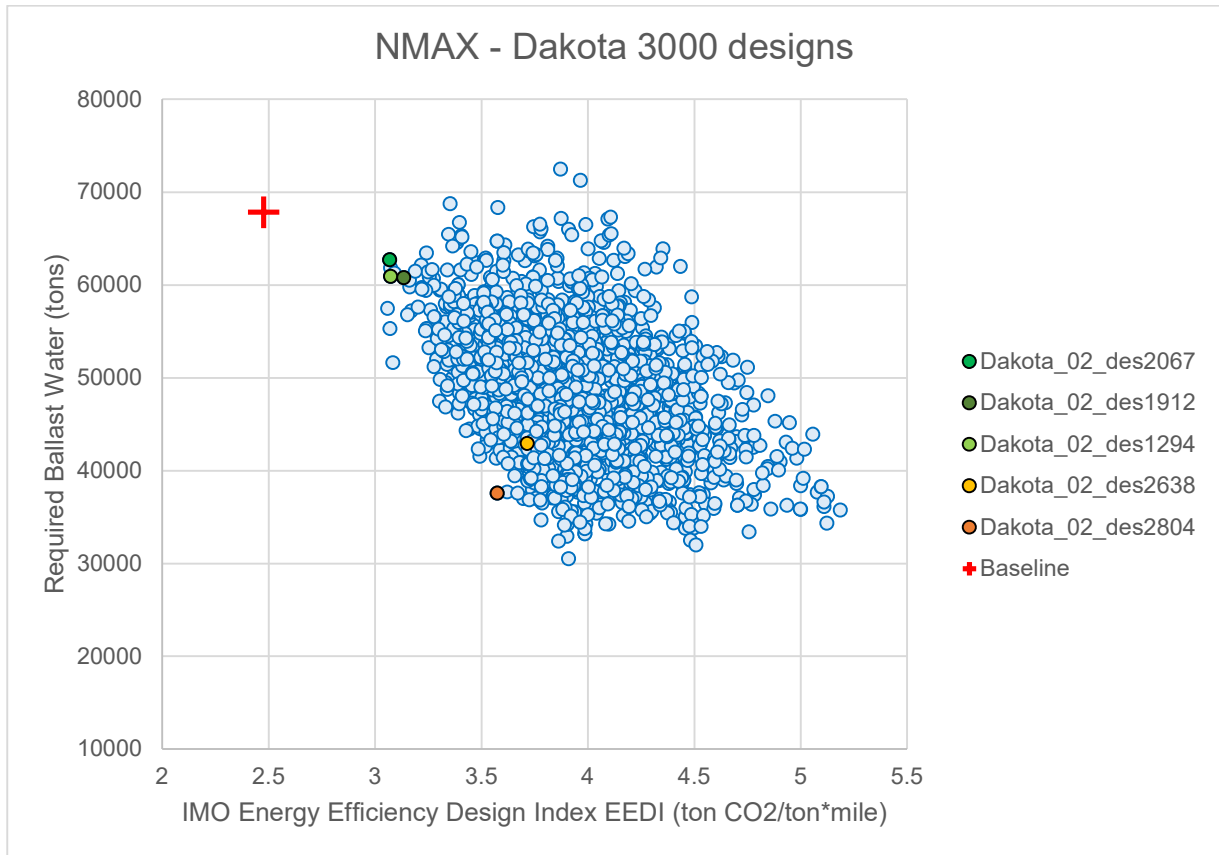


Figure 134: Det_NMAX_01 / Required Ballast Water vs. EEDI Design Scatter Diagram with Baseline Vessel and Dominant Variants superimposed.

A similar behaviour as in the previous graph is observed also in the scatter diagram between the EEDI and Required Ballast Water amount (Figure 134) due to the strong and linear correlation of EEDI and RFR. The distinctive pareto front strictly dominates all designs with EEDI above 4.0 tCO₂/ton*mile and in a sense creates an “efficiency barrier wall”. A very steep increase of required ballast amount by decreasing EEDI indicating the strong economies (in this instance “efficiencies”) of scale and the smaller EEDI values triggered by increased vessel size. This is evident even within the scope of this optimization study where the design variables are examined in a narrower design space where similar-sized vessels are examined. Again, two poles of dominant variants are generated: One of the smaller-sized vessels with increased EEDI but reduced ballast water amount and the other one of high-efficiency (low EEDI) vessels with higher required ballast water amount.

The middle area of the Pareto front is ignored by the linear utility functions imposed. The reason is that as middle areas are examined there is a deviation from the Pareto fronts of the rest of the diagrams/ target relationships. Furthermore, the derived utilities of variants of middle areas are in general lower.

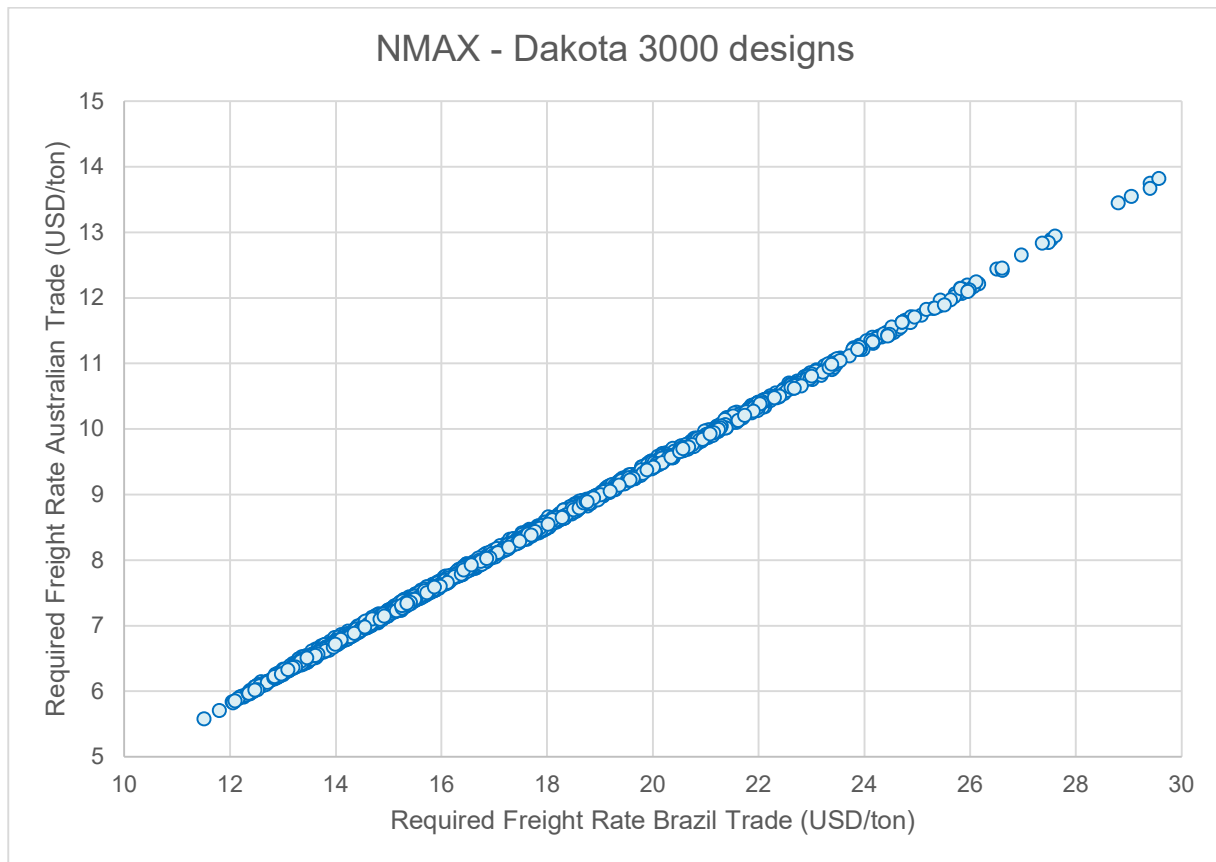


Figure 135: Det_NMAX_01 / RFR Australian Trade vs. RFR Brazilian Trade Design Scatter Diagram

The Required Freight Rate figures of each trade route have a strictly linear correlation as witnessed from the scatter diagram in Figure 135. Instead of a pareto front, the latter is reduced to one point, the local minimum, in other words, the design with the minimum RFR value that remains minimum for both trades. Such a relationship is an indication of the design robustness on one hand: If a ship is profitable in one route, it will be in all routes of the examined trade. The main reason for this strong correlation is that the RFR essentially examines the breakeven point between positive and negative monetary flows. The breakeven (in contrast to profitability) will remain the same in terms of ranking among different routes with a changing magnitude that is a function of the vessel utilization in terms of annual round trips and thus annual tons of cargo transported. For example, the Australian route which is a shorter one will allow a higher number of annual voyages compared to the Brazilian route, leading to a bigger flow of cargo per year and thus a lower value of RFR. Considering this analysis, for simplicity and efficiency purposes, only one RFR is used for the rest of the studies: Australian Trade RFR for Newcastlemax designs and Brazilian Trade RFR for VLOC designs. However, for all designs and case studies, all calculations are available and conducted.

6.4.3.2. *Newcastlemax Design – MOSA Algorithm (ID: Det_NMAX_02)*

For this optimization run (ID: Det_NMAX_02) a total number of 2874 viable designs were generated out of a total population of 3000 designs corresponding to 95.8% success rate.

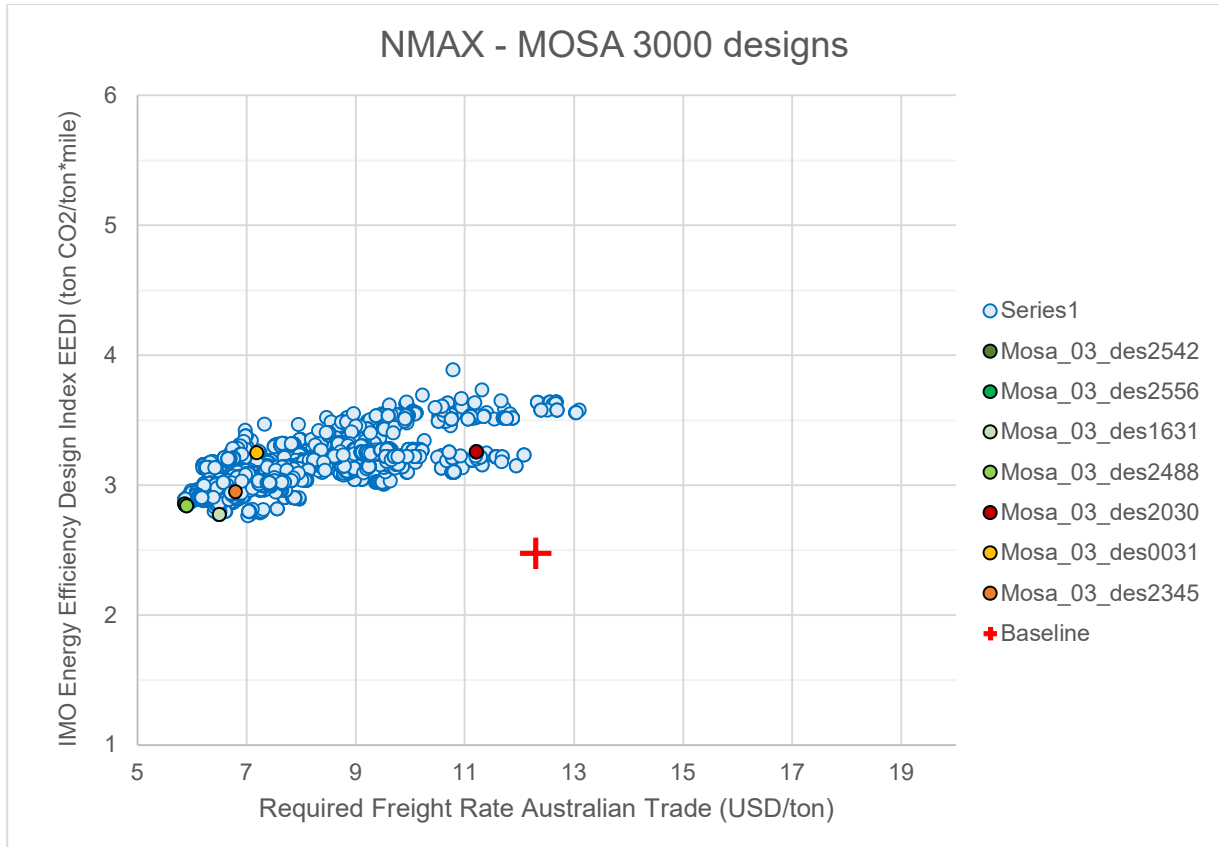


Figure 136: Det_NMAX_02 / EEDI vs. RFR Design Scatter Diagram with Baseline Vessel and Dominant Variants superimposed.

When looking at the scatter diagram of EEDI vs RFR for the Det_NMAX_02 run (Figure 136), a less dense design cloud is generated when comparing to the results of the Dakota algorithm run (Det_NMAX_01). The relationship between RFR and EEDI remains similar but less strict and with greater variance. This is witnessed by the generation of one main design cloud, with a Pareto front that is being reduced to a small peak of designs. Additionally, a branch design scatters at the region of 7-8 USD/ton RFR is observed and strictly dominates all neighbouring designs in terms of EEDI.

Designs IDs 0031 and 2345 are dominated by other ranked designs in terms of RFR however are almost on the Pareto front in terms of EEDI, while the meantime they are located in the middle of the Pareto front in Figure 137 and Required Ballast amount performance. Baseline design is far away from the design cloud with regards to RFR values, while for the EEDI it is observed that like in the previous runs it dominates and is lower than all generated designs.

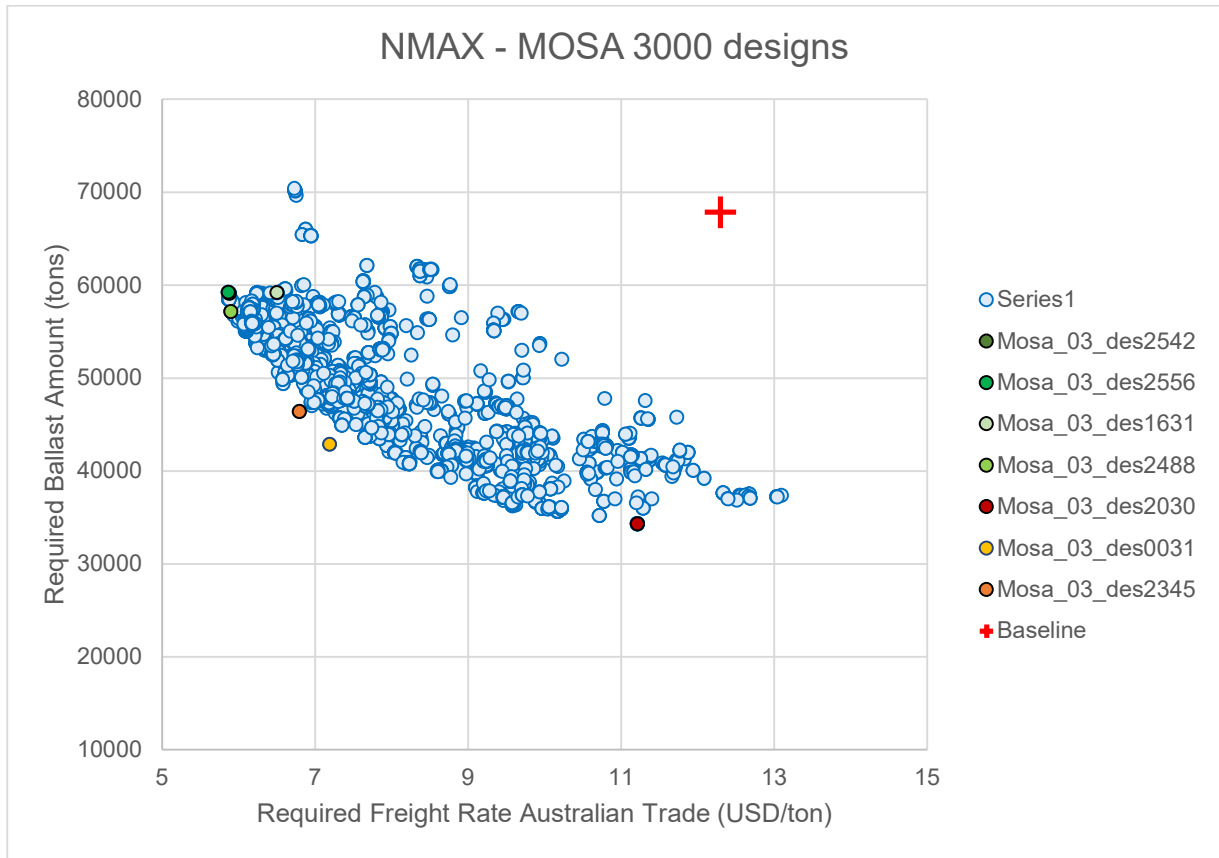


Figure 137: Det_NMAX_02 / Required Ballast Water vs. RFR Design Scatter Diagram with Baseline Vessel and Dominant Variants superimposed.

In Figure 137, the scatter diagram between the Required Ballast Water Amount and the RFR of Det_NMAX_02 is presented. Again, the cloud is observed as less dense, while the Pareto front is similar to the one of the Dakota algorithm, having a characteristic antagonistic relationship between RFR/EEDI and Ballast Water Amount. Two separate regions are again polarized by the utility functions. Two designs that lie on the Pareto front and are located in the middle area of the latter have been selected on an “ad-hoc” basis. The designs (ID 0031 and 2345) are not on the Pareto front with regards to the RFR-EEDI relationship but are not far from the latter, while design ID2345 remains on the Pareto front with regards to the relationship between Required Ballast amount and EEDI, highlighting thus its robustness. Area with concentrated designs that have been selected by the utility functions (2556, 2488, 1631, 2542) are larger vessels of full hull form and higher block coefficient that due to economies of scale feature a better EEDI and RFR but require higher ballast water amounts. A significant improvement was observed when compared to the baseline: ID2556 has an RFR of 52.3% less and requires approximately 13.8% less Ballast Water.

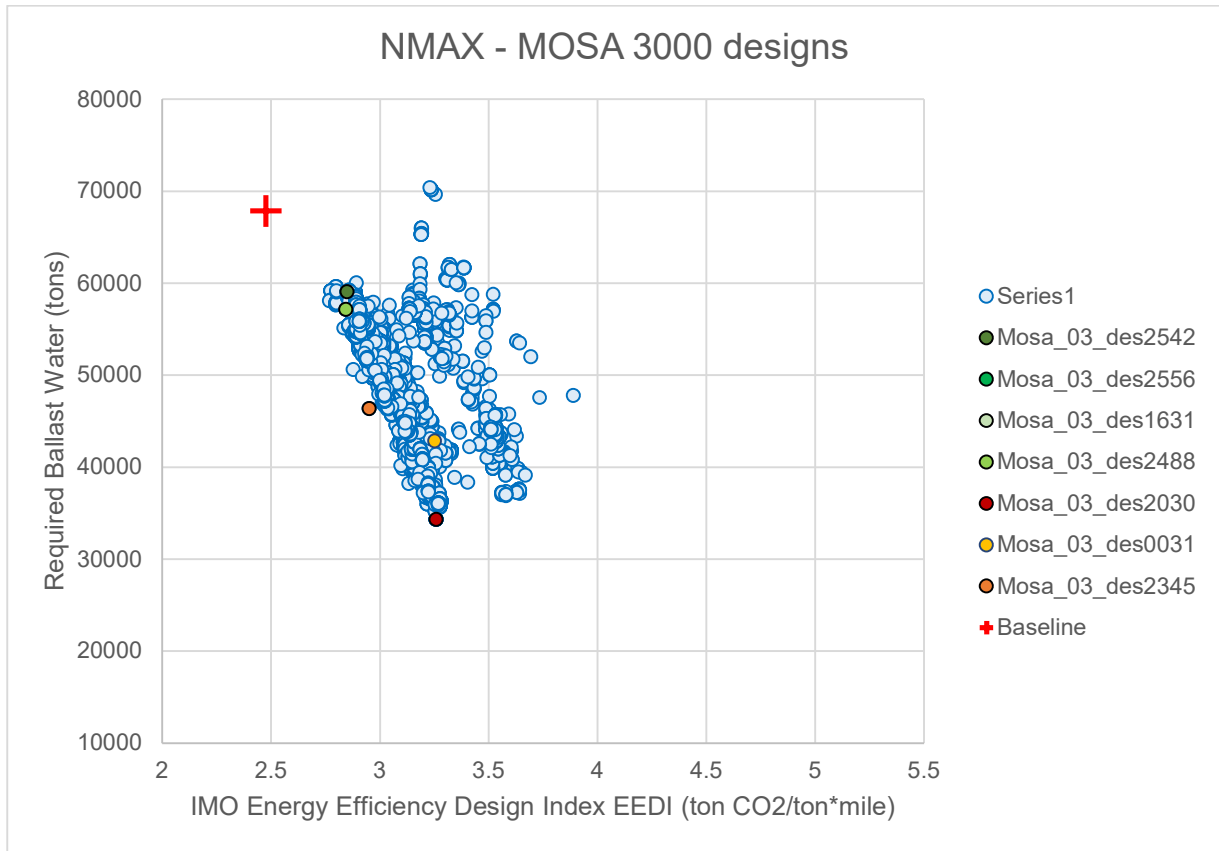


Figure 138: Det_NMAX_02 / Required Ballast Water vs. EEDI Design Scatter Diagram with Baseline Vessel and Dominant Variants superimposed.

In Figure 138, where the scatter diagram of Required Ballast Water Amount versus the EEDI for Det_NMAX_02 are represented, two different scatter clouds were generated with the left dominating the right one. Very steep Pareto front compared to previous studies. One area of selected dominant variants is characterized by larger vessels (top left) while the other is by smaller vessels. Larger vessels remain on all Pareto fronts optimal, as well as ID2345. With a compromise of 3.5% in EEDI, the Required Ballast Amount is reduced by 13.8%. The baseline is dominated by all the generated designs in terms of the Required Ballast amount.

6.4.3.3. *Newcastlemax Design – NSGAI Algorithm (ID: Det_NMAX_03)*

For this optimization run (ID: Det_NMAX_03) a total number of 2277 viable designs were generated out of a total population of 3000 designs corresponding to 75.9% success rate.

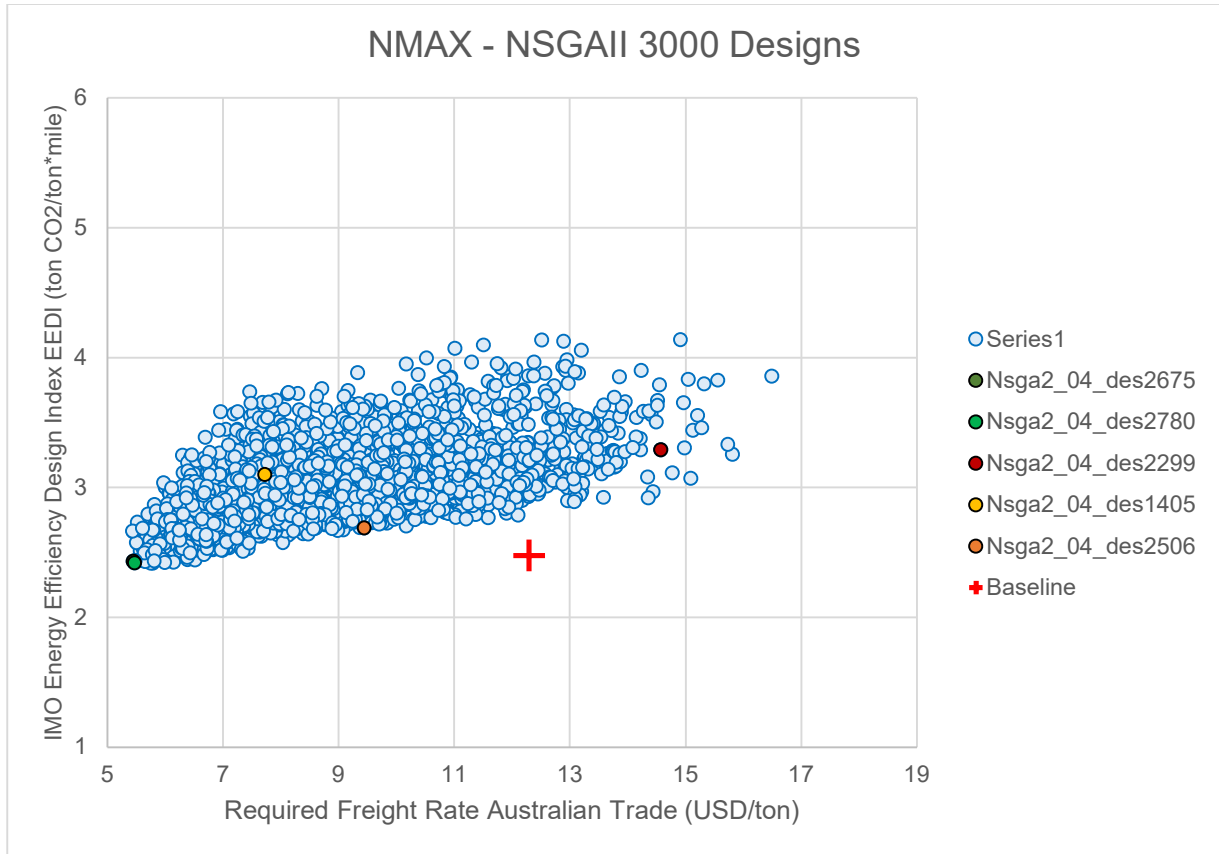


Figure 139: Det_NMAX_03 / EEDI vs. RFR Design Scatter Diagram with Baseline Vessel and Dominant Variants superimposed.

A dense cloud that is very similar to the one generated from Dakota characterizes the scatter diagram of EEDI versus RFR for the Det_NMAX_03 optimization run (Figure 139). The reason for this is that the Dakota platform is based on gradient and non-gradient based methods that create results very similar to those of evolutionary algorithms like NSGAI. Like in previous studies, the relationship between EEDI and RFR is highly linear. Compared to the similar Dakota results, the cloud is flatter. Similar to other runs, the Pareto frontier is reduced to a single peak of designs that dominate all others in terms of both EEDI and RFR. Interestingly, 70% of the generated designs have better RFR than the baseline. As in previous runs, the EEDI performance of the baseline strictly dominates all generated variants. When looking at the dominant variants, Design IDs 2780, 2675 are typically designs of larger dimensions and fuller hull form, featuring a bigger capacity and better transport efficiency leading to improved EEDI and RFR, while designs like 2506, 1405 and 2299 are smaller and more slender ships that feature considerably smaller Ballast Water amount.

When manually selecting a design at the middle of the front (ID2506) we can observe a reduction of 40.5% of the required ballast water amount at the expense of a lower performance EEDI (9.3%) and RFR (40%) when compared to designs ID2675 and ID2780. Interestingly, the RFR of ID2506 still remains more competitive than the one of the Baseline vessel.

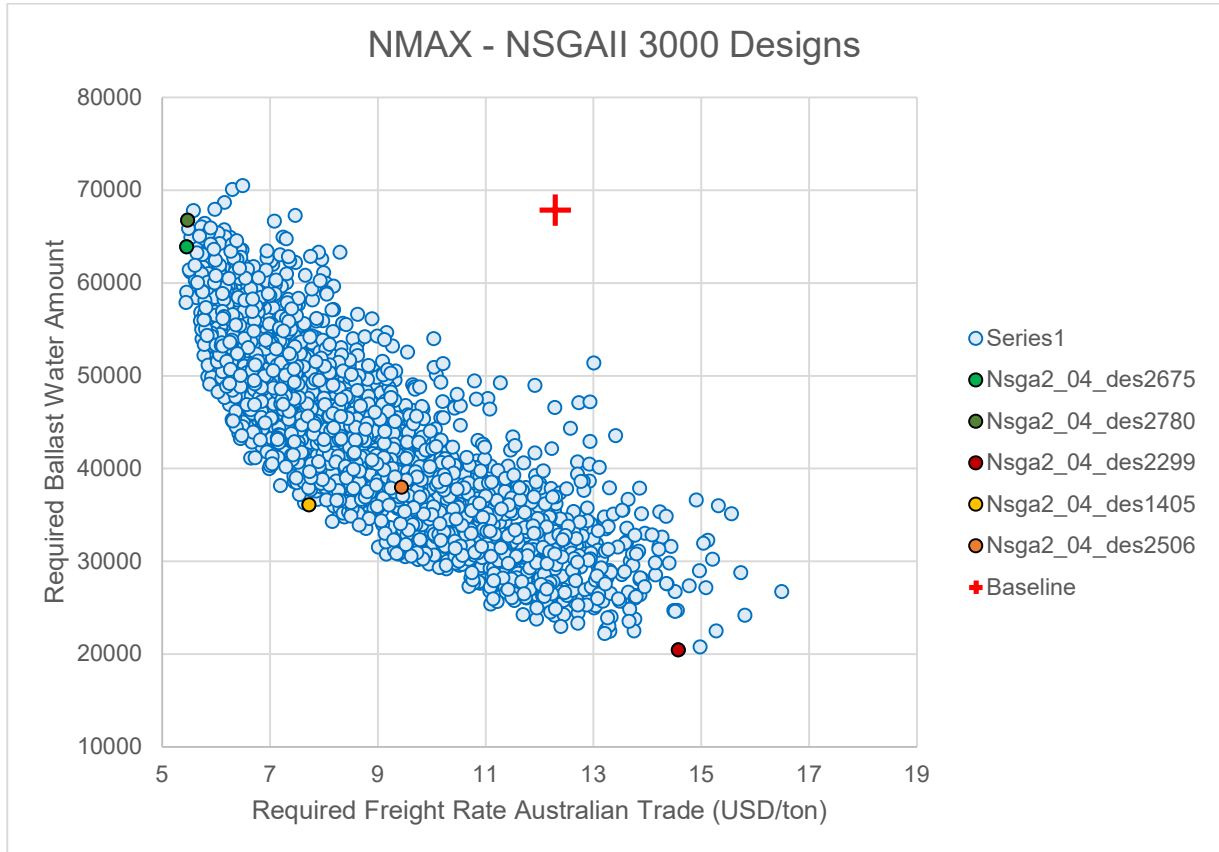


Figure 140: Det_NMAX_03 / Required Ballast Water vs. RFR Design Scatter Diagram with Baseline Vessel and Dominant Variants superimposed.

A very dense and distinct cloud has been generated, clearly highlighting the antagonistic relationship between Ballast Water Amount and RFR in Figure 140, which for lower RFR numbers is steeper. This curve however indicates relationships and optimization opportunities given that with small increases of RFR reductions of up to 10,000 tons of required ballast water (or roughly 17%) can be attained, not considering the EEDI performance. The shape of the generated cloud is also very similar to the one generated by DAKOTA indicating the close relationship between these two design engines/ optimization tools.

Interestingly, when comparing the baseline to the design cloud one case observe that for the same level of RFR, the Required Ballast Water amount is reduced significantly by more than 50% which is aligned with previous studies on the matter (Nikolopoulos, et al., 2016). With the same approach, it is interesting to observe that for the same level of required Ballast Water amount as the baseline, the RFR is reduced by more than 50%. This phenomenon indicates the serious play

and potential available in the optimization methods employed, even when they are used on a deterministic basis and with minimal information with regards to the operating profile.

The dominant variants highlighted from the EEDI-RFR graph continue to be the same for this graph as selected from the use of utility functions. Design IDs 2675, 2780 are again in the top right part of the Pareto frontier given their superior EEDI and RFR performance. An interesting observation is that design ID 1405 manually selected to be at the middle of the frontier has a reduction of the required ballast water amount at the expense of RFR. This design is not on the Pareto front neither of the EEDI-RFR plot nor of the Ballast Water amount front – EEDI front. This phenomenon highlights the importance of the use of utility functions for selecting robust designs that remain on Pareto fronts for all objectives. When manually selecting design ID 1405 that is in the middle of the generated Pareto frontier

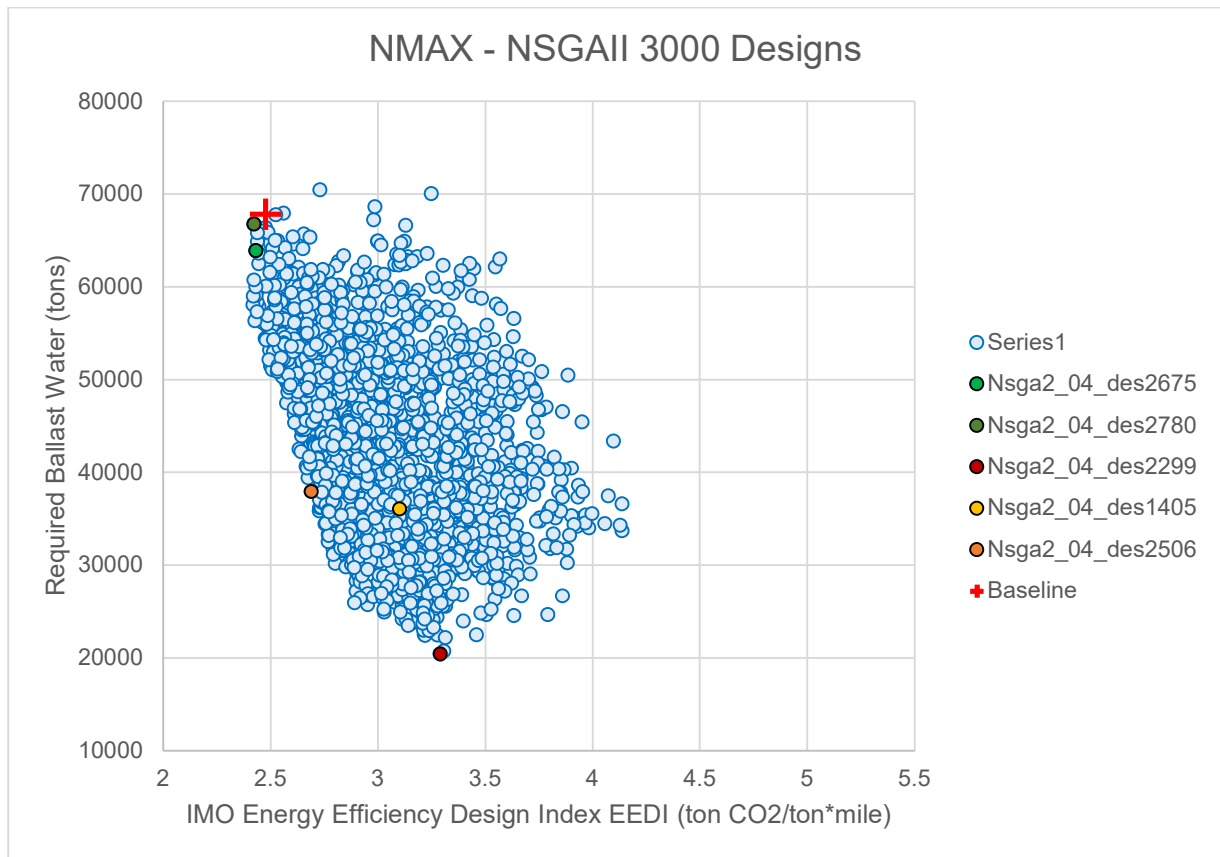


Figure 141: Det_NMAX_03 / Required Ballast Water vs. EEDI Design Scatter Diagram with Baseline Vessel and Dominant Variants superimposed.

When looking at the scatter diagram of Required Ballast Water vs. EEDI in Figure 141 it can be observed, that apart from the same density and high design concentration, a considerably steeper Pareto front is formed. Interestingly, the baseline design appears to be very close to the Pareto peak of designs. Another interesting observation is that despite the steepness of the Pareto front which can trigger considerable reductions in the required ballast water amount with a very slight

compromise in the EEDI performance, the dominant variants as picked from the utility functions (linear weight distribution) are not located in this area. This phenomenon is due to the “polarized” peaks of the Pareto fronts that are generated and are attributed to the linear correlation and synergetic behaviour of EEDI and RFR. Given that the Required Ballast Water amount vs. RFR frontier is not equally steep but smoother and parabolic, the utility functions are not directed there. Dominant variants depicted on previous graphs and picked from the utility functions remain on the peak of the Pareto front indicating robustness in their positions. A very interesting observation is that design ID2506 which was manually selected from the Pareto front of the EEDI vs. RFR cloud also appears to be on the Pareto front of the Ballast Water vs. EEDI scatter diagram, while it was dominated by a big cloud on the Ballast Water vs. RFR scatter diagram. Such observations indicate the importance of using utility functions as all designs picked with the use of such mathematical formulation remain on Pareto fronts between all optimization targets and not just independent ones.

6.4.3.4. *VLOC Design – Dakota Algorithm (ID: Det_WOZMAX_01)*

For this optimization run (ID: Det_WOZMAX_01) a total number of 2569 viable designs were generated out of a total population of 3000 designs corresponding to 85.63% success rate.

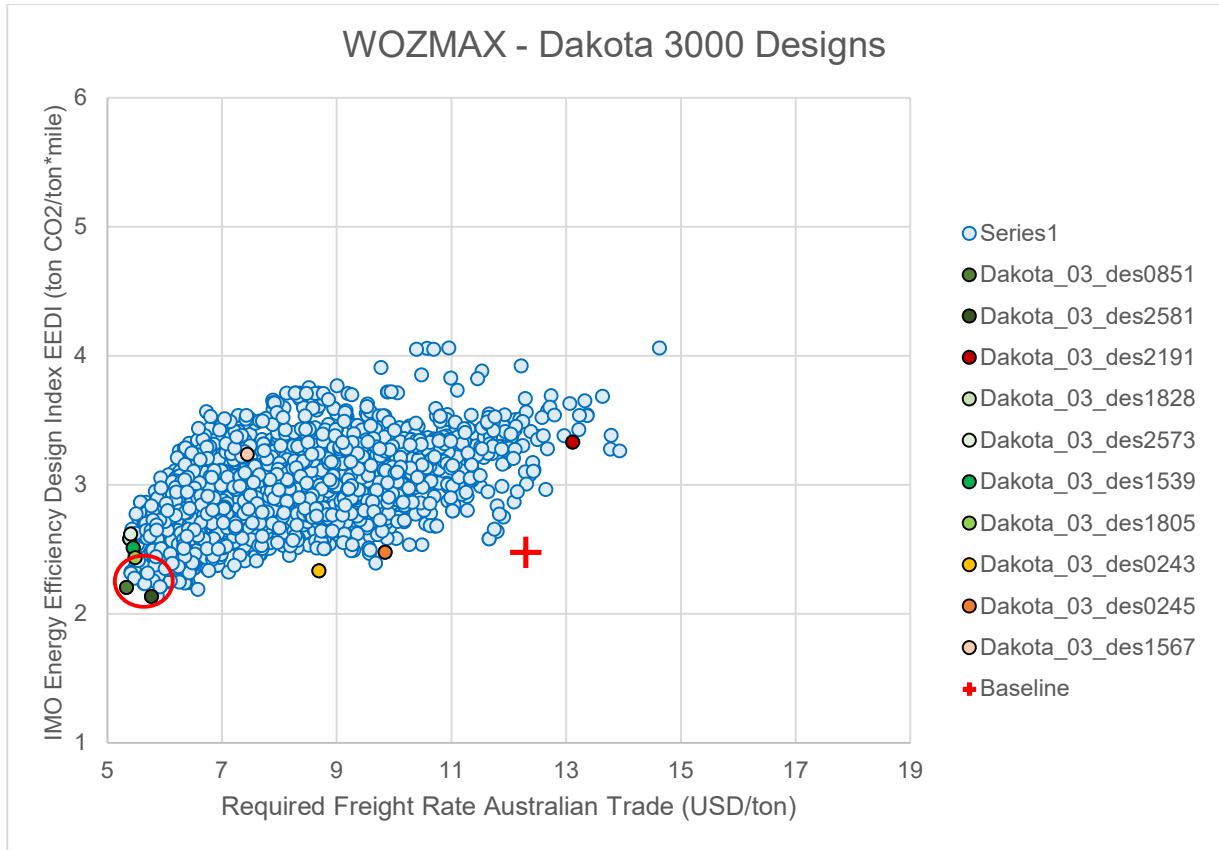


Figure 142: Det_WOZMAX_01 / EEDI vs. RFR Design Scatter Diagram with Baseline Vessel and Dominant Variants superimposed.

The scatter diagram (Figure 142) when compared to the equivalent of the Newcastlemax runs (Det_NMAX_01), has a very similar density, shape and steepness. The magnitude of RFR and EEDI are smaller and improved due to the economies of scale that generally dominate the design of large vessels. In this respect, EEDI is more influenced compared to the RFR. Again, the Pareto frontier is reduced to a single peak of designs that all feature similar characteristics in terms of dimensions. The Pareto pole has been marked with a superimposed red circle to have a better visual representation.

The baseline vessel is far away from the optimal design area and dominated by the entire design cloud. This effect is more profound for WOZMAX vessels since the size limitations previously imposed have been herein lifted. For deterministic runs a Maximum improvement of 56.6% in terms of RFR (Design ID0851) and 10.7% of EEDI (Design ID0851) have been recorded which set the boundaries of the examined design space with such approaches. From the use of utility

functions for picking dominant variants from the Pareto frontier, two types of variants have been selected similarly to previous runs:

1. Larger Vessel designs that are located on the Pareto peak featuring minimized RFR, EEDI. This represents the majority of the designs selected by utility functions, as the phenomenon of a “polarized” peak draws the linear weight distribution towards that particular area.
2. Smaller vessel variants with a minimized required Ballast Water amount.

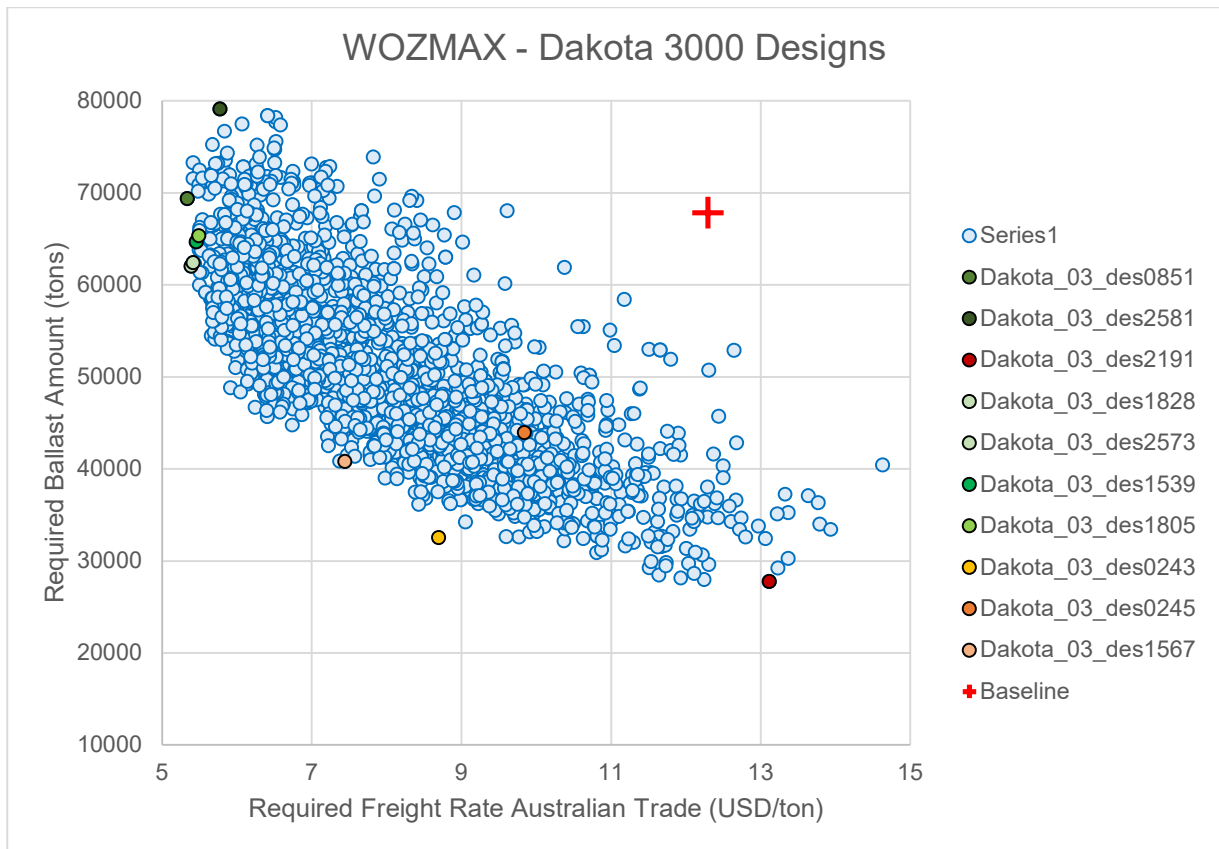


Figure 143: Det_WOZMAX_01 / Required Ballast Water vs. RFR Design Scatter Diagram with Baseline Vessel and Dominant Variants superimposed.

A very dense design cloud is generated in this scatter diagram (Figure 143), which is typical for the Dakota and NSGAI algorithms due to their evolutionary nature and lower mutation probabilities. Compared to the equivalent run for the Newcastlemax case study, the cloud has a very similar form. The magnitude of RFR is very similar as described above, while the magnitude of the Required Ballast Water amount is similar in terms of extent, with some designs with higher ballast amounts also appearing. Interestingly, this means that there is a possibility of deriving a larger vessel design that requires the same or even lower Ballast Water amount while in the meantime reaps the benefits of economies of scale both in terms of RFR and more significantly (and profoundly) EEDI.

As one moves on the distinctive Pareto front towards lower RFR the front gets increasingly steeper. At the region of 5.5 USD/ton RFR, with only an increment of 0.1-0.2 USD/ton, the required Ballast amount can be decreased by merely 10,000 tons (or 16.7%). Such regions will be a good ground for design exploration in simulation-driven runs, where the robustness of the model is considerably higher.

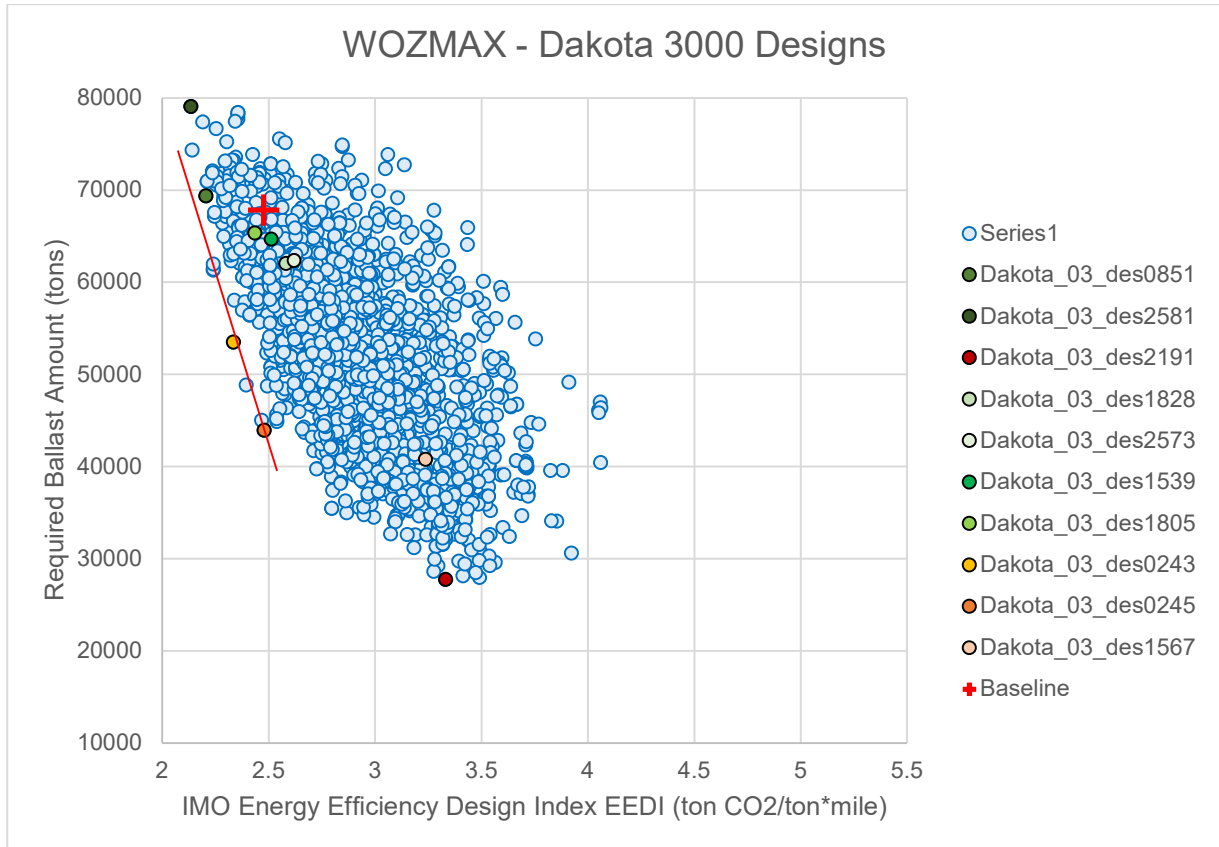


Figure 144: Det_WOZMAX_01 / Required Ballast Water vs. EEDI Design Scatter Diagram with Baseline Vessel and Dominant Variants superimposed.

When looking at Figure 144 and the scatter diagram of the Required Ballast Water amount versus EEDI, it is interesting to the observer that the Design IDs 1539, 1805, 2573, 1828 that have been on the Pareto front of the scatter diagram between Required Ballast Water amount and RFR are shifted to the inner area of the design cloud, closer to the Baseline vessel and dominated by a design population. The reason for this is the slight shift from the Pareto peak area in the scatter diagram between EEDI and RFR.

Another interesting observation in this graph is the formation of an additional front as marked with the superimposed red line of the graph. These individual designs stand out and strictly dominate the neighbouring points of the scatter diagram. In a sense, such a line and population and designs could be considered as a substitute Pareto front, that however is not at all dense and comprised only of individual points. In such cases, the next step would be to “push” the Pareto

front and bridge the gap from such designs. This can be achieved with an increase in the design population as well as the probability of mutation which in fact is the catalyst of the variation process within the algorithm.

Like in previous runs, random designs have been also picked from the Pareto front to be assessed across the scatter diagrams of all objectives. For this case, manual picking of design ID1567 from the middle of the Pareto front of the scatter diagram between the Ballast Water amount and RFR indicates that it doesn't lie on the Pareto front of the scatter diagram between RFR and EEDI. Similarly, Design ID245 appears to be on the Pareto front of the scatter diagram between Ballast Water Amount and EEDI and strictly dominates all neighbouring designs in the scatter diagram between RFR and EEDI. However, when picking Design ID243 appears to be on the Pareto front of all 3 objectives' scatter diagrams making it a more viable solution. The above observations highlight once more the importance of the use of utility functions which are the automatic and mathematic picking of the designs ensuring adequate robustness and Pareto optimality for all fronts and objectives.

The ranking of dominant variants by the use of utility functions can be seen in the bar charts of Table 49 with various utility scenarios as previously described.

6.4.3.5. *VLOC Design – MOSA Algorithm (ID: Det_WOZMAX_02)*

For this optimization run (ID: Det_WOZMAX_02) a total number of 2820 viable designs were generated out of a total population of 3000 designs corresponding to 94% success rate.

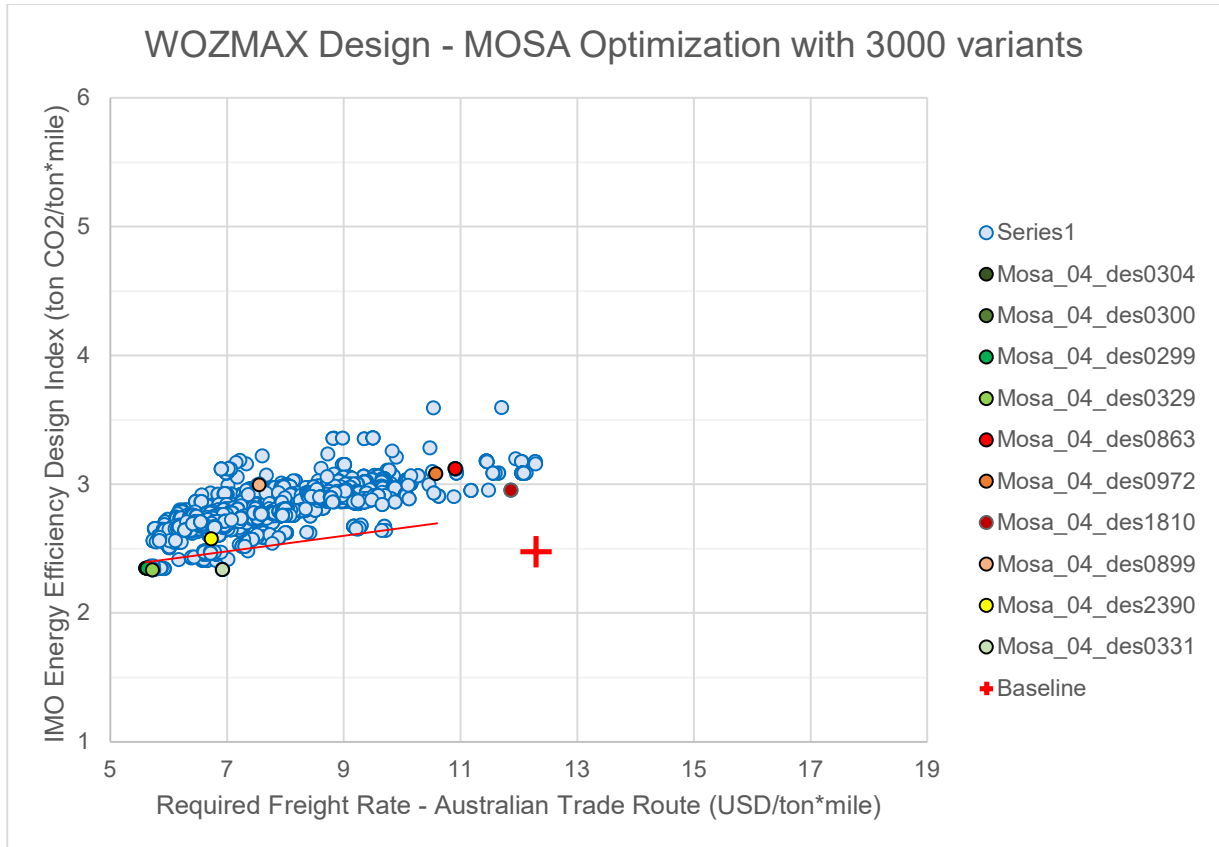


Figure 145: Det_WOZMAX_02 / EEDI vs. RFR Design Scatter Diagram with Baseline Vessel and Dominant Variants superimposed.

Similarly to the Newcastlemax runs, the MOSA algorithm for the VLOC runs produces considerably dense scatter clouds. The linear relationship between the EEDI and the RFR is flattened, and a formation of a detached Pareto front as marked with a red line in Figure 145 is observed. The maximum reduction of the RFR can be up to 53.5% and of the EEDI up to 5.6%. The two families of dominant are again distinctive and characterized by either larger vessels with better EEDI/RFR characteristics or smaller vessels with reduced Ballast Water amount.

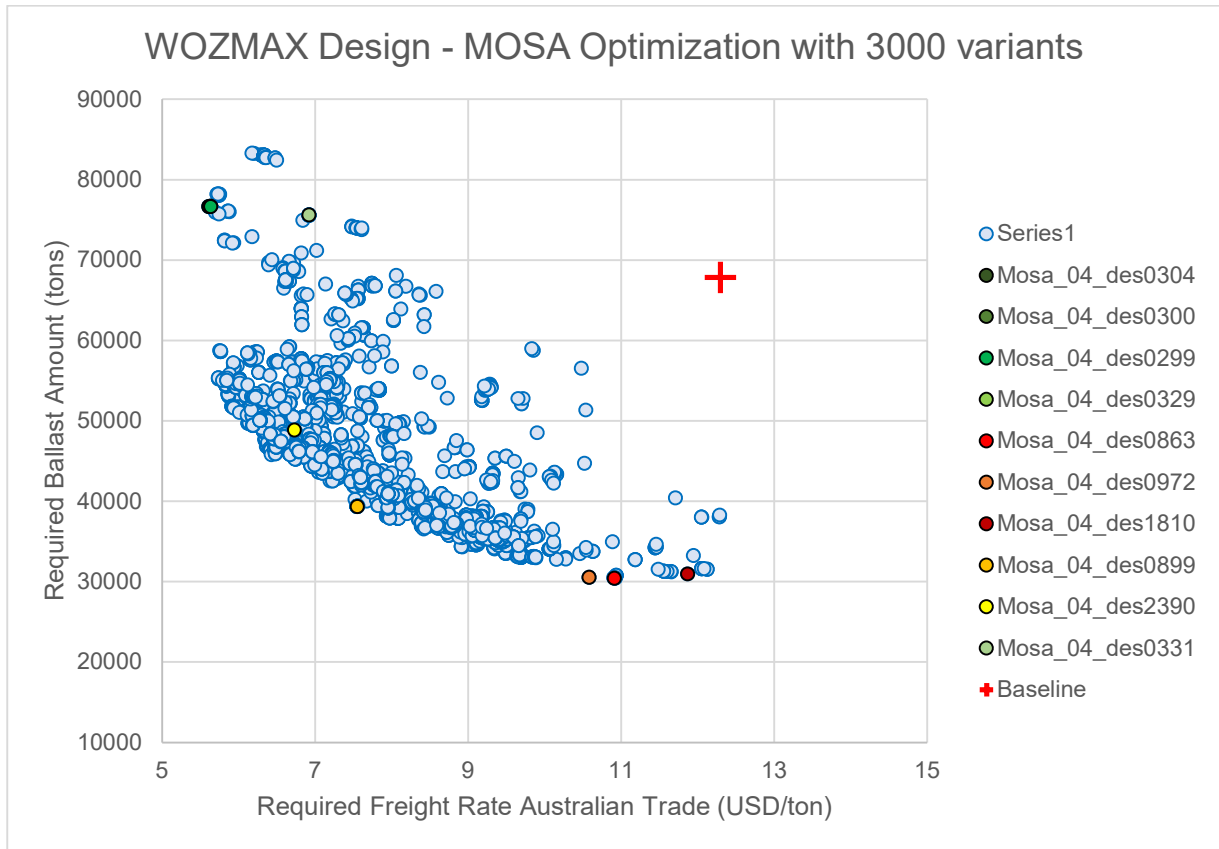


Figure 146: Det_WOZMAX_02 / Required Ballast Water vs. RFR Design Scatter Diagram with Baseline Vessel and Dominant Variants superimposed.

The antagonistic relationship of the required Ballast Water amount with both the RFR and EEDI is evident from the corresponding scatter diagrams.

When looking at the scatter diagram between the Ballast water amount and the RFR (Figure 146), a characteristic Pareto front is formulated. However, rather interestingly, not all the selected dominant variants from the utility functions are located on that front. Variants that feature a smaller ballast water amount (type two designs) and correspond to smaller vessel sizes are indeed located on the far-right region of the front. However, one might have expected that the far-left region of the front would feature dominant variants corresponding to larger vessel sizes. This is not the case, as the area in question has on one hand larger vessels with improved RFR, however, these designs have inferior performance in terms of EEDI in contrast to the ones located on the elevated peak far right with suboptimal performance regarding ballast water amount. Between this elevated peak and the far-right starting point of the Pareto frontier, there is no population of designs whatsoever, creating a void in the scattered cloud.

Taking this a step further, the effect of EEDI is considered as a limit to the optimization potential instead of being a driver to the search of designs with improved performance and thus providing apart from a “pole region” that limits the searching and picking capabilities of the utility functions also a twisting function on the searching and identification of Pareto fronts. Taking such

phenomena into account, the importance of both simulation in the optimization scheme as well as the introduction of utility functions that have weight distribution functions other than linear is elevated. Within this line of thought, the use of EEDI can be altered thanks to simulation-driven features in the next chapter from being an optimization object to instead enacting as an optimization constraint that is also in line with the upcoming IMO regulatory framework.

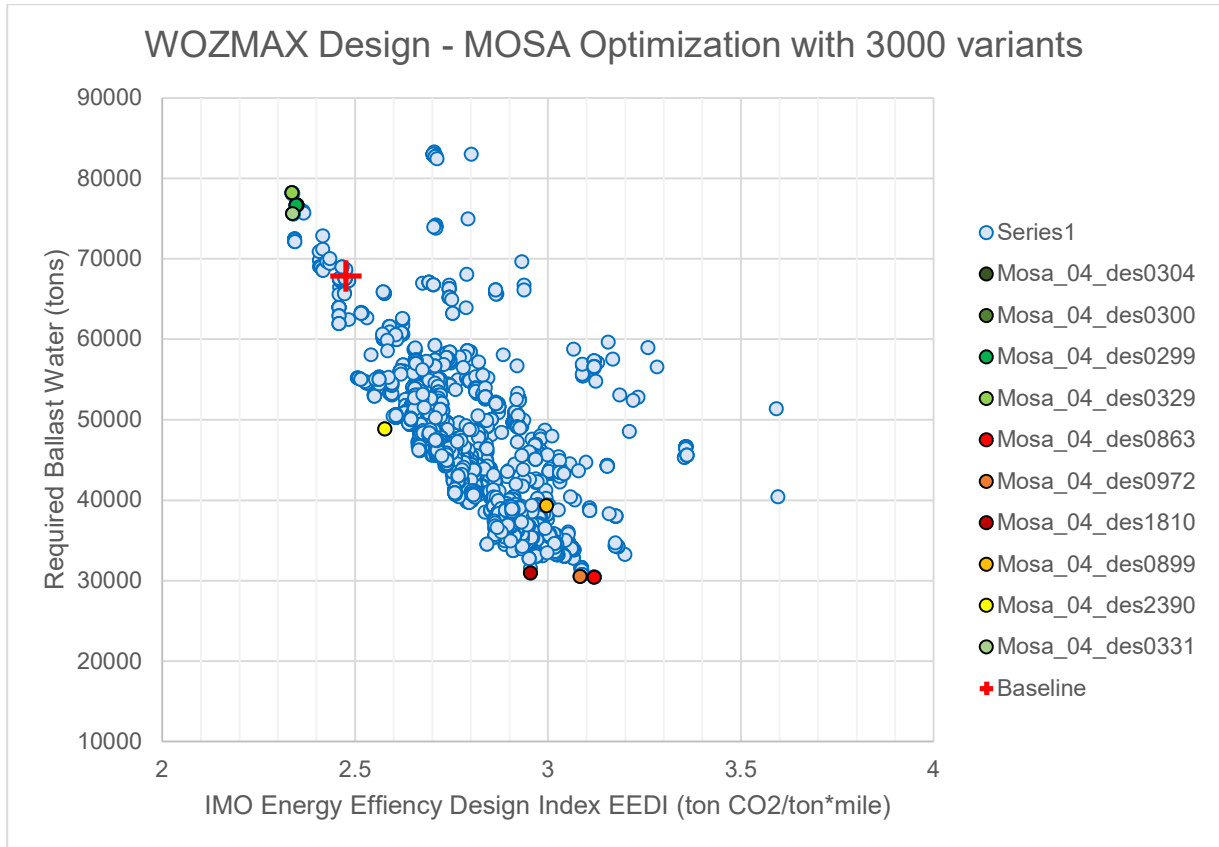


Figure 147: Det_WOZMAX_02 / Required Ballast Water vs. EEDI Design Scatter Diagram with Baseline Vessel and Dominant Variants superimposed.

When looking at Figure 147 and the scatter diagram between the Required Ballast water amount and EED, a new characteristic form emerges that wasn't previously observed and is highly linear. Furthermore, the scatter around the centreline has been considerably reduced when compared to run Det_NMAX_02. The Pareto front here is more profound than in the previous scatter diagram. Furthermore, the baseline is located at the top end, close to dominant variants due to the very good EEDI performance. Overall, the linear Pareto front is less steep than in previous runs, meaning that considerable concessions are required in terms of EEDI to reduce the required Ballast Water amount.

Further to the previous remarks, dominant variants with good RFR and EEDI performance which are larger vessels are located at the top right of the Pareto front, while smaller vessel alternatives with considerably improved required ballast amount (up to 55%) are located far left.

Like in all previous runs, designs in the middle of Pareto regions have been arbitrarily selected by the Author to identify their robustness and characteristics compared to the remaining dominant variants.

For example, Design ID 2390 has been identified to be in the middle area of the Pareto front formulated in the scatter diagram between Required Ballast Water and EEDI, however, it was far away from the Pareto front of the scatter diagram between Required Ballast Water and RFR and closer to the Pareto region/pole of the scatter diagram between EEDI and RFR. Design ID 899 which was picked from the middle of the Pareto region of the scatter diagram between Required Ballast and EEDI on the other hand, is suboptimal and far away from the Pareto regions of both the other two scatter diagrams.

6.4.3.6. *VLOC Design – NSGAI Algorithm (ID: Det_WOZMAX_03)*

For this optimization run (ID: Det_WOZMAX_03) a total number of 2340 viable designs were generated out of a total population of 3000 designs corresponding to 78% success rate.

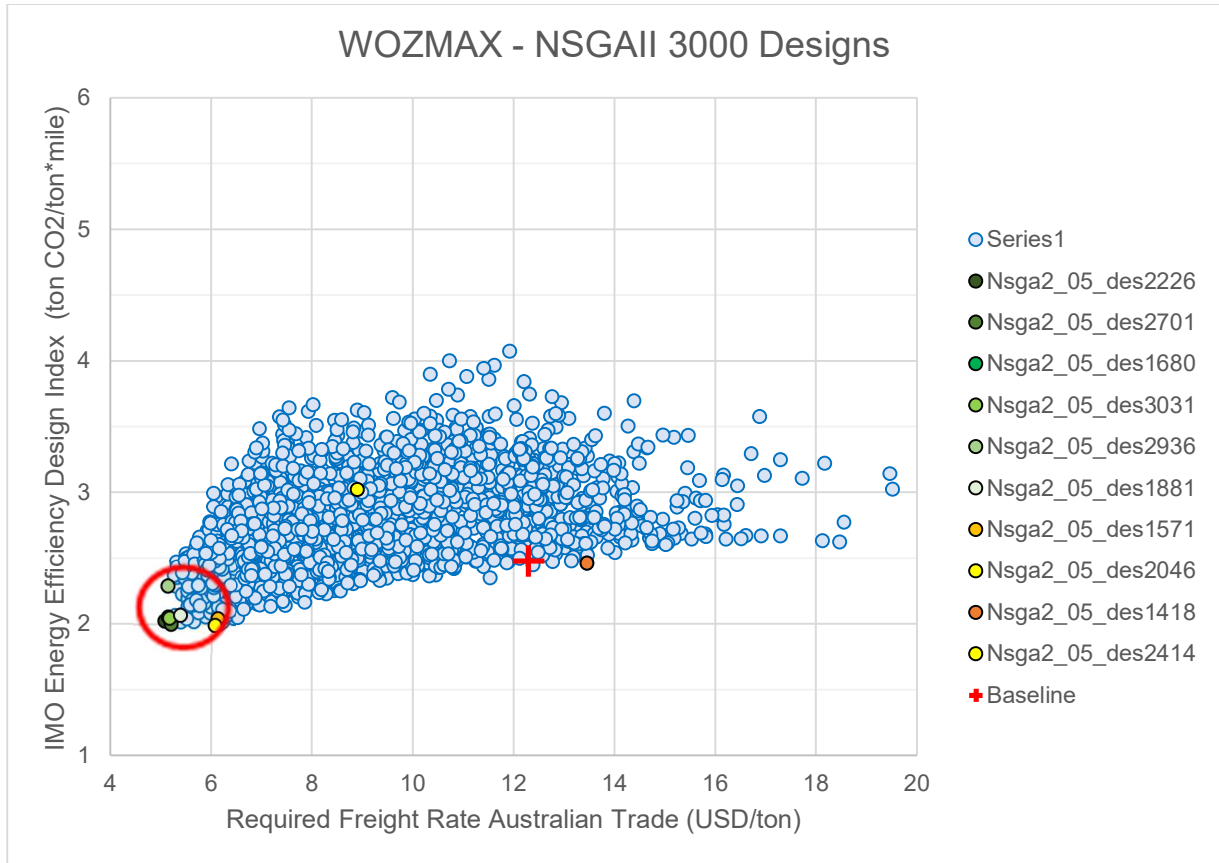


Figure 148: Det_WOZMAX_03 / EEDI vs. RFR Design Scatter Diagram with Baseline Vessel and Dominant Variants superimposed.

The design cloud for this case is very dense cloud as seen in Figure 148 illustrating the scatter diagram of the EEDI versus the RFR. In this optimization run (Det_WOZMAX_03) a linear correlation between EEDI and RFR is still identified, but considerably less steep than in the previous run (Det_NMAX_02) or the runs with Dakota algorithms (Det_NMAX_01 and Det_WOZMAX_01). The polarized Pareto peak is still evident as marked with a superimposed red circle. Most of the dominant variants corresponding to larger and fuller vessels lie there.

The increased (but) dense scatter of designs can be attributed to different calculation modules between EEDI and RFR. For simulated studies where a common input is used under the same framework between EEOI and RFR, it is expected that this wide scatter will be significantly narrower.

Due to the considerably flattened linear relationship between the two variables, the selection process for utility functions is particularly difficult with the Pareto pole dominating all other regions. Given this, it was decided that the same optimization run should be repeated with one

of the RFR values (Australian trade) removed from the objectives to increase the steepness and through the “de-polarization” of the front make the selection and ranking process easier and create bigger play and room for multi-objective optimization.

The Baseline design is on a linear extension of the Pareto region, dominating all the designs with the same RFR in terms of EEDI, however, it is far away from the pole. Thus, the best design in terms of RFR features an improvement of about 57.7%.

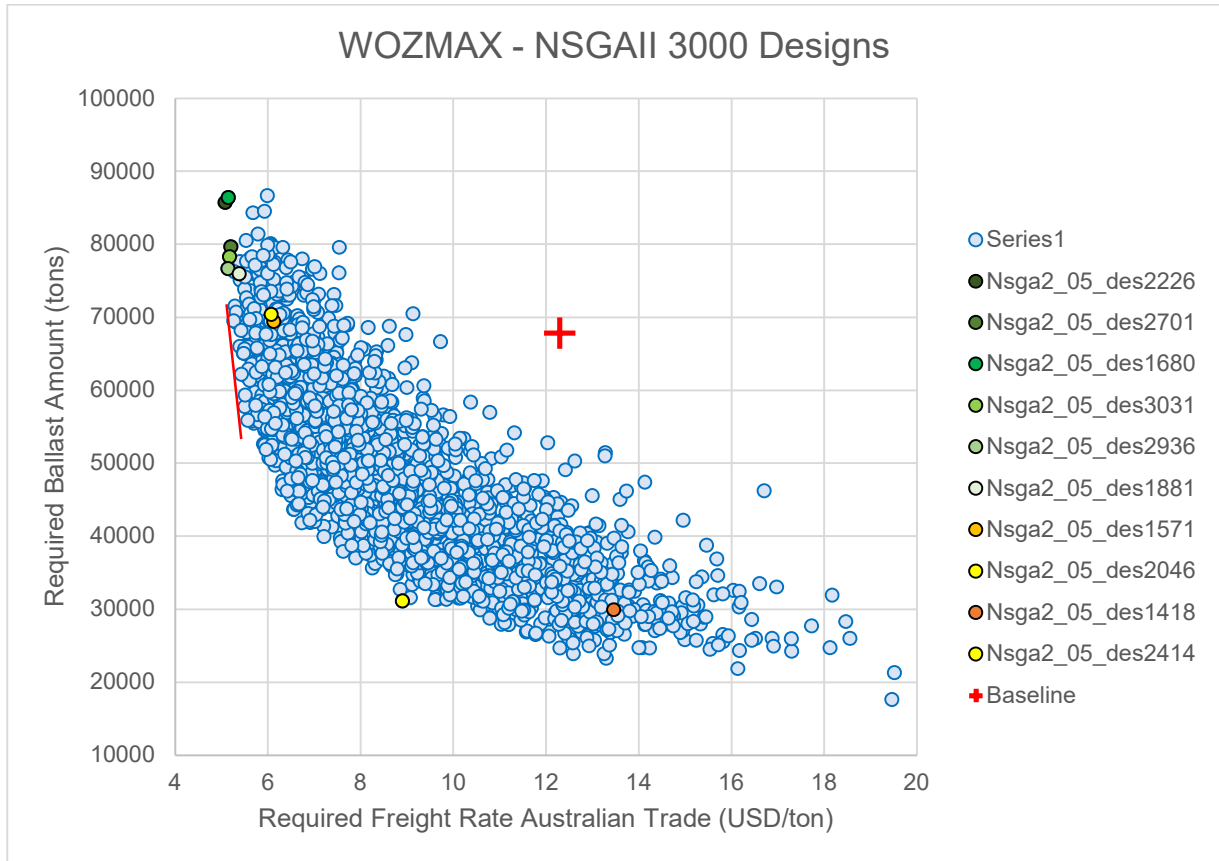


Figure 149: Det_WOZMAX_03 / Required Ballast Water vs. RFR Design Scatter Diagram with Baseline Vessel and Dominant Variants superimposed.

Interestingly, in Figure 149 a curved Pareto front has been generated. The scatter diagram remains dense, but the width for the diagram between Required Ballast and RFR is considerably narrower than the previous one. Given that the scatter diagram of Required Ballast and EEDI is very wide, this indicates that the source of the scatter and underlying uncertainty comes from the EEDI calculation and the unsuitability of the latter to be a representative design index.

An interesting observation is a region and front formulated in the area indicated by the superimposed red line in Figure 149. The sharp fall of the front and curve indicate that in the subject area there are available vessel designs that feature a sharp decrease of Ballast Water (26.4%) at a very small compromise of the RFR performance (a drop of only 8.6%) that can potentially create considerable opportunities for trade-offs. However, none of the selected

dominant variants is from this region of the scatter diagram, with the main reasons being the following:

- Linear weight distribution of utility functions. A more elastic approach using logarithmic distributions can assist in design picking and ranking instead.
- EEDI performance is not optimal, indicating that EEOI instead is a better objective and that EEDI should be a constraint instead.
- The RFR values for both trade routes (Australian and Brazilian) have been used as independent design objectives/targets, making possible trade-offs very difficult.

The baseline in this regard is completely suboptimal with all generated designs strictly dominating it. For the same level of RFR, an improvement of 60% in terms of required ballast is attained while for the same level of required ballast again an improvement of more than 50% is attained.

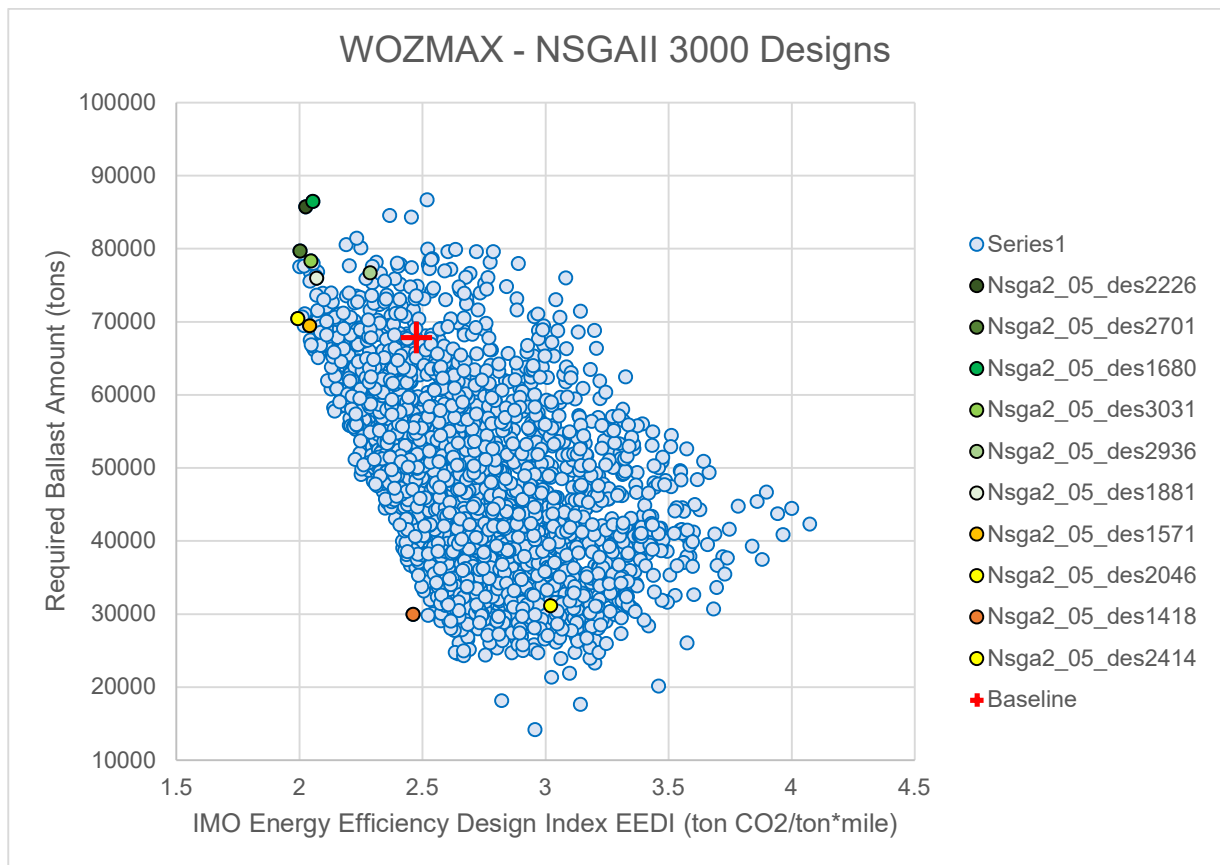


Figure 150: Det_WOZMAX_03 / Required Ballast Water vs. EEDI Design Scatter Diagram with Baseline Vessel and Dominant Variants superimposed.

The scatter diagram between the Required Ballast and the EEDI (Figure 150) is, as previously discussed, to a wider extent without losing however the characteristics of the dense population. A linear and steep Pareto frontier has been generated, with the population of the left region belonging to larger and fuller vessels while smaller vessels are in the right region of the frontier.

Again, the polarization of the first scatter diagram as well as the linear weight distribution “block” the utility functions from selecting designs located in the middle regions.

When manually selecting design ID 2414 of the Pareto middle grounds of the scatter diagram between Required Ballast Water and RFR we see that is suboptimal and away from the Pareto front of the other two scatter diagrams (BW-EEDI and EEDI-RFR).

Having concluded the first round of optimization studies using a “basic” setup of a deterministic framework, and prior to moving to the next optimization studies the following conclusions were evident:

1. The use of linear weight distribution of utility function blocks intermediate design selections with high potential trade-offs.
2. The introduction of the Required Freight Rate of both the Australian and the Brazilian Trade Routes as independent optimization objectives, further entangles the path of the optimization algorithm to the Pareto fronts and creates further anomalies.

It is thus clear that the use of only one RFR as an objective (e.g of the Australian trade route for Newcastlemax Designs and the Brazilian Trade Route for WOZMAX designs) is necessary for producing results with higher optimization potential, while the introduction of more “elastic” weight distributions (e.g logarithmic) of the utility functions can contribute to an easier, more efficient, and more robust picking of dominant variant designs.

Within this context, it was decided to repeat the last optimization run Det_WOZMAX_03, but with a reduced objective (without RFR of the Australian Trade) and introduce both linear as well as logarithmic weight distributions for the utility functions while ranking. The reason for the repetition is to have the results of these two interventions independent from the simulation clear and use them directly in simulation-driven results.

6.4.3.7. *VLOC Design – NSGAI Algorithm with refined Objectives (ID: Det_WOZMAX_04)*

The subject run is, as mentioned previously, a repeated optimization using the same variables and constraints as the original NSGAI run, but in this instance, the objective of the Required Freight for the Australian Trade was removed and only the objective for the Brazilian trade was kept to “de-polarize” the selection process and utility function use from regions that favour RFR and EEDI performance. From a first look, it is evident that the optimization results are better; the lowest EEDI attained is 1.87 compared to 2.1 which was the equivalent figure of optimization run ID Det_WOZMAX_03 (it also happens to be the best figure from all runs) corresponding to a 10.9% improvement. Furthermore, the optimization clouds are steeper and less wide, indicating a smaller variance and scatter and better opportunities for trade-offs.

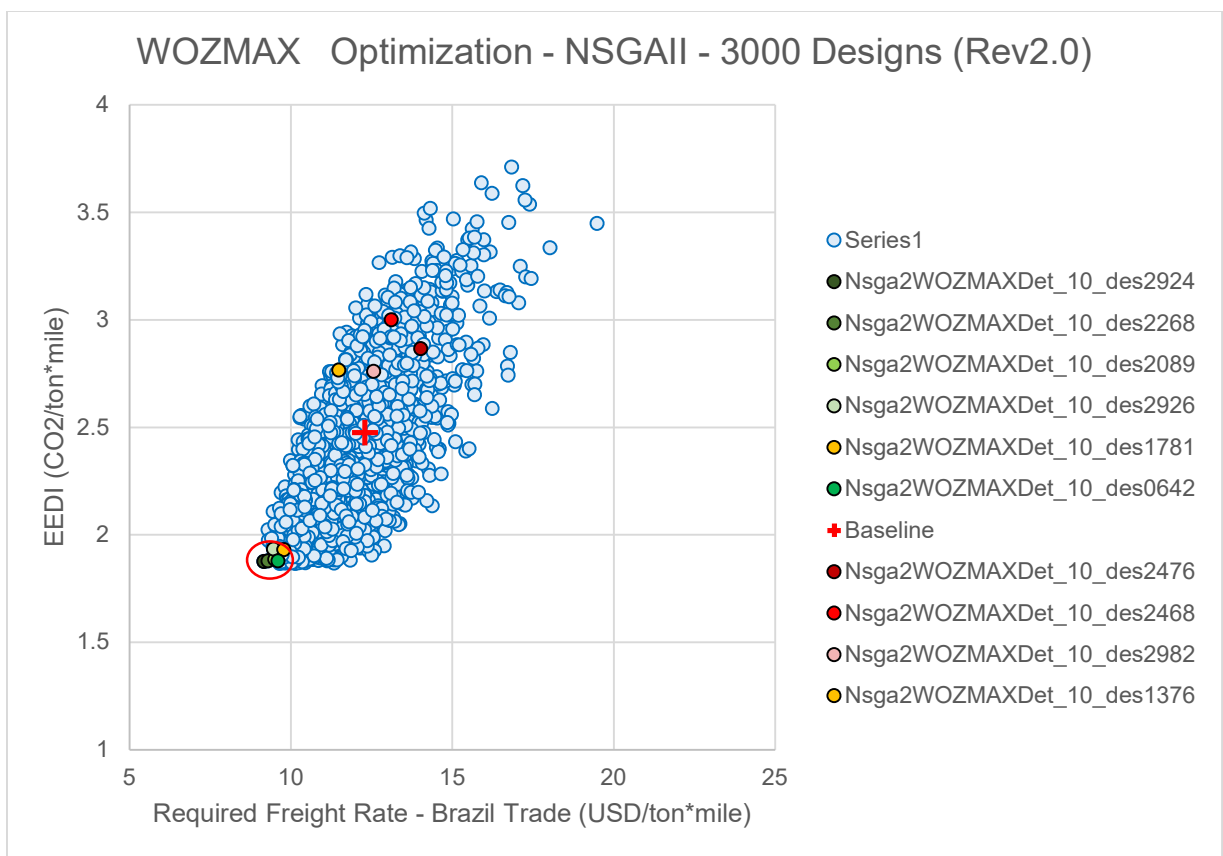


Figure 151: Det_WOZMAX_04 / EEDI vs. RFR Design Scatter Diagram with Baseline Vessel and Dominant Variants superimposed.

When looking at the scatter diagram between EEDI and RFR (Figure 151) one can observe a cloud that is considerably steeper than the ones of previous runs. It is narrower as well, creating a Pareto peak region instead of a front as marked with the red circle on the scatter diagram. Interestingly, the majority of the dominant variants lie there. In regions where the circle circumference lies and neighbouring to them are variants that are not Pareto optimal but have considerably reduced required ballast water amount at a very small expense of EEDI and RFR. An example is design ID1781, which has similar dimensions to the large vessels of the Pareto region but is slenderer,

corresponding to a considerably smaller required displacement at the ballast draft and thus ballast water amount.

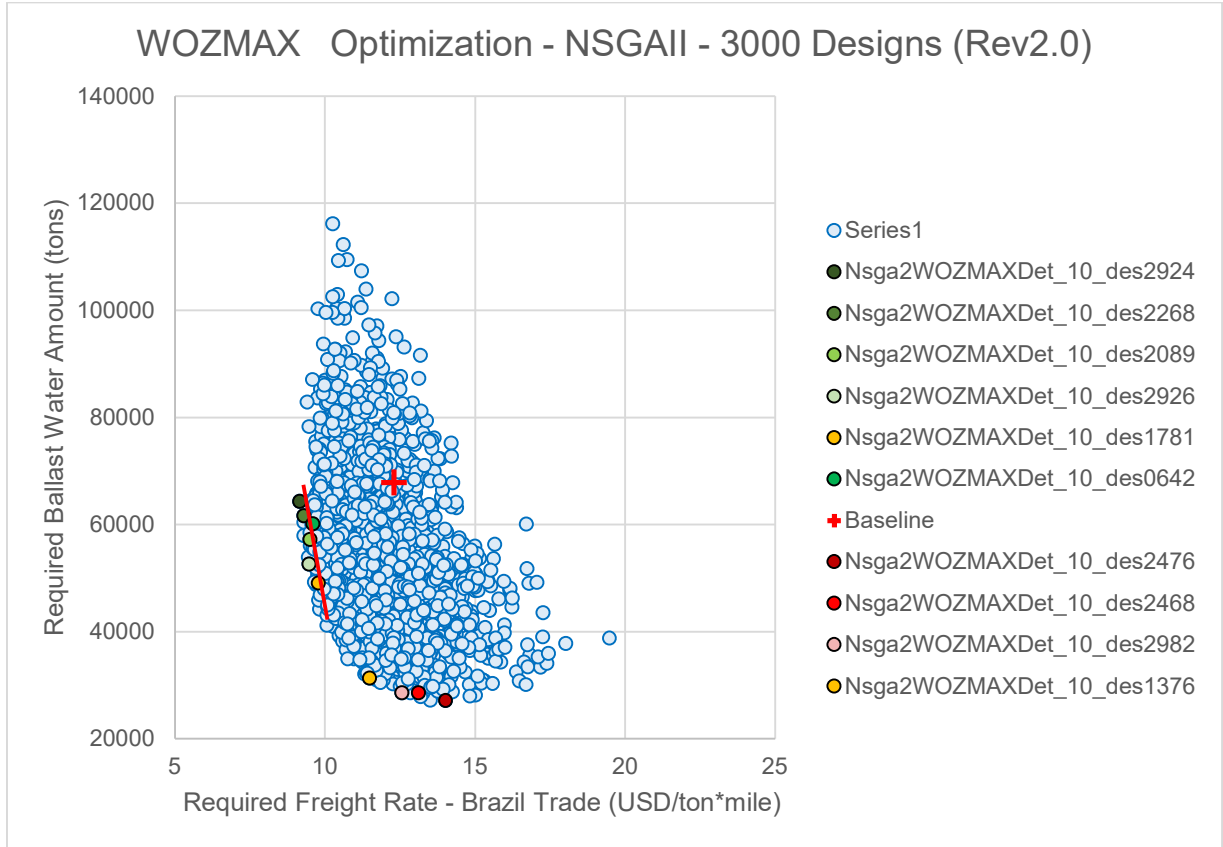


Figure 152: Det_WOZMAX_04*/ Required Ballast Water vs. RFR Design Scatter Diagram with Baseline Vessel and Dominant Variants superimposed.

The scatter diagram between Required Ballast Amount and RFR (Figure 152), features an extended Pareto front where most dominant variants lie. The Pareto front on the right-hand side is composed of a linear area that is considerably steep as marked with the superimposed red line, while after a point design variants are located on a parabolic front. The steepness of this area (similar to the equivalent in the optimization run Det_WOZMAX_03) creates an opportunity for significant trade-offs, that enable the extensive reduction of the required ballast amount at a very small expense to the RFR. The use of logarithmic weight distribution for the utility functions enabled better exploration and ranking resulting in the automatic and direct picking of designs with attractive trade-offs in intermediate regions of the Pareto frontier such as Design ID 1781. Interestingly, the subject design features a 23.7% reduction in Ballast Water amount compared to the dominant variant with the best RFR with only a 6% increase in terms of RFR compared to the same dominant variant. Design ID1781 remains also on all three scatter diagrams of Pareto regions (fronts or peaks) indicating that it is a choice of a robust design across all optimization relationships that couldn't have been picked with the use of the original formulation of utility functions but only from their logarithmic variant. This proves that the required "elasticity" of the

utility functions for picking designs with trade-offs and traditional Pareto relationships has been attained. The characteristics of the variants that have been selected remain like with previous runs with designs on the left end of the diagrams being larger vessels with improved EEDI and RFR while the right end of the Pareto fronts is characterized by smaller vessels with considerably less required ballast but inferior EEDI and RFR. In the meantime, the baseline vessel is strictly dominated by most of the generated designs both in terms of Ballast, EEDI and RFR.

Lastly, the scatter diagram between the required ballast water amount and EEDI reveals a very interesting and unprecedented pattern. Similar to the previous scatter diagram (Figure 151) but more intensely, a nearly vertical wall of designs is generated at the far-left region and prior to the formation of a Pareto frontier stretching from the left to the far right regions. This vertical wall comprises the region all the dominant variants are located, while at the bottom of the wall (where effectively a new Pareto front starts) design ID 1781 is located and shows cases of the drastic reduction of required ballast water (23.7% decrease compared to Design ID2924) with minimum expense to EEDI (3.2% increase compared to Design ID2924). The main reason the wall front can be attributed to is the limit imposed by the size constraint of the optimization (DWT constraint), which is thus limiting designs to be out of this vessel size segment and feature significantly lower EEDI values.

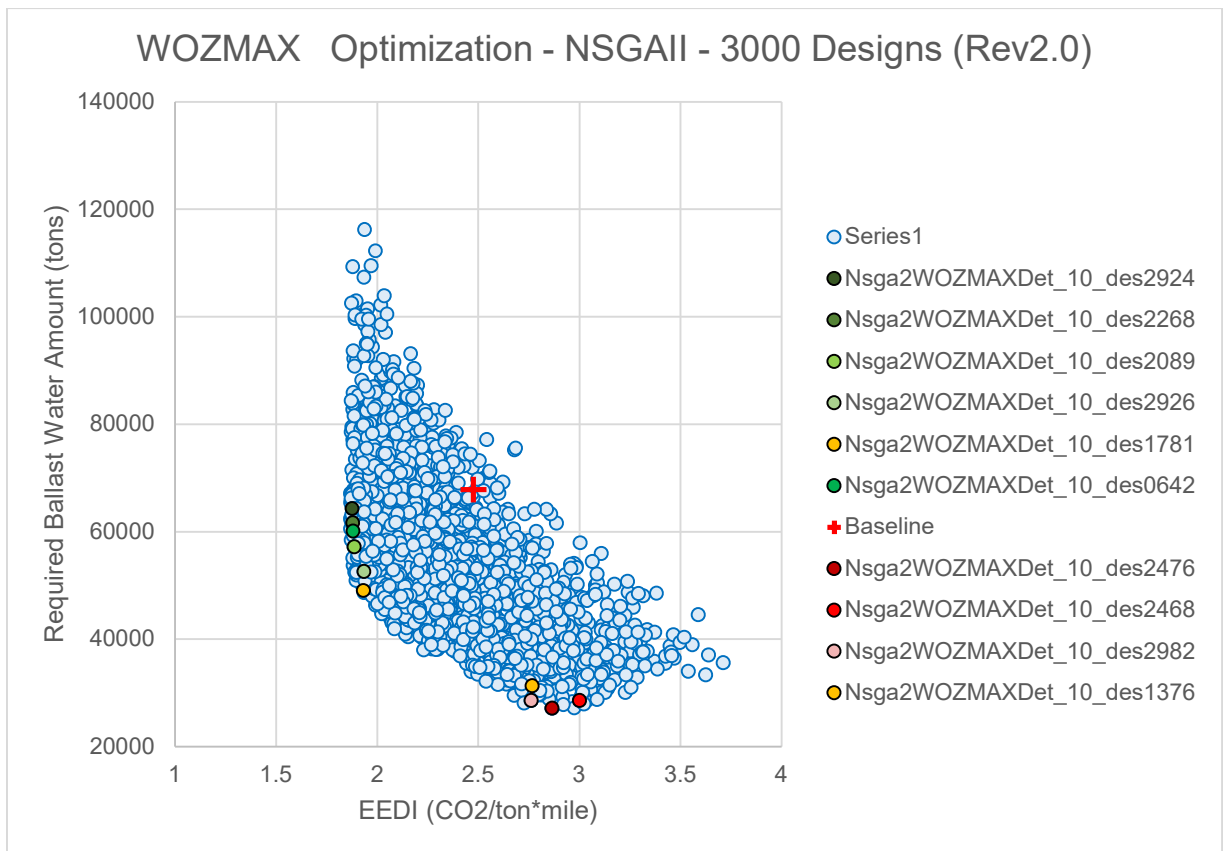


Figure 153: Det_WOZMAX_04* / Required Ballast Water vs. EEDI Design Scatter Diagram with Baseline Vessel and Dominant Variants superimposed.

Again, the logarithmic weight distribution of the utility functions enabled this enhanced exploration picking more design variants. The region creating the “knuckle” between the vertical wall of designs and the beginning of the Pareto front is the most promising in optimization terms. Such a potential can be further enhanced by the removal of the EEDI from the optimization targets and the use of the latter as a design constraint with the EEOI generated from voyage simulation studies replacing the latter.

6.4.4. Design Selection, Ranking and Discussion

6.4.4.1. *Design Selection and Ranking Per Run*

In the below tables, the ranking of the top 10 design variants for each utility weight assignment scenario (maximum weights per optimization target) and each run are depicted for the Run IDs Det_WOZMAX_01~04. For the Det_WOZMAX_04 Run ID ranking using the logarithmic weight distribution is shown as “U5 Scenario”.

An interesting observation is that for utility scenarios U1~U3, the top three variants remain the same with slight changes (if any) in the ranking between them. This phenomenon highlights the high degree of polarization and that despite the changes in the weight assignment per optimization target, the ranking process is trapped in the same set of designs and is unable to explore further the Pareto region.

A first countermeasure to tackle the above phenomenon was to set the maximum weight of EEDI to zero, to eliminate one of the strongly correlated targets. The effect of this in scenario U4 is that different designs are ranked, especially in the region of vessels with considerably lower ballast amounts but with a considerable concession in terms of RFR performance while designs with better trade-offs are again neglected by the picking function.

A second countermeasure was to have one additional optimization run (Det_WOZMAX_04) where only one RFR value was used as an optimization target. In this instance, the effect on the ranking of utility functions was none. The only case for this optimization run where the ranking was more flexible, picking also designs with better trade-off was when the logarithmic distribution function was introduced as the U5 scenario.

The basis on the rankings in Table 49 to Table 50, the dominant variants have been illustrated in the scatter diagrams of each run, in paragraph 5.4.3 and their principal particulars are shown in and discussed.

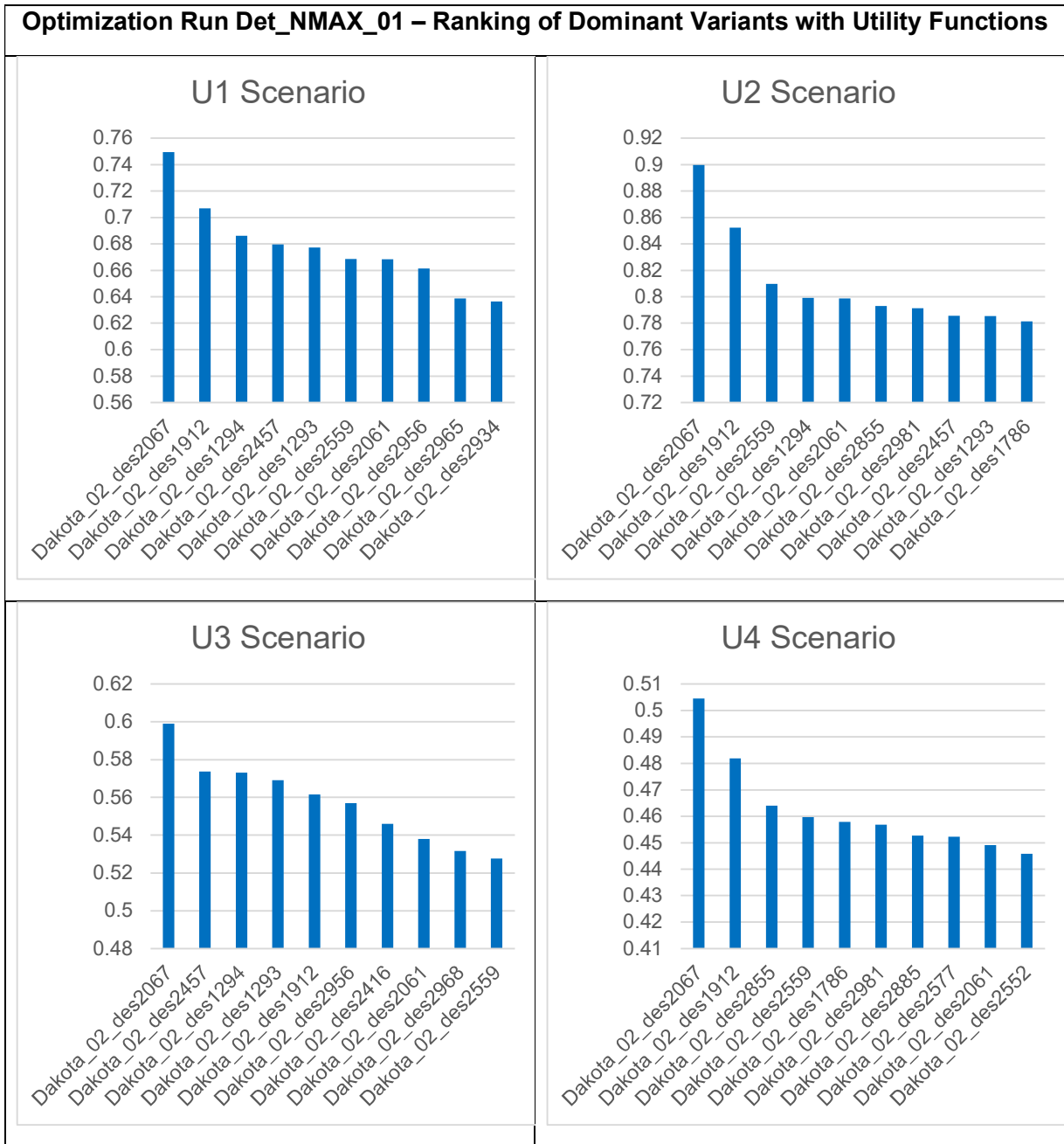


Table 49: Ranking of Optimization Dominant Variants with Utility Functions Scenarios – RUN ID Det_NMAX_01

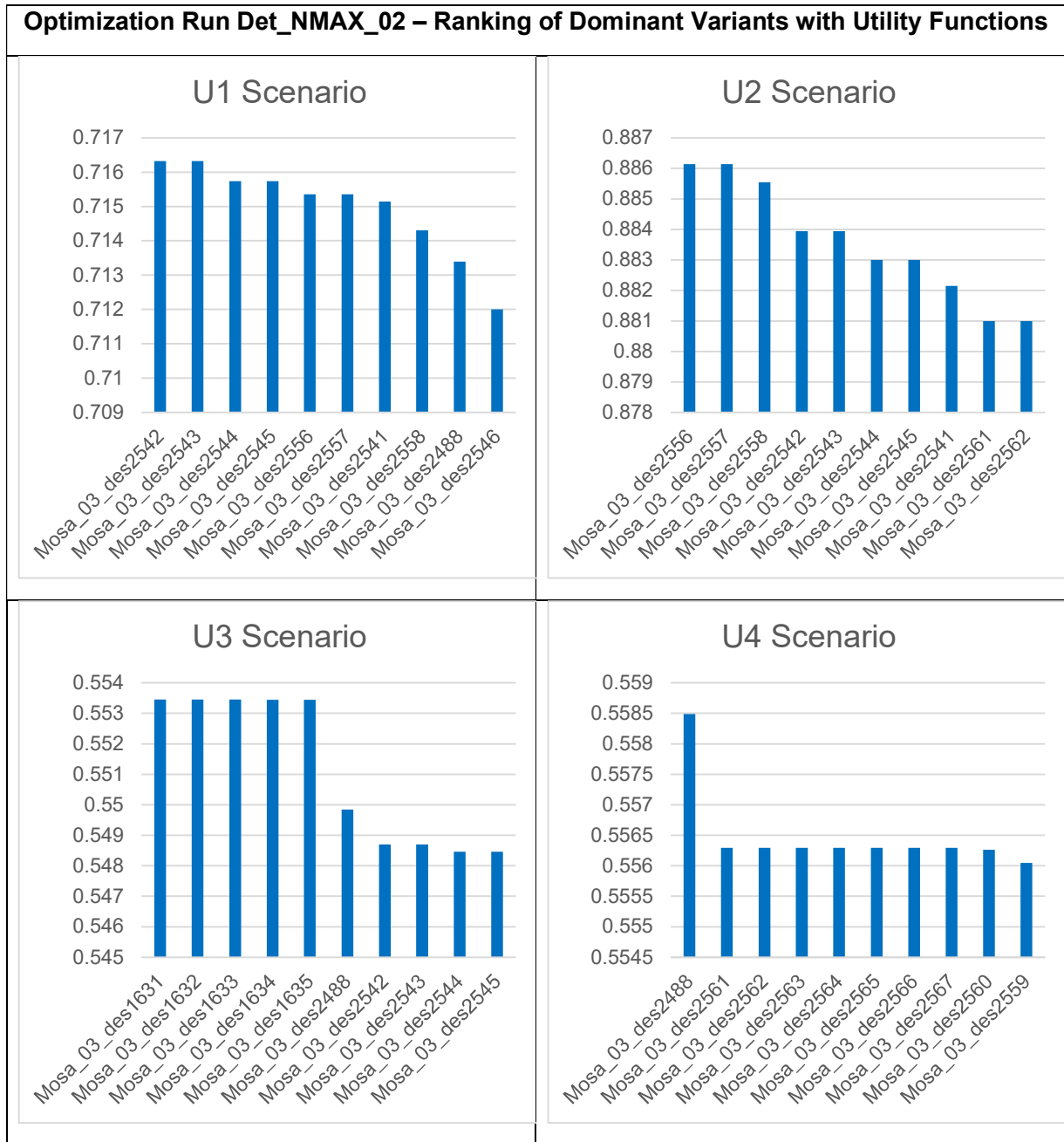


Table 50: Ranking of Optimization Dominant Variants with Utility Functions Scenarios – RUN ID Det_NMAX_02

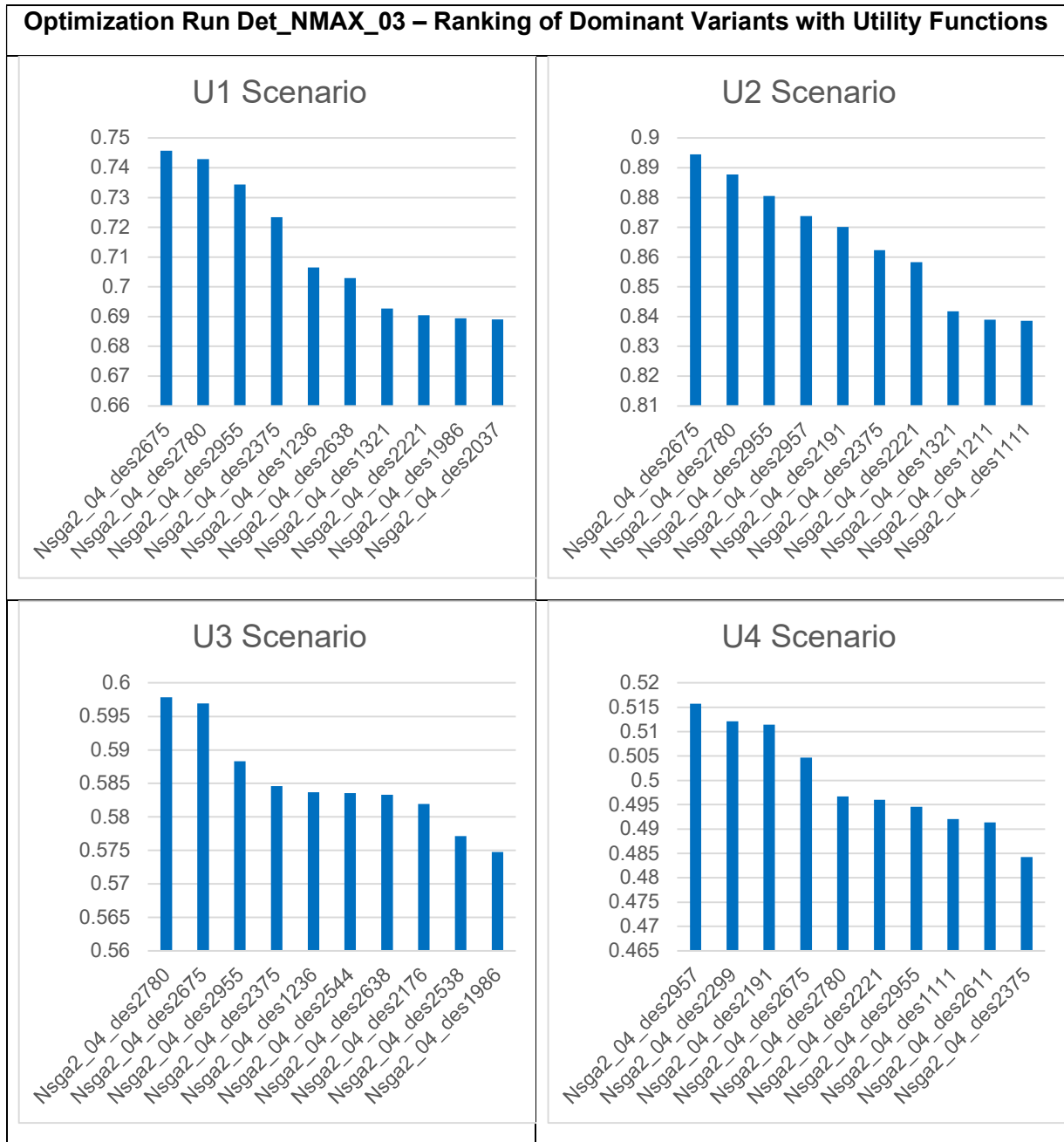


Table 51: Ranking of Optimization Dominant Variants with Utility Functions Scenarios – RUN ID Det_NMAX_03

Optimization Run Det_WOZMAX_01 – Ranking of Dominant Variants with Utility Functions

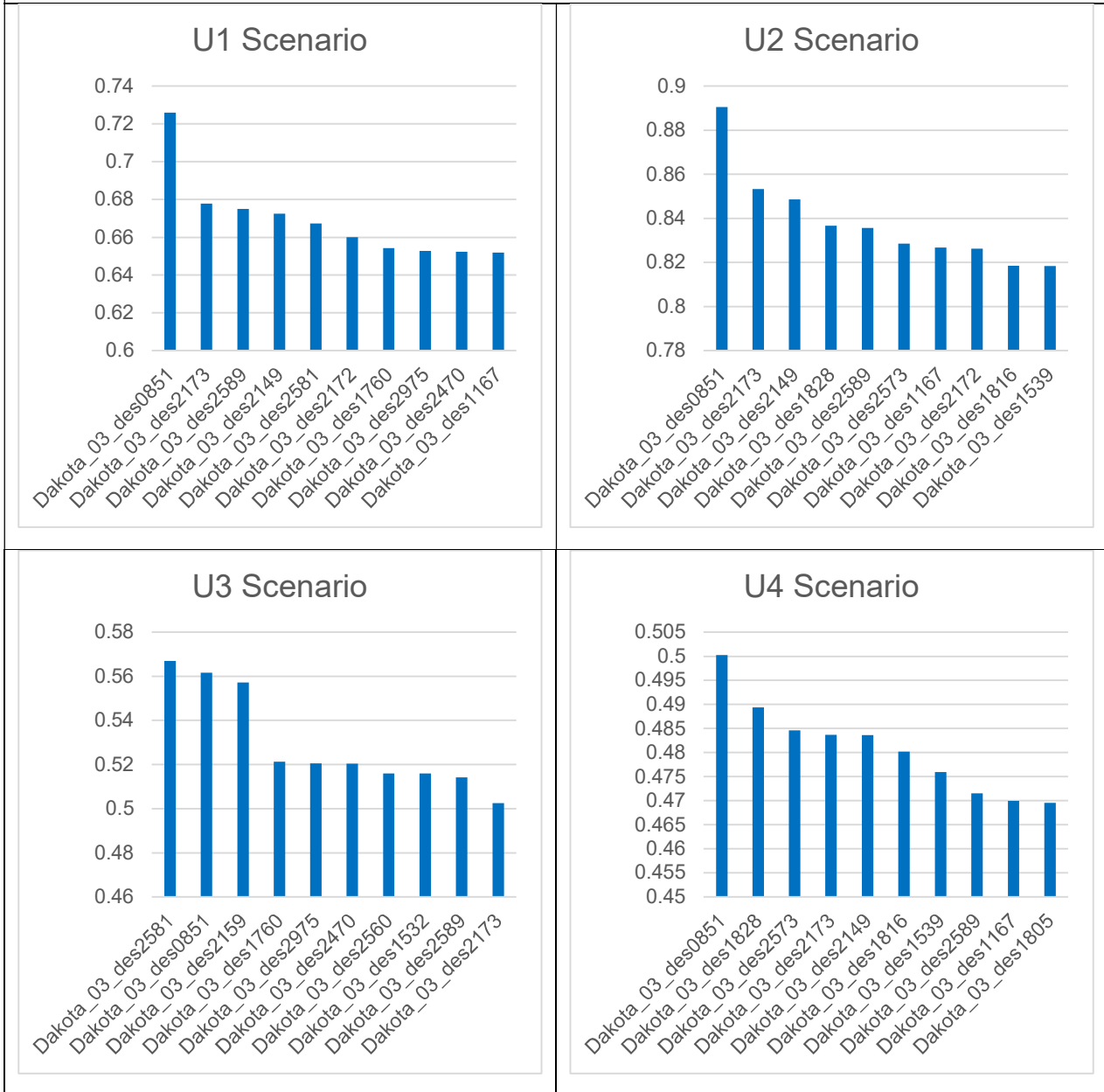


Table 52: Ranking of Optimization Dominant Variants with Utility Functions Scenarios – RUN ID Det_WOZMAX_01

Optimization Run Det_WOZMAX_02 – Ranking of Dominant Variants with Utility Functions

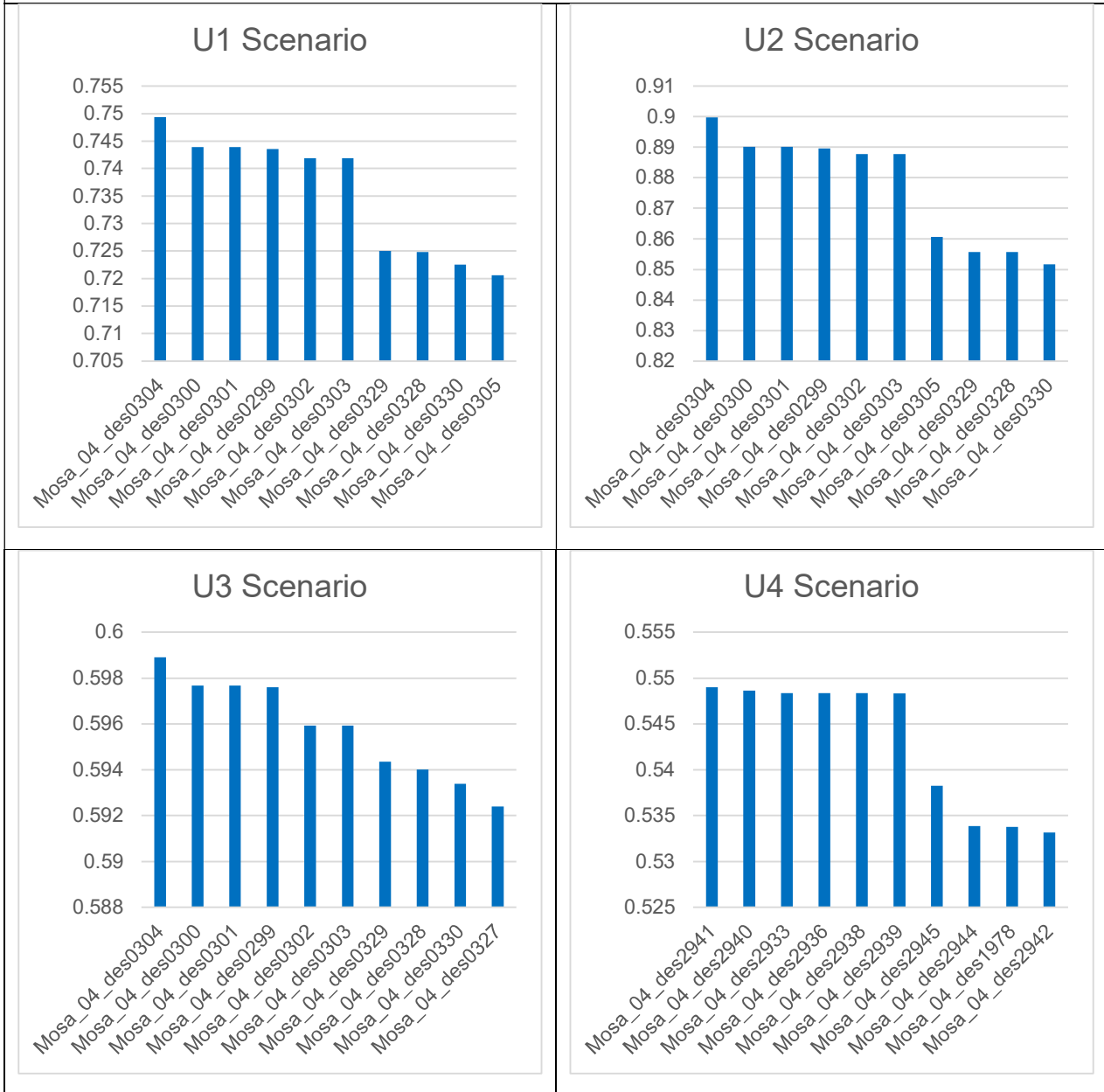


Table 53: Ranking of Optimization Dominant Variants with Utility Functions Scenarios – RUN ID Det_WOZMAX_02

Optimization Run Det_WOZMAX_03 – Ranking of Dominant Variants with Utility Functions

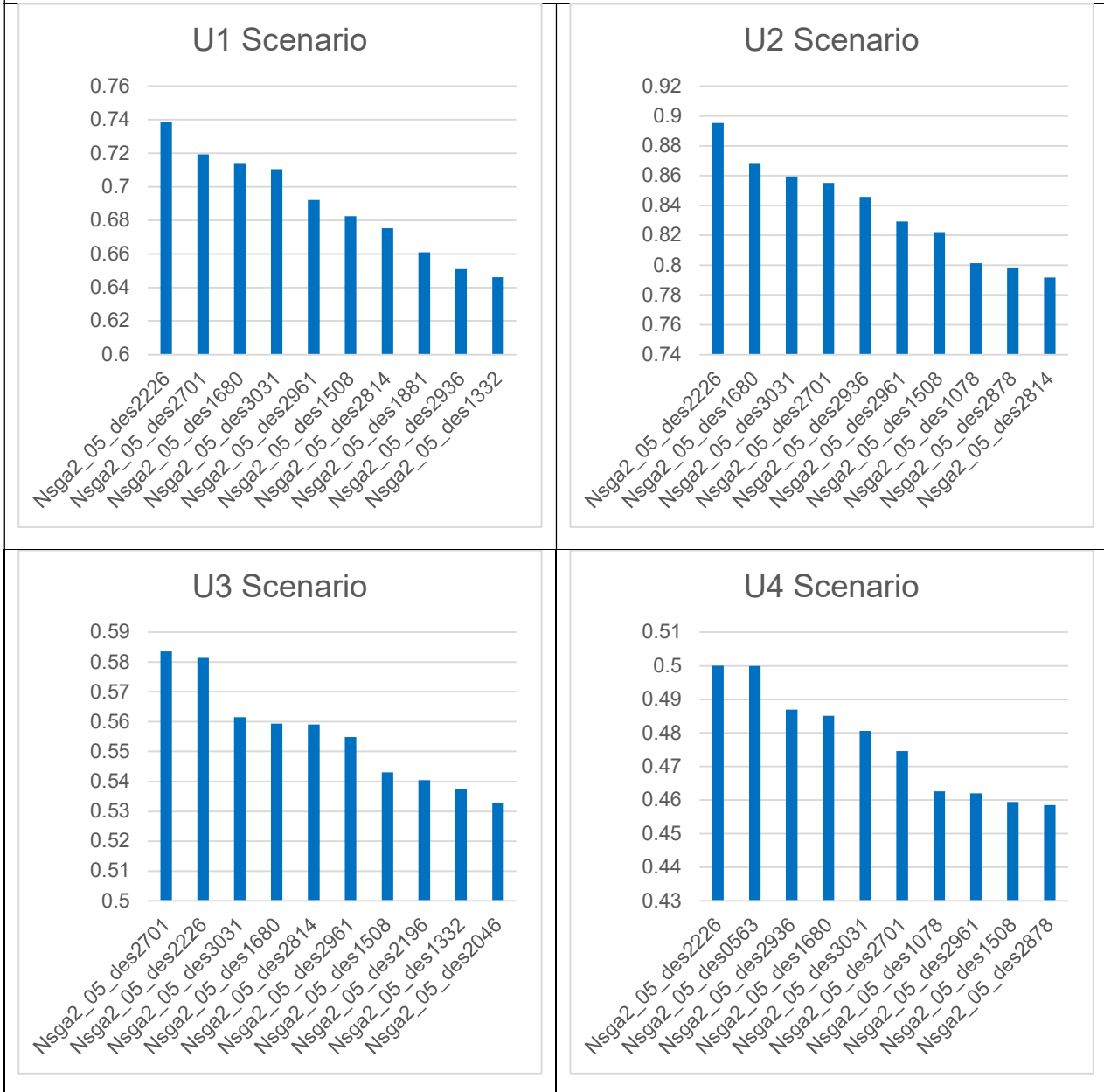
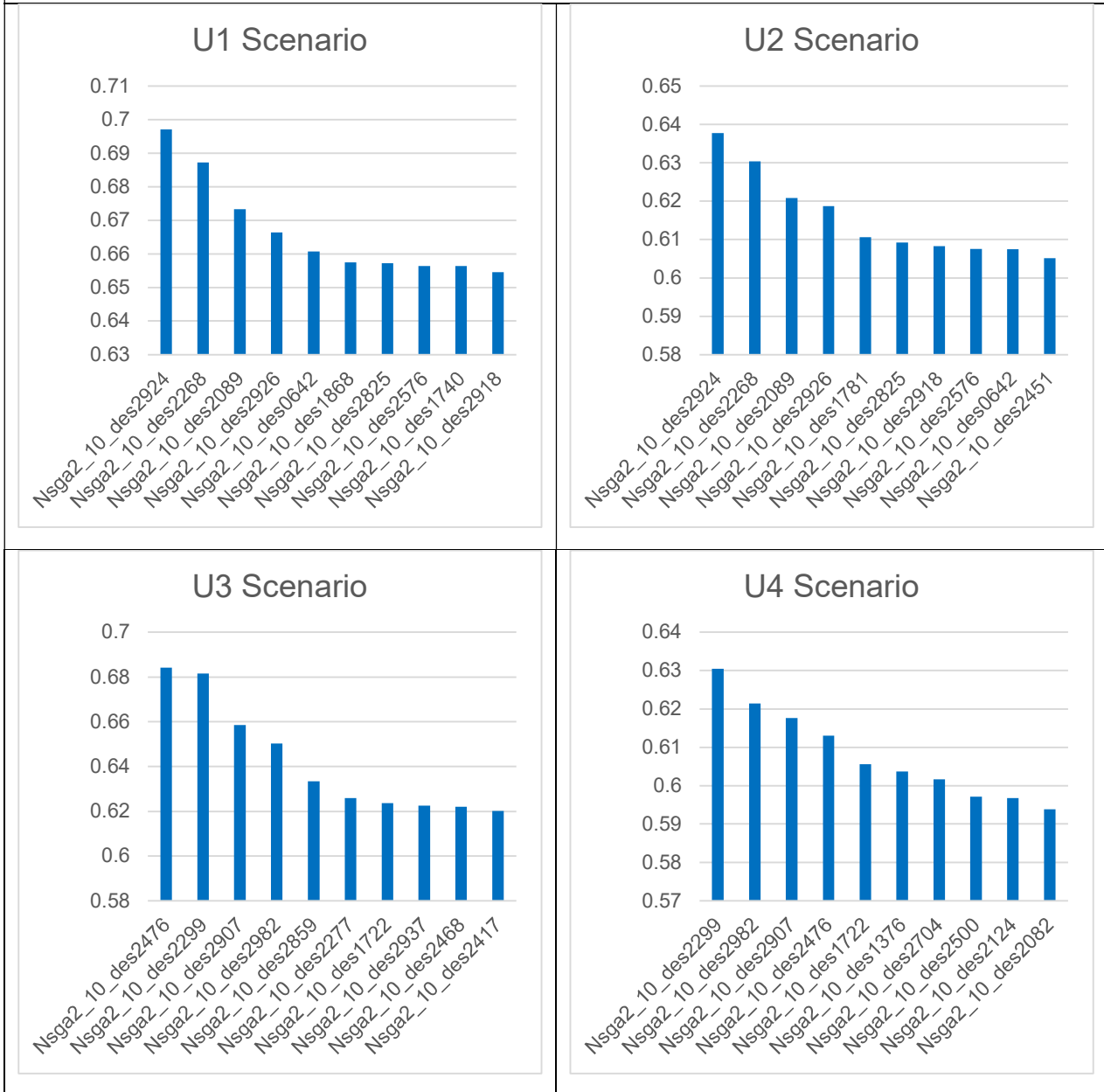


Table 54: Ranking of Optimization Dominant Variants with Utility Functions Scenarios – RUN ID Det_WOZMAX_03

Optimization Run Det_WOZMAX_04 – Ranking of Dominant Variants with Utility Functions



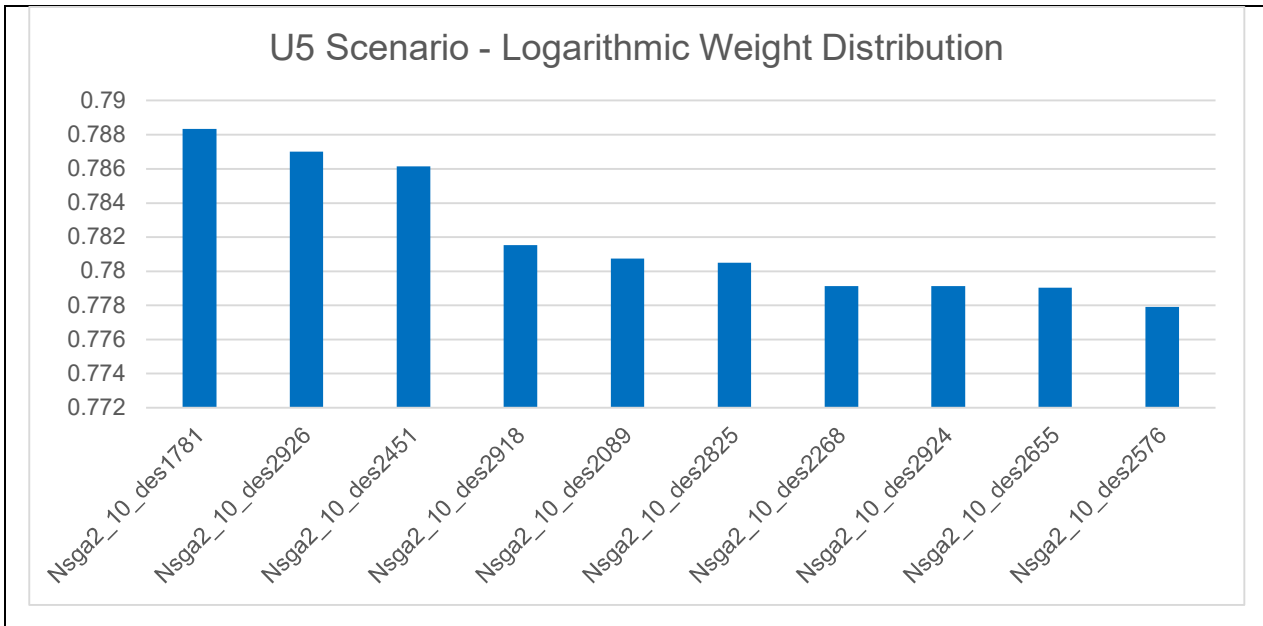


Table 55: Ranking of Optimization Dominant Variants with Utility Functions Scenarios – RUN ID Det_WOZMAX_04

6.4.4.2. *Principal Particulars of Dominant Variants.*

The principal particulars of a selected group of dominant variants from the Deterministic Optimization Pathway runs can be found in Table 56 to Table 60.

- *Observed Length*

For Newcastlemax case studies, RFR and EEDI optimal designs have lengths very close to the upper boundary (300m) of the respective optimization variable while the Required Ballast Water optimal designs have lengths very close to the lower boundary. Clearly, this is an indication of the favourable effect of the vessel's size on the RFR and EEDI and the negative effect on Required Ballast Water.

A more interesting relationship on the observed length is those of the dominant variants originating from the optimization runs of the WOZMAX case study. For these designs, even at lengths at the upper limit of the variable (close to 330 meters) variants with lower Required Ballast amounts are observed due to their lower C_b . Interestingly, also RFR and EEDI optimal designs move towards the upper limit coupled with larger beam values and considerably lower block coefficient values.

- *Observed Beam*

For the Newcastlemax variants, in contrast to the length correlation described above, the beam has a less correlated behaviour with RFR and EEDI with dominant variants having beam values well spread within the variable range. For WOZMAX case studies, beamy designs of dominant variants are found in the optimization run Det_WOZMAX_04, while in the previous runs beam values are kept at the middle to lower ranges of the variable.

- *Observed Draft*

A very interesting observation with regards to the design (summer scantling) draft of the dominant variants of both Newcastlemax and WOZMAX designs is that it converges at the range of 20.8-21.7 meters which is close to the upper limit of the subject variable range. The anticipated reason for such a phenomenon is that for higher draft values there is a penalization in terms of calm water resistance (and thus required power) while at lower draft values, displacement and capacity are lost leading to an overall increased RFR and EEDI.

- *Observed Block Coefficient (C_b)*

Newcastlemax dominant variants belong to two categories with regard to the observed C_b values. As in the case of length, larger vessels with higher block coefficients are RFR and EEDI optimal while vessels with lower block coefficients are Required Ballast Amount optimal but at a considerable expense of RFR and EEDI.

On the contrary to this, the majority of WOZMAX dominant variants have lower C_b values and still have a considerably better performance in terms of RFR and EEDI due to their larger size and “unlocked” design space and potential combinations.

- *Observed Deck Height*

Similarly to the observed draft values, the deck height for all dominant variants (either NMAX or WOZMAX) was close to the upper limit of the subject variable. The reason for this is that with a bigger depth the lightship and building cost (thus CAPEX) penalization is small compared to the positive effect on cargo hold volumes, allowable drafts (based on allowed freeboard heights) and payloads to the RFR.

- *Observed Cargo Hold Variables*

Cargo Hold variable values of dominant variables have generally a greater scatter compared to main dimensions and hull variables with considerably smaller correlation (close to none) to RFR, EEDI and practically zero correlation with regards to Required Ballast Amount. It is important to stress here that the variation and range of cargo hold variables are such to be adaptable to the surrounding hull surface changes and create meaningful structure and subdivision designs.

- *Observed Propeller Particulars*

The most interesting comment when looking at the propeller characteristics of the dominant variants (both for WOZMAX and NMAX designs) is the emergence of many designs with 5-blade propellers which for this propeller size appears less frequently in Bulk Carrier designs of this size but not uncommon. The most common value of the Pitch Ratio of the propellers of dominant variants is in the range of 0.7-0.74. The diameters of designs that are RFR and EEDI optimal are larger, leading to smaller powering requirements due to the increased efficiency but higher ballast amounts due to the larger aft draft required for full propeller immersion.

No.	Particular	ID2067	ID2638	ID1631	ID2345
-	Run ID	Det_NMAX_01	Det_NMAX_01	Det_NMAX_02	Det_NMAX_02
N_01	Length between Perpendiculars	299.789	276.490	299.4113	299.4681
N_02	Beam	48.760	45.985	48.505	46.634
N_03	Draft	21.832	21.237	20.295	21.165
N_04	Deck height	28.928	29.875	27.788	28.099
N_05	Hopper Height	10.176	7.853	8.264	9.388
N_06	Hopper Breadth (m)	3.231	3.912	4.217	4.810
N_07	Topside Height (m)	11.770	10.208	11.719	11.335
N_08	Topside Breadth (m)	7.180	13.309	9.869	11.979
N_09	Block Coefficient C _b	0.858	0.839	0.867	0.813
N_10	LCB (%Lbp)	0.522	0.511	0.518	0.522
N_11	Bilge Height (m)	3.862	3.333	6.039	6.158
N_12	Bilge Width (m)	5.521	2.767	2.599	3.235
N_13	Propeller Diameter (m)	9.168	8.046	8.385	8.313
N_14	Propeller Expanded Area Ratio	0.449	0.860	0.917	0.781
N_15	Propeller Pitch over Diameter	0.741	0.742	1.039	0.784

N_16	Propeller Number of Blades	5	5	4	5
O_1	Required Freight Rate (RFR)	5.581	6.858	6.497	6.793
O_2	EEDI	3.068	3.713	2.774	2.950
O_3	Required Ballast Water Amount	62,693	42,949	59,210	46,381
-	SMCR	20,870/75.8	23,248/91.5	22,718 /70.9	23,357 / 84.8
-	Lightship Weight	27,696	23,281	27,754	26,050

Table 56: Principal Particulars of Newcastlemax Dominant Variants (I)

No.	Particular	ID2675	ID1405
-	Run ID	Det_NMAX_03	Det_NMAX_03
N_01	Length between Perpendiculars	297.417	278.656
N_02	Beam	49.616	45.175
N_03	Draft	21.897	21.574
N_04	Deck height	29.074	29.006
N_05	Hopper Height	10.101	11.350
N_06	Hopper Breadth (m)	5.332	3.777
N_07	Topside Height (m)	5.057	7.573
N_08	Topside Breadth (m)	7.816	14.888
N_09	Block Coefficient C _b	0.867	0.814
N_10	LCB (%Lbp)	0.521	0.522
N_11	Bilge Height (m)	6.902	2.551
N_12	Bilge Width (m)	5.102	4.806
N_13	Propeller Diameter (m)	9.090	8.027
N_14	Propeller Expanded Area Ratio	0.817	0.923

N_15	Propeller Pitch over Diameter	0.708	0.713
N_16	Propeller Number of Blades	5	4
O_1	Required Freight Rate (RFR)	5.447	7.724
O_2	EEDI	2.431	3.100
O_3	Required Ballast Water Amount	63,904	36,096
-	SMCR	21,361/81.3	25,378/97.1
-	Lightship Weight	27,793	23,237

Table 57: Principal Particulars of Newcastlemax Dominant Variants (II)

No.	Particular	ID851	ID243	ID304
-	Run ID	Det_WOZMAX_01	Det_WOZMAX_01	Det_WOZMAX_02
W_01	Length between Perpendiculars	318.520	318.177	318.516
W_02	Beam	51.844	54.850	51.852
W_03	Draft	21.832	21.601	20.130
W_04	Deck height	28.748	29.889	29.086
W_05	Hopper Height	6.422	10.896	6.591
W_06	Hopper Breadth (m)	4.076	4.583	4.775
W_07	Topside Height (m)	10.500	11.858	10.566
W_08	Topside Breadth (m)	12.924	9.532	14.109
W_09	Block Coefficient C _b	0.865	0.784	0.853
W_10	LCB (%Lbp)	0.516	0.506	0.510
W_11	Bilge Height (m)	2.828	4.090	2.684
W_12	Bilge Width (m)	5.878	6.541	6.740
W_13	Propeller Diameter (m)	8.362	8.446	9.136

W_14	Propeller Expanded Area Ratio	0.887	0.642	0.724
W_15	Propeller Pitch over Diameter	0.707	1.086	0.738
W_16	Propeller Number of Blades	4	5	5
O_1	Required Freight Rate (RFR)	5.331	8.692	5.605
O_2	EEDI	2.204	2.333	2.349
O_3	Required Ballast Water Amount	69367	53514	76651
-	SMCR	21,958/97.18	32,981/69.59	20,434/77.79
-	Lightship Weight	31976	32537	31393

Table 58: Principal Particulars of WOZMAX Dominant Variants (I)

No.	Particular	ID2390	ID2226	ID2046
-	Run ID	Det_WOZMAX_02	Det_WOZMAX_03	Det_WOZMAX_03
W_01	Length between Perpendiculars	298.268	314.872	319.292
W_02	Beam	46.685	54.718	54.614
W_03	Draft	21.645	21.883	21.868
W_04	Deck height	28.394	29.776	29.961
W_05	Hopper Height	9.816	6.955	9.532
W_06	Hopper Breadth (m)	3.560	3.753	3.099
W_07	Topside Height (m)	6.287	5.720	8.237
W_08	Topside Breadth (m)	13.558	13.362	10.718
W_09	Block Coefficient C _b	0.851	0.863	0.867
W_10	LCB (%Lbp)	0.518	0.512	0.519
W_11	Bilge Height (m)	6.647	3.057	6.883
W_12	Bilge Width (m)	5.457	6.922	5.808
W_13	Propeller Diameter (m)	8.091	9.895	8.110
W_14	Propeller Expanded Area Ratio	0.604	0.559	0.942

W_15	Propeller Pitch over Diameter	1.076	0.742	1.040
W_16	Propeller Number of Blades	4	4	4
O_1	Required Freight Rate (RFR)	6.726	5.074	6.071
O_2	EEDI	2.576	2.025	1.9935565
O_3	Required Ballast Water Amount	48871	85719	70428
-	SMCR	23,843	17,423	21,866
-	Lightship Weight	26,542	32,824	33,301

Table 59: Principal Particulars of WOZMAX Dominant Variants (II)

No.	Particular	ID2924	ID1781	ID2451
-	Run ID	Det_WOZMAX_04	Det_WOZMAX_04	Det_WOZMAX_04
W_01	Length between Perpendiculars	323.843	304.025	326.017
W_02	Beam	59.362	62.505	58.338
W_03	Draft	21.458	21.93668	21.95789
W_04	Deck height	27.581	28.803	28.704
W_05	Hopper Height	7.363	8.035	6.081
W_06	Hopper Breadth (m)	5.121	4.798	3.558
W_07	Topside Height (m)	5.881	4.196	4.970
W_08	Topside Breadth (m)	11.536	10.307	9.446
W_09	Block Coefficient C _b	0.738	0.706	0.701
W_10	LCB (%Lbp)	0.523	0.512	0.514
W_11	Bilge Height (m)	2.971	3.871	5.636
W_12	Bilge Width (m)	6.147	4.516	6.410
W_13	Propeller Diameter (m)	8.701	8.050	8.036
W_14	Propeller Expanded Area Ratio	0.739	0.539	0.458

W_15	Propeller Pitch over Diameter	0.726	0.745	0.805
W_16	Propeller Number of Blades	5	5	4
O_1	Required Freight Rate (RFR)	9.161	9.779	9.745
O_2	EEDI	1.875	1.931	1.952
O_3	Required Ballast Water Amount	64319	49055	48901
-	SMCR	16975 / 79.99	18679 / 87.84	17955/85.44
-	Lightship Weight	34010	31910	33095

Table 60: Principal Particulars of WOZMAX Dominant Variants (III)

6.4.5. Discussion Of Results

In Table 61 the improvement and results of the dominant variants when compared to the baseline are shown, with improvement (reduction) percentages having negative values.

It is evident that all WOZMAX dominant variants have an overall better RFR, EEDI and Required Ballast amount strictly dominating the baseline yielding a considerable improvement in all areas. More specifically ID2924 has a reduced RFR of 25%, an improved EEDI of 39% and the Required Ballast amount reduced by 5%. If the RFR reduction is kept at 20% which still is considerable, ID 1781 offers a reduced ballast amount of 28%.

The same picture doesn't apply to Newcastlemax dominant variants. The reduction of ballast water amount comes typically with an increase of RFR and EEDI compared to the baseline. From these dominant variants, the only promising one for further optimization is ID2675 which combines a reduction of 6% in the required ballast amount with an improvement of 8% in RFR and 22% in EEDI.

It should be noted that such phenomena highlight the importance of simulation and the use of simulation-derived EEOI as an optimization target as there is an expected high uncertainty on the EEDI vs the actual performance in seaways. Furthermore, the superior capabilities in Multi-Objective Optimization with contradicting optimization targets of the NSGAI algorithm are identified, since for a highly constrained problem such as the Newcastlemax optimization runs, it is the only algorithm that can provide solutions where all optimization targets are reached. If the ballast water reduction is a core requirement for the decision-maker, the only viable Newcastlemax design would be ID 2345 that has also an improved EEDI by 5% but an inferior RFR by 5% compared to the baseline. It is thus considered critical that simulation-driven methods that weigh in uncertainty consideration as well as the vessel's actual anticipated response to real seaways are required to produce more robust designs for such highly constrained optimization problems as the Newcastlemax case study.

Design I.D	Optimization Run	RFR improvement	EEDI Improvement	Required Ballast Amount Improvement
Baseline	-	-%	-%	-%
ID2067	Det_NMAX_01	-6%	-1%	-8%
ID2638	Det_NMAX_01	15%	20%	-37%
ID1631	Det_NMAX_02	9%	-11%	-13%
ID2345	Det_NMAX_02	14%	-5%	-32%
ID2675	Det_NMAX_03	-8%	-22%	-6%
ID1405	Det_NMAX_03	30%	0%	-47%
ID851	Det_WOZMAX_01	-10%	-29%	2%
ID243	Det_WOZMAX_01	46%	-25%	-21%
ID304	Det_WOZMAX_02	-6%	-24%	13%
ID2390	Det_WOZMAX_02	13%	-17%	-28%
ID2226	Det_WOZMAX_03	-15%	-35%	26%
ID2046	Det_WOZMAX_03	2%	-36%	4%
ID2924	Det_WOZMAX_04	-25%	-39%	-5%
ID1781	Det_WOZMAX_04	-20%	-38%	-28%
ID2451	Det_WOZMAX_04	-21%	-37%	-28%

Table 61: Summary of Optimization Results on Optimization Targets for Dominant Variants // Deterministic Pathway

6.4.5.1. *Effect of vessel size*

The general expectation from Ship Design Theory is that the larger vessel variants created in WOZMAX optimization runs will clearly dominate and outperform Newcastlemax designs in terms of RFR and EEDI due to the inherent formulation economies of scale. What was not expected and is very interesting is that such designs with excellent RFR and EEDI performance can also facilitate a drastic reduction of the Required Ballast Amount despite the increase in the vessel's size. The reason for this is that the propeller diameter (and thus aft draft requirement) is

kept at a reasonable number (without any decrease in the vessel's efficiency). Furthermore, the ballast amount is minimized due to the lower block coefficient numbers that prevail in such vessels which also acts positively for both EEDI and RFR. As a result, the antagonistic relationship of RFR and EEDI with Required Ballast is softened (as witnessed from the steep Pareto fronts of far-left regions of the corresponding scatter diagrams of Det_WOZMAX_03/04) and thus the multi-objective optimization potential is higher than in Newcastlemax studies where size constraints and limitations are harder. The expansion of the vessel size also to the next size of vessels (210-250,000 t DWT) is therefore considered reasonable and of design value enabling better trade-offs and a more globalized design search for optimal transport solutions. The same effect could be seen if VLOCs or Valemax vessels were deployed in the trade accordingly.

6.4.5.2. *Effect of Algorithm use*

By comparing the results (scatter diagrams) of the Deterministic runs and having the context of optimization algorithm comparison, the following conclusions can be drawn:

1. *Best in Success Rate: MOSA*

The MOSA algorithm demonstrated both for NMAX and WOZMAX case studies a considerably higher design success rate (95.8% and 94%) compared to DAKOTA (80.3% and 85.63%) and NSGAI (75.9%, 78% and 71%). The smaller success rate of the NSGAI algorithm is attributed to the wider exploration and bigger alternations (mutations) of design variable combinations compared to MOSA that gave NSGAI a better exploration of the design space and optimization potential.

2. *Best in Convergence: MOSA*

The MOSA algorithm demonstrated a considerably faster convergence rate compared to NSGAI and DAKOTA, reaching the optimal areas from an early stage of the optimization. However, this comes at the expense of the total optimization effect where the two evolutionary approaches (NSGAI) and DAKOTA push harder towards the optimal regions.

3. *Best in Optimization Effect: NSGAI*

It is a clear observation from Table 56 to Table 60 summarizing the various dominant variants particulars as well as from Figure 136 to Figure 138 and Figure 145 to Figure 147 that the most promising values of the optimization targets were given by the NSGAI algorithms. When looking closer at the scatter diagrams of the NSGAI algorithm (for both WOZMAX and NMAX case studies), one could observe that the NSGAI design cloud albeit similar to the DAKOTA equivalent graph is "translated" and shifted towards the regions of optimality on the graph and all generated designs have better values both for RFR, EEDI and Required Ballast compared to their equivalent counterparts in DAKOTA.

4. *Best in Cloud Density and Pareto Front formation: DAKOTA / NSGAI*

Both algorithms create design clouds that are denser and more coherent on one hand (when compared to MOSA clouds) and on the other, the Pareto fronts generated are more straightforward and clearer to identify as well as work with when picking optimal designs (either by utility functions or ad-hoc).

Based on the above points 1~5 and having in mind computational power, time and effort limitation it was decided that in the next stage only NSGAI algorithms would be used for the optimization runs and the focus will be on the comparison of the results with the Deterministic Runs.

6.4.5.3. *Effect of choice of optimization targets*

As discussed in the previous paragraphs, it is evident that the reduction of optimization targets by the use of only one RFR target (Brazilian Trade RFR for WOZMAX and Australian Trade RFR for NMAX) “de-polarized” the Pareto region and enabled a much more efficient, transparent and productive use of the utility functions (either linear or logarithmic weight based).

6.4.5.4. *Effect of utility functions.*

The use of logarithmic weight distribution that was herein introduced proved to be a sound choice given the very antagonistic nature between the optimization objectives, namely between the RFR/EEDI and the Required Ballast amount. In such antagonistic relationships and with the existence of very strong (and linear) correlations between the two of the three optimization targets (RFR and EEDI), the “elasticity” of the logarithmic distribution enabled the following positive effects:

1. Proper identification of promising design trade-offs. Especially in the case of the scatter diagram between RFR and Required Ballast in Det_WOZMAX_04 (Figure 152), the trade-offs identified on the steep front in the far-left regions wouldn't have been picked with the use of linear weight distribution utility functions.
2. Identification and picking of design variants in the Pareto middle regions.
3. Broader and more holistic picking leads to better exploration and utilization of the Pareto region.

It should be noted that all these positive effects were spotted while the nominal weights of the utility functions (maximum weight for best performing design for each optimization target respectively), were equally split (1/3) among the three optimization targets.

In summary, the logarithmic weight distribution enabled the softening of the impact of a strong linear correlation between RFR and EEDI on the overall optimization outcome.

6.4.5.5. *Design decisions made for the Simulation-Driven Optimization Runs*

Given the above analysis and discussions, the following decisions were made and implemented during the Simulation-Driven Optimization Pathway runs:

1. NSGAI is used as the only Design Optimization algorithm.
2. Only one RFR is set as an optimization target for each case study respectively as explained in paragraph 6.4.5.
3. Logarithmic Distribution Utility Functions will be used in parallel with linear distribution utility functions.
4. Both case studies (NMAX and WOZMAX) will be repeated in the Simulation-Driven Optimization Pathway to have a broader comparison basis between the two pathways.

6.5. Stage 2: Multi-Objective Optimization under Simulation

In the publication of (Nikolopoulos & Boulougouris, 2015) the basis for the currently completed research work is set with the 1st Generation optimization methodology featuring an RPM curve instead of self-propulsion equilibrium at each stage and weather modelling derived from onboard data acquisition (see Paragraph 3.3). This simulation code was further refined with the self-propulsion module and resulted in results depicted in (Nikolopoulos & Boulougouris, 2018) and culminated in the publication of (Nikolopoulos & Boulougouris, 2020). When looking at the scatter plots of the resulted design pools of these runs, it is evident that the shape and correlation of EEOI and RFR remain unchanged in the herein examined 2nd Generation methodology results. On the other hand, the shapes of scatter diagrams between the Ballast Water Amount required and either EEOI or RFR have changed in shape. Similarly, it is interesting to observe that the dominant variants' relation to the optimization merits is considerably different. In general, resulting dominant variants of the 1st Generation feature higher block coefficient values compared to the results that will be presented below. The main reason for this is the differentiation of the 2nd Generation of Simulation code:

1. The weather has been modelled from matched hindcast satellite weather data and using a Joint Probability distribution function as explained in Paragraph 3.3.4.
2. The methodology has been altered to feature the updated methodology of (Liu & Papanikolaou, 2020) for predicting added resistance in waves for arbitrary wave directions after being validated and benchmarked with the Ranking Panel code results of the parent hull.
3. Spectral analysis of the added resistance in waves is conducted resulting in more reliable results for assessing performance in actual seaways.

Apart from the introduction of the parameters and equations for predicting added resistance resulting from waves of arbitrary direction, (Liu & Papanikolaou, 2020) change the modelled correlation of block coefficient and added wave resistance based on revised and new experimental and numerical data. Under this prism and refinement, slender designs of lower C_b feature a lower added resistance for certain wave encounter frequencies and corresponding wave lengths. Lastly, as a last part of the analysis of optimization, the number of generated variants is changed for a run from 1500 to 2000 in an effort to create a more dense populated Pareto front that uniformly bridges the gap between dominant variants of previous runs.

6.5.1. Optimization Problem Setup

The optimization problem here is defined in paragraph 6.3. The focus and targets of simulation-driven runs are the following:

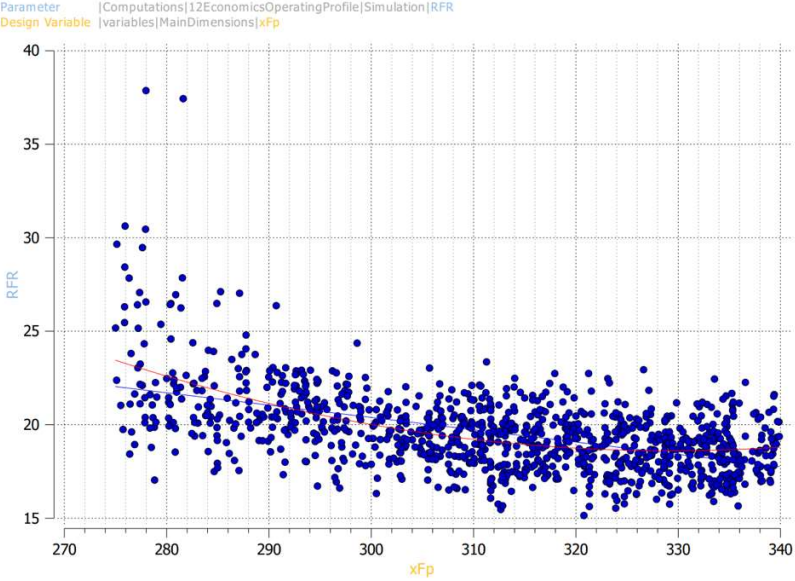
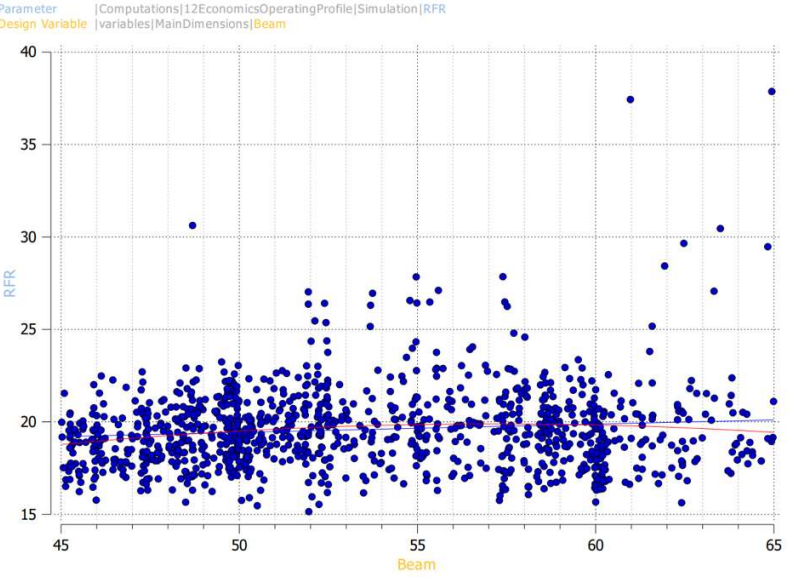
1. Use the results of the previous stage of Deterministic Optimization pathways in terms of variables and the resulting robust optimization framework as a basis for simulation drive optimization.
2. Design Space Exploration and Formal Optimization with Targets derived from Voyage Simulation.
3. Comprehensive sensitivity analysis and targets behaviour analysis
4. Explore the uncertainty of deterministic merits such as EEDI and RFR compared to simulation-driven equivalents (EEOI and RFR simulated).
5. Analyse and Assess the potential and robustness of resulting dominant variants while comparing them to deterministic peers.
6. Analyse and quantify the effect of optimization on actual variant vessel performance under realistic environmental, market and operational conditions.
7. Compare the optimization efficiency and potential to voyage simulation optimization studies.

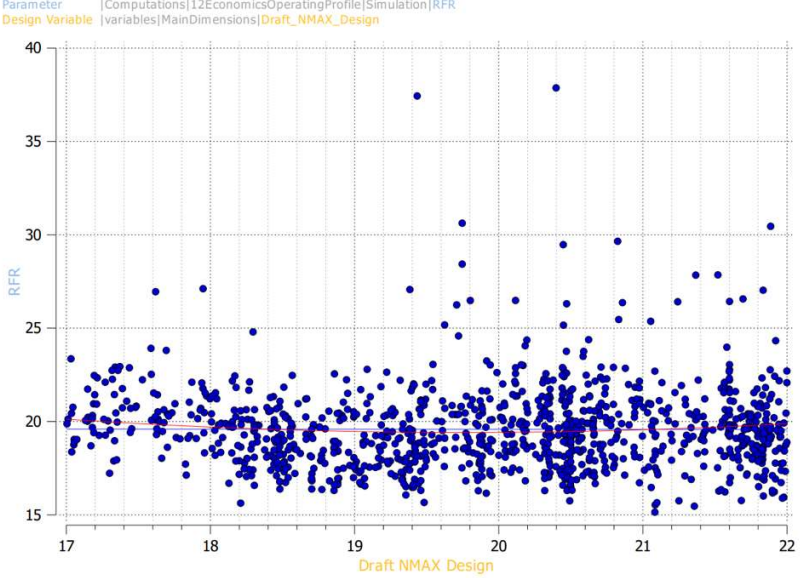
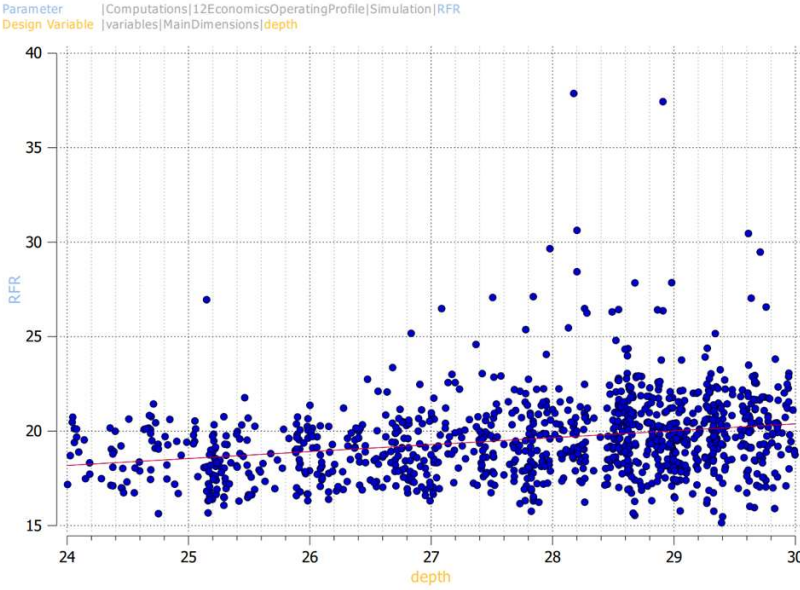
6.5.2. Sensitivity Analysis

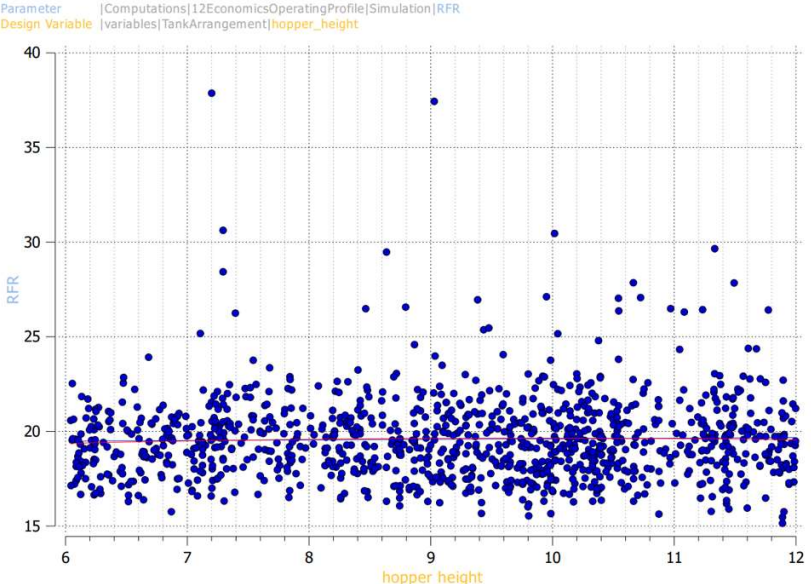
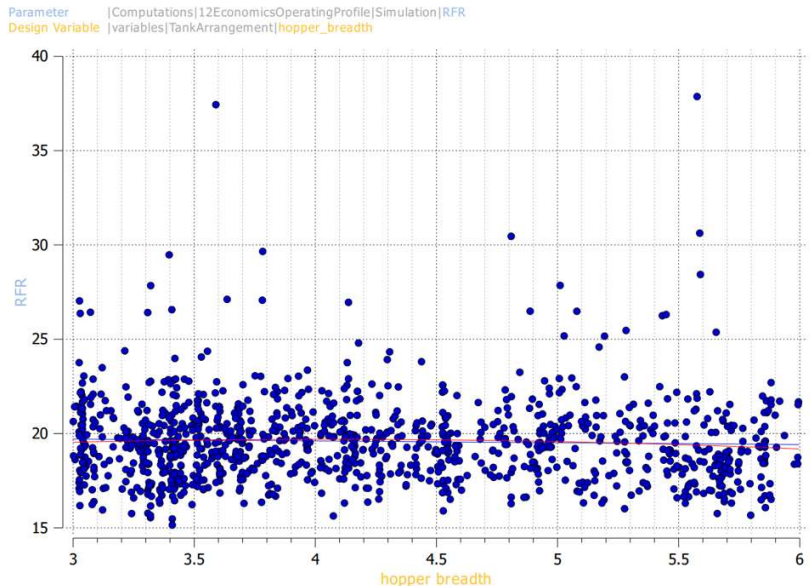
In Table 62 to Table 64 the effect of the design variables on each optimization objective can be identified for the Newcastlemax and WOZMAX case studies respectively for Simulation Driven Runs. The detailed sensitivity scatter diagrams can be found as separate documents submitted with the Thesis Material in Appendix I.

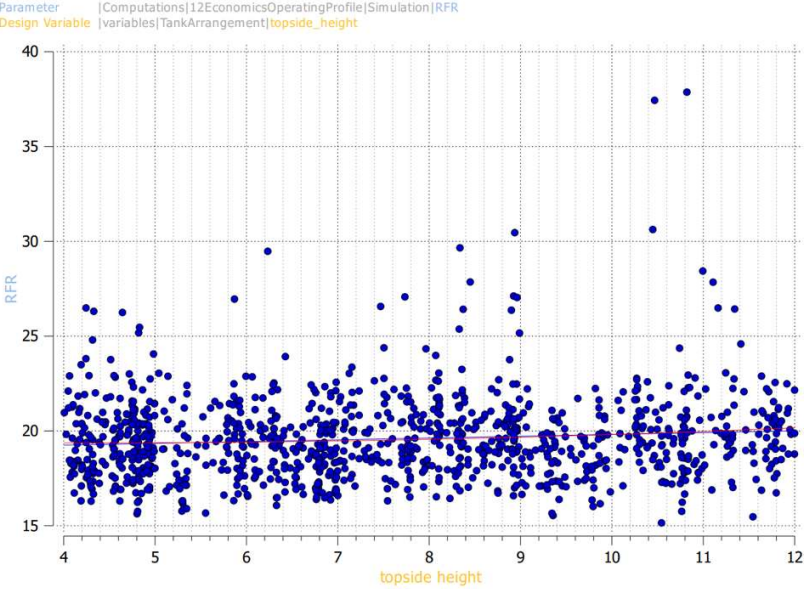
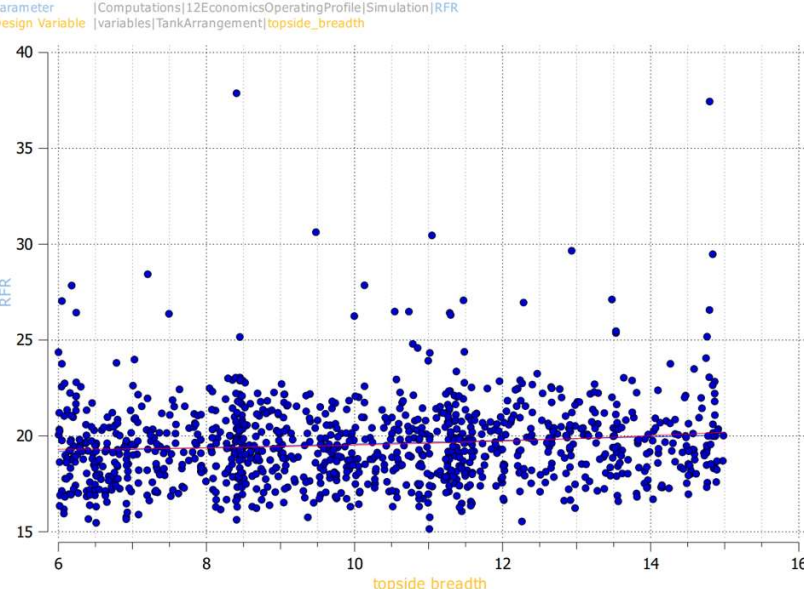
When comparing results to the sensitivity analysis results of the deterministic runs the following conclusions are withdrawn :

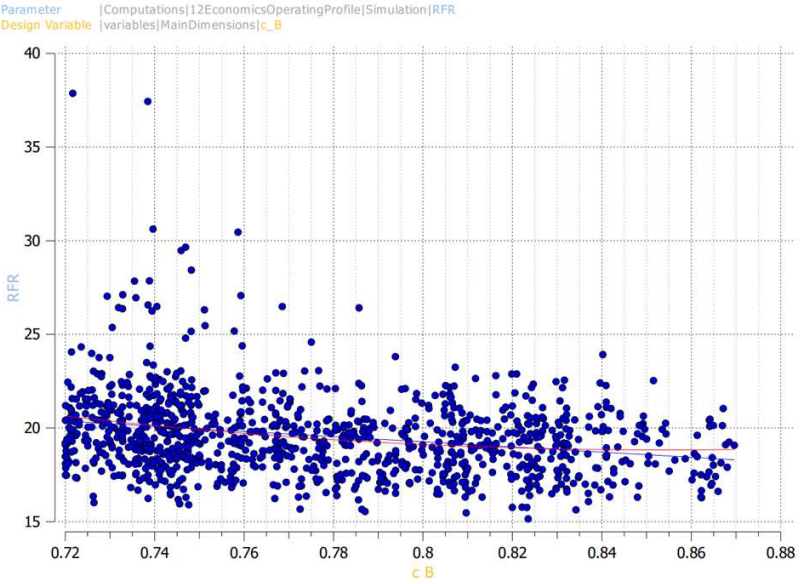
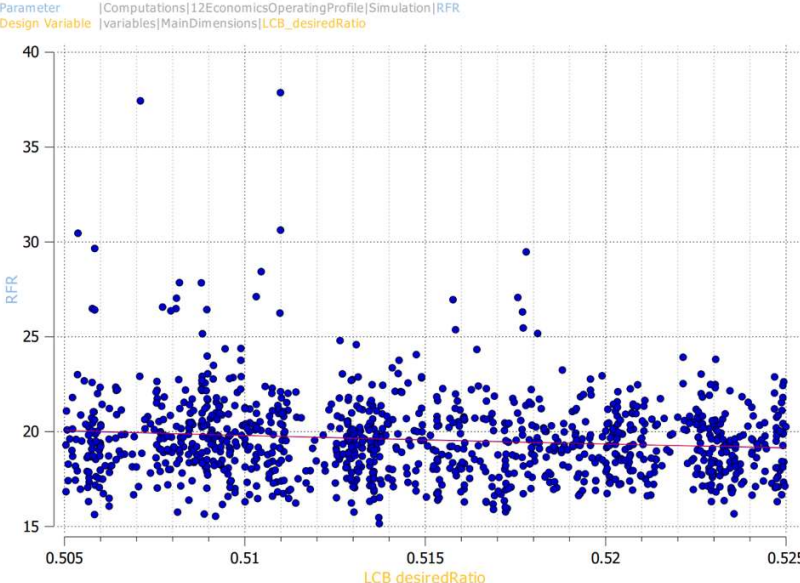
- Required Ballast Water amount sensitivity remains practically unchanged as the computational basis of the latter is outside the core RHODA simulation framework. However, a higher sensitivity in cargo hold arrangement compared to deterministic runs has been observed.
- The sensitivity of both the RFR and EEOI on the block coefficient, C_b , is smaller compared to deterministic runs for the WOZMAX case studies while in the meantime remains unchanged for Newcastlemax case studies.
- The sensitivity of both the EEOI and RFR on propulsion variables (Propeller diameter and pitch) is lighter compared to deterministic runs which can be attributed to the wider range of operating speeds examined rather than the design speed alone.
- Deck height plays a positive role for EEDI in deterministic runs but neutral to none for the EEOI in simulation driven runs.
- Deck height sensitivity of RFR in simulation driven runs is reverse from the one encountered in deterministic runs.
- Both the EEOI and RFR sensitivities on the design draft are distinctively less than the one of EEDI and RFR over the same variable at deterministic optimization runs.
- EEOI has a sensitivity (slight) on the LCB position (%) in contrast to the neutral sensitivity of EEDI over the same variable. This can be attributed to the closer link to delivered power over a wider range of speeds for the calculation of EEOI.
- The EEOI and RFR sensitivity on Bilge width and height is considerably smaller than the equivalent of EEDI and RFR in deterministic runs.
- Hopper dimensions have a smaller (zero) effect on EEOI than in EEDI.
- Cargo hold parameters (hopper and topside dimensions) have the same sensitivities for RFR as in the deterministic runs.
- EEOI sensitivity in beam (slight and close to neutral) in contrast to high sensitivity of EEDI in deterministic runs over the same parameter.

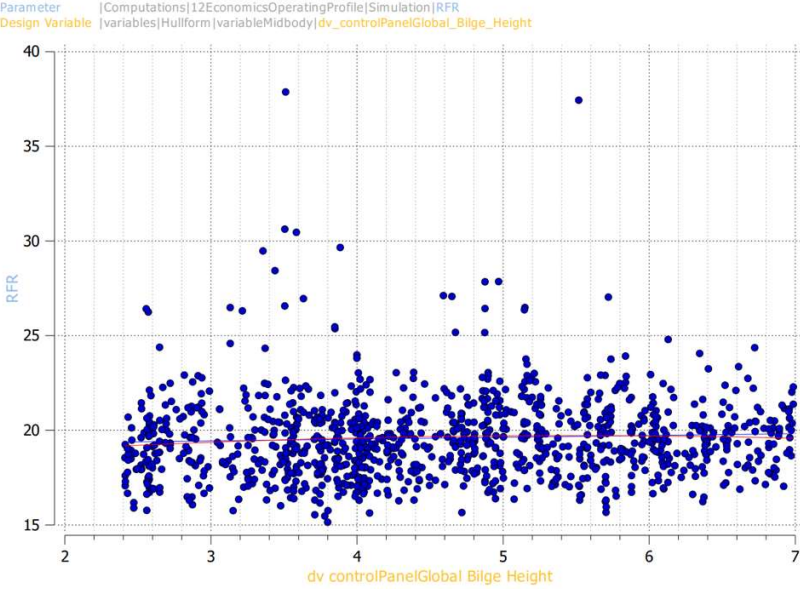
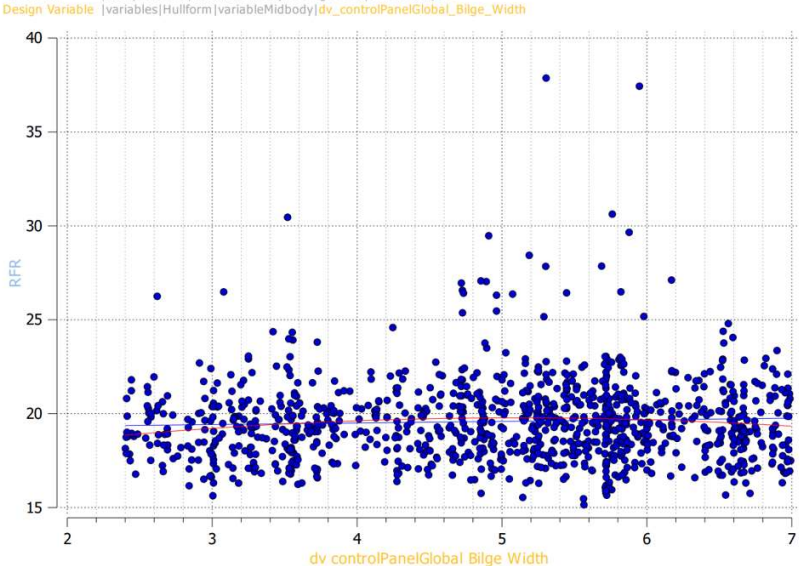
ID	Design Variable	Effect on RFR
N_01	Length between Perpendiculars	<p>High sensitivity of RFR in Length between perpendiculars: decrease of RFR by increasing length.</p>  <p>Parameter Computations 12EconomicsOperatingProfile Simulation RFR Design Variable variables MainDimensions xFp</p>
N_02	Beam	<p>Uniform, no sensitivity by increasing or decreasing beam to RFR.</p>  <p>Parameter Computations 12EconomicsOperatingProfile Simulation RFR Design Variable variables MainDimensions Beam</p>

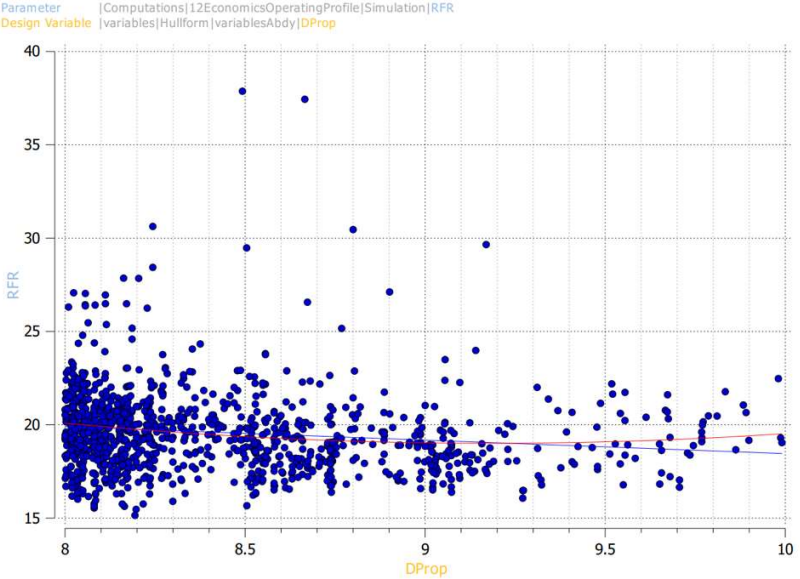
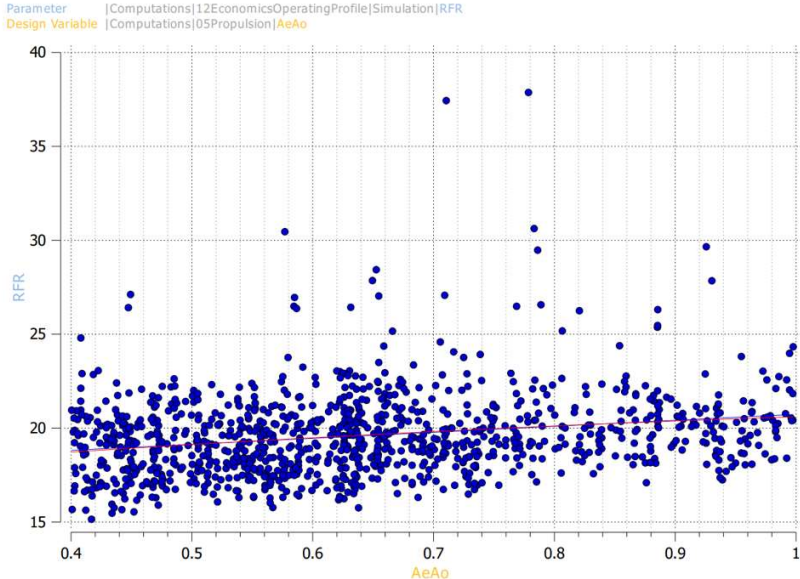
<p>N_03</p>	<p>Draft</p>	<p>By increasing draft, slight decrease on the RFR.</p> 
<p>N_04</p>	<p>Deck height</p>	<p>Slight increase of RFR by increasing Deck height, majority of feasible designs concentrated in higher deck height values.</p> 

<p>N_05</p>	<p>Hopper Height</p>	<p>Zero sensitivity of RFR in hopper height.</p>  <p>The scatter plot shows RFR on the y-axis (ranging from 15 to 40) and hopper height on the x-axis (ranging from 6 to 12). The data points are widely scattered across the x-axis, indicating that RFR is not significantly affected by changes in hopper height. A horizontal red line is drawn at approximately RFR = 19.5.</p>
<p>N_06</p>	<p>Hopper Breadth (m)</p>	<p>Almost zero sensitivity with a trend of decreasing RFR over increasing hopper breadth</p>  <p>The scatter plot shows RFR on the y-axis (ranging from 15 to 40) and hopper breadth on the x-axis (ranging from 3 to 6). The data points are scattered, but there is a slight downward trend as hopper breadth increases. A horizontal red line is drawn at approximately RFR = 19.5.</p>

<p>N_07</p>	<p>Topside Height (m)</p>	<p>Uniform distribution of designs, small sensitivity of RFR in Topside Height.</p> 
<p>N_08</p>	<p>Topside Breadth (m)</p>	<p>Uniform distribution of designs, small sensitivity of RFR in Topside Breadth.</p> 

<p>N_09</p>	<p>Block Coefficient Cb</p>	<p>High sensitivity, increasing Cb decreases the RFR up to 0.85 (then stable).</p> 
<p>N_10</p>	<p>LCB (%Lbp)</p>	<p>Uniform distribution of designs, small sensitivity of RFR in LCB.</p> 

<p>N_11</p>	<p>Bilge Height (m)</p>	<p>Uniform distribution of designs, small sensitivity of RFR in Bilge Height</p>  <p>Parameter [Computations]12EconomicsOperatingProfile[Simulation]RFR Design Variable [variables]Hullform[variableMidbody]dv_controlPanelGlobal_Bilge_Height</p>
<p>N_12</p>	<p>Bilge Width (m)</p>	<p>Uniform distribution of designs, small sensitivity of RFR in Bilge Width</p>  <p>Parameter [Computations]12EconomicsOperatingProfile[Simulation]RFR Design Variable [variables]Hullform[variableMidbody]dv_controlPanelGlobal_Bilge_Width</p>

<p>N_13</p>	<p>Propeller Diameter (m)</p>	<p>Decrease of RFR by increasing propeller diameter, higher design population in lower diameters.</p>  <p>Parameter [Computations 12EconomicsOperatingProfile Simulation RFR] Design Variable [variables Hullform variablesAbdy DProp]</p>
<p>N_14</p>	<p>Propeller Expanded Area Ratio</p>	<p>Uniform distribution with little sensitivity of RFR in Expanded Area Ratio.</p>  <p>Parameter [Computations 12EconomicsOperatingProfile Simulation RFR] Design Variable [Computations 05Propulsion AeAo]</p>

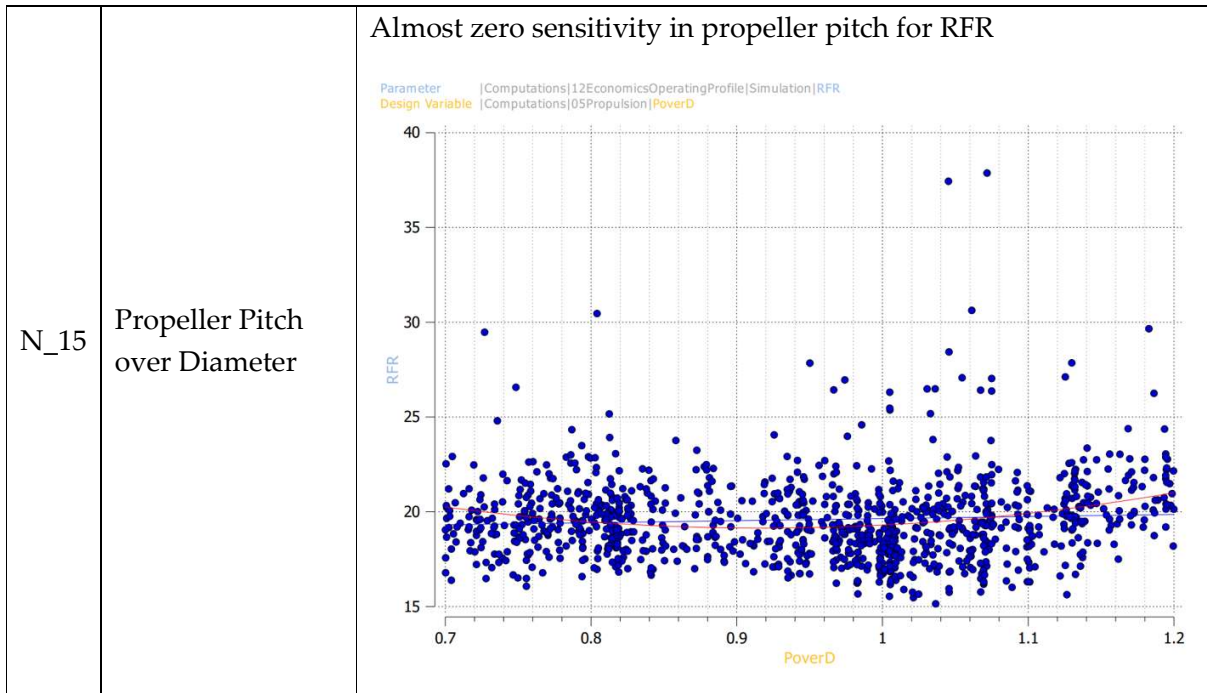
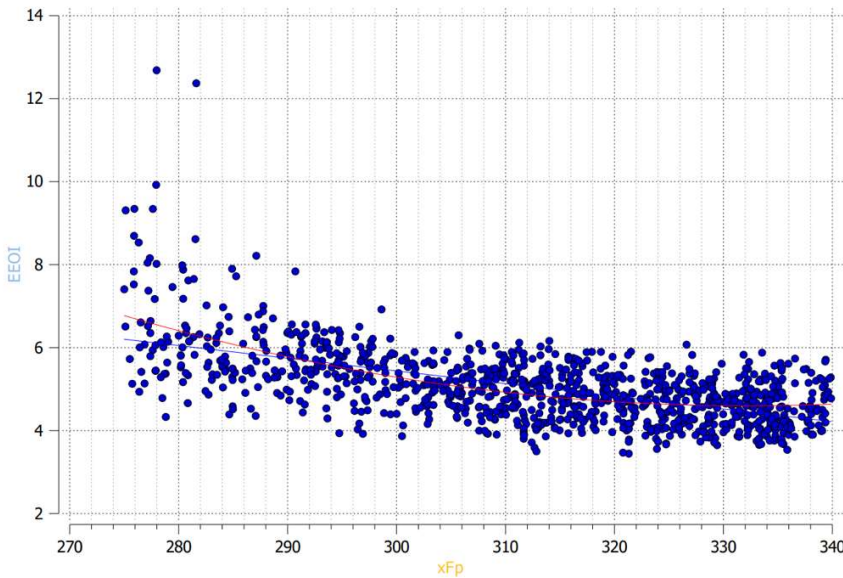
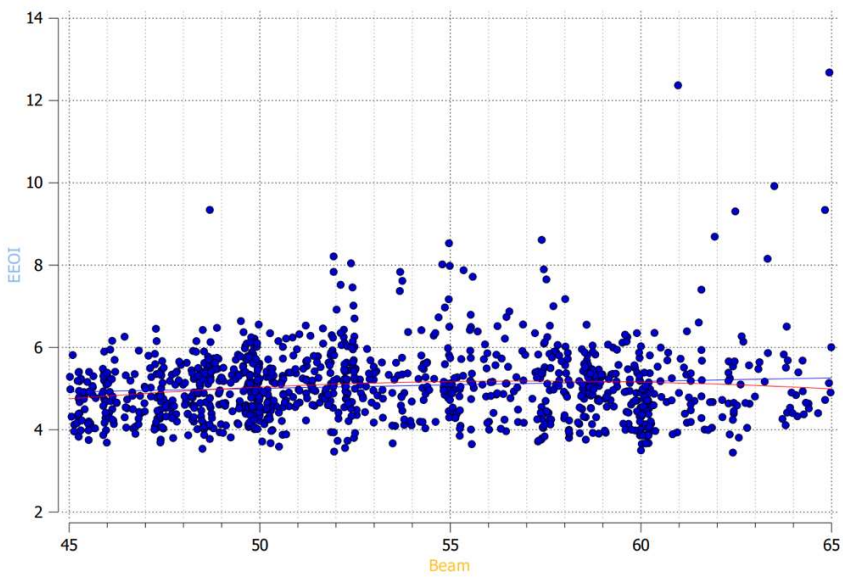
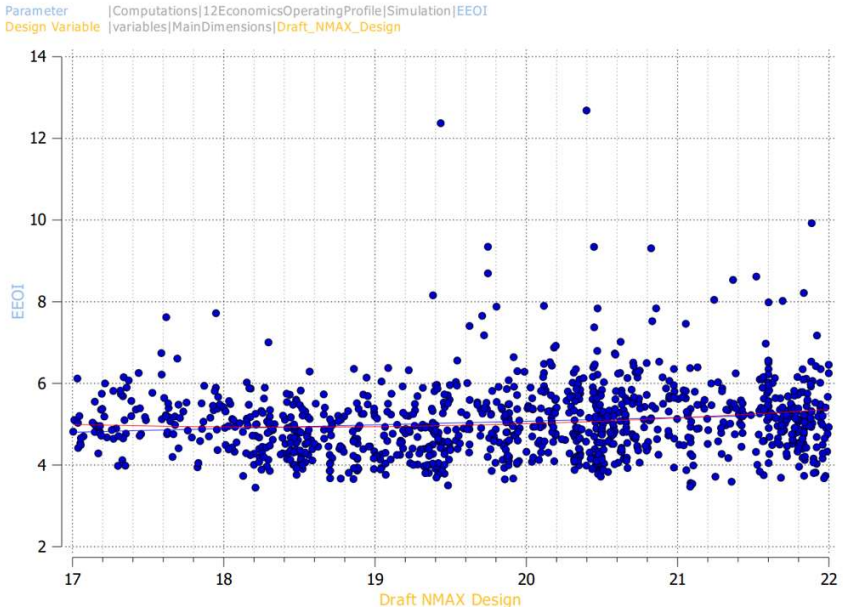
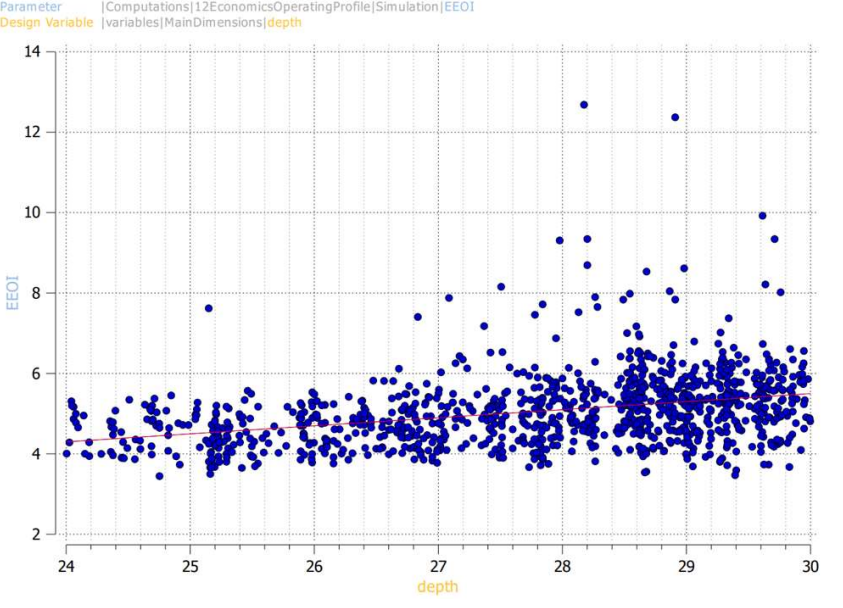
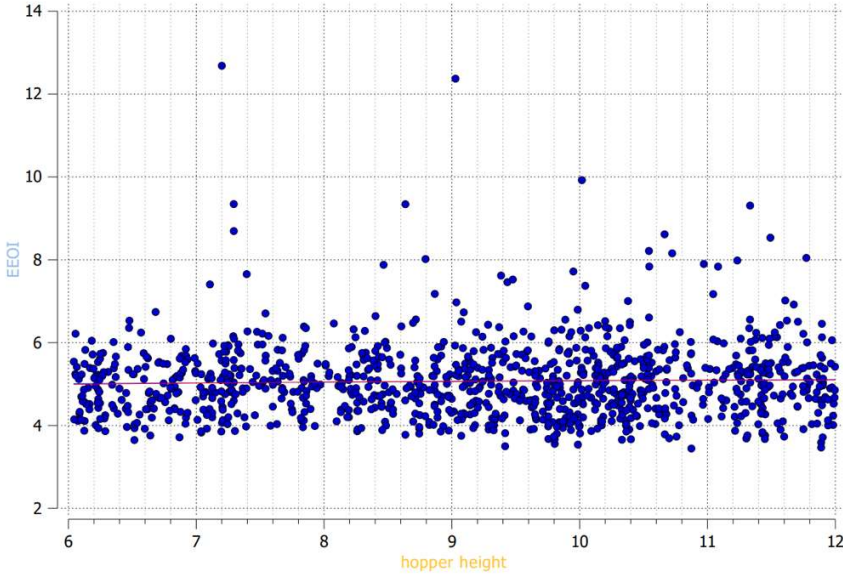
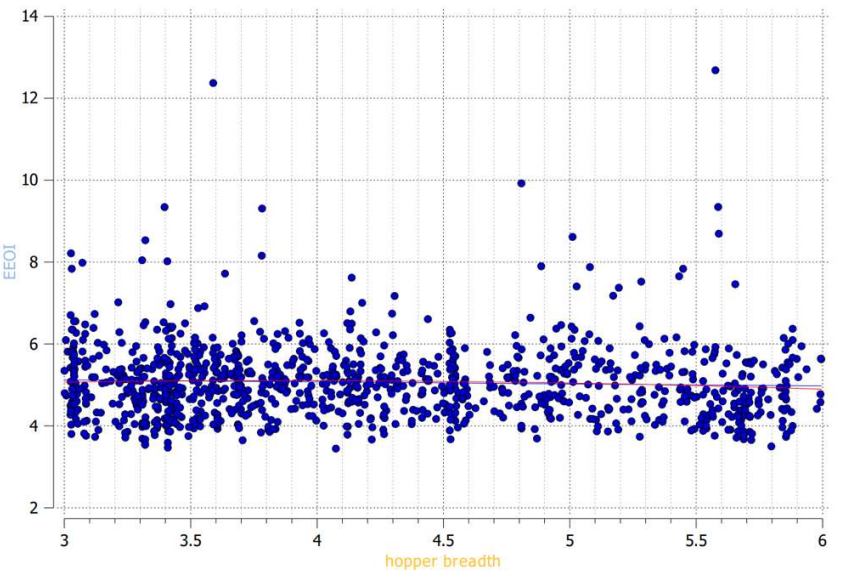
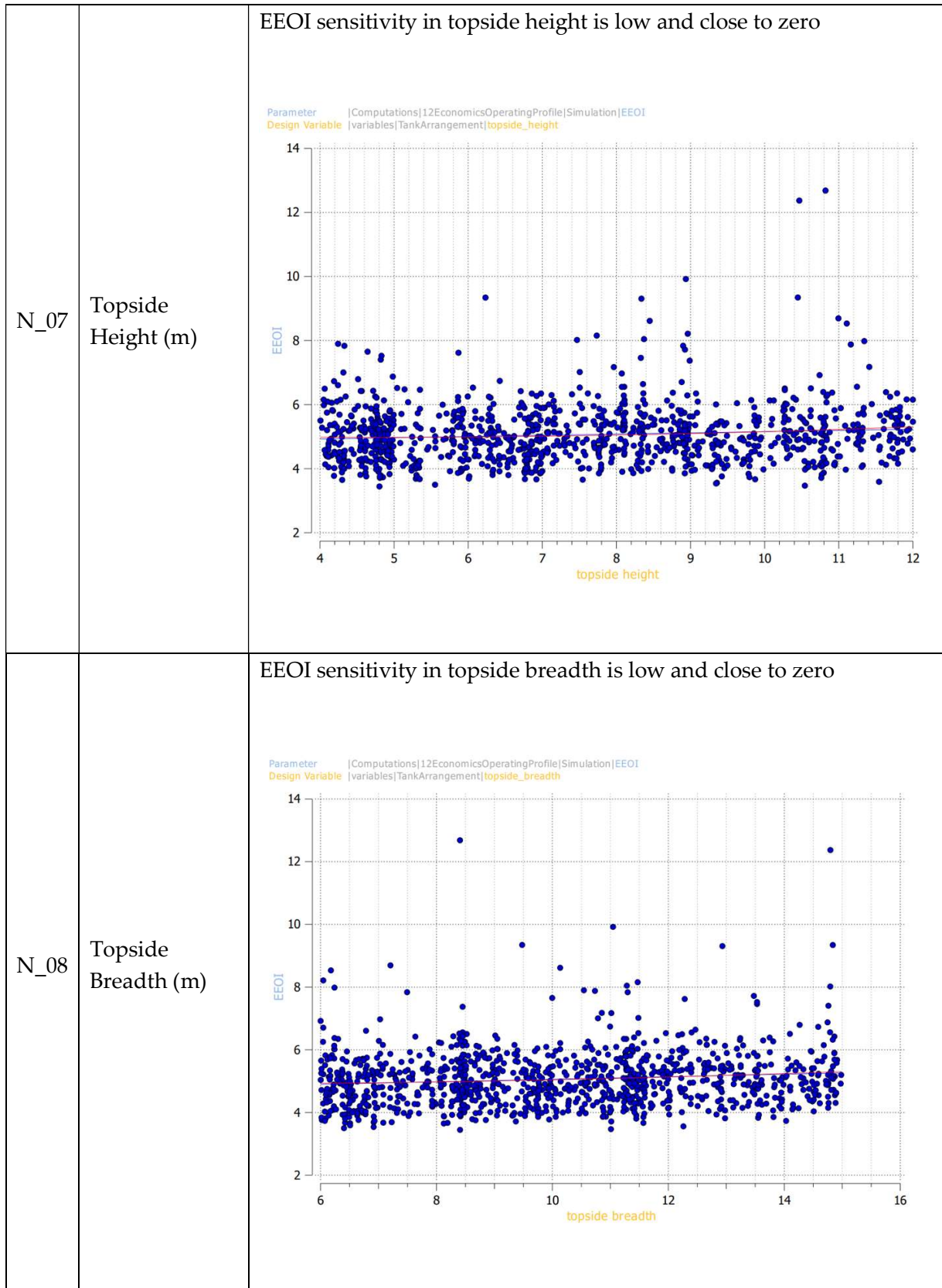


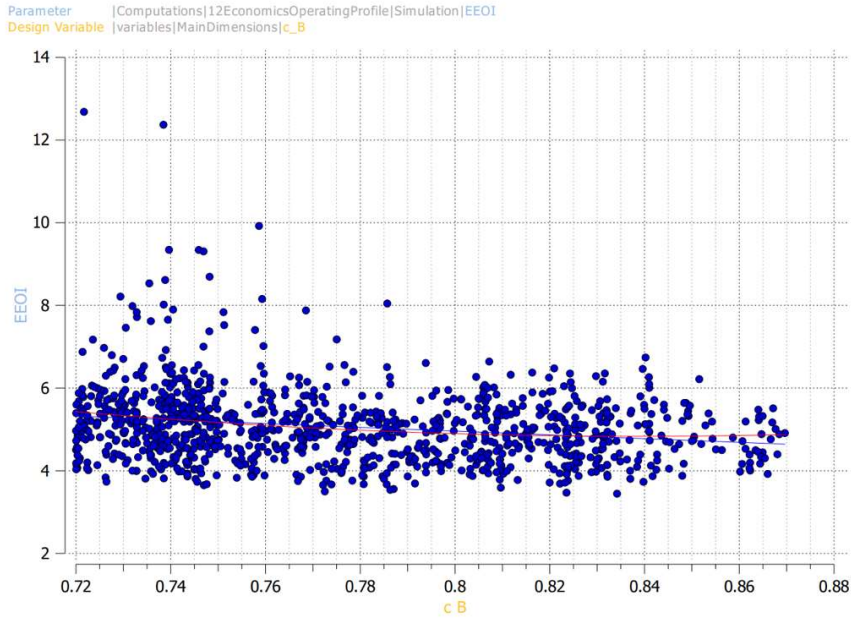
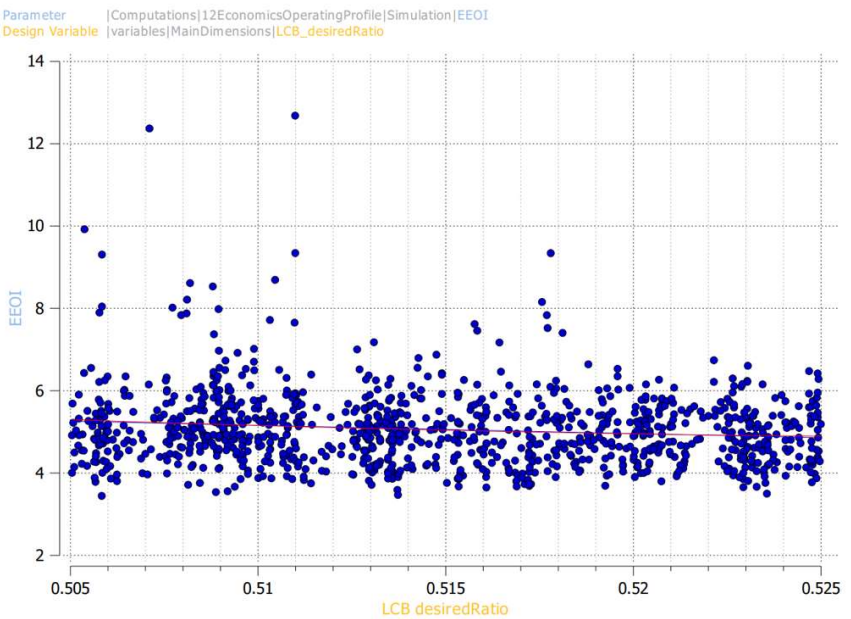
Table 62: RFR Sensitivity on Design Variables – Simulation Driven WOZMAX Case Studies

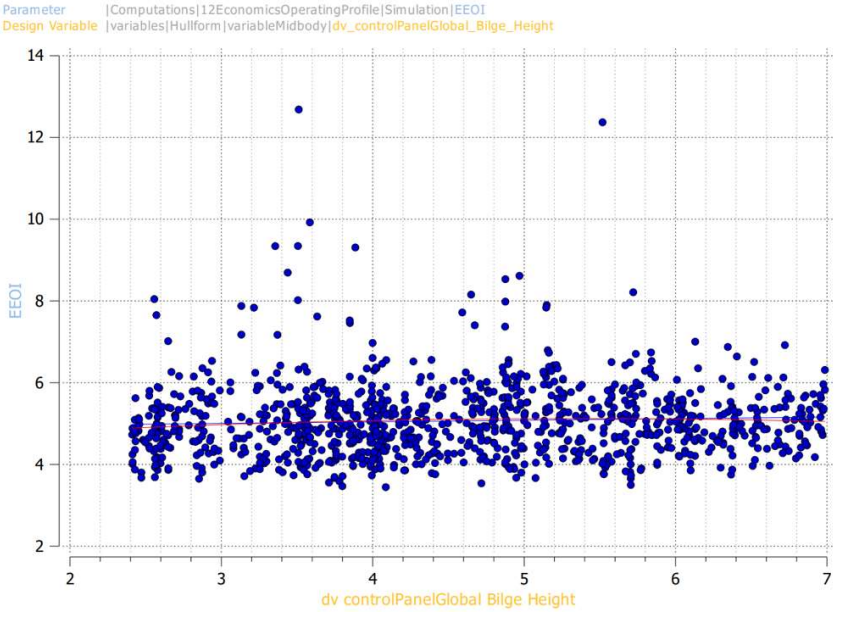
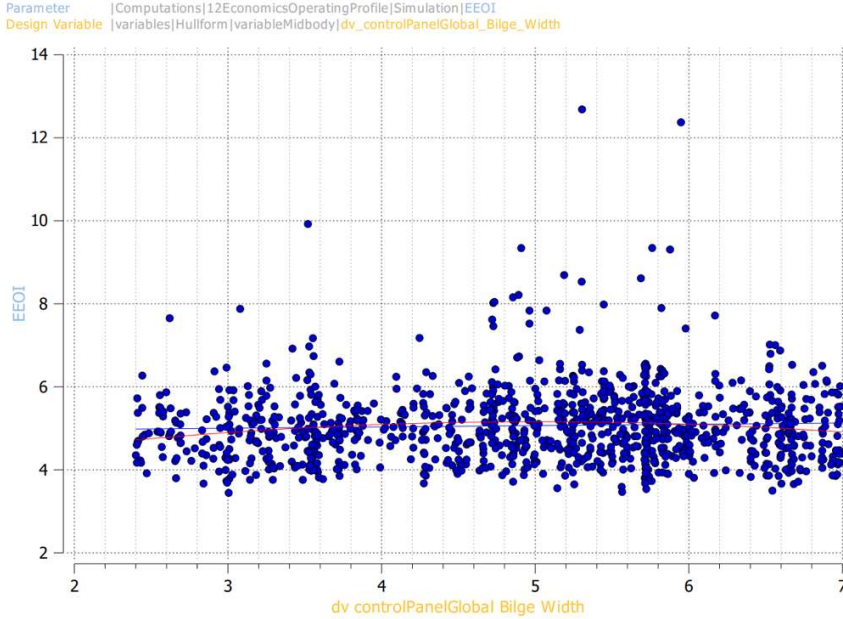
ID	Design Variable	Effect on EEOI
N_01	Length between Perpendiculars	<p>High sensitivity of EEOI in Lbp. EEOI decreases by increasing length. Small scatter of designs</p>  <p>Parameter Computations 12EconomicsOperatingProfile Simulation EEOI Design Variable variables MainDimensions xFp</p>
N_02	Beam	<p>Small to zero sensitivity of EEOI in beam.</p>  <p>Parameter Computations 12EconomicsOperatingProfile Simulation EEOI Design Variable variables MainDimensions Beam</p>

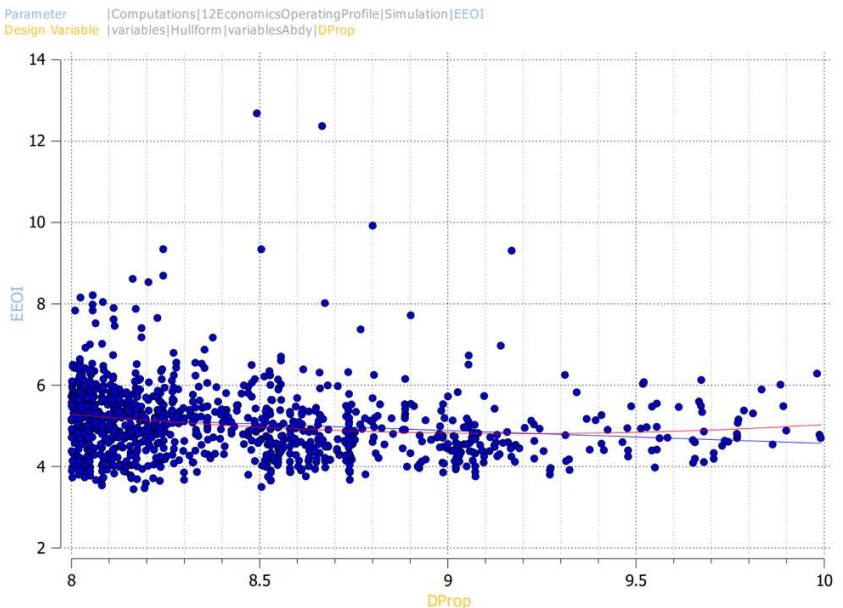
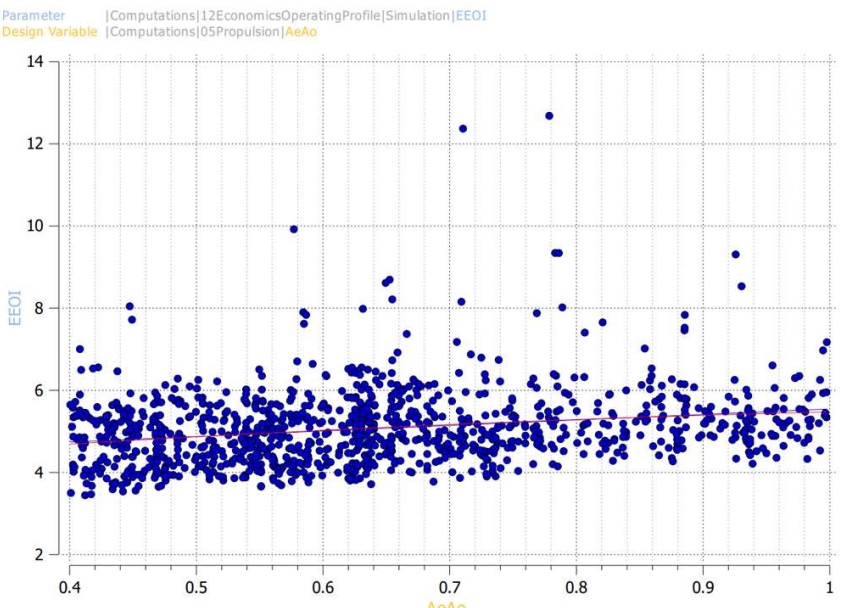
<p>N_03</p>	<p>Draft</p>	<p>Small to zero sensitivity of EEOI in Draft</p>  <p>Parameter Computations 12EconomicsOperatingProfile Simulation EEOI Design Variable variables MainDimensions Draft_NMAX_Design</p>
<p>N_04</p>	<p>Deck height</p>	<p>Smaller sensitivity of EEOI in Deck Height : EEOI decreases by increasing deck height. Scatter increases by increasing deck height and most of the design population is concentrated at higher values.</p>  <p>Parameter Computations 12EconomicsOperatingProfile Simulation EEOI Design Variable variables MainDimensions depth</p>

<p>N_05</p>	<p>Hopper Height</p>	<p>Small Sensitivity to Hopper Dimensions: Increase of Hopper Height leads to a slight increase of EEOI (through cargo capacity and deadweight).</p> <p>Parameter Computations 12EconomicsOperatingProfile Simulation EEOI Design Variable variables TankArrangement hopper_height</p> 
<p>N_06</p>	<p>Hopper Breadth (m)</p>	<p>Increase of Hopper Breadth leads to a slight decrease of EEOI (through cargo capacity and deadweight).</p> <p>Parameter Computations 12EconomicsOperatingProfile Simulation EEOI Design Variable variables TankArrangement hopper_breadth</p> 



<p>N_09</p>	<p>Block Coefficient Cb</p>	<p>Mild sensitivity of EEOI in Cb: EEOI decreases by increasing the block coefficient but not as sharply as EEDI in deterministic studies</p>  <p>Parameter Computations 12EconomicsOperatingProfile Simulation EEOI Design Variable variables MainDimensions c_B</p>
<p>N_10</p>	<p>LCB (%Lbp)</p>	<p>Mild sensitivity of EEOI in LCB position with uniform distribution of designs. Increase of LCB % (fore movement) slightly reduces EEOI.</p>  <p>Parameter Computations 12EconomicsOperatingProfile Simulation EEOI Design Variable variables MainDimensions LCB_desiredRatio</p>

<p>N_11</p>	<p>Bilge Height (m)</p>	<p>Almost no sensitivity of EEOI in Bilge Height value</p>  <p>Parameter Computations 12EconomicsOperatingProfile Simulation EEOI Design Variable variables Hullform variableMidbody dv_controlPanelGlobal_Bilge_Height</p>
<p>N_12</p>	<p>Bilge Width (m)</p>	<p>Little sensitivity of EEOI in bilge width.</p>  <p>Parameter Computations 12EconomicsOperatingProfile Simulation EEOI Design Variable variables Hullform variableMidbody dv_controlPanelGlobal_Bilge_Width</p>

<p>N_13</p>	<p>Propeller Diameter (m)</p>	<p>EEOI has a low sensitivity in the change of propeller diameter, with slight decrease of the EEOI with increasing diameter and majority of designs being populated in the small diameter regions</p> 
<p>N_14</p>	<p>Propeller Expanded Area Ratio</p>	<p>Decreasing EEOI in propellers with lower expanded area ratios</p> 

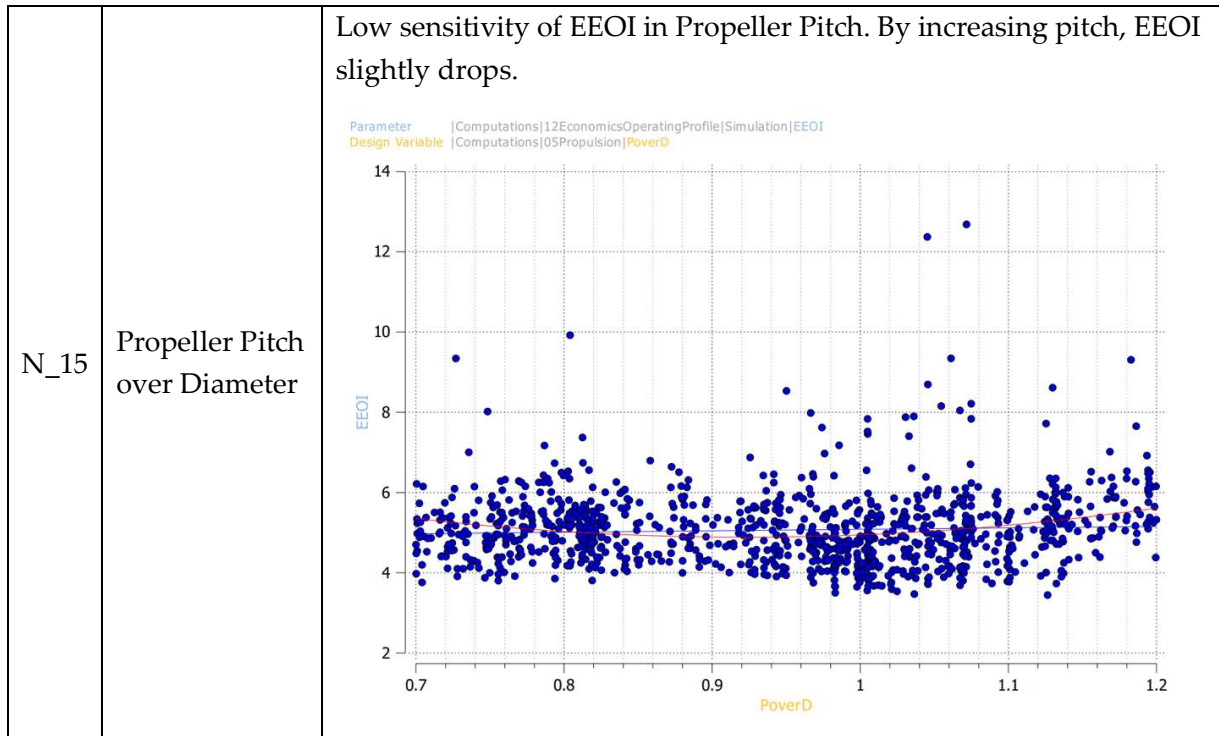
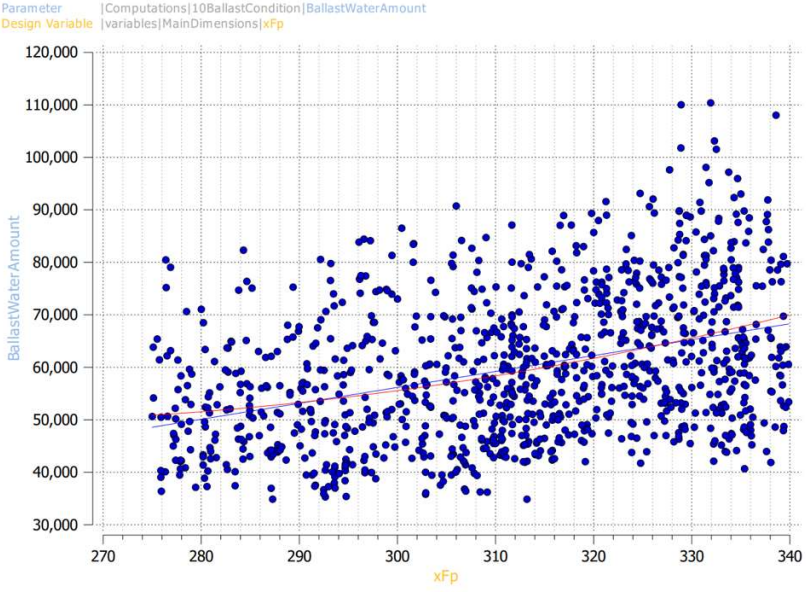
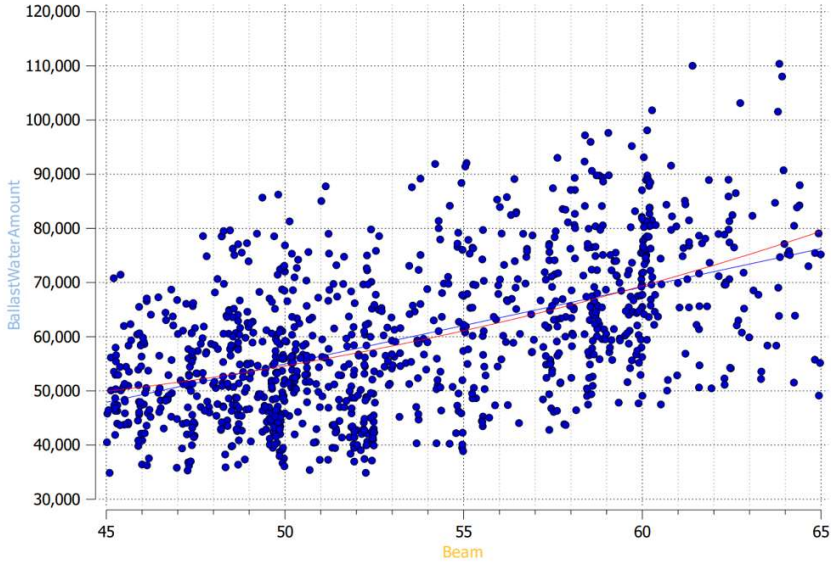
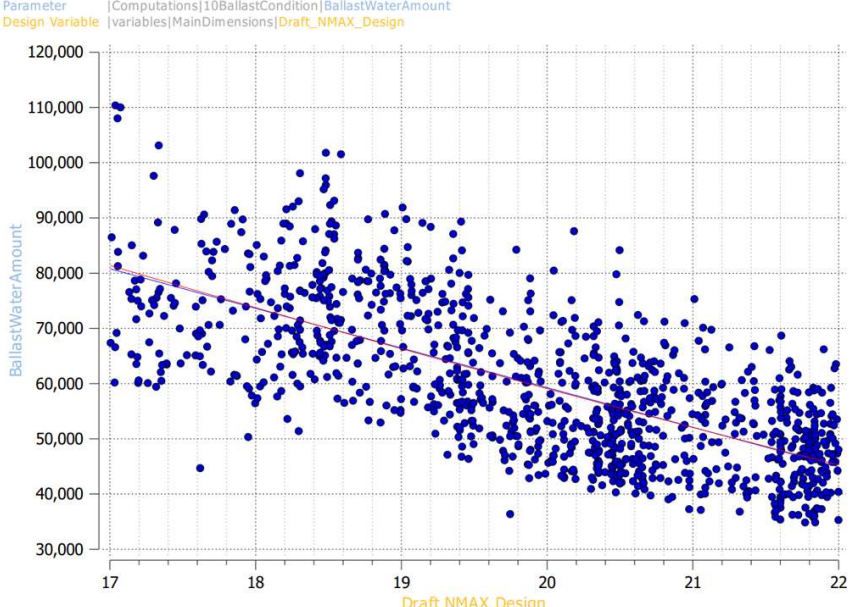
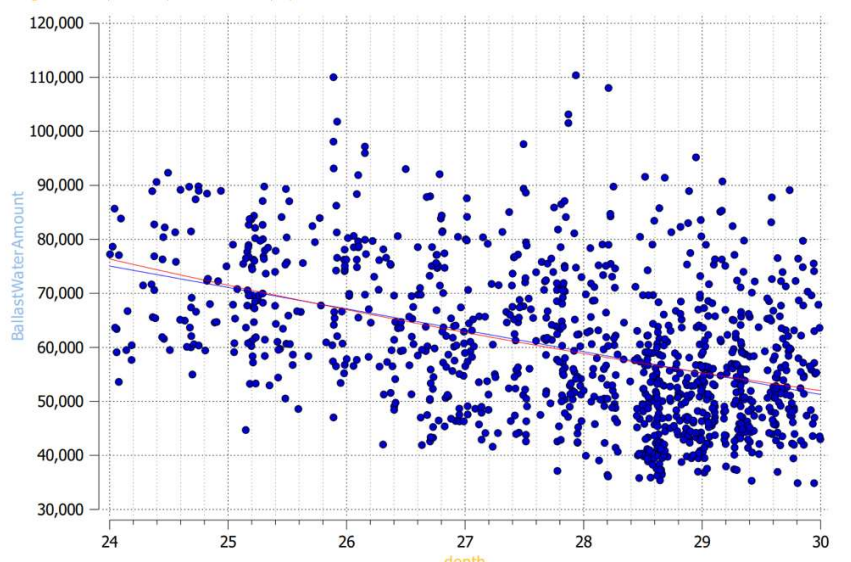
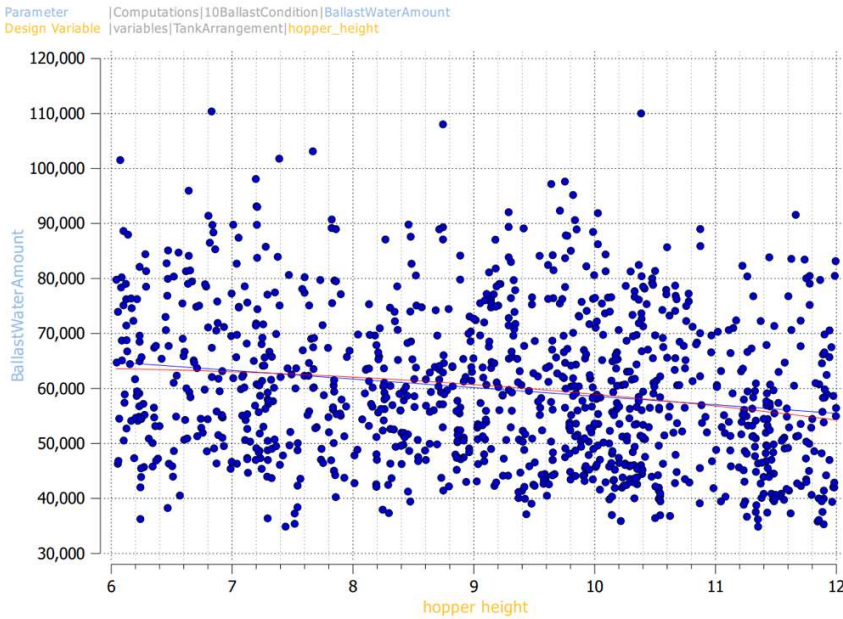
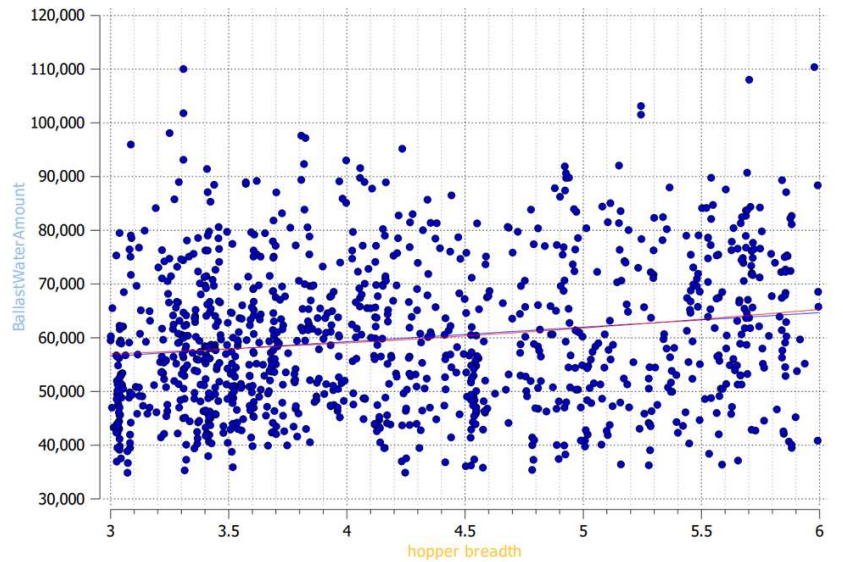
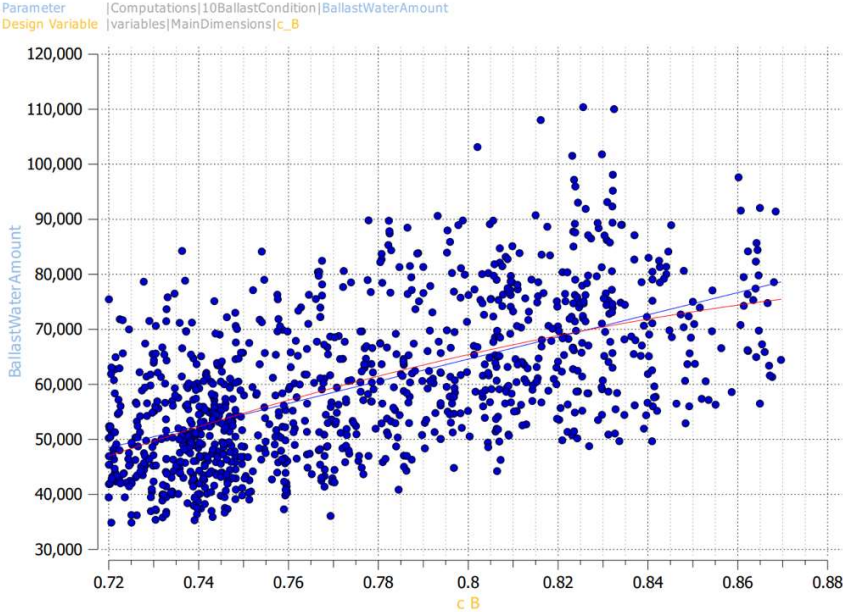


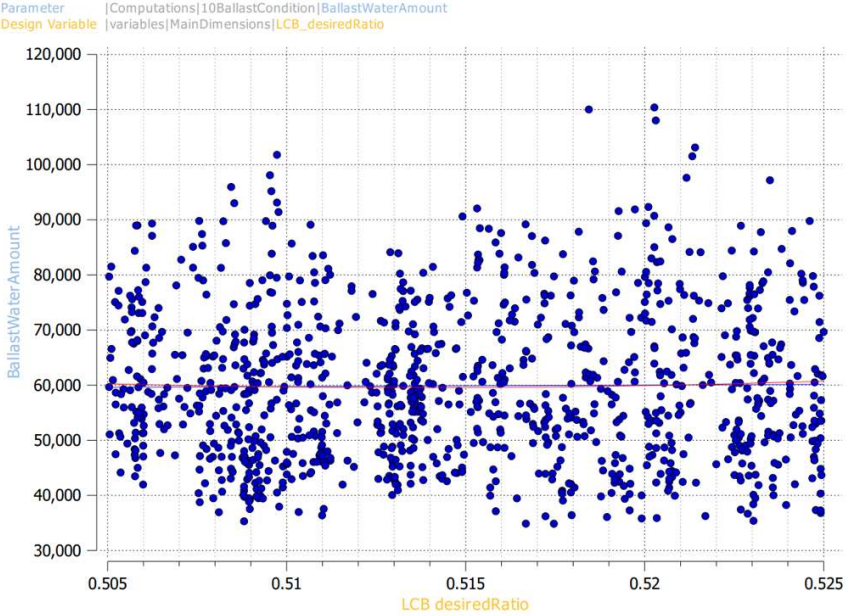
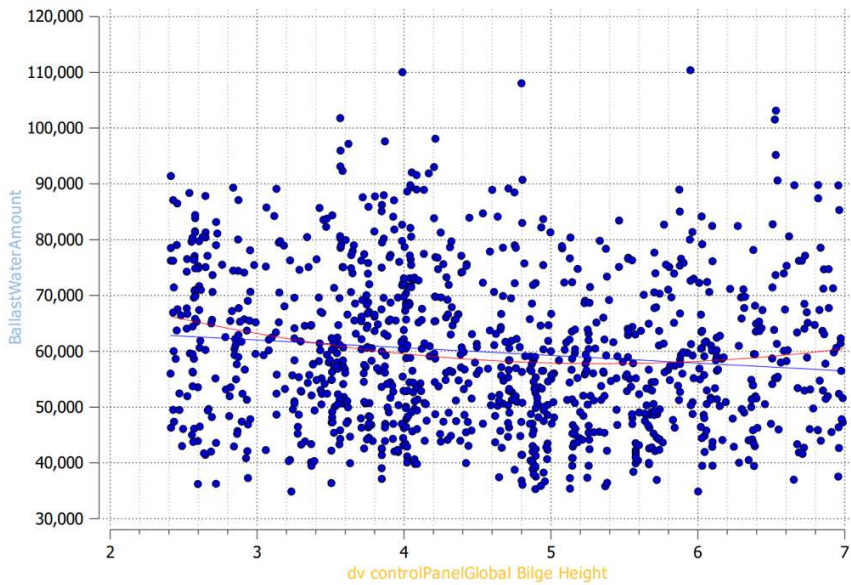
Table 63: EEOI Sensitivity on Design Variables – Simulation Driven WOZMAX Case Studies

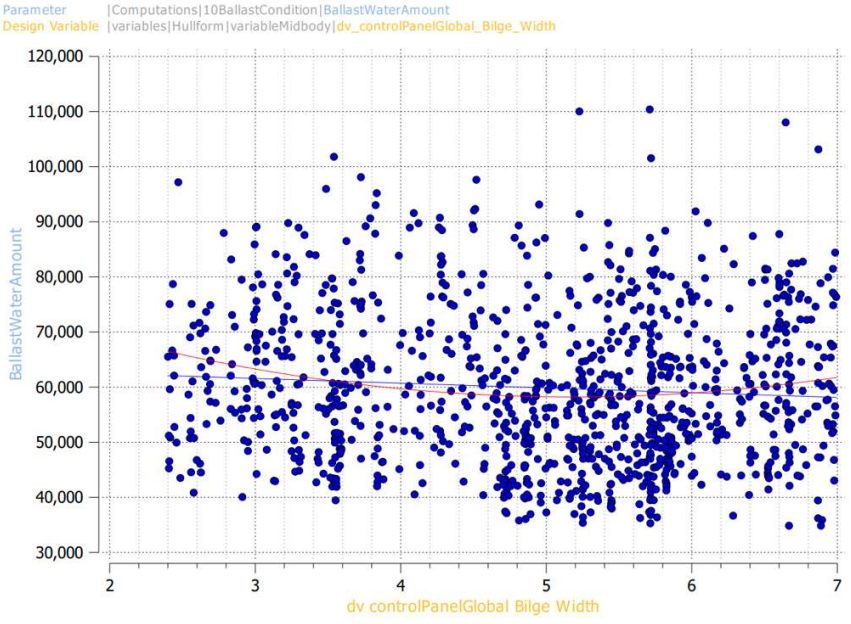
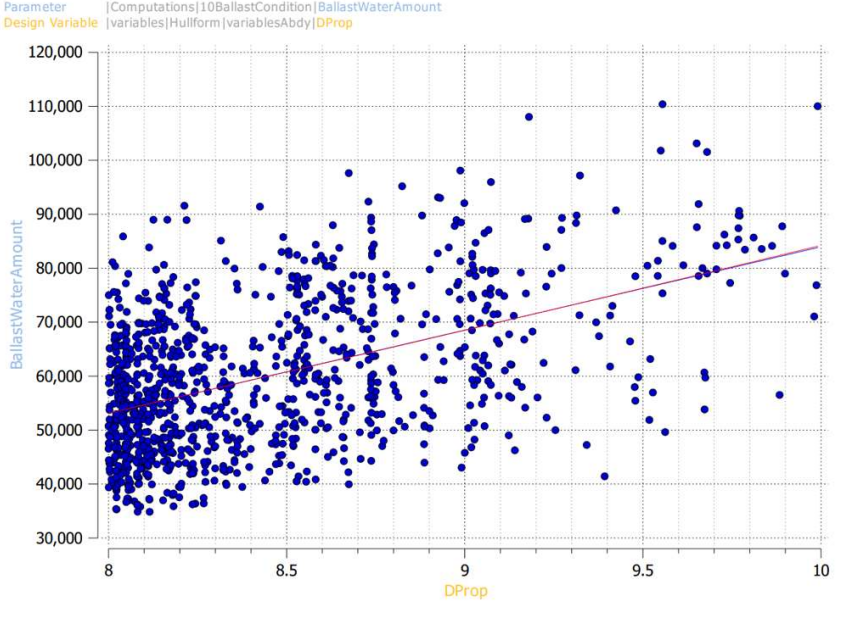
ID	Design Variable	Effect on Required Ballast Water Amount
N_01	Length between Perpendiculars	<p>High Sensitivity of BW Amount in Lbp: Increased by increasing length.</p>  <p>Parameter Computations 10BallastCondition BallastWaterAmount Design Variable variables MainDimensions xFp</p>
N_02	Beam	<p>Increased BW Amount by increasing beam.</p>  <p>Parameter Computations 10BallastCondition BallastWaterAmount Design Variable variables MainDimensions Beam</p>

<p>N_03</p>	<p>Draft</p>	<p>Low sensitivity of Ballast Water Amount in Deck Heigh: Increasing design draft leads to decreasing BW Amount</p>  <p>Parameter Computations 10BallastCondition BallastWaterAmount Design Variable variables MainDimensions Draft_NMAX_Design</p>
<p>N_04</p>	<p>Deck height</p>	<p>Increasing Deck Height leads to decreasing BW Amount</p>  <p>Parameter Computations 10BallastCondition BallastWaterAmount Design Variable variables MainDimensions depth</p>

<p>N_05</p>	<p>Hopper Height</p>	<p>While in previous runs there is no sensitivity, for simulation runs there is a sensitivity of BW Amount resulting into decreasing BW Amount by increasing hopper height</p>  <p>Parameter [Computations]10BallastCondition BallastWaterAmount Design Variable [variables]TankArrangement hopper_height</p>
<p>N_06</p>	<p>Hopper Breadth (m)</p>	<p>While in previous runs there is no sensitivity, for simulation runs there is a sensitivity of BW Amount resulting into increasing BW Amount by increasing hopper height</p>  <p>Parameter [Computations]10BallastCondition BallastWaterAmount Design Variable [variables]TankArrangement hopper_breadth</p>

N_07	Topside Height (m)	No sensitivity of BW Amount with this variable
N_08	Topside Breadth (m)	No sensitivity of BW Amount with this variable
N_09	Block Coefficient C _b	<p>High Sensitivity of BW Amount in C_b. By increasing block coefficient there is a sharp increase of the BW Amount.</p>  <p>The figure is a scatter plot with a grid. The vertical axis is labeled 'BallastWaterAmount' and ranges from 30,000 to 120,000 in increments of 10,000. The horizontal axis is labeled 'c_B' and ranges from 0.72 to 0.88 in increments of 0.02. The plot contains numerous blue data points. A red regression line is drawn through the data, showing a positive linear trend. The legend at the top left of the plot area identifies the parameter as 'BallastWaterAmount' and the design variable as 'c_B'.</p>

<p>N_10</p>	<p>LCB (%Lbp)</p>	<p>LCB has a positive effect on Ballast Water amount: by increasing the LCB % the required BW Amount slightly drops</p>  <p>Parameter Computations 10BallastCondition BallastWaterAmount Design Variable variables MainDimensions LCB_desiredRatio</p>
<p>N_11</p>	<p>Bilge Height (m)</p>	<p>Almost zero sensitivity of BW Amount to changes of the Bilge Height</p>  <p>Parameter Computations 10BallastCondition BallastWaterAmount Design Variable variables Hullform variableMidbody dv_controlPanelGlobal_Bilge_Height</p>

<p>N_12</p>	<p>Bilge Width (m)</p>	<p>Almost zero sensitivity of BW Amount to changes of the Bilge Width</p>  <p>Parameter Computations 10BallastCondition BallastWaterAmount Design Variable variables Hullform variableMidbody dv_controlPanelGlobal_Bilge_Width</p>
<p>N_13</p>	<p>Propeller Diameter (m)</p>	<p>High Sensitivity of BW Amount in Propeller Diameter: with increasing diameter, required BW Amount sharply increases (due to Aft Draft requirements)</p>  <p>Parameter Computations 10BallastCondition BallastWaterAmount Design Variable variables Hullform variablesAbdy DProp</p>

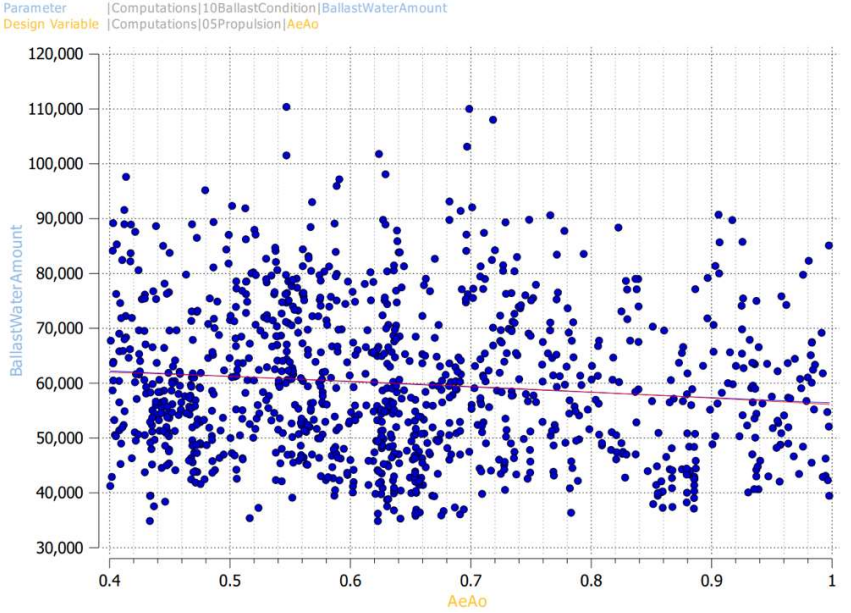
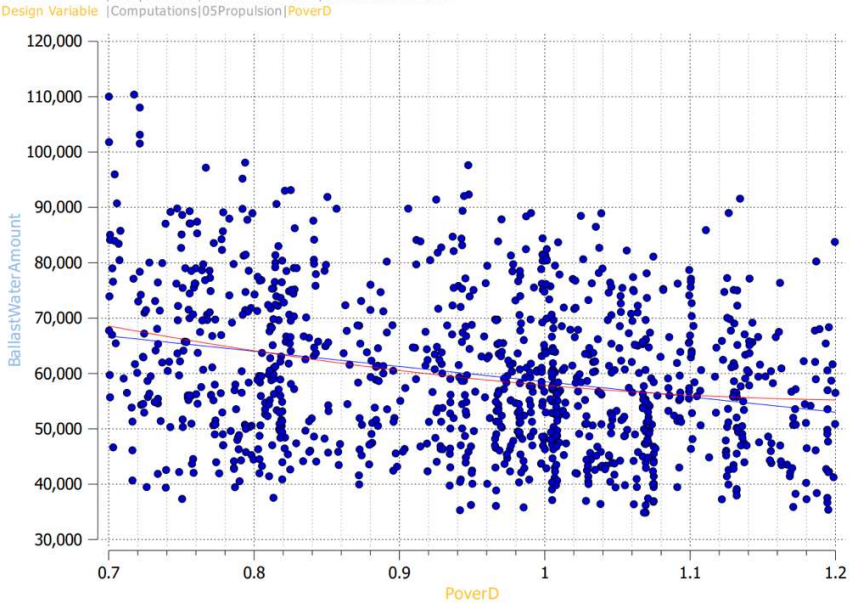
<p>N_14</p>	<p>Propeller Expanded Area Ratio</p>	<p>No sensitivity of BW Amount in Propeller Expanded Area Ratio</p>  <p>Parameter Computations 10BallastCondition BallastWaterAmount Design Variable Computations 05Propulsion AeAo</p>
<p>N_15</p>	<p>Propeller Pitch over Diameter</p>	<p>High Sensitivity of BW Amount in Pitch: Increasing pitch leads to lower BW Amount (due to propeller diameter reduction)</p>  <p>Parameter Computations 10BallastCondition BallastWaterAmount Design Variable Computations 05Propulsion PoverD</p>

Table 64 : BW Amount Sensitivity of Design Variables– Simulation Driven WOZMAX Case Studies

Apart from comparing the sensitivities of the Deterministic and Simulation Driven Optimization pathways, the most interesting observation is the comparison of the EEDI of each design with the attained from the simulation Energy Efficiency Operating Index (EEOI) as well as the comparison of the nominal calculated Required Freight Rate with the RFR derived from the products of the simulation module. This comparison of deterministic objective functions with their voyage simulation-based counterparts is the foundation of the herein proposed methodology and Thesis and reveals the robustness of simulation-driven variants as a whole new dimension that of the actual performance in real yet “off-design” conditions, which in previous research work has been unexplored, is now taken into account with the use of actual data. From the corresponding, but opposite side the degree of uncertainty of deterministic optimization products can also be identified.

In Figure 154 the scatter diagram between the nominal RFR and its simulation-based counterpart for dominant variants of the NMAX Case Study (based on Run ID Sim_NMAX_02) is depicted, while in Figure 155 the same equivalent scatter diagram of the WOZMAX Case Study (based on Run ID Sim_WOZMAX_02) is also depicted.

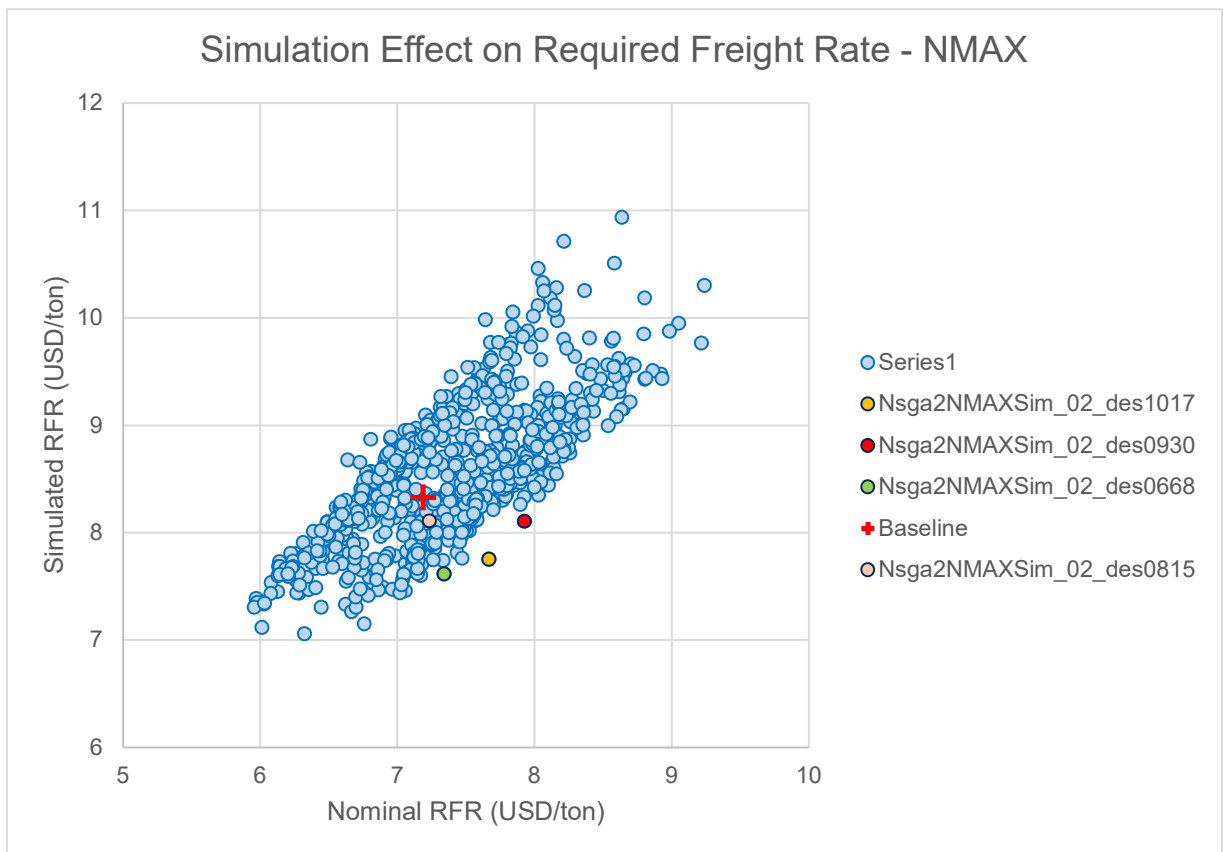


Figure 154: Sensitivity Analysis and Scatter between Nominal and Simulated Required Freight Rate – NMAX Case Study

A first and very interesting observation is of course that for both case studies the range of uncertainty for the RFR is rather large. For example in the NMAX Case Study, for a given nominal RFR of 7.0 USD/ton, the corresponding simulation-based RFR has a range from 7.4 to 9.0 USD/ton. Similarly in the WOZMAX Case study, for a given nominal RFR of 11 USD/ton, the corresponding simulation RFR values range from 13.4 to 17.1 USD/ton. Such variances that are up to 20% in magnitude showcase that the robustness of a solution when seen only from a deterministic viewpoint is not given. Another interesting observation is that as the RFR is reduced and leads to RFR-optimal regions of the Pareto fronts, the range of the variance of simulation-based RFR values is narrowed down for both cases an almost eliminated at the left-hand side peak. It should also be noted at this point, that the two scatter clouds are distinctly different from one another as the NMAX Case Study cloud features two smaller cloud regions, with the left cloud prevailing at lower RFR regions, while in the WOZMAX Case Study, the two cloud regions converge and merge into one at lower RFR values.

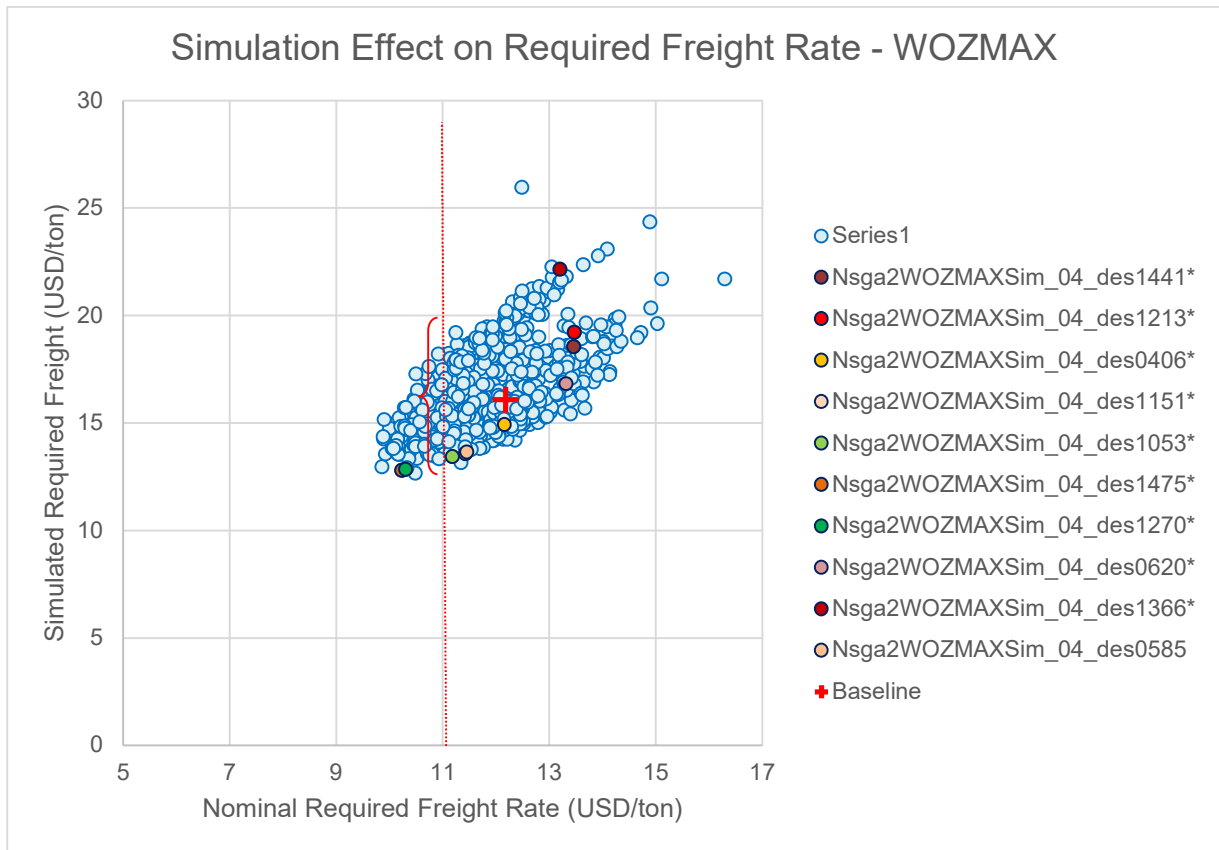


Figure 155: Sensitivity Analysis and Scatter between Nominal and Simulated Required Freight Rate – WOZMAX Case Study

The basic conclusion from the above is that even in the lowest RFR values, the nominal RFR derived from a deterministic calculation done at the vessel’s design point (Laden and Ballast nominal conditions at NCR load for the engine and corresponding speed) doesn’t represent

adequately the expected actual economic performance of the design at actual market and operating conditions. In fact for the same nominal RFR value, there are many designs with varying levels of attained RFR for the same simulated voyage (same speed profile and prevailing environmental condition). For the optimization scope and viewpoint, this creates uncertainty and reduces drastically the dominant variant robustness on one hand and the other poses limits on the378rastic of the possible design space exploration and thus optimization potential.

The uncertainty and unsuitability of EEDI as a metric of Ship Design efficiency can be clearly identified in Figure 156 for NMAX designs and in Figure 157 for WOZMAX designs. More specifically, from both graphs, it is evident that for a given EEDI value, the range of attained simulation-based Energy Efficiency Operating Index (EEOI) values is large. That means that vessels that share the same EEDI rating, might vary in terms of EEOI performance for the same simulated voyage input significantly. For example, in Figure 156 of the NMAX Case Study, for an EEDI value of 2 tonCO₂/ton*mile the levelled voyage simulation-based EEOI of different designs ranges from 4.3 to 5.4 tonCO₂/ton*mile. If we move slightly right on the same diagram, for an EEDI value of 2.2 tonCO₂/ton*mile, the simulation-based EEOI range of different designs is even higher from 4.3 to 6.5 tonCO₂/ton*mile. For the NMAX Case, similarly to the RFR, the variation range lowers as moving into areas of lower EEDI, however not effectively. In contrast to that, for the WOZMAX Case Study (refer to Figure 157), the variation remains unaffected regardless of the EEDI value and is even higher. The reason for this high variation is attributed to, is the bigger range of design variables for the case of the WOZMAX designs which trigger a larger design space and by definition magnifies all the existing model uncertainties of EEDI.

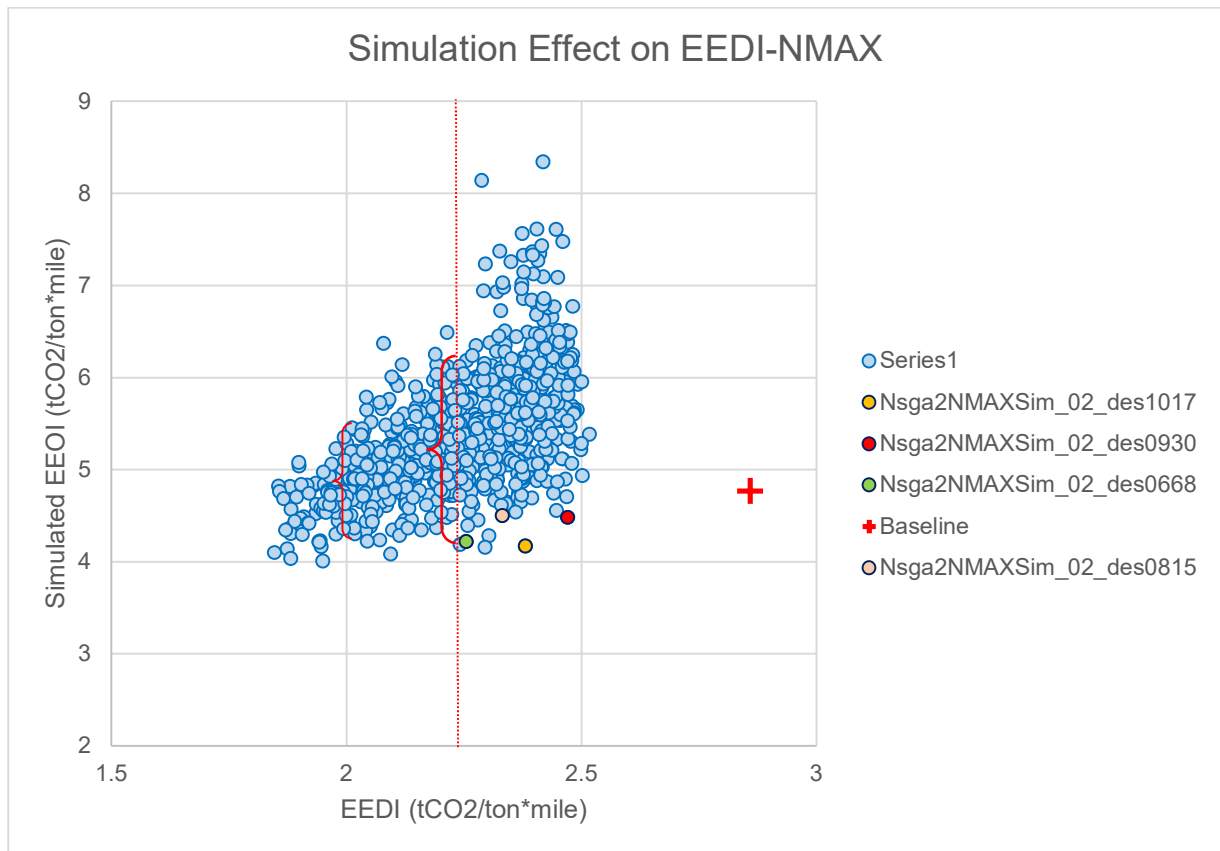


Figure 156: Sensitivity Analysis and Scatter between EEDI and Simulated EEOI – NMAX Case Studies

If want to examine now an example for WOZMAX designs, in Figure 157 and for EEDI values of 1.9 tonCO₂/ton*mile, the simulation-based EEOI of generated designs varies from 3.49 to 5.6 tonCO₂/ton*mile, not taking into account the outliers located sporadically at regions above 6.0 tonCO₂/ton*mile.

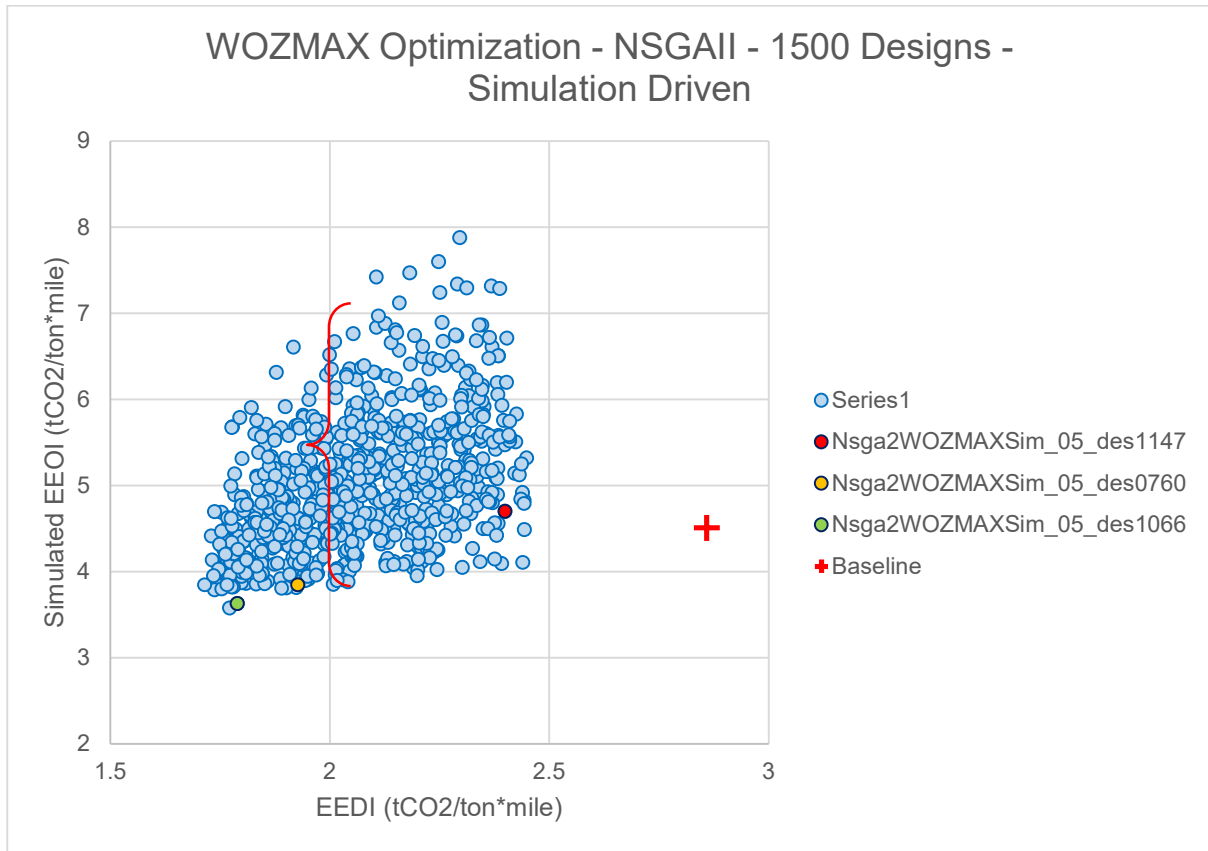


Figure 157: Sensitivity Analysis and Scatter between EEDI and Simulated EEOI – WOZMAX Case Studies

As a conclusion from the sensitivity analysis of EEDI and EEOI, it is clear, obvious and herein proven that EEDI is deemed unsuitable as a design index used in Ship Design Optimization and the use it should be done with the necessary caution. In contrast to that, a simulation-derived EEOI depicts all the sensitivities and the actual vessel performance providing a more reliable and robust comparison basis amongst generated design variants of an optimization study. However, since EEDI has been well documented and an established design metric by the existing Regulatory Framework of IMO and Flag States, it can be used for the benefit of any optimization framework more effectively as an optimization constraint rather than as an optimization target. This hybrid approach, of using simulation-based EEOI as a design target and EEDI as a constraint has been employed for all the below Simulation-Based Optimization Runs. More, specifically Phase 2 and Phase 3 reduced EEDI has been used as a constraint. Due to the demanding and strict EEDI reduction from the above phase values, the success rate of the optimization runs has been reduced from levels of 70% to roughly 56%, but simultaneously the algorithm has been “pushed” to explore higher design variants with overall lower EEOI ratings.

6.5.3. Optimization Results

6.5.3.1. Newcastlemax Design – NSGAI Algorithm (ID: Sim_NMAX_01)

The subject run has been conducted using the same variables as the deterministic runs (ID: Det_NMAX_03), the NSGAI algorithm as the design engine and the simulation-based RFR and simulation-based EEOI as optimization targets replacing their deterministic equivalents while EEDI Phase 3 has been used as a constraint instead. For this optimization run (ID: Sim_NMAX_01) a total number of 810 viable designs were generated out of a total population of 1500 designs corresponding to a 54% success rate.

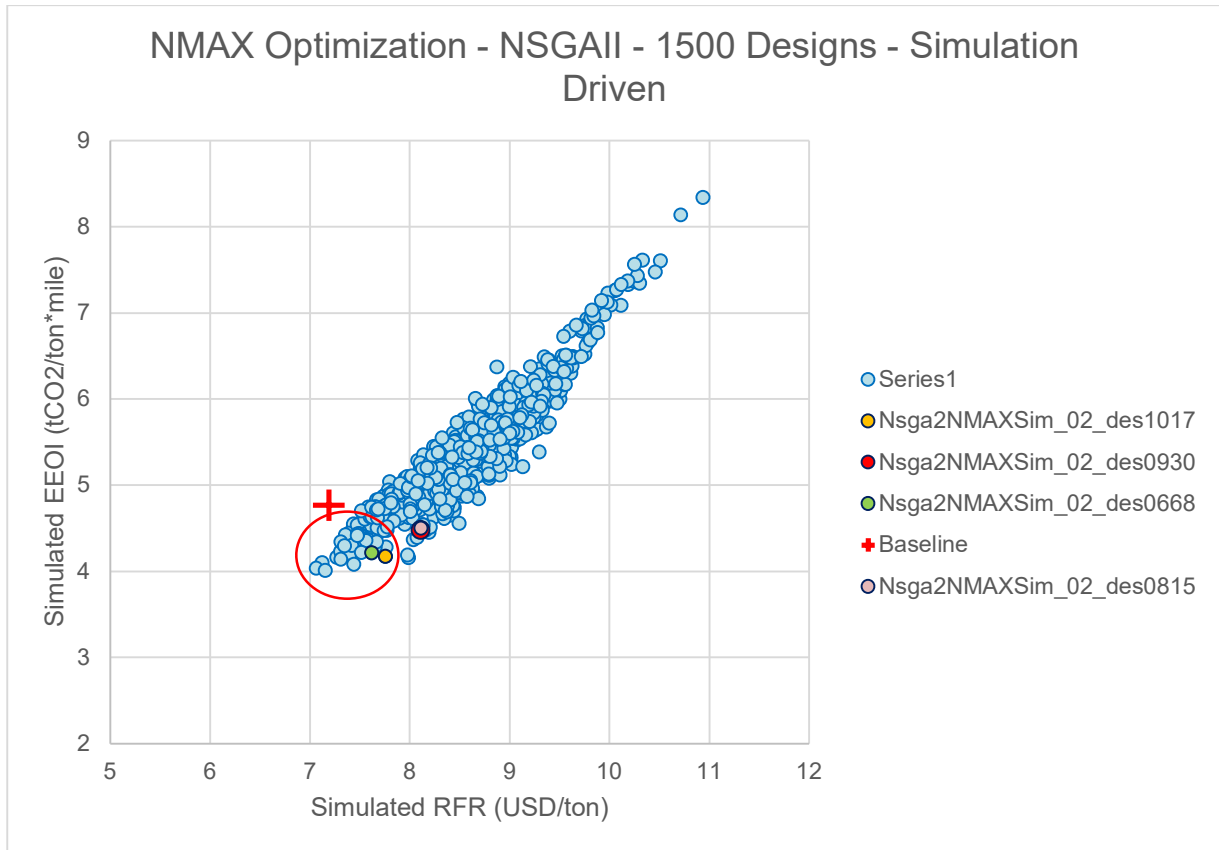


Figure 158: Sim_NMAX_01 / EEOI vs. RFR Design Scatter Diagram with Baseline Vessel and Dominant Variants superimposed.

The scatter diagram between the simulation-based EEOI and simulation-based RFR can be seen in Figure 158. From the first view, it is clear that the linear correlation between the two optimization targets is not only maintained but is considerably stronger. The scatter and range from the linear area is very narrow in contrast to the equivalent deterministic run (Det_NMAX_01). This strong linearity and the narrow band can be interpreted by the origin of the data used for the calculation of each metric. While in the deterministic runs the calculations of the RFR and EEDI were independent but assuming the same speed and power, the calculation

here is synchronous and integrated within the simulation module. This highlights the importance of simulation in converging data and metrics under the same assumptions of voyage input. The Pareto frontier in Figure 158 is reduced into a Pareto peak of a small number of dominant designs (red circle superimposed on the diagram), following an almost identical pattern to the deterministic runs due to the high-level linearity that is observed. The dominant variants, similarly to the deterministic cases are split into two regions, one region corresponding to low RFR and EEOI vessels with higher Ballast Water amount uptake and one region of significantly reduced required Ballast Water amount at the expense of a higher RFR and EEOI. However, in the case of the simulation-based runs, the variants have a smaller “distance” from one another on the same/equivalent scatter diagram. This is an indication, as it will be shown here below, that there are cases of high-performing vessel variants that for a very small trade-off can decrease considerably the required ballast water amount.

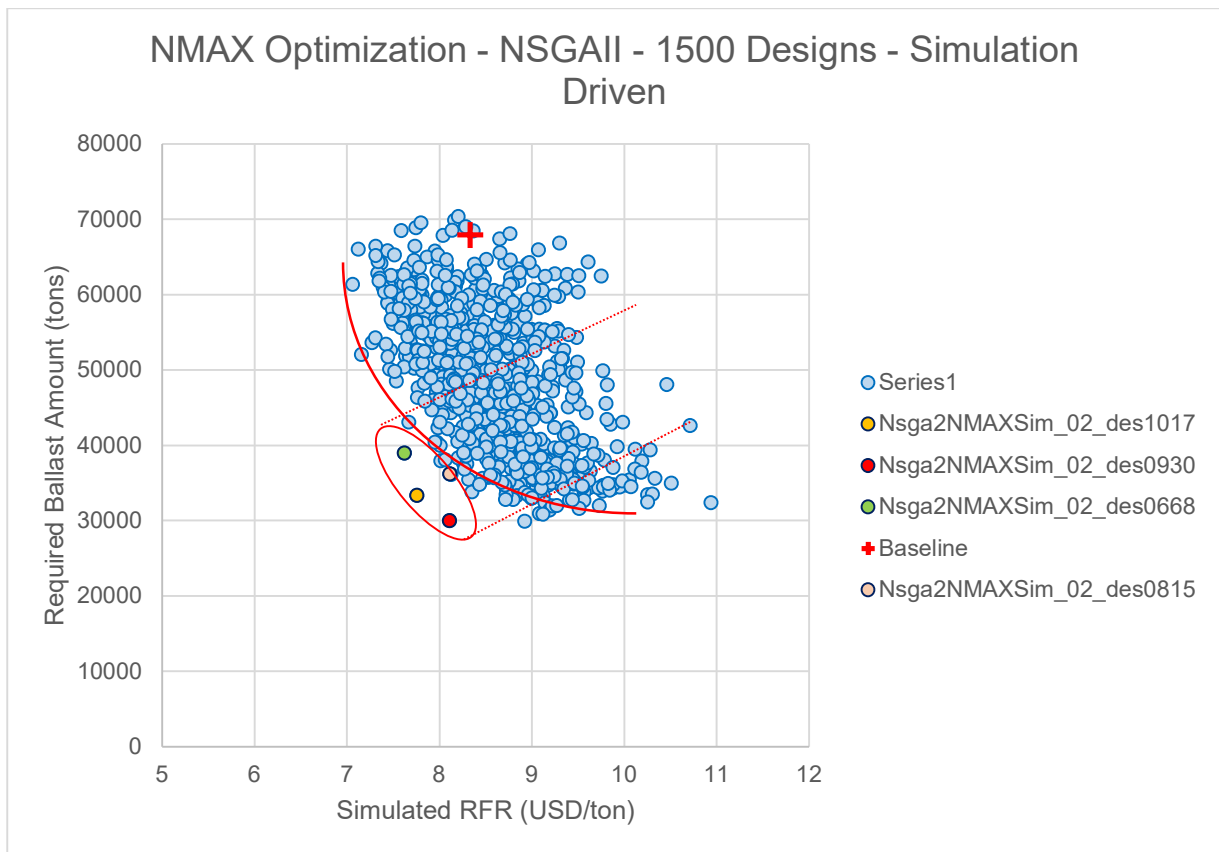


Figure 159: Sim_NMAX_01/ Required Ballast Water vs. Simulated RFR Design Scatter Diagram with Baseline Vessel and Dominant Variants superimposed.

The scatter diagram of the simulation-based RFR and Required Ballast Water amount can be seen in Figure 159. The arc-shaped Pareto frontier observed in the deterministic equivalent run (Det_NMAX_03) is preserved also in this case. However around the bending point of the arc (see superimposed red circle), there are some offset individual designs that strictly dominate the rest of the design cloud of all adjacent regions (see “band” defined by superimposed dashed red

lines). The ranking and pattern of the deterministic runs are maintained with left-hand side regions being characterized by low RFR (and low EEOI) variants that require bigger amounts of Ballast (due to bigger dimensions) while the right-hand side is comprised of vessel variants of higher RFR (and EEOI) and drastically reduced ballast water amount. The most interesting region is as previously mentioned the area where the Pareto arc is bent. The region on its left side is comprised of a very sharp increase in the Ballast Water amount with almost negligible improvement in terms of RFR. It's therefore not a surprise that all the dominant variants resulting from all utility function scenarios are situated in the said region. The vessel with the best combination of RFR and EEOI (Design 0668) is situated on top of the region in the discussion. The vessel with the least water ballast amount required (Design 0930) is situated slightly below the subject region. Interestingly, in this case, the study and run the penalization to decrease the Ballast Water amount required is significantly lower when compared to deterministic runs (Det_NMAX_03). At the same time, in the centre of the region under discussion, the designs featuring the "best compromise" are situated and promise the best trade-off between RFR/EEOI performance and minimization of Ballast Water amount, in a way that is considered the optimization outcome (Designs 0815 & 1017). If we take Design 0815 as an example, the ballast water amount when compared to the optimization baseline (also an NMAX design) is reduced by 42.6%. At the same time, the attained EEDI is 21.1% lower than the Baseline Design while the simulation-based EEOI is 11.5% better than the equivalent EEOI of the Baseline Design assuming the same voyage profile and marine environment. Following the aforementioned linear correlation, the simulation-based RFR is also reduced when compared to the Baseline Design, by a magnitude of 8.6%. Interestingly, even Design 0930 which is the vessel variant that has the highest reduction of Ballast Water Amount (55.8% compared to the Baseline Design) has an improvement both in terms of EEDI and EEOI with 13.6% and 6% respectively as well as in terms of simulation-based RFR which is 2.7% better than the equivalent for the same voyage profile. Interestingly, when ranking with Utility Function Scenario U5 (logarithmic weight distribution), the highest utility designs are Designs 1017 and the low ballast Design 0930.

The identical pattern and shape of the scatter diagram between Required Ballast Water and simulation-based RFR is also met in the scatter diagram between Required Ballast Water and simulation-based EEOI (Figure 160). The two design clouds are very similar in terms of shape and identical in terms of variant and dominant variant positioning. The primary difference is a slightly different frontier of the left-hand-side region of the BW-EEOI diagram which has a small cyrtosis towards the inner area of the cloud. The relative relationships between dominant variants and the Pareto arc bent positioning remain the same. This similarity is attributed to the strong correlation between simulation-based RFR and EEOI.

Another interesting observation from both Figure 159 and Figure 160 is that for both cases the density of the Pareto Frontier is considered lower than with the main body of the design cloud presented. More specifically, both on the edge of the formatted Pareto arc as well as on the Pareto Arc bend area, the designs that one can find are fewer and with a distance between one another.

The explanation for this lies in the design engine itself. As these results are a product of an evolutionary algorithm such as the NSGAI (genetic algorithm), the products of the last generation are the ones with the most attractive merit values (EEOI, RFR, BW etc). The lower density can be attributed to the two below algorithm run settings:

- Number of Generations: In case the number of generations is not high enough for a design problem that is modelled there might be such gaps and low densities. If the algorithm could run for a higher number of generations such gaps can be filled. The effect of the number of generations is examined in paragraph 6.5.3 and Run ID Sim_WOZMAX_02.
- Mutation Probability: The probability of mutation is the trigger of the variation process and is set at the default CAESES® value. For the problem the algorithm is performing variation, a higher number of mutations might trigger the generation of more designs with offset characteristics and merits such as 0930, 1017 and 0815. However, there is a risk of a lower feasibility % as more unfeasible designs might be generated.

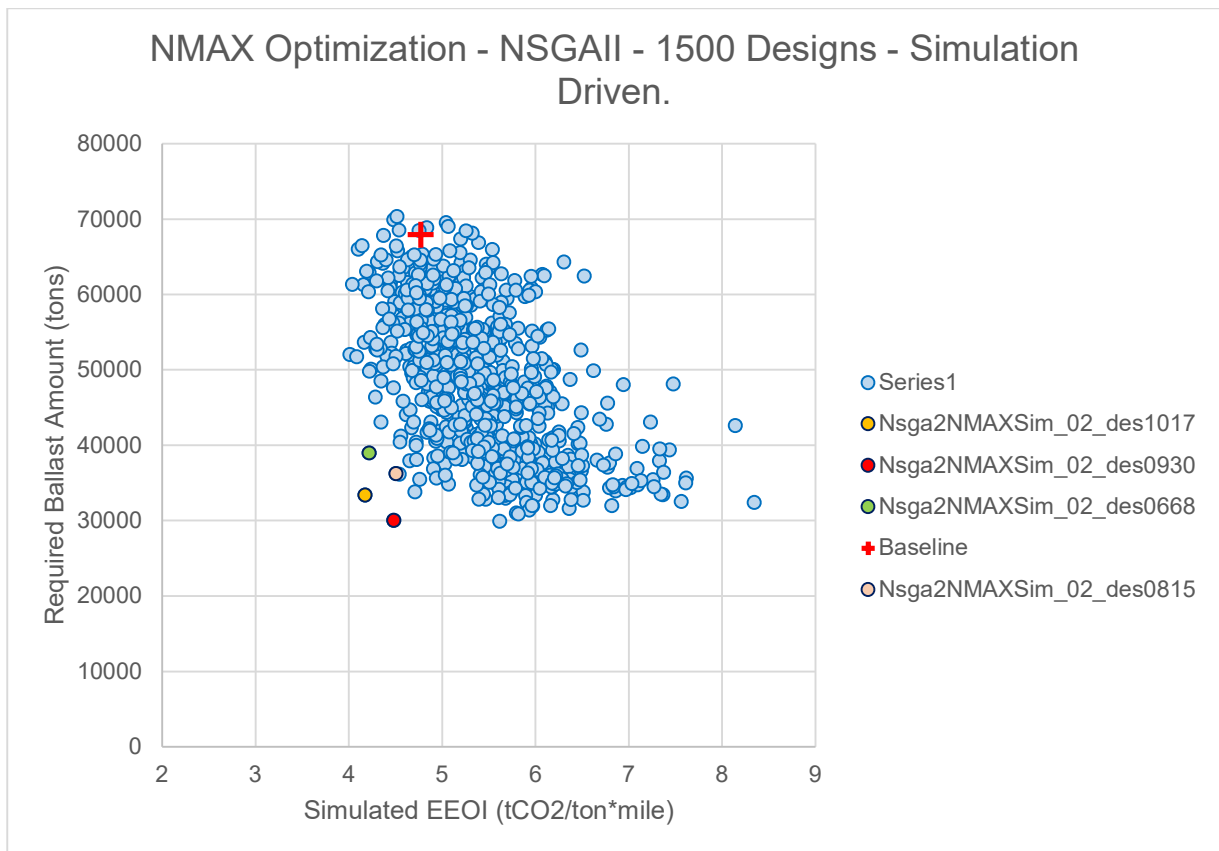


Figure 160: Sim_NMAX_01 / Required Ballast Water vs. Simulated EEOI Design Scatter Diagram with Baseline Vessel and Dominant Variants superimposed.

6.5.3.2. WOZMAX Design – NSGAI Algorithm (ID: Sim_WOZMAX_01)

Subject run (ID: Sim_WOZMAX_01), has been conducted using the same algorithm (NSGAI) and variables as the deterministic equivalent (ID: Det_WOZMAX_03), but with the difference of Total viable designs generated: 795 designs out of 1500 nominal variants Corresponding to 53% success rate.

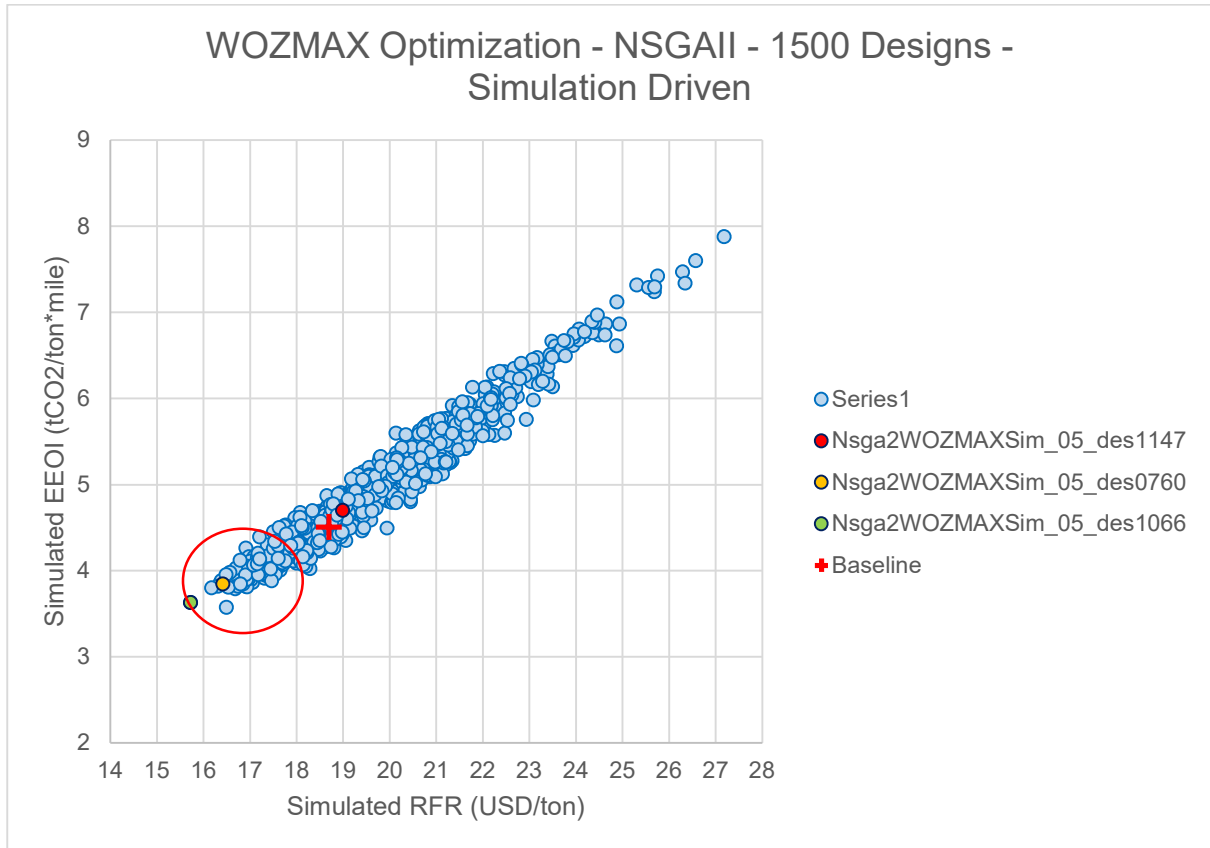


Figure 161: Sim_WOZMAX_01 / EEOI vs. RFR Design Scatter Diagram with Baseline Vessel and Dominant Variants superimposed.

A very distinctive linear relationship with a very narrow scatter of designs, unlike previous deterministic runs where EEDI and RFR were plotted against each other (Figure 161). Results agree with findings in previous optimization runs and subsequent publications (Nikolopoulos & Boulougouris, 2018) as well as the aforementioned NMAX Case study run (ID: Sim_NMAX_01) The reason for this agreement is that in both cases the EEOI is generated from the same data source and outputs of the simulation framework as those of the RFR, narrowing the width of the scatter across the centreline. Furthermore, as both variables are produced from the same voyage simulation, results are synchronous when compared to a deterministic formula for efficiency at the design speed and draft and a simplified economic assessment using the same assumptions.

Sharp Pareto peak is generated strictly dominating all designs above that. Most dominant variants originated from that peak.

The Baseline Vessel is located far away with an RFR that is 19% bigger and an EEOI that is 23.9% bigger than the best-performing designs.

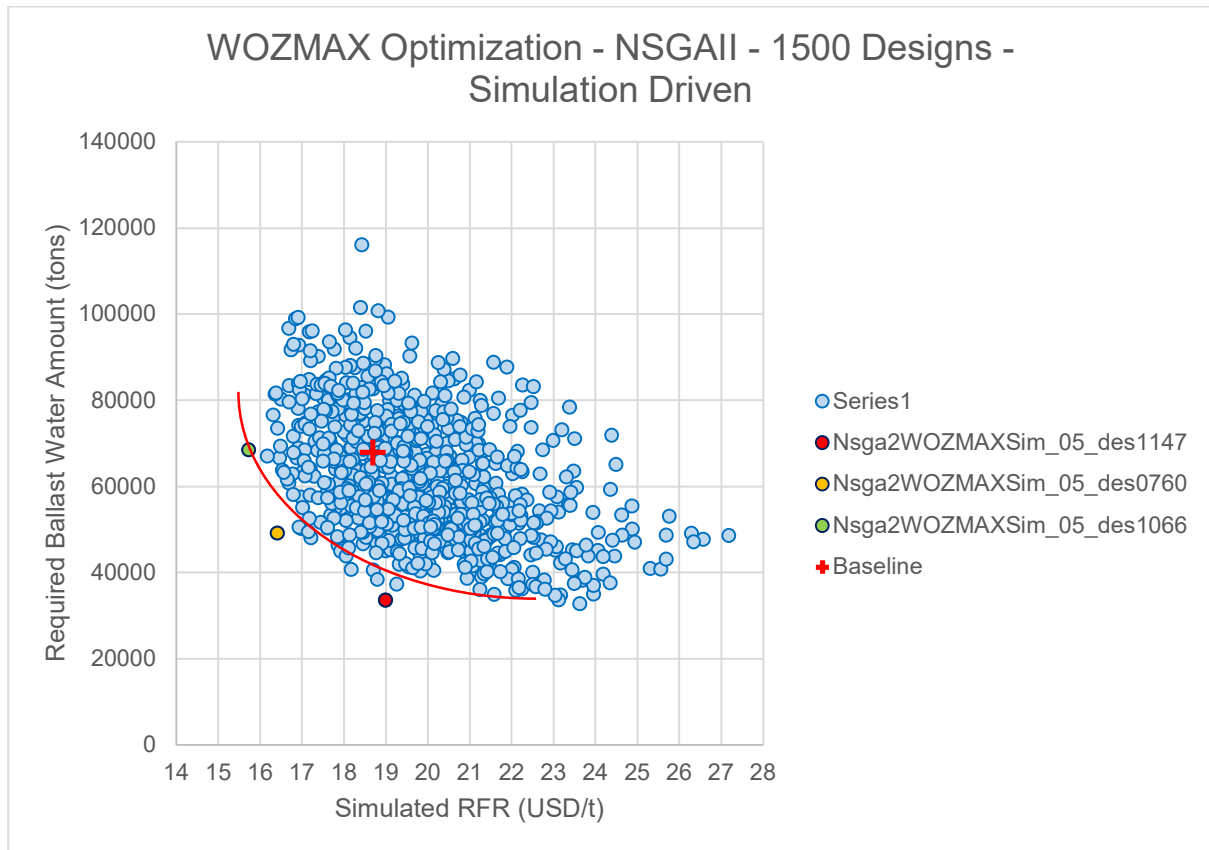


Figure 162: Sim_WOZMAX_01/ Required Ballast Water vs. Simulated RFR Design Scatter Diagram with Baseline Vessel and Dominant Variants superimposed.

When looking at the scatter diagram between the Required Ballast Water amount and the RFR, a similar pattern emerges with a distinctive Pareto front stretching from left to right (Figure 162). The shape of the design cloud is similar to the equivalent cloud from the WOZMAX NSGAI run (Det_WOZMAX_04) but with more curvature on the front and a narrower area of scatter. The use of logarithmic weight distribution for the utility functions again ensures picking designs from all regions of the front. Like in previous runs (but less profoundly), there is a region with high opportunity trade-offs in the region of the arc bent. When compared to the NMAX Case Study (ID: Sim_NMAX_01), the Pareto front is considerably smoother, continuous and with a steeper left-hand side. Like in the NMAX Case study examined the dominant variants are strictly dominating the entire design cloud and their adjacent region is less dense than the rest of the cloud. The attributed reason for that is as previously explained a potentially low number of generations. The baseline design is strictly dominated by all other designs at the same RFR level

while at the same Required Ballast Water amount level the RFR is improved up to 20%. An interesting trade-off to observe is the relationship of Design ID 760 with the best performer in terms of RFR (Design ID1066). With an increase of RFR of merely 4.3%, the Required Ballast Water amount is reduced by 28%. Given the methodology’s potential error and uncertainty as possible post-processing corrective actions (local optimization problems), the inferior RFR can be levelled by either improved hull geometry or external measures to the current methodology (e.g Energy Saving Devices).

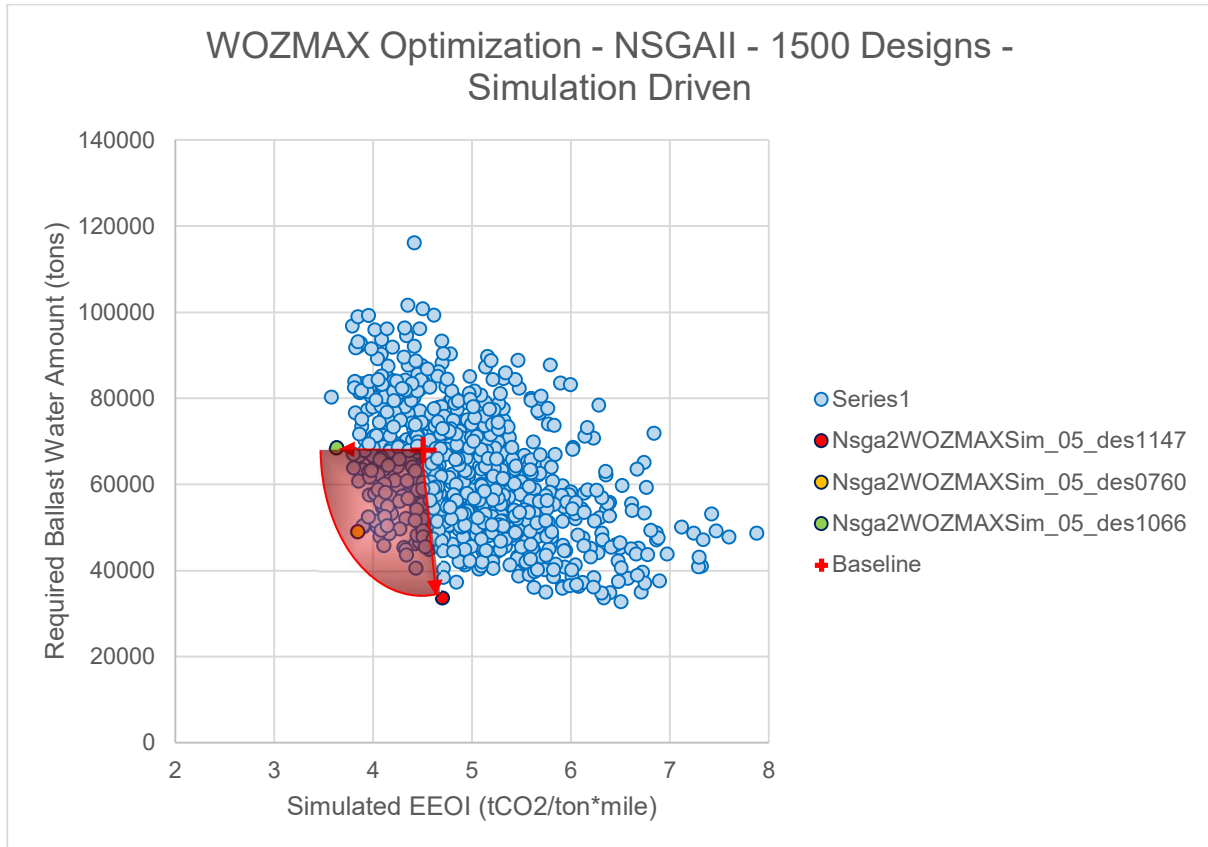


Figure 163: Sim_WOZMAX_01 / Required Ballast Water vs. Simulated EEOI Design Scatter Diagram with Baseline Vessel and Dominant Variants superimposed.

Due to the very strong correlation, common data usage and “synchronous” calculation between EEOI and RFR as described previously in Figure 161, the scatter diagram between the Required Ballast Amount and EEOI is almost identical to the previous diagram for the RFR (Figure 163). The patterns described above, trade-offs and relevant design positions and Pareto Fronts are also the same. It is thus considered that the decision to de-couple EEDI from the optimization and use in turn EEOI having the first as a constraint is highly relevant and correct given that the selection process now is clearer and allows proper exploration of the Pareto front without polarization effects and at the bottom line give a better optimization potential and the final result, highlighting and producing better and more importantly more robust vessel designs. Another interesting observation that would serve as a mathematical analogy for the mechanics of the herein-

presented optimization methodology is the superimposition shown in Figure 163. By assuming the relative location of the point in the scatter cloud corresponding to the Baseline Vessel and defining a vector that has as a start coordinate that particular location and end the coordinate of the corresponding location at the Pareto front, that vector can produce a scanning of the cloud as shown in the red highlighted area. This area is where designs are “meaningful” in terms of optimization results when compared to the Baseline vessel and all of them strictly dominate the latter. In fact, this scanned area shows the real alternatives and true optimization area. The greater it becomes when compared to the total scatter area the more efficient the optimization process is and additionally the initial solution is “worse” creating a bigger potential for improved variations of designs. On the other hand, if the subject area is smaller, that would correspond to a “better” initial solution and, potentially, a less efficient optimization process.

An interesting observation from both Figure 162 and Figure 163, lies in the density of both Pareto fronts. In both cases, there are outliers that dominate the rest of the front. To avoid this and provide a more streamlined flow of dominant variants with better trade-offs it was decided to re-run the optimization process but instead of having 15 generations of 100 designs each (1500 designs) use 20 generations of 100 designs each with the target of obtaining a more dense front.

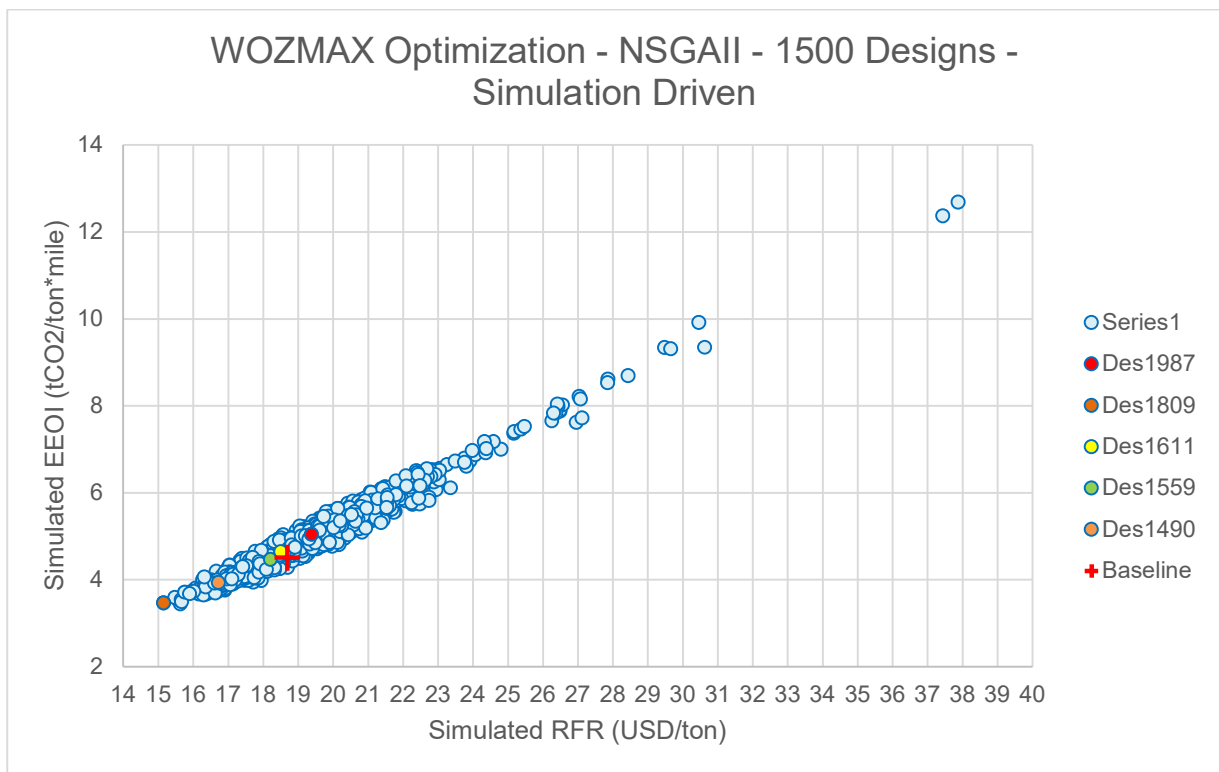


Figure 164: Sim_WOZMAX_02/Simulated EEOI vs. Simulated RFR Design Scatter Diagram with Baseline Vessel and Dominant Variants superimposed.

When looking at the expanded optimization run Sim_WOZMAX_02 with 2000 variants, it can be seen that the key relationships between optimization targets are kept the same as the previous

run Sim_WOZMAX_01 (Figure 164 to Figure 166). However, when superimposing the design scatter of Sim_WOZMAX_01 (1500 variants) under the Sim_WOZMAX_02 (2000 variants) scatter, the following two conclusions come up:

- Conclusion 1: The entire scatter, despite keeping the same shape is “pushed” to the left-hand side of the diagram, in Pareto optimal regions.
- Conclusion 2: The areas of the Pareto front that had a thin design density in Sim_WOZMAX_01 are now filled with design variants, forming in this way a more continuous and robust Pareto frontier with a greater variety of designs with optimization potential and trade-offs, especially between 60,000 and 45,000 tons of Ballast Water amount required.

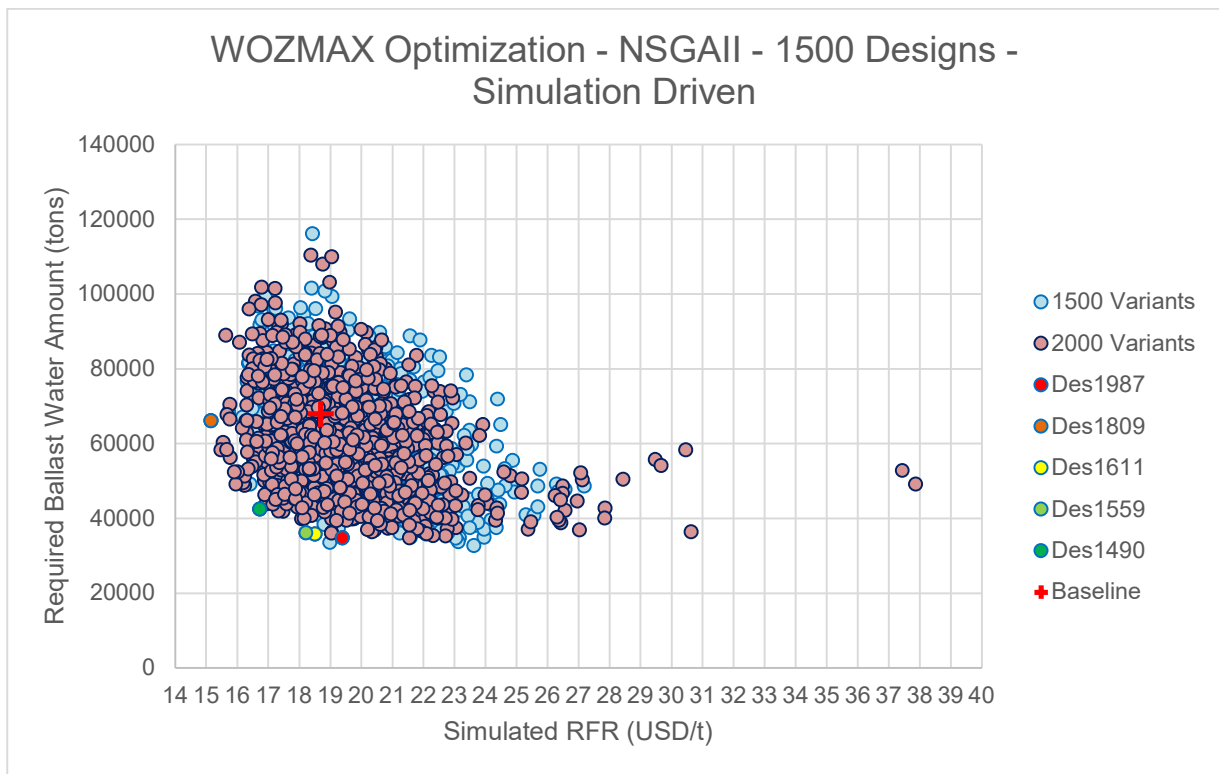


Figure 165: Sim_WOZMAX_02 / Required Ballast Water vs. Simulated RFR Design Scatter Diagram with Baseline Vessel and Dominant Variants and Sim_WOZMAX_01 design scatter superimposed

When applying the same technique of design selection with the use of utility functions (U1~U5 scenarios) with both linear and logarithmic weight distribution, it is interesting to observe that the selected designs are all above the 1000th in the order/sequence of variant generation. Since this is common with the previous run (Sim_WOZMAX_01), it is important here to stress that the optimization algorithm has a “margin” of approximately 1000 designs (from 1000th to 2000th) to create optimal and dominant variants, while previously the same margin was narrowed to 500 designs. As a result of this, it is therefore concluded that the increase of design variant number by the increase of Generation number, contributes to the magnification of the optimization effect.

This can be further validated when looking at the values of the optimization targets of the dominant variants when compared to the baseline. For example, the best performing design in terms of efficiency (RFR and EEOI) when compared to the baseline has an EEOI improved by 29% (when compared to 23% of Sim_WOZMAX_01) and an RFR improved by 24% (when compared to 20% of Sim_WOZMAX_01).

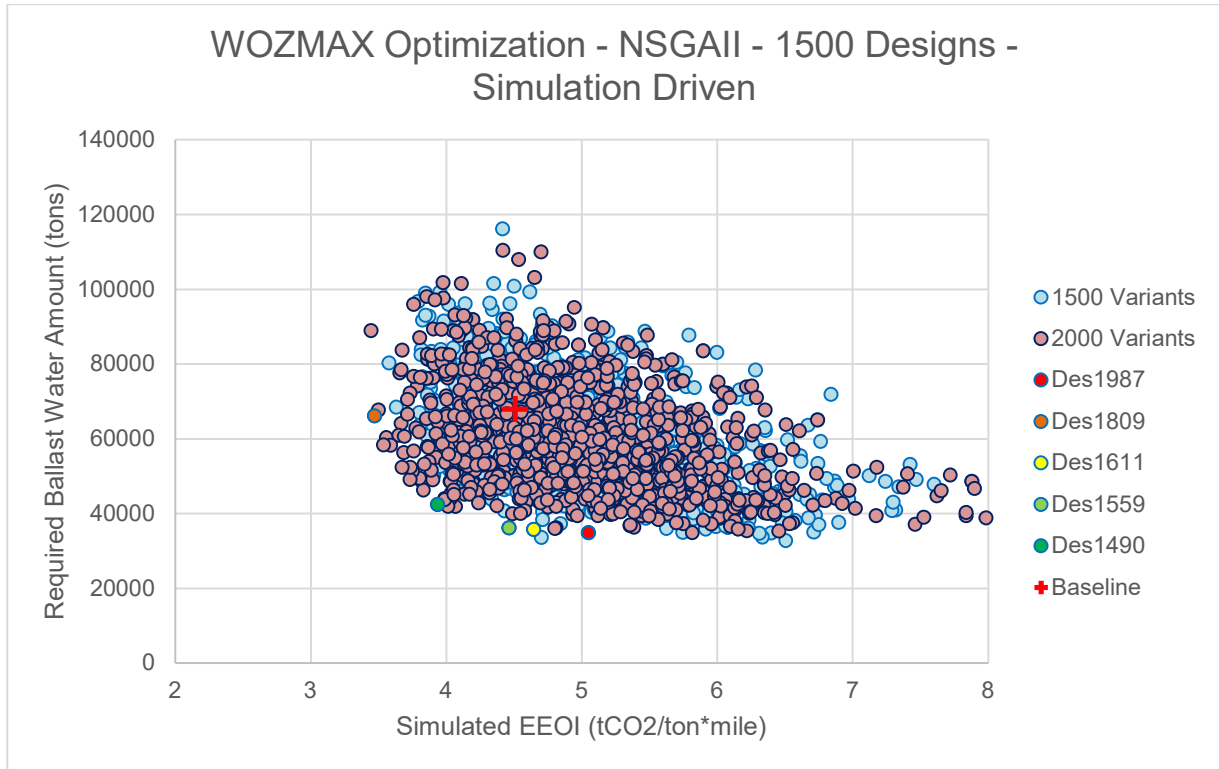


Figure 166: Sim_WOZMAX_02 / Required Ballast Water vs. Simulated EEOI Design Scatter Diagram with Baseline Vessel and Dominant Variants and Sim_WOZMAX_01 design scatter superimposed

An interesting and promising design picked from this run is Design ID 1490. This design is selected from a region of the scatter diagram that has been “filled” with variants due to the Generation number increase. This design has an improved RFR by 15% and improved EEOI by 12% while the Required Ballast Water amount has been reduced by 37%. An equivalent design from the previous run was Sim_WOZMAX_01 ID_760 which has an inferior RFR by 2%, better EEOI by 3% and increased Required Ballast Water amount by 2%.

6.5.4. Design Selection, Ranking and Discussion

6.5.4.1. *Design Selection and Ranking Per Run*

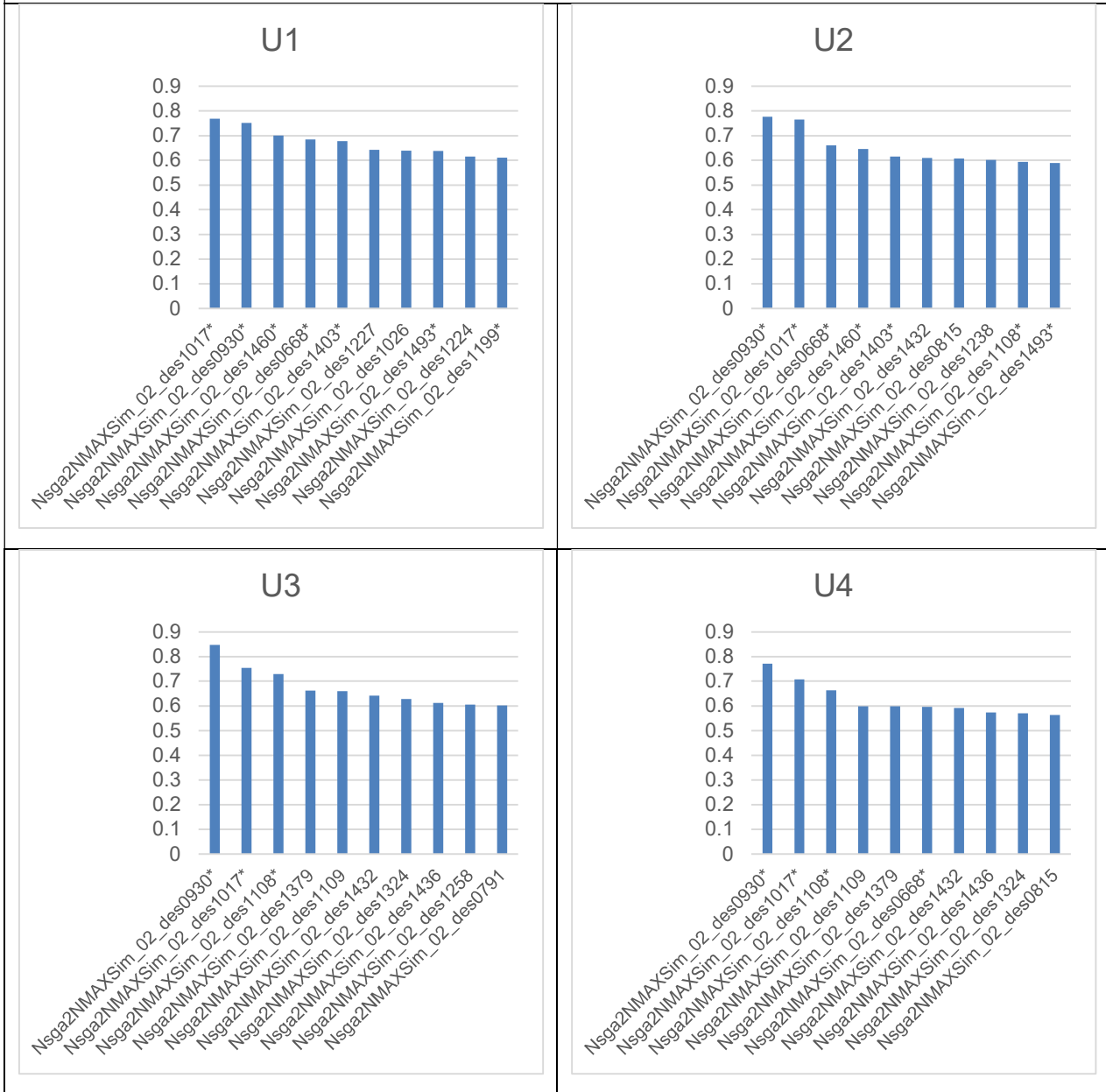
In the below Table 65 to Table 67, the ranking of the top 10 design variants for each utility weight assignment scenario (maximum weights per optimization target) and each run are depicted.

Having established the advantage of the “inelastic” logarithmic utility distribution scenario that enables ranking and picking of dominant variants with trade-offs of increased potential in the Deterministic Runs, the same standardization and approach are followed also here.

Like in the runs of the deterministic pathway, the top three designs remain unchanged (only in a different order) across different scenarios with the exception of Run ID Sim_WOZMAX_02. For this Run, Design IDs 1559 and 1611 are in the top scenarios for U2, U3 and U4 scenarios, however, many more IDs are included as well. The reason for this phenomenon is the denser Pareto frontier (due to increased population from 1500 to 2000 designs) and a thus bigger number of competing for dominant variants.

The basis on the rankings in Table 65 to Table 67, the dominant variants have been illustrated in the scatter diagrams of each run, in paragraph 4.4.3 and their principal particulars are shown and discussed in paragraph 4.4.4.2

Optimization Run Sim_NMAX_01 – Ranking of Dominant Variants with Utility Functions



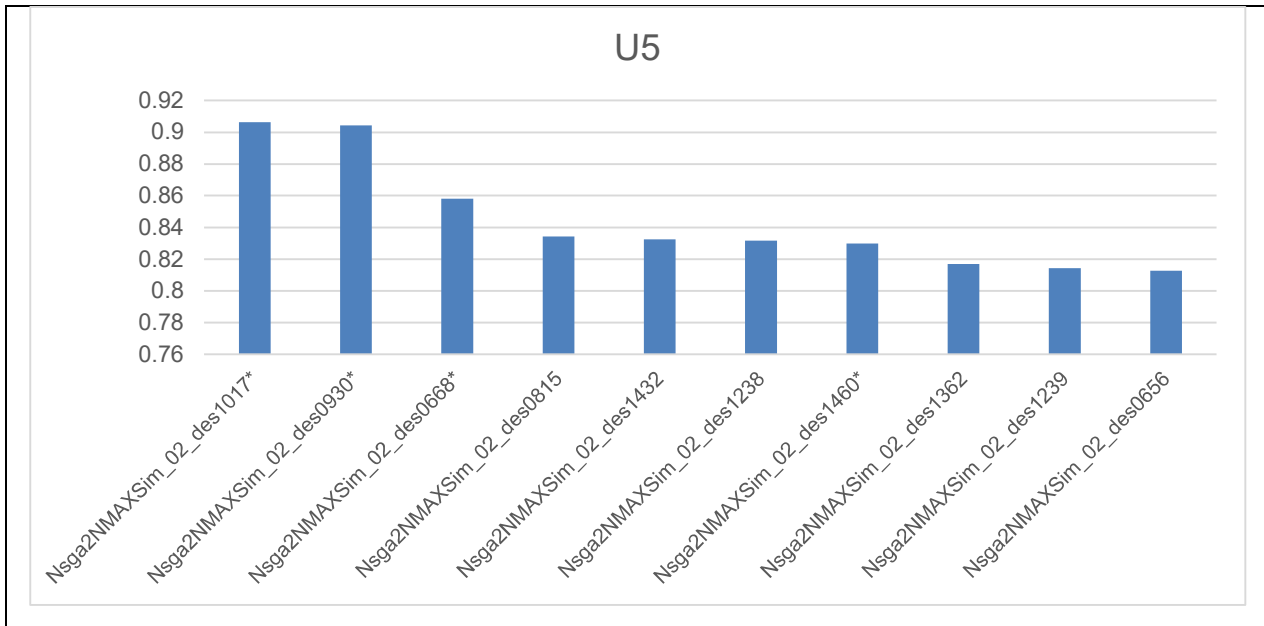
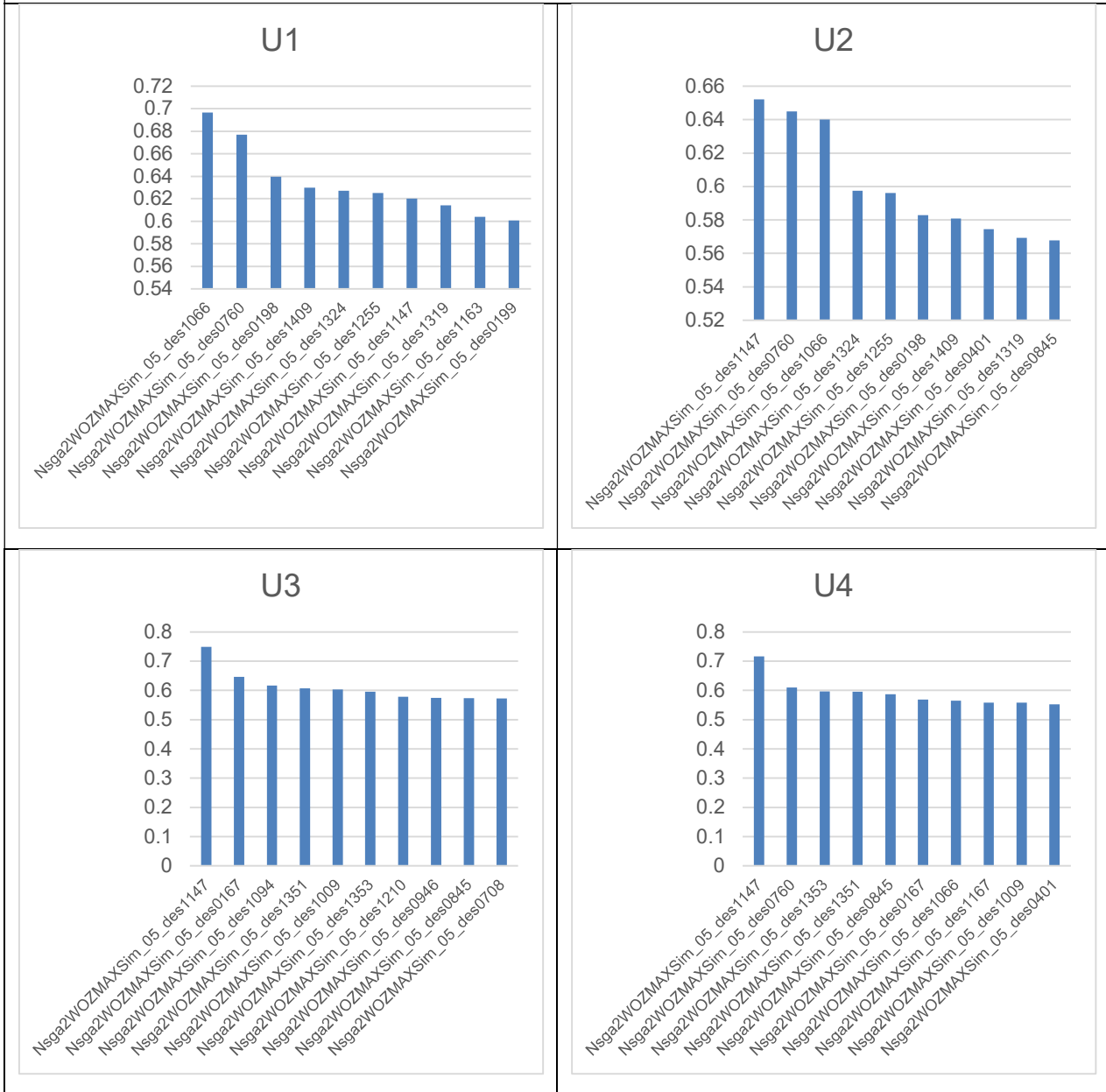


Table 65: Ranking of Optimization Dominant Variants with Utility Functions Scenarios – RUN ID Sim_NMAX_01

Optimization Run Sim_WOZMAX_01 – Ranking of Dominant Variants with Utility Functions



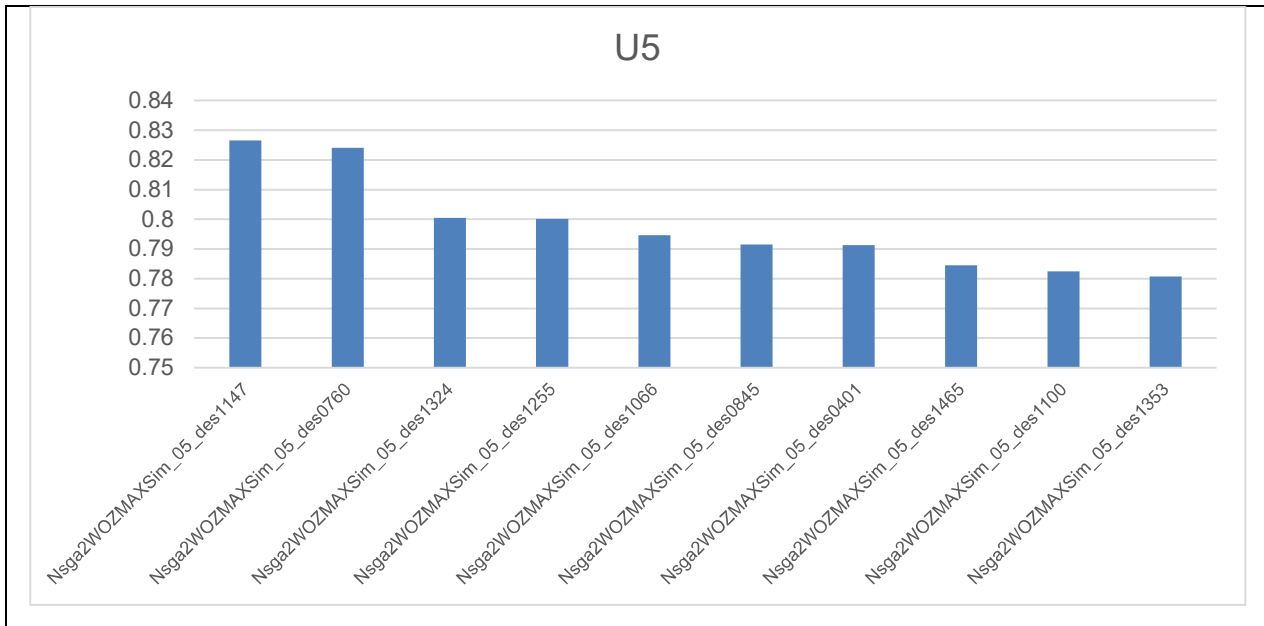
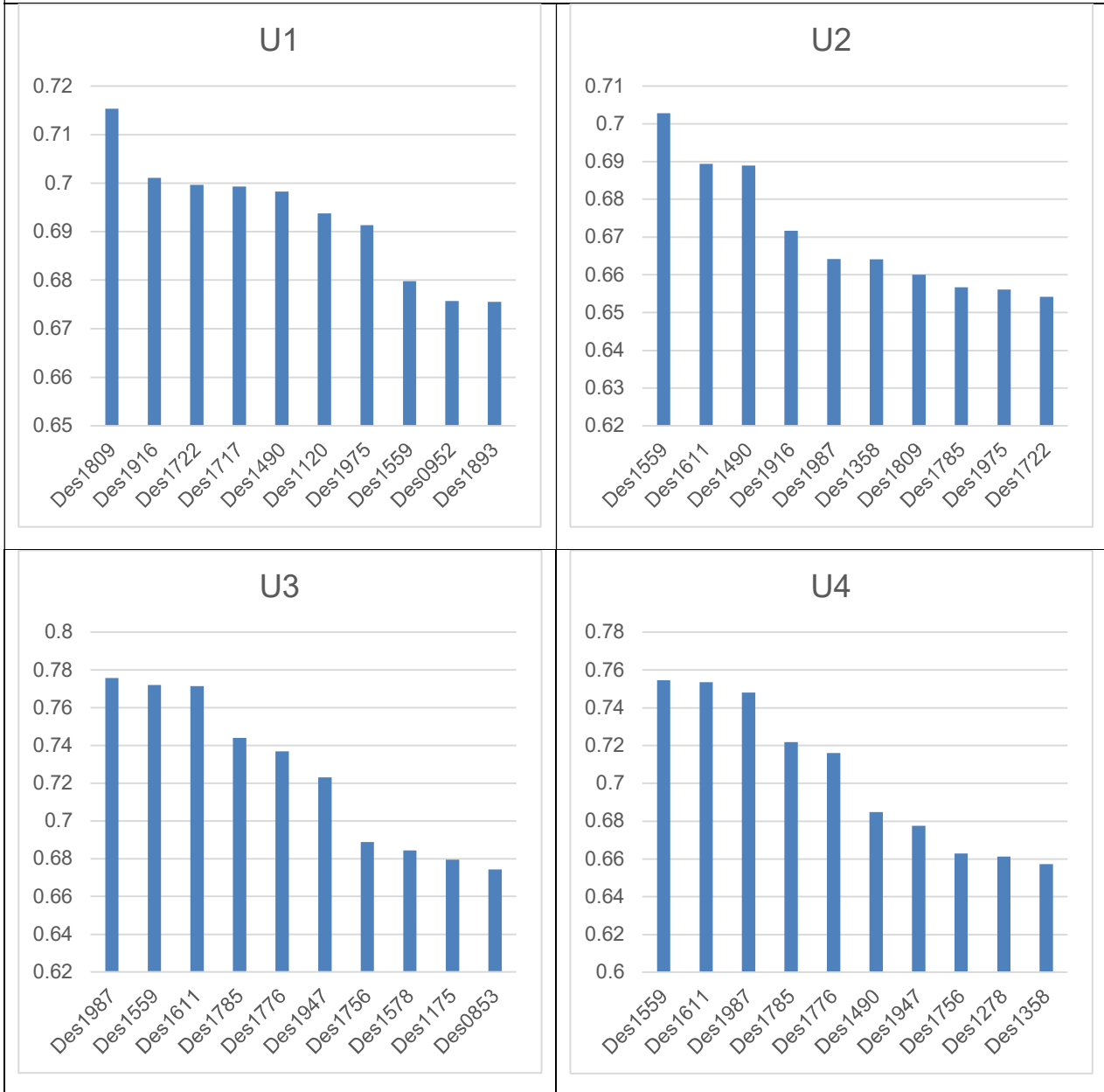


Table 66: Ranking of Optimization Dominant Variants with Utility Functions Scenarios – RUN ID Sim_WOZMAX_01

Optimization Run Sim_WOZMAX_02 – Ranking of Dominant Variants with Utility Functions



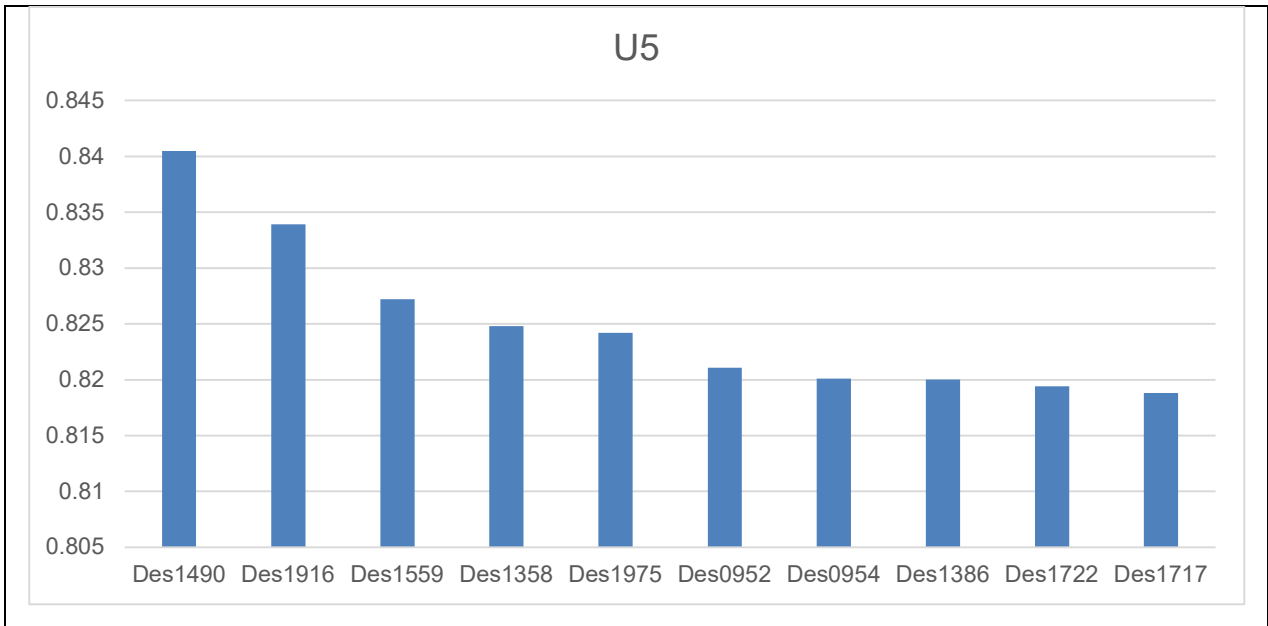


Table 67: Ranking of Optimization Dominant Variants with Utility Functions Scenarios – RUN ID Sim_WOZMAX_02

4.4.4.2 *Principal Particulars of Dominant Variants*

The principal particulars of a selected group of dominant variants from the Simulation-Based Optimization Pathway runs can be found in Table 68 to Table 70.

No.	Particular	ID1017	ID668	ID930
-	Run ID	Sim_NMAX_01	Sim_NMAX_01	Sim_NMAX_01
W_01	Length between Perpendiculars	298.386	293.095	291.936
W_02	Beam	47.944	45.041	45.042
W_03	Draft	21.151	21.943	21.865
W_04	Deck height	27.657	28.971	28.994
W_05	Hopper Height	10.005	6.896	6.849
W_06	Hopper Breadth (m)	3.487	4.431	3.177
W_07	Topside Height (m)	4.458	11.011	10.714
W_08	Topside Breadth (m)	12.193	14.844	11.690
W_09	Block Coefficient C _b	0.725	0.780	0.722
W_10	LCB (%Lbp)	0.513	0.511	0.512
W_11	Bilge Height (m)	5.193	3.511	3.511
W_12	Bilge Width (m)	4.711	4.989	5.564
W_13	Propeller Diameter (m)	8.023	8.017	8.045
W_14	Propeller Expanded Area Ratio	0.634	0.428	0.428

W_15	Propeller Pitch over Diameter	0.931	1.048	1.048
W_16	Propeller Number of Blades	5	5	5
O_1	Required Freight Rate (RFR)	8.112	7.619	8.108
O_2	EEOI	4.502	4.217	4.481
O_3	Required Ballast Water Amount	36236	38987	30033
-	SMCR	17277	18325	18243
-	Lightship Weight			
-	EEDI (Constraint)	2.331	2.254	2.470

Table 68: Principal Particulars of Sim_NMAX_01 Dominant Variants (I)

No.	Particular	ID1147	ID760	ID1066
-	Run ID	Sim_WOZMAX_01	Sim_WOZMAX_01	Sim_WOZMAX_01
W_01	Length between Perpendiculars	291.953	296.959	334.411
W_02	Beam	47.446	57.726	49.642
W_03	Draft	21.751	21.925	21.825
W_04	Deck height	28.515	28.389	28.251
W_05	Hopper Height	9.994	6.095	9.278
W_06	Hopper Breadth (m)	4.377	5.419	4.961
W_07	Topside Height (m)	6.570	11.857	9.930
W_08	Topside Breadth (m)	13.906	13.964	6.111
W_09	Block Coefficient Cb	0.728	0.731	0.808
W_10	LCB (%Lbp)	0.517	0.518	0.514
W_11	Bilge Height (m)	5.680	2.598	3.677
W_12	Bilge Width (m)	5.944	6.004	3.354
W_13	Propeller Diameter (m)	8.093	8.641	8.712
W_14	Propeller Expanded Area Ratio	0.720	0.506	0.411
W_15	Propeller Pitch over Diameter	0.919	0.912	0.910

W_16	Propeller Number of Blades	5	4	4
O_1	Required Freight Rate (RFR)	18.988	16.410	15.724
O_2	EEOI	4.701	3.848	3.631
O_3	Required Ballast Water Amount	33620	49177.	68492
-	SMCR	17582	18292	17711
-	Lightship Weight			
	EEDI (Constraint)	2.399	1.926	1.789

Table 69: Principal Particulars of Sim_WOZMAX_01 Dominant Variants (II)

No.	Particular	ID1987	ID1809	ID1559	ID1490
-	Run ID	Sim_WOZMAX_02	Sim_WOZMAX_02	Sim_WOZMAX_02	Sim_WOZMAX_02
W_01	Length between Perpendiculars	287.278	320.784	309.154	294.745
W_02	Beam	52.261	51.950	47.314	51.941
W_03	Draft	21.839	21.083	21.723	20.975
W_04	Deck height	29.805	29.391	28.632	28.649
W_05	Hopper Height	7.442	11.889	11.350	8.291
W_06	Hopper Breadth (m)	4.246	3.409	4.524	3.366
W_07	Topside Height (m)	11.295	11.295	4.921	8.753
W_08	Topside Breadth (m)	6.285	11.00	7.199	8.416
W_09	Block Coefficient C _b	0.720	0.823	0.726	0.746
W_10	LCB (%Lbp)	0.516	0.513	0.517	0.519
W_11	Bilge Height (m)	6.001	3.798	2.597	4.896
W_12	Bilge Width (m)	6.887	5.565	6.868	5.826
W_13	Propeller Diameter (m)	8.081	8.194	8.081	8.021
W_14	Propeller Expanded Area Ratio	0.433	0.416	0.622	0.478
W_15	Propeller Pitch over Diameter	1.068	1.036	1.069	0.949
W_16	Propeller Number of Blades	5	5	4	5

O_1	Required Freight Rate (RFR)	19.380	15.146	18.210	16.720
O_2	EEOI	5.048	3.468	4.462	3.936
O_3	Required Ballast Water Amount	34873	66193	36208	42470
-	SMCR	19966	19452	18867	18273
-	Lightship Weight				
	EEDI (as a constraint)	2.262	1.833	2.303	2.212

Table 70: Principal Particulars of Sim_WOZMAX_02 Dominant Variants (III)

- *Observed Length*

For Newcastlemax case studies, RFR and EEOI optimal designs have lengths very close to the upper boundary (300m) of the respective optimization variable in the same way it was applicable for Deterministic studies. In contrast to these studies, the Required Ballast Water optimal designs have lengths also close to the upper boundary (previously next to the lower boundary), leading to a considerable improvement in their RFR and EEOI performance.

When now looking at the WOZMAX case studies (Sim_WOZMAX_01 and Sim_WOZMAX_02), the best performers in terms of RFR and EEOI have the biggest Lbp values, with the shortest designs are the ones with the minimized Required Ballast Water amount. Dominant variants that have the most interesting trade-offs between RFR and Required Ballast Water amount performance have intermediate length values which are close to or slightly higher than the upper bound of the NMAX study (but with an enlarged beam).

When comparing both NMAX and WOZMAX ship types and optimization cases with the deterministic pathway counterparts, it is safe to deduct that the methodology and model sensitivity in terms of length as well as the tendency of dominant variants in terms of Lbp remains the same. However, the contribution of the simulation-based metrics (RFR and EEOI) lies in the more enhanced exploration of the design space, leading to dominant variants that have greater Lbp and almost optimal RFR values while keeping at the same time the Required Ballast amount at a certain limit. This result is more profound in the Sim_NMAX_01 optimization run.

- *Observed Beam*

For the Newcastlemax variants, the beam, similarly to the deterministic studies has a less correlated behaviour with RFR and EEOI. Again, dominant variants have beam values well spread within the variable range.

For WOZMAX case studies, the beamier designs in general are the best performers in terms of RFR and EEOI. The range of the beam is kept in the middle of the variable range and slightly higher when compared to the deterministic pathway results.

- *Observed Draft*

The tendency of increased scantling draft that was observed for the dominant variants of the Deterministic pathway Run IDs is kept the same. Interestingly, all dominant variants are further pushed to the upper limit of the draft variable range with scantling drafts at the range of 21.5 to 21.9 meters. Compared to the deterministic runs these in general are higher absolute values. The simulation-based calculations at actual operating speeds, highlight the small penalization of power due to increased draft over the benefit of increased displacement, deadweight and payload which counterbalances the loss of displacement due to a smaller block coefficient. The simulation therefore here plays an important role in pushing the variation algorithm to smaller installed power by leading to finer hulls of smaller C_b and higher scantling draft.

- *Observed Block Coefficient (C_b)*

The most interesting part of the simulation-based runs is observed in the values of the block-coefficient of dominant variants in the Simulation-Driven Run IDs. In contrast to the Deterministic Pathway, all designs are pushed at the lowest boundary of the range of block coefficient at values in the range of 0.72-0.75, which are not common in actual shipbuilding practice. Interestingly, the reduction of the C_b for simulation-based studies, apart from reducing the installed power of the M/404 drastically reduces the added resistance in actual seaways and for the most frequent operating speeds of the specific trade routes examined. An important role in this direction is played by the updated added resistance methodology which accounts for all wave directions and has an updated correction for the C_b value of the vessel. Interestingly, slender designs have considerably less added resistance in actual seaways, while the reduced payload is counterbalanced by the increased length and beam values.

- *Observed Deck Height*

Deck height for both Newcastlemax and WOZMAX studies dominant variants have been found, similarly to the Deterministic Pathway runs, to be the upper bound of the variable range with most dominant variants having a height between 28 and 29 meters. As in the deterministic runs, the deck height is increased due to the higher scantling draft to maintain compliance with the minimum freeboard constraint (calculated based on the Load Line convention of 1966. One of the reasons for the low percentage of successful designs is the non-compliance of many variants of the first optimization generations with this constraint. Another observation is that for the RUN ID Sim_WOZMAX_02, the total design population is 2000 designs (instead of 1500 of all previous

deterministic and simulation-based runs) the deck height of dominant variants is the highest amongst all run results. The bigger number of variants which creates a denser Pareto front “pushes” the algorithm towards such solutions.

- *Observed Cargo Hold Variables*

Cargo Hold variable values of dominant variables have generally a greater scatter compared to main dimensions and hull variables with considerably smaller correlation (close to none) to RFR, EEDI and practically zero correlation with regards to Required Ballast Amount. The effect of simulation here is not observed at all.

- *Observed Propeller Particulars*

For the Simulation-Driven pathway, the propeller particulars play a very decisive role in the optimization process. Instead of examining a single point (of the NCR) in the deterministic pathway, for simulation-based optimization runs, the full propeller operation is simulated under different loads, in real seaways, for actual speeds and quasi-dynamic conditions.

The effect of simulation, also identified in Table 71 and Table 72 which compare dominant variants, can be summarized below:

- Reduction of Dominant Variant Propeller Diameter.
- Reduction of Expanded Area Ratio.
- Increase of Propeller Pitch over Diameter Ratio
- More frequent dominant variants with 5 instead of 4 blades.

The reason for limited propeller diameters for dominant variants is that the aft draft in the light ballast condition is reduced and thus the required ballast amount to attain the latter loadline. The simulation-based optimization here ensures the increase of propeller efficiency for the actual speeds (and thus advance coefficients J), by leading to designs of increased propeller pitch but of relatively smaller expanded area ratio to maintain a sufficient light running margin (also ensured through the engine selection module).

The comparison of the principal particulars of dominant variants of Deterministic Pathways (Det_NMAX_02_ID2345 and Det_WOZMAX_02_ID2390) with simulation-based optimization runs can be found in Table 71 for NMAX case studies and Table 72 for WOZMAX case studies.

A Novel Methodology for Robust, Holistic, Simulation-Based Ship Design Optimization

No.	Particular	ID2345	ID668	Difference
-	Run ID	Det_NMAX_02	Sim_NMAX_01	
W_01	Length between Perpendiculars	299.468	293.095	-2.1%
W_02	Beam	46.634	45.041	-3.4%
W_03	Draft	21.165	21.943	3.7%
W_04	Deck height	28.099	28.971	3.1%
W_05	Hopper Height	9.388	6.896	-26.5%
W_06	Hopper Breadth (m)	4.810	4.431	-7.9%
W_07	Topside Height (m)	11.335	11.011	-2.9%
W_08	Topside Breadth (m)	11.979	14.844	23.9%
W_09	Block Coefficient C _b	0.813	0.780	-4.1%
W_10	LCB (%Lbp)	0.522	0.511	-2.1%
W_11	Bilge Height (m)	6.158	3.511	-43.0%
W_12	Bilge Width (m)	3.235	4.989	54.2%
W_13	Propeller Diameter (m)	8.313	8.017	-3.6%
W_14	Propeller Expanded Area Ratio	0.781	0.428	-45.2%
W_15	Propeller Pitch over Diameter	0.784	1.048	33.7%
W_16	Propeller Number of Blades	5	5	-%

O_1_a	Deterministic Required Freight Rate (RFR)	6.793	7.340	
O_1_b	Simulation-Based Required Freight Rate (RFR)	N/A	7.619	
O_2_a	Deterministic EEDI (Constraint)	2.950	2.254	-23.6%
O_2_b	Simulation-Based EEOI	N/A	4.217	
O_3	Required Ballast Water Amount	46,381	38,987	-15.9%
-	SMCR	23,357	18325	-21.5%

Table 71: Comparison of Principal Particulars of Dominant Variants of Deterministic vs. Simulation-Based Runs / Newcastlemax Case Study

No.	Particular	ID2390	ID760	ID1490	Highest Improvement %
-	Run ID	Det_WOZMAX_02	Sim_WOZMAX_01	Sim_WOZMAX_02	
W_01	Length between Perpendiculars	298.268	296.959	294.745	-1.18%
W_02	Beam	46.685	57.726	51.941	11.26%
W_03	Draft	21.645	21.925	20.975	-3.10%
W_04	Deck height	28.394	28.389	28.649	0.90%
W_05	Hopper Height	9.816	6.095	8.291	-15.54%
W_06	Hopper Breadth (m)	3.560	5.419	3.366	-5.45%
W_07	Topside Height (m)	6.287	11.857	8.753	39.22%
W_08	Topside Breadth (m)	13.558	13.964	8.416	-37.93%
W_09	Block Coefficient C _b	0.851	0.731	0.746	-12.34%
W_10	LCB (%L _{bp})	0.518	0.518	0.519	0.19%
W_11	Bilge Height (m)	6.647	2.598	4.896	-26.34%
W_12	Bilge Width (m)	5.457	6.004	5.826	6.76%
W_13	Propeller Diameter (m)	8.091	8.641	8.021	-0.87%
W_14	Propeller Expanded Area Ratio	0.604	0.506	0.478	-20.86%
W_15	Propeller Pitch over Diameter	1.076	0.912	0.949	-11.80%

W_16	Propeller Number of Blades	4	4	5	-
O_1_a	Deterministic Required Freight Rate (RFR)	12.18	11.543	12.067	-5.22
O_1_b	Simulation- Based Required Freight Rate (RFR)	N/A	16.410	16.720	-
O_2_a	Deterministic EEDI	2.576	1.926	2.212	-14.13%
O_2_b	Simulation- Based EEOI	N/A	3.848	3.936	-
O_3	Required Ballast Water Amount	48871	49177	42470	-13.10%
-	SMCR	23843	18292	18273	-23.36%

Table 72: Comparison of Principal Particulars of Dominant Variants of Deterministic vs. Simulation-Based Runs / WOZMAX Case Study

6.5.5. Discussion Of Results

In Table 73, the improvement of the key optimization targets for the dominant variants of the Simulation-Driven Pathway Run IDs can be quickly summarized.

Design I.D	Optimization Run	RFR improvement <i>*Simulation Based</i>	RFR improvement <i>*Nominal</i>	EEOI Improvement	EEDI Improvement	Required Ballast Amount Improvement
Baseline	-	-%		-%	-%	-%
ID1017	Sim_NMAX_01	-7%	+7%	-12%	-17%	-51%
ID668	Sim_NMAX_01	-9%	+2%	-12%	-21%	-43%
ID930	Sim_NMAX_01	-3%	+10%	-6%	-14%	-56%
ID1147	Sim_WOZMAX_01	1.6%	0.0%	4.3%	-16.1%	-50.5%
ID760	Sim_WOZMAX_01	-12.2%	-5.2%	-14.6%	-32.6%	-27.6%
ID1066	Sim_WOZMAX_01	-15.9%	-17.9%	-19.4%	-37.4%	+0.8%
ID1987	Sim_WOZMAX_02	+3.7%	+10.7%	+12.0%	-20.9%	-48.7%
ID1809	Sim_WOZMAX_02	-19.0%	-9.5%	-23.1%	-35.9%	-2.6%
ID1559	Sim_WOZMAX_02	-2.6%	+1.0%	-1.0%	-19.4%	-46.7%
ID1490	Sim_WOZMAX_02	-10.5%	+6.8%	-12.7%	-22.6%	-37.5%

Table 73: Summary of Optimization Results on Optimization Targets for Dominant Variants // Simulation Driven Pathway

Best Performer Variants

The most efficient design appears to be Design ID1809 of Sim_WOZMAX_02, which features a reduction of RFR by 19.0%, and a reduction of EEOI by 23.1% (EEDI reduction by 35.9%) while the Required Ballast Water amount is only slightly reduced by 2.6%. A neighbouring design is also Design ID1066 of Sim_WOZMAX_01 which for practically the same Required Ballast Amount as the baseline (0.8% increase), is improved by 15.9% in terms of RFR and 19.4% in terms of EEOI.

Least Ballast Water Amount Variants

The design with the greatest reduction of Required Ballast Water amount is ID1017 of Sim_NMAX_01 (Newcastlemax Case study). Interestingly, this design combines a reduction of the Required Ballast Water amount of 51%, while is also improved in terms of efficiency rather significantly with an improvement of 7% for RFR and 12% for EEOI (EEDI reduction by 17%). The equivalent dominant variant for WOZMAX case studies is ID1147 for which the Required Ballast amount is reduced by 50.5%, however, that comes with a penalty of 1.6% for RFR and 4.3% for EEOI.

Best Trade-Off Variants

The dominant variants which represent best the principle of RHODA (Robust Holistic Optimization Design Approach) are the designs that feature the best overall performance with the best trade-off amongst optimization merit performance. For the Newcastlemax design case, that would be ID668 of Sim_NMAX_01, which combines a reduction of 9% in RFR and 12% in EEOI with a simultaneous drop of 43% for the Required Ballast Water amount. The equivalent “play” in optimization trade-off amongst targets can be seen also for WOZMAX case studies and ID1490 of Sim_WOZMAX_02, where an improvement of 10.5% in RFR and 12.7% in EEOI is combined with a reduction of Required Ballast Amount of 37.5%. If now the Required Ballast amount reduction is of smaller value for the decision-maker (but not negligible) dominant variants with intermediate performance such ID760 of Sim_WOZMAX_01 could be considered for further development. The latter still features a considerable reduction of the Required Ballast Amount at the level of 27% and in the meantime, the RFR is improved by 12.2% and the EEOI by 14.6%. This “optimization result compromise” makes ID760 the best example of a variant with a trade-off amongst optimization targets.

Comparison with Deterministic Results

For the deterministic results, dominant variants either had a 30-40% reduction in Required Ballast or no reduction at all, whereas for these results there were many dominant variants with considerable reductions (above 50%) as well as many with intermediate numbers combined with overall improvements. The most interesting observation is the deviation of the nominal RFR and EEDI from the baseline vessel. For most dominant variants the nominal RFR appears to be higher (worse) compared to the baseline in contrast to the respective values of the simulation-based RFR which are significantly lower indicating better performance. This problematic ranking when using the nominal RFR is behind the high degree of elasticity of the Pareto fronts and ranking methods for the deterministic results and the absence of an intermediate Pareto solution (polarization discussed in paragraph 6.4). The overall EEDI improvement is higher for all variants when compared with the Deterministic Pathway results (Table 61), a result attributed to the strict constraint of IMO EEDI Phase 3 applied. When comparing results with the Deterministic Pathway Optimization Studies, it is thus evident that the first results are not Robust, since the introduction of simulation in the Optimization enabled a more enhanced design space exploration and

subsequent optimization, leading to better solutions that have both higher reduction rates in absolute magnitude and the meantime provide variants with better performance for all three optimization targets thus “relaxing” the intense competition amongst given optimization targets as discussed in paragraph 6.4.

6.5.5.1. *Effect of Simulation on RFR Improvement*

To quantify and identify the effect of the use of voyage simulation in the optimization process, it is necessary to examine the areas where the nominal RFR appears to be higher: there is a very big scatter for the values of simulation-based RFR. That means, that a small penalization in the simulation-based RFR is found to be a far greater penalization for the nominal RFR. An example of this behaviour is seen between Sim_WOZMAX_01_ID1066 and Sim_WOZMAX_01_ID760 and Figure 167. When moving from ID1066 to ID760 the simulation-based RFR is increased by roughly 0.7 USD/ton (from 15.72 USD/ton to 16.4 USD/ton) while at the same time the nominal RFR is increased by 1.5 USD/ton (from 10 USD/ton to 11.5 USD/ton). Figure 167 clearly shows this correlation from the tangent of the equivalent linear area of the scatter diagram between the two optimization targets. The practical meaning behind this is that in reality, the performance reduction of ID760 under real operating conditions (speed, weather) in the simulation module is considerably smaller than anticipated by a deterministic calculation on the NCR design point.

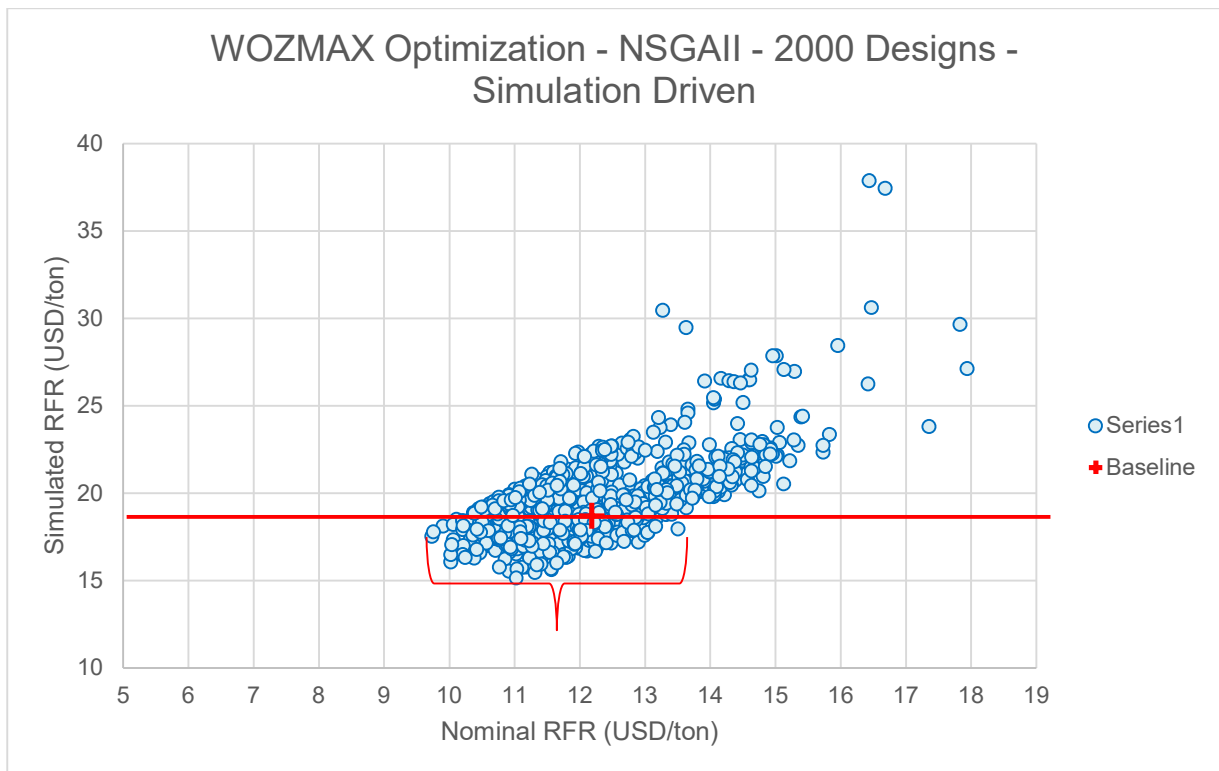


Figure 167: Scatter Diagram of Simulation-Based RFR vs Nominal RFR for Sim_WOZMAX_02 Run (2000 designs)

Another interesting example is that of Sim_WOZMAX_02_ID1490. This design variant that features an improvement of 10.5% compared to the baseline in terms of simulation-based RFR, however the nominal RFR of the same design appears to be 6.8% worse than the baseline.

To understand and visualize the above-mentioned examples better, it is useful to observe Figure 155, which is the scatter diagram between the simulated RFR vs. nominal RFR for the Sim_WOZMAX_02 with the Baseline Design and dominant variants superimposed. If a line having as ordinate the Simulation-Based RFR value of the Baseline Vessel is defined it splits the design cloud into two parts: the lower part (~35% of the total population) which corresponds to variant IDs with simulation-based RFR lower (better) than the baseline design and the upper which are designs with the higher, thus worse equivalent value. When looking now at the lower cloud, the width of the scatter corresponds to values of nominal RFR ranging from 9.5 USD/t to 13.5 USD/t (142%). For all of these values of the nominal RFR, there are points (designs) with improved simulation-based RFR values.

If now all these designs with improved simulation-based RFR but higher than the baseline nominal RFR are ignored, many design solutions with improved Required Ballast Water amount and even EEDI/EEOI values are discarded. For this reason, the herein presented methodology is considered a Robust Process.

6.5.5.2. *Effect of Simulation on EEOI Improvement*

The effect of the use of voyage simulation in the improvement of EEOI (namely the vessel's environmental performance) is profound from the above results as well as previously discussed scatter diagrams and sensitivity analysis. Voyage simulation proves the profound unsuitability of EEDI as an efficiency metric in Ship Design Optimization Studies as it is incapable of capturing the true efficiency of the vessel in actual operating conditions. For example, in the case of Design ID1147 of Sim_WOZMAX_01, an EEDI reduction of 16.1% is not matched by the EEOI, with the latter being 4.3% higher than the equivalent value of the baseline when performing the same voyages over time. The same and more profound effect is seen in ID1987 of Sim_WOZMAX_02 which is a design alternative that despite having an EEDI value that is 20.9% lower than the baseline, its actual performance and corresponding EEOI after simulation proves to be higher by 12% than the equivalent of the baseline.

Another example of EEDI's inability for ranking the efficiency of produced designs can be seen from the comparison of two NMAX optimization dominant variants; ID1017 and ID668. Both of them have the same EEOI improvement of 12% however, ID668 appears to have a better performance "in-paper" with an EEDI that 21% reduced from the baseline.

As dominant variants with increased improvement percentages from the baseline are examined, the deviation between EEOI and EEDI in terms of ranking shrinks and EEDI is linearly correlated with EEOI acting as a magnification factor only. Indeed, this observation amongst dominant variants can be also validated by the findings analysed in paragraph 6.5.2 of the Sensitivity Analysis of the Simulation-Driven Pathway runs. The degree of uncertainty for EEDI is reduced as the latter is pushed to the far-left region of Figure 156 and the lowest values of EEOI are in the design scatter diagram.

Considering all the above results, the use of EEDI in optimization studies should be limited only to a design constraint rather than an optimization target. The use as a constraint reduces the number of successful designs significantly (all runs had an overall success rate of about 55%), however, it creates a big push (considering IMO Phase 3 EEDI reduction line) for the algorithm to explore areas of the design space with maximum overall efficiency. As the algorithm is pushed to minimum simulation-based EEOI designs the degree of uncertainty is reduced significantly, and the scatter between EEOI and EEDI is reduced to a linear area. This in turn translates into a greater degree of robustness of dominant variants.

6.5.5.3. Effect of simulation on Required Ballast Water Amount

The effect of the integration of voyage simulation and application of the RHODA for ship design optimization on the reduction of the required Ballast Water amount can be witnessed also in Table 73. When comparing to the Table 61 of Deterministic Pathway optimization runs, it is evident that there is no polarization of design areas on the Pareto front and there are many intermediate solutions that represent design trade-offs between RFR/EEOI performance and required ballast water amount. Also, the steep front after the knuckle of the Pareto front described in Figure 152 shows that for a very small penalty in RFR the Required Ballast Water amount is drastically reduced. The dominant variant characteristics as shown in Table 72 further validate this observation seen all selected designs from utility function rankings (with either linear or logarithmic distribution) combine a considerable reduction in RFR and EEOI with a high magnitude reduction (region of 50%) of the Ballast Water amount. This was not feasible for the results of the Deterministic pathway where the high reduction of Ballast Water amount corresponded to a penalization of the RFR/EEDI performance and vice versa.

The combination of improvement of all merits and creation of design concepts with trade-off characteristics is solely attributed to the integration of voyage simulation inside the optimization loop and run since the performance of the vessel candidates in actual voyage scenarios rather than a single design point is assessed.

6.6. Stage 3: Multi-Objective Optimization of Zero Emission Vessel (ZEV) under Simulation and Uncertainty

6.6.1. Optimization Problem Setup

As a test case to prove the applicability of the RHODA, the application of the same methodology in the Simulation-Based optimization of Zero Emission vessels has been examined. The same optimization framework setup (with slight variations discussed here below) and an adjusted simulation module have been applied for the WOZMAX test case (using as a basis the framework under which Sim_WOZMAX_01&02 have run) but while examining ship variants that use Ammonia (NH₃) as a fuel instead of the VLSFO base of optimization runs so far. The reasons for choosing NH₃ to be the fuel for the Zero Emission Vessel test studies are the following:

1. Effectively Carbon Free

Ammonia has no carbon in its molecule and is thus effectively carbon-free by definition. The only CO₂ considerations in a well-to-wake lifecycle Green House Gas analysis are the CO₂ emissions of the pilot fuel to be used (due to the low flammability of ammonia) and the CO₂ related on the well-to-tank side of the equation related to the generation and bunkering of ammonia onboard. This results in a drastic CO₂ reduction without the mean of equivalent measures (eg carbon capturing) as in the case of synthetic methane, synthetic methanol and biofuels.

2. OPEX

The low calorific value of Ammonia (18600 kJ/kg) combined with its low density results in a considerably lower energy density when compared to other net zero or hydrocarbon-based fuels, yielding a daily vessel consumption that can 2-3 fold the one of a VLSFO equivalent design. Such OPEX implications create a drive and requirement for drastically more efficient designs due to the highly penalized RFR and thus a powerful and enhanced optimization framework.

3. CAPEX

The additional capital expenditure required for the installation of the ammonia equipment is considered excessive and high and can reach (depending on the ship type) the region of 20 million USD (reference) at the time of the writing. The reason for such high capital cost is the high volume of the required cryogenic containment system and the corresponding weight of the steel structure to support the latter as well as the cost of the Fuel Gas Supply System (FGSS), the Main Engine additional equipment and the additional safety and venting equipment required due to the toxicity of NH₃. This increase in the CAPEX leads to a consequential penalization of the RFR (following the aforementioned OPEX increase) making the RFR minimization imperative through optimization techniques.

4. Technological Considerations and Modelling

At the time of the writing, the technological development of the ammonia containment systems (either IMO C-Type tanks or membrane tanks) and the 2-stroke Main Engine technology were at such a stage where information from commercial sources and the Author’s work in the industry enabled the easier modelling and adjustment of the various models, both in terms of the Main Engine simulation model as well as the CAPEX cost assessment.

In paragraph 4.5.1.1 below, the adjustments and modifications of the methodology required to cover NH₃-powered vessels are presented. A key analysis element here is the concurrent simulation of both the VLSFO and NH₃ alternatives. So for each optimization variant, the user/designer can identify and assess both the performance as an NH₃-powered as well as a fully conventional VLSFO vessel and make more meaningful comparisons as well as understand and quantify the decarbonization impact on the operational and commercial life of the vessel.

6.6.1.1. Methodology modifications for Ammonia Powered Variant Modelling

The philosophy and process flow of the NH₃ fuel and handling system can be found in the indicative P&ID presented in Figure 168 below

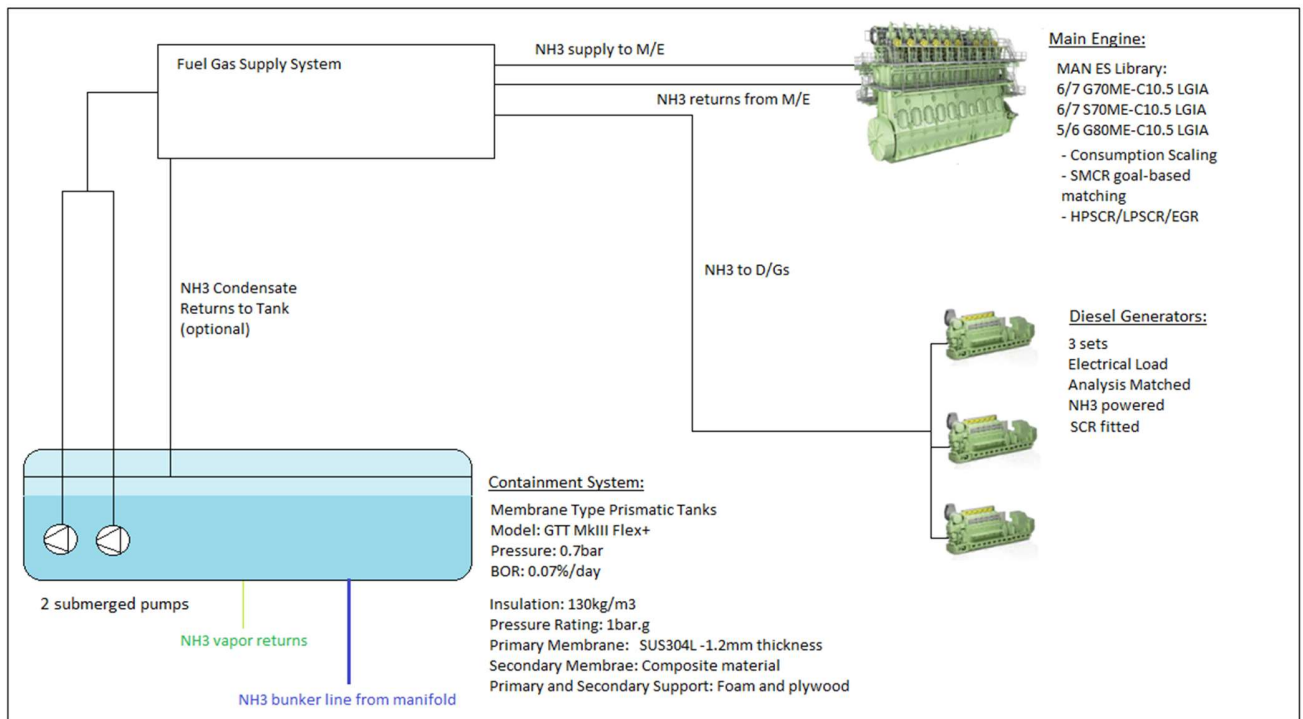


Figure 168: Indicative P&ID of the NH₃ containment, processing and consumption system.

At this point it should be highlighted that for the sake of modelling simplicity, efficiency and globality it was chosen not to examine the FGSS design but rather “macroscopically” treating it as a “black box” and modelling it as additional electrical power and steam consumer. The thermodynamic simulation of the processes in the FGSS is not considered as it is regarded as a detailed design objective. Additionally, further hybridization of the power plant with the use of

batteries and a shaft generator is also not taken into account. Given this, the adjustment of the simulation-based RHODA methodology is herein focused on the following tasks:

1. Main Engine Performance and NH₃ Consumption Modelling
2. Diesel Generators NH₃ Consumption Assumption
3. Containment System Capacity Sizing and Modelling
4. FGSS footprint assessment
5. Lightship Increase assessment
6. CAPEX Modelling
7. Probabilistic Analysis of NH₃ pricing
8. Definition of Maximum Ammonia Price (M.A.P)

Main Engine Performance and Consumption Modelling

When taking into consideration the total energy balance onboard for seagoing conditions, it is straightforward that the main engine and the energy demand of the latter constitute the primary and major consumption component of any propulsion plant. For the herein presented study of the Zero Emission Vessel Case study, a 2-stroke engine-based propulsion plant is assumed accompanied by 4-stroke Diesel Engine Generator sets. Effectively, the philosophy of the propulsion and engineering plant of the vessel is the use of the Ammonia fuelled counterparts of the existing VLSFO fuelled components. One could argue that the use of solid oxide fuel cells could replace both propulsion and electricity generation components, however, due to the very high capital intensity of this technology such applications were not examined. At the time of the code development and Thesis writing (Q2 2021), there were no available 2-stroke engines capable of burning Ammonia in operation or as readily available designs. The only contemporary Ammonia powered engine that could be used as an analysis basis was the “ME-C-LGIA” developed by MAN (MAN B&W, 2022). The data available to Authors (Table 74) however were available only for the larger bore 7 cylinders G80 engine of MAN (800mm bore), which is included in the Methodology Engine Library and repository but not frequently selected by the Engine-Propeller Matching module. Given that the same data for the same tuning are also available for the conventional, “base” engine of the G80 family (7G80ME-C10.5) and considering the thermodynamic process and the diesel cycle use of the LGIA engine, it was decided to define a load-dependent “scaling” function that will be used for all available engines in the Methodology Engine Library to convert the Specific Fuel Consumption figure (MGO basis) to Specific Ammonia Consumption. The scaling function has been modelled by deriving a logarithmic function using regression models (Figure 169), while the specific pilot consumption was defined again as a load-dependent non-dimensional function of the Specific Ammonia Consumption (Figure 170). From both the curve as well as Table 74, one can easily observe that the pilot fuel consumption is compared when compared to methane (LNG) powered or methanol engines, with the primary reason for that being the very low flammability property of ammonia. The pilot fuel is hereby assumed to be MGO or VLSFO, but can be in future analysis considered as biofuel instead.

MAN 7G80ME-C10.5 LGIA (NH3 ENGINE)				
Load	Power	RPM	SPOC	SFOC
100	24510	66.4	10.1	379.9
95	23285	65.3	10.5	375.2
90	22059	64.1	10.8	371
85	20834	62.9	11.3	367.2
80	19608	61.6	11.8	365.3
75	18383	60.3	12.3	363.7
70	17157	59	12.8	360.2
65	15932	57.5	13.5	359
60	14706	56	14.3	357.9
55	13481	54.4	15.1	357.3
50	12255	52.7	16.1	356.3
45	11030	50.9	17.3	356.3
40	9804	48.9	18.6	356.1
35	8579	46.8	20.4	354.8
30	7353	44.5	22.6	351.9
25	6128	41.8	25.6	349.4

Table 74: Performance and Consumption Engine of MAN 7G80-ME-C10.5 LGIA Engine (NH3 powered)

MAN 7G80ME-C10.5 (Conventional)				
Load	Power	RPM	SPOC	SFOC
100	24510	66.4	-	158.2
95	23285	65.3	-	156.6
90	22059	64.1	-	155.3
85	20834	62.9	-	154.2
80	19608	61.6	-	153.9
75	18383	60.3	-	153.8
70	17157	59	-	153.4
65	15932	57.5	-	153.9
60	14706	56	-	154.7
55	13481	54.4	-	155.6
50	12255	52.7	-	156.6
45	11030	50.9	-	158.0
40	9804	48.9	-	159.4
35	8579	46.8	-	160.9
30	7353	44.5	-	161.9
25	6128	41.8	-	163.9

Table 75: Performance and Consumption of Conventional "Base" 7G80-ME-C10.5 Engine

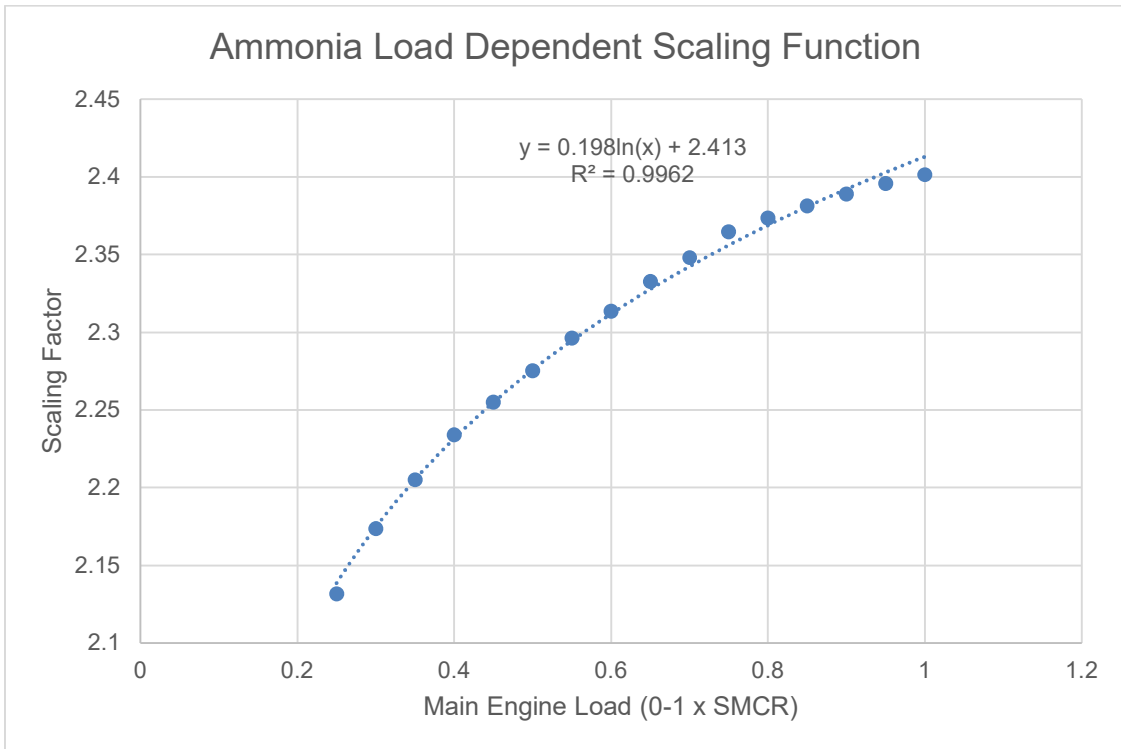


Figure 169: Modelling of Load Dependent Ammonia Specific Consumption Scaling Function

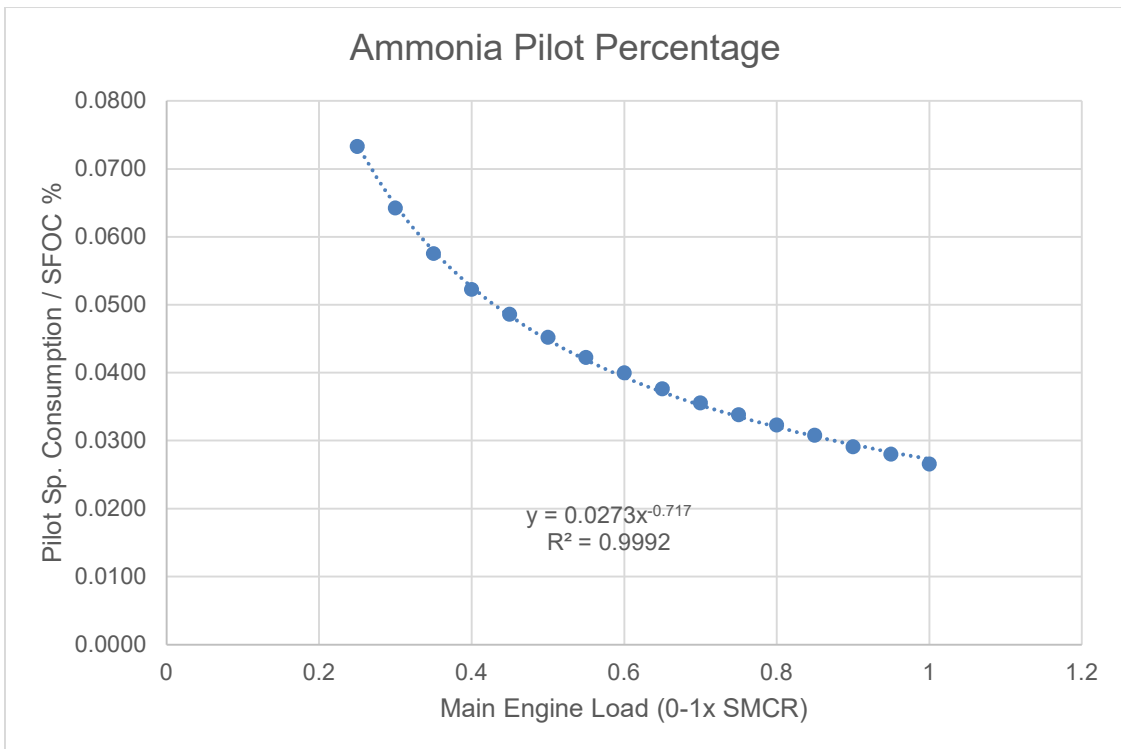


Figure 170: Modelling of Load Dependent Ammonia Specific Pilot Oil Consumption as a percentage of NH3-SFOC

Diesel Generator NH₃ Consumption Modelling

For the purposes of the present study, the diesel generators' consumption and performance modelling has been modelled by scaling the VLSFO consumption curve by the scale ratio of the Lower Calorific Values of NH₃ and VLSFO respectively.

Containment System Modelling

A membrane tank has been chosen herein as the containment system for onboard ammonia storage. More specifically, the digital twin of the GTT Mark III Flex+ prismatic membrane tank has been generated.

The capacity of the membrane tank is determined as the required capacity for performing one full roundtrip of the Brazil to China trade route without refuelling with results based on the output of the simulation code and an addition of a safety margin of 5%. Given that this is by far one of the longest routes large bulkcarrier are employed in, the calculated capacity corresponds to the worst-case scenario. The capacity of the containment system can be a separate subject of local design optimization as examined in the discussion of optimization results in paragraph 6.5.3.

Spatially, the membrane tank centre has been modelled to coincide with the midship of each vessel variant and take the same parametric prismatic shape required to match the determined required capacity. The membrane tank is located within the adjacent cargo hold with a small cofferdam around the latter. For this purpose, two additional transverse bulkheads have been added to the lightship model. The tank's special gravity, capacity and longitudinal as well as the transverse centre of gravity have been added in the Trim and Stability module, while the fuel tanks have been removed. With the above formulation, the loss of cargo as well as new loading cases have been assessed. A sketch of the relevant arrangements of the Ammonia Bunker Tank (membrane), FGSS Room, NH₃ lines and vent lines can be seen in the below Figure 171. The relevant arrangements are under the provisions of the IGF Code (IMO, 2017) .

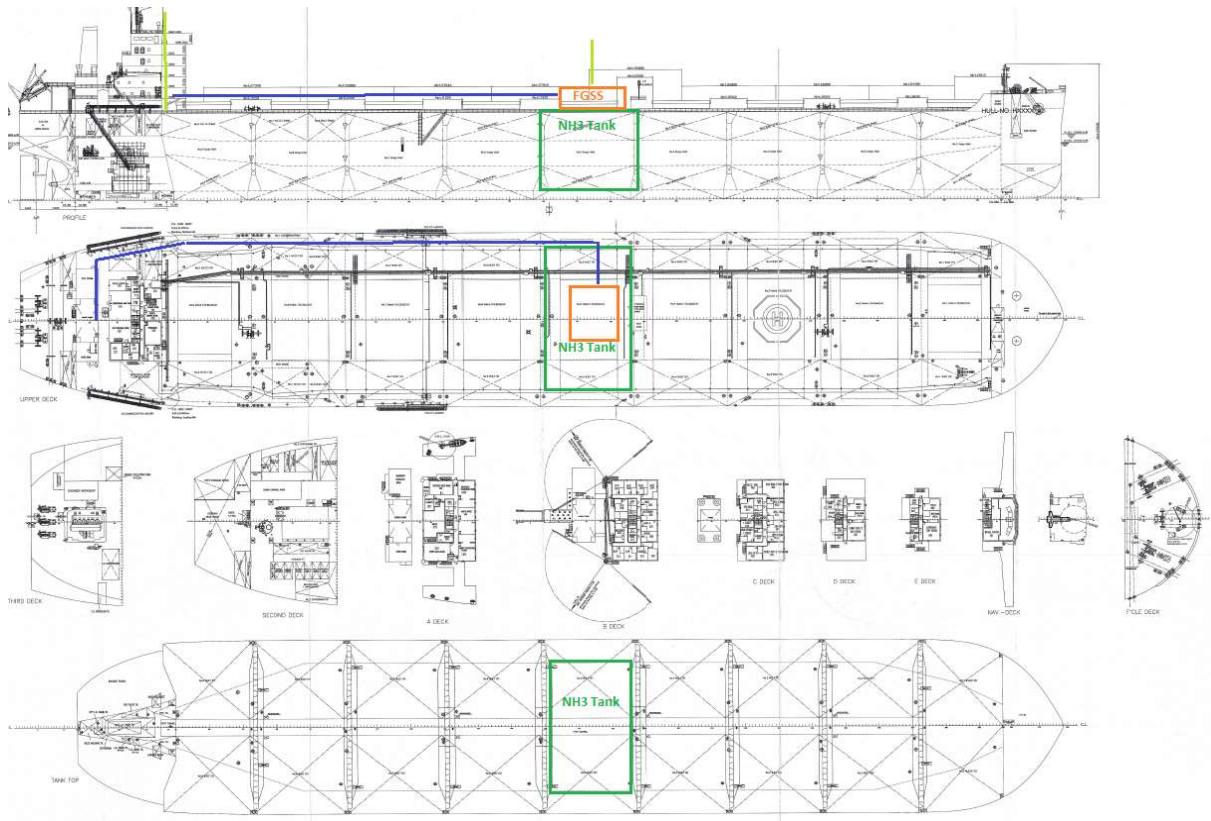


Figure 171: Sketch of the relevant locations of the NH3 tank (green) , FGSS Room (orange) , NH3 lines (blue) and Vent lines (light green)

One of the most important elements of the membrane is the cost of the latter and how this affects the additional CAPEX required for the NH3 variants. The cost has been modelled parametrically and as a function of volume based on available commercial sources of the Author (Table 76). A linear curve of the USD/m³ containment curve has been introduced in the model accordingly (Figure 172).

Nominal Capacity (m ³)	Cost	Volumetric Cost Ratio (USD/m ³)
9,000	\$ 6,000,000	667
14,000	\$ 7,500,000	536

Table 76: Cost Basis and Non-dimensional costs of cryogenic Membrane Tanks

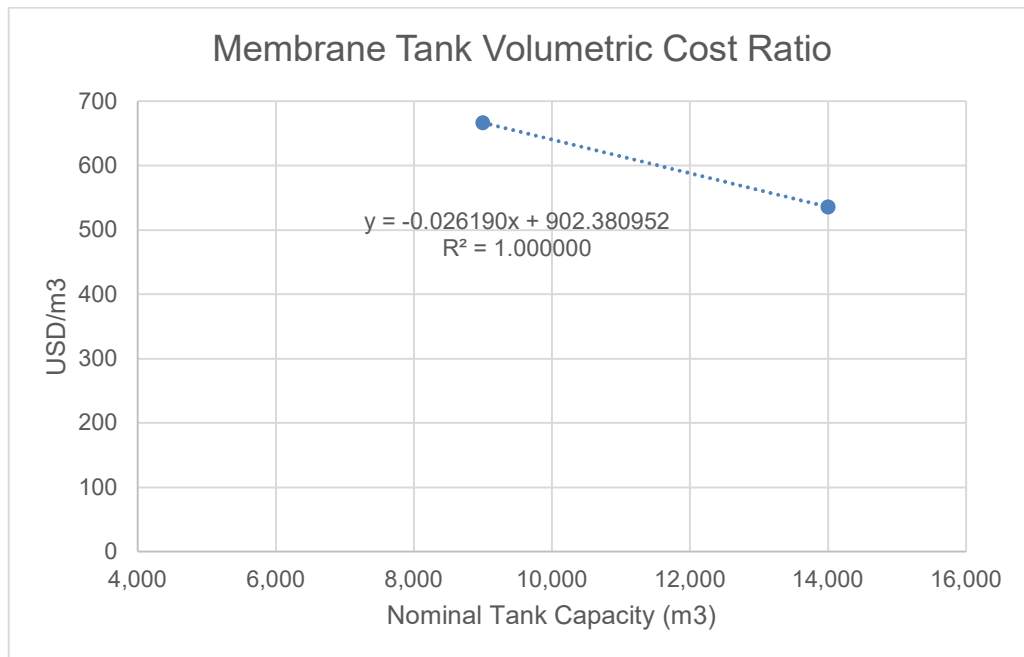


Figure 172: Membrane Tank Volumetric Cost Ratio (linear modelling)

FGSS system basic philosophy and sizing.

The FGSS system has been assumed as a black box, being modelled as only an electrical and steam consumer, with a constant load (kW) and steam consumption (kg/h) assumed. As this is a preliminary ship design context exploration it was considered sufficient.

CAPEX modelling

The assessment of the additional capital expenditure to cover the cost required for the NH3 containment, processing and combustion equipment as well as safety and venting equipment is important due to its effect on RFR. The total additional expenditure is decomposed into the categories depicted in Table 77.

Cost Category	Assumed Cost Range (USD)
Containment System	$-0.026190 * Volume + 902.380952$
Main Engine Equipment & Modifications	\$ 4,000,000
Fuel Gas Supply System	\$ 4,500,000
Structural Reinforcements	\$ 3,000,000
Venting Arrangements	\$ 500,000
Safety Equipment	\$ 100,000

Table 77: Additional CAPEX Decomposition

Ammonia Pricing probabilistic approach to uncertainty modelling.

As NH₃ has not been used as a marine fuel in the past there is little to no reference (S&P Platts, 2022) about the pricing of the latter in such a way that the distribution and bunkering networking is accounted for. Furthermore, despite the existence of references for ammonia pricing from the heavy land-based industry (fertilizers), this is primarily for “brown” ammonia as shown in Figure 173: Pricing of ammonia in various regions from 2010 to 2019 (Fertecon, 2020).

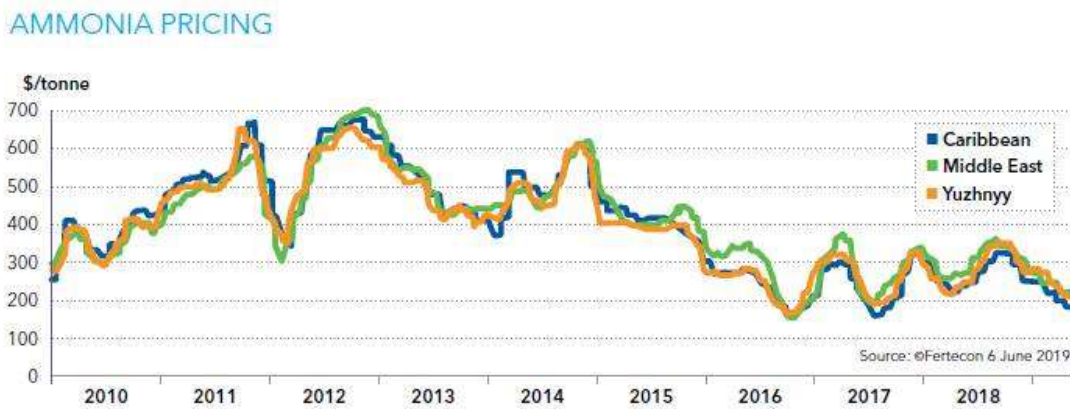


Figure 7: Ammonia pricing in various regions since year 2010. Source: Fertecon

Figure 173: Pricing of ammonia in various regions from 2010 to 2019

Brown ammonia, however, has a considerable CO₂ footprint since is typically a side product of coal-fired land power stations or from methane consumption (European Commission, 2021). If the GWP and CO₂e tons of the same source are used for the lifecycle assessment of emissions generated on a well-to-tank basis, ammonia has a heavier carbon footprint than VLSFO. For the context of the use of Ammonia in shipping decarbonization thus, only “Blue” or “Green” ammonia are hereby considered which are either product of carbon-capturing or generated from alternative hydrogen and power sources. The pricing of this, with the uplift of the marine

distribution network, is way from available and reliable. For this reason, a hybrid approach has been employed as a first attempt to price NH₃ within the context of RHODA.

In the first stage, a probabilistic, weighted average method is used in the same way as in the VLSFO based version of the methodology with the absence however of the probability distribution functions of the pricing. Instead, low, middle and high pricing are introduced at 700 USD/ton, 1200 USD/ton and 1800 USD/ton respectively. These are being attributed and matched with an equal probability of occurrence of respectively (1/3) (Table 78: Ammonia Pricing Scenarios introduced in RHODATable 78).

Price Scenario	Unit Pricing (USD/ton)	Probability of Occurrence (%)
Low	700	33.3%
Middle	1200	33.3%
High	1800	33.3%

Table 78: Ammonia Pricing Scenarios introduced in RHODA

A higher combined probability is given for the high and middle scenarios. This choice is done as in the first years of NH₃ production the unitized production is expected to be at a higher side before scaling up of the electro fuel and processes can drive the pricing down.

Definition of Maximum Ammonia Pricing (M.A.P).

A second attempt to map the pricing of NH₃ is through the introduction of a new design metric, the Maximum Ammonia Pricing (M.A.P). This metric was conceived by the Author in the preliminary assessment of NH₃-powered concepts of VLCCs Joint Industrial Projects (JIP) and has been inspired by the definition of the Required Freight Rate design metric. In this context, the Maximum Ammonia Price reflects the maximum allowable pricing of NH₃ that will allow an NH₃-powered vessel to recover the additional CAPEX as well as OPEX (due to the 3-fold daily consumption) within 10 years from delivery of the NH₃-powered vessel (or retrofit) taking into account the savings realized from the reduced CO₂ taxation. This is being realized in the below formula:

$$MAP = \frac{FOC+CO_2-FOC_{Diff}-Pilot_Cost-Pilot_CO_2cost}{Annual\ NH\ Consumption} \quad (85)$$

Where:

- $FOC_{Diff} = \frac{AddCAPEX}{Amortization}$ (86)
 - AddCAPEX is the additional CAPEX of the NH₃ onboard containment, processing and combustion equipment.

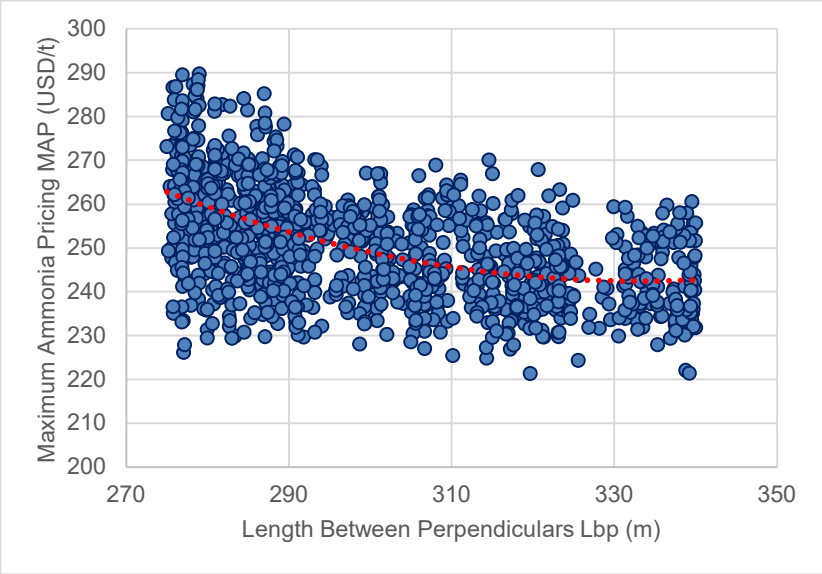
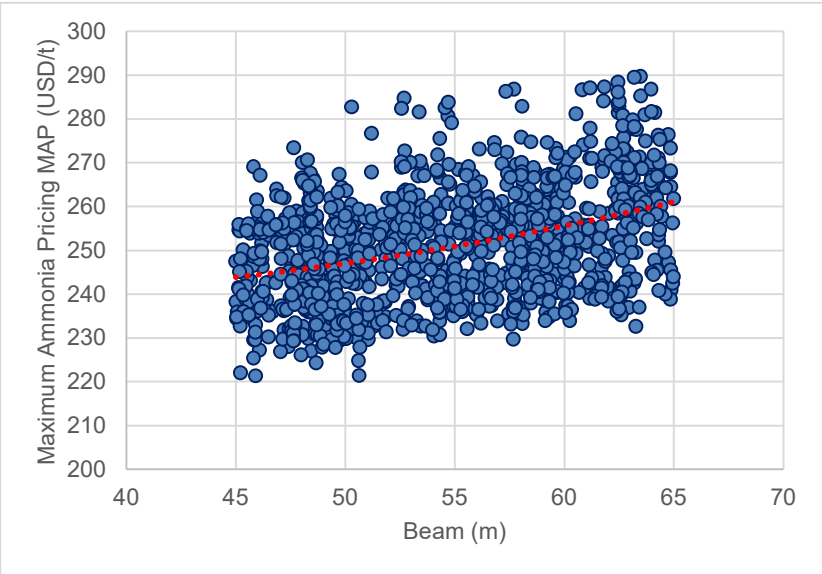
- *Amortization* is the time by which the additional investment is required to be amortized
- *FOC* is the Annual Fuel Cost of the VLSFO variant
- *CO2* is the Annual Emission tax cost of the VLSFO variant
- *Pilot_Cost* is the annual cost of the pilot fuel amount (calculated from the simulation module)
- *Pilot_CO2cost* is the annual taxation of the CO2 emitted from the combustion of pilot fuel.

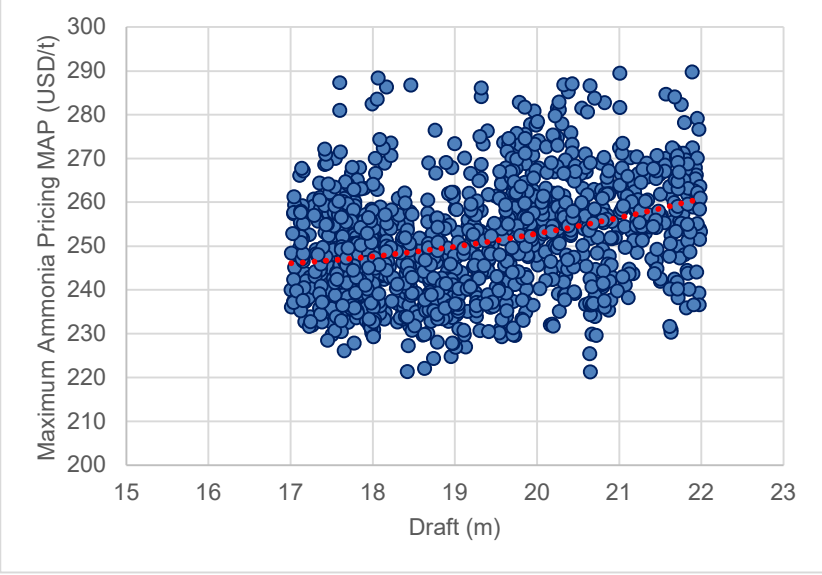
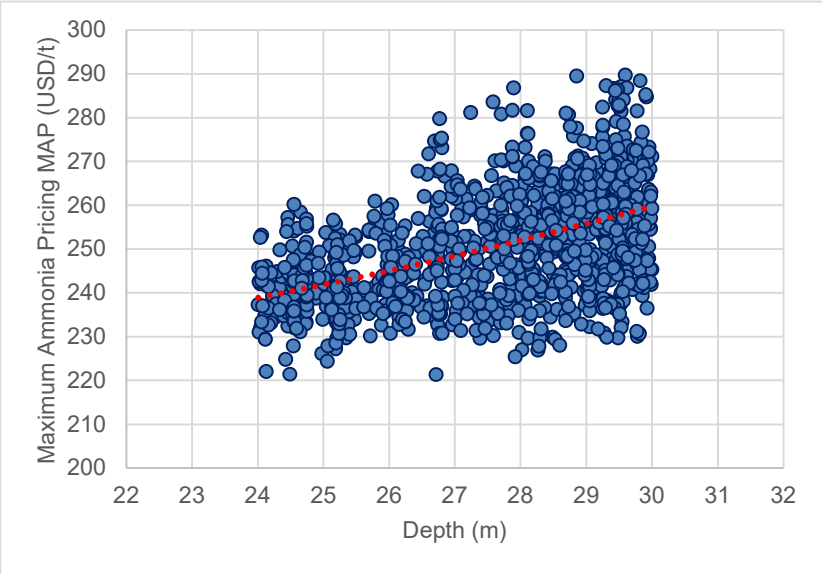
6.6.2. Sensitivity Analysis

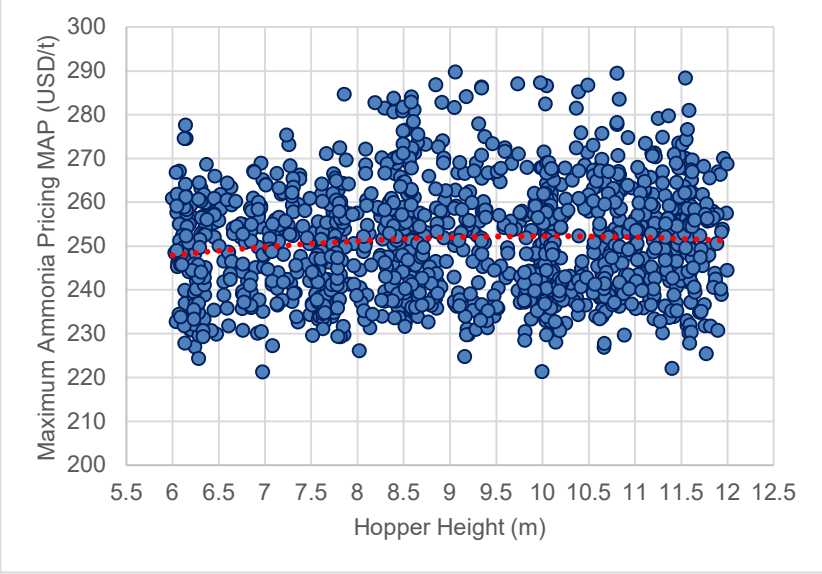
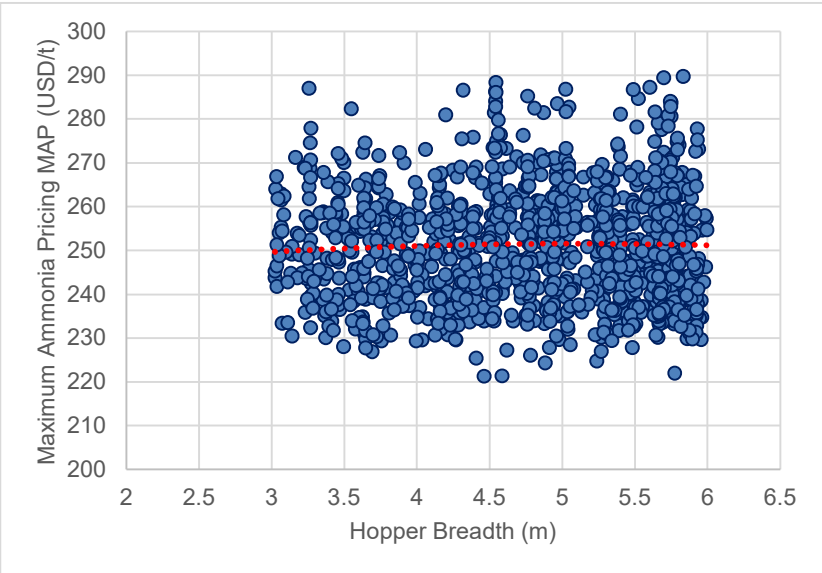
Considering that the multi-objective optimization case studies of Zero emission vessels has been based on the same RHODA model as their VLSFO powered counterparts, the focus of the sensitivity analysis in this paragraph is to expand the insights gained in paragraph 6.5.2 and focus on the sensitivity and effects of the various variables on the Maximum Ammonia Pricing (MAP) as witnessed in Table 79 below as well as Appendix I.

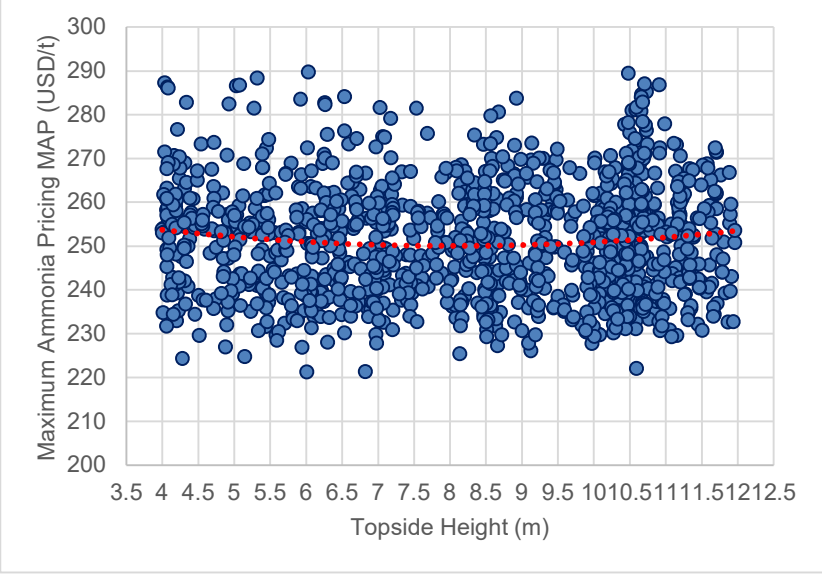
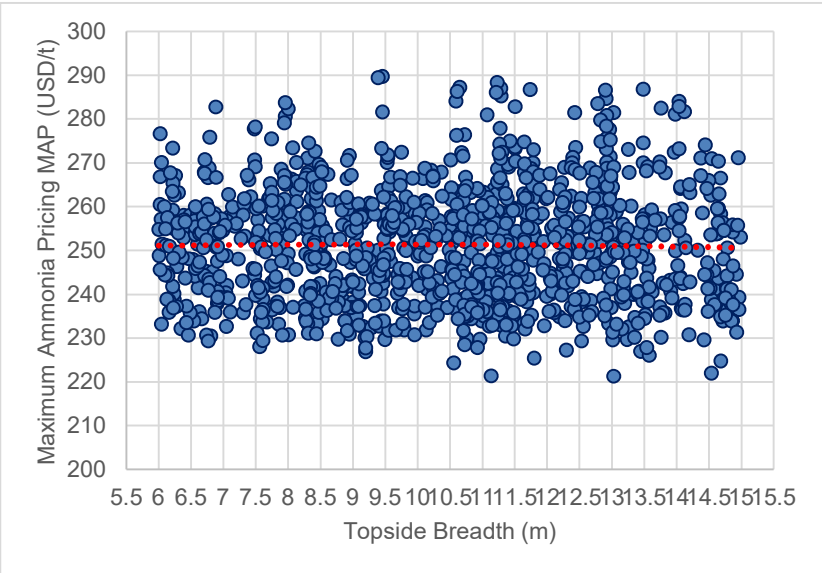
By reviewing Table 79, the following interesting observations can be withdrawn:

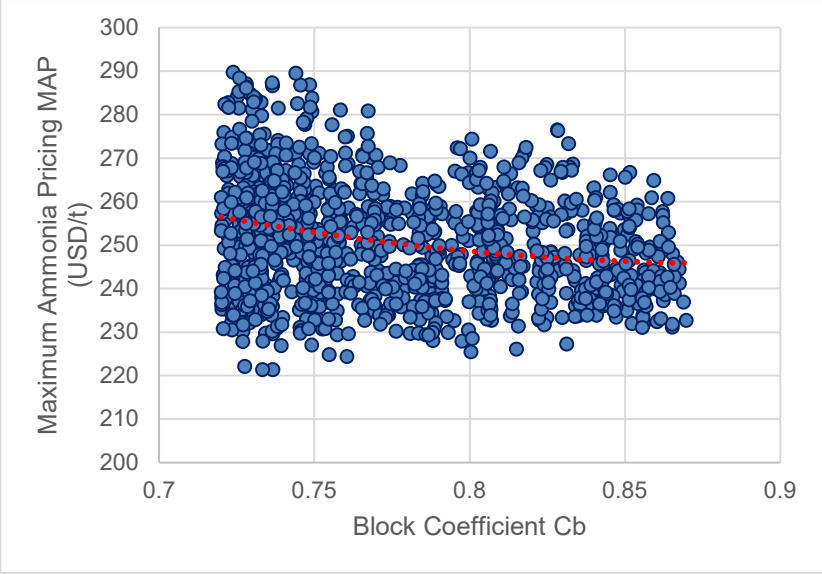
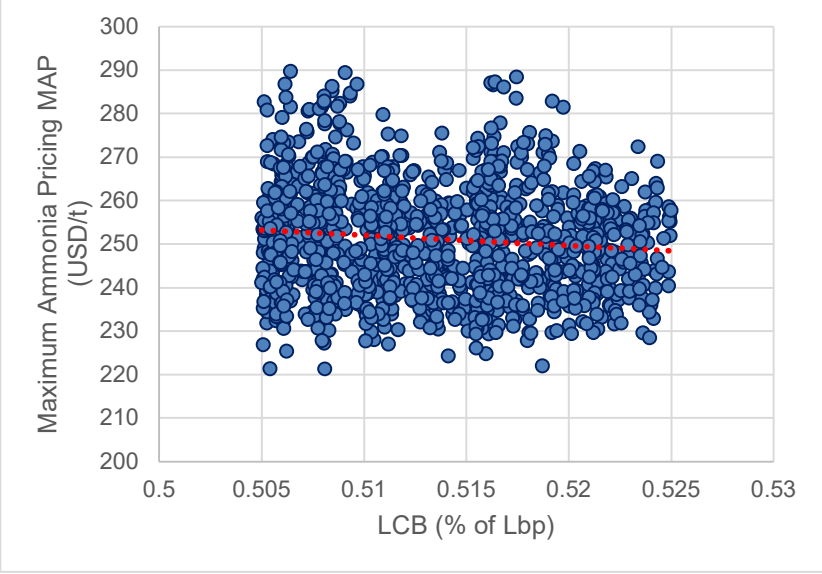
- Slender designs with short length, wide beam, deep draft and deck high have the best MAP performance making them the most economically viable Zero Emission Vessel variants.
- Cargo Hold variables have a zero effect on MAP.
- Similarly, Bilge Width and Height have also a zero effect on MAP.
- LCB that had a zero sensitivity in previous studies no has a slight sensitivity with vessels with aft LCB featuring higher MAP values. The reason for this change within simulation-driven studies results (VLSFO and NH3 runs) is that LCB ratio plays an important role in calm water resistance and can decrease the latter. When taking into account the 3-fold increase of the Specific NH3 Consumption of the engine due to the low calorific value of NH3, any effect on calm water resistance (decrease or increase) is magnified.
- Propulsion Parameters Sensitivity:
 - In general MAP is favoured by high pitch and lower diameter propellers.
 - Low Expanded Area ratio also has a positive effect (increase) on MAP.
 - High pitch is a typical design measure to increase efficiency and decrease installed power.
 - The decrease of diameter and expanded area ratio is where the algorithm is lead in order to comply with the constraints of Light Running Margin (LRM) and torque limitations of the engine.

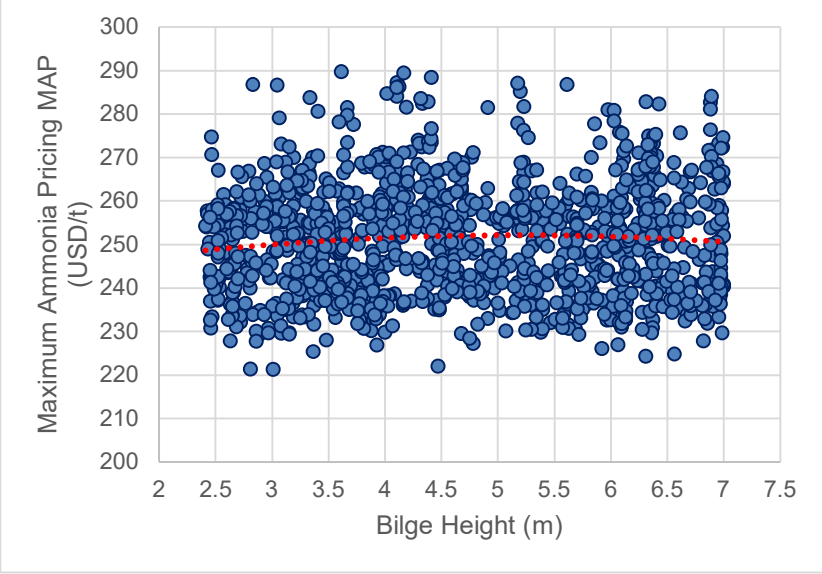
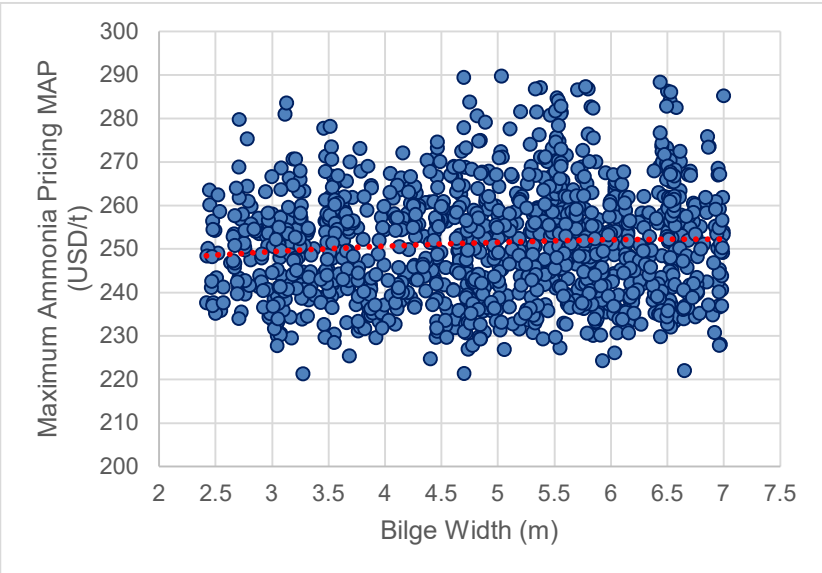
ID	Design Variable	Effect on MAP
N_01	Length between Perpendiculars	<p>By increasing Length MAP decreases (negative).</p> 
N_02	Beam	<p>By increasing Beam MAP sharply increases (positive).</p> 

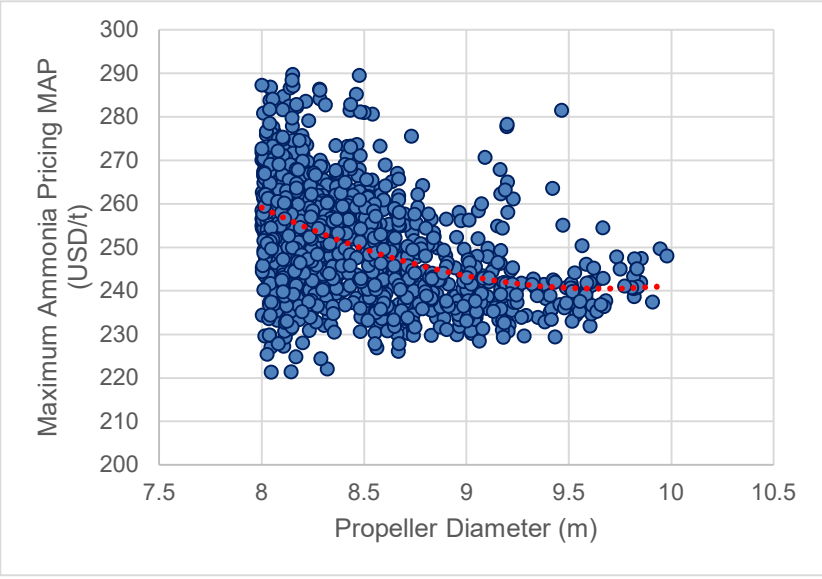
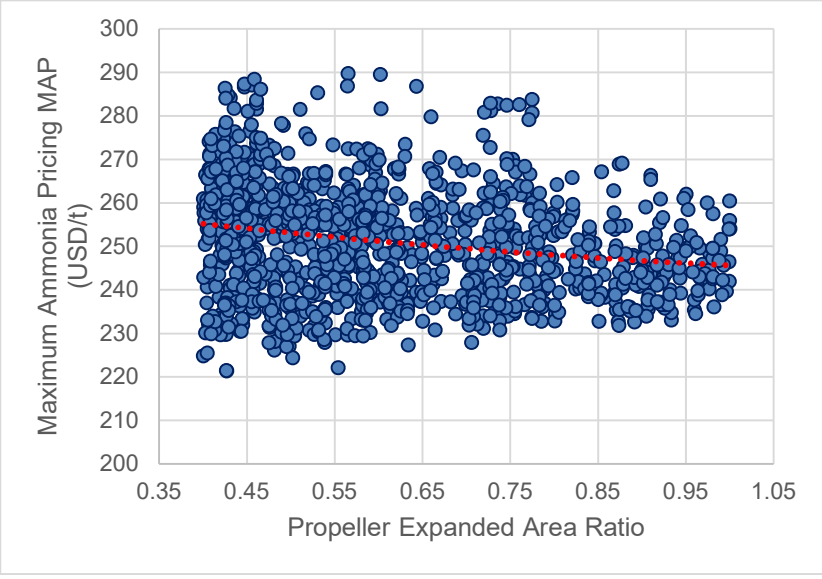
<p>N_03</p>	<p>Draft</p>	<p>By increasing draft MAP also increases (positive effect)</p> 
<p>N_04</p>	<p>Deck height</p>	<p>By increasing Deck Height MAP sharply increases (positive effect)</p> 

<p>N_05</p>	<p>Hopper Height</p>	<p>Little to zero sensitivity of MAP on Hopper Height</p> 
<p>N_06</p>	<p>Hopper Breadth (m)</p>	<p>Little to zero sensitivity of MAP on Hopper Height</p> 

<p>N_07</p>	<p>Topside Height (m)</p>	<p>Little to zero sensitivity of MAP on Topside Height</p> 
<p>N_08</p>	<p>Topside Breadth (m)</p>	<p>Little to zero sensitivity of MAP on Hopper Breadth</p> 

<p>N_09</p>	<p>Block Coefficient Cb</p>	<p>High sensitivity of MAP with decreasing Cb yielding higher MAP values (positive effect)</p> 
<p>N_10</p>	<p>LCB (%Lbp)</p>	<p>Small sensitivity, lower LCB values (towards the aft) increases MAP slightly</p> 

<p>N_11</p>	<p>Bilge Height (m)</p>	<p>Little to zero sensitivity of MAP on Bilge Height</p> 
<p>N_12</p>	<p>Bilge Width (m)</p>	<p>Little to zero sensitivity of MAP on Bilge Width</p> 

<p>N_13</p>	<p>Propeller Diameter (m)</p>	<p>High sensitivity of MAP on propeller diameter with smaller diameters yielding higher MAP values (positive effect) , wide scatter and big concentration on this area.</p> 
<p>N_14</p>	<p>Propeller Expanded Area Ratio</p>	<p>Expanded Area Ratio decrease triggers slight increase on MAP values</p> 

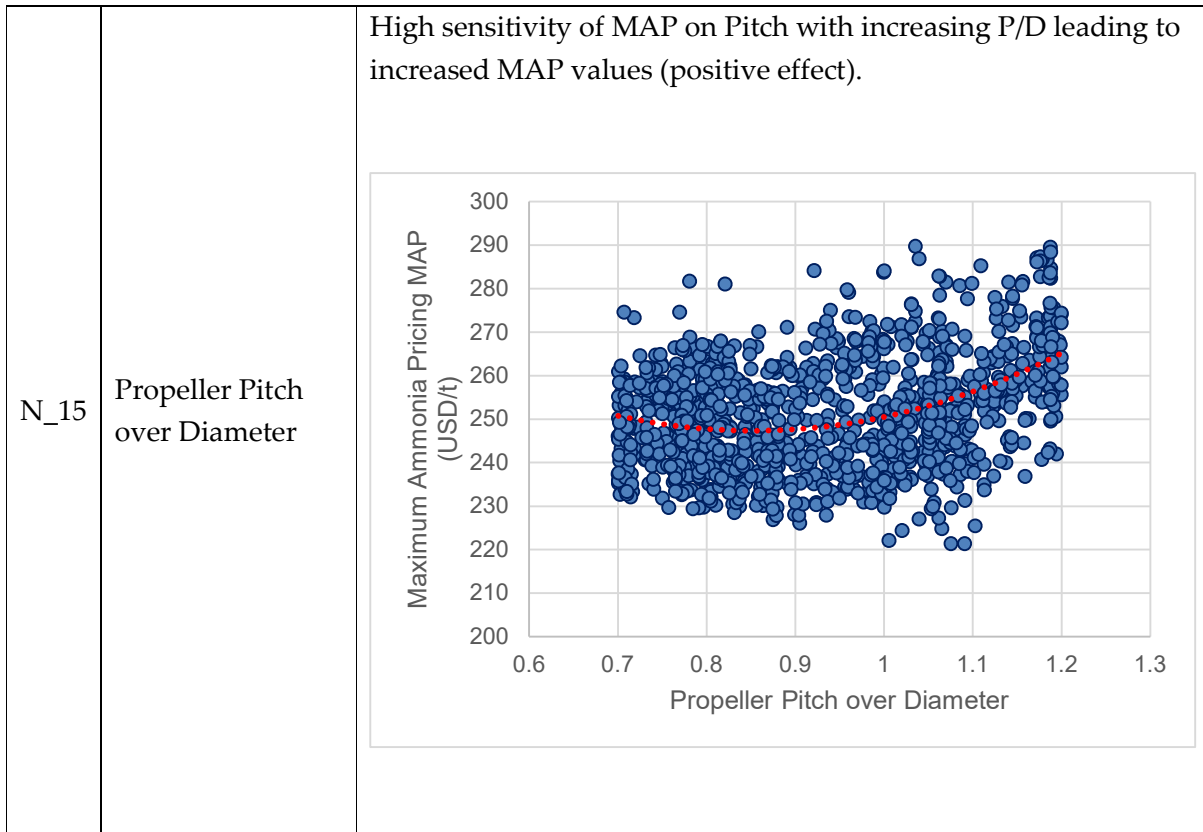


Table 79: MAP Sensitivity on Design Variables – Simulation Driven Zero Emission Vessel Case Studies

Apart from the above formal analysis of MAP sensitivity, an additional way to observe the sensitivity of the methodology for Zero Emission vessels is to examine the relationship of the optimization objectives between the VLSFO and NH3 powered designs. In Figure 174, the scatter diagram of the design variants depicts the simulation-based RFR of an NH3 powered vessel versus the simulation-based RFR of the same vessel if it was powered by VLSFO. Both merits are derived concurrently from the adapted methodology, as described above, in order for a given design variant to assess its performance (in terms of RFR and EEOI) for both VLSFO and NH3 fuels. Evidently, from Figure 174 the correlation is linear and very strong. This is to indicate the wide applicability of the herein proposed methodology, as a design that has a superior performance for VLSFO fuel will also be superior if in turn uses Ammonia as a fuel. In this sense, the methodology sensitivity remains the same, while the magnitude of the RFR is scaled up considerably.

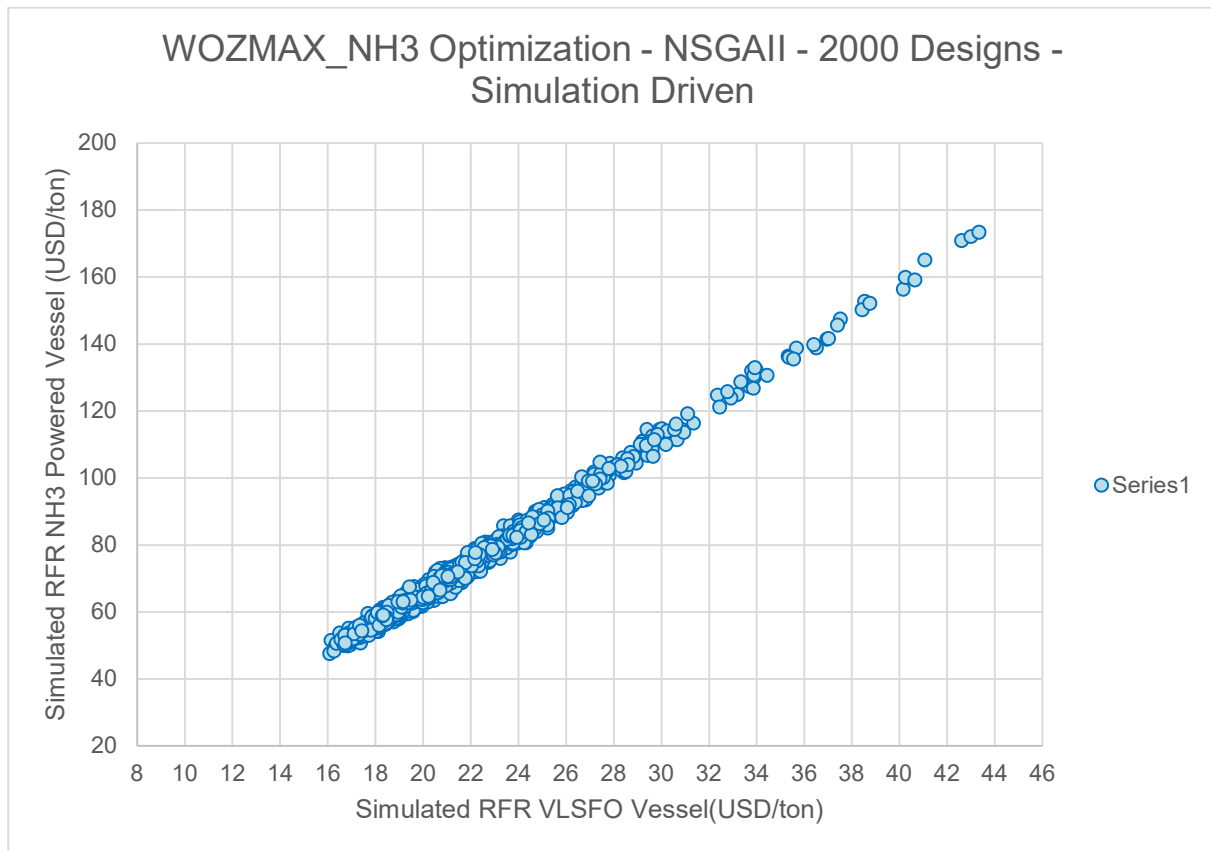


Figure 174: Sim_WOZMAX_03 / Simulated RFR of NH3 powered Vessel vs. Simulated RFR of VLSFO powered Vessel with Baseline Vessel superimposed.

If now instead a variant of the RFR calculation is introduced, namely the simulation-based RFR for NH3 powered vessels assuming these are under T/C employment. That means that the fuel cost (NH3 cost) and, presumably, the CO2 emission cost in the Laden voyages are covered under the T/C charter party agreement. When comparing this index to the previously examined simulation-based RFR for NH3 powered vessels (Figure 175), the linear correlation is as expected retained. However, due to the absence of the component and contribution of the Laden voyages in RFR, there is a region of uncertainty in the graph. For example, for a vessel with RFR for NH3 of 75 USD/ton, there is a range of RFR for NH3 under T/C from 38 to 47 USD/ton, indicating a range of uncertainty of about 19%. This percentage and the corresponding scatter are attributed to the absence of the cost of Laden voyages in the RFR under T/C. In the results analysis paragraph a further analysis is made on what is the required carbon pricing to offset the additional Total Cost of Ownership of NH3 powered variants.

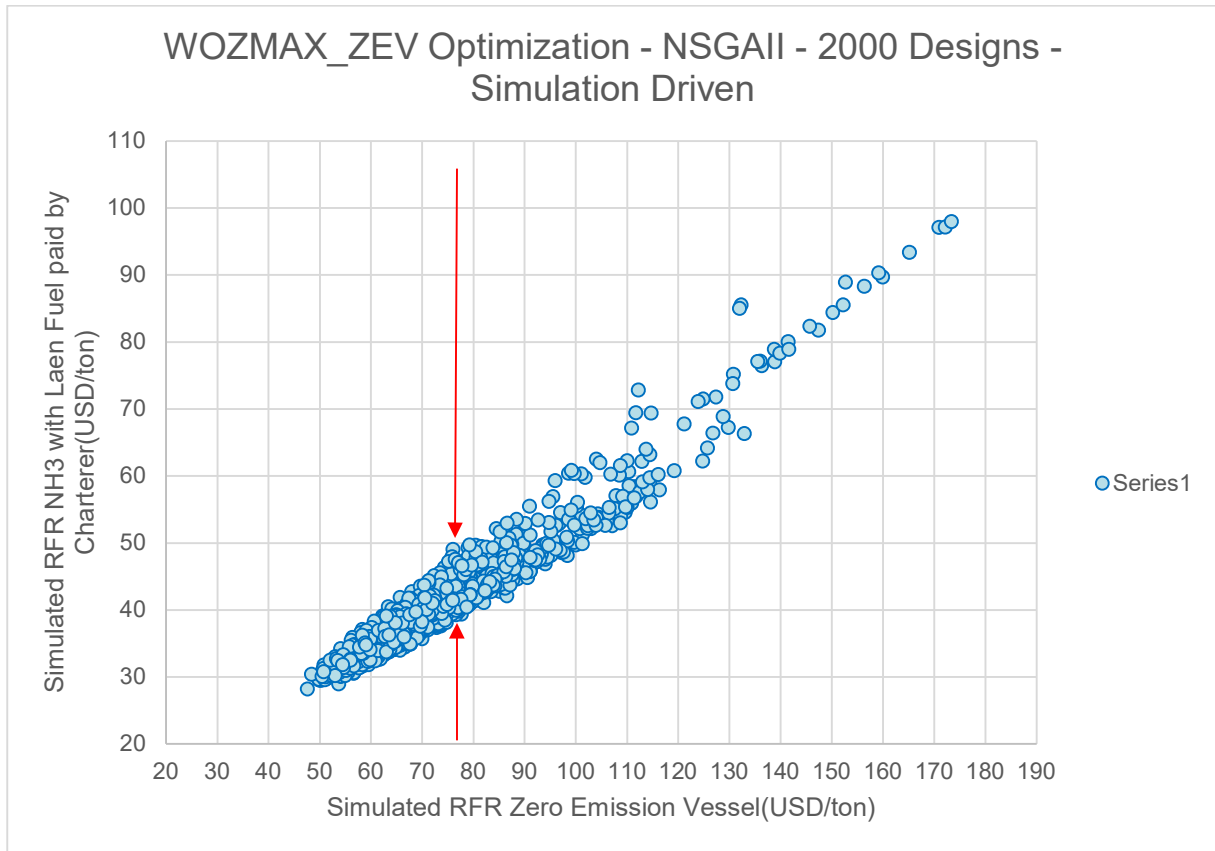


Figure 175: Sim_WOZMAX_03 / Simulated RFR of NH3 powered vessel vs Simulated RFR with Laden Consumption covered by Charterers

6.6.3. Optimization Results

The subject run has been conducted using the same variables as the simulation-driven runs for the WOZMAX ship type (ID: Sim_WOZMAX_01 & Sim_WOZMAX_02), the NSGAI algorithm as design engine with the necessary provisions and modifications to depict an Ammonia powered design as described in paragraph 4.5.1. As described there, it is important to stress that the product of the simulation module has results both for the Zero Emission Vessel variants (NH₃) as well as the VLSFO conventional counterpart of each one. The EEDI Phase 3 constraint was similarly used here, with little to no effect, since the reduction of the EEDI has been more than 80% due to the use of Ammonia as a fuel. As proven in the Sim_WOZMAX_02, the extension of the number of generations to 200 (corresponding to 2000 variants) has been similarly applied in order to positively influence the optimization effect and Pareto front structure and density. For this optimization run (ID: Sim_WOZMAX_03) a total number of 1196 viable designs were generated out of a total population of 2000 designs corresponding to 59.8% success rate.

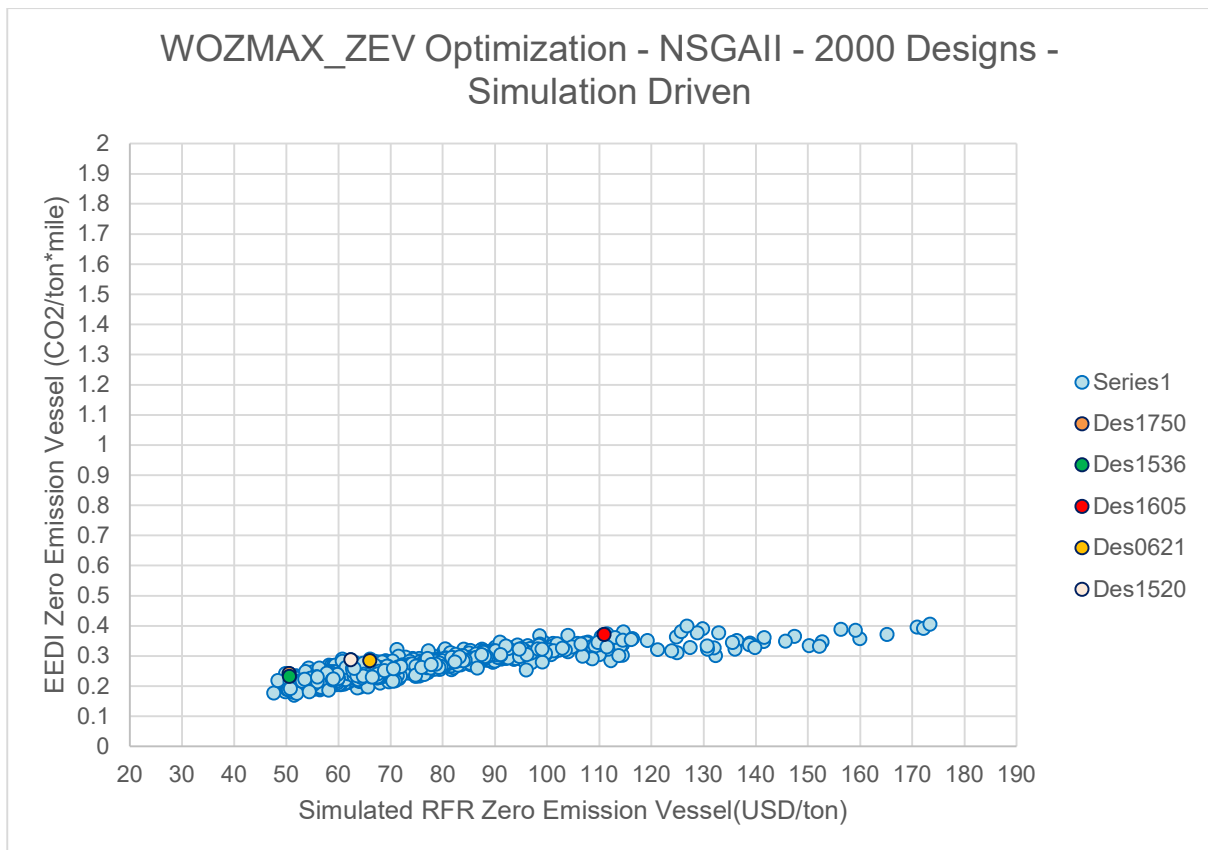


Figure 176: Sim_WOZMAX_03 / EEDI vs Simulated RFR of NH₃ powered Vessel with Baseline Vessel and dominant variants superimposed.

In Figure 176 the drastic reduction of the EEDI value is clearly identified. From previous runs the EEDI of dominant variants for WOZMAX ship types was in the region of 1.8 to 2.0 tCO₂/ton*mile, while for the cases examined here the equivalent range is between 0.2 to 0.4 tCO₂/ton*mile, corresponding to a reduction at the range of 78-90%. Such a drastic reduction, contributed to the absence of carbon in the molecule of Ammonia (NH₃), removes completely both the EEDI as well as the EEOI from affecting the design decisions and sensitivities as in previous optimization studies, reducing the optimization problem to examining trade-offs in the relationship of Required Ballast Water amount and simulation-based RFR and the minimization of both such merits.

The relationship between the simulation-based RFR for the Zero-emission vessel variants retains the same relationship with the Required Ballast Water amount as in the simulation-based runs for conventional vessels (Figure 177). The structure, density and Pareto front characteristics are the same as in the previous runs, while the trade-off in corresponding variant design characteristics and parameters remains also the same.

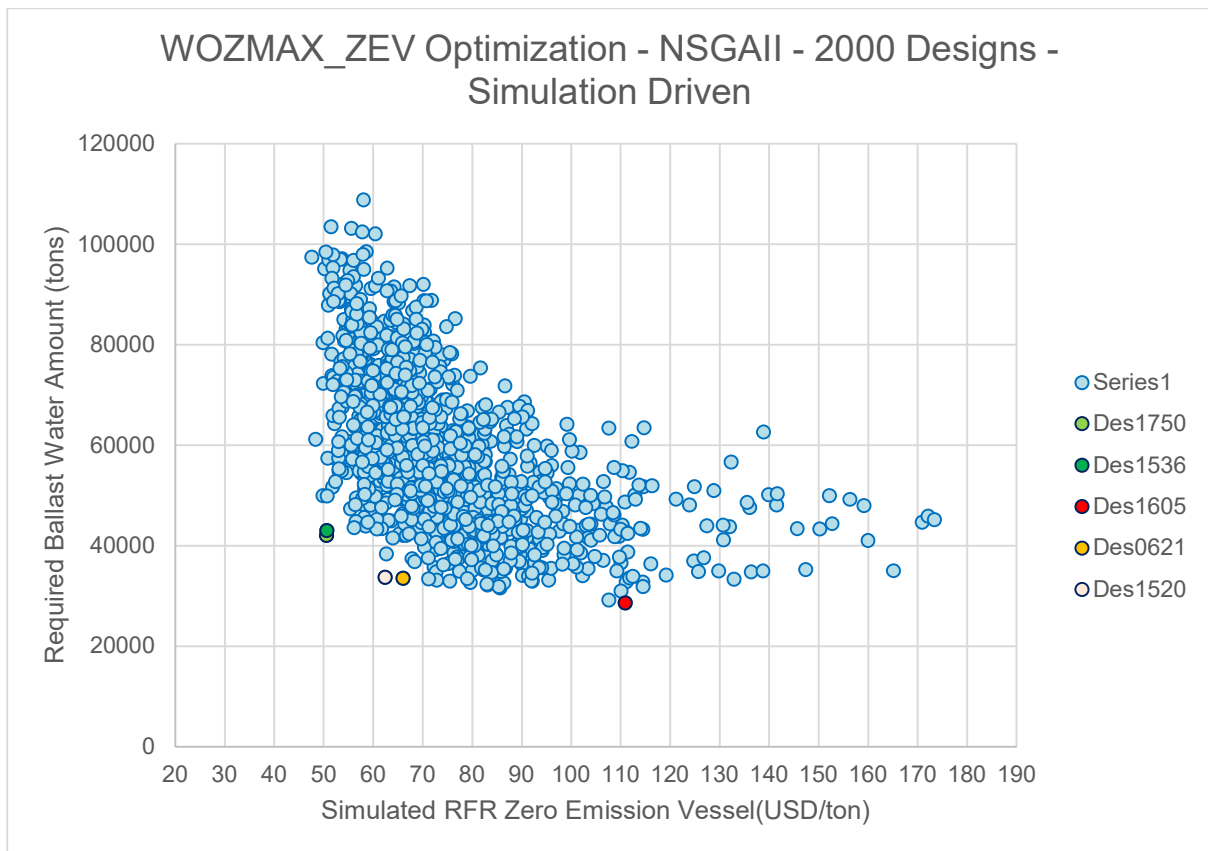


Figure 177: Sim_WOZMAX_03 / Required Ballast Water Amount vs Simulated RFR of NH₃ powered Vessel with Baseline Vessel and dominant variants superimposed.

The steep end at the left-hand side of the Pareto front remains the same. The RFR minimization remains here of paramount importance, especially when taking into account the magnification of the latter due to the ammonia consumption (3 times fold when compared to the VLSFO

equivalents). Using the same utility function picking techniques, the dominant variants have been identified. The variant with the lowest Required Ballast Amount (ID 1605) in this case is not to be considered for further exploration since a decrease in the Ballast amount of 33% (from 43,000 tons of the nearest dominant variant to 28,600 tons) leads to an increase of the RFR of almost two-fold. When considering now the already very high magnitude of the RFR (when compared to conventional designs) such an increase makes mentioned designs economically unfeasible.

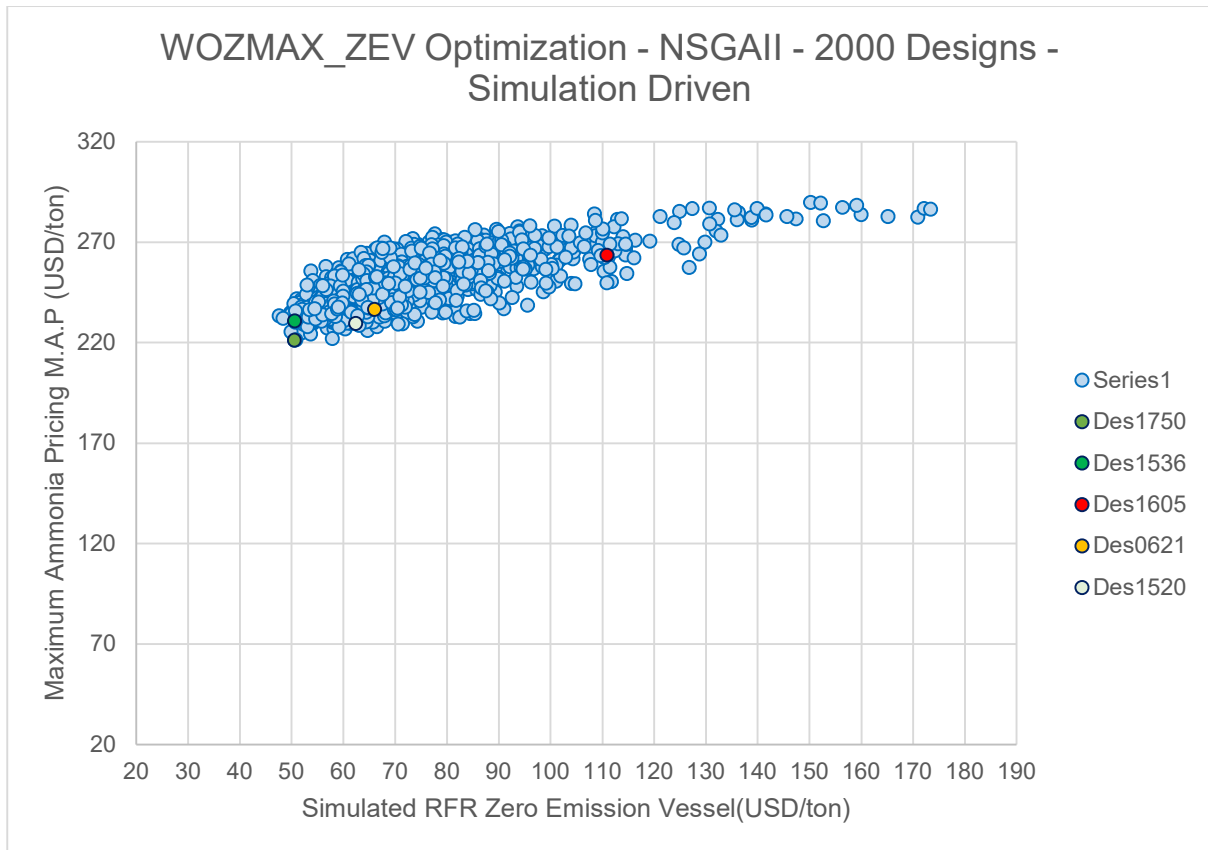


Figure 178: Sim_WOZMAX_03 / Maximum Ammonia Pricing (MAP) vs Simulated RFR of NH3 powered Vessel with Baseline Vessel and dominant variants superimposed.

In Figure 178, the newly defined Maximum Ammonia Pricing (M.A.P) scatter diagram versus the simulation-based RFR is depicted. Interestingly, despite the relatively flat shape of the scatter cloud, an upwards trend of the MAP values by increasing RFR is observed. This means that design variants with a higher simulation-based RFR also have a higher MAP and thus a higher margin on the maximum allowable value of NH3 unit pricing in order to be profitable. This is explained by the fact that such designs correspond to designs that have inherently higher fuel consumption and powering requirements (both in calm sea and actual seaways) and thus their annual fuel consumption and corresponding CO2 taxation could favour the use of NH3 instead. The reason behind this is that for a VLSFO-powered vessel the CO2 emission factor is 3.114 (European Commission, 2021) and thus the penalization in consumption is even harsher when

CO2 taxation is considered. This trend is validated by Figure 179 and the scatter diagram between MAP and the Required Time Charter Equivalent Daily rate⁶.

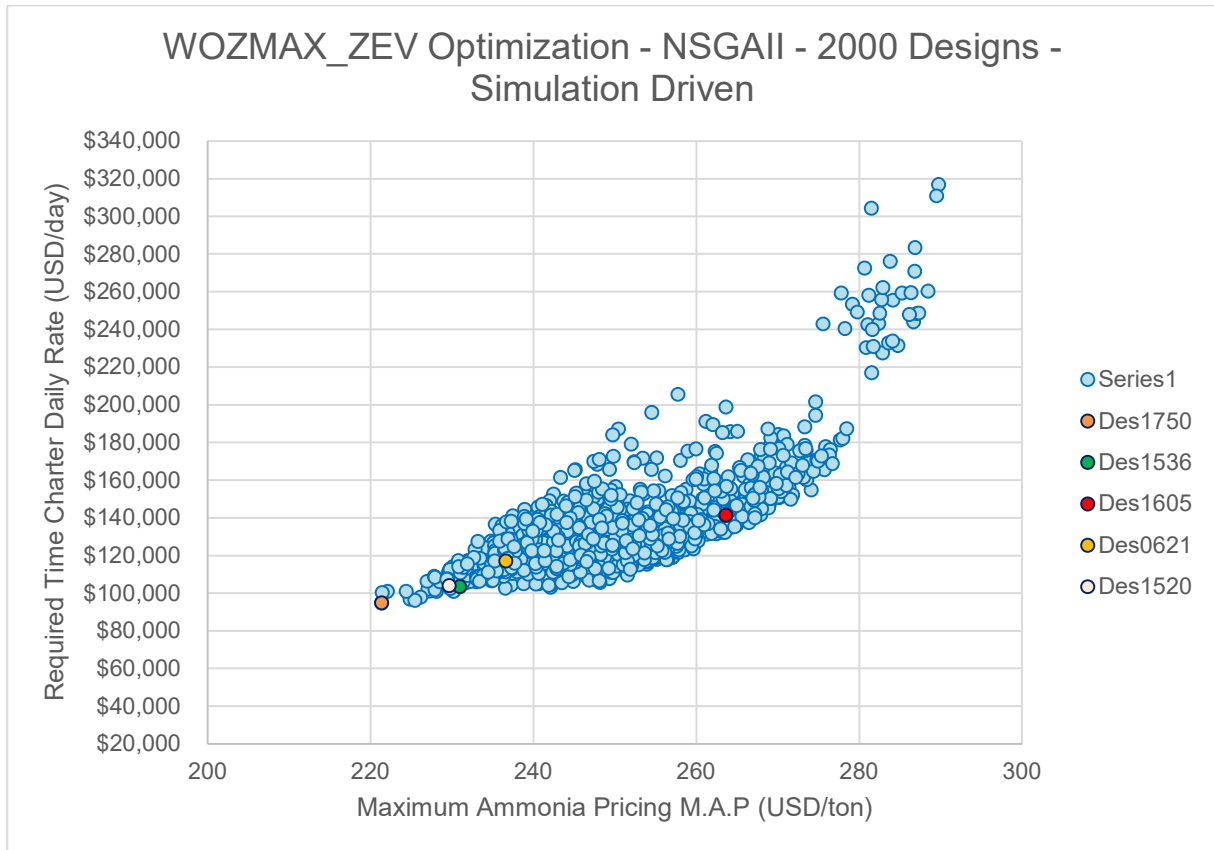


Figure 179: Sim_WOZMAX_03 / Required Time Charter Equivalent Daily Rate (TCE) vs Maximum Ammonia Pricing (MAP)

For this case, the relationship between simulation based Required TCE Rate and MAP is much cleared. By increasing MAP, the required TCE increases following a 2nd to 3rd order power curve. This relationship is stronger as the simulation based Required TCE is supposed to cover all fuel and CO2 taxation costs over the period of the charter among other economic coverages. The number and magnitude of the MAP are also converging with the calculations performed for VLCCs in industrial studies (region of 300 USD/ton) which are larger and higher consuming vessels than WOZMAX bulk carriers. This gives a preliminary estimation of where the NH3 bunkering market should move in order for the latter to make an attractive business case.

The validity and utility of RFR as a design metric are re-verified by Figure 180, representing the scatter diagram between the simulation-based Required TCE Daily Hire Rate and the simulation-

⁶ The daily charter hire if the vessel was to be Time-Chartered. It reflects the minimum hire rate to cover capital recovery in 10years , OPEX, Dry Docking costs, fuel costs for both the Laden and Ballast Condition and the CO2 taxation cost.

based RFR. These two metrics indicate a strong and linear correlation of medium inclination tangent.

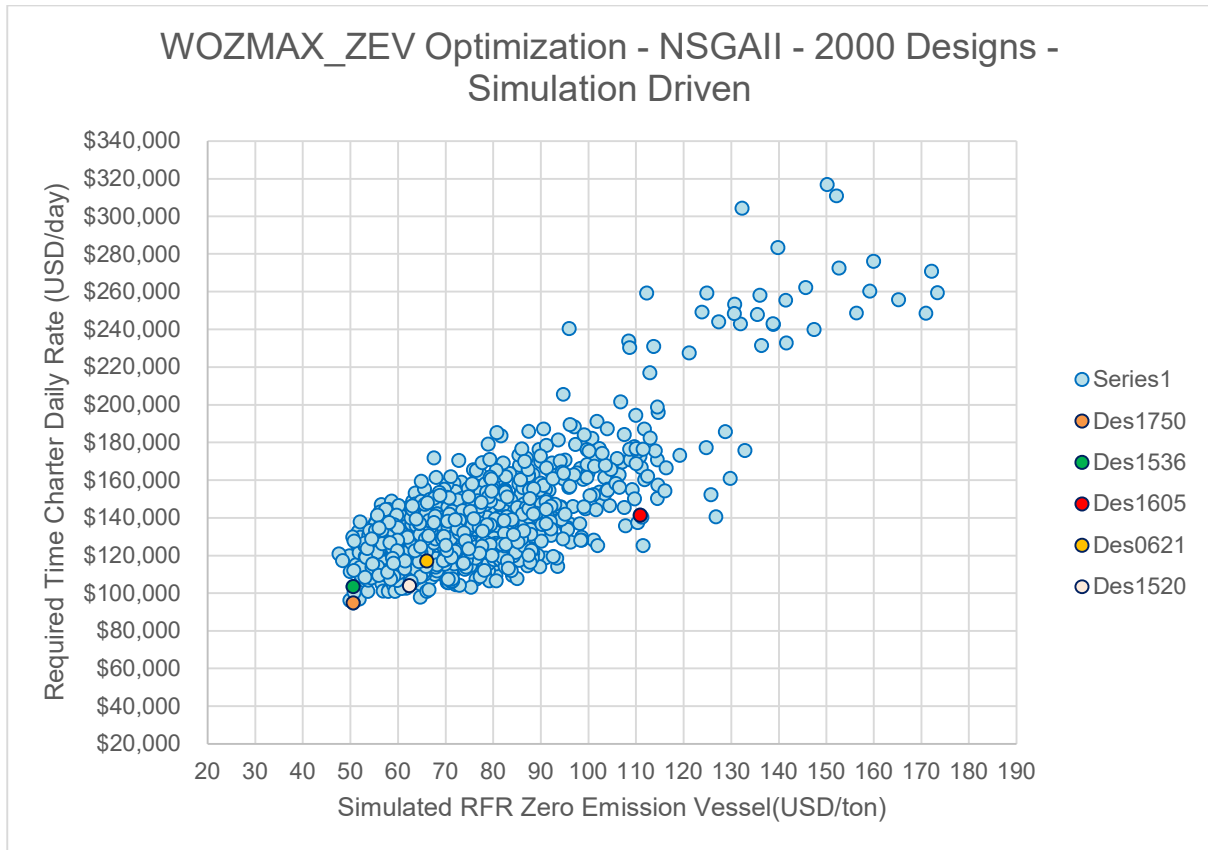


Figure 180: Sim_WOZMAX_03 / Required Time Charter Equivalent Daily Rate (TCE) vs Simulated RFR of NH3 powered Vessel with Baseline Vessel and dominant variants superimposed.

6.6.4. Design Selection, Ranking and Discussion

6.6.4.1. *Design Selection and Ranking per Run*

In the below Table 80, the ranking of the top 10 design variants for each utility weight assignment scenario (maximum weights per optimization target) and each run are depicted.

Like in previous runs of both Deterministic and Simulation-Driven Pathways, the top three designs remain unchanged (only in a different order) across different scenarios.

The basis on the rankings in Table 80, the dominant variants have been illustrated in the scatter diagrams of each run, in paragraph 6.5.3 and their principal particulars are shown and discussed in paragraph 6.5.4.2.

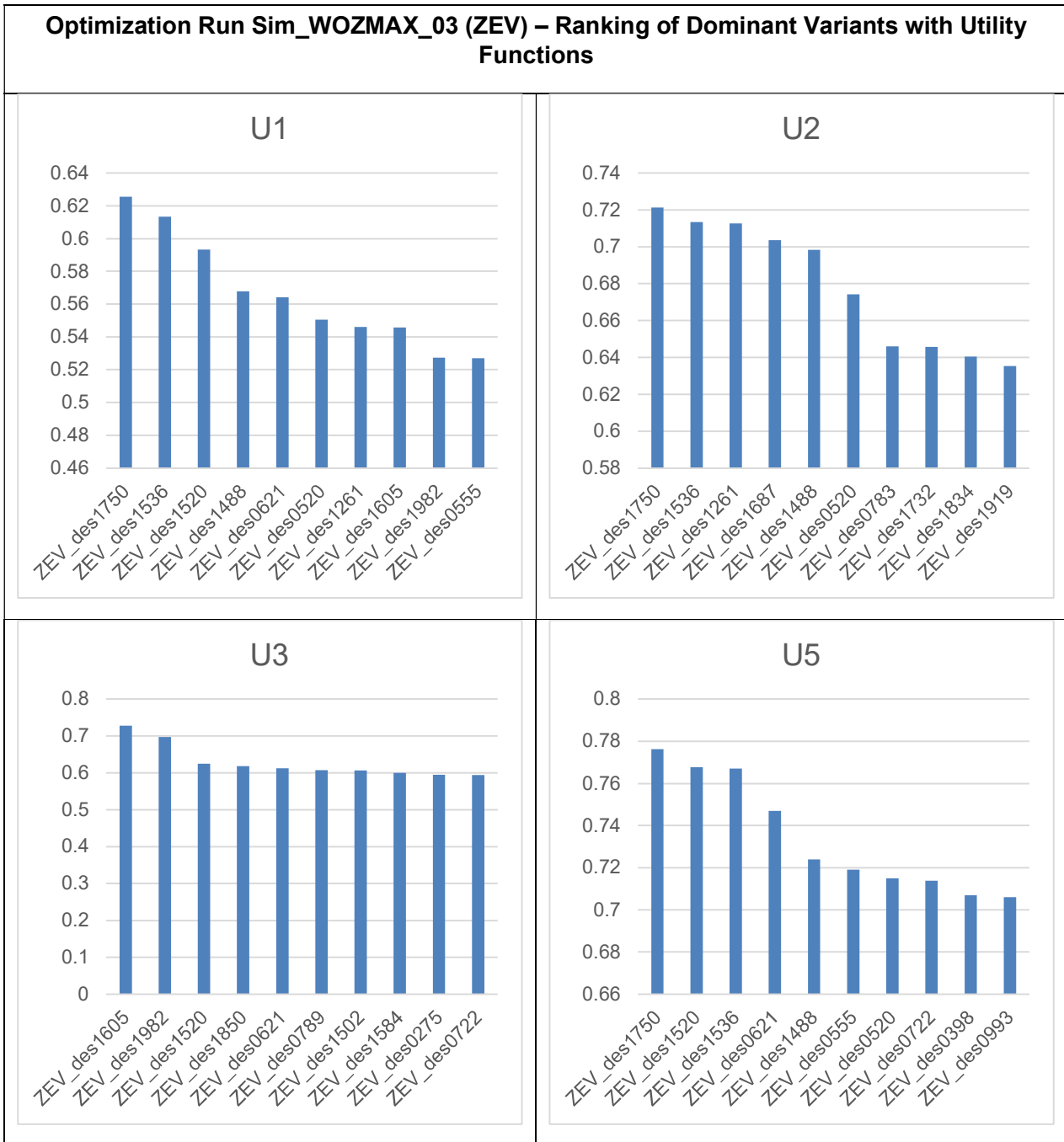


Table 80: Ranking of Optimization Dominant Variants with Utility Functions Scenarios – RUN ID Sim_WOZMAX_03 (ZEV)

6.6.4.2. *Principal Particulars of Dominant Variants*

The principal particulars of a selected group of dominant variants from the Simulation-Based Optimization Pathway runs applied for Zero Emission Vessels (Sim_WOZMAX_03 pathway_ can be found in Table 81. It should be highlighted that the role of RHODA with a simulation-based assessment for actual operating speeds is quite important in order to explore the new local minima and robust solutions considering vessels that are NH3 powered by design (not just NH3 powered versions of existing designs) with each variant however being compared to its conventional counterpart as well. With this “synchronous” optimization approach it is possible to capture the different algorithm responses, optimization effect, Pareto front formations, dominant variant characteristics and overall pathway result for a Zero Emission Vessel against a VLSFO-powered counterpart.

No.	Particular	ID1750	ID1536	ID1520
-	Run ID	Sim_WOZMAX_03	Sim_WOZMAX_03	Sim_WOZMAX_03
W_01	Length between Perpendiculars	319.663	306.659	291.792
W_02	Beam	45.911	48.606	45.813
W_03	Draft	20.648	21.631	20.722
W_04	Deck height	26.716	27.977	28.111
W_05	Hopper Height	6.973	6.205	6.286
W_06	Hopper Breadth (m)	4.462	5.263	4.035
W_07	Topside Height (m)	6.009	7.200	11.154
W_08	Topside Breadth (m)	13.030	8.948	13.013
W_09	Block Coefficient Cb	0.736	0.747	0.736
W_10	LCB (%Lbp)	0.508	0.511	0.523
W_11	Bilge Height (m)	3.008	6.369	3.080

W_12	Bilge Width (m)	3.274	4.880	3.920
W_13	Propeller Diameter (m)	8.047	8.232	8.015
W_14	Propeller Expanded Area Ratio	0.426	0.419	0.550
W_15	Propeller Pitch over Diameter	1.090	0.977	1.075
W_16	Propeller Number of Blades	4	4	4
O_1a	Required Freight Rate (RFR) <i>NH3 Powered Vessel</i>	50.554	50.591	62.380
O_1b	Required Freight Rate <i>NH3 Powered Under TC</i>	31.000	30.627	37.846
O_1c	Required Freight Rate <i>VLSFO Variant (for reference)</i>	16.755	16.445	19.110
O_2	Required Time Charter Rate	94808	103442	103976
O_3	Maximum Ammonia Pricing (M.A.P)	221	230	229

O_4	Required Ballast Water Amount	42028	43014	33738
O_5a	EEOI <i>NH3 Powered</i>	0.288	0.272	0.355
O_5b	EEOI <i>VLSFO Equivalent</i>	3.732	3.864	4.682
-	SMCR	17339	18103	18335
-	Lightship Weight	27,096	26,833	23,826
-	EEDI <i>(as constraint)</i>	VLSFO: 2.372 NH3: 0.242	VLSFO: 2.184 NH3: 0.231	VLSFO: 2.603 NH3: 0.288

Table 81: Principal Particulars of Sim_WOZMAX_02 Dominant Variants (ZEVs)

- *Observed Length*

Similarly to the previous optimization runs Sim_WOZMAX_01 and Sim_WOZMAX_02, the best performers in terms of RFR have higher Lbp values but are closer to the middle of the variable range, with the shortest designs are the ones with the minimized Required Ballast Water amount. The isolation and decoupling of EEOI from the optimization objectives (since the current case study concerns vessels designed for NH3 fuel) lead to a relevant relaxation of the requirements for the length, so the optimized RFR and Ballast Water amount values were found more efficiently.

- *Observed Beam*

Interestingly and in contrast to the previous runs, the beam of dominant variants has been restrained below the 50-meter threshold, and lower than the results of the simulation-based optimization runs presented in Chapter 4.4. The reason for this is that the EEOI has been lifted as an optimization objective (depolarizing the Pareto frontier from “best performer” designs)

- *Observed Draft*

The tendency of increased scantling draft that was observed for the dominant variants of all previous Optimization Pathways (Deterministic and Simulation-Driven) is not so obvious for the results of Sim_WOZMAX_03. The scantling draft is again on the high end of the variable range

but at lower values when compared to the Sim_WOZMAX_01 & Sim_WOZMAX_02. Again, as in the case of Length the decoupling of EEOI from the optimization targets and thus relaxation on the requirement from common minimization of both RFR and EEOI, combined with the simulation-based calculations at actual operating speeds, leads to solutions that are Pareto optimal without the need of maximizing the scantling draft.

- *Observed Block Coefficient (Cb)*

Considering that Sim_WOZMAX_03 uses the same, updated added resistance methodology (for arbitrary waves directions and updated Cb correction) as in the Simulation-Based runs Sim_WOZMAX_01 & Sim_WOZMAX_02 the observed values of the block coefficient follow the same tendency with these runs. The reason for this is that, as previously explained, slender designs have considerably less added resistance in actual seaways, while the reduced payload is counterbalanced by the increased length and beam values. As a result again all Cb values are at the range of 0.73.

- *Observed Deck Height*

The Deck height of the dominant variants has been found, in contrast to the Deterministic and Simulation-Driven pathways, to be the middle (instead of upper) bound of the variable range with most dominant variants having a height between 26 and 27 meters. Since the deck height from one hand actively contributes in the increase of the lightship and thus building cost and thus initial CAPEX and consecutively RFR, and from the other the current case study concerns CAPEX intensive vessels (due to the increased CAPEX from NH3 application), the deck height of the dominant has been restrained in this case by the algorithm in order to prevent the overshoot of the CAPEX value resulting into RFR penalization with an adverse effect on the optimization effect. This correlation and behaviour highlights the robustness of RHODA and its effect on the optimization algorithm and result since the change in the methodology (required to facilitate the NH3 fuel technology and its effect on ship design) which lead to higher CAPEX drove the algorithm to find different variable combinations than before in order to achieve the optimization target.

- *Observed Cargo Hold Variables*

Cargo Hold variable values of dominant variables continue to have generally a greater scatter compared to main dimensions and hull variables with considerably smaller correlation (close to none) to RFR, EEDI and practically zero correlation with regards to Required Ballast Amount.

- *Observed Propeller Particulars*

For this optimization run, since itself is also part of the Simulation-Driven pathway runs, the same relationships and behaviour of propeller particulars as in Sim_WOZMAX_01 & Sim_WOZMAX_02 are observed. The only difference is that for subject application, dominant

variants are restricted to 4 blade applications instead of some 5 blade alternatives previously appeared.

The comparison of the principal particulars of dominant variants of Deterministic Pathways (Det_NMAX_02_ID2345 and Det_WOZMAX_02_ID2390) with simulation-based optimization runs can be found in Table 82.

No.	Particular	ID2390	ID760	ID1750
-	Run ID	Det_WOZMAX_02	Sim_WOZMAX_01	Sim_WOZMAX_03
W_01	Length between Perpendiculars	298.268	296.959	319.663
W_02	Beam	46.685	57.726	45.911
W_03	Draft	21.645	21.925	20.648
W_04	Deck height	28.394	28.389	26.716
W_05	Hopper Height	9.816	6.095	6.973
W_06	Hopper Breadth (m)	3.560	5.419	4.462
W_07	Topside Height (m)	6.287	11.857	6.009
W_08	Topside Breadth (m)	13.558	13.964	13.030
W_09	Block Coefficient C _b	0.851	0.731	0.736
W_10	LCB (%Lbp)	0.518	0.518	0.508
W_11	Bilge Height (m)	6.647	2.598	3.008
W_12	Bilge Width (m)	5.457	6.004	3.274
W_13	Propeller Diameter (m)	8.091	8.641	8.047
W_14	Propeller Expanded Area Ratio	0.604	0.506	0.426
W_15	Propeller Pitch over Diameter	1.076	0.912	1.090

W_16	Propeller Number of Blades	4	4	4
O_1_a	Deterministic Required Freight Rate (RFR)	6.726	11.543	12.728
O_1_b	Simulation-Based Required Freight Rate (RFR)	-	16.410	16.755
O_1_c	Zero Emission Vessel Required Freight Rate (RFR)	-	-	50.554
O_2_a	Deterministic EEDI	2.576	1.926	VLSFO: 2.372 NH3: 0.242
O_2_b	Simulation-Based EEOI	-	3.848	3.732
O_3	Required Ballast Water Amount	48871	49177	42028
-	SMCR	23843	18292	17339

Table 82: Comparison of Deterministic vs. Simulation-Driven and vs. Simulation Driven (NH3 powered) optimization run results.

6.6.5. Discussion of Results

In Table 83, the improvement of the key optimization targets for the dominant variants of the Simulation-Driven Pathway Run for the Zero Emission Vessel case study is depicted.

Design I.D	RFR improvement <i>NH3 Variant</i>	RFR improvement <i>VLSFO Variant</i>	EEOI Improvement <i>NH3 Variant</i>	Global CO2 Reduction	Required Ballast Amount Improvement	Required TCE Improvement
Baseline	-%		-%	-%	-%	-%
ID1750	-14.13%	-8.50%	-17.19%	-89.78%	-38.13%	-12.91%
ID1536	-14.07%	-10.19%	-14.28%	-89.38%	-36.68%	-4.98%
ID1520	+5.95%	+4.36%	4.03%	-88.93%	-50.33%	-4.49%

Table 83: Summary of Optimization Results on Optimization Targets for Dominant Variants // NH3 Powered Variants

The lifecycle CO2 emissions are reduced dramatically by design due to the Ammonia Powered concept, with 10% of residual emissions being accounted for by the pilot fuel used for the Main Engine and Diesel Generators as explained in Paragraph 4.5.

Best Performer Variants

The most efficient design appears to be Design ID1750, which features a reduction of RFR by 14.1% for the NH3 variant which corresponds to a reduction 8.50% for the VLSFO powered equivalent. In the meantime, the EEOI is further reduced when compared to the baseline by 17.19% contributing itself as well to the CO2 reduction. In the meantime, the Required TCE as defined in paragraph 4.5.1.1, is improved by 13% when compared to the baseline. A neighbouring design is also Design ID1536 which has the same level of RFR improvement for the NH3 powered variant, while the simulation-based RFR of the VLSFO variant is further reduced by 10% when compared to the baseline. The most interesting observation here however is that for both “best performers” there has been no penalization at all with regards to the Required Ballast Water amount. On the contrary, both designs feature an almost 40% reduction of the Ballast Water amount. The underlying reason for this is that the sorting and ranking algorithms detect and pick directly as dominant variant similar to designs incorporating “Best Trade-Offs” in Simulation Pathway Runs (Sim_WOZMAX_01& 02) as such designs combine a reduced CAPEX combined with size to allow economies of scale.

Least Ballast Water Amount Variants

The design with the greatest reduction of Required Ballast Water amount is ID1520. This design combines a reduction of Required Ballast Water amount of 50%, but the RFR and EEOI is worse than the Baseline by 5%. Interestingly however, the Required TCE is improved by 4.5%. The reason for this contradiction is the use of M.A.P (Maximum Ammonia Pricing) as an objective as well. For the MAP, the best designs are larger consumers for which carbon taxation is so big that can make them more attractive even at higher prices of Ammonia. This is the reason also for having a smaller TCE than the baseline.

Comparison with Deterministic Results

When comparing the results with the equivalent results of the baseline, it is interesting to see that, apart from the Global CO₂ reduction due to the use of Ammonia as a fuel, the level of reduction for RFR (either for NH₃ or VLSFO variants), EEOI and Required Ballast Water remains the same as the results of Sim_WOZMAX_01 & Sim_WOZMAX_02. This proves the wide applicability of the RHODA and the linearity of the latter since the Pareto frontiers as well as principal particulars of the dominant variants remain similar. It is therefore concluded that the optimization solution and pathway to optimal combinations of designs remain the same despite the model adaptations introduced in paragraph 4.5.1.1 showing on one hand robustness of the original RHODA solutions and the other the prevailing “mechanisms” in Preliminary Ship Design that transcend in some cases even fuel and powerplant options and continue dominate the design space.

From Table 81, the magnitude of the RFR values as well as that of the TCE appear considerable large, despite their improvement due to optimization studies. Such values can be even considered not sustainable in the modern shipping market. In view of this , Design ID1750 has been picked for a further sensitivity analysis post-optimization in the form of changing key design assumptions in the form of costs in order to illustrate ways of making the Shipping Decarbonization more economically sustainable.

When looking at the RFR and Required TCE values of all NH₃ powered generated designs as well as dominant variants it is evident that their economic performance is considerably burdened compared to their VLSFO equivalents. The reason for this is the 3-fold increase in Ammonia fuel mass consumption when compared to VLSFO due to the very low energy intensity of the first. In view of this the following post-optimization design queries are made for the selected dominant variant selected (ID1750) in order to assist the readers to comprehend the sensitivities and true cost of decarbonization along the shipping value chain.

What is the true cost of decarbonization?

	Baseline	Sim_WOZMAX_03_ID1750
Total Cost of Ownership <i>VLSFO Variant</i>	\$ 219,089,401	\$ 191,652,427
Total Cost of Ownership <i>NH3 Powered Variant</i>	\$ 647,468,102	\$ 527,808,087

Table 84: Comparison of discounted Total Cost of Ownership between Baseline and ID1750

In order to assess the cost of decarbonizing the supply chain that large bulk carriers are employed in, given that the optimization results are based on dynamic simulation of voyages over each vessel’s entire lifecycle and all key economic metrics are calculated, the analysis is reduced in comparing the Total Cost of Ownership (TCO) discounted to Net Present Value (NPV) between the NH3 powered vessel and its VLSFO counterpart that has been concurrently calculated in the simulation module. Indeed this has been done and presented in Table 84, where it is evident that the cost to decarbonize the Baseline vessel is an additional 428,378,701 USD to the discounted TCO, whereas the cost to decarbonize ID1750 is an additional 336,155,660 USD to the discounted TCO. It thus significant to mention at this point is that the application of the RHODA methodology lead to a reduction of 92,223,041 USD of decarbonization cost (21.5%) and an overall 18.48% reduction of the discounted TCO of the NH3 powered vessel.

What is the global effect of the attained CO2 reduction if applied to the entire population of large Bulk Carriers?

The CO2 emissions of the global commercial vessel fleet has been examined systematically in (Psaraftis & Kontovas, 2009). In this study, the annual CO2 emissions of the entire fleet of Dry Bulk Carriers corresponds to a total of 151.03 million tons of CO2, with large bulkers herein studied (above Panamax size) having a footprint of 36.27 million tons of CO2. If the EEOI reduction of 89.78% that was witnessed for Sim_WOZMAX_03_ID1750 is assumed as the basis, then the global effect of applying such designs across the supply chain would be the elimination of 32.56 million tons of CO2 per annum and 814.08 million tons of CO2 for a lifecycle of vessels (25 years). In order put this reduction into scale, in 2019 the annual emissions of the entire Scotland where 47.8 million tonnes of CO2e (Statista, 2022), the annual emissions of the entire United Kingdom 468 million tonnes (Statista, 2022), and for the entire world 36,700 million tons CO2e (Statista, 2022).

How improving the RFR by 1 USD/ton would change the Total Cost of Ownership (TCO)?

For Sim_WOZMAX_03_ID1750, the total Net Present Value (NPV) of the Total Cost Of Ownership as derived from the lifecycle simulation is 527,808,087 USD and a simulation-based RFR of 50.554 USD/ton. The VLSFO equivalent vessel of ID1750 in turn has a TCO NPV of 191,652,427 USD and a simulation-based RFR of 16.75 USD/ton (Table 85). The equivalent values for the Baseline Design are TCO NPV 647,468,102 USD and RFR 58.875 USD/ton for the NH3 powered and TCO NPV 219,089,401 USD and RFR 18.31 USD/ton for the VLSFO counterpart. So, it can be deduced that while “navigating” on the Pareto frontier of the NH3 powered designs, a difference/increment of 1 USD/ton RFR among dominant variants would translate to 14,380,485 USD discounted Total Cost of Ownership. Similarly, for a VLSFO powered vessel, an RFR difference of 1 USD/ton among design candidates would correspond to 17,587,573 USD discounted Total Cost of Ownership.

	Baseline	Sim_WOZMAX_03_ID1750
Required Freight Rate (USD/ton)	18.31	16.75
Total Cost of Ownership NPV	\$ 219,089,401	\$ 191,652,427
Required Freight Rate <i>NH3 Powered Variant</i> (USD/ton)	58.875	50.554
Total Cost of Ownership <i>NH3 Powered Variant</i> NPV	\$ 647,468,102	\$ 527,808,087

Table 85: RFR Sensitivity and Translation to Total Cost of Ownership

What would be the RFR of a Zero Emission Vessel if Ammonia pricing would be at a market of the minimum MAP observed (200 USD/ton). What would be for the case of 1800 USD/ton? What would it take to take Ammonia at a price of 200 USD/ton?

From Table 86 the reader can see the sensitivity of the ID1750 optimization merits and overall economic performance in changes in the Ammonia pricing. Using the probabilistic approach applied in optimization studies. for Ammonia pricing (see paragraph 4.5.1.1) the ID1750 has an RFR of 50.55 USD/ton and a Required TCE of 94,808 USD/day. With an Ammonia price of 200 USD/ton, the ID1750 would have an RFR of 17.39 USD/ton and a Required TCE of 42,764 USD/day. In the extreme case of 1800 USD/ton for Ammonia pricing, the cost overshoots to 68.73 USD/ton RFR and 123,349 USD/day TCE.

	NH3 Probabilistic Pricing	NH3 at 200 USD/ton	NH3 at 1800 USD/ton
Required Freight Rate (USD/ton)	50.55	17.39	68.73
Required TCE (USD/day)	94,808	42,764	123,349

Table 86: Effect of NH3 pricing on key economic metrics of Sim_WOZMAX_03_ID1750

From the above analysis it is evident that the importance of scaling “green” NH3 worldwide production and distribution to reduce the cost to a level of the MAP will make Zero Emission vessels sustainable. The matter of NH3 production scaling is preliminary discussed in the literature (Osman, et al., 2020).

What would be the necessary Carbon Tax Rate to Offset the additional NH3 costs?

Another interesting question that is very relevant currently is what would be the necessary carbon tax imposed that will offset the rise of the Total Cost of Ownership (TCO) both for the baseline and the selected dominant variant. This is a simple calculation of dividing the rise of the discounted TCO between the VLSFO and NH3 powered variants of each case (baseline and dominant) by the abated tons of CO2 respectively with the results being shown in Table 87.

	Sim_WOZMAX_03_ID1750
Delta Total Cost of Ownership (USD)* <i>*Increase of NH3 Compared to VSLFO Variant</i>	\$ 336,155,660
Abated Lifecycle CO2e Emissions (tons)	959,467
Required CO2e Tax (USD/ton)	350.35

Table 87: Required CO2e Tax to Offset the increase of TCO for NH3 Variant

When seeing the derived required CO2 tax to offset the TCO increase for NH3 powered variants, it is very interesting to compare it with the assumed CO2 tax probabilistic values assumed in the herein presented studies of 50 , 100 and 200 USD/ton scenarios respectively. In general it is a number higher than any assumption currently in the industry and can be used as a benchmark for carbon levy studies. An extensive discussion of the carbon taxation and market based measures can be found in the literature in (Psaraftis, et al., 2021), (Psaraftis, 2021).

What would be the effect on RFR by prolonging the vessel's age?

The next major design question is that of the Design Lifetime of the vessel. When looking at ships that are capital intensive (e.g LNG Carriers, Cruise and Passenger Ships etc) they typically have a (structural) design life of 40 years that in most cases coincides with the commercial life of the vessel. The reason for targeting such prolonged vessel lifetimes is to spread the capital expenditure over a longer period of time and in the meantime prolong the years of operation and thus income in order to lead to maximization of NPV. Due to the significant increase in the required additional CAPEX in order to invest in an NH3 powered vessel to achieve zero emissions, this is one of the sensitivities that need to be taken into account in order to prolong the vessel's lifetime as a technique for creating a more attractive RFR.

	ZEV Required Freight Rate (USD/ton)
Total Lifetime 25 years	50.554
Total Lifetime 40 years	34.69

Table 88: Effect of Vessel's Lifetime on Required Freight – Sim_WOZMAX_03_ID1750

What can be seen in Table 88 is the result of this sensitivity examination. For ID1750, the lifetime of the vessel (Economic Simulation Module input) was changed from 25 to 40 years. After repeating all calculations, the RFR for the NH3-powered ZEV has been shrunk considerably from 50.554 to 34.69 USD/ton corresponding to a 31.33% improvement,

What is the effect of the containment system capacity to the RFR? Examine the RFR change if the containment system was designed for a single leg of the Brazil trade route instead of roundtrip.

The biggest component of the additional CAPEX for an Ammonia Powered Zero Emission Vessel is the containment system used for the storage, namely the cryogenic tanks which for the herein presented case study is a single membrane type tank.

As described in paragraph 4.5.1.1, the methodology has modelled the unitized cost of the membrane tank (USD/m³ of tank) as a function of the tank capacity. Given the linearity and cost magnitude, an immediate design consideration (which the Author has encountered also in Commercial Ship Design and Building Case studies) would be how the Range Requirement would affect the CAPEX and thus the Required Freight Rate and if the total asset cost could be thus optimized. If a bunkering stop in Singapore is assumed, the simulation module has been recalculated using the half requirement for Range and thus resulting in a tank of 50% capacity.

	Capacity (m3)	ZEV Required Freight Rate (USD/ton)
Containment System Designed for Brazil→ China Roundtrip	15479	50.554
Containment System Designed for Brazil→ China Single Leg* <i>*Bunkering in Singapore</i>	7739	48.041
Containment System Designed for Brazil→ China Single Leg* and 40 years lifetime <i>*Bunkering in Singapore</i>	7739	32.98

Table 89: Effect of Containment System Capacity of RFR of Sim_WOZMAX_03_ID1750

The result of this re-assessment is depicted in Table 89 above, for which a further improvement of 4.9% is achieved with the tank reduction, making the point of cost optimization through capacity restriction valid and thus highlighting the necessity of scaling up the bunkering and infrastructure network for Zero Emission Fuels (in this case Ammonia). The reason the improvement is not higher is attributed to the economy of scale of membrane tanks for Shipbuilders with the unitized cost per cubic meter being shrunk by the increase of capacity.

Summarizing the above analysis, it is evident that the most profound RFR sensitivity is, as expected, that of the Fuel Price. However, given fuel pricing reductions highly depend on the scalability of the fuel production and procurement supply chain, Owners and designers the below two techniques to further improve the RFR by order of improvement magnitude:

1. Prolonging the Vessel’s Design and Commercial Life.
2. Reducing the containment system volume for NH3.

Chapter 7: Discussion, Results and Conclusion

7.1. General Remarks

In the present and last section an overview of the Research work undertaken is summarized and conclusions from the Original work are withdrawn.

In **Chapter 1**, the Author highlighted the major Contemporary and future Challenges of commercial shipping affecting Ship Design, Construction and Operation / Utilization as widely perceived by the academia and industry. The current and traditional Ship Design Practice has been examined and how the future of Ship Design will be able to cope with the functional, commercial and technical requirements that are created and continuously grow from the major challenge of decarbonization. Having this in mind, the main Rationale of the Thesis was produced having as an aim the systematic development and assessment of a Robust and Holistic Optimization Design Approach which is attained through a simulation-based parametric CAE environment. Based on this rationale a set of tangible Objectives has been deployed as a main Roadmap for the methodology creation. In order to meet the set Objectives the Strategy devised structured the Thesis under two phases of implementation: developing independent methodology component modules as products of empirical formulae, numerical methods or combinations and producing a finalized synthesis of such models. The second Phase is comprised by the application in multiple optimization studies the differentiation of each study highlights the introduced novelty compared to the previous.

In **Chapter 2**, following a comprehensive survey of the current literature and Research on the matter following a structured review under taxonomy, the predominant Research Gaps were identified in relation to Ship Design Optimization Studies.

The design, computational and mathematical modelling of the subject's Robust Holistic Optimization Design Approach (RHODA) was setup and described in **Chapter 3, 4 and 5**. The resulting methodology flowchart is shown in Figure 4 of Chapter 3 and is comprised of the below main modules :

- Geometrical Core
A fully parametric hull surface model is the basis under which all variants are generated.
- Hydrostatics & Lackenby transformation.
The module that does the necessary hydrostatic calculations of the first generated hull surface and uses the Lackenby transformation to attain the required C_b , Displacement and LCB.

- Cargo Hold Arrangement modelling
A part of the Geometric core that using the resulting hull surface as a template builds a fully parametric internal compartmentation structure for the cargo and ballast tanks areas respectively.
- Calm Water Resistance Module
Utilized the results of the Author re-calibration of Holtrop and Mennen Method using experimental data that are up to date from existing and widely acceptable commercial ship designs (Nikolopoulos & Boulougouris, 2019).
- Added Resistance in Seaways:
The module that estimates the additional resistance of a vessel in seaways uses the method of Fujiwara for the calculation of added resistance due to wind. For the added resistance in waves this method is the First Ship Design approach to utilize the new method of Liu for added resistance in arbitrary waves following benchmark with panel code runs.
- Fouling resistance.
The module that estimates the aging of the hull due to increase of the hull roughness from biological fouling and quantifies the impact on the resistance of the vessel.
- Self-propulsion equilibrium & Propeller matching.
The module solves the propulsor self-equilibrium thus matching the hull and propeller.
- Main Engine matching
This module features a novel, goal-based approach (instead of prescriptive) with which the entire Engine Room is dimensioned and its high-level operation parameters simulated (Level 2 approach).
- Lightship Weight, Stability and Loading conditions
The module uses established Ship Design methods with calibrated data to produce the basic Loading Conditions and performs the Trim and basic stability calculations.

In **Chapter 4**, all the known and adapted established methods for the above RHODA processes are described and viewed. In **Chapter 5**, the processes that have been derived from Original research work have been described in detail. Among them, an Enhanced Simulation Code has been developed tightly integrated within the methodology and the CAESSES design environment with the inherent ability to perform a robust and quasi-dynamic simulation of actual voyages explicitly defined, broken into voyage fragments (legs). The enhanced simulation code has unique modelling of weather conditions comprised of developed Probability Distribution Functions and spectral analysis based on a blend of Onboard acquired data, Satellite Weather Data matched by timestamp and coordinates as well as a Global Weather model (DNV, October 2010) as shown in the Figure 67.

The validity of the blend of computational methods and resulting Simulation Code has been benchmarked against actual voyage data and onboard measurements with very good results as described in paragraph 5.3.7. In this paragraph the novel simulation model of the RHODA studied herein has illustrated a very powerful capability for accurate power and speed production. Such powerful predictions and simulation tools haven't been previously deployed in Ship Design studies making this point a key novelty of the herein presented Research work.

In **Chapter 6**, the RHODA Methodology application has been deployed in a wide array of applications using as a Baseline the case of a Newcastlemax/VLOC Bulk Carrier. Firstly, the optimization problem is defined and its mathematic formulation is approached. Then two different Pathways of Optimization runs are set as a means to distinguish results using the same input variables.

The First pathway (deterministic) utilized known optimization principles known from previous research work on the herein presented environment but without any simulation and using a static and constant operating point for the vessel (assuming a constant speed at the Normal Continuous Rating – NCR). The rationale for running a deterministic pathway first is multi-fold:

- Explore the design space, assess the code efficiency and behaviour, adjust the optimization variables and after assessing the sensitivities quantify the boundaries of improvement.
- Assess the effectiveness and performance characteristics of various optimization algorithms (herein referred to as design engines) within the end-to-end optimization process.
- Provide a reference baseline for comparison with results where voyage simulation and uncertainties are enabled accordingly.

The Second pathway (simulation-based) therefore, using the experience gained from deterministic runs has used the NSGAI algorithm for deploying the full extent of the RHODA approach herein developed with a primary focus on simulation-based runs with different layers of uncertainty per run and examining the Simulation Effect on both the Optimization Discipline as well as the results of the optimization either in terms of improvement boundaries or resulting Ship Design characteristics. When comparing overall the results of RHODA with its deterministic counterpart, the most interesting observation is the deviation of the nominal RFR and EEDI from the baseline vessel. One of the most interesting aspects, is the effect of the use of voyage simulation in the improvement of EEOI (namely the vessel's environmental performance). The presented RHODA results and scatter diagram proves undoubtedly the profound unsuitability of EEDI as an efficiency metric in Ship Design Optimization Studies due to its inherent inability to capture the true efficiency of the vessel in actual operating conditions.

When examining on the other hand, the effect of simulation on RFR, there is a very big scatter for the values of simulation-based RFR. A small penalization in the simulation-based RFR is found to be a far greater penalization for the nominal RFR and thus creates barriers and bottlenecks in multi-objective optimization problems with antagonistic objective functions. In reality, the performance reduction of several dominant variants under real operating conditions (speed, weather) in the simulation module is considerably smaller than anticipated by a deterministic calculation on the NCR design point. This sensitivity highlights the Robustness component of the developed RHODA proving that only under the light of voyage simulation the true boundaries of the design space can be properly explored and hinder better design solutions/combinations.

This powerful capability of RHODA for enhanced optimization with robust results makes it an ideal tool in the Design and Optimization of Zero Emission Vessels (ZEVs). Due to the increased cost and low energy density of the majority of zero carbon or carbon neutral fuels (e.g Ammonia), the introduction of Voyage Simulation in the design process is imperative as the volatility and sensitivity of designs is greater. The applicability of RHODA was therefore proven with the deployment of the latter in the multi-objective optimization case study of an innovative Ammonia-Powered VLOC with membrane tank arrangement. The subsequent analysis and discuss of Optimization results revealed some considerable findings that should be considered in the future designs to match the decarbonization effort. The effect of optimization in the Total Cost of Ownership magnified by the increased cost of running with NH₃ is one of them as well as the profound effect of prolonging the vessel's commercial and technical lifetime which can in turn shrink the RFR.

In the below paragraph 7.2, some more focused Ship Design questions with regards to RHODA are discussed in order to further showcase its value, novelty and potential importance in Commercial Ship Design applications.

7.2. Ship Design Optimization Conclusions and Thesis Contribution

Having concluded with an overview of the novelties and contribution of the Thesis, in this paragraph follows a more Global review of the generalized conclusions on the position of the herein presented RHODA approach in Ship Design Optimization and its contribution.

7.2.1. What is the effect of Simulation-Based RHODA on the Optimization Process and Targets?

The biggest effect and differentiation of Simulation-Based to Deterministic Runs has been the largest exploration and utilization of the available design space. With the use of simulation, the search and variation process has been enhanced in such a way that bottlenecks and barriers by contradicting optimization targets are reduced or even eliminated. The best example in this respect is to look into the combined reduction of the RFR, EEOI and Required Ballast Water Amount for the simulation-based optimization variants (Table 73 in paragraph 6.4.5) where a synchronous improvement of RFR by 10%, of EEOI by 12% and of Required Ballast Water Amount by 40% was achieved a combination which was impossible in Deterministic Runs. In this respect the Robustness of the solutions is evident. Such an approach makes the RHODA an ideal candidate for the development of future Ship Designs compliant with Decarbonization visions.

7.2.2. What is the macroscopic effect of the optimization result?

The macroscopic effect of the optimization result is the effect on a Global Basis as it can be understood and received by a non-expert. Such an analysis has been made in paragraph 4.5.5 for the Simulation-Based optimization of Zero Emission Vessels to put the results of the optimization runs into the larger picture of Commercial Shipping. From this analysis, it can be observed that the RHODA method contributed to the reduction of the discounted Total Cost of Ownership (TCO) over the entire lifecycle of an NH₃-powered Large Bulk Carrier by 119,660,015 USD or 18.48%. On the other hand, it is estimated that a fleet-wide application of Zero Emission Vessels can contribute to an annual CO₂ reduction equivalent to the annual CO₂ emissions of Scotland.

7.2.3. What is the most effective use of IMO Efficiency Indices (EEDI, EEOI etc) in the optimization process?

Considering all the above results, the use of EEDI in optimization studies should be limited only to a design constraint rather than an optimization target. The use as a constraint reduces the number of successful designs significantly (all runs had an overall success rate of about 55%), however, it creates a big push (considering IMO Phase 3 EEDI reduction line) for the algorithm to explore areas of the design space with maximum overall efficiency. As the algorithm is pushed to minimum simulation-based EEOI designs the degree of uncertainty is reduced significantly, and the scatter between EEOI and EEDI is reduced to a linear area. This in turn translates into a greater degree of robustness of dominant variants.

7.2.4. How robust are the Designs generated from the optimization process?

A design could be characterized as Robust if it attains the same performance (and for optimization superior performance compared to its peers) over different operating and exogenous conditions affecting its voyage execution. A very good example of how Robust the RHODA are generated designs have been previously discussed in Paragraph 6.4.5 is Sim_WOZMAX_01_ID1066 and Sim_WOZMAX_01_ID760 and Figure 158. When moving from ID1066 to ID760 the simulation-based RFR is increased by roughly 0.7 USD/ton (from 15.72 USD/ton to 16.4 USD/ton) while at the same time the nominal RFR is increased by 1.5 USD/ton (from 10 USD/ton to 11.5 USD/ton). Figure 154 clearly shows this correlation from the tangent of the equivalent linear area of the scatter diagram between the two optimization targets. The practical meaning behind this is that in reality, the performance reduction of ID760 under real operating conditions (speed, weather) in the simulation module is considerably smaller than anticipated by a deterministic calculation on the NCR design point. Another interesting example is that of Sim_WOZMAX_02_ID1490. This design variant that features an improvement of 10.5% compared to the baseline in terms of simulation-based RFR, however the nominal RFR of the same design appears to be 6.8% worse than the baseline. Similarly, the Robustness in terms of EEDI and EEOI performance has been previously discussed with the case of Design ID1147 of Sim_WOZMAX_0 where an EEDI reduction of 16.1% is not matched by the EEOI (being 4.3% higher than the equivalent value of the baseline when performing the same voyages over time). On the other hand, ID1987 of Sim_WOZMAX_02 which is a design alternative that despite having an EEDI value that is 20.9% lower than the baseline has an actual performance and corresponding EEOI which is considerably worse (12% higher than the equivalent of the baseline).

7.2.5. Benefits from the use of actual operating data in the optimization process.

The use of actual operating data makes a realistic voyage simulation possible to be embedded within the Preliminary Ship Design and Optimization stage and highlights the actual design robustness over different operating speeds. Such an approach is missing from modern Ship Design and Construction and will be necessary to incorporate given the increased cost of Decarbonization as witnessed in paragraph 6.6.

7.2.6. Use in the Design Optimization of Zero Emission Vessels.

The powerful computational and simulation capability and its inherent robustness enabled RHODA to be an ideal candidate for use in the Design Optimization of Zero Emission Vessels since the cryogenic nature of many zero-carbon fuels require increased capital investment for integrating the corresponding containment and handling systems and thus any benefits from the sizing of these can be achieved from Voyage simulation.

7.3. Future Work and Reception by Industry Stakeholders

Future Work and further development of the herein presented RHODA approach can include but not be limited to:

- Incorporation and standardization of more fuel and propulsion plants (e.g methanol, hydrogen, nuclear etc) with the development of the corresponding code libraries in CAESES™ .
- Improvement of the methodology programming environment and further code enhancement to accelerate the code and results generation.
- Use for optimizing also local design problems instead of Global Optimization such as local hull form optimization and voyage execution (operating speed optimization).

The RHODA reception by Industry can potentially accelerate the evolution of current Ship Design practices to the needs of shipping for the next decades. The most affected users are Shipyards and Engineering offices. From the Author's activities in the Technical Management of Newbuilding construction vessels for commercial shipping, it is perceived that within 2030 RHODA methods will be incorporated into the design process. The role of consultants and Classification Societies is important to act as a catalyst and feedback to the Shipyards. From the Author's industrial experience such approaches begin to take shape if the form of Approvals In Principle (AiPs) and Joint Development Projects (JDPs) between Classification Societies, Shipyards and Shipowners.

Appendix I – List of Publications

The developed methodology within the Thesis for covering the requirements of the degree of Doctor of Philosophy (PhD) has also led to the publication of the following original research contributions:

1. *Application of Holistic Ship Optimization in Bulkcarrier Design and Operation*, Presentation in EUROGEN 2015 Conference as well as Chapter in Book: *Advances of Evolutionary and Deterministic Methods for Design, Optimization and Control in Engineering and Sciences*. (Nikolopoulos & Boulougouris, 2015)
2. *Applications of Holistic Ship Theory for the Simulation Driven Optimization of the Design and Operation of Large Bulk Carriers*, presentation at the Energy Efficient Ships 2016 Conference by the Royal Institution of Naval Architects. (Nikolopoulos, et al., 2016)
3. *A Study on the Statistical Calibration of the Holtrop and Mennen Approximate Power Prediction Method for Full Hull Form, Low Froude Number Vessels*, Peer Reviewed Paper in the Journal of Ship Production and Design of the Society of Naval Architects and Marine Engineers (SNAME) (Nikolopoulos & Boulougouris, 2019)
4. *Multi-Criteria decision-making methodology for the selection of cargo hold coatings for bulk carriers*, Peer Reviewed Paper in the Journal of Ships and Offshore Structures (Arabatzis, et al., 2019)
5. *A Methodology for the Holistic, Simulation Driven Ship Design Optimization under uncertainty*, Presentation at the 2018 International Marine Design Conference/IMDC2018 (Nikolopoulos & Boulougouris, 2018)
6. *A novel method for the Holistic, Simulation Driven Ship Design Optimization under uncertainty in the Big Data Era*, Peer Reviewed Paper in Ocean Engineering Journal
Peer Reviewed Paper in Ocean Engineering Journal
(Nikolopoulos & Boulougouris, 2020)
7. *A Robust Holistic Optimization Ship Design Approach using Simulation* , Peer Reviewed Paper in Ocean Engineering Journal.
Paper Under Submission
8. *Simulation Drive Robust Design Optimization of Zero Emission Vessels*
Paper Under Submission.

References

- (2016), “. m. f. t. s. p. o. a. c. s., 2016. Mao, W.; Rychlik, I.; Wallin, J.; Storhaug, G.;. *Journal of Ocean Engineering*, Volume 126.
- Abt, C., Brenner, M. & Harries, S., 2009. *Feature Modeling and Simulation-driven Design for Faster Processes and Greener Products*. Shanghai, China, Royal Institution of Naval Architects.
- Abt, C. & Harries, S., 2007. FRIENDSHIP-Framework – integrating ship-design modelling, simulation, and optimisation. *The Naval Architect*, January.
- Abt, C. & Harries, S., 2007. Hull Variation and Improvement using the Generalised Lackenby Method of the FRIENDSHIP-Framework. *The Naval Architect*, September.
- Abt, C., Harries, S., Heimann, J. & Winter, H., 2003. *From Redesign to Optimal Hull Lines by means of Parametric Modeling*. Hamburg, Germany, s.n.
- Adams, B. et al., 2009. “*Dakota, A Multilevel Parallel Object-Oriented Framework for Design Optimization, Parameter Estimation, Uncertainty Quantification, and Sensitivity Analysis: Version 5.1 User’s Manual*,” s.l.: Sandia Technical Report SAND2010-2185.
- Aldous, L., Smith, T., Buckhall, R. & Thompson, P., 2015. Uncertainty Analysis in ship performance monitoring. *Ocean Engineering*, Issue 110, pp. 29-38.
- Alizadeh, A., Strandenes, S. & Thanopoulou, H., 2016. Capacity retirement in the dry bulk market: A vessel based logit model. *Tranportation Reserach Part E: Logistics and Transportation Review*, Volume 92, pp. 28-42.
- Alwan, S., n.d. Simulation-based ship design and system engineering.
- Andrews, D., Kana, A., Hopman, J. & Romanoff, J., 2018. *State of the art report on design methodology*. International Marine Design Conference (IMDC) 2018, Helsinki, Finland, Francys Taylor Group.
- Andrews, D., Papanikolaou, A. & Singer, D., 2012. *DESIGN FOR X, State of The Art Report*. Glasgow, s.n.
- Ang, J., Jirafe, V., Goh, C. & Li, Y., 2018. *Smart design of hull forms through hybrid evolutionary algorithm and morphing approach*. International Marine Design Conference (IMDC) 2018, Helsinki, Finland, Taylor and Francis Group.
- Anon., 2017. <https://www.offshore-energy.biz/capesize-newbuild-handed-over-to-k-line/>. [Online] [Accessed 2017].
- Anon., 2017. *Offshore Energy*. [Online] Available at: <https://www.offshore-energy.biz/capesize-newbuild-handed-over-to-k-line/>

- Anon., 2017. *Offshore Energy*. [Online]
Available at: <https://www.offshore-energy.biz/capesize-newbuild-handed-over-to-k-line/>
- Anon., n.d. <https://www.offshore-energy.biz/capesize-newbuild-handed-over-to-k-line/>. [Online].
- Arabatzis, I. et al., 2019. Multi-Criteria decision-making methodology for the selection of cargo hold coating for bulk carriers. *Ships and Offshore Structures*, 14(6), pp. 609-630.
- Aristotle & Ross, W. D., 1981. *Aristotle's Metaphysics*. Oxford [England], : Clarendon Press.
- Bauk, S. & Ivosevic, S., 2010. Corrosion Wastage Modeling for Different locations of aged bulk carriers. *Journal of Maritime Research*, VII(I), pp. 27-40.
- Bekker, A., 2018. *Exploring the blue skies potential of digital twin technology for a polar supply and research vessel..* International Marine Design Conference (IMDC) 2018, Helsinki, Finland, Taylor Francis Group.
- Belanger, D., Furth, M., Jansen, K. & Reichard, L., 2018. *Towards the use of big data in smart ships*. International Marine Design Conference (IMDC) 2018 , Helsinki, Finland, Taylor and Francis Group.
- Bergstrom, M., Erikstad, S. & Ehlers, S., 2015. *Assessment of the effect of uncertainties in design parameters on the design of arctic ships*. Tokyo, Japan, s.n.
- Bernitsas, M., Ray, D. & Kinley, P., 1981. *KT, KQ and efficiency curves for the Wageningen B-series propellers*, Ann Arbor, Michigan: University of Michigan, Department of Naval Architecture and Marine Engineering.
- Birk, L. & Harries, S., 2000. *Automated Optimization – A Complementing Technique for the Hydrodynamic Design of Ships and Offshore Structures*. Potsdam, Berlin, Germany, s.n.
- Blenderman, W., 1993. *Schiffsform und Windlast-Korrelations-und Regressionanalyse von Windkanal-messungen am Modell*. Hamburg: Institut für Schiffbau der Universität Hamburg-Harburg.
- BMTI, 2020. https://www.bmti-report.com/baltic-capesize-index-bci/?fbclid=IwAR1gXyk98C73f4rKCzTVkCbEbECE5eyg78zSykpsMOTTt447c_AxZybc4M. [Online] [Accessed May 2020].
- Boese, P., 1970. *Eine einfache Methode zur Berechnung der Widerstandserhöhung eines Schiffes in Seegang*. Technical Report 258 ed. Hamburg: Institut für Schiffbau der Universität Hamburg.
- Bose, N. & Molloy, S., 2009. *Reliability and accuracy of ship powering performance extrapolation*. Trondheim, Norway, s.n.
- Bouhlef, M. & Martins, J., 2019. Gradient-enhanced kriging for high-dimensional problems. *Engineering with Computers*, 35(1).
- Brent, P. et al., 2006. *A methodology for the logistics-based ship design*. Ann-Arbor, Michigan, s.n.

- Britner-Gregersen, E. & Haver, S., 1991. *Joint Environmental Model for Reliability Calculations*. Edinburgh, United Kingdom, s.n.
- Campana, E. et al., n.d. A Multi-objective DIRECT algorithm for ship hull optimization.
- Campana, E., Stern, F. & Diez, M., 2015. *Hydrodynamic Ship Design Optimization considering Uncertainty*. Lecco, Italy, s.n.
- Chen, X. et al., 2015. High-fidelity global optimization of shape design by dimensionality reduction, meta-models and deterministic particle swarm. *Eng. Optim.* 2015, 47, p. 473–494..
- Cichowicz, J., Theotokatos, G. & Vassalos, D., 2015. Dynamic Energy Modelling for ship life-cycle performance assessment. *Journal of Ocean Engineering*, Volume 110.
- Cichowicz, J., Theotokatos, G. & Vassalos, D., n.d. Dynamic Energy Modelling for ship life-cycle performance assessment.
- Cinquegrana, D. & Iuliano, E., 2019. Efficient Global Optimization Method for Multipoint Airfoil Design. In: E. Minisci, et al. eds. *Advances in Evolutionary and Deterministic Methods for Design, Optimization and Control in Engineering Sciences*. s.l.:Springer International Publishing, pp. 95-117.
- Clarich, A. & Russo, R., 2019. Innovative Methodologies for Robust Design Optimization with a Large Number of uncertainties using ModeFrontier. In: E. Minisci, et al. eds. *Advances in Evolutionary and Deterministic Methods for Design, Optimization and Control in Engineering Sciences*. s.l.:Springer International Publishing , pp. 335-352.
- Clarksons Shipping Intelligence, 2015. *Clarksons Shipping Intelligence Database*. [Online] Available at: <https://sin.clarksons.net> [Accessed January 2016].
- Coatings, I. M., 2003. *Propeller*, January, Issue 15.
- Corrigan, P. et al., 2018. *System engineering based design for safety and total cost of ownership*. International Marine Design Conference (IMDC) 2018, Helsinki , Finland, Francis Taylor Group.
- Couser, P., Harries, S. & Tillig, F., n.d. Numerical Hull Series for Calm Water and Sea-Keeping.
- Darwin, C., 1859. *On the origin of species by means of natural selection, or the preservation of favored races in the struggle for life*. London: John Murray.
- Deb, K., Pratap, A., Agarwaj, S. & Meyarivan, T., 2002. A fast and elitist multiobjective genetic algorithm: NSGA-II. *IEEE Transaction on Evolutionary Computation* , 3(2).
- Demo, N. et al., 2018. *Shape optimization by means of proper orthogonal decomposition and dynamic mode decomposition*. NAV 2018, Trieste, Italy, s.n., p. 212–219.

- Di Pierro, F., Khu, S. & Savic, D., 2009. Many-Objective Evolutionary Optimisation. In: *Encyclopedia of Artificial Intelligence*. London: s.n., pp. 1042-1048.
- Diez, M. & Peri, D., 2010. Robust Optimization for ship conceptual design. *Ocean Engineering*, Issue 37, pp. 966-977.
- Diez, M. & Peri, D., 2010. *Two-stage Stochastic Programming Framework for Ship Design Optimization under Uncertainty*. s.l., s.n.
- Diez, M., Peri, D., Fasan, G. & Campana, E., 2010. *Multi-Disciplinary Robust Optimization for Ship Design*. Pasadena, California, s.n.
- DNVGL, 2019. *Maritime Forecast to 2050*, Oslo: DNVGL.
- DNV, October 2010. *Recommended Practice DNV-RP-C205 Environmental Conditions and Environmental Loads*, Oslo, Norway: Det Norske Veritas.
- Energy, O., 2017. <https://www.offshore-energy.biz/capesize-newbuild-handed-over-to-k-line/>. [Online] Available at: <https://www.offshore-energy.biz/capesize-newbuild-handed-over-to-k-line/>
- Energy, O., 2017. <https://www.offshore-energy.biz/capesize-newbuild-handed-over-to-k-line/>. [Online] Available at: <https://www.offshore-energy.biz/capesize-newbuild-handed-over-to-k-line/>
- Erikstad, S. & Rehn, C., 2015. *Handling Uncertainty in Marine Systems Design - State-of-the-Art and Need for Research*. Tokyo, Japan. , s.n.
- European Commission, 2021. *Regulation of the European Parliament and of the council on the use of renewable and low-carbon fuels in maritime transport amending Directive 2009/16/EC*, Brussels: European Commission.
- Evans, J., 1959. *Basic Design Concepts*.
- Faltinsen, O., Minsaas, K., Liapis, N. & Skjørdal, S., 1980. *Prediction of resistance and propulsion of a ship in a seaway*. Tokyo, s.n., pp. 505-529.
- Ferrante, M., Chalfant, J. & Chryssostomidis, C., n.d. Adding simulation capability to Early-Stage Ship Design.
- Fertecon, 2020. *Fertecon Price Methodology*, s.l.: IHS Markit.
- Flikkema, M., van Hees, M., Verwoest, T. & Bons, A., 2019. HOLISPEC/RCE: Virtual Vessel Simulations. In: A. Papanikolaou, ed. *A Holistic Approach to Ship Design, Volume 1: Optimization of Ship Design and Operation for Life Cycle*. Athens, Greece: Springer, pp. 465-485.
- Fujii, H. & Takahashi, T., 1975. *Experimental study on the resistance increase of a ship in regular oblique waves*. Ottawa, Canada, International Towing Tank Conference (ITTC).

- Fujiwara, T., Ueno, M. & Ikeda, Y., 2005. A New Estimation Method of Wind Forces and Moments acting on Ships on the basis of Physical Component Models. *The Japan Society of Naval Architects and Ocean Engineers*, Volume 2, pp. 243-255.
- Fusi, F., Congendo, P., Geraci, G. & Iaccarino, G., 2019. An Alternative Formulation for Design Under Uncertainty. In: E. Minisci, et al. eds. *Advances in Evolutionary and Deterministic Methods for Design, Optimization and Control in Engineering Sciences*. s.l.:Springer International Publishing, pp. 405-417.
- Garbatov, Y. & Guedes Soares, C., 2008. Corrosion wastage modeling of deteriorated bulk carrier decks. *International Shipbuilding Progress*, pp. 109-125.
- Garbatov, Y. & Guedes Soares, C., 2011. Corrosion Modeling in Marine Structures. In: C. Guedes Soares, ed. *Marine Technology and Engineering*. London: s.n., pp. 1121-1156.
- Gaspar, H., Ross, A., Rhodes, D. & Erikstad, S., 2012. *Handling Complexity Aspects in Conceptual Ship Design*. Glasgow, UK, s.n.
- Gerritsma, J. & Beukelman, W., 1972. Analysis of the Resistance Increase in Waves of a Fast Cargo-ship. *International Shipbuilding Progress*, Volume 18, p. 217.
- Good, N., 2006. *Multi-Objective Design Optimization considering Uncertainty in a Multi-Disciplinary Ship Synthesis Model*. Blacksburg, Virginia: s.n.
- Goodrum, C., Taylordean, S. & Singer, D., 2018. *Understanding initial design spaces in set-based design using networks and information theory*. International Marine Design Conference (IMDC) 2018, Helsinki, Finland, Taylor Francis Group.
- Grin, R., 2012. *On the prediction of wave added resistance*. Glasgow, UK, s.n.
- Guerrero, J., Cominetti, A., Pralits, J. & Villa, D., n.d. Surrogate Based Optimization using an open source framework: the bulbous bow shape optimization case.
- Guo, B. & Steen, S., 2011. Evaluation of added resistance of KVLCC2 in short waves. *Journal of Hydrodynamics*, 23(6), pp. 709-722.
- Guo, B., Steen, S. & Den, G., 2012. Seakeeping prediction of KVLCC2 in head waves with RANS. *Applied Ocean Research*, Volume 35, pp. 56-67.
- Hannapel, S., 2012. *Development of Multidisciplinary Design Optimization Algorithms for Ship Design under Uncertainty*. PhD Thesis, University of Michigan: s.n.
- Hannapel, S. & Vlahopoulos, N., 2010. *Robust and Reliable Multidiscipline Ship Design*. AIAA/SSMO Multidisciplinary Analysis Optimization Conference, Fort Worth, Texas, American Institute of Aeronautics and Astronautics.

- Harries, S., 1998. *Parametric Design and Hydrodynamic Optimization of Ship Hull Forms*. 1st ed. Berlin: Mensch-und-Buch-Verl..
- Harries, S., 2008. *Serious Play in Ship Design*. Berlin, s.n.
- Harries, S. & Abt, C., 1998. *Parametric Curve Design Applying Fairness Criteria*. Postdam/Berlin, Germany, Teubner Verlag.
- Harries, S. & Abt, C., 2019. CAESES- The HOLISHIP Platform for Process Integration and Design Optimization. In: A. Papanikolaou, ed. *A Holistic Approach to Ship Design, Volume 1: Optimization of Ship Design and Operation for Life Cycle*. Athens, Greece: Springer, pp. 246-293.
- Harries, S. et al., n.d. Software Platform for the Holistic Design and Optimisation of Ships.
- Harries, S. & Nowacki, H., 1999. *Form Parameter Approach to the Design of Fair Hull Shapes*. Cambridge, MA, MIT.
- Hassani, V., Rindaroy, M., Kyllingstad, L. & Nielsen, J., 2016. *Virtual Prototyping of Maritime Systems and Operations*. Busan, South Korea, ASME.
- Hiekata, K. et al., 2015. *A Ship Design Evaluation Method to Maximize Operational Value under Uncertainty*. Tokyo, Japan, s.n.
- Holtrop, J., 1984. A statistical re-analysis of resistance and propulsion. *International Shipbuilding Progress*, 31(363), pp. 272-276.
- Holtrop, J. & Mennen, G., 1982. An approximate power prediction method. *International Shipbuilding Progress*, 29(335), pp. 166-170.
- I.T.T.C, 2014. *Specialist Committee on CFD in Marine Hydrodynamics, Final Report and Recommendations to the 27th ITTC*, Copenhagen: ITTC.
- Ichinose, Y. & Tahara, Y., 2018. *Development of an automatic hull form generation method to design specific wake field..* International Marine Design Conference (IMDC) 2018, Helsinki, Finland, Taylor and Francis Group.
- IMO, 2017. *International Code of Safety for Ships using Gases or other Low-Flashpoint Fuels (IGF Code)*. s.l.:s.n.
- International Maritime Organization (IMO), 1966. *International Convention on Load Lines*. London: IMO.
- International Maritime Organization (IMO), 1966. *International Convention on Load Lines (ILCC)*. 2nd ed. London: IMO.
- International Maritime Organization (IMO), 2008. *Adoption of International Code on Intact Stability (2008 IS Code) , Resolution MSC.267(85).*, London: IMO.

- International Maritime Organization (IMO), 2009. *MEPC.1/Circ.684: Guidelines for voluntary use of the Ship Energy Efficiency Operational Indicator (EEOI)*, London: IMO.
- International Maritime Organization (IMO), 2011. *Resolution MEPC.203 (62): Amendments to the annex of the protocol of 1997 to amend the international convention for the prevention of pollution from ships, 1973, as modified by the protocol of 1978 relating thereto*, London: IMO.
- International Maritime Organization (IMO), 2013. *2013 Interim Guidelines for Determining Minimum Propulsion Power to Maintain the Maneuverability of Ships in Adverse Conditions*, London: IMO.
- International Maritime Organization (IMO), 2014. *Resolution MEPC.251(66): Amendments to MARPOL Annex VI and the new NOx Technical Code 2008*, London: IMO.
- International Maritime Organization (IMO), 2016. *IMO Train the Trainer Course on Energy Efficient Ship Operation - Module 2: Ship Energy Efficiency Regulations and Related Guidelines*. 1st ed. London: IMO.
- International Maritime Organization, 2018. *ADOPTION OF THE INITIAL IMO STRATEGY ON REDUCTION OF GHG EMISSIONS*, London, United Kingdom: IMO.
- International Organization for Standardization (ISO), 2016. *ISO19030-1:2016 - Ships and Marine Technology - Measurement of changes in hull and propeller performance - Part 1: General Principles*. 1st ed. Geneva: ISO.
- Isherwood, R., 1973. Wind Resistance of Merchant Ships. *RINA Supplementary Papers*, Volume 115, pp. 327-338.
- ISO15016:2015, 2015. *Ships and marine technology -- Guidelines for the assessment of speed and power performance by analysis of speed trial data*. s.l.:International Organization for Standardization.
- ITTC, 2014. *Speed and Power Trials, Part 2 Analysis of Speed/Power Trial Data*, s.l.: Specialist Committee on Performance of Ships in Service, 27th International Towing Tank Conference.
- Iuliano, E. & Quagliarella, D., 2019. Application of Surrogate-Based Optimization Techniques to Aerodynamic Design Cases. In: E. Minisci, et al. eds. *Advances in Evolutionary and Deterministic Methods for Design, Optimization and Control in Engineering Sciences*. s.l.:Springer International Publishing, pp. 65-95.
- Iwashita, H. & Ohkusu, M., 1992. The Green function method for ship motions at forward speed.. *Ship Technology Research*, 39(2), pp. 3-21.
- Jinkine, V. & Ferdinante, V., 1974. A method for predicting the added resistance of fast cargo ships in head waves. *International Shipbuilding Progress*, 238(21), pp. 149-167.
- Joosen, W., 1966. *Added Resistance in Waves*. Washington, 6th Symposium on Naval Hydrodynamics.

- Kalyanmoy, D. et al., 2015. *Optimal Ship Design and valuable knowledge discovery under uncertain conditions*. 2015 IRRR Congress on Evolutionary Computation (CEC), Sendai , Japan, s.n.
- Kashiwagi, M. 2., 2009. *Impact of hull design on added resistance in waves - application of the enhanced unified theory*. Trondheim, Norway, s.n.
- Killaars, T., van Bruinessen, T. & Hopman, J., 2015. *Network Science in Ship Design: Applying network science to control the interation between ship-elements in ship design*. Tokyo, s.n.
- Kim, K. & Kim, Y., n.d. Numerical Study on added resistance of ships by using a time-domain Rankine panel method.
- Kim, Y. et al., n.d. Prediction of Added Resistance in Waves using RANS based Analysis.
- Koepke, M. et al., 2014. *Holistic optimization of high efficiency and low emission containership*. Paris, France, s.n.
- Kostas, K., Ginnis, A., Politis, C. & Kaklis, P., 2015. *Ship-Hull Shape Optimization using BEM-Isogeometric Solvers*. Tokyo, Japan, s.n.
- Koutroukis, G., 2012. *Parametric Design and Multi-Objective Optimization study of an ellipsoidal containership*. Athens, Greece: National Technical University of Athens.
- Koutroukis, G. et al., 2013. Multi-Objective optimization of a containership design. *Mediterranean Marine Science*.
- Kwon, Y., 2008. Speed loss due to added resistance in wind and waves. *The Naval Architect*, Volume 3, pp. 14-16.
- Lackenby, H., 1950. On the systematic geometrical variation of ship forms. *Transactions of the RINA*, Volume 92, pp. 289-315.
- Lamb, T., 2003. *Ship Design and Construction*. 3rd ed. Jersey City , New Jersey: The Society of Naval Architects and Marine Engineers.
- Lammeren, W., van Manen, J. & Oosterveld, M., 1969. The Wagenigen B-screw series. *Trans. SNAME*, Volume 77, pp. 269-317.
- Lassahn, G., 1985. Uncertainty Definition. *Journal of Fluids Engineering*, 2(107).
- Le Nena, R., Guegan, A. & Rafine, B., 2019. Systemic Approach to Ship Design. In: A. Papanikolaou, ed. *A Holistic Approach to Ship Design, Volume 1: Optimization of Ship Design and Operation for Life Cycle*. Athens, Greece: Springer, pp. 123-138.
- LEAN MARINE, 2022. <https://yaramarine.com/vessel-optimization/fuelopt/>. [Online] Available at: <https://yaramarine.com/vessel-optimization/fuelopt/>

- Ley, J., Onorato, M., Oberhageman, J. & Moctar, O., n.d. Simulations of Ships in Severe and Extreme Sea Conditions,.
- Li, J., Bouhleb, M. & Martins, J., 2018. *A data-based approach for fast airfoil analysis and optimization*. 2018 AIAA/ASCE/AHS/ASC Structures, Structural Dynamics, and Materials Conference, Kissimmee, FL, USA, 8–12 January 2018., s.n.
- Liu, S. et al., 2020. Rational processing of monitored ship voyage data for improved operation. *Applied Ocean Research*, November. Volume 104.
- Liu, S. & Papanikolaou, A., 2015. Fast Approach to the estimation of the added resistance of ships in head waves. *Ocean Engineering*, Volume 112, pp. 211-225.
- Liu, S. & Papanikolaou, A., 2020. Regression analysis of experimental data for added resistance in waves of arbitrary heading and development of a semi-empirical formula. *Ocean Engineering*, Volume 206.
- Liu, S. & Papanikolaou, A., n.d. Added Resistance of Ships in Quartering Seas.
- Liu, S. & Papanikolaou, A., n.d. Time-domain hybrid method for simulating large amplitude motions of ships advancing in waves,.
- Liu, S., Papanikolaou, A. & Zaraphonitis, G., 2015. *Practical Approach to the Added Resistance of a Ship in Short Waves*. Hawaii, USA, International Society of Offshore and Polar Engineers (ISOPE).
- Liu, S., Papanikolaou, A. & Zaraphonitis, G., n.d. Practical Approach to the added resistance of a ship in short waves.
- Liu, S., Papanikolaou, A. & Zaraphonitis, G., n.d. Prediction of added resistance of ships in waves.
- Liu, S., Shang, B., Papanikolaou, A. & Bolbot, V., 2016. An Improved Formula for Estimating the Added Resistance of Ships in Engineering Applications.
- Löhrman, J. & Hochbaum, A., n.d. Simulation of Seakeeping Tests using OPENFOAM.
- Lorkowski, O. et al., 2018. *Application of a goal based approach for the optimization of contemporary ship designs*.. International Marine Design Conference (IMDC) 2018, Taylor Francis Group.
- Loshchilov, I., Schoenauer, M. & Sebag, M., 2010. Comparison-Based Optimizers Need Comparison- Based Surrogates. *Parallel Problem Solving from Nature XI (PPSN 2010)*, Sep 2010, Krakow, Poland..
- Lu, R. et al., 2015. A semi-empirical ship operational performance prediction model for voyage optimization towards energy efficient shipping. *Ocean Engineering*, Issue 110, pp. 18-28.

- MacCallum, K. & Duffy, A., 1989. Computer representation of numerical expertise for preliminary ship design. *Marine Technology*, 26(4), pp. 289-302.
- Maggioncalda, M. et al., 2019. Life Cycle Performance Assessment (LCPA) Tools. In: A. Papanikolaou, ed. *A Holistic Approach to Ship Design, Volume 1: Optimization of Ship Design and Operation for Life Cycle*. Athens, Greece: Springer, pp. 383-412.
- MAN B&W, 2022. *MAN B&W Ammonia Engine*. Melbourne Australia, Ammonia Energy Association.
- MAN, 2015. *Market Update Note (MUN) 2015-3 on Light Running Margin*, Copenhagen: MAN.
- MAN, 2017. *Marine Engine Program*, Copenhagen: MAN Energy Solutions.
- MAN, 2020. *MAN B&W G70ME-C9.5*, Copenhagen: MAN Energy Solutions.
- Mandel, P. & Leopold, R., 1966. Optimization methods applied to ship design. *Transactions SNAME*, Volume 74.
- Manderbacka, T. & Haranen, M., 2018. *Feedback to design power requirements from statistical methods applied to onboard measurements*. International Marine Design Conference (IMDC) 2018 , Helsinki, Finland, Taylor and Francis Group.
- Mao, W., Rychlik, I., Wallin, J. & Storhaug, G., 2016. Statistical models for the speed prediction of a container ship. *Journal of Ocean Engineering*, Volume 126.
- MARIN, 2010. *Holtrop-Mennen founders reveal the secret of method's long-lasting success*, Wagenigen: MARIN.
- Maruo, H., 1957. The Excess Resistance of a Ship in a Rough Seas, International Shipbuilding Progress 4(85). *International Shipbuilding Progress*, Volume 4, p. 85.
- Maruo, H., 1960. The drift of a body floating on waves. *Journal of Ship Research*, Volume 4, pp. 1-10.
- Maruo, H., 1963. Resistance in waves. *The Society of Naval Architects of Japan, 60th Anniversary Series*, Volume 8, pp. 67-102.
- Marzi, J., 2019. Introduction to the HOLISHIP Project. In: A. Papanikolaou, ed. *A Holistic Approach to Ship Design, Volume 1: Optimization of Ship Design and Operation for Life Cycle*. Athens, Greece: Springer, pp. 21-28.
- Marzi, J. et al., n.d. HOLISTIC ship design optimization.
- McKesson, C., 2014. *Introduction to Ship Design - Unpublished lecture notes*. New Orleans: University of New Orleans.

- Meyer, J., 2002. *A Risk-Based Approach to Optimal Margins in Ship Design*. Cambridge, MA: Massachusetts Institute of Technology, Diploma Theis.
- Murphy, R., Sabat, D. & Taylor, R., 1965. Least cost ship characteristics by computer techniques. *Journal of Maritime Technology*, Issue 2, p. 2.
- Nakamura, Y., 2015. *Possibility of Design Feedback by big data*. Tokyo, Japan, s.n.
- Nikolopoulos, L., 2012. *A Holistic Methodology for the Optimization of Tanker Design and Operation and its Applications*. Athens, Greece: National Technical University of Athens.
- Nikolopoulos, L. & Boulougouris, E., 2015. Application of Holistic Ship Optimization in Bulker Design and Operation. In: E. Minisci, et al. eds. *Advances in Evolutionary and Deterministic Methods for Design, Optimization and Control in Engineering Sciences*. s.l.:Springer International Publishing AG, pp. 229-255.
- Nikolopoulos, L. & Boulougouris, E., 2018. *A Methodology for the Holistic, Simulation Driven Ship Design Optimization under Uncertainty*. Espoo, Finland, International Marine Design Conference.
- Nikolopoulos, L. & Boulougouris, E., 2019. A Study on the Statistical Calibration of the Holtrop and Mennen Approximate Power Prediction Method for Full Hull Form, Low Froude Number Vessels. *Journal of Ship Production and Design*, Volume 35, pp. 41-68.
- Nikolopoulos, L. & Boulougouris, E., 2020. A novel method for the Holistic, Simulation Driven Ship Design Optimization under uncertainty in the Big Data Era. *Ocean Engineering*.
- Nikolopoulos, L., Boulougouris, E. & Khorasanchi, M., 2016. *Applications of Holistic Ship Theory for the Simulation Driven Optimization of the Design and Operation of Large Bulk Carriers*. London, Royal Institution of Naval Architects.
- Nikolopoulos, L. et al., 2014. *Holistic Approaches in Containership Design*. London, UK, Royal Institution of Naval Architects .
- Noor, A., 2005. Perspectives on nondeterministic approaches. In: E. Nikolaidis, M. Ghiocel & S. Singhal, eds. *Engineering design reliability handbook*. Boca Raton: CRC Press, pp. 2-19.
- Nowacki, H., 2019. On the History of Ship Design for Life Cycle. In: A. Papanikolaou, ed. *A Holistic Approach to Ship Design, Volume 1: Optimization of Ship Design and Operation for Life Cycle*. Athens, Greece: Springer, pp. 43-73.
- Nowacki, H., Brusis, F. & Swift, P., 1970. Tanker Preliminary design – an optimization problem with constraints.. *Transactions SNAME*, p. 78.
- Ohkusu, M., 1985. *Added resistance in waves of hull forms with blunt bow*. s.l., s.n., pp. 135-147.
- Oosterveld, M. & van Oossanen, P., 1975. Further computer-analyzed data for the Wagenigen B-screw series. *International Shipbuilding Progress*, Volume 22, pp. 251-262.

- Osman, O., Sgouridis, S. & Sleptchenko, S., 2020. Scaling the production of renewable ammonia: A techno-economic optimization applied in regions with high insolation. *Journal Of Cleaner Production*, October. Volume 271.
- Papanikolaou, A., 2009. *Risk-Based Ship Design*. Berlin: Springer-Verlag Berlin Heidelberg.
- Papanikolaou, A., 2010. Holistic ship design optimization. *Computer-Aided Design*, Issue 42, pp. 1028-1044.
- Papanikolaou, A., 2014. *Ship Design, Methodologies of Preliminary Design*. 1 ed. s.l.:Springer Netherlands.
- Papanikolaou, A., 2019. Holistic Ship Design Optimization. In: A. Papanikolaou, ed. *A Holistic Approach to Ship Design, Volume 1: Optimization of Ship Design and Operation for Life Cycle*. Athens, Greece: Springer, pp. 9-42.
- Papanikolaou, A., 2022. Holistic Approach to Ship Design. *Journal of Marine Science and Engineering*, Volume 10.
- Papanikolaou, A. et al., 2009. *State of the Art Report on Design for X*. Trondheim, s.n.
- Papanikolaou, A. & Daphnias, N., 1998. Re-optimisation of the hull form of a fast displacement catamaran ferry. *Ship Technology / Schiffstechnik*.
- Papanikolaou, A., Harries, S. & Hooijmans, P., 2020. A Holistic Approach to Ship Design: Tools and Applications. *Journal of Ship Research*.
- Papanikolaou, A., Harries, S., Wilken, M. & Zaraphonitis, G., 2011. *Integrated Ship Design and Multiobjective Optimization Approach to Ship Design*. Trieste, Italy, Royal Institution of Naval Architects.
- Papanikolaou, A., Kaklis, P., Koskinas, C. & Spanos, D., 1996. *Hydrodynamic Optimization of fast displacement catamarans*. Trondheim, Norway, s.n.
- Papanikolaou, A., Tuzcu, C., Tschlis, P. & Eliopoulou, E., 2007. *Risk-Based Optimization of Tanker Design*. s.l., s.n.
- Papanikolaou, A. et al., 2010. Multi-Objective Optimization of an AFRAMAX Oil Tanker Design. *Journal of Marine Science and Technology*, 15(4).
- Papanikolaou, A., Zaraphonitis, G., Skoupas, S. & Boulougouris, E., 2010b. An integrated Methodology for the design of Ro-Ro passenger ships. *Ship Technology / Schiffstechnik*, 57(1).
- Park, D., Kim, Y., Seo, M. & Lee, J., 2015. Study on added resistance of a tanker in head waves at different drafts. *Ocean Engineering*, Volume 111, pp. 569-581.
- Park, D., Lee, J. & Kim, Y., 2015. Uncertainty analysis of added resistance experiment of KVLCC2 ship. *Ocean Engineering*, Volume 95, pp. 143-156.

- Parker, M., Taylor, P. & Holth, K., 2019. *A Global Framework for responsible ship finance*, s.l.: Poseidon Principles.
- Parry, I., Heine, D., Kizzier, K. & Smith, T., 2018. *Carbon Taxation for International Marine Fuels: Assessing the options*, s.l.: International Monetary Fund (IMF).
- Perez Arribas, F., 2007. Some methods to obtain the added resistance of a ship advancing in waves. *Ocean Engineering*, Volume 34, pp. 946-955.
- Peric, R., n.d. Applications of Wave Generation inside solution domain of simulations based on Navier Stokes Equation.
- Peri, D. & Tinti, F., 2012. A multi-start gradient-based algorithm with surrogate model for global optimization. *Commun. Appl. Ind. Math.* 2012, 3, p. 1–22..
- Plessas, T. & Papanikolaou, A., 2015. *Stochastic life cycle ship design optimization*. VI International Conference on Computational Methods in Marine Engineering MARINE 2015, s.n.
- Plessas, T., Papanikolaou, A., Liu, S. & Adamopoulos, N., 2018. *Optimization of Ship Design for life cycle operation with Uncertainties*. International Marine Design Conference (IMDC) 2018, Helsinki, Finland, Taylor and Francis Group.
- Prebeg, P., Andric, J., Rudan, S. & Jamberic, L., 2018. *Multiobjective ship structural optimization using surrogate models of an oil tank crash worthiness*. International Marine Design Conference (IMDC) 2018, Helsinki, Finland, Taylor Francis Group.
- Priftis, A., Turan, O. & Boulougouris, E., 2018. *Parametric design and holistic optimization of post-panamax containerships*. International Marine Design Conference (IMDC) 2018, Helsinki, Finland, Taylor and Francis Group.
- Psaraftis, H., 2021. Shipping decarbonization in the aftermath of MEPC 76. *Cleaner Logistics and Supply Chain*.
- Psaraftis, H. N. & Kontovas, C. A., 2009. CO2 emission statistics for the world commercial fleet. *WMU Journal of Maritime Affairs*.
- Psaraftis, H., Zis, T. & Lagouvardou, S., 2021. A comparative evaluation of market based measures for shipping decarbonization. *Maritime Transport Research*.
- S&P Platts, 2022. <https://www.spglobal.com/commodityinsights/en/about-commodityinsights/media-center/press-releases/2022/042622-sp-global-commodity-insights-launches-platts-ammonia-forward-curve-assessments>. [Online].
- Sadat-Hosseini, H., Wu, P., Carrica, P. & Kim, H., 2013. CFD verification and validation of added resistance and motions of KVLCC2 with fixed and free surge in short and long head waves. *Ocean Engineering*, Volume 59, pp. 240-273.

- Salvesen, N., 1974. *Second-order steady state forces and moments on surface ships in oblique regular waves*. London, s.n., pp. 212-226.
- Sames, P. et al., 2011. *BEST Plus – Better Economics with Safer Tankers*. Houston Texas, Society of Naval Architects and Marine Engineers (SNAME).
- Sand, P., 2019. *Tanker Report*, s.l.: BIMCO.
- Sandvik, E., Asbjornlett, B., Steen, S. & Johnsen, T., 2018. *Estimation of fuel consumption using discrete-event simulation – a validation study*. International Marine Design Conference (IMDC) 2018, Helsinki, Finland, Taylor and Francis Group.
- Schmode, D., Bertram, V. & Tenzer, M., n.d. *Simulating Ship Motions and loads using OPENFOAM*.
- Sea Trials Analysis JIP, 2006. *Recommended Analysis of Speed Trials*, Wagenigen: MARIN.
- Sen, P. & Yang, J., 1998. *Multiple criteria decision support in engineering design*. London: Springer.
- Seo, M., Park, D., Yang, K. & Kim, Y., 2013. Comparative study on computation of ship added resistance in waves. *Ocean Engineering*, Volume 73, pp. 1-15.
- Shields, C., Brefort, D., Parker, M. & Singer, D., 2015. *Adaptation of Path Influence Methodology for Network Study of Iteration in Marine Design*. Tokyo, s.n.
- Shields, P., Rigterink, D. & Singer, D., n.d. Investigating physical solutions in the architectural design of distributed ship service systems.
- Singer, D., Doerry, N. & Buckley, M., 2009. What is Set-Based Design. *Naval Engineers Journal*.
- Smith, D., Veitch, B., Khan, F. & Taylor, R., 2018. *Using FRAM to evaluate ship designs and regulations*. International Marine Design Conference (IMDC) 2018, Helsinki, Finland, Taylor and Francis Group.
- Smith, T., 2019. *Definition of Zero Carbon Energy Sources*, s.l.: Getting to Zero 2030 Coalition.
- Smuts, H. J., 1927. *Holism and Evolution*. 1st ed. London: Macmillan And Company Limited.
- Sobol, I., 1976. Uniformly distributed sequences with an additional uniform property. *Zh.Vych. Mat. Mat.* , pp. 1332-1337.
- Söding, H. & Poulsen, I., 1974. Methods for programming for tasks in ship design. *Jahrbuch Schiffbautechnische Gesellschaft (STS)*, Volume 68.
- Söding, H. et al., n.d. Computing Added Resistance in Waves-Rankine Panel Method vs. RANSE Method.
- Soultanias, I., 2014. *Parametric Ship Design and Holistic Design Optimization of a 9000 TEU Container Carrier*. Athens, Greece: National Technical University of Athens.

Statista, 2022. *Statista*. [Online]

Available at: <https://www.statista.com/statistics/367892/greenhouse-gas-emissions-scotland-annually/>

Statista, 2022. *Statista*. [Online]

Available at: <https://www.statista.com/statistics/276629/global-co2-emissions/>

Statista, 2022. *Statista*. [Online]

Available at: <https://www.statista.com/statistics/486129/co2-emission-uk/>

Strom-Tejse, J., Yeh, H. & Moran, D., 1973. Added Resistance in Waves. *SNAME*, Volume 81.

Takahashi, T., 1988. A practical prediction method for added resistance of a ship in waves and the direction of its application to hull form design (in Japanese). *Transactions, West-Japan Society of Naval Architects*, pp. 75-95.

Tillig, F. & Ringsberg, J., 2018. A 4 DOF simulation model developed for fuel consumption prediction of ships at sea. *Ships and Offshore Structures*, December.

Tillig, F., Ringsberg, J., Mao, W. & Ramme, B., n.d. A generic energy systems model for efficient ship design and operation.

Townsin, 2003. International Marine Coatings. *Propeller*, August, Volume 16.

Townsin, 2003. International Marine Coatings. *Propeller*, August, Volume 15.

Townsin, R. & Kwon, Y., 1983. Approximate formulae for the speed loss due to added resistance in wind and waves. *Transactions, RINA*, Volume 125.

Tsitsilonis, K. & Theotokatos, G., 2018. A Novel Systematic Methodology for Ship Propulsion Engines Energy Management. *Journal of Cleaner Production*, Issue 204, pp. 212-236.

Tsitsilonis, K. & Theotokatos, G., 2018. A Novel Systematic Methodology for Ship Propulsion Engines Energy Management. *Journal of Cleaner Production*, August.

Ulungu, E., Teghem, J., Fortemps, P. & Tuytens, D., July 1999. MOSA method: a tool for solving multiobjective combinatorial optimization problems. *Journal of Multi-Criteria Decision Analysis*, 8(4).

Umetani, N. & Bickel, B. L., 2018. Learning Three-dimensional Flow for Interactive Aerodynamic Design.. *ACM Trans. Graph.*, 37(doi:10.1145/3197517.3201325.).

UNCTAD, 2017. *Review of Maritime Transport*, New York: United Nations.

United Nations, 1997. *UNFCCC (1997) Kyoto Protocol to the United Nations Framework Convention on Climate Change adopted at COP3*.. Kyoto, Japan, s.n.

United Nations, 2015. *C.N.63.2016.TREATIES-XXVII.7*. Paris, s.n.

- United States Coastguard, 2016. *Marine Safety Center Technical Note (MTN) No.,04-95, CH-2: Lightship Change Determination: Weight - MOment Calculations vs Deadweight Survey vs Full Stability Test*, US: USCG.
- Van Berlekom, W., Tragardh, P. & Dellhag, A., 1975. LARGE TANKERS-WIND COEFFICIENTS AND SPEED LOSS DUE TO WIND AND SEA. *Naval Architect*, January, pp. 41-58.
- Van Den Boom, H., Van Der Hout, I. & Flikkema, M., 2008. *Speed-Power Performance of Ships during Trials and in Service*. s.l., Society of Naval Architects and Marine Engineers (SNAME).
- Vasile, M., 2019. Polynomial Representation of Model Uncertainty in Dynamical Systems. In: E. Minisci, et al. eds. *Advances in Evolutionary and Deterministic Methods for Design, Optimization and Control in Engineering Sciences*. s.l.:Springer International Publishing, pp. 419-432.
- Vassalos, D., 2009. Risk Based Ship Design. In: A. Papanikolaou, ed. *Risk-based ship design: methods, tools and applications*. Berlin: Springer.
- Vettor, R. & Guedes Soares, C., 2016. Development of a ship weather routing system. *Journal of Ocean Engineering*, Volume 123.
- Yan, C. & Huang, F., n.d. An overview of simulation-based hydrodynamic design ship hull forms.
- Yondo, R., Bobrowski, K., Andres, E. & Valero, E., 2019. A Review of Surrogate Modeling Techniques for Aerodynamic Analysis and Optimization: Current Limitations and Future Challenges in Industry. In: E. Minisci, et al. eds. *Advances in Evolutionary and Deterministic Methods for Design, Optimization and Control in Engineering Sciences*. s.l.:Springer International Publishing, pp. 19-35.
- Yuan, H. & Singer, D., 2018. *Performance Analysis through fuzzy logic in set-based design*. International Marine Design Conference (IMDC) 2018, Helsinki, Finland, Taylor Francis Group.
- Zaraphonitis, G., Boulougouris, E. & Papanikolaou, A., 2013. *Multi-objective optimization of cruise ships considering the SOLAS 2009 and GOALDS damage stability formulations*. Shanghai, China, s.n.
- Zaraphonitis, G., Kanellopoulou, A., Papanikolaou, A. & Shigunov, V., 2016. *Ship optimization for efficiency and maneuverability in adverse sea conditions*. Hamburg, Germany, 6th International Maritime Conference on Design for safety.
- Zaraphonitis, G. & Papanikolaou, A., 1993. Second-order Theory and Calculations of Motions and Loads of Arbitrarily Shaped 3D Bodies in Waves. *Marine Structures*, pp. 165-185.
- Zaraphonitis, G. et al., 2019. Parametric Optimisation in Concept and Pre-contract Ship Design Stage. In: A. Papanikolaou, ed. *A Holistic Approach to Ship Design, Volume 1: Optimization of Ship Design and Operation for Life Cycle*. Athens, Greece: Springer, pp. 209-245.

Zaraphonitis, G., Skoupas, S., Papanikolaou, A. & Cardinale, M., 2012. *Multi-objective optimization of watertight subdivision of ROPAX ships considering the SOLAS 2009 and GOALDS factor formulations*. Athens, Greece, s.n.

Zou, L. & Larsson, L., n.d. A Verification and Validation Study Based on Resistance Submissions to the Gothenburg 2010 Workshop on Numerical Ship Hydrodynamics.